



THE UNIVERSITY OF
SYDNEY

COPYRIGHT AND USE OF THIS THESIS

This thesis must be used in accordance with the provisions of the Copyright Act 1968.

Reproduction of material protected by copyright may be an infringement of copyright and copyright owners may be entitled to take legal action against persons who infringe their copyright.

Section 51 (2) of the Copyright Act permits an authorized officer of a university library or archives to provide a copy (by communication or otherwise) of an unpublished thesis kept in the library or archives, to a person who satisfies the authorized officer that he or she requires the reproduction for the purposes of research or study.

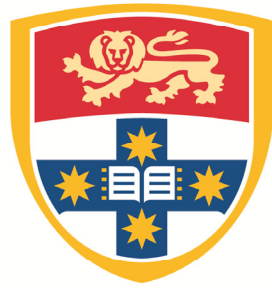
The Copyright Act grants the creator of a work a number of moral rights, specifically the right of attribution, the right against false attribution and the right of integrity.

You may infringe the author's moral rights if you:

- fail to acknowledge the author of this thesis if you quote sections from the work
- attribute this thesis to another author
- subject this thesis to derogatory treatment which may prejudice the author's reputation

For further information contact the University's Director of Copyright Services

sydney.edu.au/copyright



THE UNIVERSITY OF
SYDNEY

**BEHAVIOUR OF SANDY SOIL SUBJECTED TO
DYNAMIC LOADING**

YAHYA NAZHAT

BSc., MSc.

A thesis submitted in fulfilment of the requirements for the
degree of Doctor of Philosophy

Faculty of Engineering & Information Technologies

School of Civil Engineering

University of Sydney

2013

COPYRIGHT AND USE OF THIS THESIS

This thesis must be used in accordance with the provisions of the Copyright Act 1968.

Reproduction of material protected by copyright may be an infringement of copyright and copyright owners may be entitled to take legal action against persons who infringe their copyright.

Section 51 (2) of the Copyright Act permits an authorized officer of a university library or archives to provide a copy (by communication or otherwise) of an unpublished thesis kept in the library or archives, to a person who satisfies the authorized officer that he or she requires the reproduction for the purposes of research or study.

The Copyright Act grants the creator of a work a number of moral rights, specifically the right of attribution, the right against false attribution and the right of integrity.

You may infringe the author's moral rights if you:

- fail to acknowledge the author of this thesis if you quote sections from the work
- attribute this thesis to another author
- subject this thesis to derogatory treatment which may prejudice the author's reputation

For further information contact the University's Director of Copyright Services

sydney.edu.au/copyright

SYNOPSIS

This thesis presents the kinematics occurring during lab-based dynamic compaction tests using high speed photography and image correlation techniques. High speed photography and X-ray microtomography have been used to analyse the behaviour of sandy soil subjected to dynamic impact. In particular, the densification mechanism of granular soils due to dynamic compaction is the main theme of the thesis.

Image correlation and X-ray scans revealed the formation, rate and growth of narrow tabular bands of intense deformation and significant volumetric change and provided answers towards a better understanding of the densification mechanism in dry granular soils due to dynamic compaction. As a quantitative tool, high speed photography has allowed the propagation of localised deformation and strain fields to be identified and has suggested that compaction shock bands control the kinematics of dynamic compaction. The displacement and strain results from high speed photography showed that soil deformation in the dynamic tests was dominated by a general bearing capacity mechanism similar to that widely stated in classic soil mechanics texts.

Simulations of the physical models were carried out using LS-DYNA finite element formulations for comparison and verification purposes. The FE simulations verified the general characteristics from the photography findings. However, simulation results were unable to predict the exact details of the strain localisation due to surface impacts during physical model tests.

PREFACE

The work described in this thesis was carried out during the period 2009-2012 in the School of Civil Engineering at the University of Sydney. The candidate was supervised by Professor David Airey.

The By-Laws of the University of Sydney require that the original sections of a thesis submitted for the degree of Doctor of Philosophy be indicated. In accordance with the By-Laws, information obtained from other sources has been appropriately acknowledged and referenced in the text. The author claims originality for the following work:

In Chapters 3 and 4: the design and development of the test apparatus for both the PIV tests including the 1-g scale models and the computerised tomography technique, sample preparation techniques for sand-silt soil and instrumentation installation.

In Chapters 5 and 6: The densification mechanism reported by the photography, X-Ray computerised tomography and instrumentation results. Interpretation of the experimental data of both homogenous sand and sand-silt soil models that are not explicitly acknowledged.

In Chapter 7: the numerical analyses conducted for the simulation of the physical models; and the identification of the principles of verification. The candidate used the powerful structure of the existing finite element code of LS-DYNA as the basis for his programming. However, the scheme of validating the photography strain localisation by finite element programme is claimed to be original.

The following papers were published by the author in conjunction with others during the course of the PhD candidature. These are submitted in support of this thesis, they are:

1. Airey, D, **Nazhat, Y**, Moyle, R & Avalle, D 2012, 'Dynamic compaction-insights from laboratory tests', *International Conference on Ground Improvement and Ground Control (ICGI 2012)*, 30 Oct. – 2 Nov., Wollongong, Australia.
2. **Nazhat, Y** & Airey, D 2012, 'The effect of different tamper geometries on the dynamic compaction of sandy soils', *International Symposium on Ground Improvement, ISSMGE - TC 211*, IS-GI Brussels, Belgium, 31 May - 1 June.
3. **Nazhat, Y** & Airey, D 2011, 'Applications of high speed photography and X-ray computerised tomography (Micro CT) in dynamic compaction tests', *International Symposium on Deformation Characteristics of Geomaterials*, Seoul, Korea, September 1-3, pp. 421-427.
4. **Nazhat, Y** & Airey, D 2011, 'validation of high speed photography and PIV in large strain measurements of granular materials', *9th International Symposium on Particle Image Velocimetry – PIV11*, Kobe University, Japan, July 21-23.
5. Chow, SH, **Nazhat, Y** & Airey, DW 2010, 'Applications of high speed photography in dynamic tests', *7th International Conference on Physical Modelling in Geotechnics (ICPMG 2010)*, 28 June - 1 July, Zurich, Switzerland, pp. 313-318.

ACKNOWLEDGEMENTS

Throughout this research work, numerous people have provided support and encouragement. I would like to extend my sincere thanks to my supervisor Professor David Airey for his enthusiasm, insights, and continuous support throughout this work over the last four years. Likewise, I appreciate the interest and insights of my co-supervisor Professor Itai Einav.

I am indebted to many people for their interest and assistance during the course of this work. I have very much valued my time in the School of Civil Engineering; I have learned a great deal and made some lifelong friends. In this regard, I would like to thank various members of the staff, in particular Professor Robert Herbertson, Associate Professor Peter Ansourian, Associate Professor Abbas El-Zein, Dr. Gwénaëlle Proust; special thanks to Dr. Steve Cochard for his valuable comments and advices on high speed photography and image analysis. In the process of performing the numerical analyses for this research, several people shared their knowledge and offered advice. I would like to thank Dr. Nigel Balaam and Dr. Luming Shen. To my postgraduate colleagues Dr. Arghya Das, Dr. Faham Tahmasebinia, Dr. Oded Ben-Nun, Dr. Shiao Huey Chow, Mr. Benjamin Marks, Mr. Thomas Miller, Mr Youventharan Duraisamy and Mr. Fahim Tonmoy; It has been a pleasure to work with them.

My graduate work would not have been possible without the generous financial support of the Australian Postgraduate Award, the Australian Research Council, and the Civil Engineering Foundation.

Special thanks to Mr. Dennis Dwarte (Senior Microscopist) of the Australian Centre for Microscopy and Microanalysis at the University of Sydney for his kind help and assistance in performing the X-ray microtomography CT scans.

To Mr. Ross Baker and Sergio De Carvalho, the School Technical Officers, I wish to express my deep gratitude and sincere thanks for, generous assistance, and continuous help during my entire period of candidature.

Yahya Nazhat

NOTATIONS

All notation and symbols are defined where they first appear in the text. For convenience, the most frequently used notations and their meanings are given here. Some symbols may have a different definition in different chapters. In these cases, the chapter numbers relevant to the definition are given in brackets preceding the definitions.

English Letters

a	acceleration
A	area
ALE	Arbitrary Lagrangian - Eulerian
B	foundation width
CID	isotropically consolidated drained
CT	computerised tomography
CPT	cone penetration test
d_{50}	Particle-size diameter corresponding to 50% finer
D	drop
D[3]	Diameter
DC	dynamic compaction
DIC	digital image correlation
D_{max}	maximum depth of improvement
DMT	flat plate dilatometer
D_r	relative density
DSM	dynamic settlement modulus
e	void ratio
E [7]	total energy
E, E_{max}	Young's modulus, maximum Young's modulus
EPC	earth pressure cell
Eq	equation
F[4]	filtered image
F[6]	net impact force

FE	finite element
fps	frames per second
g	earth gravitational force
G, G _{max}	shear modulus, maximum shear modulus.
GVS	global volumetric strain
H	height
IFFT	inverse discrete Fourier transform
IS	induced shifting
K	bulk modulus
K _{un}	unloading bulk modulus
k _{dy}	peak dynamic stiffness
k _o	coefficient of lateral earth pressure at rest
k _s	spring constant
LAG	Lagrangian
m	mass
MIS	maximum impact stress
n	porosity
N	number of drops
NC	net contraction
NCV	net contracted volume
NF	non filtered image
N _e	number of elements
N _p	number of patches
n _s	attenuation coefficient
N _γ	bearing capacity factor
P	impact pressure
p'	effective mean stress
PI	plasticity index
PIS	pre-impact surface
PIV	particle image velocimetry
PMT	pressuremeter test
q	deviator stress
q _c	cone resistance

q_u	ultimate bearing capacity
r	radial coordinate from the centre of impact
SD	standard deviation
SPH	smoothed particle hydrodynamic
SPT	standard penetration test
t	time
T	kinetic energy
$U_{\text{dissipation}}$	dissipated energy
v	impact velocity
V	volume
V_e	volume of soil represented by a single strain element
V_m	volume of soil covered by GeoPIV mesh
V_p	compression wave velocity
V_s	shear wave velocity
VS_e	GeoPIV element's volumetric strain
V_R	Rayleigh wave velocity
W	pounder mass
z	vertical coordinates from the centre of the impact

Greek Letters

α [2.1.1]	attenuation coefficient (damping)
α [2.3.1]	density ratio
ε_v	volumetric strain
ϵ	pounder relative displacement: pounder penetration/pounder width
δ	angle of interface friction
ϕ	friction angle
$\Delta\phi$	change in friction angle
ν	Poisson's ratio
ρ	mass density of the soil
ρ_{max}	maximum possible soil density
γ	unit weight of soil
σ_a	axial stress
σ_c	confining stress
σ_e	elastic limit vertical stress
u_s	contact deflection on the soil,
\dot{u}_s	contact velocity

LIST OF TABLES

<u>Table no.</u>	<u>Title</u>	<u>page</u>
Table 2.1.	Dynamic compaction terminology	23
Table 2.2.	Suitability of soil for dynamic compaction (Lukas, 1986).	25
Table 2.3.	Suggested value of empirical coefficient “n” (Yee, 1999).	29
Table 3.1.	List of instrumentation specifications	89
Table 3.2.	List of dynamic compaction tests	92
Table 3.3.	List of Static Load tests	100
Table 3.4.	Maximum dry densities and optimum moisture contents of sand:silt	104
Table 4.1.	Correlation of GeoPIV precision verses patch size	121
Table 5.1.	Coordinates and accumulated volumetric strain at locations shown in Figure 5.30	159
Table 5.2.	GeoPIV strain analysis of first impact during test DC24	163
Table 6.1.	Ranges of P-wave and S-wave velocities measured during DC tests	214
Table 7.1.	LS-DYNA possible Geomaterial models	239
Table 7.2.	Selected consistent system of units for LS-DYNA inputs and results	239
Table 7.3.	List of soil parameters required for LS-DYNA material 014 input card	240
Table 7.4.	Parameters used to define the soil materials using MAT_014 formulation	245
Table 7.5.	List of LS-DYNA models	248
Table 7.6.	List of LS-DYNA sensitivity analysis models	252
Table 7.7.	Pounder penetrations by LS-DYNA simulations and physical models.	266
Table 7.8.	Impact velocities from two types of measurements	270
Table A3.1.	Object space coordinates of 101 stationary calibration dots	A-22
Table A3.2.	Control markers object space coordinates with reference to the 101 calibration dots (Figure A3.1. & Table A3.1.)	A-23
Table A3.3.	Control markers object space coordinates with reference to the coordinates of the top let corner control marker	A-24
Table A5.1.	Details of triaxial tests.	A-36

LIST OF FIGURES

<u>Figure no.</u>	<u>Figure Title</u>	<u>page</u>
Figure 1.1.	Dynamic compaction equipment- crane and tamper (courtesy of Keller Australia).	3
Figure 1.2.	Dynamic compaction using 23 tonne and 30 tonne pounders at Port Ras Laffan, Qatar (courtesy of Menard).	4
Figure 2.1.	One dimensional compaction model (Scott and Pearce, 1975)	13
Figure 2.2.	Axial deformation of confined compactable loose granular soil	14
Figure 2.3.	Densification mechanism of saturated deposits (Menard and Broise, 1975)	15
Figure 2.4.	Schematic diagram of wave propagation due to surface impact (Graff, 1975)	16
Figure 2.5.	Dynamic compaction energy partitioning components (Shenthan <i>et al.</i> , 2004).	17
Figure 2.6.	Modulus variations with strain level	18
Figure 2.7.	Grouping of soils for dynamic compaction (Lukas, 1986).	26
Figure 2.8.	Suitability of different ground stabilisation methods verses grading range of problem soils (Mitchell <i>et al.</i> , 1998).	26
Figure 2.9.	Descriptive pattern of soil improvement by DC (Lukas, 1986).	27
Figure 2.10.	Typical energy-depth of influence chart for DC (Slocombe, 1993).	31
Figure 2.11.	Comparison of various prediction models - depth of influence (Berry <i>et al.</i> , 2000).	31
Figure 2.12.	Lateral ground movement at 3 m and 6 m from impact point (Lukas, 1995)	32
Figure 2.13.	Predicted residual horizontal stresses after compaction (Ferreira, 1983).	32
Figure 2.14.	Lateral stresses measured in sand foundation at the Jackson Lake dam site in Wyoming, USA, (left) before and (right) after dynamic compaction. (Handy, 2011)	33
Figure 2.15.	CPT test results from before and after dynamic compaction at Pointe Noire deep sea harbour (Dumas and Beaton, 1988).	35
Figure 2.16.	1-D theoretical model of dry soil deformation due to surface impact (Smits and De Quelerij, 1989)	38

Figure 2.17.	The one-dimensional wave equation model (Chow <i>et al.</i> , 1992a).	39
Figure 2.18.	A semi-prolate-spheroid approximation for DC density contours (Poran <i>et al.</i> , 1992).	44
Figure 2.19.	Dynamic compaction model by centrifuge test (Oshima <i>et al.</i> , 1997).	45
Figure 2.20.	Definition of compacted area and comparison of compacted areas under different ram weights (Oshima <i>et al.</i> , 1997).	47
Figure 2.21.	Image of Ottawa sand in contact with the steel plate (Guler <i>et al.</i> , 1999).	52
Figure 2.22.	Displacement vectors from image analysis (Guler <i>et al.</i> , 1999).	53
Figure 2.23.	Schematic diagram showing set up for slicing transparent synthetic soils (Sadek <i>et al.</i> , 2003).	54
Figure 2.24.	Example of the image from a plane strain foundation test (White <i>et al.</i> , 2005).	55
Figure 2.25.	Shear band patterns from plane strain bearing capacity by (a) experiment and (b) by numerical simulation (Tatsuoka <i>et al.</i> , 1994 and 1997).	55
Figure 2.26.	Vertical displacement increments (a); horizontal displacement increments (b); maximum shear strain (c); and volumetric strain increments (d) in reinforced dense sand (Michalowski and Shi, 2003).	56
Figure 2.27.	Evolution of the volume strain ε_v and deviatoric strain ε_p in a funnel flow silo after 1, 3, 5 and 7 sec of flow for initially dense sand and very rough walls (Slominski <i>et al.</i> , 2007).	57
Figure 2.28.	Volumetric (a) and shear (b) strains revealed by digital image correlation (DIC) technique (Hall <i>et al.</i> , 2010).	58
Figure 2.29.	PIV image analysis technique (White <i>et al.</i> , 2001a).	60
Figure 2.30.	Typical digital image of the strip footing model and sand displacement fields by ACC algorithm (Liu and Iskander, 2004).	61
Figure 2.31.	X-ray image analysis of bio-cemented Ottawa sand specimens: (a) porosity; (b) shear strain by DIC; (c) cement density (Tagliaferri <i>et al.</i> , 2011).	63
Figure 2.32.	Deformation and vertical (Z) stresses in Lagrangian model by LS-DYNA (a) 250 mm of penetration and, (b) 420 mm of penetration (Bojanowski and Kulak, 2010).	67
Figure 2.33.	A 2-D mesh for a dynamic compaction test, and the contours of typical displacement due to monotonic loading (Parvizi and Sharif, 2011).	68

Figure 3.1.	Schematic diagram of the small size model type 1 (a), and a snapshot shows the lighting and cameras set up in front of the test model (b).	76
Figure 3.2.	Control markers positioned on the front window between the Perspex sheets.	77
Figure 3.3.	Set up of the small sized model, Type 2.	78
Figure 3.4.	The soil container of small model Type 2 rotated through 90o to the horizontal with its backside removed and top of the container plugged to facilitate sample preparation.	78
Figure 3.5.	The large size model soil container full of sand to a height of 1.0m.	79
Figure 3.6.	Configuration of flat and non-flat based pounders.	79
Figure 3.7.	Microscopic images of Sydney sand and Feldspar non-plastic silt	80
Figure 3.8.	Natural colours and texture of Sydney sand, feldspar silt and 2sand:1silt mixture.	80
Figure 3.9.	Grading curves of Sydney sand, Feldspar silt and 2sand:1silt mixture	81
Figure 3.10.	Set up of sand raining apparatus above the large model.	83
Figure 3.11.	Texture of sand grains in a sand B/W image (a), relative size of the embossing powder marker particles (b), texture by black marker on the front of a 2sand:1silt model (c) and the texture by the markers in a 2sand:1silt B/W image (d).	85
Figure 3.12.	Captured field of view (1024 x 1024 pixel) by the high speed camera on the windows of the small and large DC models.	86
Figure 3.13.	Schematic diagram shows locations of CPT tests within the DC model viewed from above.	87
Figure 3.14.	Schematic diagram shows distribution of instrumentation within the DC model.	88
Figure 3.15.	Images of accelerometer types 3022 and 3038 and EPC type PS-C.	88
Figure 3.16.	Schematic diagram shows the EPC calibration chamber.	90
Figure 3.17.	Extracted sand-resin lumps prior to trimming.	94
Figure 3.18.	Preparing the extracted sand-resin lump by a cutting wheel equipped with a diamond blade.	95
Figure 3.19.	CT scan trimmed ready sand-resin specimens	95
Figure 3.20.	A ready sand-resin specimen in the Skyscan1172 Micro CT scanner.	96
Figure 3.21.	Bender elements affixed to triaxial pedestal and specimen cap.	96

Figure 3.22.	Set up of triaxial test apparatus with wave velocity measurement.	97
Figure 3.23.	Set up of oedometer experiment for k_0 measurement.	99
Figure 3.24.	Set up of the oedometer cell with the caps used to seal the ring during calibration.	99
Figure 3.25.	Set up of steady rate static load test experiment	101
Figure 3.26.	Set up of pseudo-static load test experiment	102
Figure 3.27.	Dry densities verses moisture contents from modified and standard proctor compaction tests of sand:silt mixture.	103
Figure 4.1.	Flowchart of the GeoPIV analysis procedure (White and Take, 2002).	107
Figure 4.2.	Illustration of camera calibration Concept (Zhao et al., 2007).	110
Figure 4.3.	Simulation of barrel distortion (a), pincushion distortion (b) and moustache distortion (c) in photography (http://en.wikipedia.org/wiki/Distortion (optics)).	113
Figure 4.4.	Black dot patterns as calibration sheets for the control markers (indicated by red arrows).	114
Figure 4.5.	Frequency of pixel-level intensities of filtered and non-filtered images.	116
Figure 4.6.	Raw and Matlab processed images.	117
Figure 4.7.	Variation in grayscale intensities of 24 random stationary images.	118
Figure 4.8.	Artificially induced encoded displacements.	119
Figure 4.9.	GeoPIV precision verses patch size (Artificially shifted raw images).	120
Figure 4.10.	Displacement fields from non-filtered (raw) and filtered images.	122
Figure 4.11.	Cumulative displacement vectors at end of drop1 from high speed photographs (a) and displacement vectors at end of drop1 from still camera before and after impact (b).	123
Figure 4.12.	Illustration of the overlapped field of view merged by the high speed camera and digital still camera fields of view.	124
Figure 4.13.	Comparison of displacement profiles from GeoPIV patches.	125
Figure 4.14.	History of lateral displacements at 2 locations around the impact centreline from GeoPIV patches at different elevations.	126
Figure 4.15.	History of vertical displacements along the impact centreline from GeoPIV patches at different elevations.	127

Figure 5.1.	Stress-Displacement responses of steady rate static tests in loose (a) and dense (b) sands.	131
Figure 5.2.	Figure 5.2. Cumulative displacement vectors at (a) 7mm and (b) 51mm displacements (end of static test ST-R3)	134
Figure 5.3.	Displacement trajectories of soil elements tracked through a steady rate static test	134
Figure 5.4.	The evolution of total shear strain caused by (a) 13mm, (b) 33mm and (c) 51mm footing displacements during static test ST-R3	136
Figure 5.5.	Total volumetric strain at the end of test ST-R3	137
Figure 5.6.	Total shear strain (a) and total volumetric strain (b) at the end of test ST-R4	137
Figure 5.7.	Illustration of soil displacement tracked by GeoPIV patch (Extracted from Figure 5.2b)	138
Figure 5.8.	Load-displacement curve for 25mm and 35mm pads during ST-P1 and ST-P4 tests.	139
Figure 5.9.	Cumulative displacement vectors (magnified 4 times) at the end of 150N (a) and 550N (b) static load applications (Test: ST-P4)	141
Figure 5.10.	Evolution of total shear strain due to 150N, 350N, 450N and 550N during ST-P4	142
Figure 5.11.	Comparison of total shear strain at 70kPa stress level during ST-P4 (a) and ST-R3 (b) static tests.	142
Figure 5.12.	Evolution of shear strain subsequent to load increase from 150N to 250N during ST-P4.	143
Figure 5.13.	Schematic diagrams of general bearing capacity and shear strain localisation in pseudo-static mechanisms.	144
Figure 5.14.	Cumulative displacement vectors at end of drop1 of tests DC11 (57mm poulder, Dr: 25%) and DC4L (57 mm poulder, Dr: 29%).	146
Figure 5.15.	Effect of imparting energy level on poulder penetration and soil heave.	146
Figure 5.16.	Effect of energy levels on poulder penetrations.	147
Figure 5.17.	Incremental displacement vectors at four different times following the impact of drop no.1 (Test DC11).	148

Figure 5.18.	Cumulative shear strain at 0.008, 0.010, 0.015 and 0.025 sec during drop no.1 of Test DC11 (compare with incremental displacement shown Figure 5.17).	149
Figure 5.19.	Cumulative volumetric strains at 0.01 and 0.025 sec during drop no.1 (Test DC11).	150
Figure 5.20.	Cumulative shear (a) and volumetric strains (b) and end of drop 1 during DC11.	151
Figure 5.21.	Cumulative shear strain after 2 (a) and 4 (b) drops (Test DC11-sand)	152
Figure 5.22.	Cumulative shear strains after 1, 3, 6 and 12 drops (Test DC1L)	153
Figure 5.23.	Cumulative volumetric strains after 6 and 12 drops during test DC1L (DC1L: sand of Dr 8%, 35mm poulder and 49.4N.m/drop).	154
Figure 5.24.	Cumulative volumetric strains after 6 and 12 drops during test DC6L (DC6L: sand of Dr 30%, 105mm poulder and 82N.m/drop).	154
Figure 5.25.	Cumulative shear strains after 1 and 3 drops (Test DC20)	155
Figure 5.26.	Cumulative shear strains after 1 and 3 drops (Test DC22)	155
Figure 5.27.	Cumulative shear strains after 0.008 and 0.01 seconds from drop 1 (Test DC12).	156
Figure 5.28.	Cumulative shear strain after 2 (a) and 4 (b) drops (Test DC36-sand:silt)	157
Figure 5.29.	Fluctuation of volumetric strain along the centreline of impact at times 0.005sec, 0.020 sec and end of drop 1 (Test DC30).	159
Figure 5.30.	Cumulative volumetric strain after 1, 6 and 12 drops with zoomed in windows that illustrate the fluctuation of strain at 5 selected locations (Test DC24).	160
Figure 5.31.	GeoPIV pre-impact patches for DC primary zone of influence calculations.	161
Figure 5.32.	Variation of the net contracted volume parameter over the 12 impacts of DC24.	164
Figure 5.33.	CPT soil resistance along the centreline of impact from before and after 8 drops of test DC3 with GeoPIV shear and volumetric strain.	166
Figure 5.34.	CPT soil resistance at 115mm off the impact centreline from before and after 8 drops of test DC3 with GeoPIV shear and volumetric strain.	167
Figure 5.35.	Bands of localised shear stain following the 1 st drop during test DC2.	168
Figure 5.36.	Bands of localised volumetric following 1st and 4th drops during test DC2.	169

Figure 5.37.	Schematic diagram demonstrates the sliced X-Ray images by NRecon software and the 3D volumetric reconstruction by CTAn software of a scanned sand-resin sample.	170
Figure 5.38.	Correlation between sand porosity and CTScan mean greyscale index (Loose sand).	171
Figure 5.39.	Correlation between sand porosity and CTScan mean greyscale index (Dense sand).	171
Figure 5.40.	Sensitivity of greyscale thresholds and estimated sand porosity (Loose reference sample - void ratio, $e=0.668$ - porosity, $n=0.40$).	173
Figure 5.41.	Sensitivity of greyscale thresholds and estimated sand porosity (Dense reference sample - void ratio, $e=0.58$ - porosity, $n=0.367$).	173
Figure 5.42.	Change of sand porosity as estimated from the Micro-CTScan images at the location of a predetermined strain localisation at the end of Drop No. 1 during DC16.	174
Figure 5.43.	Characteristic features of DC selected measurements	175
Figure 5.44.	Calculation example of global volumetric strain	176
Figure 5.45.	Calculation example of percentage of net contraction (NC) within the Z4 region.	176
Figure 5.46.	Cumulative displacement vectors (magnified x 2 for clarity) after 6 impacts – sand models (1000 pixels = 400mm).	178
Figure 5.47.	Cumulative displacement vectors (magnified x 2 for clarity) after 6 impacts – Sand- Silt mixture models (1000 pixels = 400mm).	179
Figure 5.48.	Total Shear Strain (a), and total volumetric strain (b) at end of 6 impacts on dry sand models using four types of tampers	180
Figure 5.49.	Total Shear Strain (a), and total volumetric strain (b) at end of 6 impacts on sand-silt models using four types of tampers	181
Figure 5.50.	Incremental shear strains and history of total shear strain over the course of 6 impacts on a sand model using tamper type A (test DC30).	182
Figure 5.51.	History of total shear strain over the course of six impacts on a sand-silt model using tamper type A (test DC36).	182
Figure 5.52.	Variation of the NCV parameter over the course of 6 impacts on sand models using four types of tampers.	183
Figure 5.53.	NCV ratios (NCV of drop “n” /NCV of drop “n” by tamper type A) from DC tests on sand models.	184

Figure 5.54.	Variation of the NCV parameter over the course of 6 impacts on sand-silt models using four types of tampers.	185
Figure 5.55.	NCV ratios (NCV of drop “n” /NCV of drop “n” by tamper type A) from DC tests on sand-silt models.	185
Figure 5.56.	Variation in volumetric strain intensities - arranged from smallest to largest NCV (a) and DC measured characteristic features - arranged from smallest to largest Z3 (b).	186
Figure 5.57.	Variation in global volumetric strain with respect to tamper geometries (a) and correlation between the global volumetric strains (GVS) and adjudicator net contraction (NC) and (NCV) parameters within the region of Z4 (b.)	187
Figure 5.58.	Correlations between tamper geometries, key DC aspect ratios and intensities of net contracted volume (NCV) in sand and sand-silt models.	189
Figure 5.59.	History of accumulated total shear strain over the course of 12 drops due to three levels of imparting energy on three loose sand models (Dr: 13-17%).	191
Figure 5.60.	Variation in the NCV parameter by three energy levels over the course of 12 drops (sand models of void ratio 0.76-0.77) with their linear correlations.	192
Figure 5.61.	Variation in the NCV parameter by three energy levels over the course of 12 drops (sand models of void ratio 0.76-0.77) with their logarithmic correlations.	192
Figure 5.62.	Effect of the imparting energy on the NCV parameter over the course of 5 drops (sand models of void ratio 0.71-0.77) with their logarithmic correlations.	193
Figure 5.63.	Normalised NCV (NCV of drop “n” / NCV of drop 1) from three DC tests in sand models employing three energy levels.	194
Figure 5.64.	History of accumulated volumetric strain over the course of 6 drops due to two levels of imparting energy on sand-silt models (Dr: 55-57%).	195
Figure 5.65.	Variation in the NCV parameter by two energy levels over the course of 6 drops (sand-silt models of void ratio 0.65-0.66) with their logarithmic correlations.	196
Figure 5.66.	Normalised NCV (NCV of drop “n” /NCV of drop 1) from two DC tests in sand-silt models employing two energy levels.	196
Figure 5.67.	DC tests with 180mm (DC38) and 85mm (DC39) of sand overlaid sand-silt soil.	197

Figure 5.68.	Variation in the NCV parameter by same energy input over the course of 5 drops (sand-silt models overlaid by sand) with their logarithmic correlations.	198
Figure 5.69.	Separation of NCV values among the sand (A) and sand-silt (B) portions along the Z4 regain shown by Figure 5.67.	198
Figure 5.70.	Separation of normalised NCV ratios among the sand (A) and sand-silt (B) portions along the Z4 regain shown by Figure 5.67.	199
Figure 6.1.	Time history of two embedded accelerometers signals (a) and time shift by IFFT cross-correlation (b).	205
Figure 6.2.	Correlation between measured poulder penetration by poulder acceleration, and poulder penetration tracked by GeoPIV.	207
Figure 6.3.	Correlation between measured soil displacements from integrated accelerations and tracked GeoPIV patches.	207
Figure 6.4.	Peak soil accelerations at 150mm (a) and 250mm (b) below point of impact over 12 drops on loose sand models.	209
Figure 6.5.	Peak soil accelerations at 150mm (a) and 250mm (b) below point of impact over 12 drops on dense sand models.	210
Figure 6.6.	Variation in shock passing velocities in dense sand models.	210
Figure 6.7.	Variation in shock passing velocities in dense (a) and loose (b) sand models.	211
Figure 6.8.	Soil accelerations at 150 and 250mm depths during drop no. 1 on loose sand model (a) and dense sand model (b) employing the same energy level.	212
Figure 6.9.	Soil accelerations at 150 and 250mm depths during drop no. 2 on loose sand model (a) and dense sand model (b) employing the same energy level.	213
Figure 6.10.	Variation of Rayleigh wave, P-wave, and S-wave velocities with Poisson's ratio (after Richart <i>et al.</i> , 1970).	214
Figure 6.11.	Trends of compaction band velocities by GeoPIV	215
Figure 6.12.	Variation in DSM values for three DC tests employing three energy levels on loose sand models (Dr: 13-17%).	218
Figure 6.13.	Variation in maximum impact stress for tests on loose sand models using 35mm poulder falling from 100 and 200mm heights.	219

Figure 6.14.	Correlation of accumulated NCV with DSM (a), peak dynamic stiffness (b) and MIS (c) from DC tests on loose sand models using 35mm pounder.	221
Figure 6.15.	Pounder work verses NCV values of individual impacts (a) and correlation between accumulated NCV and accumulated pounder work from DC tests on loose sand models using 35mm pounder with 17.4N.m/drop (b), 11.6N.m/drop (c) and 5.8N.m (d)over the course of 12 impacts.	222
Figure 6.16.	Accumulated pounder work over the course of 12 drops from both small size models (DC27 and DC30) and large size models (DC1L, DC2L, DC5L and DC6L).	222
Figure 6.17.	Variation in impact stresses with number of drops for two energy levels calculated from pounder post impact decelerations (a) and measured by pounder EPC (b).	224
Figure 6.18.	Correlations between maximum impact stresses (MIS) calculated from pounder post impact decelerations and impact stresses measured by pounder EPC form DC tests by two energy levels.	225
Figure 6.19.	Contact stress against rigid pounder penetrating sand.	225
Figure 6.20.	Effect of the non-flat disturbed soil surface on the contact stress against rigid pounder penetrating sand.	226
Figure 6.21.	EPC soil stresses from dynamic compaction during DC11 and DC12 tests – (for clarity, results from the first and second drops are shown separately). The range of impact stresses from the pounder accelerations are enclosed by dashed lines.	227
Figure 6.22.	Typical time domain of pounder acceleration and its integrated velocity and displacement – drop 1 test DC1.	228
Figure 6.23.	Typical after impact pounder deceleration and displacement verses pounder penetration velocity (drop 1 test DC1).	229
Figure 6.24.	Typical time domain signals of the dynamic soil acceleration (drop 1 of DC2 - Dr: 95%).	230
Figure 6.25.	Typical time domain signals of soil dynamic pressure measured by earth pressure cells during drop 1 of DC11.	231
Figure 6.26.	Records of after impacts pounder accelerations (decelerations).	232
Figure 6.27.	Pounder displacements (by double integration of pounder accelerations).	233
Figure 6.28.	Examples of pounder net impact force history (a), pounder net impact force vs. displacement (b) and history of work done by the pounder (c).	234

Figure 6.29.	Pounder impact stresses verses pounder relative displacements (strain) from two different setups (pounder widths, energy levels and model sizes).	235
Figure 7.1.	Schematic of geomaterial general compression response	241
Figure 7.2.	Triaxial and uniaxial compression response (strain dependency) of sand	244
Figure 7.3.	Uniaxial compression response (strain dependency) of sand:silt mixture	244
Figure 7.4.	LS-DYNA two parts, two sections and two materials model	246
Figure 7.5.	History of pounder displacements from the model M3 generated by three different mesh sizes.	250
Figure 7.6.	History of soil body internal energies from the model M3 generated by three different mesh sizes.	250
Figure 7.7.	History of maximum shear stress in soil elements immediately beneath the impacting contact from the model M3 generated by three different mesh sizes.	251
Figure 7.8.	Effect of the soil model parameters on predicted pounder penetration	252
Figure 7.9.	Effect of soil strength (a), stiffness (b), density (c) and stress-strain responses on predicted pounder penetration.	254
Figure 7.10.	History of Soil body internal energies from four different soil model parameters.	254
Figure 7.11.	Total internal and hourglassing energies from M1 models.	256
Figure 7.12.	Pounder displacements from M1A-LAG (Lagrangian) and M1A-ALE models.	257
Figure 7.13.	Maximum shear stress in soil elements immediately beneath the impacting contact from M1A-LAG (Lagrangian) and M1A-ALE models.	257
Figure 7.14.	Progressing displacements (a, b and c) and end displacement vectors at 100 milliseconds (d) for model M1-SA3 (DC11).	261
Figure 7.15.	Progressing displacements (a, b and c) and end displacement vectors at 100 milliseconds (d) for model M3-SA3 (DC30).	262
Figure 7.16.	Progressing displacements (a, b and c) and end displacement vectors at 100 milliseconds (d) for model M4-SSL2 (DC36).	262
Figure 7.17.	Progressing displacements (a, b and c) and end displacement vectors at 100 milliseconds (d) for model M5-SA3 (DC6L).	263

Figure 7.18.	History of poulder displacement and surface soil heave from model M1-SA3.	263
Figure 7.19.	Displacement vectors by GeoPIV and LS-DYNA simulation (at 50 milliseconds) for model M1-SA3 (DC-11) - displacement vector scale x 1.0.	264
Figure 7.20.	Response of sand:silt mixture during drop 1 captured by the high speed photography (a) and by LS-DYNA simulations (b, c and d) for DC36.	264
Figure 7.21.	Displacement at time 300 milliseconds from simulations M3-SA3 (a) and M4-SSL2 (b).	265
Figure 7.22.	Total soil body internal energy and Rayleigh damping dissipated energy during simulations M1-SA3 (a) and M5-SA3 (b).	265
Figure 7.23.	Measured (GeoPIV) and predicted (LS-DYNA) poulder penetrations (results are only for simulations of the small size DC models using sand).	266
Figure 7.24.	Soil accelerations measured during DC11 and simulated by model M1-SA3.	268
Figure 7.25.	Lateral stress at 150mm depth at the wall of the DC container simulated by model M1-SA3 (DC11), (-ve is for stress in compression).	268
Figure 7.26.	Contours of maximum shear strain during M3-SA3 simulation (DC30).	271
Figure 7.27.	Contours of maximum shear strain after 49.998 milliseconds from impact during M3-SA3 simulation (DC30).	271
Figure 7.28.	Contours of maximum shear strain during M5-SA3 simulation (DC6L).	272
Figure 7.29.	Soil accelerations at 150 and 250 mm depths by M3-SA3 -DC30.	272
Figure 7.30.	Soil accelerations at 150 and 250 mm depths by M5-SA3-DC6L	273
Figure 7.31.	Velocities of propagated shear strain bands tracked from LS-DYNA simulations (note: mm/ms = m/sec).	273
Figure A2.1.	Calibration of EPC- PS-2KC- Rated capacity 200 kPa – Loose Sand	A-12
Figure A2.2.	Calibration of EPC- PS-5KC- Rated capacity 500 kPa – Dense Sand	A-12
Figure A2.3.	Calibration of EPC- PS-5KC- Rated capacity 500 kPa – Loose Sand	A-13
Figure A2.4.	Calibration of EPC- PS-5KC- Rated capacity 500 kPa – 2Sand:1Silt	A-13
Figure A2.5.	Calibration of EPC- PS-10KC- Rated capacity 1000 kPa – Loose Sand	A-14
Figure A2.6.	Calibration of load cell – Steady rate static test	A-15

Figure A2.7.	Calibration of oedometer ring strain gauges	A-16
Figure A3.1.	Calibration of control markers by 101 stationary dots	A-21
Figure A5.1.	Correlation between G_{\max} and mean effective stress (p') in sand	A-37
Figure A5.2.	Correlation between G_{\max} and mean effective stress (p') in sand:silt mixture	A-37
Figure A5.3.	Stress ratio vs axial strain from triaxial tests (sand).	A-38
Figure A5.4.	Stress ratio vs axial strain from triaxial tests (sand:silt).	A-38
Figure A5.5.	Stress paths of triaxial tests (sand).	A-39
Figure A5.6.	Stress paths of triaxial tests (sand:silt).	A-39

TABLE OF CONTENTS

SYNOPSIS	iii
PREFACE	iv
ACKNOWLEDGEMENTS	vi
NOTATIONS	vii
LIST OF TABLES	xi
LIST OF FIGURES	xii
TABLE OF CONTENTS	xxv

CHAPTER I: INTRODUCTION

1	PREFACE	2
1.1	DYNAMIC COMPACTION	2
1.1.1	Principles of Dynamic Compaction	4
1.1.2	Types of Soil Improved	6
1.1.3	Limitations and Offsite Restrictions	7
1.2	AIMS OF THE THESIS - RESEARCH SCOPE & OBJECTIVES	7
1.3	OUTLINE OF THE THESIS	9

CHAPTER II: LITERATURE REVIEW

2	OVERVIEW	12
2.1	DYNAMIC RESPONSE OF GRANULAR MATERIALS	12
2.1.1	Energy Emission due to Surface Impact	15
2.1.2	Wave Propagation and Stress-Strain Behaviour of Soils	18
2.1.3	Energy Attenuation due to Surface Impact	21
2.2	HISTORY OF DYNAMIC COMPACTION	22
2.2.1	Modern Applications of Dynamic Compaction	24
2.2.2	Types of Soils Improved by Dynamic Compaction	24

2.2.3	Philosophy and Design of Dynamic Compaction	27
2.2.4	Quality Control and Assessment of Dynamic Compaction	33
2.2.5	Environmental Concerns	35
2.3	RESEARCH WORKS OF DYNAMIC COMPACTION	36
2.3.1	Dynamic Compaction by Analytical and Mathematical Models Derived From Field or Experimental Observations	36
2.3.2	Dynamic Compaction by Physical Models Laboratory Testing	43
2.3.2.1	Application of Spatial Deformations and Strain Measurement by Image-based Displacement in Geotechnical Physical Modelling & Laboratory Testing	49
2.3.2.2	X-Ray Tomography (CT-Scan)	62
2.3.3	Dynamic Compaction by Finite Elements Models	64
2.4	SUMMARY	69

CHAPTER III: TESTING APPARATUS AND EXPERIMENTAL PROCEDURES

3	OVERVIEW	72
3.1	MERITS AND LIMITATIONS OF SMALL SCALE MODEL TESTING IN GEOMECHANICS	72
3.2	PHYSICAL MODELLING OF THIS RESEARCH	74
3.2.1	Set-up of 1-g Dynamic Compaction Models	75
3.2.2	Pounders (Tampers)	77
3.2.3	Materials Used	80
3.2.4	Models Preparation	82
3.2.5	High Speed & Still digital cameras	84
3.2.6	Cone Penetrometer Test (CPT)	86
3.2.7	Instrumentation	87
3.2.7.1	Instrumentation Calibration	89
3.3	DYNAMIC COMPACTION TEST PROCEDURE	91

3.4	EXTRACTING UNDISTURBED SAND SPECIMENS FROM POST DC TEST MODELS FOR CT-SCAN TESTS	93
3.5	TRIAxIAL TESTING WITH SHEAR WAVE VELOCITY MEASUREMENTS.	96
3.6	LABORATORY INVESTIGATION OF LATERAL STRESSES k_0 COEFFICIENT	98
3.7	STATIC LOAD TESTS	100
3.8	COMPACTION AND DENSITY TESTS	102

CHAPTER IV: CAMERA CALIBRATION AND VALIDATION OF DISPLACEMENT MEASUREMENTS

4	OVERVIEW	106
4.1	PRINCIPLES OF GeoPIV ANALYSIS AND VALIDATION	106
4.2	ACCURACY AND PRECISION IN GeoPIV MEASUREMENTS	107
4.3	CAMERA CALIBRATION TECHNIQUE FOR PIV	109
4.4	PILOT ASSESSMENT OF THE PHOTOGRAPHY SYSTEM	111
4.4.1	Camera Calibration for Image Distortions	112
4.4.2	Image Quality - Noise and Filters	115
4.4.3	Sensitivity of Camera Sensor	117
4.4.4	GeoPIV Evaluation	119
4.5	HIGH SPEED VERSUS STILL PHOTOGRAPHY FOR DC TESTS	122
4.6	SUMMARY	128

Chapter V: EXPERIMENTAL RESULTS – PHOTOGRAPHY

5	OVERVIEW	130
5.1	PHOTOGRAPHY RESULTS - ANALYSIS OF SOIL MOVEMENT	130
5.1.1	Soil Displacement During Static Load Tests	131
5.1.1.1	Steady Rate Static Load Tests	131

5.1.1.2	Pseudo-Static Load Tests	138
5.2	THE KINEMATICS OF DYNAMIC COMPACTION	144
5.2.1	Displacement Patterns & Soil Response to Impact Loading	144
5.2.2	Strain Uniformity and Micromechanics	158
5.3	QUANTIFYING THE DYNAMIC COMPACTION TESTING RESULTS	165
5.3.1	Cone Penetration Tests (CPT)	166
5.3.2	X-Ray Microtomography	168
5.3.3	Image analysis	174
5.3.3.1	Effect of Different Tamper Geometry on the Kinematics of Dynamic Compaction	177
5.3.3.2	Effect of Imparting Energy	190
5.3.3.2.1	Effect of Imparting Energy on Sand Models	190
5.3.3.2.2	Effect of Imparting Energy on Sand:Silt Models	194
5.4	SUMMARY	200

CHAPTER VI: EXPERIMENTAL RESULTS – PHYSICS OF DYNAMIC COMPACTION

6	OVERVIEW	202
6.1	THE ROLE OF INSTRUMENTATION IN DC TESTS	202
6.2	MEASUREMENT VALIDITY	203
6.2.1	Soil-instrumentation interaction	203
6.2.2	Effect of Reflected Signals	204
6.2.3	Signal noise	204
6.3	VALIDATION OF PHOTOGRAPHY RESULTS	206
6.4	INSTRUMENTATION RESULTS	208
6.4.1	Accelerometers	208
6.4.1.1	Soil Accelerations	208
6.4.1.2	Pounder Accelerations	216

6.4.2	Stress Cell (EPC) Data	223
6.4.2.1	Impact Stresses by Pounder EPC	223
6.4.2.2	Dynamic Soil Stresses	226
6.5	TYPICAL RESULTS DURING DC TESTS	228
6.6	SUMMARY	236

CHAPTER VII: SIMULATION OF DYNAMIC COMPACTION BY FINITE ELEMENT

LS-DYNA CODE

7	OVERVIEW	238
7.1	THE LS-DYNA CODE	238
7.2	LS-DYNA SYSTEM OF UNITS	239
7.3	SELECTION OF SOIL MODELS	240
7.4	LABORATORY TESTS TO CHARACTERISE THE GEOMATERIALS	240
7.4.1	Derivation of Soil Parameters for LS-DYNA Material Model	243
7.5	MODEL DEVELOPMENT	245
7.6	SENSITIVITY STUDY	248
7.6.1	Sensitivity of the results to the FE mesh size	248
7.6.2	Sensitivity of the Soil Model Material Parameters	251
7.6.3	Model Stability	255
7.6.4	Lagrangian verses ALE models	256
7.6.5	Summary of preliminary sensitivity analysis	258
7.7	SIMULATION RESULTS	258
7.8	SUMMARY OF THE LS-DYNA MODELLING RESULTS	274

CHAPTER VIII: SUMMARY, CONCLUSIONS, AND RECOMMENDATIONS FOR FURTHER STUDIES

8.1	SUMMARY	276
8.2	CONCLUSIONS	277

8.3	RECOMMENDATIONS FOR FURTHER STUDIES	279
	REFERENCES	281
	APPENDIX I	
A1.1	Data sheets of the data Acquisition System – StrainSmart 6000	A-2
A1.2	Accelerometers Data Sheets	A-5
A1.3	Stress cell data sheet	A-9
A1.4	Megapoxy data sheet	A-10
	APPENDIX II	
A2.1	Calibrations of earth pressure sensors	A-12
A2.2	Calibration of load cell- Steady rate static test	A-15
A2.3	Calibrations of oedometer ring strain gauges	A-16
	APPENDIX III	
A3.1	Syntaxes and algorithms of the Matlab routine "histeq"	A-18
A3.2	Syntaxes and algorithms of the Matlab routine "wiener2"	A-20
A3.3	Calibration of control markers object-space coordinates	A-21
	APPENDIX IV	
A4.1	Theoretical backgrounds of LS-DYNA soil models (extracted from LS-DYNA theory manual)	A-26
A4.2	Examples of LS-DYNA model	A-28
	APPENDIX V	
A5.1	Triaxial testing results	A-36

Chapter I: Introduction

Table of Contents

1	PREFACE.....	2
1.1	DYNAMIC COMPACTION	2
1.1.1	Principles of Dynamic Compaction	4
1.1.2	Types of Soil Improved	6
1.1.3	Limitations and Offsite Restrictions	7
1.2	AIMS OF THE THESIS - RESEARCH SCOPE & OBJECTIVES	7
1.3	OUTLINE OF THE THESIS	9

1 PREFACE

The aim of this chapter is to provide a concise overview of ground improvement by dynamic compaction, including its development, applications, and limitations. The advantages and benefits of dynamic compaction are discussed and the reasons behind its popularity are explained. Why research is needed, and the need for the research that is the focus of this thesis is explained

In this study, the research reviews and aims will be addressed by examining the following key questions:

- How does dynamic compaction work;
- What is the design procedure for dynamic compaction;
- How to estimate the depth and extent of improvement;
- How should dynamic compaction be operated.

1.1 DYNAMIC COMPACTION

Based on dropping a heavy weight from a large height, dynamic compaction was introduced to the engineering market in the 1970s by the late Frenchman, Louis Menard. Since then, dynamic compaction (DC) has become one of the more regularly used in-situ ground improvement techniques to mitigate undesirable subsurface conditions. Today, ground improvement by dynamic compaction is a viable alternative due to its simplicity and cost-effectiveness especially for improving large areas.

Dynamic compaction has proven to be an economical alternative to other available methods such as excavation and replacement, surcharging, compaction grouting and other soil improvement techniques. Dynamic Compaction relies entirely on the compaction method without the need for soil removal or replacement or the introduction of any material into the treated soils.

For sites underlain by deep layers of fill or soft or loose soils, conventional practice (prior to dynamic compaction) was to either remove and replace the unsuitable soils, or to adopt expensive deep foundations. The primary goal of dynamic compaction is to improve the

density of loose soil deposits by transforming these deposits into ones that have uniform and better engineering properties. Dynamic compaction is used to improve the engineering properties of soils at depth, both above and below the groundwater level. Dynamic compaction is sometimes used in conjunction with other ground improvement techniques. As the availability of suitable construction sites decreases due to developments of urban areas, the need to utilize sites with poor bearing and settlement characteristics (sites underlain by deep layers of fill or soft or loose soils) for foundation support increase. The dynamic compaction market is well established with steady growth expected because of the number of old landfill sites that were previously not considered for development.

Essentially, dynamic compaction consists of providing high energy impacts at the ground surface by repeatedly dropping steel or concrete tampers, 5 to 40 tonnes in weight, from heights ranging from 10 to 50 m. Figures 1.1 and 1.2 show examples of typical dynamic compaction equipment and operations.



Figure 1.1. Dynamic compaction equipment- crane and tamper (courtesy of Keller Australia).

1.1.1 Principles of Dynamic Compaction

Dynamic Compaction comprises the imparting of high energy from a large mass dropping from considerable height, onto the ground. Thus, dynamic compaction is similar to a Proctor compaction test, in that there is a physical displacement of soil particles into a denser configuration.



Figure 1.2. Dynamic compaction using 23 tonne and 30 tonne pounders at Port Ras Laffan, Qatar (courtesy of Menard).

The widely accepted explanation for how dynamic compaction works, is that imparted energy is transmitted from the surface of the ground to deeper layers of soil by the propagation of shear and compression waves forcing the soil into a denser state. Dynamic compaction also produces a low frequency vibration, in the range of four to ten cycles per second, which, along with the energy input, reduces the void ratio and increases the relative density. The densification improves the bearing capacity and enhances the soil settlement characteristics. After dynamic compaction, the soil strength is increased, and its compressibility has decreased as a result of the densification. The intent of dynamic

compaction is to make a heterogeneous mass, either man-made or natural, a more homogeneous mass with a lower void ratio, a higher shear strength, and therefore a higher bearing capacity.

Dynamic compaction is typically performed with multiple passes over a pre-determined grid pattern, in a systematically controlled pattern of drops. The grid spacing, number of drops per impact point, applied energy, and number of passes depend upon the conditions of the soil, such as the initial ground response, depth to the groundwater and the dissipation of pore water pressure. At the present comprehensive field monitoring and engineering judgement of the ground response are the only methods to specify DC grid spacing. The initial grid spacing generally approximates the thickness of the compressible layer of soil. Typically, 5 to 15 blows per grid point are applied. Often, the proximity of groundwater or excessively deep craters, limits the number of blows that can be applied at each location to avoid getting the tamper stuck, and to allow for the dissipation of pore water pressure. Standard practice is to curtail the application of energy when a crater is deeper than one and a half to two times the height of the tamper, or when the groundwater surface rises into the crater. When this occurs, additional passes after backfilling the crater and levelling (ironing) the ground are required to complete the required number of drops.

In principle, the degree of soil improvement depends to a large degree upon the total amount of energy applied to the soil, i.e., the more energy input to the soil, the greater the degree of improvement. When the technique is successful, the results of treatment by dynamic compaction are dramatic and immediate. Depending on the looseness of soil deposit, surface settlement is typically five to ten percent of the thickness of the material being treated and is noticed immediately. Pore pressure increase is instantaneous, and dissipation usually occurs rapidly in granular soils; often accompanied by rising groundwater levels or localized boiling at the surface. Strength and compressibility, as measured by in situ tests, are typically improved by a factor of two to four. The significant developments in dynamic compaction over the past two decades are the expansion of its applications, uses, and purposes. The list of applications continues to grow, but dynamic compaction has been mainly used in the following applications:

- To increase soil bearing capacity to allow higher loads to be supported,
- To reduce total and differential settlements,
- To improve resistance to liquefaction,
- To treat environmentally questionable sites by not uncovering or exposing them.

1.1.2 Types of Soil Improved

The single most important factor in determining the suitability of a type of soil to be improved by dynamic compaction is its ability to dissipate excess pore pressure quickly. During dynamic compaction, soil particles are compressed. If voids are saturated an instant rise in pore water pressure occurs and little densification can occur because of the incompressible nature of water. It is necessary for this pressure to dissipate before additional densification can occur under repeated high energy drops. If this is not allowed to happen, then repeated drops from the tamper only cause displacement of the ground, and not densification. (Menard and Broise, 1975)

Associated with the increase in applications of dynamic compaction over the last two decades, there has been an increase in the types of materials treated. Originally, the predominant types of soil considered suitable for dynamic compaction only included granular soils. But, because of the economic advantages of dynamic compaction, a multitude of materials have since been improved, including uncontrolled fills, silts containing mostly non-plastic silt, gravel and occasionally clayey soils, except for sensitive clays (Lukas, 1986). Fills can include the entire spectrum of natural soils, man-made debris, by-products, and any combination of the three. Dynamic compaction works best, however, on dry and unsaturated granular fills, including sand, gravel, ash, rock, and steel slag.

For deposits below the water table, the impact vibrations cause an increase in pore pressure, and after a number of impact passes, can cause a sufficient rise in pore pressure to induce liquefaction. Once this occurs, additional energy application is ineffective until the pore pressure dissipates. Additional compaction following pore pressure dissipation produces more low frequency vibrations that reorganises the particles into a denser configuration (Nashed, 2005).

1.1.3 Limitations and Offsite Restrictions

Because of the high-energy impact of a heavy tamper hammering the ground, dynamic compaction produces vibration and noise. Since dynamic compaction results in improved inter particle contact of the treated soils, vibration levels tend to increase towards the end of the treatment operation even though the final impact energy levels are significantly lower than those performed in earlier passes. With close monitoring, vibrations can be maintained well below vibrations that would cause any structural damage; however, public awareness of noise and vibrations, particularly in residential areas often precludes the use of dynamic compaction (Lukas, 1980, Mayne, 1985 & 1988 and Hwang & Tu, 2006).

1.2 AIMS OF THE THESIS - RESEARCH SCOPE & OBJECTIVES

Large numbers of case studies have demonstrated that DC can increase the density and bearing capacity of treated granular soil deposits and improve their resistance to liquefaction. Despite the wide use of DC as a ground improvement technique for granular soil sites, there are no established design procedures because there is no clear understanding of the kinematic mechanism of the densification process, taking place beneath the ground surface.

It is traditionally considered that the imparted energy is transmitted from the ground surface to the deeper soil layers by the propagation of shear and compression waves, which force the soil particles into a denser state. Only a limited study focusing on in situ measurements referring to the decay of soil surface vibration caused by the falling weight after each impact to correlate the soil mass interaction and provide a site-specific optimisation to the dynamic compaction practise (Adam *et al.*, 2007) has been reported. There are currently no subsurface real time measurements that have been obtained during the dynamic compaction process, and the depth and extent of the soil improvement is often difficult to predict.

Before the development of mathematical prediction tools, typical prototypes of DC behaviour were based on trial in-situ test results which relied on surface measurements, observations and experience, but provided little scientific explanation. Current practice for the design, feasibility assessment, and determination of optimum field operations relies on past experience, case studies and expensive field pilot tests. Typical dynamic compaction projects

are still planned using empirical design criteria (such as impact mass, impact grid pattern and grid spacing, number of impacts per grid point, time delay between impacts, and total number of passes) that are based on field trials, verified by before and after field investigations.

Typically, field verification testing includes conventional standard penetration tests (SPT), cone penetration tests (CPT), pressuremeter tests, and static load tests. Verification tests are expensive and time consuming, and may not provide a comprehensive picture of the degree of improvement, particularly at the impact grid points where the resulting denser soils often obstruct testing equipment. Such design and practice fails to account for key factors such as the pre-impact relative density of the soil and the required level of relative density or SPT/CPT penetration resistance. Dynamic compaction is a complicated process and a better understanding of the DC process in granular soil deposits such as sand, and silty sand soil deposits, is required to aid the current design practice.

This research work investigates the kinematics occurring during lab-based 1-g models, using high speed photography and image correlation techniques. To date, researchers have studied soil dynamic behaviour using still digital photography to capture the before and after spatial deformation. These cameras can not take images of the soil deformation quick enough to capture the real motion of the soil particles during time dependent episodes such as during dynamic compaction application. The camera with high frame rate used in this research has made possible the visualization of the high speed motion of the soil particles during the dynamic compaction process. In this research, particle image velocimetry (PIV) combined with high speed photography and X-ray microtomography have been applied to capture the dynamic motion of soil particles inside the soil mass while it is repeatedly compacted.

The main objectives of this research are to:

- Capture the real-time kinematic mechanism of the dynamic compaction densification process taking place below the soil surface using physical models with transparent windows for sub-surface observations using high speed photography.
- Develop an improved understanding of the behaviour of granular soils, including sands and silty sand treated by dynamic compaction.

- Establishing a scientific relationship between magnitudes, patterns, and distribution of volumetric strain within the imparted soil mass, and levels of applied energies.
- Explore the ability of finite element (FE) numerical models to simulate the DC physical models.
- Evaluate the effect of fines content, pre-compaction relative density, and tamper geometry on crater size, the achievable influence depth and level of improvement.

1.3 OUTLINE OF THE THESIS

Chapter 2 presents a literature review for the historical background of the following:

- Dynamic compaction; a review of its applications and recent research, modelling, design and field advances.
- Displacement and strain measurements in geotechnical materials.
- The application of photography in geotechnical physical modelling to study the mechanism and behaviour of soil deformation.
- Digital image correlation (DIC), Particle image velocimetry and X-ray Computerised Tomography (CT) as strain measurements tools.
- Numerical modelling of dynamic compaction.

Chapter 3 presents the experimental set up, materials tested, apparatus, and instrumentation used.

Chapter 4 discusses camera calibration, displacement measurement technology, validation of high speed photography techniques, and using the PIV algorithm to measure large strains in granular materials.

Chapter 5 presents the results of the dynamic compaction behaviour captured by the high speed photography and microtomography focusing on:

- The internal densification mechanisms
- The presence of localised deformation and strain bands
- The role of CT scan in quantifying the density of soil within the localised strain bands.

- The effect of different tamper geometries on the response from sand and sand:silt soils.

Chapter 6 discusses the role of instrumentation in capturing the physics of the DC process.

Chapter 7 presents the results of numerical modelling of dynamic compaction by finite element code LS-DYNA.

Chapter 8 summarises the major findings of this research and makes recommendations for further studies.

Chapter II: Literature Review

Table of Contents

2	OVERVIEW	12
2.1	DYNAMIC RESPONSE OF GRANULAR MATERIALS.....	12
2.1.1	Energy Emission due to Surface Impact.....	15
2.1.2	Wave Propagation and Stress-Strain Behaviour of Soils.....	18
2.1.3	Energy Attenuation due to Surface Impact.....	21
2.2	HISTORY OF DYNAMIC COMPACTION.....	22
2.2.1	Modern Applications of Dynamic Compaction.....	24
2.2.2	Types of Soils Improved by Dynamic Compaction.....	24
2.2.3	Philosophy and Design of Dynamic Compaction.....	27
2.2.4	Quality Control and Assessment of Dynamic Compaction.....	33
2.2.5	Environmental Concerns.....	35
2.3	RESEARCH WORKS OF DYNAMIC COMPACTION.....	36
2.3.1	Dynamic Compaction by Analytical and Mathematical Models Derived From Field or Experimental Observations	36
2.3.2	Dynamic Compaction by Physical Models Laboratory Testing.....	43
2.3.2.1	Application of Spatial Deformations and Strain Measurement by Image-based Displacement in Geotechnical Physical Modelling & Laboratory Testing	49
2.3.2.2	X-Ray Tomography (CT-Scan).....	62
2.3.3	Dynamic Compaction by Finite Elements Models	64
2.4	SUMMARY	69

2 OVERVIEW

This research work has required knowledge of the dynamic response of granular materials, analysis of shearing and strain localisation in granular materials, and physical and numerical modelling in geotechnical engineering. It has made use of close-range photogrammetry, particle image velocimetry (PIV), digital image correlation (DIC) and X-ray microtomography techniques, image based tools that have been used to measure strain and displacement in geomaterials. This chapter provides a review and synthesis of the state of development and the most recent research related to these topics.

2.1 DYNAMIC RESPONSE OF GRANULAR MATERIALS

The behaviour of fine-grained soils under cyclic loading has been traditionally reported as the result of three main deformation mechanisms. These mechanisms are cumulative plastic shear strain, cumulative consolidation, and cumulative compaction (O'Reilly and Brown, 1991). When dynamic compaction is applied at the surface of dry or partially saturated deposits, the densification process is “essentially identical” to that of impact Proctor compaction in the laboratory (Varaksin, 1981). The engineering properties of the deposit are improved by reducing the void ratio and increasing the relative density of the deposit by physical rearrangement of particles.

It has long been believed that the densification achieved in dry soils by dynamic compaction is mainly due to shockwaves inducing high intergranular stresses that deform the soil skeleton. Based on this assumption, a simple one-dimensional model has been developed to simulate the process combining the effects of impact inertia forces and soil body stress waves (Scott and Pearce, 1975). In this model, the vertical stress-strain behaviour of the loose granular soil under confined compression has been idealised by the elasto plastic relationship shown in Figure 2.1.

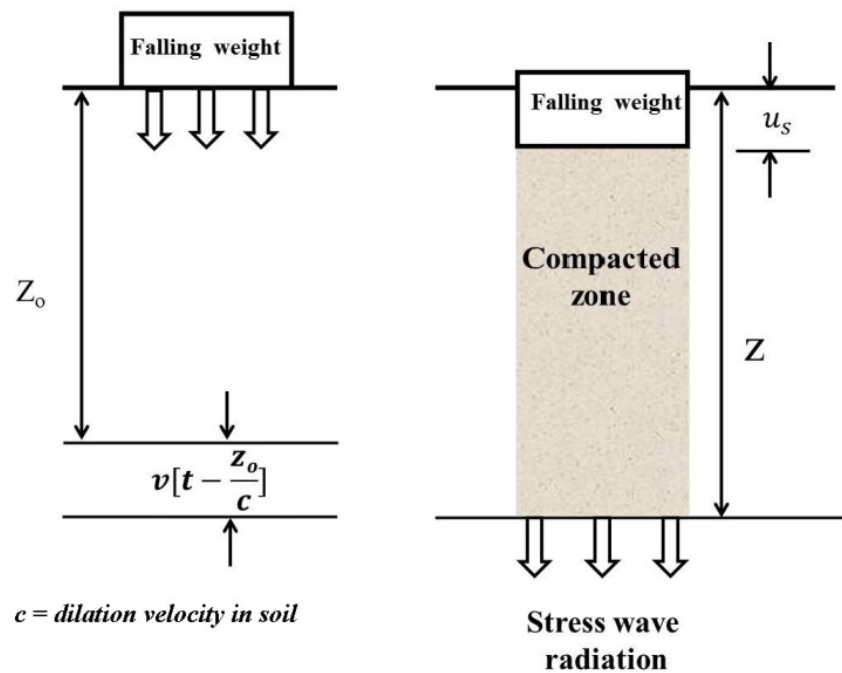


Figure 2.1. One dimensional compaction model (Scott and Pearce, 1975)

The falling poulder applies a sudden dynamic loading to the loose granular soil, which can cause the vertical stress to exceed its elastic limit σ_e (Figure 2.1), causing the soil to deform plastically. The poulder then punches through the soil forcing a growing cylinder of soil downwards, assuming no lateral spread of the cylindrical compacted zone. The soil inside the cylindrical volume is forced into a state of confined compression due to the punching. The equation of motion can be derived by considering the equilibrium of the stress applied at the bottom surface of the falling weight and can be expressed as (Scott and Pearce, 1975):

$$m_s \frac{\partial}{\partial t} (\dot{u}_s - v) = \rho \frac{\partial}{\partial t} \left[(z - u_s) \frac{\partial}{\partial t} (u_s - vt) \right] + \sigma_e \quad (2-1)$$

where m_s is mass per unit area of the falling weight, u_s is the contact deflection on the soil, \dot{u}_s is the contact velocity, v is the particle velocity in a radiated stress wave, ρ is the mass density of the soil, z is the instantaneous position of the wave front, and σ_e is the elastic limit stress (Figure 2.2).

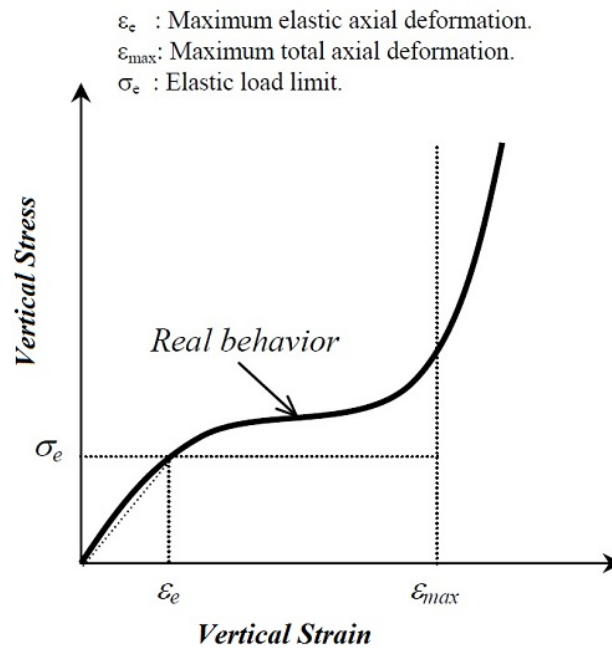


Figure 2.2. Axial deformation of confined compactable loose granular soil

For saturated soils, Menard and Broise (1975) have suggested a densification mechanism different from that for dry or partially saturated soils. They believed that if the surface impact increases to a critical stage, a significant rise in pore water pressure will induce liquefaction similar to that caused by earthquakes. This DC induced liquefaction results in the soil being subjected to very high shear strains, while its shear strength declines due to the build up of pore pressure and falling effective stress. The low frequency vibrations caused by further stress impulses will then reorganise the particles into a denser state.

Menard and Broise illustrated their densification mechanism of dynamic compaction by time histories (Figure 2.3) of accumulated imparting energy, corresponding variation of volume in the soil, dissipation of pore pressure (degree of liquefaction) and change in the soil bearing capacity. Since it is fundamental that reduction in the volume of soil can only take place by expulsion of water from the soil voids, it is not clear why Menard and Broise's scheme shows no concurrent volume change taking place with the pore pressure dissipation.

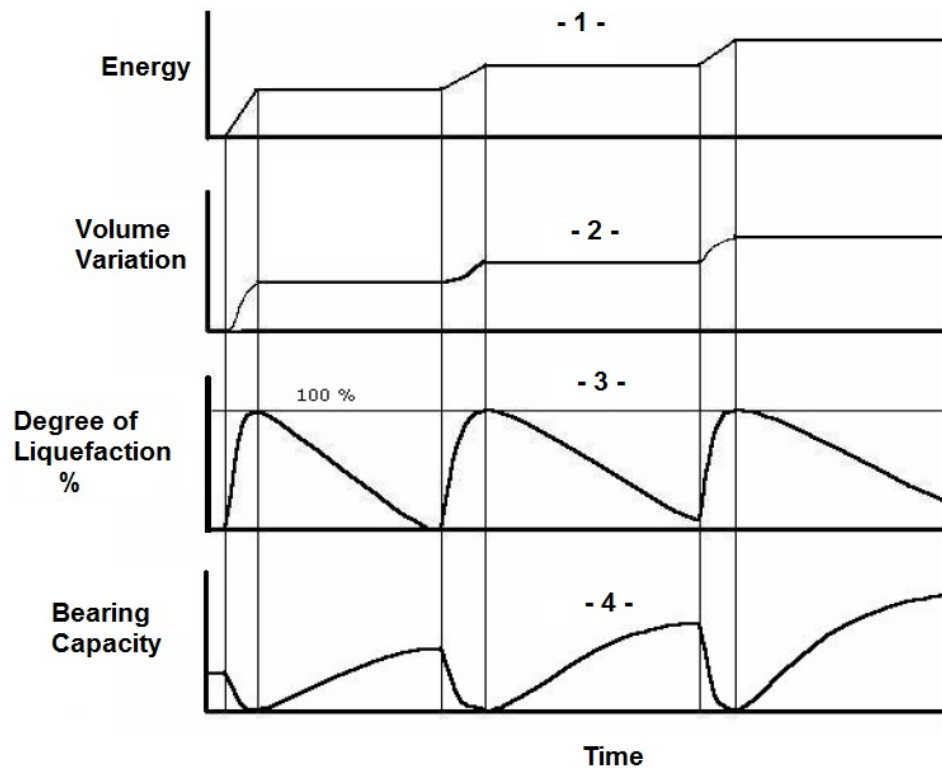


Figure 2.3. Densification mechanism of saturated deposits (Menard and Broise 1975)

It is recognized in the literature that liquefaction is a process involving energy dissipation due to frictional loss along grain contacts during dynamic or cyclic loading leading to collapse of the soil structure and that this knowledge can be applied to develop methods for liquefaction mitigation design applications (Berrill and Davis 1985; Figueroa *et al.*, 1994; Thevanayagam *et al.*, 2000; Green and Mitchell 2004). During liquefaction, undrained loading of a saturated cohesionless soil causes an accumulated increase in pore pressure and a decrease in effective stress. The energy required to cause liquefaction mainly depends on the density of packing of the grains and the confining stress. To mitigate liquefaction, dynamic compaction is generally applied to loose sand deposits that are susceptible to liquefaction.

2.1.1 Energy Emission due to Surface Impact

The energy delivered at the impact zone by the falling weight propagates through the surrounding soil as body waves (primary, P-waves and secondary, S-waves) and surface waves (primarily Rayleigh waves). Wave type is defined by the direction of particle motion relative to the direction of wave propagation. The primary, P-waves are compression waves

that propagate as alternating compressions and extensions to the medium and are characterized by particle motions in the directions of propagation. The secondary, S-waves are shear waves that propagate as distortions in an elastic medium without volume change and are characterized by particle motion perpendicular to the direction of propagation. Rayleigh waves are surface waves that travel near the surface of solids. Rayleigh waves include both longitudinal and transverse motions that decrease exponentially in amplitude as distance from the surface increases. There is a phase difference between these component motions. A schematic diagram illustrating the different types of waves induced from an impact on the surface of a half-space, is shown in Figure 2.4.

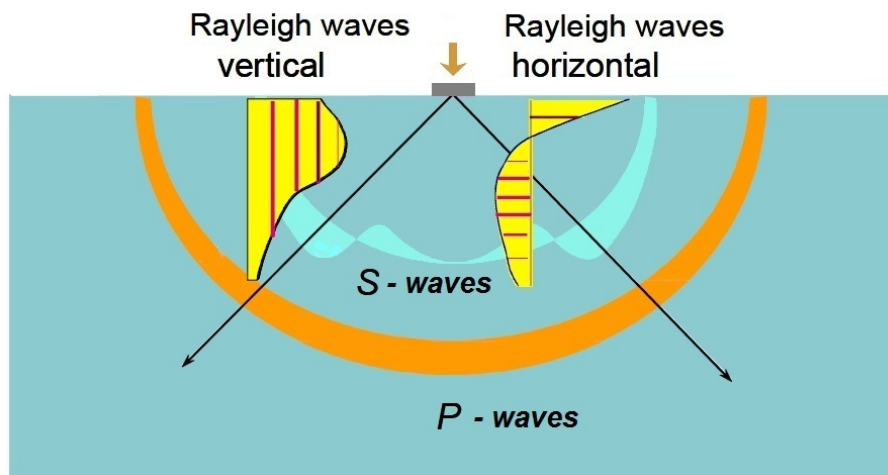


Figure 2.4. Schematic diagram of wave propagation due to surface impact (Graff 1975).

Geotechnical engineers have long recognised that Rayleigh waves offer a useful non-invasive method of investigating the ground in situ (*e.g.* Hertwig, 1931; Jones, 1958; Heukolom & Foster 1962; Abbis, 1981). A solution to the partition of an energy source on the surface of homogeneous, isotropic elastic half-space is available. It has been shown that as a first order approximation, the energy loss per unit volume of soil due to these Rayleigh waves W_R and body waves W_B , respectively, are given by (Shenthan *et al.*, 2004):

$$W_R(r, z) = F(0.67WH)(\alpha e^{-2\alpha r})/\pi r \quad (2-2)$$

$$W_B(r, z) = (0.33WH)(\alpha e^{-2\alpha R})/\pi R^2 \quad (2-3)$$

where W is the dropped weight in tonnes, H is the height of drop in meters, α is the attenuation coefficient due to material damping, $R = \sqrt{r^2 + z^2}$, F is an integral function, and r and z are radial and vertical coordinates from the centre of the impact surface, respectively. Figure 2.5 shows the dynamic compaction energy partitioning components.

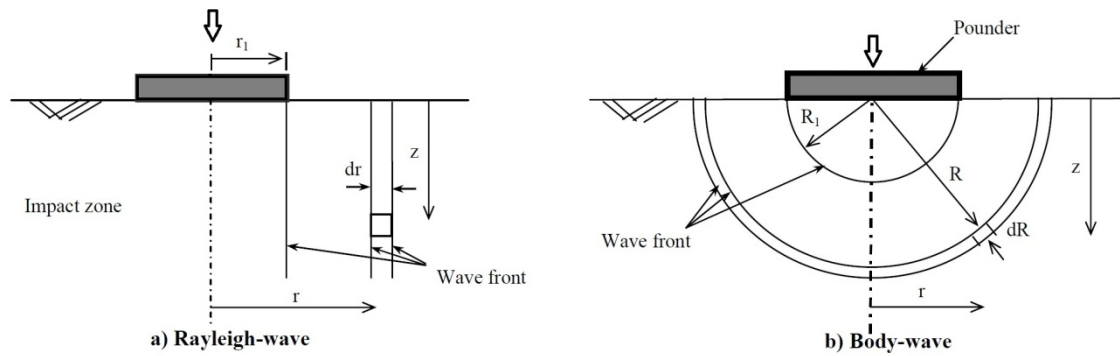


Figure 2.5. Dynamic compaction energy partitioning components (Shenthan *et al.*, 2004).

The cumulative energy loss at any point is given by:

$$W_C = W_R + W_B \quad (2-4)$$

The building up of excess pore pressure under rapid loading is a common phenomenon that affects the strength and the deformability of saturated cohesionless soils. Based on a large experimental database and theoretical considerations, excess pore water pressure generated due to undrained cyclic loading of saturated sands and non-plastic silty soils has been related to frictional energy loss in the soil (Thevanayagam *et al.*, 2003):

$$r_u = 0.5 \log_{10} (100W_C/W_L) \quad \text{provided } (W_C/W_L) > 0.05 \quad (2-5)$$

where, r_u is the excess pore pressure ratio (u/σ'_o), σ'_o is the initial mean effective confining pressure, W_C is the cumulative energy loss per unit volume of soil, and W_L is the energy per unit volume required to cause liquefaction. Assuming this relationship holds true for loading due to Rayleigh and body waves as well, impact-induced excess pore pressure at any point in the soil surrounding the impact zone can be obtained by substituting Equation 2-4 for W_C in Equation 2-5. Using this approach, Nashed (2005) developed a simulation model to evaluate the spatial distribution of energy dissipation per unit volume of soil from ground surface

impact during dynamic compaction. The simulation model was verified through simulating well-documented case histories, in which reasonable agreements were claimed. Despite this agreement the application of this method in general is unlikely to be reliable. This is because the problem of energy emission at the surface of a non-homogenous, nonlinear, elastic-plastic soil deposit during DC is more complex than energy calculations based on theory of elasticity.

2.1.2 Wave Propagation and Stress-Strain Behaviour of Soils

The amount of strain developed when a material undergoes a loading depends upon the level of stress applied. For typical soils, the modulus observed at high strain levels will be smaller than those observed at low strain levels as shown in Figure 2.6. Small-strain parameters play an important role in understanding the mechanical behaviour of soils. According to Atkinson and Salfors (1991) and Lai and Rix (2002), the stress-strain curve is linear at strain levels below 0.001% for uncemented coarse-grained soils. The slope of the linear portion of the shear stress-strain curve is the same as the initial slope of an unloading and reloading curve after nonlinear deformation has taken place (Figure 2.6).

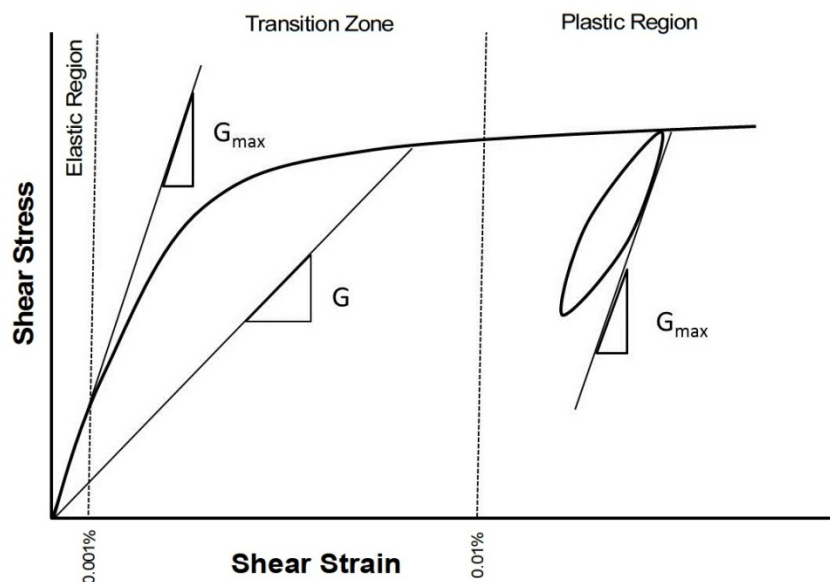


Figure 2.6. Modulus variations with strain level

The modulus value over the linear portion of the curve in the stress-strain curve is known as the material's maximum modulus, commonly denoted E_{max} , maximum Young's modulus, or G_{max} , maximum shear modulus. These maximum moduli allow for a direct comparison of stiffness since they are relatively constant at small strains.

Pre-failure stiffness plays a crucial role in modelling typical geotechnical problems. Mathematically modelled soil behaviour with non-linear elasticity, is characterized by a strong variation of soil stiffness, which depends on the magnitude of strain occurring during loading and unloading of the soil. The shear modulus of soils at a small strain level (0.0001 – 0.001%) is a required parameter in simulating dynamic event in soils as the wave propagation produced by DC induces low levels of strain in the soil mass away from the loading source. On the other hand, large strains are induced in soils within close proximity to the poulder during DC. Dynamic properties of the soil such as shear modulus and damping ratio (ratio of viscous to critical damping) and their variation with stress and strain level are critical in evaluating soil dynamic responses. Material damping occurs as a result of the loss of energy due to hysteresis damping and internal sliding of soil particles. The energy loss depends on the frequency of loading, soil type, stress conditions, and strain level.

To determine the stiffness at very small strains many authors have made use of bender elements placed in the end platens of test apparatus or buried in the soil. As bender elements are used in this research they are discussed briefly here. Many researches on the small strain shear modulus of cohesive soils and sands by the bender element test have been performed. Shirley and Hampton (1978) pioneered the use of bender elements for measuring the shear wave velocity in marine sediments. Dyvik and Madshus (1985) were the first to use bender elements to measure the shear wave velocity in conventional soil testing equipment. Viggiani and Atkinson (1995), Arulnathan *et al.*, (1998), Lohani *et al.*, (1999), Santamarina *et al.*, (2001), and Leong *et al.*, (2005) advanced the state-of-the-art on bender element data analysis. This approach allows the shear wave velocity " V_S " to be determined. Assuming the soil is an isotropic linear elastic medium this enables G_{max} and hence E_{max} to be determined. Based on the theory of elasticity, Richart *et al.*, (1970) provided a relationship between the characteristic velocity of shear waves V_S and Rayleigh waves V_R in an elastic medium, and Matthews *et al.*, (1996) outlined the relationship between the maximum shear modulus or

stiffness G_{max} , and the shear wave velocity. In an isotropic elastic medium, the velocity of a compression wave V_P , is given by:

$$V_P = \sqrt{\frac{K + \frac{4}{3}G}{\rho}} \quad (2-6)$$

The velocity of a shear wave V_S is:

$$V_S = \sqrt{G/\rho} \quad \text{or} \quad G_{max} = \rho V_S^2 \quad (2-7)$$

where K is the bulk modulus, G is the shear modulus and ρ is the mass density. According to the theory of elasticity, Young's modulus E , is related to G and K thus:

$$K = \frac{E}{3(1-2\nu)} \quad (2-8)$$

and

$$G = \frac{E}{2(1+\nu)} \quad (2-9)$$

where ν is Poisson's ratio. Thus, G can be obtained from the measurements of V_S alone, but V_S and V_P are needed to determine E , K , and ν . The relationship between the velocity of shear waves V_S and Rayleigh waves V_R in an elastic medium is given by:

$$V_R = CV_S \quad (2-10)$$

The constant C is dependent on Poisson's ratio and may be found from the expression:

$$C^6 - 8C^4 + 8\left(3 - \frac{1-2\nu}{1-\nu}\right)C^2 - 16\left(1 - \frac{1-2\nu}{2(1-\nu)}\right) = 0 \quad (2-11)$$

The range of C is from 0.911 to 0.955 for the range of Poisson's ratio associated with most soils, if anisotropy is ignored. The maximum error in G arising from an erroneous value of C is less than 10%.

2.1.3 Energy Attenuation due to Surface Impact

The analysis of any problems in soil dynamics also requires knowledge of the attenuation characteristics of waves propagating in the ground. A considerable amount of research has been dedicated to the subject of construction vibrations and wave attenuation (Siskind *et al.*, 1980; Wiss, 1981; Mayne, 1985 and Hwang *et al.*, 2006). Most of the studies have involved field measurements of the vibrations and development of empirical relationships, taking into consideration the amount of discharged energy, the distance from source, and the frequency of vibration and type of soil.

The impact energy applied to the ground surface results in densification of the deposit to a certain depth governed by the energy radiation and attenuation with depth. Due to the difference in expanding wave fronts between different types of waves, the decreasing rate in amplitude due to geometrical spreading (damping) differs. In the dynamic compaction process both body waves and surface waves are produced from surface impact. The body waves expand along a hemispherical wavefront, which encompasses a significantly large area, and the surface waves expand along a cylindrical wavefront, as shown in Figure 2.5. Consequently, the energy per unit area of an expanding body wave decreases at a significantly greater rate than a surface wave and the amplitude of the wave motion decreases in proportion with this reduction in the energy level of the expanding wave front. In terms of distance from the source r , the attenuation of the body wave amplitude is proportional to $1/r^2$ along the surface, and $1/r$ elsewhere, while attenuation of the surface wave amplitude is proportional to $1/r^{0.5}$ (Richart *et al.*, 1970). The geometric spreading can be expressed by:

$$A^* = A_1^* \left(\frac{r_1}{r} \right)^{n_s} \quad (2-12)$$

where A_1^* is the amplitude of vibration at a distance r_1 from the source, A^* is the amplitude of vibration at a distance r from the source, and n_s is an attenuation coefficient. The value of the attenuation coefficient n_s depends on the type of wave, and the position and size of the source. The geometric spreading does not result in any energy loss.

2.2 HISTORY OF DYNAMIC COMPACTION

There is evidence that the compaction of loose deposits by repeatedly lifting and dropping stone weights took place in China about 4000 years ago, and later by the Romans (Kerisel, 1985). In 1871, a Mexican war cannon filled with lead densified the soil for the St. George Mormon Temple in St. George, Utah (Welsh, 1986). Deep dynamic compaction by heavy tamping has been applied in Austria and Germany since the 1930s, but was initially limited to weights of about 10 tonnes and falling heights of about 10 m. The United States Army Corps of Engineers experimented with heavy tamping at the Franklin Falls Dam construction in 1936.

In 1955, DC was used in South Africa to densify loose soils for the foundations of a 76 m diameter crude oil tank. In Russia, heavy tampers were used to compact silty and sandy soils in the early 1960s (Elias *et al.*, 1999). With the advent of large crawler cranes in the early 1970s, the modern DC technique was promoted by the late French engineer Louis Menard (Schaefer 1997). The application of high energy tamping levels of 20 to 25 tonnes dropping from heights up to 25 m has been regularly used in France since 1970, in Britain since 1973, and in North America since 1975 (Slocombe, 1993). With the development of ‘gigamachines’ for dynamic compaction, a falling weight up to 2000kN (200tonnes) from heights up to 40 m is not uncommon nowadays.

For treating granular fill up to 3 - 4 meters depth, a form of dynamic compaction called "Rapid Impact Compaction (RIC)" was developed in the United Kingdom in 1990s for rapid densification of soils to repair bomb craters on runways. RIC consists of an excavator-mounted hydraulic pile-driving hammer striking a circular plate that rests on the ground. Typically, a 70 kN hammer is hydraulically raised to a height of 1.2m and then allowed to free-fall, resulting in a maximum energy per blow delivered to the plate of 85kN.m. The tamper typically strikes the plate at a rate of 30 to 40 blows per minute and generally 10 to 30 blows are applied per compaction location. A detailed review of the impact compaction literature has been undertaken by Paige- Green (1998). He made the observation that "*Impact compaction results in compaction at depth, with disturbance of the upper portion of the layer*". He also noted that "larger loads and larger contact areas are better for deep compaction".

Dynamic compaction and RIC are similar in that both utilise a falling weight to compact the ground. The major difference between the two techniques is that a portion of the energy applied with RIC is lost before it reaches the ground as it must overcome the inertia of the plate resting on the ground. RIC works well for shallow compaction but it is not suitable for moderate or deep compaction of soils, no matter how rapidly or how many times the tamper is dropped (Serridge and Synac, 2006). Development of dynamic compaction throughout the world has resulted in a large number of technical terms, some of which can have different meanings in different areas. Table 2.1 summarises the most common terms which have been adopted mainly in the UK and South Africa.

Table 2.1. Dynamic compaction terminology

Term	Description
Effective depth of influence	Maximum depth at which improvement is attained
Zone of major improvement	Typically half to two thirds of the effective depth
Drop energy or impact energy	Energy per blow, which equals mass multiplied by drop height (normally expressed in tonnes.m)
Total energy	Sum of energy of each pass i.e. number of drops multiplied by drop energy divided by respective grid areas (normally expressed in tonnes. m/m ²)
Threshold energy	Energy input beyond which no further improvement can be practically achieved
Pass	The performance of each grid pattern over the whole treatment area
Over-tamping	A condition in which the threshold energy has been exceeded, causing remoulding and dilation of the soil
Phase	Part of a pass. For example, every other drop point of the grid pattern receives the specified energy as phase 1, then after completing phase 1, the intermediate points receive the same energy as phase 2
Recovery period	The period of time required between passes to allow the excess pore water pressures to dissipate to a low enough level for the next pass
Induced settlement	The average reduction in the general site level.
Shape test	Detailed measurement of imprint volume and surrounding heave which permits comparison of overall volumetric change with increasing energy input
Imprint	The crater formed by the weight at the point of impact

2.2.1 Modern Applications of Dynamic Compaction

The modern DC technique involves high energy impacts to the ground surface which are achieved by repeatedly dropping heavy weights of 50–300kN from heights ranging from 10m to 30m with an impact energy in the range of 0.5 to 9.0MJ to the soil, over impact grids that are typically 5–15 m apart. Following the application of high level energy, the surface of the deposit is normally in a loose condition to a depth equal to the depth of the craters. This surface layer is then compacted using a lower level of energy and this process is referred to as ironing.

A review of the pertinent literature reveals that a wealth of research has been conducted in the past two decades into dynamic compaction. The research focuses were mainly the applicability for different types of soils, development of design procedures and guidelines, physical modelling and numerical simulations. The following sections review the most relevant literature associated with: the suitability of the technique for different soils; the effective depth of influence (DI); field measurements like crater depth and surface heave; design aspects for DC operation such as grid pattern, energy per drop point and number of passes; compaction waves and their propagation behaviour in soil bodies; and the simulation and prediction by numerical models.

2.2.2 Types of Soils Improved by Dynamic Compaction

At the beginning, the technique was called heavy tamping and was generally used in good quality fill deposits such as sand, rock waste, and rubble. Later on the technique was expanded to accelerate the consolidation of saturated fine grained soil deposits and the name was changed to dynamic consolidation (Elias *et al.*, 1999). Mayne *et al.*, (1984) showed that DC is an economically attractive solution for preparing subgrades and conventional shallow foundations. The deposits considered most suitable for DC, both below or above the water table, are permeable granular soils which include natural sands and gravels, and fill deposits consisting of building rubble, granular mine spoil deposits, industrial waste fills such as slag, and decomposed refuse.

Clayey soils with impervious characteristics do not allow the rapid dissipation of excess pore-pressure, which makes the technique impractical for such deposits. Saturated clayey soils have been classified as not suitable for DC, as they have low hydraulic conductivities, since densification can not occur unless the induced pore pressure dissipates. However, partially saturated clayey fill deposits above the water table and with adequate surface drainage do experience some improvement by dynamic compaction. Varaksin (1981) proposed a formula to predict the increase in pore water pressure under saturated conditions. He noticed that once the point of liquefaction is reached, a rest period is required for the pore water pressures to dissipate. Lukas (1986) has categorized different soil deposits for their suitability for DC based on conventional soils properties such as soil permeability and plasticity index (PI) as shown in Table 2.2. Figure 2.7 shows the range of soil gradation for the zones categorised in Table 2.2. Mitchell *et al.*, (1998) provided a chart (Figure 2.8) that recommends the suitability of various ground improvement techniques based on the soil gradation range. According to this chart, ground improvement by dynamic compaction can be used to treat soils that range from 4mm (gravel) at the coarser end to 0.0015mm (silt/clay) at the finer end. Because of the chart's wide spectrum of grading ranges that may suit different ground improvement methods, the chart provides only a general guide as other site specific conditions should be taken into consideration upon the selection of any particular ground improvement technique.

Table 2.2. Suitability of soil for dynamic compaction (Lukas, 1986).

Soil Category (Figure 2.7.)	Soil Type	Soil Hydraulic Conductivity /PI	Suitability for DC
Zone 1 Most favourable	Permeable Soil - Sands, gravel, granular fill	$k > 10^{-5}$ m/sec PI= 0	Improvement is achievable
Zone 2 Intermediate	Silty sands, silts and clayey silts	$10^{-5} > k > 10^{-8}$ m/sec $0 < PI < 8$	With adequate dissipation of induced pore pressure
Zone 3 Unfavourable	Impervious clayey soils	$k < 10^{-8}$ m/sec PI > 8	Not recommended

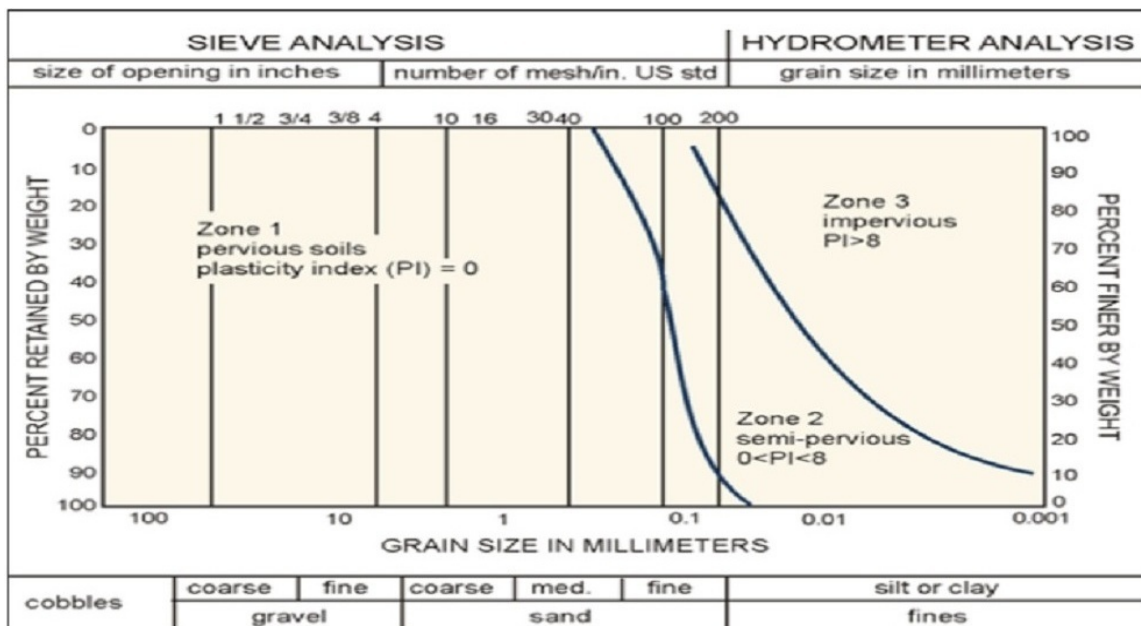


Figure 2.7. Grouping of soils for dynamic compaction (Lukas, 1986).

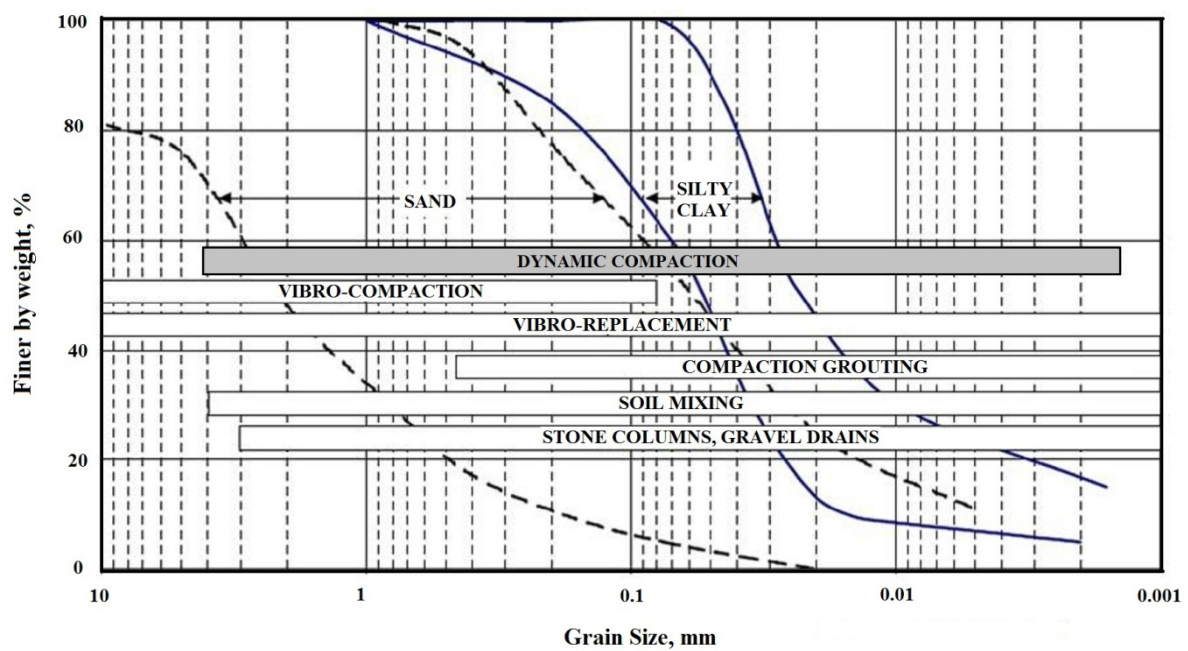


Figure 2.8. Suitability of different ground stabilisation methods verses grading range of problem soils (Mitchell *et al.*, 1998).

2.2.3 Philosophy and Design of Dynamic Compaction

Initially, before the development of any mathematical prediction tools, typical designs for dynamic compaction were based on trial and error and in-situ field investigations. The most useful of these models is given by Lukas (1986). Figure 2.9 shows Lukas's descriptive pattern of soil improvement by dynamic compaction.

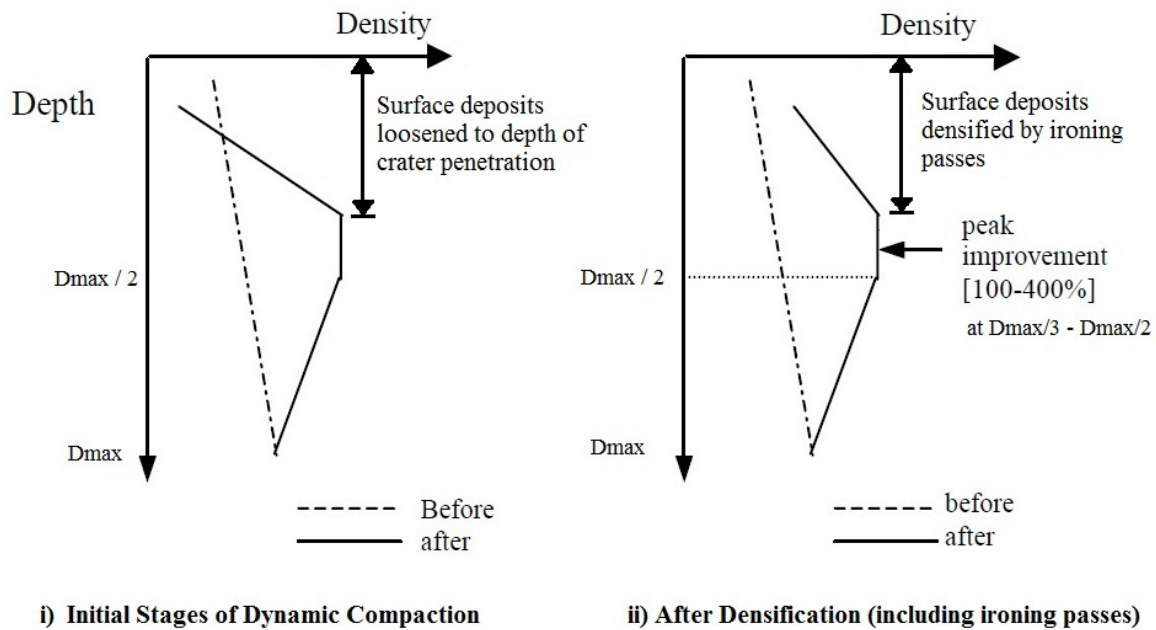


Figure 2.9. Descriptive pattern of soil improvement by DC (Lukas, 1986).

This improvement pattern is consistent with the observation by Paige-Green (1998), that the surface is loosened and compaction takes place deeper down. For ground improvement practitioners, one of the most important questions that needs answering is the depth to which improvement is reached (D_{max}). This is often estimated using the formula:

$$D_{max} = n\sqrt{W \cdot H} \quad (2-13)$$

where W =pounder mass (tonne), H =drop height (m) and n =an empirical coefficient

The formula was originally developed by Menard and Broise (1975) with $n=1$, but later modified by Lukas (1980) who suggested " n " took values 0.3-0.8 depending on soil type. This simple design approach suffers from several drawbacks. First, a wide range of values have been suggested for the empirical factor " n " resulting in considerable uncertainty in the application of this equation. Without a rational means for determining " n ", it is not clear if a single coefficient is sufficient to account for the effects of the many site specific factors and various soil properties that can potentially affect the achieved improved depth. Lukas (1986) correlated the value of " n " to the soil permeability and plasticity index, but the effects of other factors such as compressibility, initial relative density, tamper area, applied energy and tamper momentum, remain unknown. However, the modified Menard equation (2-13) is still widely used in the industry. The empirical coefficient " n " of Menard equation was further differentiated by Varaksin (1981) as $n = C \cdot \alpha$, where " C " is a speed damping factor and " α " is a stratigraphic coefficient due to heterogeneity of the soil. He suggested $C=0.9$ for cable drop and $C=1.2$ for free fall and stated that 67% of the impact energy is dissipated in the Rayleigh surface wave, which is represented by the α coefficient ($\alpha=0.7$). Table 2.3 summarises the values reported by different researchers of the dynamic compaction empirical factor " n ". Except for the case of Menard and Broise, in which the n -value was taken to be unity, the data suggests some consistency in the values for some soil types. Typical n values of 0.35, 0.5 and 0.65 were reported by various authors for municipal waste, clayey sand and silty sand respectively. These " n " values indicate that deeper zones of influence (depth of improvement) by dynamic compaction are achievable in granular soils.

Another drawback of the simple design approach of Equation (2-13) is that it only allows a limiting depth of improvement to be predicted, after some number of blows have been imparted to the ground. Quantifying the degree of improvement within the improved zone and the variation of such improvement with depth can not be predicted. Furthermore, the interim depth of improvement after a certain number of tamper blows also can not be estimated. Thus, the number of tamper blows cannot be readily adjusted to the required degree and depth of improvement of the ground.

Table 2.3. Suggested value of empirical coefficient “n” (adopted from Yee, 1999).

Source	n-values	Soil Type
Menard and Broise (1975)	1.0	all soils
Leonards, Cutter and Holtz (1980)	0.5	-
Smoltczyk (1983)	0.5	soils with unstable structure
	0.67	silts and sands
	1.0	pure frictional soils
Lukas (1980)	0.65 – 0.8	-
Mayne, Jones and Dumas (1984)	0.3 – 0.8	-
Gambin (1985)	0.5 – 1.0	-
Qian (1987)	0.65	fine sand
	0.66	soft clay
	0.55	loess
Van Impe (1989)	0.65	silty sand
	0.35	municipal waste
	0.5	clayey sand
Yee, Setiawan and Baxter (1998)	0.5	calcareous sand / coral sand
Faisal, Yee and Varaksin (1997)	0.33 – 0.39	municipal waste

Slocombe (1993) provided a typical energy-depth of influence chart (Figure 2.10) from Equation (2-13) without offering any clear explanation for how the depth of influence has been established. It is not very clear whether Slocombe’s chart was based on real dynamic compaction measurements, or it is his own interpretation to Menard’s equation towards the range of treatment depths, soil initial strength, soil type and energy input. Nevertheless, Slocombe’s chart suggests limiting depths of influence that, depending on the soil initial strength, imply the improvement depths will not increase proportionally to the input energy.

Berry *et al.*, (2000) summarised the models found in the literature available for ground improvement using impact compaction equipment. They concluded that the parameters that are most critical to a comprehensive predictive model are the mass of the compacter, the height of the drop, the contact area of the poulder, and the total energy (or total momentum). Contrary to Slocombe’s chart (Figure 2.10), the DC data presented by Berry *et al.*, (Figure

2.11) shows that the depth of influence continues increasing indefinitely. The inconsistent results from different authors and their wide range of predictions for the depth of influence indicate the limitations of the Menard type equation and the importance of selecting an appropriate value for “n” in Eq. 2.13.

From field results and a review of heavy-tamping projects, Lo *et al.*, (1990) suggested that the ground improvement is related to the enforced plastic settlement behaviour and that this is uniquely related to the energy input and the pressuremeter limit pressure (pressure at which failure occurs). They specified “energy intensity” as a function of the energy imparted per unit area and the pressuremeter limit pressure. The method indicates a “saturation energy intensity” beyond which further densification would be relatively insignificant. The method also relates the level of ground improvement to the enforced surface settlement. The essential parameters required by this method are the input energy and the limit pressure of the soil. However, the selection of the treated depth was left unlimited, which leaves the method open to overestimation of this parameter. This approach also falls short in clearly describing the influence of soil moisture and gives no guidance as to the distribution of the improvement with depth.

There is no established procedure to predict lateral ground movements resulting from the tamper impact during DC. Reliance has been placed on experience and measured field data. As part of the US Federal Highway Administration (FHWA) study on dynamic compaction (Lukas, 1995), three project sites were instrumented with inclinometers located at distances of 3.0m and 6.0m (Figure 2.12) from the point of impact. At a distance of 3.0m from the point of impact, lateral displacements ranging from 152 to 318mm were measured within a zone 6.1m below grade. At 6.0m from the point of impact, the lateral ground displacements were 19 to 76mm within the zone of 6.1m below grade. The reported lateral displacements data are site specific and depend on the soil type. As there is no model to predict this behavior, it is difficult to generalise from these observations.

Duncan *et al.*, (1986) predicted the residual stress profile following impact compaction using a method developed by Ferriera (1983). The method was originally used to predict the increase in horizontal stresses against retaining structures by compaction plant, but may also be used to predict horizontal stresses away from structures. Figure 2.13 shows the profile of

predicted residual horizontal stresses against retaining structures after compaction. It is interesting to note that there is a peak in the residual lateral stress diagram which is a function of the assumed active and passive pressure lines, and the applied dynamic stress profile.

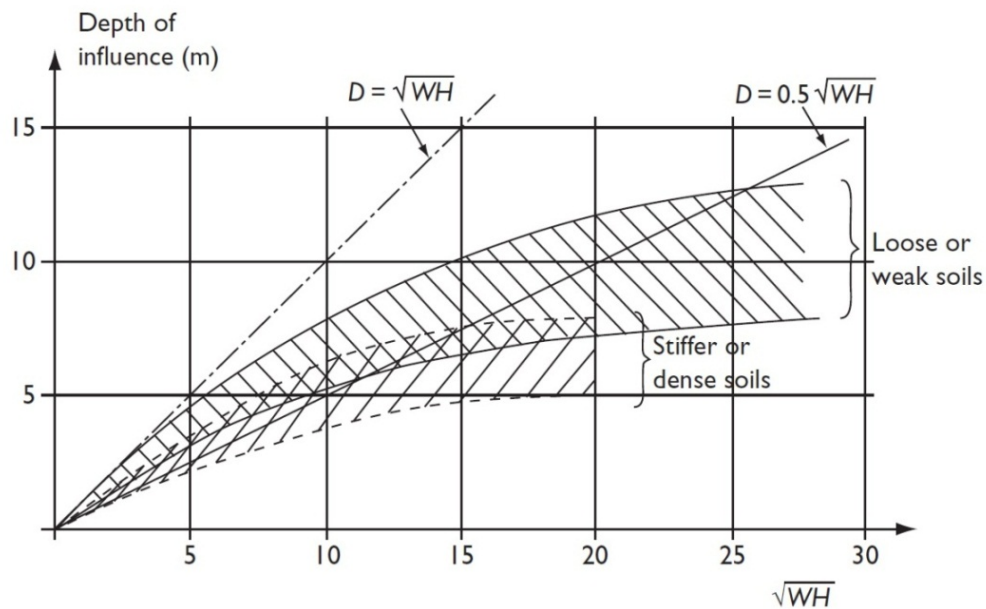


Figure 2.10. Typical energy-depth of influence chart for DC (Slocombe, 1993).

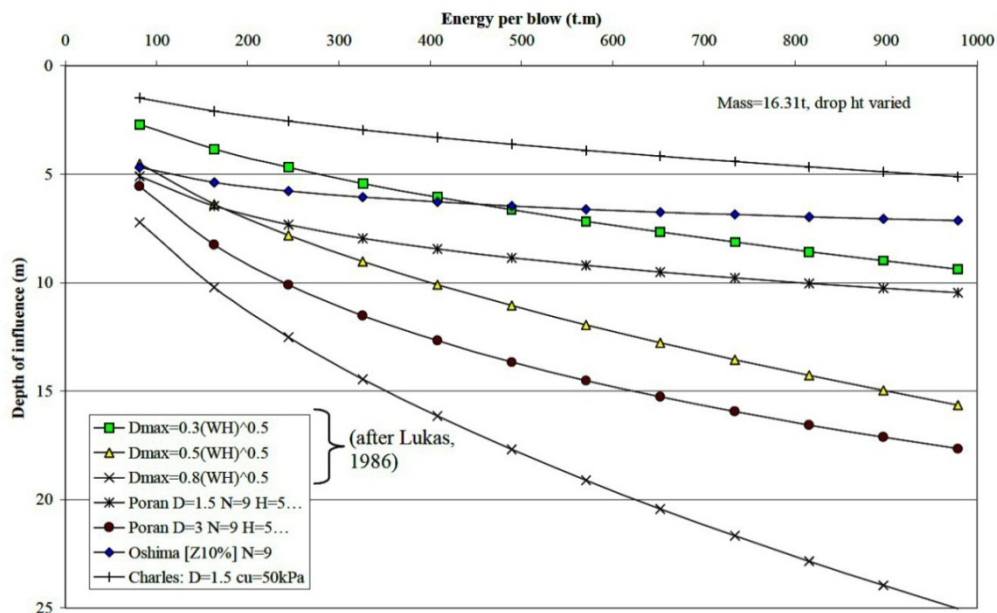


Figure 2.11. Comparison of various prediction models - depth of influence (Berry *et al.*, 2000).

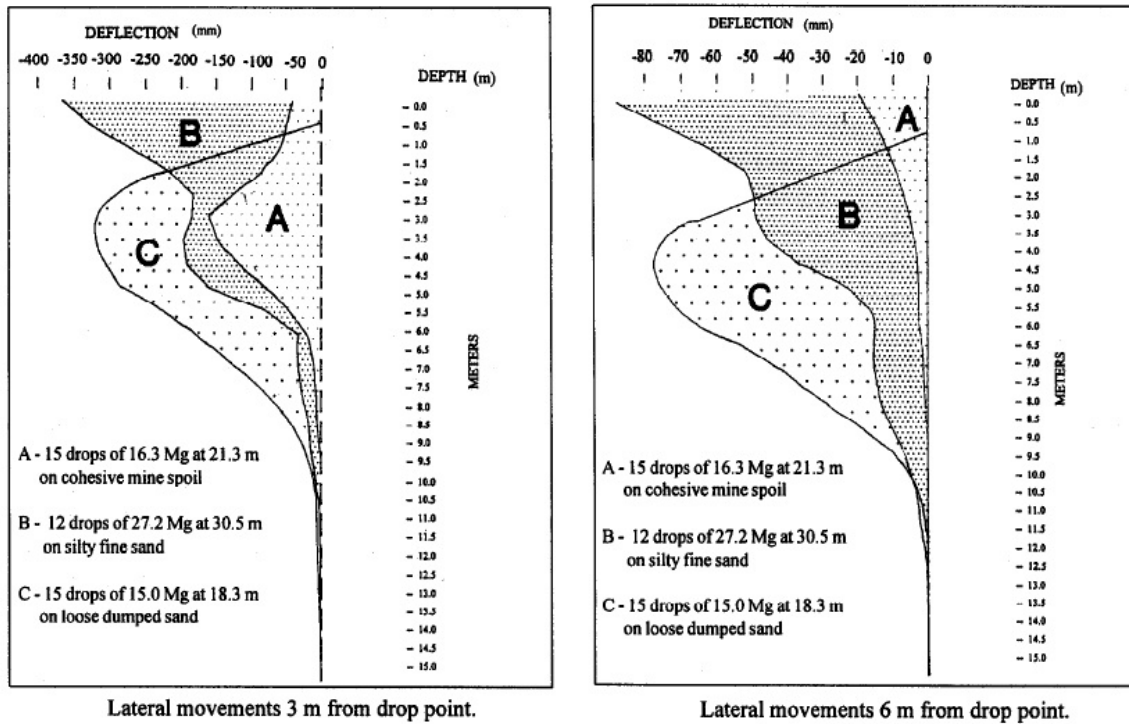


Figure 2.12. Lateral ground movement at 3 m and 6 m from impact point (Lukas, 1995)

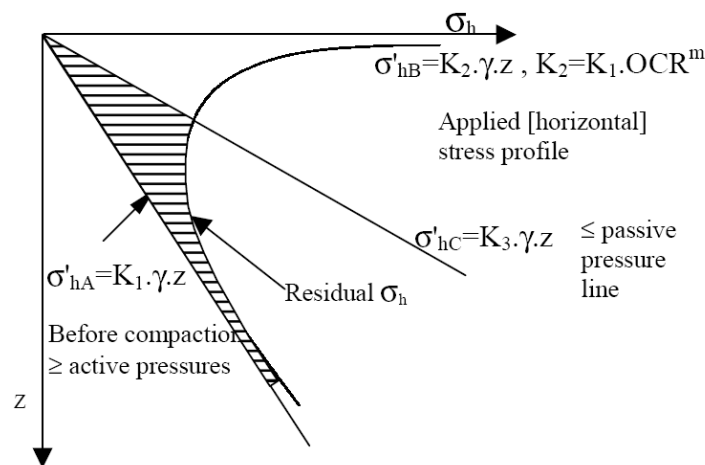


Figure 2.13. Predicted residual horizontal stresses after compaction (Ferriera, 1983).

Handy (2011) reported results from k_o (at rest lateral earth pressure) Stepped Blade tests conducted before and after dynamic compaction that involved the dropping of a 100 tonne weight for the densification of the sand foundation at the Jackson Lake dam site in Wyoming, the United States (Figure 2.14). Dynamic compaction was found to cause a substantial

increase in lateral stress, such that the after compaction average k_o is about 1.0. The narrow range of lateral stresses measured before compaction ($\pm 10\%$ from the mean) compared with $\pm 50\%$ after compaction, indicated a variability that was considered as real and not assigned to random experimental error. Handy suggested that the uneven distribution of lateral stress after compaction was the result of localized shearing that concentrated stress in one area while reducing it in another.

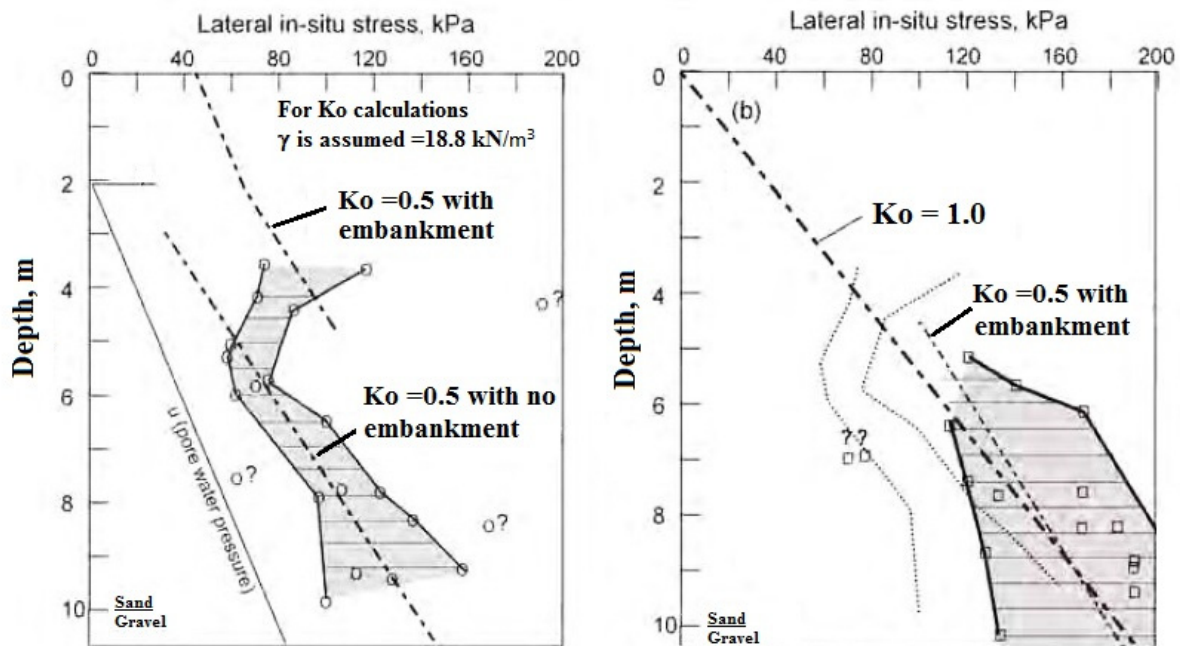


Figure 2.14. Lateral stresses measured in sand foundation at the Jackson Lake dam site in Wyoming, USA, (left) before and (right) after dynamic compaction. (Handy, 2011)

2.2.4 Quality Control and Assessment of Dynamic Compaction

The majority of DC projects are still bidded on a performance basis where the design requirement is to meet specified acceptance criteria, either tolerable settlement criteria, or specified testing requirements. A variety of methods of monitoring and quality control have been used with varying degrees of success. Quality control is an essential part of the dynamic compaction treatment to ensure that the desired result is achieved.

Engineers use cone penetration tests (CPT), standard penetration tests (SPT) and to a lesser extent pressuremeter tests (PMT) as dynamic compaction control measures to verify the

achievement of the desired degree of improvement. A list of supplementary specialty testing techniques that can be used in dynamic compaction verification may extend to include flat plate dilatometer (DMT), spectral analysis of surface waves (SASW), nuclear borehole geophysics and borehole sonic logging, borehole shear tests and seismic topography. The placement of a static load is also used, particularly in evaluations of landfills. CPT data has been found to be extremely useful for evaluation of deep compaction techniques such as, vibro-flotation, dynamic compaction, compaction by vibratory rollers and stone columns. However, cone resistance is influenced by soil density and in-situ stresses, and because dynamic compaction induces significant changes in the horizontal stresses as well as density (Handy, 2011), there are some challenges in interpreting the CPT data. Since the ultimate aim of the dynamic compaction technique is usually to improve the soil strength and compressibility characteristics, CPT data can be used directly to monitor changes in these characteristics. Sometimes this may involve the use of the term “apparent relative density”, since the real relative density is not known or required but the apparent change in relative density is of more importance. Schmertmann *et al.*, (1986) stated that increases in cone tip resistance “ q_c ” increased with the number of drops for dynamic compaction (i.e. related to energy input). Using dynamic compaction to densify 6 to 17m thick hydraulically placed fill of medium to coarse sand for a deep sea harbour project, Dumas and Beaton (1988) reported improvement of soil strength with depth following dynamic compaction and they also suggested that increases in “ q_c ” were related to energy input. No sensitivity was observed.

Sands often exhibit a drop in cone penetration resistance immediately after compaction, but cone resistance values have then been observed to increase for several weeks after compaction, which has been attributed to “static fatigue” (Michalowski *et al.*, 2012). Studies carried out by Mitchell and Keaveny (1986), Schmertmann *et al.*, (1986) and Dumas *et al.*, (1988) have shown the importance of time after the application of deep compaction techniques. For example, Dumas *et al.*, (1988) reported up to 100% increase in cone penetration resistance between tests performed immediately after compaction and tests performed 18 days later. Figure 2.15 shows cone penetration test results at one area at three different times: immediately after placement of hydraulic fill, immediately after dynamic compaction, and 8 days after the first pass of dynamic compaction. In this case, DC causes a dramatic increase in cone resistance “ q_c ” and this continues to increase with time.

Despite the wide range of verification testing available, none is ideally suited to DC applications due to the huge variation in subsurface conditions at different sites. Monitoring of the ground response, however, is probably the most important control during DC production work. Crater depth, ground heave and vibrations are all useful to determine whether the desired compaction is occurring or if the field programme needs to be modified.

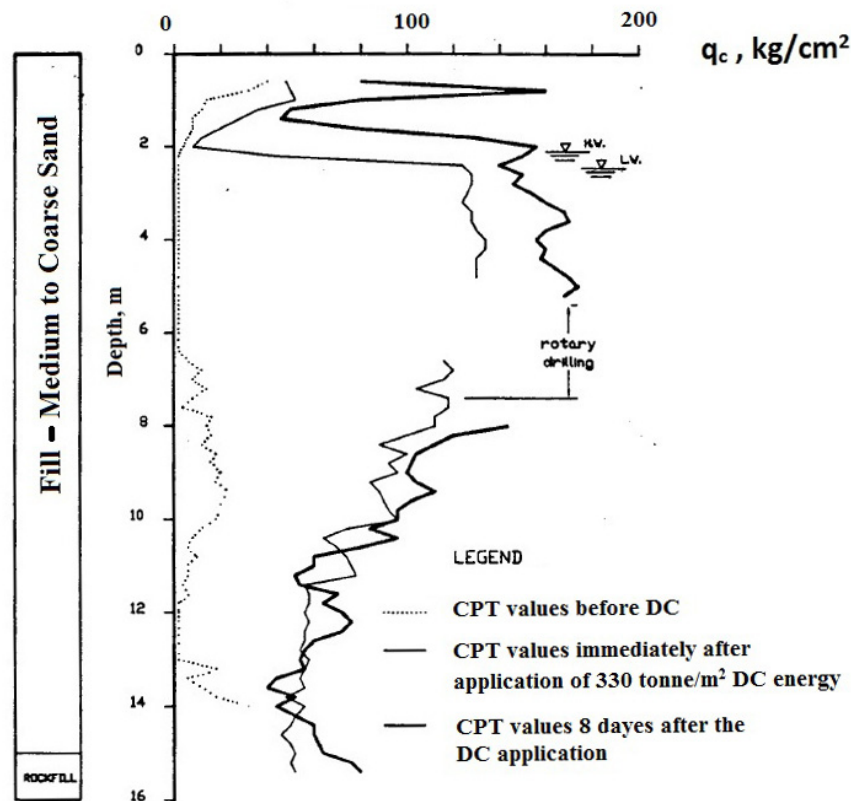


Figure 2.15. CPT test results from before and after dynamic compaction at Pointe Noire deep sea harbour (Dumas and Beaton, 1988).

2.2.5 Environmental Concerns

Dynamic compaction utilises large, highly visible equipment. The process creates high levels of noise and vibration, which must be considered in the planning of any dynamic compaction project, particularly the effect of vibration from dynamic compaction on adjacent structures. For many years, a limiting peak particle velocity of 50 mm/s has been considered as the structural damage criteria for one or two story buildings, although the tolerance to vibrations

depends upon the condition of the structure. The primary sources of data for this criterion came from blasting records of surface mining operations near residential communities (Mayne, 1985). For buried structures; particle velocity measurements have been made with a seismograph on the ground over buried utilities by Wiss (1981). He reported that pipelines and mains utilities were not affected by particle velocities of 76 mm/sec.

By studying the effect of ground vibrations on structures, Siskind *et al.*, (1980) established threshold particle velocities beyond which cracking in walls of modern houses may occur. Measurements from dynamic compaction projects have indicated that the frequency of ground vibrations from dynamic compaction is generally between 6 to 10 Hz. At this frequency range, the U. S. Bureau of Mines criteria indicates that the particle velocities should be less than 13 and 19 mm/sec for old and modern structures respectively, to prevent walls from cracking.

2.3 RESEARCH WORKS OF DYNAMIC COMPACTION

In the last 30 years, studies of dynamic compaction have considered three main approaches; (1) analytical and mathematical models based on laboratory experimental data and in-situ measurements from case histories or full scale tests, (2) physical models and (3) finite element numerical models and simulations. The following sections present the most prominent of these approaches:

2.3.1 Dynamic Compaction by Analytical and Mathematical Models Derived From Field or Experimental Observations

Early attempts at assessing the effects of a dynamic load on the soil surface were based on estimating the impact stress. The impact stress can be used with elastic stress distribution formulas to predict stress distributions in the ground. Lewis (1957) proposed an equation (2-14) that related the contact stress to the impact energy ($\frac{1}{2}mv^2$) and a spring stiffness representing the ground response.

$$p = \sqrt{\frac{1}{2}mv^2 \cdot \frac{k_s}{A}} \quad (2-14)$$

P = impact pressure, m =mass, v =impact velocity,

A =base area, k_s = spring constant

Even if it is acceptable that the soil provides a constant stiffness it is not practical as applying equation (2.14) to maintain a constant impact pressure, the impact energy must be proportional to the square root of the base area or, for a square base, proportional to the side dimension. This is not a very practical approach since it is difficult to keep the contact stresses down by raising the energy level without adjusting the side dimension of the tamper.

Wallays (1983) suggested an indirect method to predict the settlement profile at various depths below the compacted surface. The energy from the drop of the mass is equated to the work done by the vertical stress induced in the soil, plus the work done in moving the soil mass by residual settlement. This derivation results in equations predicting surface stress, surface settlement, and settlement profile. This method can also be used or extended to predict variations in the density of soil or the void ratio within the deformed profile, but it does not clearly indicate the in situ ground condition, or the presence of the ground water table. Material properties were dealt with indirectly through soil stiffness in the derivations. Charts showing results of measured settlement compared to the predicted settlement were provided, but there is not any record of the use of this method.

Smits and De Quelerij (1989) reported a case study of DC in deposits of dry, loose and dense sand, where CPTs were performed at and between the impact locations. Contrary to everyone else's work but consistent with their 1-D theoretical model, the CPT results showed that compaction was concentrated immediately below the drop locations and there was no lateral spread of the compacted zones. The field observations were used to justify the validity of one-dimensional modelling of DC in dry sand. Their model computes the extent of the plastic zone (influence depth) based on the impact velocity, tamper mass, contact area, and elastic soil properties using an extension of the approach developed by Scott and Pearce (1975), which has been discussed above, as:

$$D = \frac{m}{\rho_{max} A} \left[-1 + \left(\frac{\sigma_e + \alpha V_0^2}{\sigma_e} \right)^{0.5} \right] \quad (2-15)$$

where

D : compacted zone = $Z_p - Z_s$ (Figure 2.16)

ρ_{max} : maximum possible soil density

m : falling mass

A : contact area

σ_e : vertical stress at elasticity limit

V_0 : Impact velocity

α : density ratio

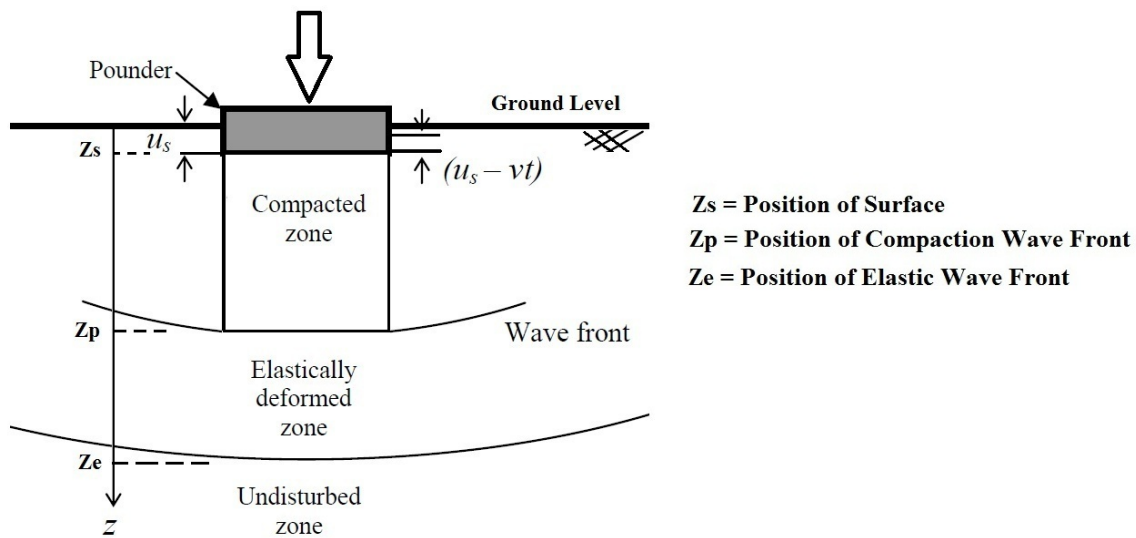


Figure 2.16. 1-D theoretical model of dry soil deformation due to surface impact
(Smits and De Quelerij, 1989)

Chow *et al.*, (1992a) and (1992b) proposed a different analytical approach where the one-dimensional wave equation model for analysing pile driving was modified by replacing the pile with a column of soil extending to at least the anticipated depth of ground improvement. In their method, the soil surrounding the soil column was modelled as linear elastic springs and linear dashpots (Figure 2.17). They proposed an implicit finite element method to solve the equation of the motion of the soil column. The developed wave-equation model enabled a rational selection of some operational parameters like the poulder mass, drop height, number of drops per pass, and number of passes but could not provide a solution to determine the print spacing. This method indirectly predicts the reduction in the void ratio as measured by

the relative density “ Dr ”. Good correlation was found between predicted and measured parameters. However, because the problem is three dimensional, due to the stress wave propagation involved within the process, this simple one dimensional model can not correctly represent the physics of the problem.

Rollins *et al.*, (1998) studied the influence of moisture content on dynamic compaction efficiency at six field test cells at the base of the Wasatch Mountain Range in Nephi, Utah. Using energy levels comparable to those employed in the field, the optimum moisture content and the maximum dry unit weight were found to be similar to those predicted by laboratory proctor testing (standard proctor, modified proctor, and 1/3 of the standard proctor). In this study, the compaction efficiency was evaluated by: (1) crater depth measurements, (2) cone penetration tests before and after compaction, and (3) undisturbed samples before and after compaction. Results showed that crater depth increased by a factor of 4 as moisture content increased while the degree of improvement increased up to a moisture content of about 17% (similar to the optimum moisture content predicted by laboratory proctor testing) and then declined. The work concluded the concept of optimum moisture content can be valid for dynamic compaction, with crater depth and depth of improvement increasing slightly as the moisture content increases. However, crater depths became excessive at moisture contents beyond the optimum resulting in difficult and time consuming poulder extraction.

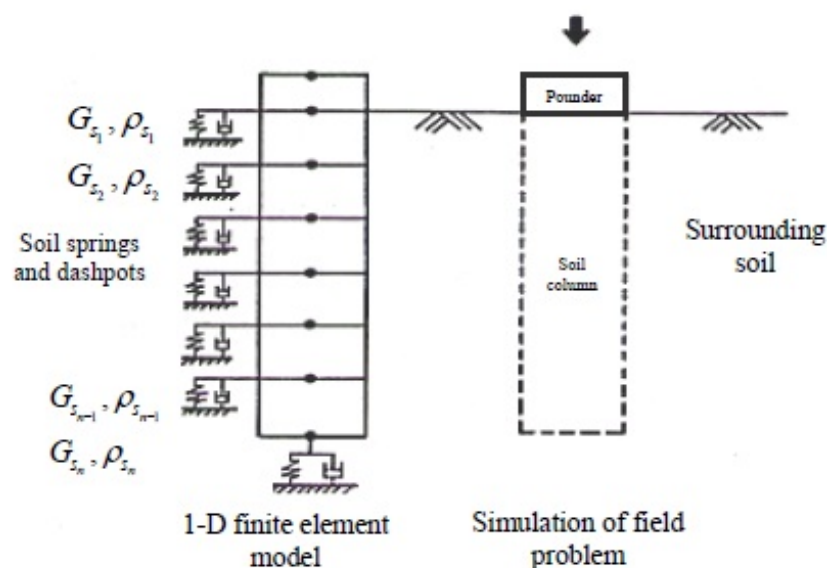


Figure 2.17. The one-dimensional wave equation model (Chow *et al.*, 1992a).

In DC, the grid spacing has a significant effect on the soil improvement within the grid but so far has received little attention. Since the intensity of applied energy is defined as the total applied compaction energy per unit print area:

$$I = \frac{nWH}{S^2} \quad (2-16)$$

where:

n = total number of blows; W = pounder weight;

H = drop height; and S = print spacing, center-to-center.

Assuming that the densification effect is proportional to the energy intensity (I), then the same densification effect should result from simultaneously increasing the number of drops, impacting energy and the grid spacing. However, field evidence (Choa *et al.*, 1979) suggests that this is not the case.

Chow *et al.*, (1994) studied the influence of print spacing on the dynamic compaction of loose granular soils and developed an approach to predict the lateral extent of soil improvement around the pounder in terms of change in the friction angle of the soil. This change in the friction angle was described by Equation (2-17). At a distance three times the diameter of the tamper, the effect of the DC becomes negligible. They concluded that the critical locations are at the centre of the grid and at the middle of the side of the grid where the least amount of improvement occurs.

$$\frac{\Delta\phi}{\Delta\phi_b} = 0.642 - 1.180 \log \frac{X}{D} \quad (2-17)$$

where:

$\Delta\phi$: Change in friction angle at distance X from the centre

$\Delta\phi_b$: Change in friction angle beneath the tamper

D : Tamper diameter

X : Distance measured from the centre of tamper

By analysing the field data and field testing results from three case histories of dynamic compaction projects, Chow *et al.*, (1994) computed the change in the friction angle after a number of DC passes and found them to agree reasonably well with those estimated from the measured CPT results.

Nouri *et al.*, (2008) reported a case history from the Shahid Rajaei Port Complex Development on the shores of Persian Gulf near Bandar-Abbas where dynamic compaction was used to treat reclaimed layers susceptible to liquefaction (silty sand with maximum depths of 7 to 12 metres and a fines content of 20% – 40%). They investigated reducing the dimensions of the tamper (for the same mass) and compensating the decrease in the tamper area by reducing the grid spacing from 9×9m to 6×6m to increase the applied energy per unit area of the DC print pattern. By comparing the values of the depth of influence from empirical formulae with the pre/post CPT results to validate the densification process at trial locations, they noticed that decreasing the tamper area by 55%, together with a 25% reduction in the grid spacing, provided a satisfactory depth of improvement of about 13m, despite the presence of high fines content. Their back calculated values of the coefficient "n" in the empirical relationship ($D_{max} = n\sqrt{WH}$) resulted in an average value of 0.42, which was in reasonable agreement with their first assumption of n= 0.40. They claimed that a better overlap of the stress distribution in the underlying layers was responsible for a deeper level of improvement in the soil layers and more effective dynamic compaction program was achieved from the reduced tamper area and grid spacing.

Thevanayagam *et al.*, (2009) and Nashed *et al.*, (2009a) and (2009b) together presented a series of three papers dealing with the theory, current design, and results of a numerical simulation of DC of saturated sands and silty sands supplemented with wick drains. Adopting the theoretical solution outlined in Sections 2.1.1 and 2.1.3 for energy partition and geometric radiation of impact energy respectively, the authors proposed a theoretical model for spatial distribution of the energy dissipated in the soil during dynamic compaction, a pore pressure model based on energy principles to estimate the spatial distribution of pore pressures induced during dynamic compaction, and a coupled consolidation model for the dissipation of pore pressure and densification of the soil. This theoretical model was later used in a numerical scheme to implement the theoretical models in simulating dynamic compaction at three different sites and to obtain post improvement densities and resistance to penetration.

They assumed that the energy attenuation model is valid under different confining stresses, and is not affected by changing soil density and stiffness under successive impacts. They also stated that these assumptions need to be verified using field tests before using the model in different cases. The authors proposed a set of simplified design charts that can be used to determine the post improvement resistance to penetration of saturated sands and non-plastic silty sands supplemented with pre-installed wick drains. The validity of the proposed design charts has not been established by independent case studies.

Bo *et al.*, (2009) studied the dynamic compaction densification method utilised at the Changi East reclamation site in Singapore to improve reclaimed sandy fill. Using the field data, they investigated the effectiveness of the densification method and the effect of various factors affecting the depth of influence such as the shape of the poulder (including square, hexagonal and circular), the drop height (12.5 – 25.0m), the lifting and dropping mechanism (crane and tripod), and the rate of pore pressure dissipation. They concluded that the depth of influence can be estimated by applying the established and generalised empirical correlation ($D_{max} = n\sqrt{WH}$), although the equation can be slightly different depending upon the geometry of the poulder and the dropping mechanism. In contradiction to the results of Smits and De Quelerij (1989), they suggested that the centroid point within a compaction pattern is the most well-compacted, and that directly under the poulder is often the least compacted and should not be used as a quality control point.

Adam *et al.*, (2007) have conducted in situ measurements (measuring the acceleration of the falling mass and the soil) in which the falling height was changed frequently, and theoretical investigations of the decay of free soil vibrations caused by the falling weight after each impact were compared with measurements. They established that the interactive behaviour between the soil and the falling mass allows for a site-specific optimisation of the heavy tamping technique. Adam *et al.*, (2007) and Kopf *et al.*, (2010) used the decay of the amplitudes of the free vibrations to determine a damping coefficient and a damped natural frequency, which were used to determine the Poisson's ratio and the modulus of elasticity of the ground after each impact. They assumed that the soil behaves like a linear elastic half space during the free vibration phase and, therefore, the Poisson's ratio and the modulus can be derived from their measurements. The aim of the work was to gain a reliable indicator of the degree of compaction of the soil immediately after each impact, hence a method for

controlling the compaction and documentation. Both Adam *et al.*, (2007) and Kopf *et al.*, (2010) assumed an elastic decay of the free soil vibrations even though still increasing pore water pressures following impact meant that effective stresses would not be truly representative of the compacted state. This assumption provided a theoretical approximation to the model that could be solved similar to a viscous-damped single degree of freedom (SDOF) system.

2.3.2 Dynamic Compaction by Physical Models Laboratory Testing

To better understand dynamic compaction, several scholars have conducted centrifuge experiments and 1-g scaled physical models to study the dynamic compaction processes.

Wetzel and Vey (1970) conducted a number of 1-g physical model tests in which they measured the stress and strain in Ottawa sand models with relative densities of 37% - 86% generated due to the impact of a tamper on the model surfaces. Measurements were made by soil stress and strain gauges embedded in the soil beneath the impact footprint and an accelerometer mounted on the falling mass. The test results showed that the distribution of vertical stresses with depth, due to the impact, was similar to the Boussinesq solution. Jessberger and Beine (1981) conducted 1-g model testing with an accelerometer attached to a falling mass to determine the relationship between the decelerations and impact velocity. They concluded that the contact stress is proportional to the force of the impact for a constant base area, and proposed a stress distribution formula based on Fröhlich's (1934) equation.

Mayne and Jones (1983) proposed a slightly different form of Jessberger and Beine's equation, based on the integral of the area under the deceleration-time graph. The formula Mayne and Jones gave for the deceleration ratio (peak deceleration of the weight at the ground surface normalised to the gravitational constant) presents values close to those measured by Heyns (1998) on the tube axles of impact compaction plant. The one-dimensional model of Mayne and Jones (1983) has been widely used to estimate the impact stresses. Poran and Rodriguez (1992a) and Poran *et al.*, (1992) developed a relationship based on the total energy rather than momentum. They conducted a number of 1-g physical model tests and studied the effects of different parameters on the results of dynamic compaction. They used dry Boston sand for the 1.22x1.22x1.22 m³ models and presented some design

curves based on the experimental results. They derived a correlation between the dimension of the plastic zone, which is assumed to have a semi-spheroid shape (Figure 2.18), and the input energy. Equations (2-18) and (2-19) show the dimensions of the plastic zone they proposed as a function of the normalised energy input.

$$\frac{b}{D} = j + k \log \left(\frac{NWH}{Ab} \right) \quad (2-18)$$

$$\frac{a}{D} = l + m \log \left(\frac{NWH}{Ab} \right) \quad (2-19)$$

where

a : Spheroid base radius

W : Falling weight

b : Spheroid height

H : Falling height

D : Diameter of the falling mass

A : Tamper area

N : Number of drops

j, k, l, m : Regression constants

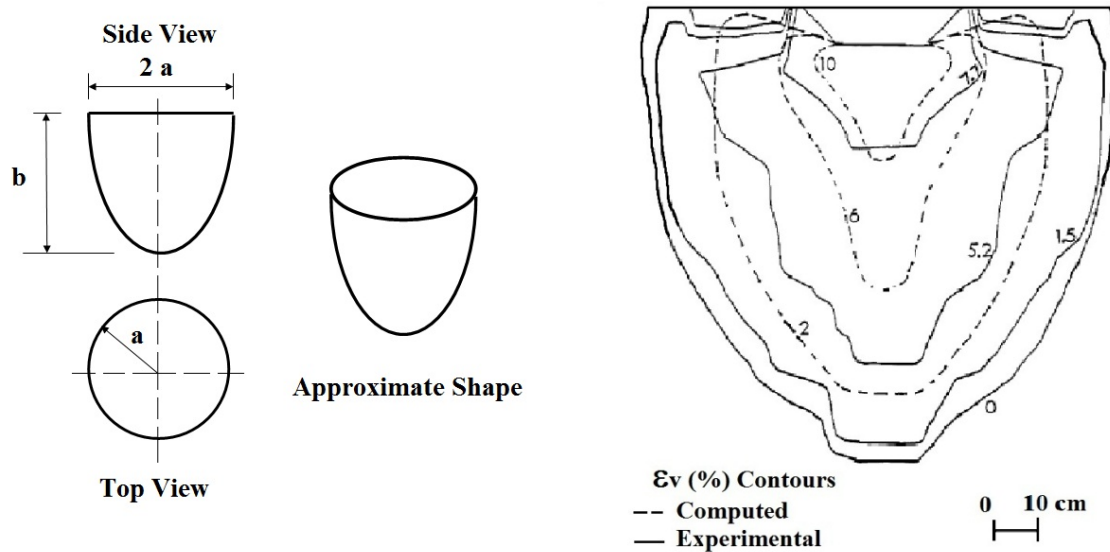


Figure 2.18. A semi-prolate-spheroid approximation for DC density contours (Poran *et al.*, 1992).

The significance of this approach arises for being the first attempt to establish a relationship between the number of impacts “N”, the diameter of the falling mass “D” and the size of affected zone (the semi-prolate-spheroid) as expressed by Equation 2-19.

Oshima and Takada (1994 and 1997) used data obtained from site tests and centrifuge model tests to study the momentum of a tamper and presented some graphs to estimate the depth of improvement during dynamic compaction. Their centrifuge model tests were conducted in a semi-cylindrical container of 30cm in diameter and 20cm in height (Figure 2-19). The work investigated the use of multiple drops using sandy soil with a water content of 4 % compacted to 50% relative density. Experiments were conducted with tamping taking place at centrifugal acceleration of 100 g. Soil deformation was observed through a glass plate on the front face of the model container. Their experimental results suggested that the crater depth could be related to the momentum of the falling weight and that the crater depth is proportional to the square root of the number of drops. Refer to Equations (2-20) and (2-21).

$$P = c \frac{mv_o}{A} \quad (2-20)$$

$$P_N = c \frac{mv_o}{A} \sqrt{N} \quad (2-21)$$

where:

P : Crater depth due to single impact

A : Tamper contact area

P_N : Crater depth to N numbers of impacts

v_o : Impact velocity

m : Tamper mass

c : constant coefficient ($m^2 \text{sec/tonne}$).

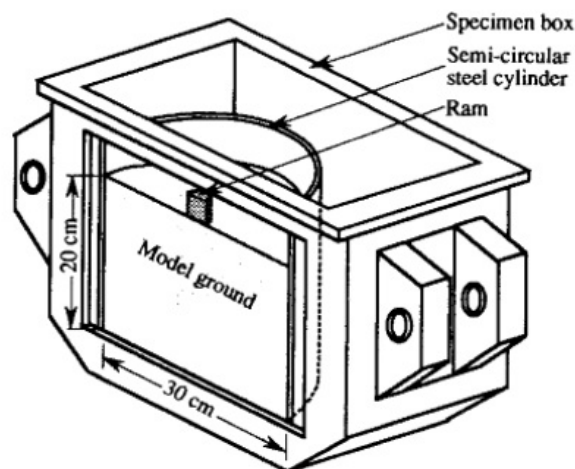


Figure 2.19. Dynamic compaction model by centrifuge test (Oshima *et al.*, 1997).

From 1-g model impact tests, Thilakasiri *et al.*, (1996) studied the stress history of soft soils under impact loading using analytical and experimental techniques. They proposed an improved analytical model to estimate the surface stress and surface deformation, while accounting for the non-linearity of soil immediately below the poulder as well as in the immediate vicinity of the poulder. In their procedure the impact zone is modelled by three distinct zones; (1) a zone beneath the falling weight undergoing non-linear axial deformation while in vertical motion, (2) an inner zone immediately surrounding zone 1 with non-linear shear deformation, and (3) an outer zone undergoing a relatively lower degree of (linear) shear deformation. The constitutive parameters of the soil that were pertinent to this model were obtained from a modified dynamic compression test that simulated the impact conditions. The results showed good agreement between the analytical predictions of the impact stress history and penetrations. The analytical predictions were verified by a series of impact tests in the laboratory that were measured with pressure transducers and accelerometers. This analytical formulation requires the amount of deformation around the poulder (radius of zone 1) as an input to determine the radius of the non-linear shear zone. This leaves the methodology depending on past experience or pilot tests.

Using centrifuge models of sand, Oshima and Takada (1997 and 1998) reported that the depth and radius of ground improvement increased with the impact momentum even when the impact energy was constant. They attributed this effect to an enhanced transfer of energy to the ground as the momentum increased. They proposed an empirical model, described by Equations 2-22 and 2-23, that predicts the degree of compaction achieved in terms of the total momentum of the poulder and constants that depends on the relative density of the soil.

$$Z = a_z + b_z \log(mvN) \quad (2-22)$$

$$R = a_R + b_R \log(mvN) \quad (2-23)$$

where :

Z =the vertical depth of improvement, N =number of impacts

R =radial improvement,

a & b are empirical constants from laboratory testing.

mvN = ram momentum,

In this model, the compacted area is defined by the depth Z and radius R of the bulb shaped area as indicated in Figure 2.20. Empirical constants “a” and “b” were evaluated for changes in D_r of 40%, 20%, and 10% respectively, corresponding to an initial D_r of 35%. A notable omission from this model is the base area of the poulder, which has been shown to influence the effective zone in other studies (Chow *et al.*, 2000), and there is no indication of how the empirical constants vary with other DC conditions.

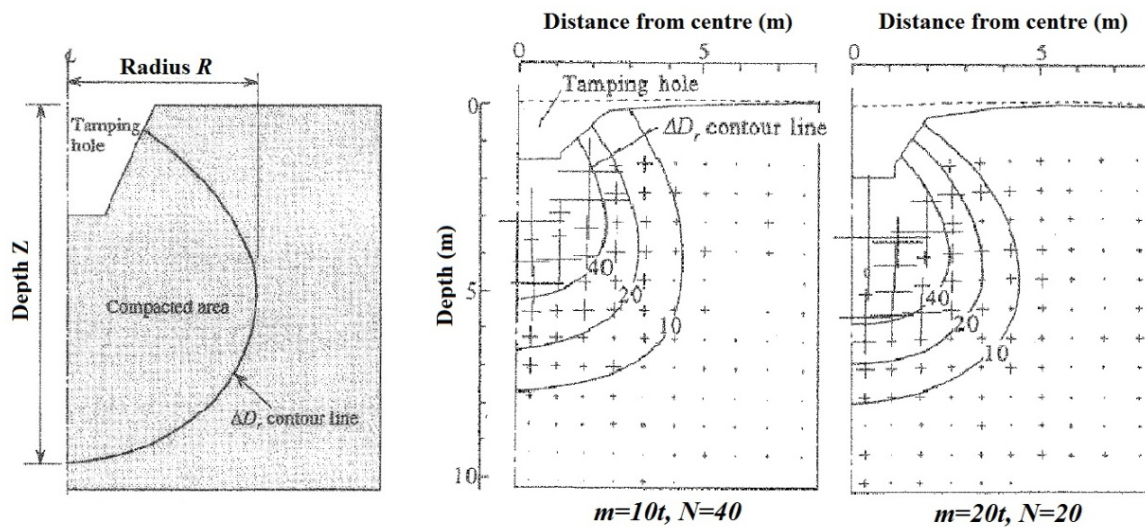


Figure 2.20. Definition of compacted area and comparison of compacted areas under different ram weights (Oshima *et al.*, 1997).

Jafarzadeh (2006) conducted a series of 1-g physical model tests studying the parameters affecting the DC method on loose dry sand models instrumented by total stress gauges and accelerometers. The author suggested a design curve for estimating the improvement depth due to dynamic compaction by employing combinations of compaction energy level, tamper weight, drop height and drop number. Results from this study suggested that the presented Equation 2-21 by Takada and Oshima underestimates the normalized crater depth, compared with the measured data in low compaction energy levels (2 and 5 N tampers), the situation being opposite for high energy levels (10 and 23 N tampers).

By means of centrifuge models and instrumentation, Parvizi and Merrifield, (2004) and Parvizi (2009) monitored the response of soil in terms of magnitude, arrival times of peak particle velocity (PPV) and peak pressure at various locations within 1:20 scale model at 20 g subjected to surface impacts. The authors used the concept of WAK (Wave Activated

Stiffness) test to monitor the degree of improvement during this process. The results, presented against relative density and distance from the point of impact, showed evidence of change in soil response (peak particle velocities and peak pressures) due to changes in the relative density of the soil.

Research works acknowledge that the effect of densification is strongly influenced by the dynamic response of the soil as well as the falling weights (or tampers). Previous studies of tamper geometry in DC have suggested that tamper shape may have some bearing on how the soil responds. This has been primarily assessed by the volume displaced at the surface, expressed in terms of the geometry of the crater through its shape, area, depth and heave around the circumference (Mullins *et al.*, 2000 and Feng *et al.*, 2005), but these quantities are not obviously related to densification at depth. For example, an empirical correlation between the depth of improvement and initial shear strength of soils, depth of the crater (penetration), and impact energy per unit area has been proposed by Mullins *et al.*, (2000). The effect of different tamper geometries on the depth of improvement has been quantified by subsurface investigations by conducting cone penetration tests or using a portable nuclear density gauge before and after DC impacts.

DC physical model tests using Mai-Liao and Ottawa sands with 90° apex angle conical and flat bottomed tampers have been performed by Feng *et al.*, (2000). The conical tampers were claimed to be more efficient than flat bottom tampers in Mai-Liao sand, but to provide a similar performance in Ottawa sand. Similarly to conventional footings, the difference was considered to arise from the different dilatancy of the two sands. Conical and flat bottom tampers were reported to provide near identical depths of improvement, as interpreted from cone penetration tests (Feng *et al.*, 2005), when Mai-Liao sand was mixed with fines for fines contents between 3.4% and 14%. However, the authors claimed that better overall performance was gained with conical bottom tampers as a result of more lateral densification. In a study using well graded Sakarya River sand, the results showed that conical bottomed tampers produced deeper influence zones than flat bottomed tampers, and also created deeper and wider craters, again suggesting that the shape of the tamper could influence the efficiency of dynamic compaction (Arslan *et al.*, 2007). Based on the displaced volumes (size of crater), they concluded that the energy consumed to obtain a given amount of improvement with the conical-bottom tampers was less than half that with the flat-bottom tampers.

Using cylindrical, oval, square, and conical tampers in DC tests of loose Arak sand (Ghazavi *et al.*, 2010), a greater depth of improvement was claimed from flat, cylindrical tampers than flat square and conical tampers for the same dropped mass, but the method used to assess the depth of improvement was not specified.

Nevertheless, some of these studies were limited because the stress dependent behaviour of soil was not properly accounted for in the small scale 1-g models, which made it difficult to make quantitative interpretations of the experimental data. Centrifuge models may well address the stress level issue but they make it difficult in most cases to host measuring instrumentation and/or to include sufficient details to reproduce the essential features of the prototype environment because of the much smaller centrifuge models. Details of the governing scaling laws are given in Taylor (1995) and Chandrasekaran (2001), with the latter also highlighting the limitations associated with the modelling of dynamic loading in centrifuges such as the conflict in the dynamic time relationship and diffusion time relationship and resonance conditions in the centrifuge machine due to dynamic force.

2.3.2.1 Application of Spatial Deformations and Strain Measurement by Image-based Displacement in Geotechnical Physical Modelling & Laboratory Testing

The effectiveness of dynamic compaction from field measurements has been quantified mainly using pre- and post-compaction CPT tests, as well as taking surface measurements of the impact such as the size of crater and induced ground heave around the impact location. Both approaches are only indicative since they can not explain the actual mechanism of the dynamic compaction process. The theoretical analysis of CPT results is difficult and, hence, limited since the cone tip resistance “ q_c ” is affected by the horizontal stress near the cone tip in addition to the relative density of soil. On the other hand, field studies that have used measurements from stress sensors and accelerometers have been very limited and have not provided sufficient information to explain the densification mechanism that takes place at depth.

Employing full scale models is usually not possible during the design process of most geotechnical projects, because of the cost, scale, and complexity of these projects. The needed repetition of full scale models to accommodate the range of DC parameters making

this option totally infeasible. Hence, geotechnical engineers have been making use of reduced-scale physical models to study the performance and/or to verify the behavior of geotechnical systems. One of the main challenges of physical modeling is to make soil deformation measurements of reasonable accuracy. The development of methods for observing deformation patterns in soil has been pursued by soil mechanics researchers for many years, and a brief review of these developments is provided here.

With the development of the digital photography and X-ray tomography techniques over the last twenty years, studies on spatial deformation and strain localisation have grown at a very rapid pace offering better characterisation of internal stress distribution and local deformations at scales intermediate between the granular and sample scales while high speed photography offers potential for the real time evolution of stress/strain localisations in dynamic loading. Several methods have been used to measure continuous spatial deformations in soils. The use of markers embedded in soil models is perhaps the oldest imaging technique reported for measuring deformation and hence strain levels in soil models and this has usually involved tracking the planar movement of markers at the glass boundaries of plane strain models. Image-based displacements within a soil mass were first studied using an X-ray method and embedded lead markers by Gerber (1929). Successive radiographs were taken to follow the movement of these markers. Roscoe *et al.*, (1963) used this system studying incremental strain patterns in large sand models and shear apparatus. James (1965) successfully used this technique to generate contours of shear and volumetric strain with a precision of 0.1% through large (2.0 m × 0.5m) models. In the 1960s and early 1970s, Robinsky and Morrison (1964), Kirpatrick and Belshaw (1968), Butterfield and Andrawes (1971), Bransby and Milligan (1975) and more recent Bourdeau (1993) contributed to the study of spatial deformations in soil using x-ray photography and lead markers embedded in models to track the markers motion. Results from those experiments were typically limited by the fact that embedded markers do not provide a continuous image of the measured field. Furthermore, markers other than coloured sand particles exhibit static and dynamic characteristics that are often different from those of the surrounding soils and therefore can change the response of the measured field. More importantly is the limitation that deformation and strain localisation have only been measured at a macro scale, i.e., the scale of the specimen.

More recently, newer techniques such as computerized axial tomography (CAT scan) and magnetic resonance imaging (MRI) have been used by Shi *et al.* (1999), Wong (1999), and Ng *et al.* (1996) for experimental modeling of geotechnical problems. However, the far-reaching applications of these techniques are limited by the relatively high cost of the apparatus, difficulties in the experimental setup, and interpretation of results. Other advanced optical techniques have also been utilized in soil mechanics research for deformation measurements. Woods *et al.*, (1974) used holographic interferometry (a technique which enables static and dynamic displacements of objects with optically rough surfaces to be measured to optical interferometric precision - i.e. to fractions of a wavelength of light) for studying the effectiveness of slurry-filled trenches for dynamic isolation of footings. Photoelasticity, which allows visualisation of stress distribution in granular materials, has been used by Drescher (1972) and Drescher *et al.*, (1976) to explore the stress distribution and transferring of stresses between granular particles.

With the development of geotechnical centrifuge modeling conventional photography was introduced to record the movement of markers through window exposing a plane of the soil model into which target markers are placed. Close-range photogrammetry in centrifuge modeling was first reported by Taylor *et al.*, (1998). The photogrammetry allows the image-space measurements of target displacement to be corrected for image distortion and camera movement.

With the rapid development in digital photography and information technology, image-based displacement and strain measurement in geotechnical testing has become more reliable and feasible. At the same time, recent developments in computer imaging and digital photography have resulted in wide-spread use of optical techniques in industrial settings and academic experiments. Digital imaging has also allowed for computerized target tracking, which permits faster and more accurate analysis. Raschke *et al.*, (1996), Gustafsson *et al.*, (1996), and Guler *et al.*, (1999) studied micro-deformation of granular soils by analyzing particle-level movement. Digital photography and computerized tracking software allowed for larger scale deformations to be tracked by monitoring a grid of patches on soil samples, Alshibli and Sture (1999) and Saada *et al.*, (1999). Nevertheless, these advances do not permit monitoring deformation inside opaque soil models. Optical methods have been used to measure the response of soil-like transparent materials, which model specific soil properties. Allersma

(1982) has studied the stress distribution under simple shear using translucent media made of crushed glass and a matched refractive index fluid, and this approach has been used as well to study the response of saturated embankments under seismic loading by Konagai *et al.*, (1992, 1994).

Guler *et al.*, (1999) measured particles movement in granular soils using image analysis by adapting two techniques (MATCH and BMAD) to determine soil particle displacement vectors using the images from direct shear tests. In their study, images of Ottawa sand at the interface with a steel plate were acquired using a microscope camera. Then the images were analyzed by block matching and individual particle tracking methods. Images of sand particles in contact with a steel plate and displacement vector of sand particles from image analysis of are shown in Figures 2.21 and 2.22 respectively. Alshibli and Sture (2000) conducted a series of plane strain experiments on sands. A grid pattern was imprinted on the latex membrane for each specimen and images were taken to analyze shear band formation. White *et al.*, (2003) used the particle image velocimetry (PIV) technique to investigate the installation of a displacement pile. Take (2003) inspected the progressive failure under moisture cycles in a clay embankment model using PIV. White and Take (2002) have developed a MatLab script called "GeoPIV". It allows the user to choose individual pixels of targets placed on the surface within a digital image and a known search area for each point.

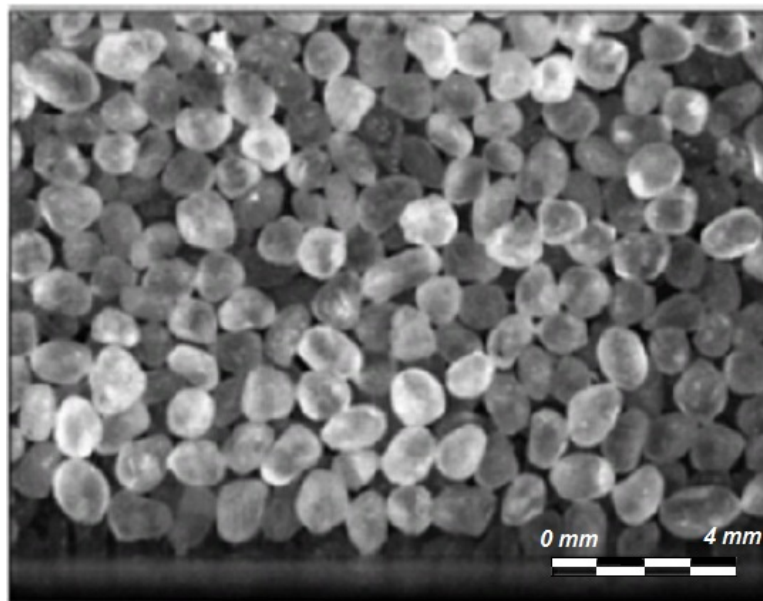


Figure 2.21. Image of Ottawa sand in contact with the steel plate (Guler *et al.*, 1999).

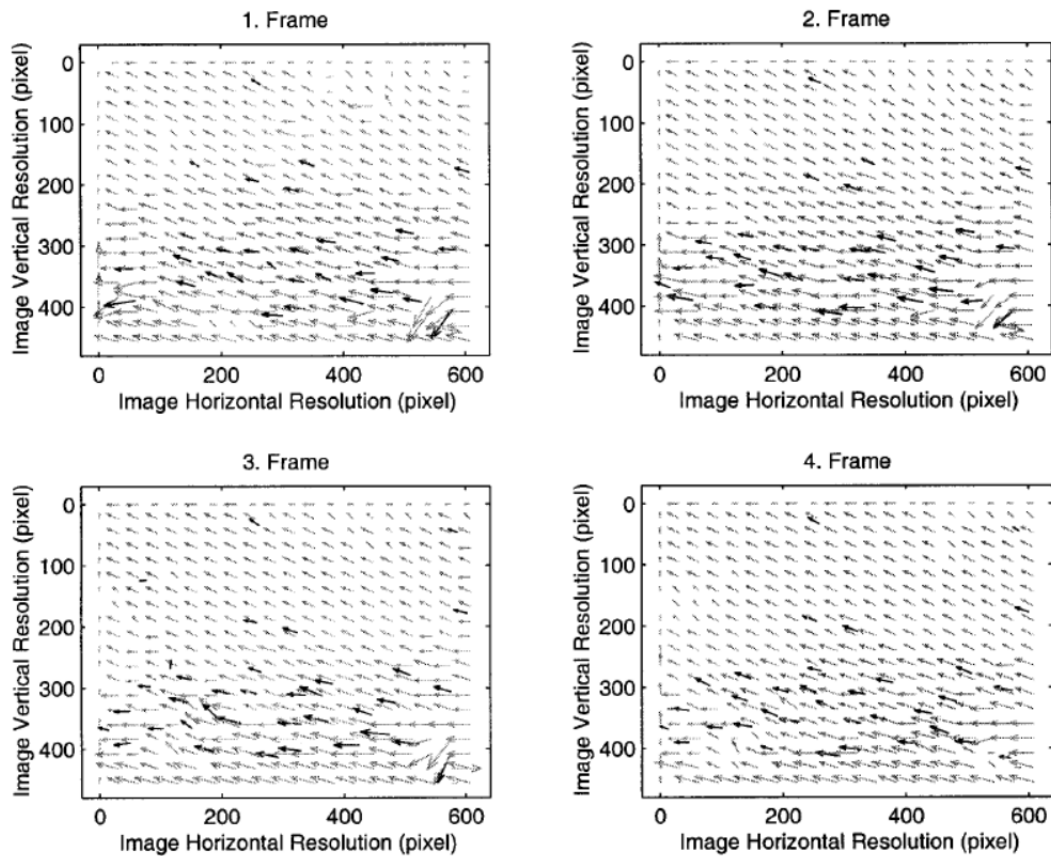


Figure 2.22. Displacement vectors from image analysis (Guler *et al.*, 1999).

Sadek *et al.*, (2003) applied DIC (digital image correlation) which is based on a similar image analysis algorithm to PIV in measuring the spatial deformation throughout a transparent soil model and compared measurements with the result of finite-element analysis. The setup of the experiment is illustrated in Figure 2.23. The setup consists of a transparent soil model, a laser source, a sheet generator lens, and a digital camera. The model container is made of Plexiglas and was filled with fine silica gel (grain size 0.5-1.5 mm). A rigid footing with a footprint of 50 mm x 50 mm was mounted on the surface of the silica gel. The footing was pushed into the model using a loading system. The accuracy of the DIC was evaluated based on a scheme of predefined digital movement of synthetic soil images. Displacement results of a constant error on the order of 0.1 pixel was obtained for a low-resolution zoom level of 0.11 mm/pixel.

Without using markers on the latex membrane, Rechenmacher and Finno (2004) used the DIC technique to quantify the localized displacements on dense sands in plane strain compression experiments. White *et al.*, (2005) applied this technique to study the instantaneous velocity field at failure of a skirted strip foundation under an eccentric vertical load in the centrifuge test. The physical model studied by White is shown in Figure 2.24.

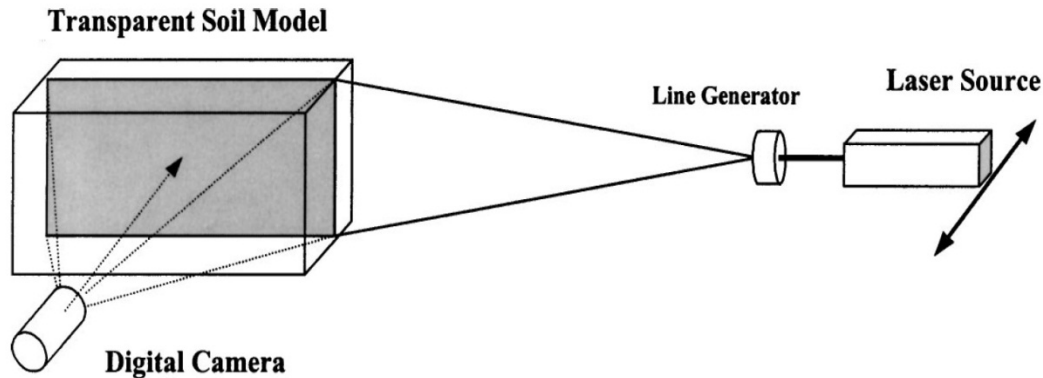


Figure 2.23. Schematic diagram showing set up for slicing transparent synthetic soils (Sadek *et al.*, 2003).

The application of the PIV technique in geotechnical engineering does not need induced markers or seeding particles. Soils such as sands have their own texture, and they will produce different image density profile on the image sensor. Clay can be covered with powder to provide a specific texture in order to be identified. However, the observed soil behaviour is restricted only to the soil surface boundary. Researchers (White, 2002; White *et al.*, 2005; Take, 2003; Sadek *et al.*, 2003; Rechenmacher and Finno, 2004) have used the PIV technique in various geotechnical problems under static loading conditions. To date there appears to have been no use of PIV in soil dynamic experiments possibly due to the limited capabilities of the camera and laser power equipment used in their research works.

Internal strains, strain evolution and localisation are key issues in understanding the behaviour of granular soils. Knowledge of shear zones distribution and the distribution of shear and volumetric strain within shear zone in granular materials is important to explain the mechanism of granular deformation and to calibrate enhanced constitutive models.

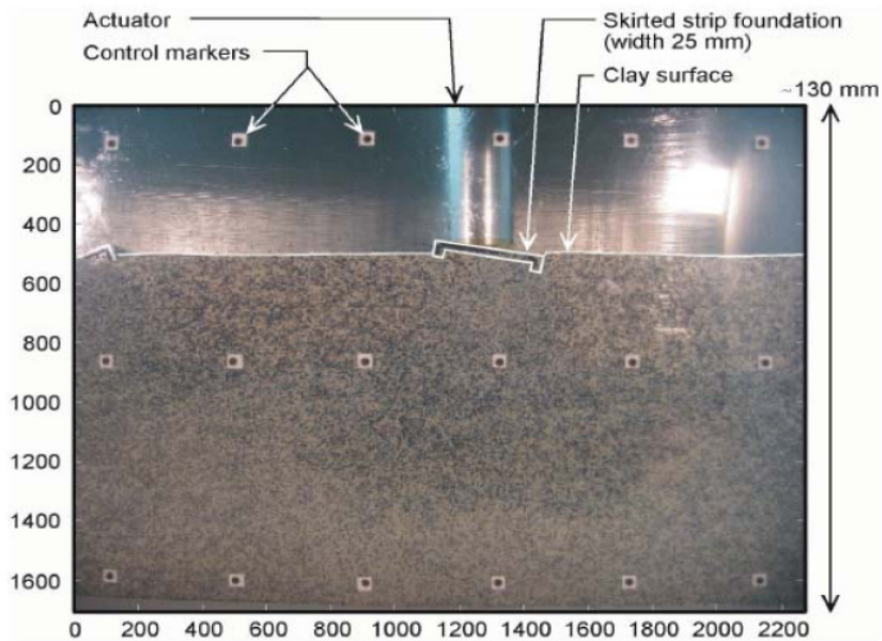


Figure 2.24. Example of the image from a plane strain foundation test (White *et al.*, 2005).

Studying the relationship between progressive failure mechanism and shear band direction and the effect of granular material particle sizes on the bearing capacity of footings in plane strain tests, Tatsuoka *et al.*, (1991, 1994 and 1997) observed shear band patterns in bearing capacity experiments of model footing on sand and predicted similar evolution of shear bands from numerical simulations as shown in Figure 2.25.

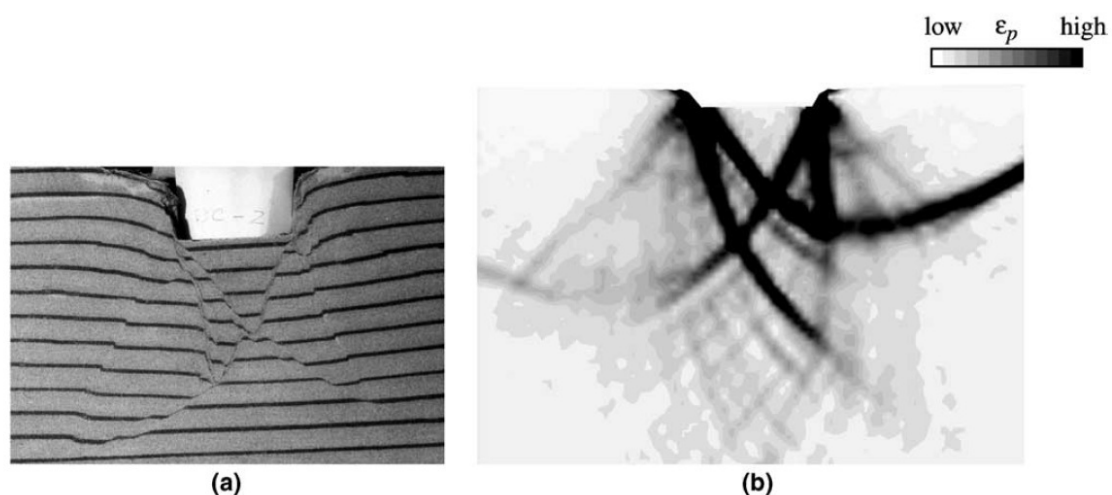


Figure 2.25. Shear band patterns from plane strain bearing capacity by (a) experiment and (b) by numerical simulation (Tatsuoka *et al.*, 1994 and 1997)

Michalowski and Shi (2003) performed laboratory tests on model strip footings to investigate the kinematics of the collapse of sand reinforced with a layer of flexible reinforcement by recording the deformation field under a model footing using a digital colour camera. They correlated the captured incremental displacements and strains under a strip footing model with depth and number of reinforcement layers. They reported the occurrence of distinct shear bands along the reinforcement region. Figure 2.26 shows examples of displacement and strain fields reported by Michalowski and Shi.

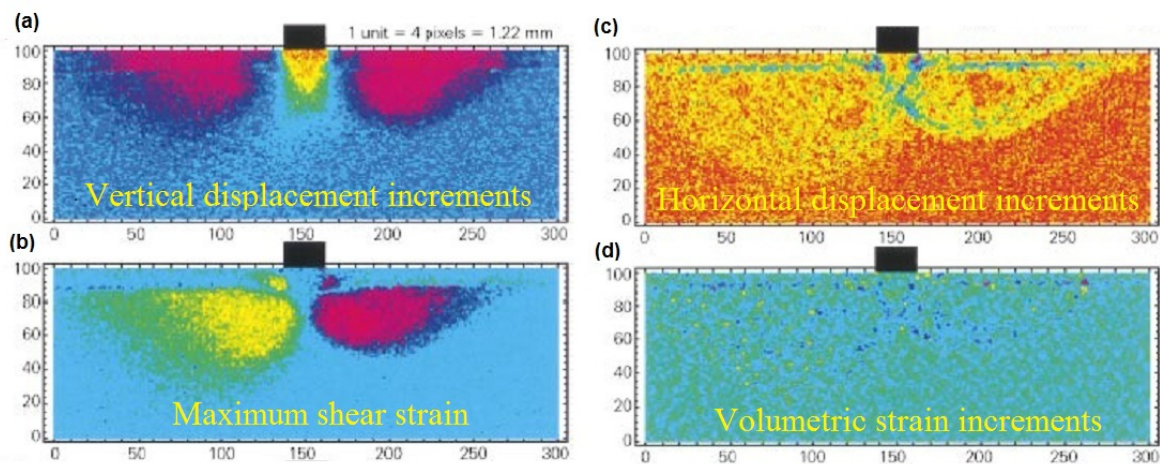


Figure 2.26. Vertical displacement increments (a); horizontal displacement increments (b); maximum shear strain (c); and volumetric strain increments (d) in reinforced dense sand (Michalowski and Shi, 2003).

Slominski *et al.*, (2007) studied the kinematics of flowing sand in a laboratory model silo using PIV for deformation measurement during granular silo flow. The measurements were carried out for granular flow in model silos without inserts and in a funnel flow silo equipped with three different types of inserts. The effect of the initial sand density and roughness of silo walls on the volumetric and deviatoric strain in sand was investigated. The results were qualitatively compared with sand displacements obtained with coloured sand layers and with the aid of X-ray imaging. Figure 2.27 shows examples of the evolution of the volume strain ϵ_v and deviatoric strain ϵ_p in a funnel flow using PIV.

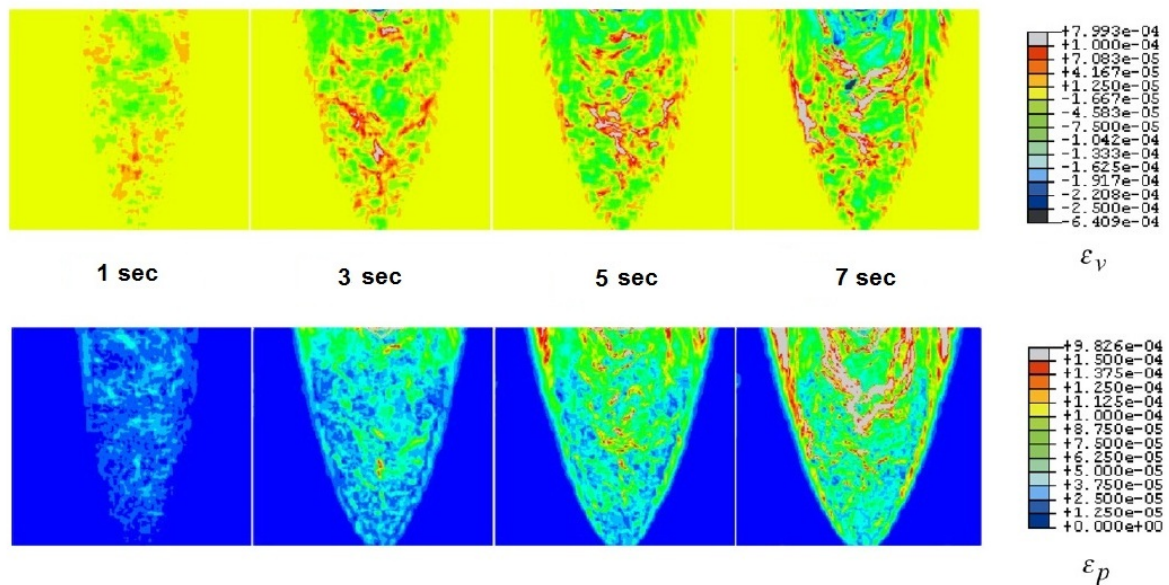


Figure 2.27. Evolution of the volume strain ε_v and deviatoric strain ε_p in a funnel flow silo after 1, 3, 5 and 7 sec of flow for initially dense sand and very rough walls (Slominski *et al.*, 2007).

Using a biaxial shear apparatus that allows the application of general stress or strain conditions, Hall *et al.*, (2009) studied the deformation patterns of what is called a Schneebeli material (a 2D analogue granular material formed of a combination of 1.5, 3 and 3.5mm diameter 60mm long PVC rods) by digital image correlation of pairs of consecutive photographs taken during the tests. The DIC analyses showed the evolving internal structures of deformation, which consisted of bands of localised deformation and ‘cells’ of low deformation between the bands. They identified that the orientations of the localised bands and cells are a function of the applied strain path. The results characterise the orientation of the bands and qualitatively identified the spacings between bands (cell size). Interpretation of the localised deformation patterns and spacings were not provided. Figure 2.28 illustrates examples of the strain plots from this work.

Hajjalilue-Bonab and Rezaei, (2009), used the PIV technique to investigate the performance of low-energy dynamic compaction on fine dry loose sand in 1-g physical models. Based on PIV displacement and strain fields, changes in relative density due to impacts at different depths have been evaluated. The results provided prediction of the influence depth of improvement in relation to the total volumetric strains and DC parameters.

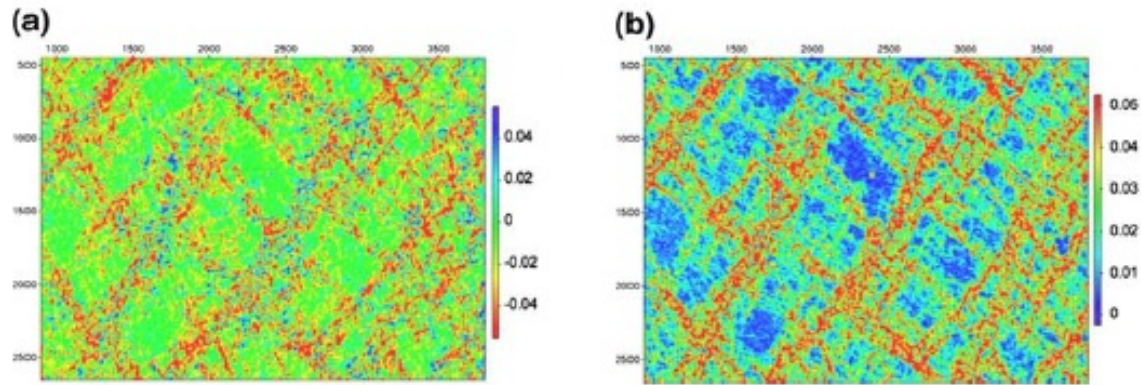


Figure 2.28. Volumetric (a) and shear (b) strains revealed by digital image correlation (DIC) technique (Hall *et al.*, 2010).

Niedostatkiewicz *et al.*, (2011) experimentally investigated the evolution of shear zones in dry sand for an earth pressure problem of a retaining wall using physical models and particle image velocimetry. Like Slominski *et al.*, (2007), the results for initially dense sand were qualitatively compared with corresponding ones obtained with X-rays. By comparing between surface and internal measurements, they reported similar patterns of shear zones obtained with PIV and X-rays in initially dense sand but localised shear zones were not detected in initially loose sand. The similarity of shear band patterns at the surface and internally is significant as it suggests friction at the Perspex face does not adversely affect the results and interpretation of the PIV results.

Using an artificial soil made of transparent clay, sand and gravel to approximate moist sandy loam soil, Beckett and Augarde (2011) captured soil movement under compaction in 1-g compaction chamber physical model using flatbed scanner placed attached to the chamber's window. However, the suitability and applicability of a flatbed scanner as an imaging tool is limited as flatbed scanners have zero focal length (i.e. set to focus on targets that are in contact with the scanning glass).

Still digital cameras with a megapixel resolution can not take images of the soil deformation quickly enough to capture the real motion of the soil particles during time dependent episodes such as seismic events or during dynamic compaction. Thus, recent research works have started employing high-speed photography to overcome this limitation. Using high speed photography to study landslide problems in centrifuge models, Wolinsky and Take (2010),

developed a signal processing technique to use in calculating velocities and accelerations from PIV deformation measurements to minimise the noise in the PIV time-displacement history. The technique enabled the separation of velocity and acceleration trend from the overlaying PIV noise.

Photogrammetry is a technique that uses photographic images to determine the geometric properties of an object. The technique involves digitising an imaged pattern on an object before and after deformation has occurred. PIV is a non-intrusive, image based measurement technique that was originally developed in the field of experimental fluid mechanics to recover instantaneous velocity fields from photographs of seeded flow (Adrian 1991). The PIV system originally used in early fluid mechanics researches consists of a laser light sheet (for illumination), fluid flow with seeding particles, an image recording system (camera), and an image data processing system. There has been a steady increase in the applications of the PIV technique and an acceptance in a variety of engineering disciplines. It has been applied to fluid mechanics, aerodynamics, multiphase flow, supersonic flow, and hypersonic flow. Sousa (2002) studied the mean turbulent flow structure around a cube mounted on the surface of a water channel with an open surface.

The PIV technique has also found an application in fluid structure interaction and impact wave studies. PIV has also been used to study the granular flow phenomena. Lueptow *et al.*, (2000) adapted PIV to measure particle displacement and velocity fields in granular flows. "Seeding" is achieved by using light and dark particles. This technique has recently been applied to geotechnical modelling (White *et al.*, 2001a, 2001b, 2002, 2003) and it is sometimes referred to as digital image correlation (DIC) (Sadek *et al.*, 2003; Rechenmacher and Finno, 2004), or block matching (Michalowski and Shi, 2003).

The principle behind DIC is the technique of matching the image pattern. Assume that two images (I_1 and I_2) were captured at different time intervals, and these two images were then divided into smaller patches (sub-sets, sub-windows, interrogation windows, or interrogation patches). Then each sub-window in the image I_2 was compared with the corresponding sub-window in the image I_1 . The cross correlation between the two sub-windows is defined as:

$$R=(s,t) = \sum_{m=0}^{M-1} \sum_{n=0}^{N-1} I_1^{i,j}(m,n) \cdot I_2^{i,j}(m-s, n-t) \quad (2-23)$$

where $I_1^{i,j}$ is the sub-set number (i,j) in the first image; and $I_2^{i,j}$ is the sub-set number (i,j) in the second image.

When this expression reaches its maximum value, the two subsets will be almost matching each other, and the subset has deformed “ s ” and “ t ” units in “ i ” and “ j ” directions, respectively. Figure 2.29 illustrates the principle behind the PIV technique. This technique provides higher field deformation data during the test instead of measuring displacements at given marker locations where conventional induced instrumentation (sensors) and markers are within the soil specimens.

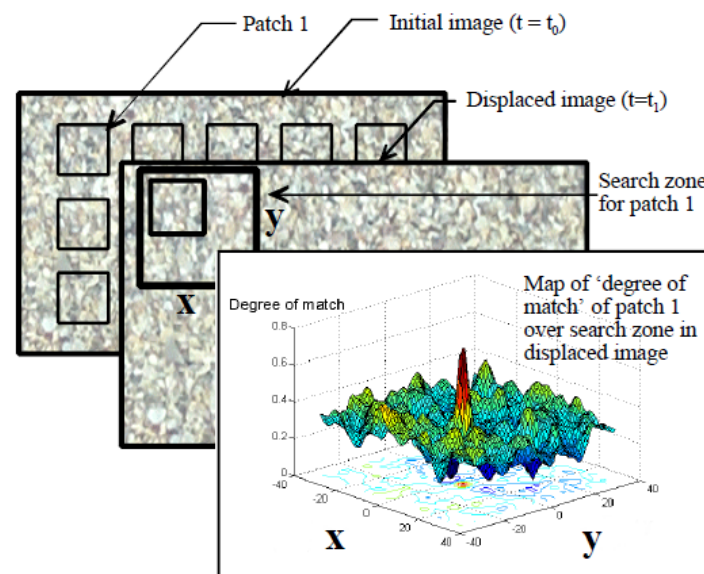


Figure 2.29. PIV image analysis technique (White *et al.*, 2001a).

As an advanced form of conventional DIC, Liu and Iskander (2004) reported the use of an adaptive cross correlation (ACC) algorithm that utilises variable size windows and methods for shifting windows to reduce the errors associated with conventional DIC. By using a scheme of predefined digital and physical movements, the ACC demonstrated improved

accuracy and range over the DIC. A typical digital image of the strip footing model and sand displacement fields calculated using adaptive cross correlation (ACC) are shown in Figure 2.30.

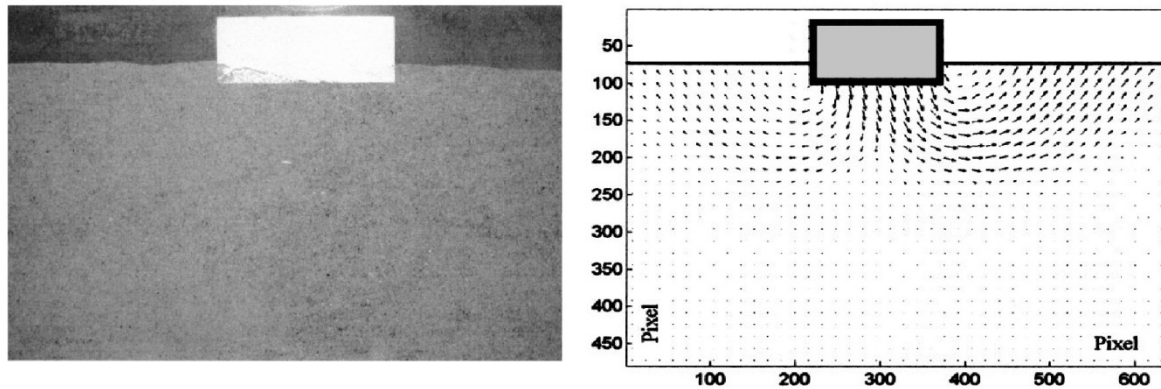


Figure 2.30. Typical digital image of the strip footing model and sand displacement fields by ACC algorithm (Liu and Iskander, 2004).

With the constant development of high resolution image acquisition equipment, the 2D-DIC method has currently become one of the most active optical measurement technologies, and demonstrates increasingly broad application prospects. Pan *et al.*, (2009) provided an extensive review of 2D-DIC for in-plane displacement and strain measurement over the last 20 years. The review summarised the 2D-DIC basic principles, applications, limitations, adopted correlation criteria, sub-pixel displacement algorithms, displacement error analysis due to image noise, distortions and estimation of the strain fields. They acknowledged the capability of the 2D-DIC of quantitatively measuring microscale deformation. Combined with a high-spatial-resolution camera, the 2D-DIC can provide full-field displacements to sub-pixel accuracy. Using artificial images to simulate the absence of experimental and field induced errors associated with camera misalignment and lighting, Lee *et al.*, (2011) proved that 2D-DIC strain measurement has the potential to provide the same strain accuracy as foil and vibrating wire strain gauges for materials experiencing homogeneous strain. With a sub-pixel interpolation techniques that was developed to reduce bias error, they demonstrated that the 2D-DIC technique could measure strain with the same accuracy as conventional strain gauges when used under ideal conditions.

The greatest impact of digital photography has been the ability to estimate the sub-pixel peak position by means of the Gaussian function, while allowing for the displacements to be determined with improved accuracy. This has enabled smaller interrogation patches to be used, leading to an increase of spatial resolution (number of vectors) in the digital PIV.

2.3.2.2 X-Ray Tomography (CT-Scan)

X-ray computed tomography (CT) is a non-destructive technique with wide applications in various disciplines. This technique allows the internal structure of objects to be visualised, mainly by variations in density and/or atomic composition. It requires the acquisition of radiographs from different positions during a step wise rotation around a central axis. This is followed by the reconstruction of two-dimensional cross sections perpendicular to the axis of rotation. It was first known for its medical applications in the early 1970s (Hounsfield 1972, 1973), but since then computerised tomography (CT) has become a common tool in the engineering field, resulting in large numbers of publications from the early 1980s onwards. Early applications include studies in the fields of soil science (Petrovic *et al.*, 1982; Hainsworth and Aylmore 1983) and geotechnical engineering (Raynaud *et al.*, 1989).

As a strong contrast mainly exists between solid phases and voids within the skeleton of the soil, studying the soil porosity, became an important application of X-ray CT. Examples of applications in this field include studies of soil macro-porosity (Perret *et al.*, 1999). 3D-CT analysis can produce large numbers of contiguous parallel cross sections which allows for 3D visualisation of selected features and quantification of 3D volumes. Pierret *et al.*, (2002) provided examples of applications that exploit this aspect of X-ray CT that include studies of the macro-porosity of soil. Mess *et al.*, (2003) presented general information about the technique and a brief overview of its applications in geosciences.

Microtomography has also developed rapidly, taking advantage of the constant improvement of image acquisition and processing techniques. The application of microtomography has been extended to study strain localisations in geomaterials. The microstructural factors of non-cohesive soils including particle size, shape and orientation, and the pore space have been examined by several researchers using this technique (Ringrose-Voase 1993; Tovey *et*

al., 1994; Yue *et al.*, 1995; Yue and Morin 1996, Shi *et al.*, 1999 and Lade, 2003). Viggiani *et al.*, (2004) conducted experiments that have used synchrotron radiation microtomography to evaluate the onset and evolution of localized deformation in a saturated fine-grained stiff (Beaucaire Marl) soil under deviatoric loading.

Microtomography allowed very detailed observations of strain localization fields. Both dilating shear bands and cracks were observed to form and to interact in the course of deformation with no gradual change of soil density from the zone of localization to the zones of the specimen far from the crack. Studying the effect of bio cementation, Tagliaferri *et al.*, (2011) conducted 3D in-situ (during loading) x-ray microtomography during triaxial compression tests of bio-cemented Ottawa 50–70 sand and non-cemented sand specimens. The tomography allowed a high quality quantitative 3D digital image analysis including porosity, cement-density and strain field measurements. Figure 2.31 illustrates the x-ray images of triaxial tests on cemented Ottawa sand specimens.

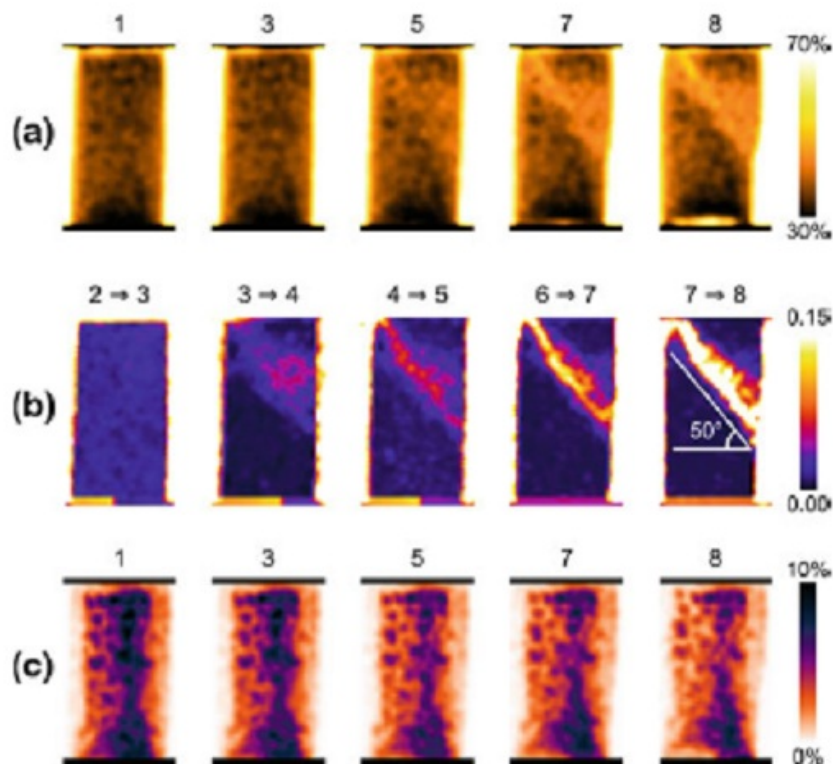


Figure 2.31. X-ray image analysis of bio-cemented Ottawa sand specimens: (a) porosity; (b) shear strain by DIC; (c) cement density (Tagliaferri *et al.*, 2011).

2.3.3 Dynamic Compaction by Finite Elements Models

Obtaining valid and sufficient field results to explain the mechanism of DC is unlikely to be successful because of the high costs involved. On the other hand, conducting centrifuge experiments and/or reliable scale 1-g physical models to study dynamic compaction is a particularly time consuming and highly laborious task. In such a setting, numerical modeling and in particular finite element analysis, are an alternative approach scientists have used to investigate dynamic compaction. The computerised simulation models also provide a tool assisting engineers in predicting the DC effect at preliminary design stages, before conducting more detailed in-situ investigations.

Poran and Rodriguez (1992b) developed two Drucker-Prager type dynamic finite element codes with a variety of soil models and computational algorithms. The codes were evaluated by laboratory investigation and experimental data. By either applying acceleration records from experimental data as a load history to a continuum composed by the soil and the tamper, or by using a numerical formulation to compute the interaction of a tamper impacting the sand surface with a known initial velocity, they claimed good correlation between computed and experimental results in relatively loose sand, but when densification occurs in the impact field, the computed results depart significantly from the experimental data. They also reported that a strongly graded mesh can lead to problems of element degenerations due to the development of very large near-field deformations during the highly non-linear DC analysis.

Using the ABAQUS finite element software package, Pan and Selby (2001 and 2002) performed two-dimensional finite element models on dry loose soils under dynamic compaction, but the validity of the results derived from using this model were not very accurate in most cases because the constitutive laws that were used were not specifically suitable for dynamic loadings. Other models by Valliappan *et al.*, (1995), Diebels and Ehlers (1996), Arduino and Macari (2001), Li *et al.*, (2004), Chen *et al.*, (2006) are also available in the literature, but they have a limited practical application because they are based on excessively simple constitutive relationships that mainly focus on numerically analysing the transmission of dilatational waves in elastic saturated porous media, or on validating certain computational procedures.

Gu and Lee (2002) studied the mechanics of dynamic compaction using two-dimensional finite element analyses with a large strain dynamic formulation and a cap model for the behaviour of soil. The study was conducted using the dynamic FE software CRISDYN (Goh, 1995 and Goh *et al.*, 1998), which has an updated Lagrangian large strain formulation for dynamic problems that are incorporated to reflect the large strains in the soil during impact. The analyses show that, in the initial blows, the propagation of stress waves induces transient elasto-plastic K_o compression due to lateral inertia. This preserves the wavefront of the plane and reduces the attenuation rate of the dynamic stresses with depth. With multiple blows the effect changes to triaxial compression, which sets a limit on the degree of improvement that can be achieved in the near field. Deeper down, the wavefront adopts a bullet shape and the rate of attenuation rises, which sets a limit on the depth of improvement.

Lee and Gu (2004) proposed a new method for estimating the degree and depth of improvement that results from the dynamic compaction of sand. Their method was based on two-dimensional finite element analyses benchmarked by the results of the centrifuge model tests of Oshima and Takada (1997) and Kampung Pakar Site, Malaysia (Lee *et al.*, 1989). Their approach was to normalise the results from a wide range of soil properties such as the initial relative density, and operating parameters such as momentum per blow, energy per blow, and number of blows. The results were summarised into a number of graphs for predictive purposes. L'opez-Querol *et al.*, (2008) developed "Pastor-Zienkiewicz" (PZ) constitutive model for sands undergoing dynamic consolidation. It is a numerical model for computing dynamic consolidation problems in saturated sandy soils with a code formulated in terms of the displacement of both solid and fluid phases instead of the conventional approach based on displacement of the solid phase and excess pore water pressure. The authors claimed that this approach is required to obtain reliable results in dynamic problems such as DC.

Currently, there are a few commercial shock and high strain rate physics codes including ABAQUS, LS-DYNA, CTH, ALEGRA, ALE-3D, and RADIOSS. The suitability of many of the finite element codes and their material models to simulate large deformation in soils depends on the performance of the software and the in-built material models. Some of these software were originally designed for military applications to simulate landmine blasts and aircraft crashes, so these software attracted engineers studying soil dynamic problems.

Penetration drop tests of airframe structure into sand were simulated by LS-DYNA (Fasanella *et al.*, 2008). The pre-test predictions of accelerations, velocities, and displacement-time histories were correlated with test data to explore the suitability of several LS-DYNA material models to provide reasonable dynamic loading and unloading behaviour.

Qin *et al.*, (2008) used the LS-DYNA finite element software package to predict the effect of ground vibration on an 80m diameter liquid storage tank at Dalian Harbour, from anticipated dynamic compaction 43m from the edge of the tank. The results from the finite element simulation were compared with actual vibration data collected by surface acoustic wave vibration transducers during the dynamic compaction process, and suggested a good agreement between the predicted and measured ground vibration.

Ghassemi *et al.*, (2009) used the finite element code PISA (Chan and Morgenstern, 1988) to investigate the applicability and accuracy of the Menard formula, and the effect of soil parameters and impact energy on the depth of improvement. By adopting the centrifuge results by Oshima and Takada (1997), the authors reported a good agreement between numerical and experimental results, but as the total momentum increases, the deviation between the numerical and experimental results gradually increases. This deviation was attributed to the soil stiffening under the high energy (or momentum) of dynamic compaction. Therefore, the Menard empirical relation (Equation 2.14) for determining the depth of improvement is useful when the weight of the tamper and the drop height are in ordinary ranges. For heavy tampers and higher impact energies, this relationship over estimates the depth of improvement. They also demonstrated that the depth of improvement does not increase linearly with the applied energy, and the concept of a limiting impact energy is valid. To determine the interim depths of improvement, the real values are rather smaller than those proposed by Lee and Gu (2004). Ghassemi *et al.*, (2010) also performed a numerical investigation on the improvement of saturated soils using the DC treatment method, with a focus on the coupled hydro-mechanical effects of impact loads on a saturated granular layer, while taking into consideration the effects of the degree of saturation, pore fluid compressibility, and coefficient of permeability along with several factors that are generally involved in the numerical modelling of dynamic compaction. They claimed good agreement between the predicted pore pressure and actual generated pore pressure in the ground. The investigation evaluated the interaction between the solid phase and fluid phase in saturated

porous media under impact load, to predict the stresses, displacements, and pore pressures using a coupled hydro-mechanical formulation.

Bojanowski and Kulak (2010) presented a comparative study of the performance of LS-DYNA soil material model (MAT_005, Soil and Crushable Foam) using a Lagrangian, a multi-material Lagrangian- Eulerian, and a Smoother Particle Hydrodynamic approach for modelling large deformation in soils. The results showed that the three formulations can produce reasonable predictions of large deformations in soils. Figure 2.32 shows the deformation and vertical stresses predicted by LS-DYNA FE code using the Lagrangian approach.

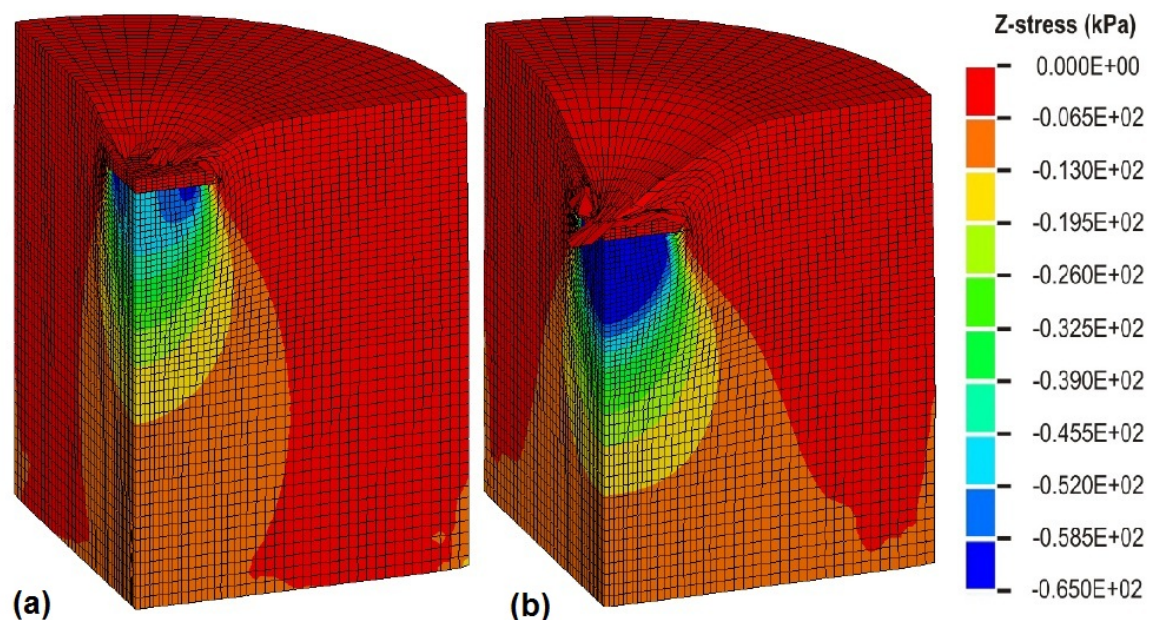


Figure 2.32. Deformation and vertical (Z) stresses in Lagrangian model by LS-DYNA (a) 250 mm of penetration and, (b) 420 mm of penetration (Bojanowski and Kulak, 2010).

Parvizi and Sharif (2011) presented a series of experiments and numerical (3-D mesh FE analysis by ABAQUS software package) tests to simulate the densification of a sandy soil by a low energy dynamic compaction (LEDC). They demonstrated that soil stiffness obtained during impact tests (experimental and numerical) and the stiffness obtained through static load test (experimental and numerical) all agreed reasonably well. Changes in the stiffness of

the soil due to dynamic compaction have been derived using WAK test and static load test methods (Parvizi, 1999). A 2-D view of Parvizi's FE model by ABAQUS and its predicted contours of displacement are shown in Figure 2.33.

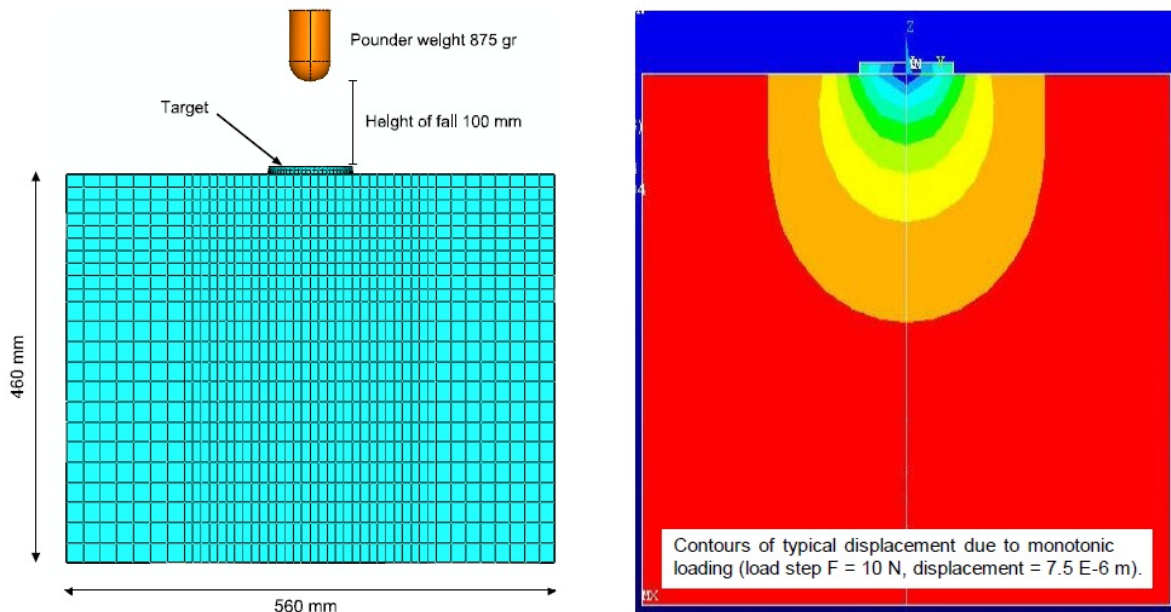


Figure 2.33. A 2-D mesh for a dynamic compaction test, and the contours of typical displacement due to monotonic loading (Parvizi and Sharif, 2011).

2.4 SUMMARY

Dynamic Compaction is one of the oldest forms of deep soil improvement. The technique consists of repeatedly dropping a heavy weight (tamper) in a pre-determined pattern onto weak ground that is going to be compacted. In dry soils, DC improves the soil by reducing the void ratio and increasing the relative density of the deposit by physical displacement, and low frequency excitation. The impacts lead to slippage and rearrangement of the soil particles resulting in enhanced bearing capacity and improved settlement. The densification process of saturated soil is different as DC causes gradual liquefaction and rapid dissipation of pore pressures under repeated impacts. Despite its wide use, the design of DC work is still essentially empirical in nature, falling back on the designer's experience, and a significant amount of costly trials and post-treatment verification tests because as yet, there is no tangible evidence of the densification mechanism taking place beneath the surface.

A wide range of verification testing is available but none is ideally suited to DC application due to the huge variation in the subsurface conditions at different sites. As such, the ground response is probably the best available control test during DC production work. Observations, such as whether the crater depth continues to increase; unusual ground heave occurs; and vibrations increase with numbers of drop are all useful to determine if the desired achievement is occurring and for modifying the field programme if required. Clearly, the current practice for D.C. processes still depends mainly on previous experience or field test programmes to determine the applicability and make site-specific design choices.

Both physical and numerical models will continue to be important components of DC research. While computer based models can serve many of the same purposes as physical models, they are entirely governed by the mathematical relationships of the soil property variables, and these are difficult to define numerically. Till the development of FE codes that can model the dependency of the soil elastic modulus on the stress state and are capable of simulating the permanent increase of soil stiffness after each blow based on the increase in relative density of the soil under impact, designing DC exclusively by numerical simulations will remain challenging. For porous materials like sand, water saturation may have a significant influence on the soil behaviour. Under such conditions, soil constitutive models developed for numerical simulations must adequately account for the water, while the

capacity of these models must be validated for a large range of dynamic loading conditions, soils and water contents.

Most available models do not directly address the effect of parameters such as the initial void ratio, the initial moisture content, depth of the water table, soil grading, plasticity, Poisson's ratio, cementation, and soil structure. Available DC models may be used as an initial indication but no single model can confidently be used to predict the compaction. It is likely that combining or modifying the models currently available into one model may be required for reliable predictions. The rapid development of digital photography and X-ray tomography techniques offers a robust tool, with a considerable potential for their application in geotechnical laboratories. The rather low price, high resolution digital cameras and high speed data processing technology available, have started a new era in spatial deformation and strain localisation in geotechnical physical modelling research.

Chapter III: Testing Apparatus and Experimental Procedures

Table of Contents

3	OVERVIEW	72
3.1	MERITS AND LIMITATIONS OF SMALL SCALE MODEL TESTING IN GEOMECHANICS.....	72
3.2	PHYSICAL MODELLING OF THIS RESEARCH.....	74
3.2.1	Set-up of 1-g Dynamic Compaction Models	75
3.2.2	Pounders (Tampers).....	77
3.2.3	Materials Used	80
3.2.4	Models Preparation	82
3.2.5	High Speed & Still digital cameras.....	84
3.2.6	Cone Penetrometer Test (CPT).....	86
3.2.7	Instrumentation	87
3.2.7.1	Instrumentation Calibration.....	89
3.3	DYNAMIC COMPACTION TEST PROCEDURE.....	91
3.4	EXTRACTING UNDISTURBED SAND SPECIMENS FROM POST DC TEST MODELS FOR CT-SCAN TESTS	93
3.5	TRIAXIAL TESTING WITH SHEAR WAVE VELOCITY MEASUREMENTS. 96	
3.6	LABORATORY INVESTIGATION OF LATERAL STRESSES k_0 COEFFICIENT	98
3.7	STATIC LOAD TESTS	100
3.8	COMPACTION AND DENSITY TESTS.....	102

3 OVERVIEW

This chapter outlines the experiment-related developments for this research work. First, the merits of conducting physical modelling and the limitations of small scale testing in geotechnical experiments are discussed. This is followed by an introduction to the physical modelling adopted for this research, which includes two different size models and a number of testing programmes. The chapter then describes the test apparatus used, which includes 2-D models of dynamic compaction experiments at normal gravity (1-g). The chapter then provides the basic classification and engineering properties of the soil materials used and sample preparation technique applied to create homogenous soil for the model tests. This is followed by a description of the experimental procedures used for the dynamic compaction tests and the instrumentation. The method of obtaining undisturbed sand samples for the CT scan tests and the laboratory tests used to measure the dynamic properties of the soils are discussed. The static load tests used to compare the soil static plane strain response with dynamic impact response are presented. Finally compaction-density tests are also reported as a reference of the possible degree of compaction the tested sand:silt mixture can reach.

3.1 MERITS AND LIMITATIONS OF SMALL SCALE MODEL TESTING IN GEOMECHANICS

The use of scale models in geotechnical engineering offers a more economical option than the corresponding full-scale test in simulating complex systems under more controlled conditions. Scale model test results can provide calibration benchmarks for analytical methods, or to make quantitative predictions of the prototype response. For such applications it is important to have a set of scaling rules that relate the observed model and predicted prototype behaviour. Rocha (1957) was the first to systematically describe scale modelling for problems in soil mechanics by differentiating between total stress and effective stress conditions and deriving separate similitude relationships for each case. To account for the different stress level present in a 1-g scale model from the prototype, he proposed that the soil constitutive behaviour must be scaled, and therefore assumed that both the stress and strain should maintain a linear relationship between the model and prototype.

Scaling test results from 1-g geotechnical models to the geometric model/prototype ratio is not usually sufficient to enable the results to be directly applied to predict the behaviour of a

prototype geotechnical problem. The prediction must also reflect the stress levels acting in the soil of the model test in reference to those at corresponding points in the soil of the prototype. Three scale ratios should ideally apply between a model and a prototype: (1) the geometric scale ratio, (2) the stress scale ratio and (3) the stress-gradient scale ratio. For proper modelling of the prototype conditions, the product of the geometric scale ratio and the stress-gradient ratio must be equal to unity. Then, the displacement ratio between the model and the prototype will be equal to the geometric scale ratio (Altaee and Fellenius, 1994).

The dynamic response of soil and the response of soil-structure interfaces to dynamic loading would ideally be investigated by conducting instrumented full scale field tests. However, where the test arrangement and equipment are very large such as for dynamic compaction, it is usually impractical because of the high costs involved, and the potential danger to human life. Small-scale model tests are considerably cheaper and also more flexible, which allows changes in test conditions to be made easily. Moreover, advances in system control, sensors, data acquisition systems and experimental design have significantly improved the performance of physical modelling while minimizing the effects of instrumentation inclusion and boundary conditions on the model response. As a result, this allows more thorough investigation of the response of the test models at a much lower cost.

The main limitation of small-scale 1-g tests is that they do not reproduce the stress gradient with depth that occurs in the field. In some situations, these stress gradients can affect the failure mechanism and this introduces uncertainty into the extrapolation of the results for full scale prototype cases. The differences in a number of aspects such as the soil stress level, the presence of model boundaries and the soil response often invalidate straightforward extrapolation of the 1-g data to large-scale studies. Nevertheless, small-scale 1-g model tests can reveal the general trend of the response of the prototype under the testing conditions and provide fine details of the generic behaviour that can be expected from the prototype. This, when coupled with numerical investigations, can provide a more comprehensive picture of the investigated soil behaviour, which is the aim of the small-scale model testing presented in this thesis.

Model testing can be classified into three main categories: (1) centrifuge model testing which allows the use of 'prototype' soil at prototype stress levels and under approximately correct conditions of stress and strain paths; (2) which considers that the model as a small prototype itself and compares its behaviour with that predicted by some method of analysis; and (3) for

which the model is designed specifically to reveal detailed stress and deformation information about certain geotechnical problems which are not specifically related to a prototype (James, 1971).

For dynamic similarity, the model and prototype experience must experience homologous forces. More importantly for the 1-g model to simulate the prototype DC event, the loose granular soil must be able to satisfy the scale modelling criteria of shear strength and dynamic shear modulus, which will require an impractically large scale model if not close to the prototype. As such, the physical models adopted in this work falls under the third category (above) since the prime objective of this work is to increase the understanding of the soil behaviour, such that new methods of analysis may be developed which then will lead to better understanding and improved design rules for use in the future.

3.2 PHYSICAL MODELLING OF THIS RESEARCH

Physical models of the dynamic compaction process have been performed to explore the sub-surface soil response during plane strain experiments. These have made use of high speed photography and digital image correlation (DIC) techniques to investigate the deformation patterns, calculate soil strains and observe strain localisation. The tests were conducted with two different sized models. Each of the different sized models has its benefits and disadvantages. For the small model tests, their flexibility provided more control of the experiments, allowing better investigation of many of the photography parameters, accommodating instrumentation within the soil body and required less material handling. The big model tests, on the other hand, achieved relatively higher soil stress levels and had less boundary interaction than the small models, but they required more material handling.

In this research, the dynamic compaction mechanism was investigated in 6 different testing programmes using high speed photography:

- i. Small scale models with dry sand (at different initial relative density),
- ii. Small scale models with dry sand (employing X-ray microtomography),
- iii. Small scale models with dry sand (with different tamper geometries),
- iv. Small scale models with sand: silt mixtures (at different initial relative density),

- v. Small scale models with sand: silt mixtures (with different tamper geometries),
- vi. Large scale models with dry sands (at different initial relative density).

Details of the apparatus, materials and experimental procedures of the above tests are presented in the following sections of this chapter.

3.2.1 Set-up of 1-g Dynamic Compaction Models

The testing apparatus used here comprises a fabricated steel container open at the top with a clear acrylic (Perspex) front window that retains the soil and a system for delivering a free falling steel poulder to impact the soil surface. Two different methods were used to operate the free-falling poulder which required different apparatus configurations. These are referred to as Type 1 and Type 2 below. For the small sized model with Type 1 arrangement, shown in Figure 3.1, the soil container is a steel frame that extends to a height of 2.8 m above the floor with a fixed pulley system resting on an axle positioned at the top of the frame. A steel poulder is fastened beneath a steel trolley, as shown in Figure 3.1, that slides up and down within the frame. The fall height is controlled by manually lifting it to the desired height via the cable and pulley. The guiding trolley and attached poulder can free fall up to 1 m onto the surface of the sample. The internal dimensions of the soil container are 350 mm (W) x 150 mm (D) x 750 mm (H). The front face is made from two Perspex sheets bolted to the front of the frame. The outer sheet is 25 mm thick and the inner sheet is a thinner, 5 mm sheet. The thin inner sheet is replaceable and is used to prevent scratching and damage of the main Perspex sheet. This system has enabled good quality photographs to be obtained without the need to replace the costly main Perspex sheet. A set of control markers, as shown in Figure 3.2, are placed between the Perspex sheets for camera calibration and to validate the conversion from image space to real space measurements. The steel frame is separated from the floor by rubber pads to prevent vibrations being transmitted through the floor to the camera.

The rigidity of the Perspex window during the impulsive nature of the DC tests is considered to be important in maintaining a 2-D plane strain condition. The strong fixity of the 30mm Perspex window to the container steel frame limited the maximum deflection to less than 1mm at the top centre of the window (0.3% of the 350 mm length) for the anticipated stress

levels (*Section 6.4.2.1*) during DC tests. Additionally, a thicker cover glass could have a significant impact on the resolution as more image distortion would be expected due to refraction through a thicker viewing window.

For the small sized model, the Type 2 arrangement to control the pounder is shown in Figure 3.3. The steel frame affixed to the container was shortened and an electromechanical gearbox and motor were mounted 500mm above the container top. The gearbox is connected to a power supply that enables the gearbox clutch to be released and allows the pounder to free-fall. The trigger switch that releases the clutch also enables synchronization of each drop with the high speed camera.

The gearbox and motor allows the pounder, and the 25mm diameter shaft connected to it, to be lifted to a pre-specified height at which the gearbox clutch is engaged allowing the freefall of the pounder and shaft. The soil container of model Type 2 was modified so that it could be rotated through 90° to the horizontal via two hinges at its base to facilitate sample preparation as shown in Figure 3.4. Steel bolts secure the container hinges to the steel frame once the container is vertical prior to testing.

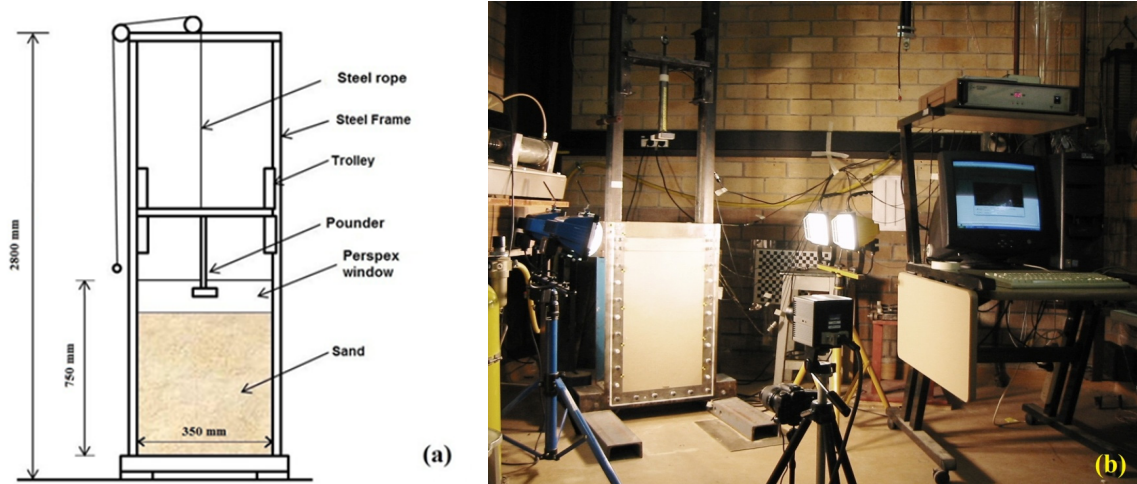


Figure 3.1. Schematic diagram of the small size model type 1 (a), and a snapshot shows the lighting and cameras set up in front of the test model (b).

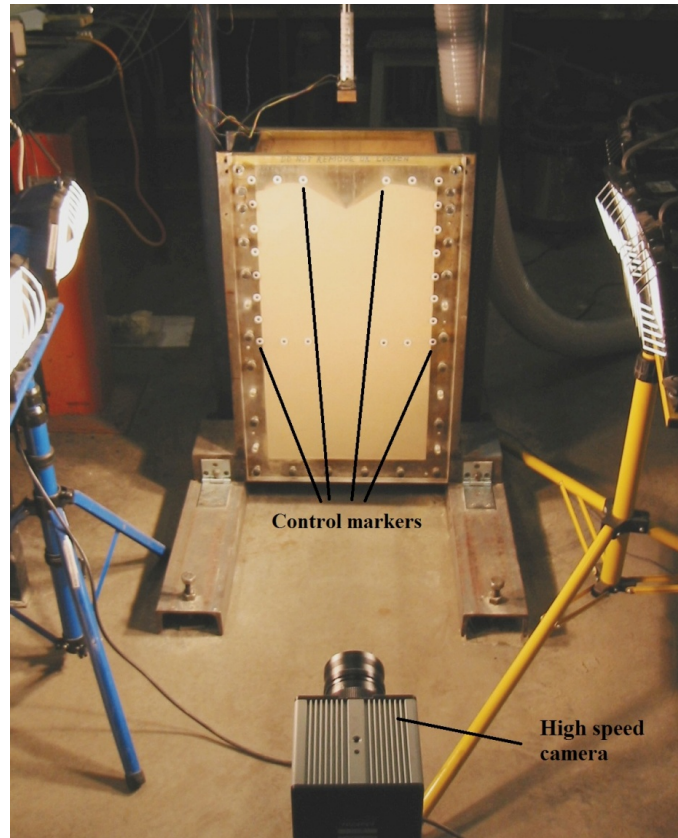


Figure 3.2. Control markers positioned on the front window between the Perspex sheets.

The soil container of the large size model is 1000 mm (W) x 300 mm (D) x 1100 mm (H) internally, and the pounder mechanism is similar to that used in the type 2 small model tests. Figure 3.5 shows the large model container with a specimen of sand that is 1.0m high.

3.2.2 Pounders (Tampers)

Pounders of different weights and geometries were used in this work. All pounders were made so that the pounder depth was equal to that of the container (2mm less to avoid the pounder making contact with the container walls) in use to ensure a 2-D, plane strain configuration.

For tests in the small container using the Type 1 configuration, DC tests were performed using a 57mm wide pounder. The weight of the free falling assembly was 160N. The weights of the free falling assembly (pounder and shaft) were 56 N and 58 N for the 25mm wide and 35mm wide pounders respectively for tests in the small container using the Type 2 configuration.

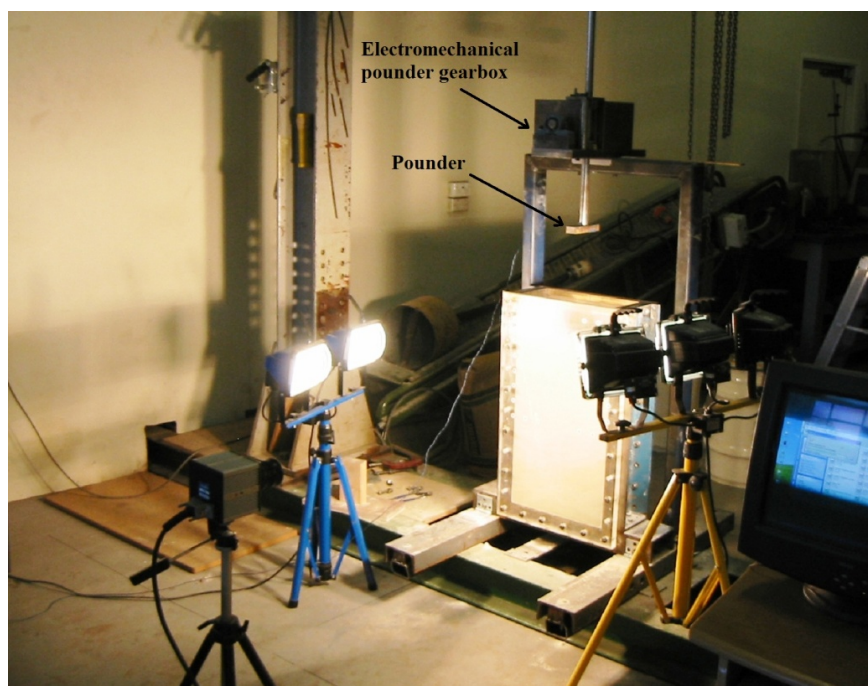


Figure 3.3. Set up of the small sized model, Type 2.



Figure 3.4. The soil container of small model Type 2 rotated through 90° to the horizontal with its backside removed and top of the container plugged to facilitate sample preparation.

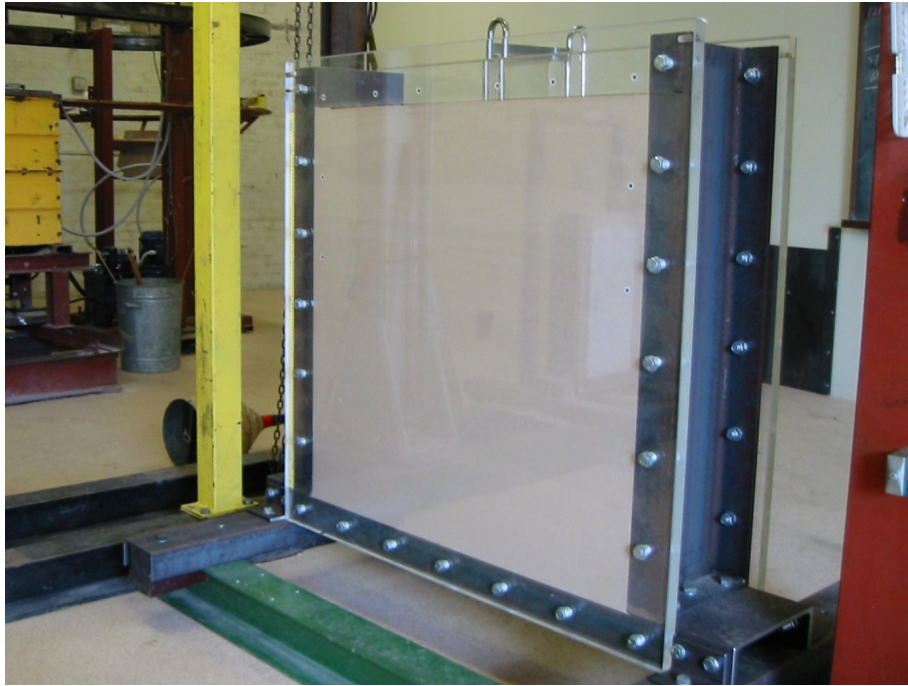


Figure 3.5. The large size model soil container full of sand to a height of 1.0m.

Similarly, 66N, 75N and 110N weights of the free falling assembly (pounder and shaft) were used with the large sized model for 35mm wide, 57mm wide and 105mm wide pounders, respectively. A set of 35mm wide non-flat based pounders were tested in the small sized, Type 2 configuration, and are referred to here as pounder Types B, C, and D for conical, shell, and curved based pounders respectively, while the standard flat-base pounder was given the designation, Type A. Configurations of the different pounder geometries are shown in Figure 3.6. The weight of the free falling assembly (pounder and shaft) was 56N for types B, C, and D pounders.

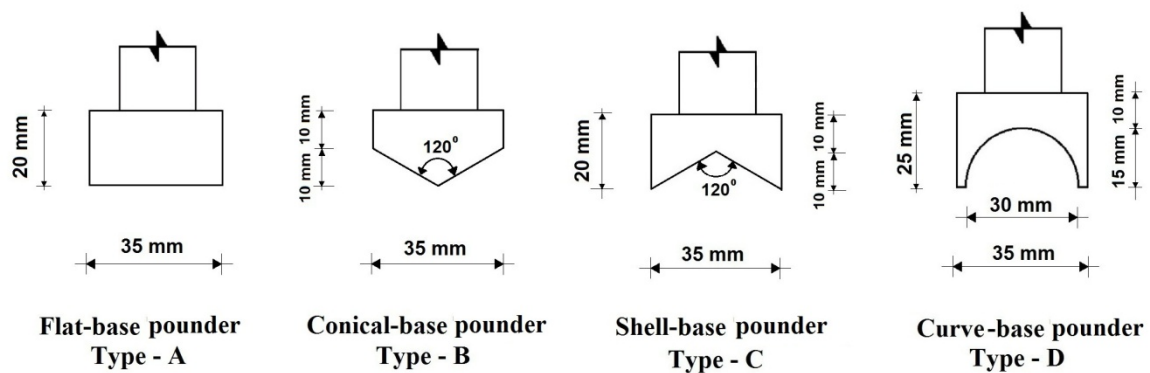


Figure 3.6. Configuration of flat and non-flat based pounders.

3.2.3 Materials Used

Medium to fine grained dry Sydney sand and sand-feldspar silt (2sand:1silt) mixtures were used in this work to study the mechanism of the dynamic compaction process. The microscopic structures, natural textures and colours of Sydney sand and the feldspar silt are shown in Figures 3.7 and 3.8 respectively. The sand has the properties $d_{50} = 0.3$ mm, $c_u = 3$, $e_{\max} = 0.80$, $e_{\min} = 0.58$, and when the non-plastic feldspar fines have been mixed with the sand to form a 2sand:1silt mixture the properties were $d_{50} = 0.2$ mm, $c_u = 22$, $e_{\max} = 0.89$, $e_{\min} = 0.51$. Grading curves of the sand, the feldspar silt and the sand:silt mixture are shown in Figure 3.9. The sand and feldspar silt have specific gravities of 2.65 and 2.63 respectively.

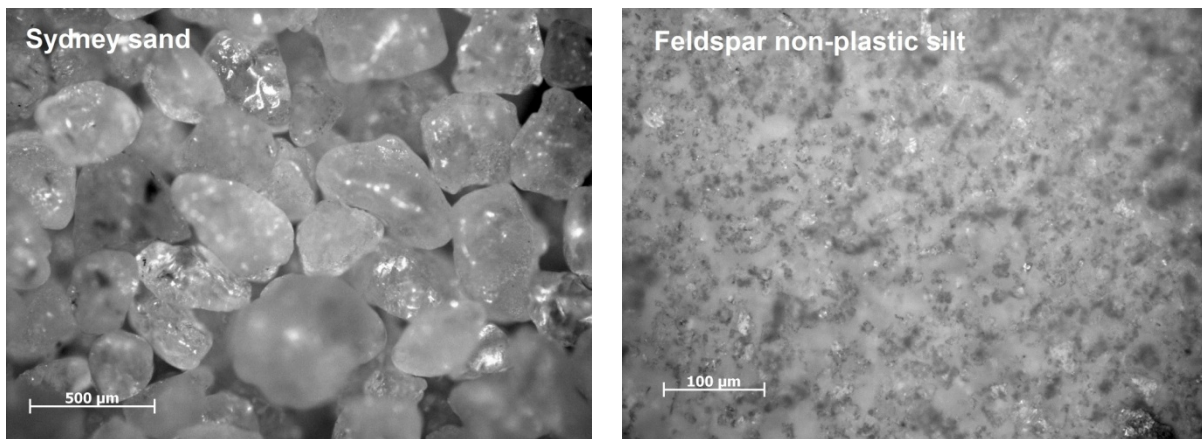


Figure 3.7. Microscopic images of Sydney sand and Feldspar non-plastic silt

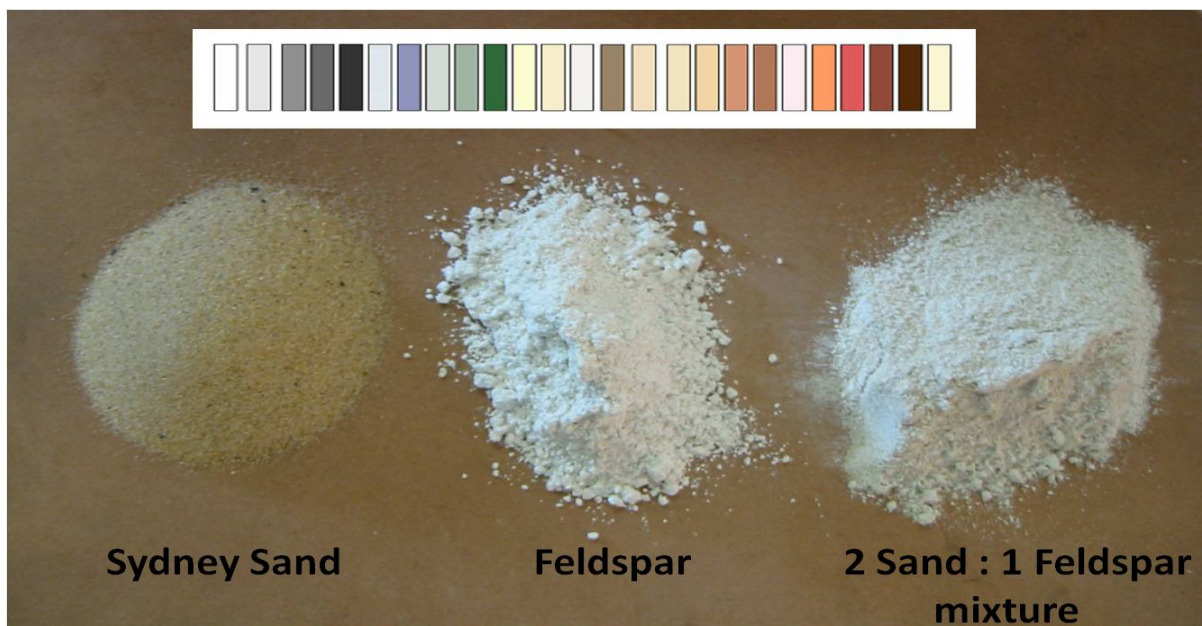


Figure 3.8. Natural colours and texture of Sydney sand, feldspar silt and 2sand:1silt mixture.

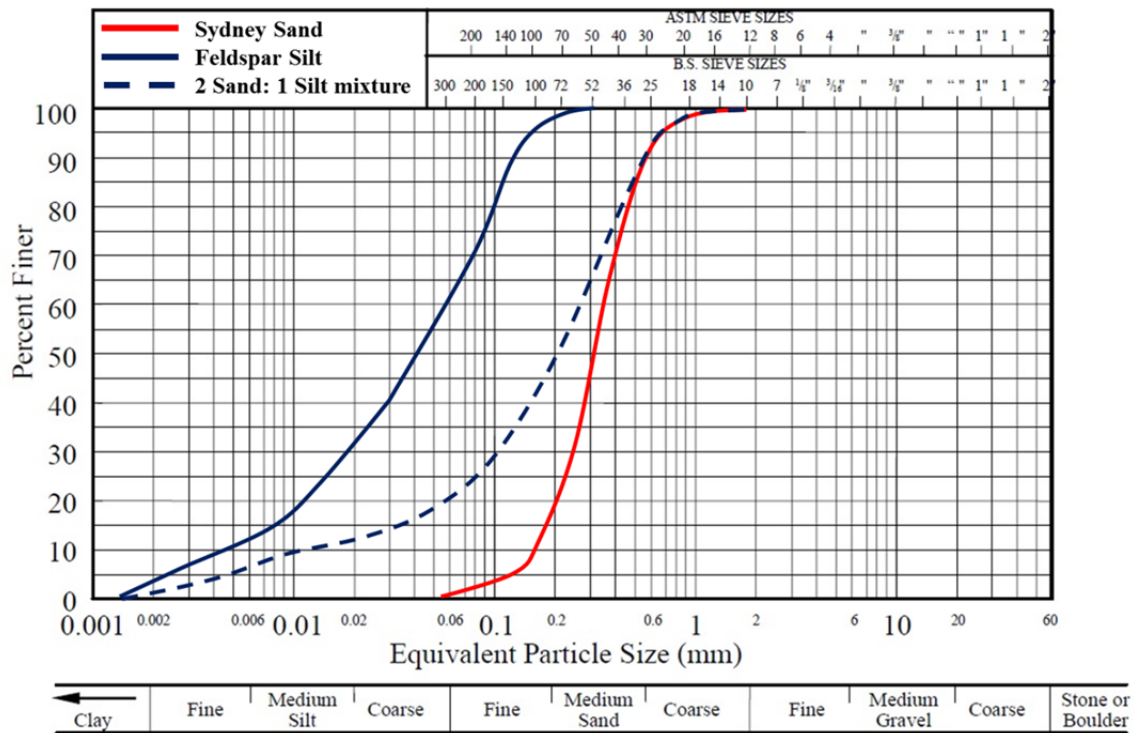


Figure 3.9. Grading curves of Sydney sand, Feldspar silt and 2sand:1silt mixture.

Classification tests were carried out in accordance with the following Australian standards:

- AS 1289.3.6.1-2009: Determination of the particle size distribution of a soil – sieving
- AS 1289.3.6.3-2003: Determination of the particle size distribution of a soil – hydrometer
- AS: 1289.3.5.1-2006: Determination of the soil particle density (specific gravity)

A series of compaction and density tests were also carried out using 40% of standard compactive effort (238 kJ/m^3), standard compactive effort (596 kJ/m^3) and modified compactive effort (2703 kJ/m^3) to determine the relationship between moisture content and dry density of the sand:silt mixtures. Compaction and density tests were carried out in accordance with the following standard procedures (except for the non- standard 40% compactive effort):

- AS 1289.5.1.1-2003: Determination of the dry density/moisture content relation of a soil using standard compactive effort.
- AS 1289.5.2.1-2003: Determination of the dry density/moisture content relation of a soil using modified compactive effort.

3.2.4 Models Preparation

To prepare the sand specimens the container was fixed in its vertical position and sand was dry-rained (air-pluvation) into the container from specific heights to produce uniform beds of sand. Figure 3.10 shows the hung sand raining funnel and strainer above the large size model. The raining apparatus (funnel, hose and strainer) were suspended from an overhead crane girder that allowed the apparatus to be easily moved across the container width as well as allowing continuous adjustment of its height to maintain a constant gap between the soil surface and the strainer outlet. Preliminary experiments were conducted to determine the uniformity of the process and how sand density changes with raining from different heights. Results from raining the sand from different elevations over known volume pans placed on the model floor demonstrated that uniform sand density could be achieved across the width of the model. By adjusting the pluvation height different sand densities were obtained. The trial results suggested that the distance between the strainer and top of the sand should be 100 mm and 300mm in order to produce uniform, loose (D_r : 8-25%) and dense (D_r : 65-75%) sand beds, respectively.

The variability in the colour of the sand grains provided sufficient texture for the GeoPIV-DIC algorithm tracking the displacement of the sand particles. The relatively pale colour and larger portion of fines of the sand/feldspar mixture required an artificial texture to be added on the face of the soil so that displacement could be easily tracked by the GeoPIV-DIC algorithm. This was performed by unfastening the container's hinges, rotating the container 90° to horizontal, removing the back of the container, placing a plug to form the upper side of the model as shown in Figure 3.4, sprinkling black, embossing powder on the Perspex window followed by dry-raining the sand-feldspar mixture, then replacing the back of the container and rotating the container back to its vertical position and securing it to the steel frame.

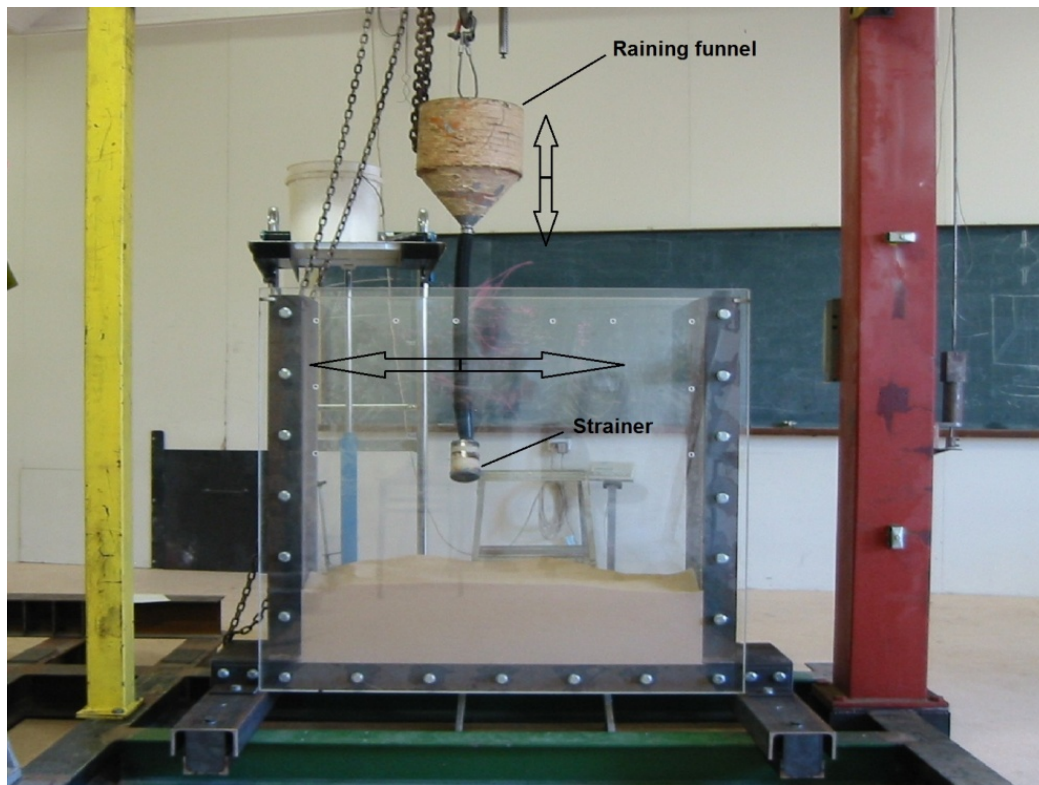


Figure 3.10. Set up of sand raining apparatus above the large model.

The contrast between the pale light grey sand:silt mixture and the black sprinkled powder provided sufficient greyscale information in the captured images. Figure 3.11 shows the natural texture of the grains of sand in a black and white (B/W) image, the size of the embossing powder particles, the texture created by the speckled black embossing powder on the inside face of the Perspex window, and the texture resulting from the speckled black embossing powder in a B/W 2sand:1silt image. Sand models were prepared with a pre-compaction void ratio that ranged from 0.79 (relative density of 3% and a unit weight of 14.49 kN/m^3) to 0.59 (relative density of 95% and a unit weight of 16.35 kN/m^3). Dry sand-silt models were prepared with a pre-compaction void ratio that ranged from 0.75 (relative density of 31% and unit weight of 14.95 kN/m^3) to 0.6 (relative density of 70% and unit weight of 16.3 kN/m^3). The method used for pluviating sand did not succeed with sand:silt mixture as the silt in the mixture interrupted the material flow by building up on the sides of the raining apparatus and blocking the strainer. The sand:silt mixture was placed by raining it in small quantities using a scoop. This procedure allowed reasonably uniform soil beds to be made successfully.

The magnitude of the sand/boundary interface shear is characterized by δ (angle of interface friction) and depends on parameters, such as the rigidity and smoothness of the boundary, and on the soil, angularity, size and relative density. In general δ for a granular soil is taken to be between $\phi/2$ and $\phi/3$ where ϕ is the angle of internal friction of the soil (O'Rourke *et al.*, 1990). This is consistent with the reported sand/Perspex δ value of 25° (Santamarina *et al.*, 1989). Since the sand-Perspex interface friction angle is significantly lower than the sand friction angle. Therefore, failure will occur at the sand-Perspex interface rather than within the soil body. This, and the tight fit of the model front and rear Perspex faces, ensures that the movement observed at the Perspex window should be similar to that present through the soil model. Since lubrication in the form of grease, oils, or silicones had little effect in reducing the ratio of interface to the sand friction angle (δ/ϕ) along the model boundaries (Santamarina *et al.*, 1989), lubrication between the soil and the Perspex faces was not considered to be important. More significantly, using any lubricant on the Perspex faces would greatly affect the quality of the photography results in observing the pattern of soil deformations during the tests, and therefore it was omitted.

3.2.5 High Speed & Still digital cameras

A high speed digital camera (model FASTCAM 1024 PCI) manufactured by Photron Inc (<http://www.photron.com>) fitted with a Navitron 50 mm lens with focal length of 0.95 m was used in this work. Images were captured at a rate of 1000 fps (frames per second) at full 1024 x 1024 pixel resolution. A shutter speed of 1/3000 second and 1000 fps provided the optimum frame sequence, field of view and image brightness for the 1024 x 1024 pixel image resolution. The high-speed camera was mounted on a tripod placed on the floor and positioned approximately 1.2m and 1.8m from the small and large model testing apparatus respectively. The field of view of the 1024 x 1024 pixel image was 403 mm x 403 mm and 680 mm x 680 mm giving object space pixel sizes of 0.39 mm and 0.67mm in the tests of the small sized and large sized models respectively (*see Section 4.3 for details of camera calibration*). The high speed camera was placed facing the centreline of the falling poulder (middle of the container) in the tests in the small sized model to capture the entire width of the model within the camera field of view.

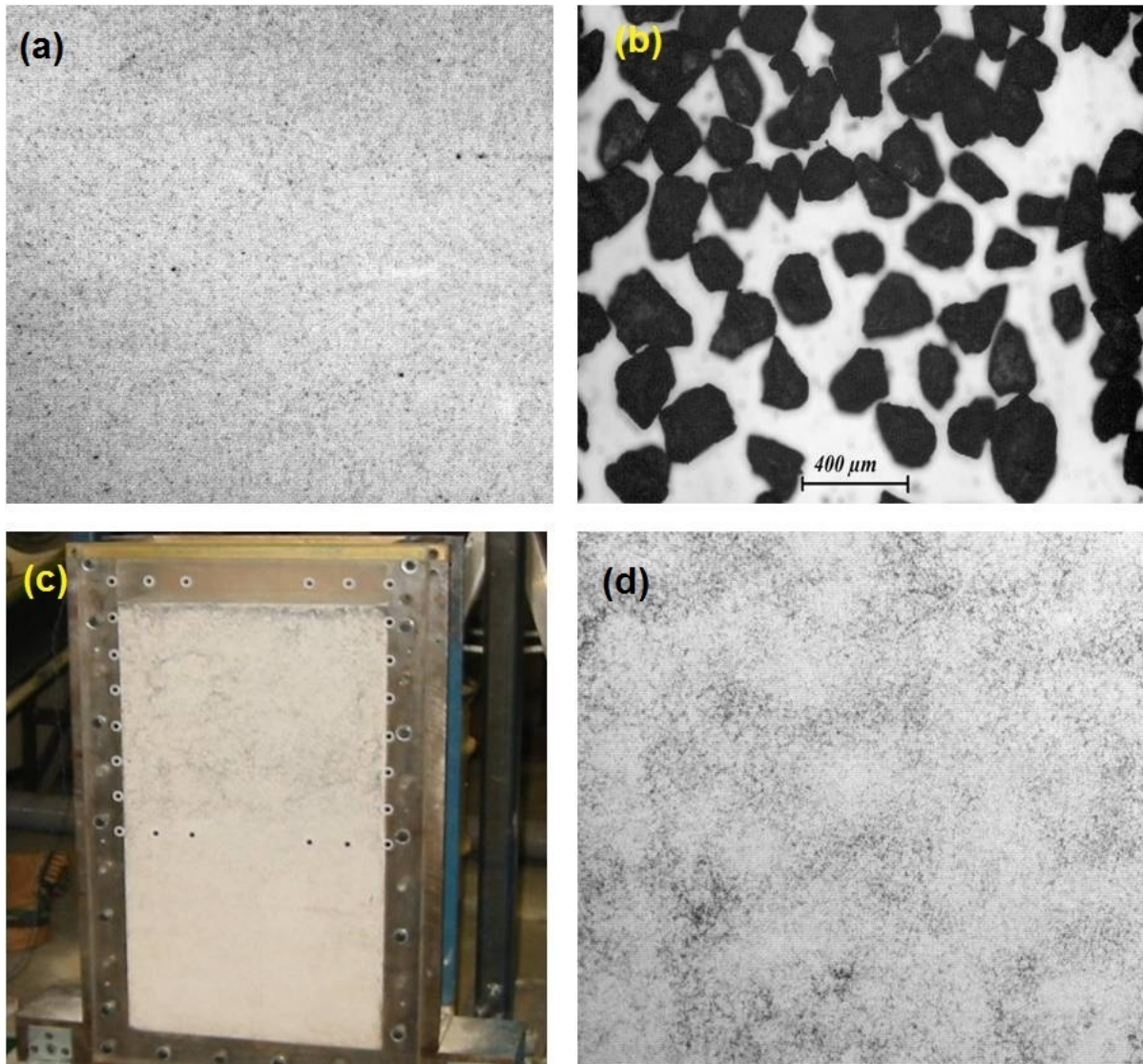


Figure 3.11. Texture of sand grains in a sand B/W image (a), relative size of the embossing powder marker particles (b), texture by black marker on the front of a 2sand:1silt model (c) and the texture by the markers in a 2sand:1silt B/W image (d).

This was not desirable with the large sized model as the high speed camera would have to be positioned further away from the model resulting in an image resolution of about 1.0mm. Therefore, the high speed camera was placed off the centreline to capture a field of view of about $\frac{2}{3}$ of the model width without compromising the image resolution. This was considered satisfactory due to the symmetrical nature of the physical 2D model along the impact centreline. Figure 3.12 illustrates the captured fields of view on the faces of the small and large DC models.

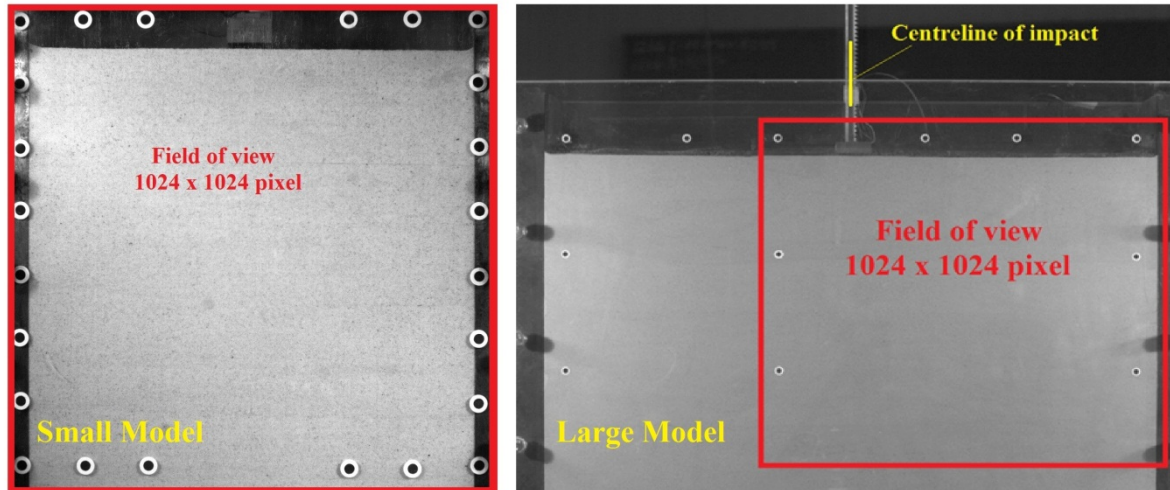


Figure 3.12. Captured field of view (1024 x 1024 pixel) by the high speed camera on the windows of the small and large DC models.

The camera was connected to a Windows PC via PCI bus, and controlled using the Photron Fastcam Viewer (PFV) software provided by the manufacturer. To avoid undesirable reflections and shadowing, lighting was provided by two sets of 2 x 500W spotlights located at the sides between the camera and the apparatus, as shown in Figures 3.1, 3.2, and 3.3. A digital SLR camera (model Canon EOS 350D) fitted with SF-S 50mm lens was also used to take high resolution (3504 x 2336 pixel) digital still photographs before and after impact, for comparison with the high speed photographs. The field of view of the 3504 x 2336 pixel still images was 380.2 mm x 253.4 mm corresponding to an object space pixel size of 0.1085 mm.

3.2.6 Cone Penetrometer Test (CPT)

Preliminarily cone penetrometer tests were performed that involved the pushing of a 5mm diameter, 30° apex angle, cone at a rate of 17mm per second through the soil. The cone was secured to the steel frame of the Type 1 arrangement, positioned above the target locations and pushed into the soil by a motorised jack. The cone was attached to a load cell that was connected to a data acquisition system (Strainsmart 6000). CPT tests were performed before and after DC tests to assess the increase in soil density following several DC drops. CPT tests were performed at locations 75mm from the Perspex front (centre of the 150mm wide container) along the centreline of the impact and at 115mm between the impact centreline and the container sidewall as shown in Figure 3.13. This arrangement provided clearances of more than 10 times the cone diameter from any of the model hard boundaries which has been

shown to minimise the boundary effects (Bolton *et al.*, 1999). The cone load cell was calibrated prior to using it for the before/after DC tests.

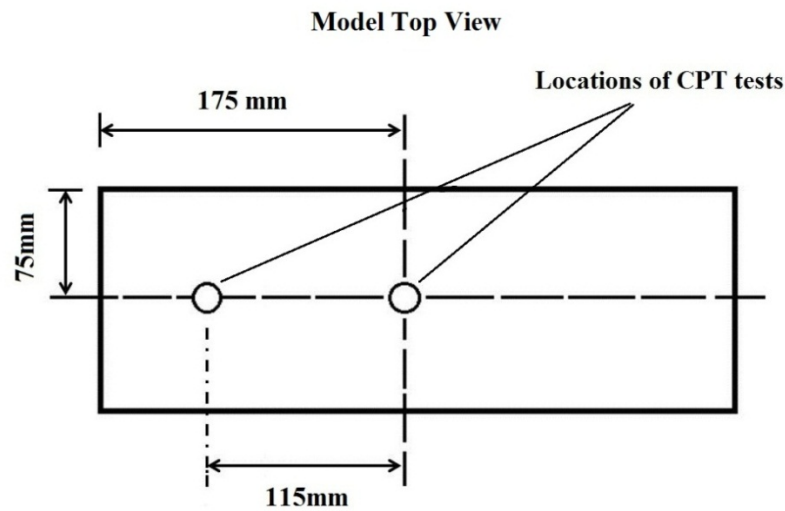


Figure 3.13. Schematic diagram shows locations of CPT tests within the DC model viewed from above

3.2.7 Instrumentation

To investigate the response of the soil to the application of dynamic compaction, earth pressure cells (EPCs) and accelerometers were embedded within the soil body in the locations and orientations shown in Figure 3.14. The instruments were concentrated in the area beneath the impact to a distance 250 mm beneath the pre-impact soil surface along the centreline of the model. The poulder was also instrumented with an accelerometer placed on its upper side and a stress cell attached to its base. Stress cells were also mounted on the sides of the soil container. All the instruments were placed halfway across the model depth in order not to interfere with the displacement taking place at the front face.

The selection of sensors of suitable size and stiffness, and the careful design of the emplacement procedure are important in obtaining reliable results of maximum reproducibility. To minimise the influence of buried instruments on the soil deformation, miniature earth pressure cells (EPCs) and miniature piezoresistive accelerometers were used. The active EPCs diameter to grain size ratio (D/d_{50}) is 10, which is twice the recommended minimum to ensure a continuum response between the soil and the EPC active face (Weiler and Kulhawy (1982). Details of the instrumentation used in this work are shown in Figure

3.15 and summarised in Table 3.1. The data acquisition system and instrumentation data sheets are provided in Appendix I. The EPCs were used to measure the total pressure on the soil at the target locations and for estimating the total stresses due to the impact of the pounder on the surface of the models. Instrumentation records were acquired and recorded by a 12 channel data acquisition system model *Strainsmart 6000* at a frequency of 10000 readings per second per channel.

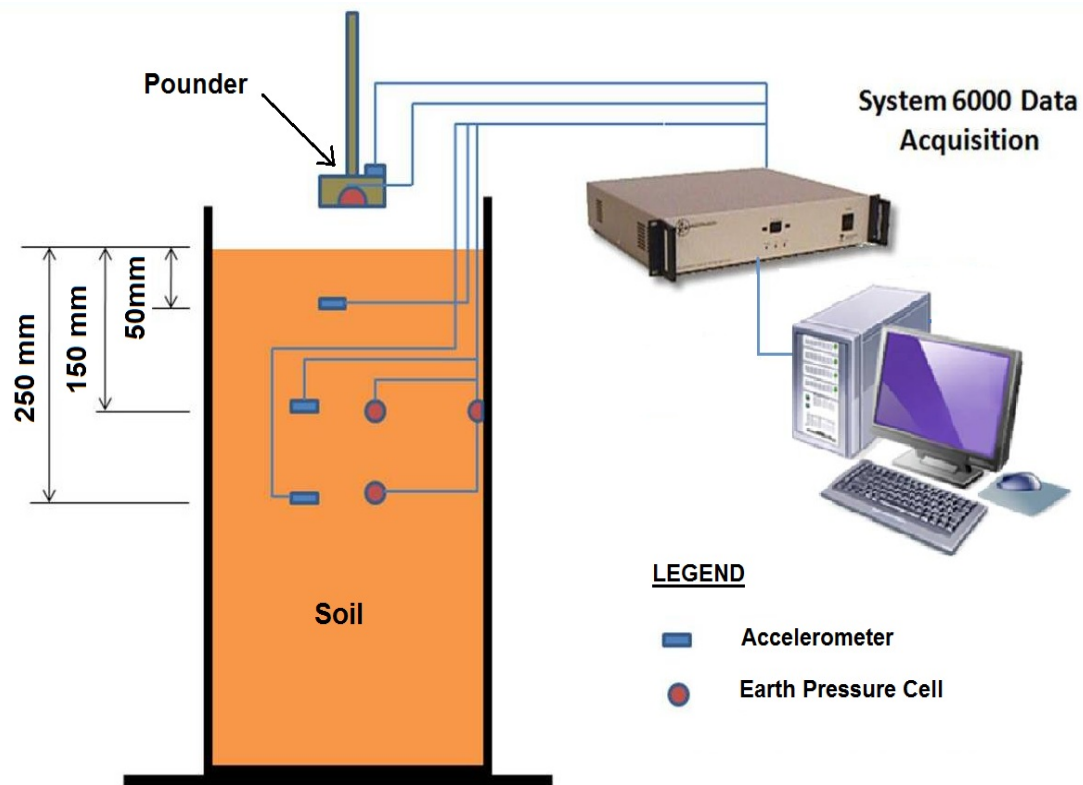


Figure 3.14. Schematic diagram shows distribution of instrumentation within the DC model.

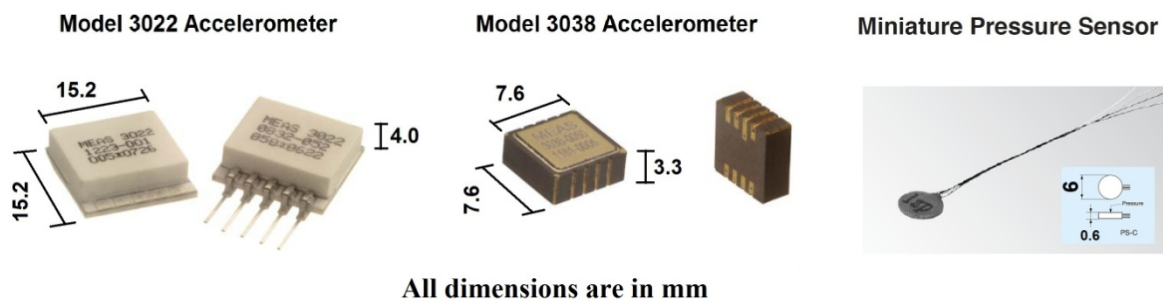


Figure 3.15. Images of accelerometer types 3022 and 3038 and EPC type PS-C.

Table 3.1. List of instrumentation specifications

Type/Model	Rated capacity	Sensitivity	Natural Frequency	Dimensions, mm	Manufacturer
EPC/ PS-2KC	200 kPa*	$\pm 1\%$ **	14 kHz	6 mm dia. 0.6 mm thick	Kyowa
EPC/ PS-5KC	500 kPa*		20 kHz		
EPC/ PS-10KC	1000 kPa*		37 kHz		
Accelerometer/ 3022	20g	1.5 mV/g	1500 Hz	15.2x15.2x4.0	Measurement Specialties, Inc.
Accelerometer/ 3038	50g	1 mV/g	4000 Hz	7.6x7.6x3.3	

* 150% safe overload rating

** Over the pressure range

3.2.7.1 Instrumentation Calibration

The basic stress sensor calibration procedures used in this study follow those outlined in Weiler and Kulhawy (1982) for earth pressure sensors in geotechnical practice. Besides the calibration of stress sensors in a fluid by the manufacturer, the use of these pressure sensors embedded in a soil body required calibration against a known stress field in the soil. Fundamentally, that is in soil, stress sensors register the component of the local stress vector, which acts normal to the sensor's plane, independent of the value of the shear stress. A steel cylindrical testing chamber 305mm in diameter and of 110mm height was used for the calibration of the stress sensors. A schematic drawing of the calibration chamber is shown in Figure 3.16. In this chamber, the vertical stress in soil was controlled with a flexible rubber membrane driven by pressurised water. The miniature size of the stress sensor relative to the calibration chamber dimensions enabled the creation of a homogeneous stress field in the central part of the soil body around the sensor. Twenty calibration experiments involving cycles of loading and unloading tests were carried out varying the position of the sensors being resting on the chamber's base to being at the middle of the chamber using both materials (sand only or sand: silt mixture) and for each varying the initial relative density.

Interpretation of soil responses from the EPC signals during the DC tests should allow for the different responses observed during the EPCs calibration such as hysteretic behaviour due to

cycles of loading/unloading and not returning to zero after the removal of load. The used calibration chamber applies k_0 (no lateral strain) conditions to the soil in which the tangent modulus of the soil normally increases with increasing axial stress level. Therefore, k_0 calibration hysteresis becomes large on subsequent load cycles due to the lateral stress buildup in the soil during loading (Weiler and Kulhawy, 1982). The calibration loading responses were used for the EPCs loading cycles; however the EPCs unloading responses were corrected in accordance with the calibration unloading responses. Calibration examples of the earth pressure sensors are provided in Appendix II.

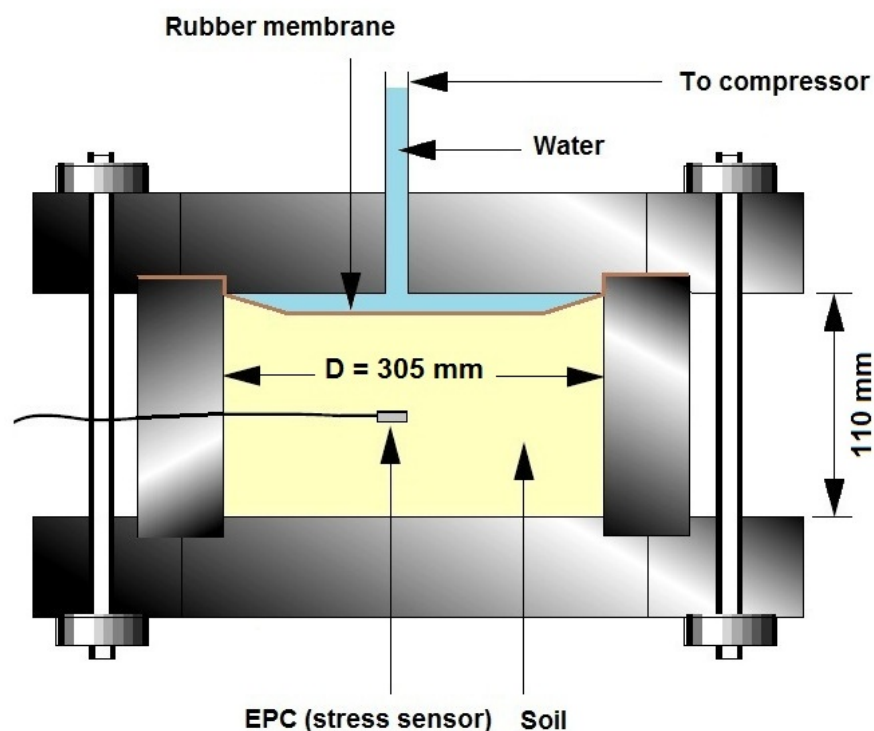


Figure 3.16. Schematic diagram shows the EPC calibration chamber.

For the accelerometers the calibrations provided by the suppliers have been used. Every accelerometer calibration was verified by conducting a free-fall test to confirm its performance prior to using it in any experiment.

3.3 DYNAMIC COMPACTION TEST PROCEDURE

A typical DC test involved 5 -12 drops of the pounder, with black and white (B/W) high speed photographs recorded at 1000 fps over 3.2 seconds for each drop. Additionally, before and after, colour photographs have been taken with a higher resolution 8 Megapixel still camera for measurement comparison. All experiments were conducted in a way that resembles the principles outlined in the previous sections, following the procedure described below:

1. The model container was cleaned, and the soil sample was rained to a specific height in steps, to allow for the placement of instrumentation, and the surface was levelled.
2. The high speed and still digital cameras and lighting system were then set up to capture the zone of interest.
3. A pre-impact image was captured by the still digital camera.
4. The instrumentation system was checked, signals zeroed then the instrumentation data acquisition system was set running.
5. The high speed camera was then started, followed by the dropping of the pounder from a scheduled height.
6. The captured images have been replayed and typically about 100 images, which had captured the dynamic loading, were saved to a computer.
7. Collect and save the instrumentation records.
8. A post-impact image was then captured by the still digital camera.
9. Repeating of the above steps for the next drop.
10. PIV analyses were subsequently conducted on the images taken using several patch size/patch spacing combinations depending on the detail required.

Depending on the required level of impacting energy, the pounder was able to free fall up to 1000mm, in the set up of the small model, type 1 tests, up to 600 mm in the set up of the small model, type 2 tests and up to 1200mm, in the large model tests. The dynamic compaction process was studied by conducting tests on dry Sydney sand and sand:silt mixtures at different pre-impact relative densities. Tests were performed with different pounder shapes to investigate the effect of different tamper geometries on both sand and sand:silt mixtures. Details of the experiments including: tested material, initial relative density, pounder type, number of drops and delivered energy are listed in Table 3.2.

Table 3.2. List of dynamic compaction tests

SAND - small sized model, Type 1 configuration									
Test Number	Soil Unit Weight kN/m ³	Void Ratio (e)	Dr%	Tamper width, mm	Weight of the falling assembly, kN	Drop height, m	Energy/drop, joule (N.m)	No. of Drops	Total energy, joule (N.m)
DC1	15.52	0.68	57%	57	0.16	0.3	48	3	144.0
DC2	16.35	0.59	95%	57	0.16	0.3	48	4	192.0
DC3	14.52	0.79	4%	57	0.16	0.3	48	8	384.0
DC4	16.11	0.61	85%	57	0.16	0.3	48	5	240.0
DC5	15.98	0.63	79%	57	0.16	0.3	48	5	240.0
DC6	15.67	0.66	64%	57	0.16	0.3	48	4	192.0
DC7	14.87	0.75	24%	57	0.16	0.3	48	5	240.0
DC8	15.03	0.73	32%	57	0.16	0.3	48	5	240.0
DC9	15.22	0.71	42%	57	0.16	0.3	48	4	192.0
DC10	15.09	0.72	35%	57	0.16	0.3	48	5	240.0
DC11	14.89	0.75	25%	57	0.16	0.3	48	5	240.0
DC12	15.19	0.71	40%	57	0.16	0.3	48	5	240.0
DC13	15.56	0.67	59%	57	0.16	0.3	48	2	96.0
SAND - small sized model, Type 2 configuration									
DC14	14.49	0.79	3%	25	0.056	0.2	11.2	4	44.8
DC15	15.63	0.66	62%	25	0.056	0.2	11.2	5	56.0
DC16	14.52	0.79	4%	25	0.056	0.2	11.2	4	44.8
DC17	16.37	0.59	96%	25	0.056	0.2	11.2	4	44.8
DC18	14.75	0.76	17%	25	0.056	0.1	5.6	6	33.6
DC19	14.49	0.79	3%	35	0.058	0.2	11.6	4	46.4
DC20	15.63	0.66	62%	35	0.058	0.2	11.6	5	58.0
DC21	14.54	0.79	5%	35	0.058	0.2	11.6	4	46.4
DC22	16.30	0.59	93%	35	0.058	0.2	11.6	4	46.4
DC23	15.41	0.69	51%	35	0.058	0.1	5.8	11	63.8
DC24	14.75	0.76	17%	35	0.058	0.1	5.8	12	69.6
DC25	15.57	0.67	59%	35	0.058	0.1	5.8	12	69.6
DC26	16.20	0.60	89%	35	0.058	0.1	5.8	12	69.6
DC27	14.67	0.77	13%	35	0.058	0.2	11.6	12	139.2
DC28	15.68	0.66	65%	35	0.058	0.2	11.6	12	139.2
DC29	15.95	0.63	77%	35	0.058	0.2	11.6	12	139.2
DC30	14.71	0.77	15%	35	0.058	0.3	17.4	12	208.8
DC31	16.03	0.62	81%	35	0.058	0.3	17.4	12	208.8
DC32	14.72	0.77	15%	35-Type B	0.056	0.3	16.8	6	100.8
DC33	14.81	0.76	20%	35-Type C	0.056	0.3	16.8	6	100.8
DC34	14.77	0.76	18%	35-Type D	0.056	0.3	16.8	6	100.8
DC35	14.80	0.76	19%	35-Type D	0.056	0.3	16.8	6	100.8

Table 3.2. List of dynamic compaction tests (*continued*).

SAND:SILT - small sized model, Type 2 configuration									
Test Number	Soil Unit Weight kN/m ³	Void Ratio (e)	Dr%	Tamper width, mm	Weight of the falling assembly, kN	Drop height, m	Energy/drop, joule (N.m)	No. of Drops	Total energy, joule (N.m)
DC36	15.57	0.65	57%	35	0.058	0.3	17.4	6	104.4
DC37	15.47	0.66	55%	35	0.058	0.1	5.8	6	34.8
DC38	15.64	0.64	59%	35	0.058	0.2	11.6	5	58.0
DC39	14.95	0.75	31%	35	0.058	0.2	11.6	5	58.0
DC40	16.30	0.60	70%	35	0.058	0.2	11.6	4	46.4
DC41	17.37	0.65	57%	35	0.058	0.2	11.6	4	46.4
DC42	15.77	0.63	63%	35-Type B	0.056	0.3	16.8	6	100.8
DC43	15.62	0.64	59%	35-Type C	0.056	0.3	16.8	6	100.8
DC44	15.83	0.62	65%	35-Type C	0.056	0.3	16.8	6	100.8
DC45	15.93	0.61	68%	35-Type D	0.056	0.3	16.8	6	100.8
DC46	15.78	0.63	63%	35-Type D	0.056	0.3	16.8	6	100.8
SAND - large sized model									
DC1L	14.58	0.78	8%	35	0.0658	0.75	49.4	12	592.65
DC2L	15.86	0.64	73%	35	0.0658	0.75	49.4	12	592.65
DC3L	15.24	0.71	43%	57	0.0753	0.75	56.5	12	678.07
DC4L	14.97	0.74	29%	57	0.0753	0.75	56.5	12	678.07
DC5L	15.83	0.64	71%	105	0.1092	0.75	81.9	12	982.67
DC6L	14.98	0.74	30%	105	0.1092	0.75	81.9	12	982.67

Note: Where tamper type is not mentioned, it is a flat based tamper (Type A).

3.4 EXTRACTING UNDISTURBED SAND SPECIMENS FROM POST DC TEST MODELS FOR CT-SCAN TESTS

To observe and quantify the local void ratio distribution at target locations (refer to *Chapter 5* for details of the CT-Scan technique and the criterion used in selecting specimens for the CT-scan analysis) within the sand soil models at the end of the dynamic compaction process, X-ray digital microtomography was used. This technique provides a means to quantitatively analyse the microstructure of the specimens and determine differences in their density from before and after the compaction process. Undisturbed sand specimens were recovered from varying depths up to about 350 mm below the sand model surface. To obtain undisturbed samples of dry granular material, a special resin was slowly injected at the target depths with a 100ml syringe through a 1.5mm diameter plastic needle into locations identified from the high speed photography as being of interest. The resin used was a solvent free epoxy resin

(MEGAPOXY HX) that has applications in repairing cracked concrete by gravity penetration. The resin is 100% reactive, hydrophilic of very low viscosity, and has a density of 1.1 g/cm^3 . For successful computerized tomography it was essential that the resin have a low density to ensure a strong contrast between the solid particles and the pore space in the X-ray images. The resin has a setting time of about 48 hours. The data sheet of the MEGAPOXY HX resin is provided in Appendix I.

The low viscosity and quick setting time properties of the selected resin provided the essential characteristics needed for solid specimens to be formed and extracted with minimal disturbance. Figure 3.17 shows examples of the extracted sand-resin lumps. Extracted sand-resin lumps were then trimmed to cubical shapes with maximum specimen dimensions of $50 \text{ mm} \times 20 \text{ mm} \times 20 \text{ mm}$ so that samples could fit in the CT scanner. Smooth faces were created using a special wheel cutter equipped with a diamond blade as shown in Figure 3.18. Examples of the CT-scan ready trimmed smooth faced specimens are shown in Figure 3.19.



Figure 3.17. Extracted sand-resin lumps prior to trimming.

X-ray imaging was then performed using the micro CT scanner model *Skyscan1172* shown in Figure 3.20. The X-ray imaging comprised a full 360° scan with an exposure time of 1770 ms using a 100kV source voltage to generate images with a pixel resolution of between 5 and $17.23 \mu\text{m}$.

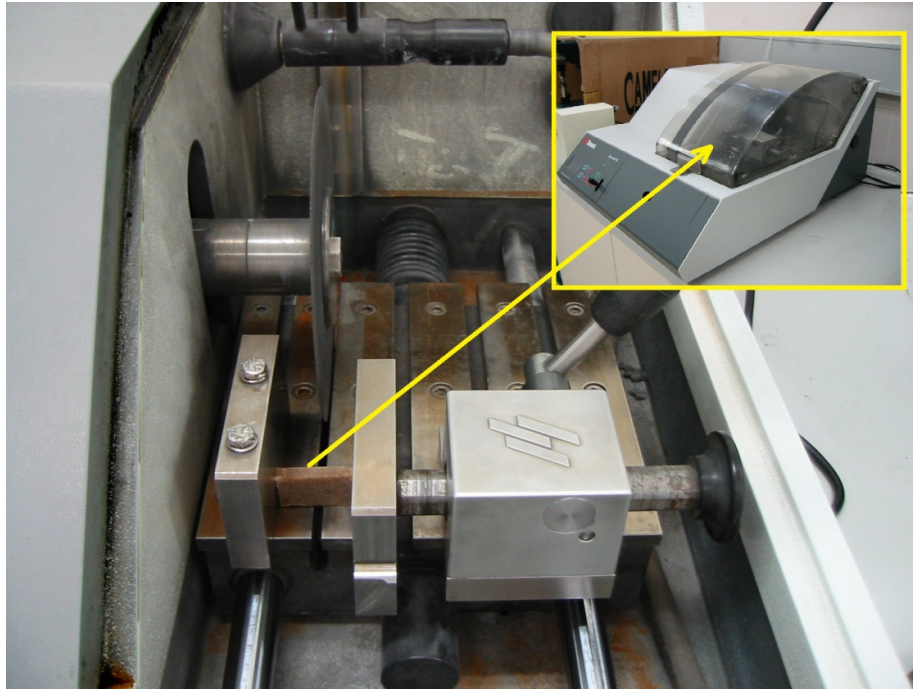


Figure 3.18. Preparing the extracted sand-resin lump by a cutting wheel equipped with a diamond blade.

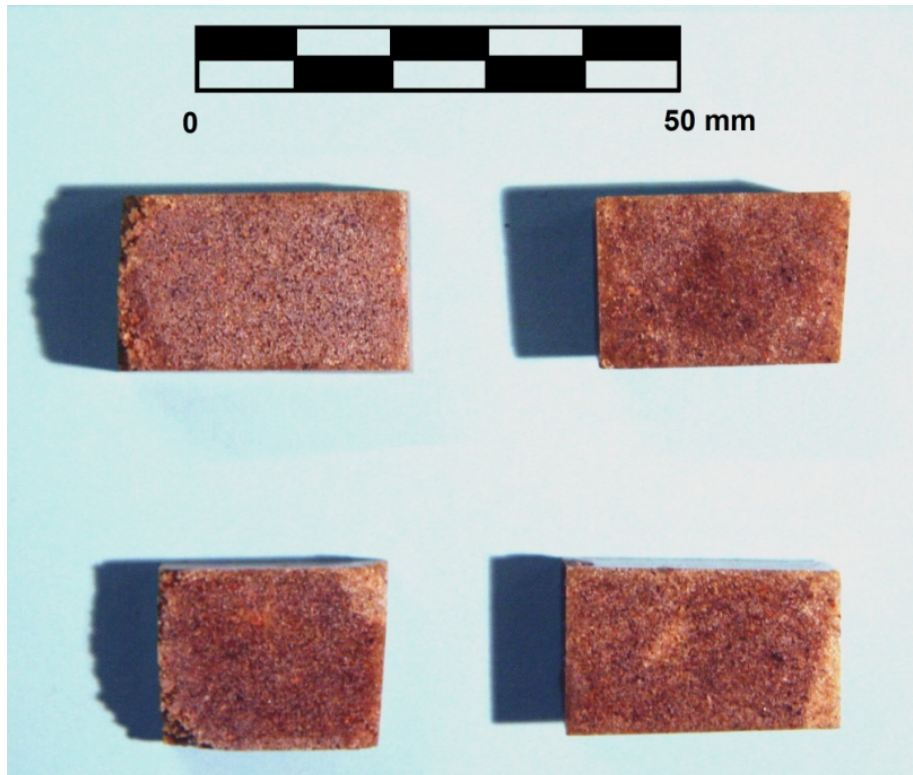


Figure 3.19. CT scan trimmed ready sand-resin specimens

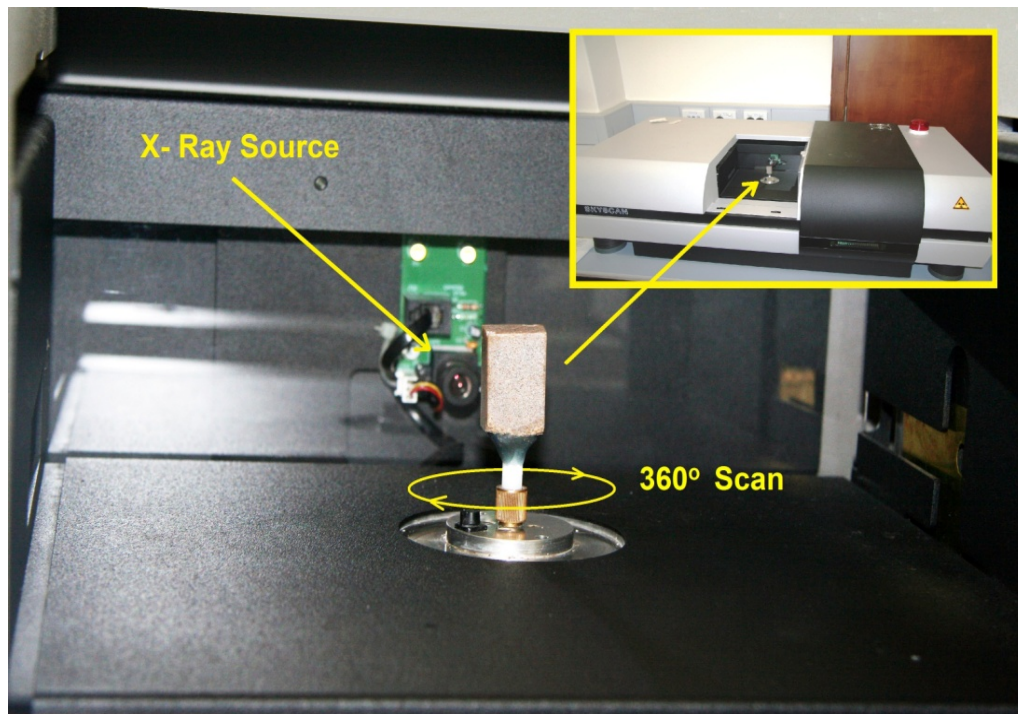


Figure 3.20. A ready sand-resin specimen in the Skyscan1172 Micro CT scanner.

3.5 TRIAXIAL TESTING WITH SHEAR WAVE VELOCITY MEASUREMENTS.

To measure the dynamic properties of the soils, a series of triaxial tests were performed on specimens made of Sydney sand and sand:silt mixtures having different dry densities. In these tests, cylindrical samples of soil were subjected to CID tests with bender elements affixed to the triaxial pedestal and specimen cap, as shown in Figure 3.21.

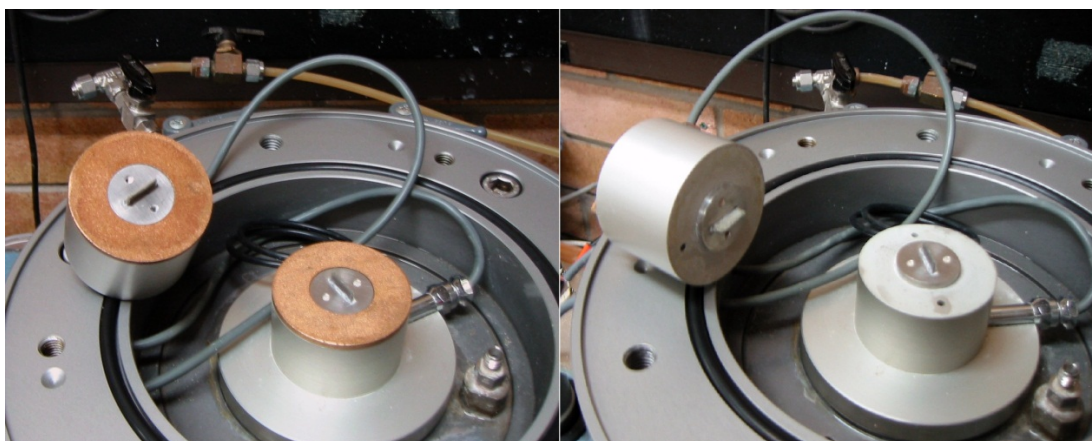


Figure 3.21. Bender elements affixed to triaxial pedestal and specimen cap.

The triaxial apparatus employed in this study has a motor controlled system so small unloading/ reloading cycles under strain control can be applied accurately to the soil specimen in the vertical direction. To measure the vertical stress, a load cell is located just above the top cap inside the triaxial cell in order to eliminate the effects of piston friction. The load cell measurement was also backed up by another load cell located above the triaxial cell. The vertical strain was measured with an external displacement transducer. The surrounding stress was applied through the water in the cell and was controlled and measured by GDS advanced pressure and volume controller which is a microprocessor-controlled screw pump for a precise regulation and measurement of fluid pressure and volume change. Another GDS system was used as a back pressure (pore pressure) controller. The triaxial cell was equipped with two vertically positioned benders at the specimen pedestal and top cap. A HP33120A function/arbitrary waveform generator was used to send the input pulse to the transmitter bender, and a Yokogawa DL1520L digital oscilloscope monitored the input and received waveforms from the bender elements. A schematic diagram of the triaxial test apparatus is shown as in Figure 3.22.

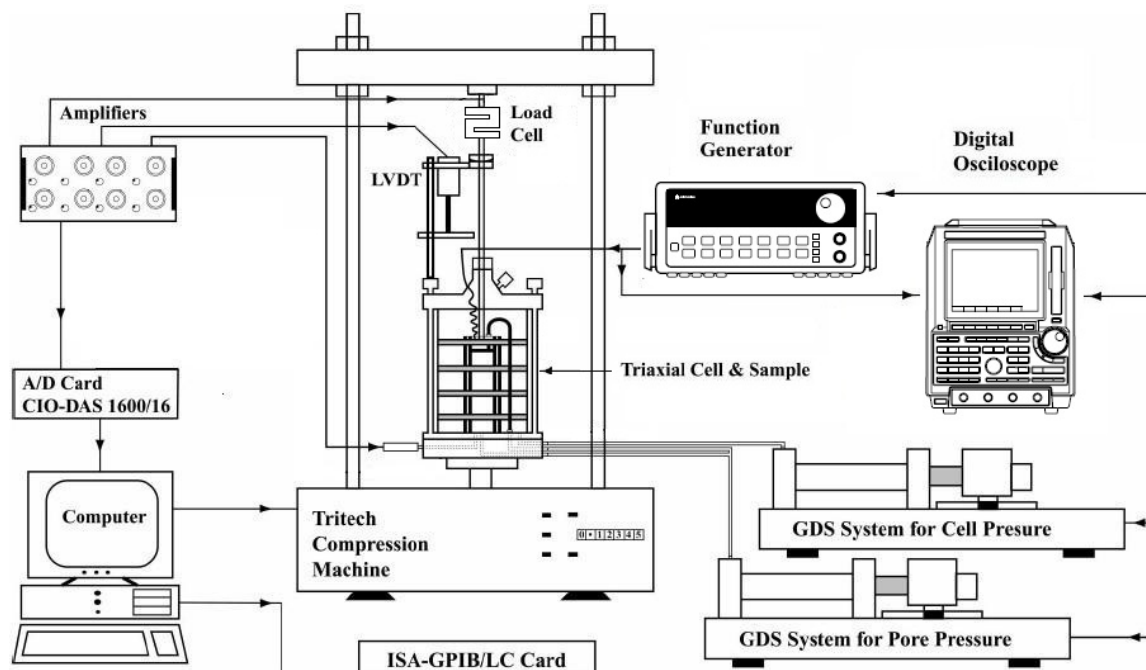


Figure 3.22. Set up of triaxial test apparatus with wave velocity measurement.

Knowing the distance between the tips of the two bender elements and the time for the wave to pass through the specimen the shear wave velocity can be determined. A cross-correlation between the input and output waveforms from the bender elements was performed and the peaks in the cross-correlation function are recorded. Evaluation of the recorded signals was carried out by taking the fast Fourier transforms of both signals in accordance with the approach described by Mohsin and Airey (2003).

3.6 LABORATORY INVESTIGATION OF LATERAL STRESSES k_0 COEFFICIENT

A series of 1-D compression tests were performed to provide stress-strain responses of the DC tested soils. It was also helpful to establish the lateral earth pressures for initial loading given by the K_0 parameter from 1-D compression tests to determine the variation in stress state induced by vertically loading the soil during the DC experiments. A conventional consolidation equipment oedometer apparatus has been used. The set up comprises a semi-rigid confining oedometer brass ring (34.45mm in diameter) of a wall thickness of 1.65mm with strain gauges affixed around the ring exterior. The thickness of the ring was chosen in such a way that the circumferential strain generated by the radial stress exerted by the specimen on the ring is measurable by strain gauges, but very small, so that quasi-oedometric conditions are ensured. The ring height is 27.0 mm.

Three SHOWA N11-FA-5-120-11 uniaxial strain gauges with resistance of 120 ohm, were mounted equally spaced, around the outer central surface of the ring parallel to the horizontal plane. The resistance changes in the strain gauges are read from the data acquisition Strainsmart 6000 at a frequency of 50 readings per second per channel. Soil samples were loaded in stages to a maximum vertical stress of 224 kPa and then unloaded. Each load stage continued until there was no further change in displacement and no change in lateral pressure. Vertical displacement was recorded by an external displacement transducer (LVDT). The oedometer rig set up for K_0 measurement is shown in Figure 3.23. The device is calibrated to known lateral pressures. Calibration was performed by loading the ring with compressed air using specially made metal caps with O-rings to seal the oedometer cell as shown in Figure 3.24. Calibrations of the strain gauges are provided in Appendix II.



Figure 3.23. Set up of oedometer experiment for k_0 measurement



Figure 3.24. Set up of the oedometer cell with the caps used to seal the ring during calibration.

3.7 STATIC LOAD TESTS

Two kinds of static load tests on dry sand were carried out for comparison with the well established static plane strain response (Vesic, 1973), and with the dynamic impact response. One of the flat based tampers was loaded incrementally and controlled by two different means of displacement application. The first method involved using a 10MPa hydraulic ram. The ram was mounted at the centre on the soil container and affixed to the steel frame as shown in Figure 3.25. Pressure was applied manually to produce rates that varied between 0.2mm/sec to 0.4mm/sec using the hydraulic ram to push the pad footings into the sand. The average contact pressure with the soil was measured by a load cell mounted between the hydraulic ram and the pad footing. Vertical displacements were recorded by an external displacement transducer (LVDT). The calibration of the load cell is provided in Appendix II. Images were recorded at a rate of around 1 frame every 3 seconds, using the still digital camera. The time between frames was determined from a stopwatch. Table 3.3 summarises the details of the static load tests.

Table 3.3. List of Static Load tests

SAND - pseudo-static load tests					
Test Number	Soil Unit Weight, kN/m ³	Void Ratio (e)	Dr%	Tamper width, mm	Imposed loading, N
ST-P1	14.53	0.79	5	25	140 - 440
ST-P2	15.63	0.66	62	25	140 - 440
ST-P3	16.35	0.59	95	25	140 - 640
ST-P4	14.53	0.79	5	35	150 - 550
ST-P5	15.63	0.66	62	35	150 - 650
ST-P6	16.35	0.59	95	35	150 - 850
SAND – steady rate load tests					
Test Number	Soil Unit Weight, kN/m ³	Void Ratio (e)	Dr%	Tamper width, mm	Peak Imposed loading, N
ST-R1	14.66	0.77	12	25	197.3
ST-R2	16.17	0.68	87	25	615.0
ST-R3	14.75	0.76	17	35	385.0
ST-R4	15.67	0.66	64	35	704.1
ST-R5	14.82	0.76	21	57	633.6
ST-R6	15.63	0.66	62	57	1838.8

The second method of load application was carried out by applying dead load increments (pseudo-static loading) on the tamper assembly starting with the assembly resting on the surface of the soil model as shown in Figure 3.26. Tests were started by placing either 140N or 150N on the trolley resting on the 25mm and 35mm pads, respectively. Load was then increased in 100N increments to make total loads of 440N and 550N acting on the 25mm and 35mm pads, respectively. After each load increment, sufficient time was allowed for the tamper displacement to cease and measurement of displacement was then recorded. Real time photographs (at 1000 fps) recorded the soil response throughout each load increment to capture the movement of the soil skeleton.

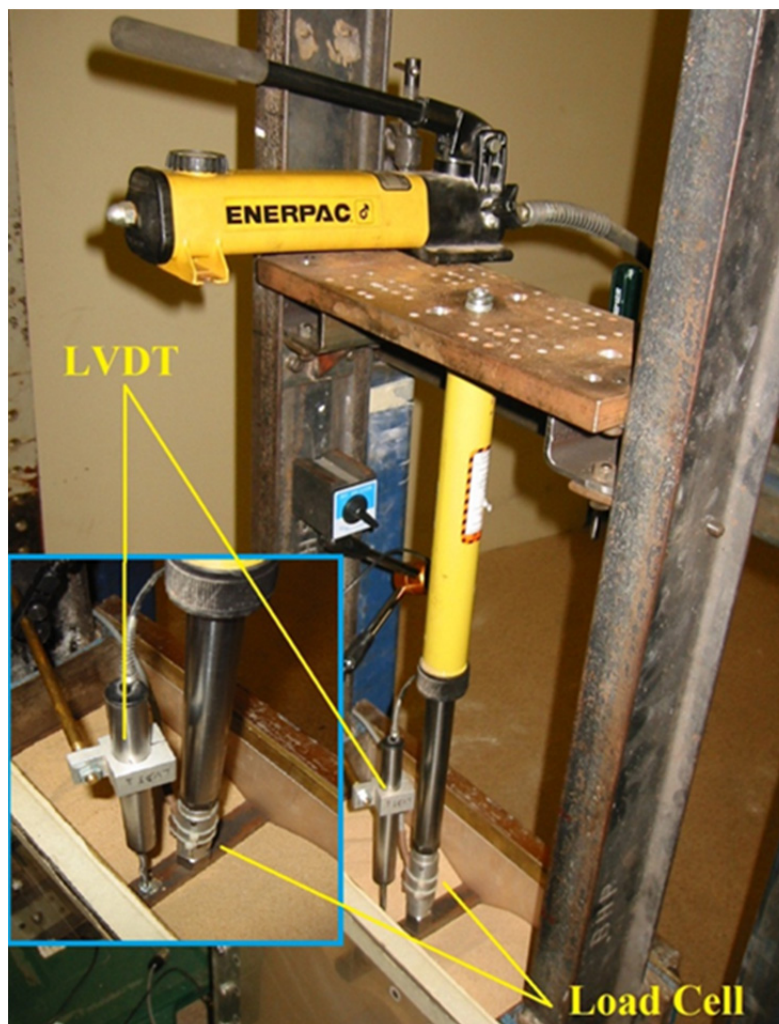


Figure 3.25. Set up of steady rate static load test experiment

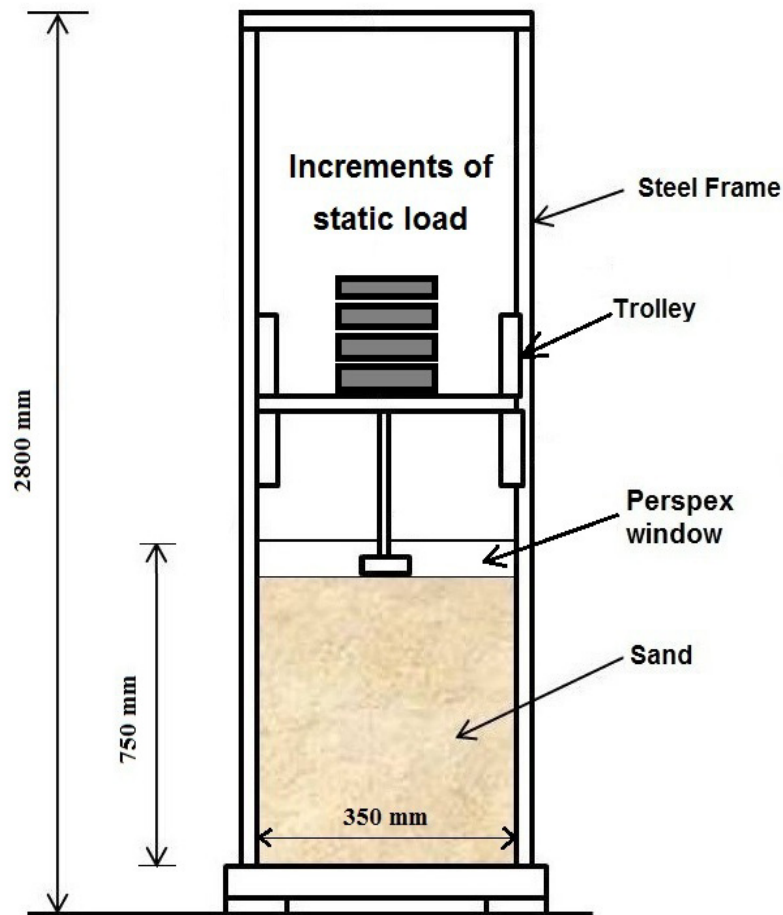


Figure 3.26. Set up of pseudo-static load test experiment

3.8 COMPACTION AND DENSITY TESTS

A series of proctor compaction test were carried out to determine the optimal moisture content at which the tested sand:silt mixture would become most dense and achieve its maximum dry density. The compaction tests were performed employing three energy levels, the standard compactive effort of 596 kJ/m^3 , the modified compactive effort of 2703 kJ/m^3 , and a non-standard compactive effort of 238 kJ/m^3 (40% of standard compactive effort). Results of the compaction tests are shown in Figures 3.27. This test is not possible to be performed on sand and therefore results are limited to compaction tests of the sand:silt mixture.

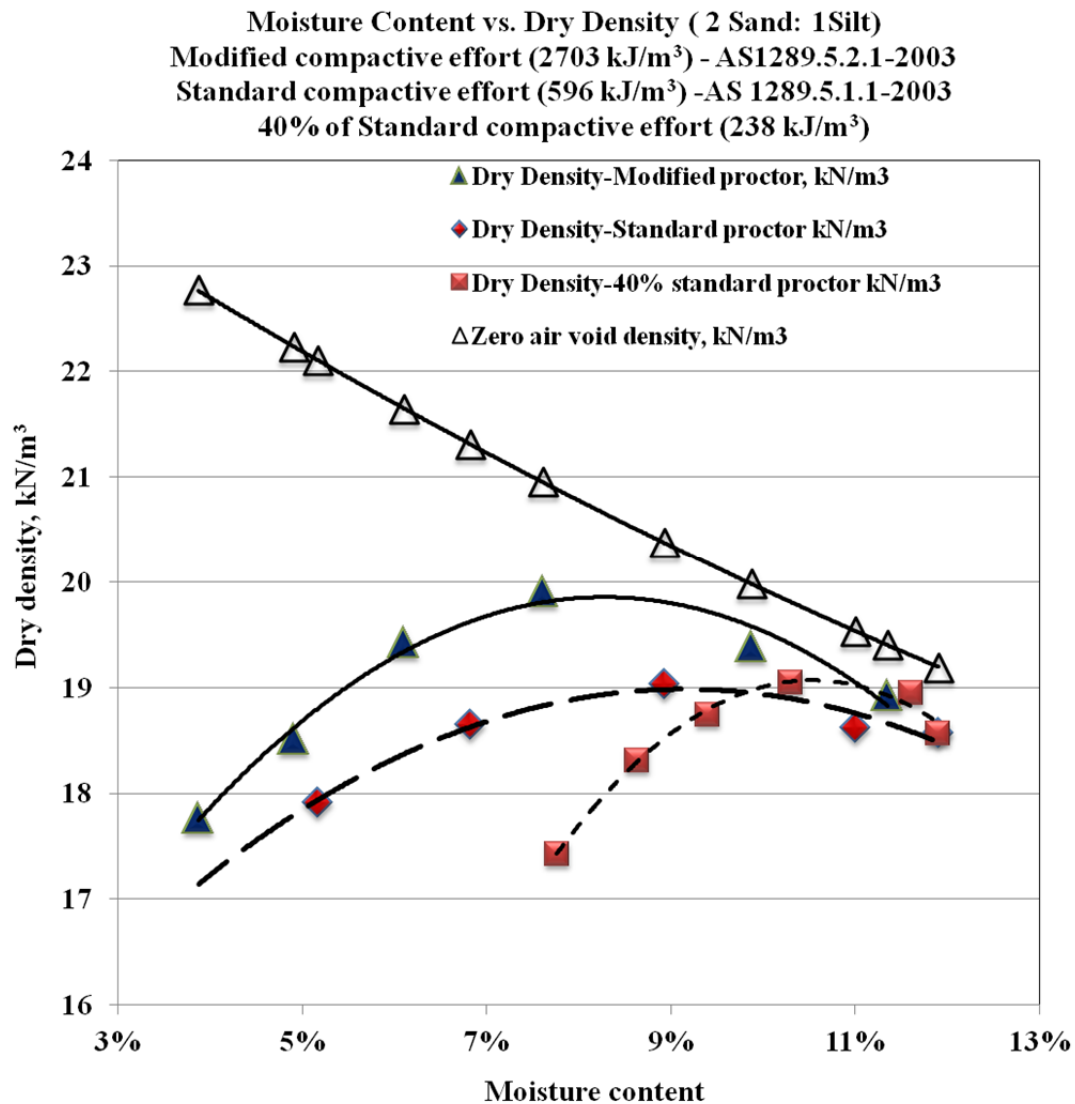


Figure 3.27. Dry densities verses moisture contents from modified and standard proctor compaction tests of sand:silt mixture.

The estimated maximum dry densities and corresponding optimum moisture contents are listed in Table 3.4. As expected, the degree of compaction increases with the increased compaction effort and can be achieved at lower optimum moisture content. The results show that it is possible to obtain the maximum dry density of the standard proctor test by 40% of the standard energy but at higher moisture content. The slightly higher maximum dry density achieved by the 40% proctor over the standard proctor was possibly related to difficulties in obtaining reliable moisture content and maximum dry density measurements from the permeable sandy soil mixture. The value of these tests is only informative since the DC tests

were performed on dry sand:silt mixture employing much lower stress levels than the compaction-density tests.

Table 3.4. Maximum dry densities and optimum moisture contents of sand:silt mixture

Compaction test	Maximum dry density, kN/m ³	Optimum moisture content, %
40% of standard proctor compaction test	19.05	10.4
Standard proctor compaction test	19.03	8.9
Modified proctor compaction test	19.97	8.3

Chapter IV: Camera Calibration and Validation of Displacement Measurements

Table of Contents

4	OVERVIEW	106
4.1	PRINCIPLES OF GeoPIV ANALYSIS AND VALIDATION	106
4.2	ACCURACY AND PRECISION IN GeoPIV MEASUREMENTS	107
4.3	CAMERA CALIBRATION TECHNIQUE FOR PIV	109
4.4	PILOT ASSESSMENT OF THE PHOTOGRAPHY SYSTEM.....	111
4.4.1	Camera Calibration for Image Distortions.....	112
4.4.2	Image Quality - Noise and Filters.....	115
4.4.3	Sensitivity of Camera Sensor	117
4.4.4	GeoPIV Evaluation	119
4.5	HIGH SPEED VERSUS STILL PHOTOGRAPHY FOR DC TESTS.....	122
4.6	SUMMARY	128

4 OVERVIEW

The image processing and algorithm validation described in this chapter represents a necessary and important part of the process of assessing high speed photography and digital image correlation analysis for dynamically loaded granular soils. However, the process cannot provide a direct check of the displacement and strain fields, and further validation tests by means of finite element modelling or X-ray micro tomography images were carried out for strain validation at the micro-scale level as will be discussed in the following chapters.

The first part of this chapter briefly describes the principles of GeoPIV analysis and its concept as an image-based deformation measurement tool. The chapter then discusses the performance (accuracy and precision) of GeoPIV for deformation measurements of geomaterials. This is followed by a description of the techniques adopted in this work to perform camera calibration and to validate the function of the GeoPIV algorithm in large deformation measurements. Advantages of using high speed photography over digital still photography for displacement and strain measurements of dynamically loaded granular soils are also presented.

4.1 PRINCIPLES OF GeoPIV ANALYSIS AND VALIDATION

In the application of image-based deformation measurement to geotechnical experiments, the performance of the system depends on the ability of the image analysis algorithm to track soil particles during a test. The analysis process used in the GeoPIV software is indicated by the flowchart shown in Figure 4.1. GeoPIV operates by tracking the texture (i.e. the spatial variation of brightness) within an image of soil through a series of images. The reference (pre-impact) image is divided up into a mesh of PIV test patches. The displaced location(s) of any patch in a subsequent image, is computed by correlating between the subject patch extracted from the reference image (at time = t_1) and a larger patch (called the search patch) from a subsequent image (at time = t_2). The location at which the highest correlation is obtained, is taken to indicate the displaced position of the patch. The location of the correlation peak is established to sub-pixel precision by fitting a bi-cubic interpolation around the highest correlation peak. This operation is repeated for the entire mesh of patches within

the image, and then repeated for each image within the series, to produce complete trajectories (displacement vectors) of each patch.

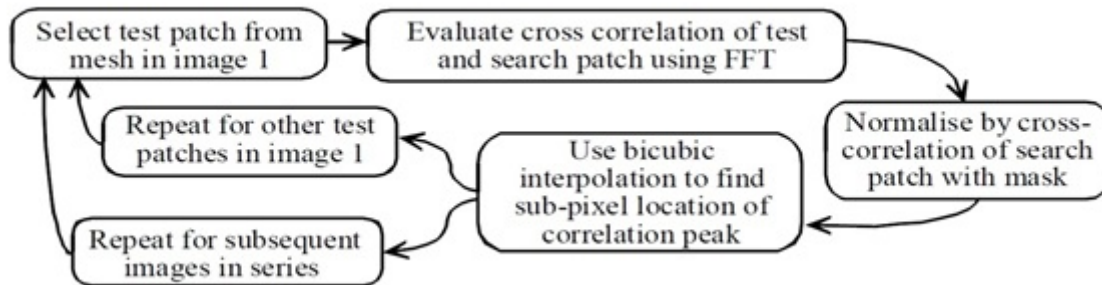


Figure 4.1 Flowchart of the GeoPIV analysis procedure (White and Take, 2002).

For statically-loaded physical element and model tests of granular soils, such as shear box and triaxial tests, soil deformations take place sufficiently slowly that they can be truly measured during and after the tests. When using image-based deformation measurement techniques, such as digital image correlation to study these models, the precision of the measurement technique can be physically quantified and backed up with measurements from the models. This can be achieved by conducting a series of controlled rigid-body movement experiments to assess the employed camera and GeoPIV algorithm. Similarly, when using GeoPIV in studying the behaviour of clayey soils in centrifuge models, the image correlation analysis can be verified by physically tracking the deformation of the artificial texture marked on the clay surface. The precision of GeoPIV over small displacement increments was initially evaluated by White *et al.*, (2001), and was further considered in greater detail by White (2002) and Take (2002). However, in this thesis soil is subjected to dynamic loading and the measurement can not be physically quantified. Thus a different approach is required, and is discussed in subsequent sections.

4.2 ACCURACY AND PRECISION IN GeoPIV MEASUREMENTS

The performance of any measurement system can be assessed by considering the errors associated with accuracy and precision. Accuracy is the systematic difference between a measured quantity and its true value, while precision is the random difference between multiple measurements of the same quantity (White *et al.*, 2002). GeoPIV is a deformation

measurement system based on image analysis, which operates by constructing the displacement field between two images and converting this displacement field from image-space (i.e. coordinates in terms of "pixels" in the digital image) to object-space (i.e. coordinates in term of "mm" in the observed field). In an ideal optic system free of lens distortions, the conversion from image-space to object-space can be carried out by assuming a constant image scale across the entire field of view. However, systematic errors associated with the accuracy of image based displacement measurement systems arise if the spatial variation in image-scale (i.e. the ratio between measurements in object- and image-space) is ignored.

The precision of the measurement system depends on the method used to construct the displacement field. White *et al.*, (2003) have demonstrated that the precision of the displacements, the random difference between multiple measurements of the same quantity, achieved using GeoPIV depends primarily on the image texture and patch size. Thus, a photogrammetry technique must be implemented to establish the image-space to object-space transformation more accurately. Taylor *et al.*, (1998) and White *et al.*, (2001b) presented systems based on the principles of close range photogrammetry. White (2002) described the photogrammetric reconstruction procedure used in the latter system.

Take (2002) describes the target location technique used to perform accurate photogrammetric reconstruction, and assesses the accuracy of transforming deformation measurements from image-space to object-space. The precision of GeoPIV over small displacement increments was initially evaluated by White *et al.*, (2001a), and was considered in greater detail by White (2002) and Take (2002). The precision of GeoPIV was evaluated by comparing the displacement vectors deduced from a grid of PIV patches overlying the soil. Since the soil translates as a rigid body, the displacement vectors should be identical; the random variation within the measured vectors indicates the system precision.

The size of the patch has been found to be critical to the accuracy of the measured displacements, as discussed by De Jong *et al.*, (2003), White *et al.*, (2003), Yaofeng *et al.*, (2007) and Pan *et al.*, (2008). White *et al.*, (2003 and 2005) reported that displacement measurements with precisions better than 0.005 and 0.002 of a pixel, for GeoPIV patches greater than 16x16 pixels and 50x50 pixels respectively, were obtained from examining

images of rigid body movements of sand and textured clay samples. Chow *et al.*, (2010) reported GeoPIV precisions of 0.0039 pixels and 0.0815 pixels for patches of 32x32 pixels for slow moving and free falling objects respectively. The lesser precision in the latter case was attributed to difficulties in obtaining uniform spatial extent (relationships between shapes, colours, spaces, and areas) throughout all the images of a free falling moving object in close range photography. This left some images alternating between being “in focus” and “out of focus”.

However, this verification is not possible for the dynamically loaded tests considered in this research because the granular material samples experience large and non-uniform displacements. This makes it difficult, if not impossible, to physically trace individual particles for the purpose of verifying the image-based deformations. Alternative verification techniques like X-ray CT (computerised tomography) scanning, or finite element modelling are limited by the difficulty of obtaining undisturbed sub-samples for high resolution scanning or disturbance to the bulk sample during its movement into the CT scanner, and by the limitations of existing constitutive models and the unproven reliability of large displacement dynamic finite element codes. Further discussion of these techniques is provided in the following chapters. Validation of the GeoPIV software required the precision of this technique to be established for dynamically loaded soil that exhibits large deformations. Therefore, it was considered essential to assess and calibrate both the high speed camera performance and effect of the characteristics of the captured images in measuring transient deformations in a dynamic test and to formulate an indirect procedure for validating the GeoPIV correlation algorithm.

4.3 CAMERA CALIBRATION TECHNIQUE FOR PIV

The accuracy of the image based measurement system depends on the resolution of the image-acquiring system and calibration of the system to handle various distortion errors. Camera calibration is a critical component of the PIV system. The data obtained from PIV analysis are in the form of image space, therefore it is essential that the camera system be calibrated to be able to find a point $P(x, y)$ in the object plane coordinate system through its

corresponding point $P(u, v)$ in the image plane coordinate system. The concept of calibrating the camera is illustrated in Figure 4.2 (Zhao *et al.*, 2007).

The deformation data obtained in image space coordinates (in pixels) must be converted into object space coordinates. Several methods for geometric camera calibration are presented in the literature. With idealised (distortion-free) imaging, the simplest way to calibrate the camera is through the pinhole camera method, which is based on the principle of co-linearity (Heikkila and Silven 1997), where all the imaging rays from object to image are assumed to pass through a single point or pinhole. In this correlation, a linear relationship between the point of an object and its image point is assumed. Because cameras usually deform the image, and the object is commonly behind a transparent material, a simple relationship between the points of the object and the image does not exist.

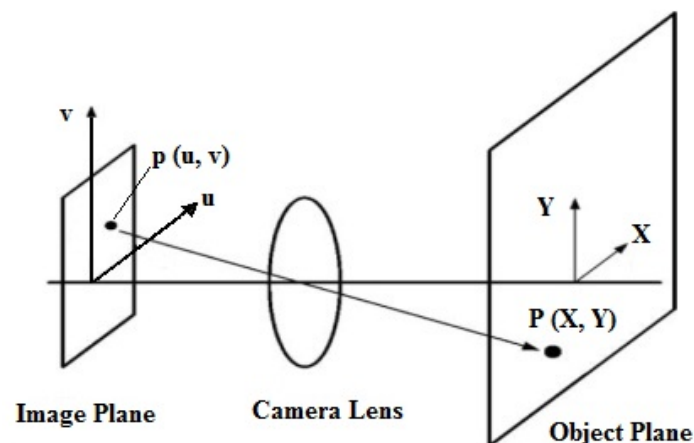


Figure 4.2. Illustration of camera calibration Concept (Zhao *et al.*, 2007).

Taylor *et al.*, (1998) first applied close range photogrammetry in centrifuge modelling. In their camera calibration model, nine parameters are needed, including two orthogonal offsets between the centre of the charge coupled device (CCD) array and the intersection of the optical axis of the camera with the array, the focal length of the camera, three polynomial coefficients representing radial geometric lens distortions, two polynomial coefficients corresponding to the tangential geometric lens distortions, and a differential scale parameter in the image, to account for the non-square pixels. This nine-parameter model can correct image distortions such as fisheye and barrelling. Paikowsky and Xi (2000) used a polynomial

function to fit the points in the object plane to their image points in the image plane. The absolute error can reach ± 0.4 mm. The classical approach that first came from the field of photogrammetry solves the problem by finding the minimum value of a non-linear error function (Slama, 1980). This method is slow and requires a lot of computation effort.

Closed form solutions have been also suggested by Abdel-Aziz *et al.*, (1971), Tsai (1987), and Melen (1994), but these methods are based on certain simplifications in the camera model, and therefore, they do not provide results as good as the non-linear minimisation. Melen (1994) and Weng *et al.*, (1992) also proposed another procedure for calibration which utilises both non-linear minimisation and a closed form solution. In these two step methods, the initial values of the parameter are computed linearly and the final values are obtained with non-linear minimisation. Heikkil and Silven (1997) proposed a four step procedure for calibrating cameras with implicit image correction using 14 parameters for their image based system for measuring deformation in centrifuge experiments. This four step method is an extension of the two step methods of calibration with an additional step to compensate for distortion caused by circular features, and a step for correcting the coordinates of the distorted image.

White *et al.*, (2003) developed the 14-parameter model of Heikkila and Silven (1997) to perform the task of calibration. Although this method still requires a lot of computational effort, the refined calibration method works very well for calibrating the camera, taking into account the majority of possible errors. The calibration control points were obtained through multiple threshold centroiding.

4.4 PILOT ASSESSMENT OF THE PHOTOGRAPHY SYSTEM

Accurate measurements of soil deformations and strains can only be obtained by correlating good quality successive images captured at different time intervals by the same camera CCD (charge-coupled device) sensor. However, the DIC analysis can be affected by misalignments of the camera, lens distortions, erratic lighting and subsequent variation in shadowing, refraction through the viewing window, image noise and most importantly the robustness of the image correlation algorithm. Thus, the following steps were adopted to assess the accuracy of the measurement system prior to conducting DC model tests. The assessment

technique comprised the following essential checks and benchmark tests of image variability and translation:

- Calibration of camera lens for image distortions for the 2D close range photography
- Evaluating noise levels in the digital images
- Assessment of the sensitivity of the camera CCD sensor
- Validation of the GeoPIV algorithm

These are discussed in detail in the following sections.

4.4.1 Camera Calibration for Image Distortions

In pinhole projection, the magnification of an object is inversely proportional to its distance to the camera along the optical axis so that a camera pointing directly at a flat surface reproduces that flat surface. However, this is far from real and even if the image is sharp, it may be distorted compared to ideal pinhole projection. Thus, it was crucial to assess the amount of distortion in the high speed camera system used in this work in order to establish the accuracy of spatial deformation measurements made during the DC tests.

For an ideal frame camera, a straight line in the object space will be a straight line in the image space in the absence of distortions. Distortion can be thought of as stretching the image non-uniformly, or, equivalently, as a variation in magnification across the field. While "distortion" can include arbitrary deformation of an image, the most pronounced modes of distortion produced by conventional imaging optics is "barrel distortion", in which the centre of the image is magnified more than the perimeter (Figure 4.3a). The reverse, in which the perimeter is magnified more than the centre, is known as "pincushion distortion" (Figure 4.3b). This effect is called lens distortion. Camera internal parameters that a calibration process is catered for are:

- Focal length: It is the distance from the centre of the lens to the focal point of the lens, which is a measure of how strongly the system converges or diverges light.
- Principal point: A point from which the focal length is measured. The principal point of a simple lens is located at the centre of the lens.
- Skew coefficient: defining the angle between the x and y pixel axes
- Distortions: The image distortion coefficients (radial and tangential distortions).

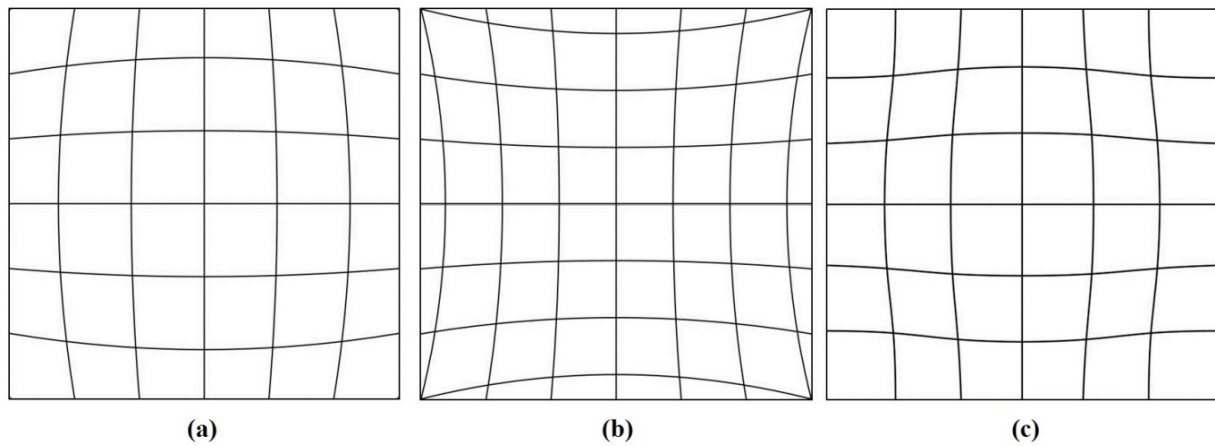


Figure 4.3. Simulation of barrel distortion (a), pincushion distortion (b) and moustache distortion (c) in photography (<http://en.wikipedia.org/wiki/Distortion> (optics)).

Reconstructing 3-D structures from multiple images (object in motion, stereo photometric, etc) requires the detection of a 3-D object of known geometry and camera calibration must then be performed by detecting a calibration object whose geometry in the 3-D space is known with very good precision. Currently, there are several available camera calibration algorithms like the camera calibration toolbox for Matlab, which utilizes a bias correction procedure for circular control points. However, for the application of close range photography in studying 2-D soil models, the main concern is to establish the accuracy of the measurements, which is the difference between the measured and true values. As such, a plane calibration technique was developed and performed as a relevant method of conversion from a plane in the image-space to a plane in the object-space. In this work, the conversion from image-space to object-space was carried out using a set of control markers placed around the captured field of view (FOV) adopting the tactic presented by Taylor *et al.*, (1998) and White *et al.*, (2001).

The exact real-space coordinates of control markers is an important factor in achieving high accuracy in the conversion process. However, these control markers were manually placed on the back of the Perspex window and their (X,Y) coordinates from direct measurements could not be used for the conversion process, because they could not be precisely located regardless of the care taken in affixing them. To obtain the exact real space coordinate of the 24 control markers, a calibration technique was performed using a pattern of uniformly spaced features on a single plane. A high contrast between the pattern features and the background was required. For this purpose, a pattern of uniformly spaced black dots on a white background

were used as calibration sheets. They were computer generated and laser printed with accurate dimensions as shown in Figure 4.4.

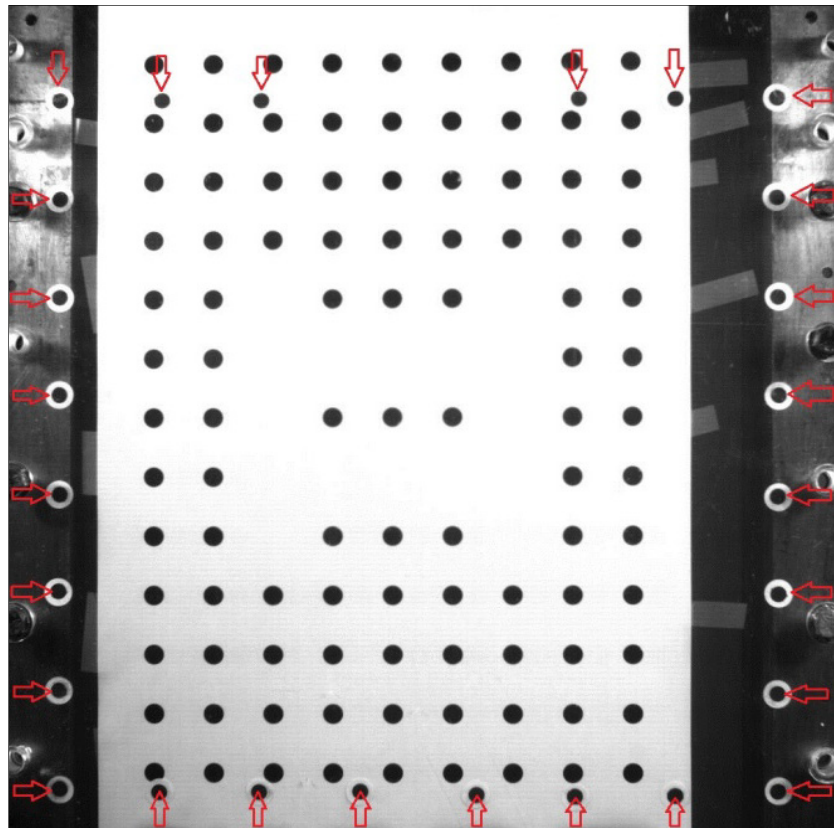


Figure 4.4. Black dot patterns as a calibration sheet for the control markers (indicated by red arrows).

Facing the stationary high speed camera, the calibration sheets were placed on the Perspex window from the inside and images were recorded using the exact set up, as outlined in Section 3.2.5, to be used later for the dynamic compaction model tests. By adopting this technique, the known coordinates on the calibration sheets (centres of the black dots) acted as control markers in the GeoPIV algorithm to establish the real-space coordinates of the real control markers that would be used later in the conversion process in the DC model tests. As the GeoPIV software constructed the displacement fields of the real control markers (which are stationary) in image-space coordinates, conversion from image-space to object-space, was then carried out subsequent to the PIV analyses to obtain the exact coordinates of the control markers. The coordinates of the control markers will remain unchanged. Distortion was found to be minimal and the image space/object space conversion was consistent over all the photographs. The control markers object-space coordinates are provided in Appendix III.

4.4.2 Image Quality - Noise and Filters

For strain mapping and pattern recognition applications based on digital image correlation, capturing good quality successive images is critical to success. In digital photography, the photographs are always affected to some extent by noise, because noise is always present in any electronic device that transmits or receives a signal, such as a camera sensor. The image noise produces a random variation in the brightness or light intensity which modifies the grayscale information in the images produced by the camera sensor.

The greyscale digital image can be represented by a matrix and defined as a two dimensional function, $f(u,v)$, where u and v are the image spatial (plane) coordinates, and the amplitude f at any (u,v) coordinate represents the intensity of the image at that point. If we consider two stationary images, denoted by α and β , captured by the same sensor with the same settings we would not expect them to be identical because of noise. The difference between α and β is a matrix ρ ($\rho = \alpha - \beta$) of the same size as α and β . The elements of “ ρ ” are noise values for the different pixels. Ideally, the displacement fields between α and β should be zero since the object hasn't moved and any apparent non-zero displacement fields are the result of the noise “ ρ ”. This procedure has been used to assess the noise produced by the camera sensor.

Two Matlab image post-processing routines were used in an attempt to improve image quality prior to the digital image correlation analysis. The routines “*histeq*” and “*Wiener2*” were used to enhance the contrast of the captured images using histogram equalization and adaptive noise-removal filtering respectively. The routine, $J = \text{histeq}(I, n)$ transforms the intensity image “ I ”, returning an intensity image “ J ” with “ n ” discrete gray levels. A roughly equal number of pixels is mapped to each of the “ n ” levels in “ J ”, so that the histogram of “ J ” is approximately flat. The “*Wiener2*” routine is a 2-D adaptive noise-removal filtering routine. This low pass filter is used with grayscale images that have been degraded by constant power additive noise. *Wiener2* uses a pixelwise adaptive Wiener method based on statistics estimated from the local neighbourhood of each pixel (Image Processing Toolbox 7; Matlab, 2010). The syntaxes and algorithms of the Matlab routines “*histeq*” and “*wiener2*” are provided in Appendix III.

Histograms depicting pixel-level intensities (grayscale levels) of the acquired non-filtered and filtered images together with their corresponding images are shown in Figures 4.5 and 4.6

respectively. The effect of the adopted image processing on the PIV analysis will be discussed in the following sections.

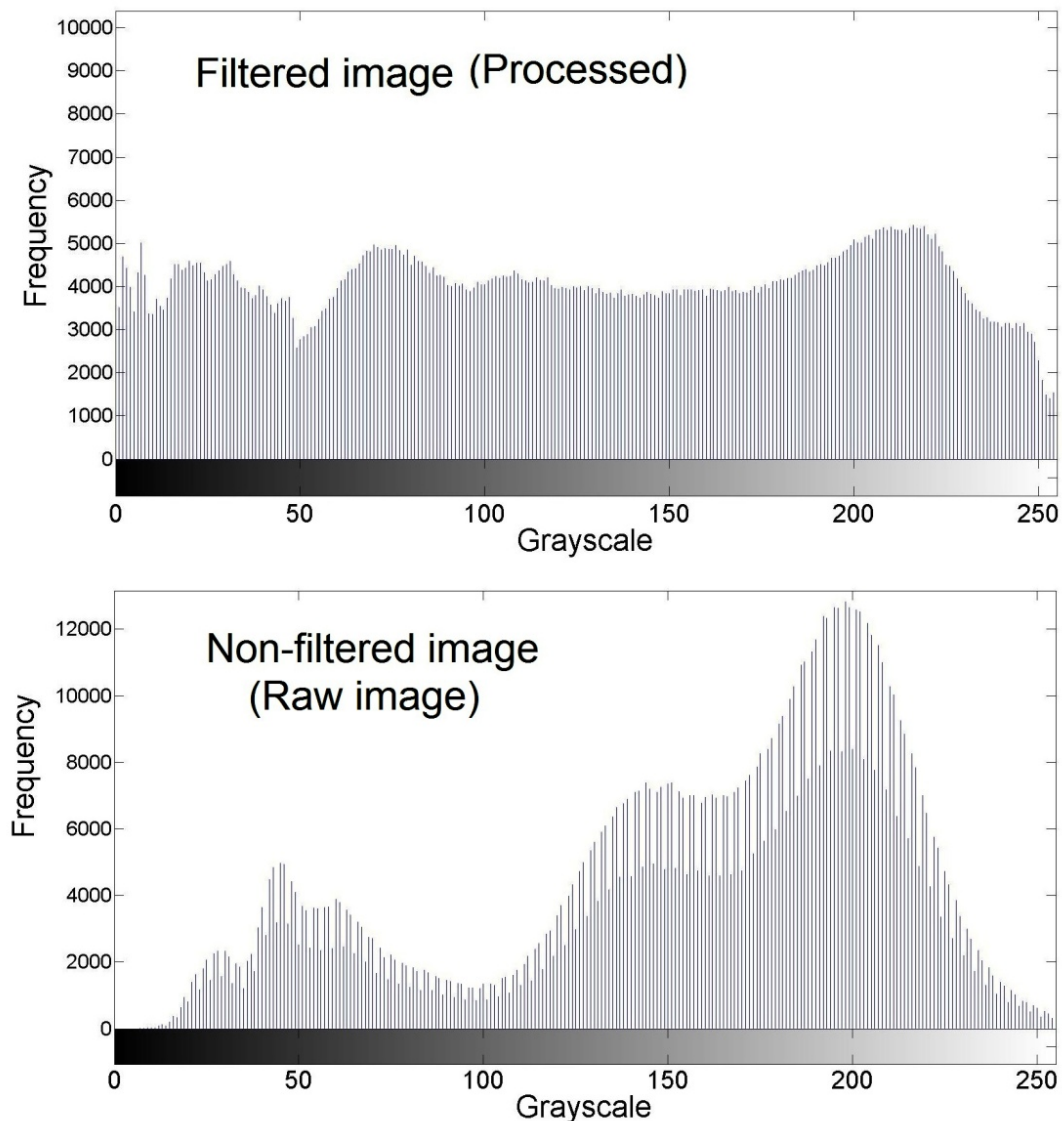


Figure 4.5. Frequency of pixel-level intensities of filtered and non-filtered images.

Filtering the noise out of the captured images or digitally enhancing their contrast using histogram equalization has been found to be unnecessary as this image processing led to an increase in the number of wild vectors. Reliable determination of the strain field requires accurate displacement fields free from wild vectors. Because of the high strain gradients in regions of close proximity to the pouncer soil interface, some wild vectors are inevitable and must be eliminated to obtain sensible strain data. The random occurrence of large displacement gradients (wild vectors) precludes automating this procedure, and requires

manual wild vector removal. As the digital image correlation using the raw data produced less wild vectors, there appears to be no advantage from using frequently recommended image manipulation techniques, and in the data processing only raw image data has been used.

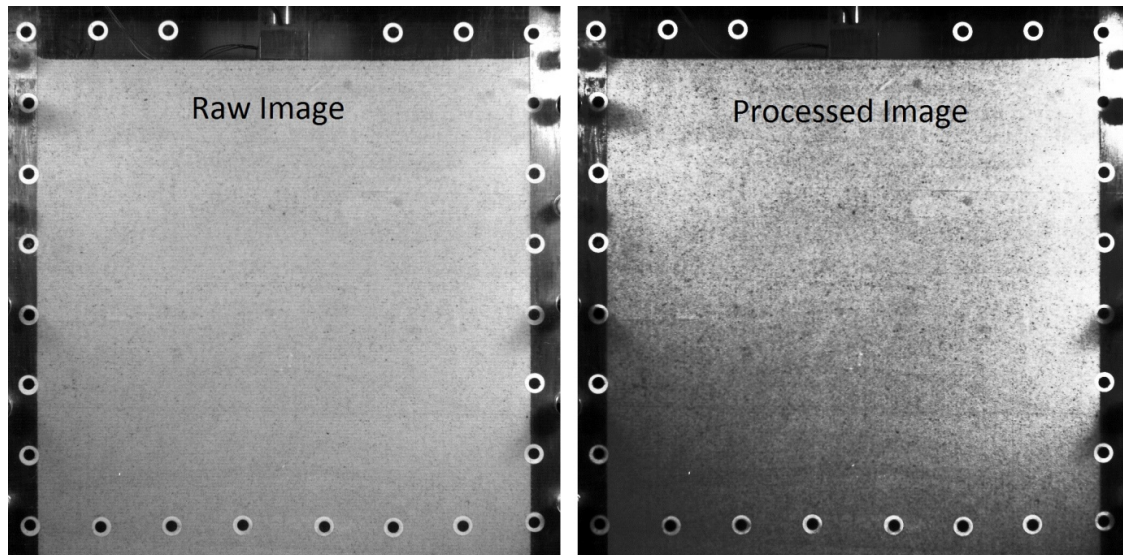


Figure 4.6. Raw and Matlab processed images.

4.4.3 Sensitivity of Camera Sensor

As the transient deformations due to a sequence of dynamic impacts were to be estimated by performing the GeoPIV image correlation between images acquired during different time intervals, it was considered essential to evaluate intensity variations between any two identical images taken by the same camera sensor at different instants of time. To this end, a set of images were recorded at 1000 fps of a stationary model (prior to dropping the poulder on the soil specimen).

While keeping all the camera settings (aperture and shutter speed, lighting, and trigger mode) the same to maintain the same optical path for any two images under consideration, the only source of digital variation should now be due to the inevitable image noise. As described in *Section 3.2.5*, the camera was secured on a tripod isolated from any movement, and the camera trigger was controlled electronically through the connected PC, to assure having a stationary camera while recording the images, which was essential to the accuracy of this process.

Values of the captured pixels from 24 randomly selected images (out of 3200 frames recorded over 3.2 seconds) were stored. Filtered and unfiltered intensity values from the analysed images, normalised by the average grayscale intensity (the image's overall grayscale mean), are shown in Figure 4.7. As expected, the processed images show less variation in grayscale intensity. However, the variance in grayscale intensities of grayscale of the raw images is insignificant as the GeoPIV analysis showed little difference in the spatial displacements and strains between processed and raw images. In this case, the acquired raw images have sufficient texture for the PIV algorithm and the camera sensor to be considered stable over the test period. The standard errors of mean (the standard deviation of the sample-mean's estimate of a population mean) grayscale values were $1.88E+5$ (0.13% dissimilarity) and $4.44E+3$ (0.003% dissimilarity) for raw and processed images respectively. This approach of indirect assessment demonstrates that the camera sensor should experience very little variation in light intensity, apart from random sensor noise, during the recording of actual images during the rapid dynamic compaction experiments.

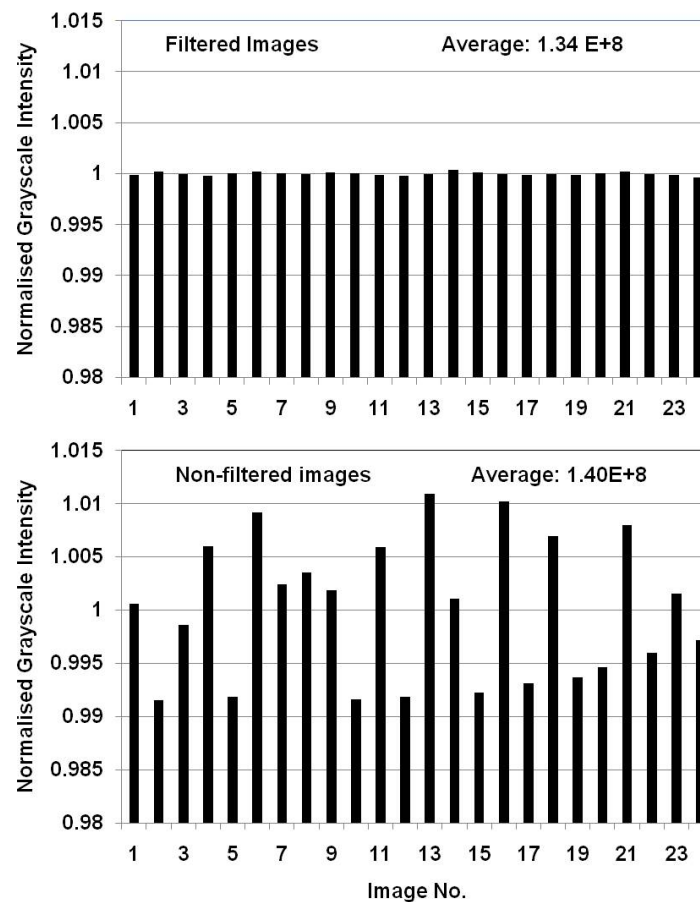
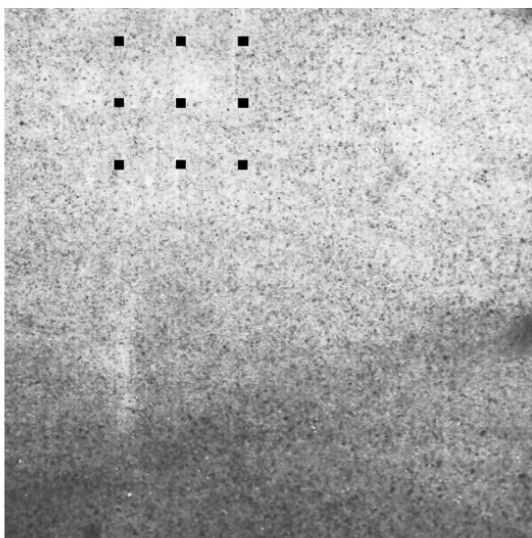


Figure 4.7. Variation in grayscale intensities of 24 random stationary images.

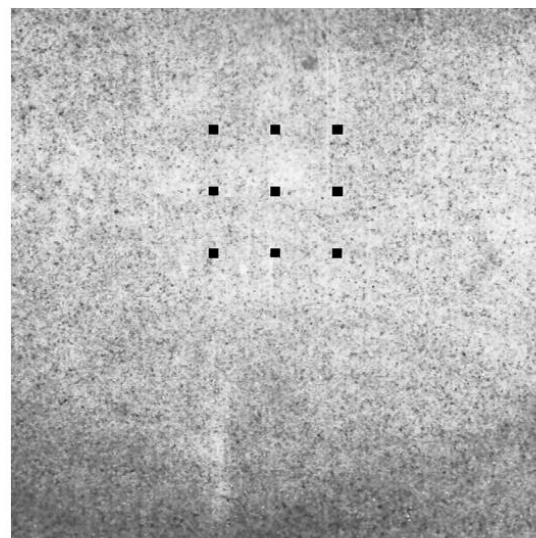
4.4.4 GeoPIV Evaluation

Since deformations in the dynamic compaction test vary across the test model, this makes it difficult to verify the spatial deformations generated by the digital correlation analysis with actual displacements. Therefore, artificial image translations were created using Matlab tools. From a stationary captured image, a window of a 600 x 600 pixel matrix was artificially shifted by 100 pixels along predetermined u-v planes of deformation as shown in Figure 4.8. These artificial displacements would represent about 15% and 10% of the extensional and shear strains within the field of view in the real dynamic compaction experiments.

In the GeoPIV image analysis, the patch size specifies the sizes of the local reference and target patches between which the displacements are sought. The patches must contain sufficient unique and identifiable features to achieve a reliable and accurate displacement determination. This patch size is a user defined input parameter, and the chosen patch size has been found to be critical to the accuracy of the measured displacements as discussed previously.



Processed image with digitally induced 9 black dots



The same image with shifted 100 pixels to the right (u) and 100 pixels down (v).

Figure 4.8. Artificially induced encoded displacements.

To assess the precision of the image correlation in tracking the imposed particle flow, 9 black colour dots were artificially created by changing the intensity of the pixel values behind these

dots to zero. Analysis by GeoPIV was then carried out to evaluate the precision of its algorithm as well as the influence of different patch sizes. The results obtained from the GeoPIV match very well with the artificially imposed displacement values. The mean and standard deviations of the displacement fields were computed and compared with the applied values. Results are summarised in Figure 4.9 and Table 4.1, which show the standard deviations in the u and v displacements. For the validation tests using the images with the artificially shifted displacements it can be seen from Table 4.1 that higher standard deviations are obtained from the images that had been pre-processed to adjust the image quality for two different patch sizes.

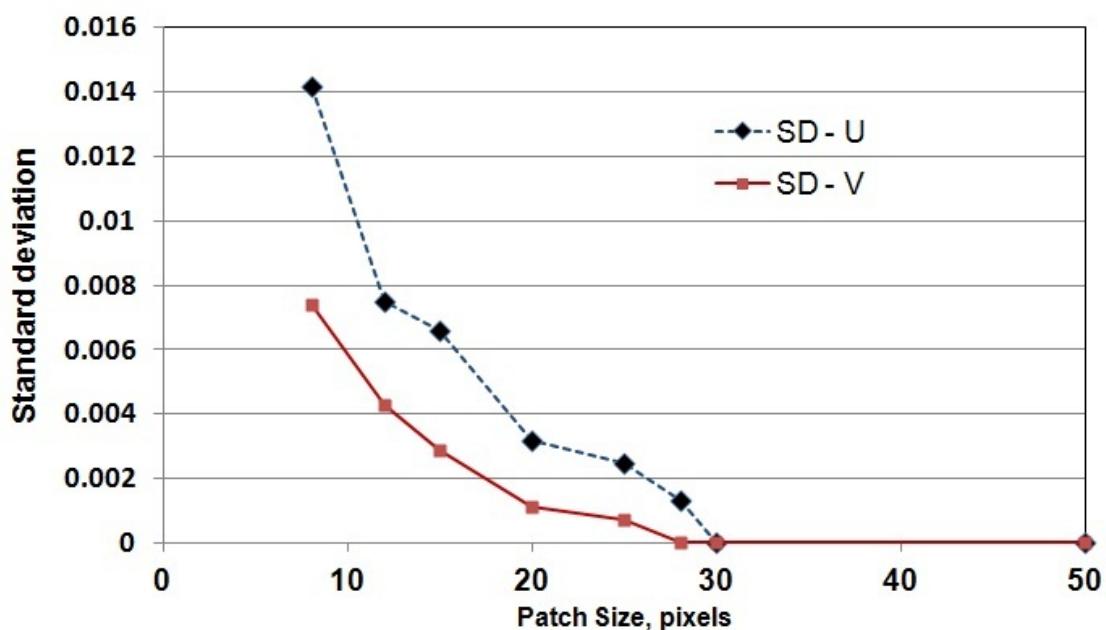


Figure 4.9. GeoPIV precision verses patch size (artificially shifted raw images).

Some soil particles during dynamic loading will be moving in and out of the plane of view and the PIV precision could be less than the precision indicated by the low standard deviations achieved from the digital experiment of artificial image translations. However, this should have a minor effect on the measured displacements because successive images should all be affected equally. Results presented in this work were obtained from GeoPIV analysis employing 30 x 30 pixels and 80 x 80 pixels for 1024 x 1024 pixel and 3504 x 2336 pixel images respectively.

Pre-processing the images by enhancing image contrast and/or noise removal appeared to have no significant effect on the precision of the displacement and strain measurements. However, comparative GeoPIV analyses with raw and digitally modified images showed some adverse effects from using the filtered and de-noised images, with the modified images leading to greater numbers of wild displacement vectors.

Table 4.1. Correlation of GeoPIV precision verses patch size

Subset (patch) size pixels	Type of Image	Induced digital shifting, pixels		Average Measured Shifting, pixels by GeoPIV		Standard deviation, SD (see Figure 4.9)	
		u	v	u	v	u	v
8 x 8	NF	100	100	99.99	99.99	0.0142	0.0074
8 x 8	F	100	100	99.99	99.99	0.0317	0.0257
12 x 12	NF	100	100	99.99	100	0.0075	0.0043
15 x 15	NF	100	100	99.99	100	0.0066	0.0029
20 x 20	NF	100	100	100	100	0.0032	0.0011
25 x 25	NF	100	100	100	99.99	0.0025	0.005
25 x 25	F-IS	100	100	100	100	0.0041	0.0007
28 x 28	NF	100	100	100	100	0.0013	0
30 x 30	NF	100	100	100	100	0	0
30 x 30	F	100	100	100	100	0.0043	0.0039
50 x 50	NF	100	100	100	100	0	0
50 x 50	F-IS	100	100	100	100	0	0

F: filtered images, NF: non filtered images (raw), IS: induced shifting

The occurrence of some wild displacement vectors is inevitable at the locations where large strains occur. This can be related to many factors including the quality of the captured images, the magnitude of displacements in relation to the selected size of the search patch, some sand particles moving away from the surface, and due to the limitation of the digital image correlation algorithm. As shown in Figure 4.10, GeoPIV analysis of post-processed images from a dynamic compaction test generated not only more wild vectors, but also some wild vectors in unanticipated locations. For the reasons discussed here unfiltered images have been used in all subsequent PIV analysis.

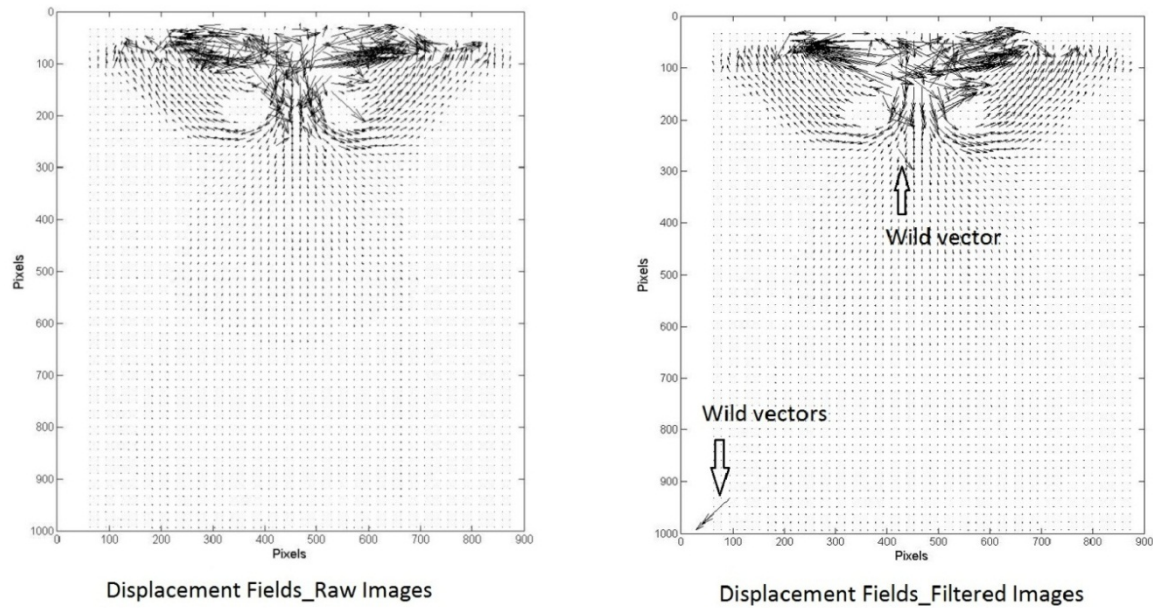


Figure 4.10. Displacement fields from non-filtered (raw) and filtered images.

4.5 HIGH SPEED VERSES STILL PHOTOGRAPHY FOR DC TESTS

To optimise the effectiveness of high speed photography required assessing the influence of various frame rates and image resolution on the spatial deformation measurements. The high speed camera offered a full resolution of 1024 x 1024 pixel images (object space pixel sizes of 0.39mm) at 1000 fps compared to the higher resolution of 3504 x 2336 pixel (object space pixel sizes of 0.1085mm) the still digital camera provided. Impacts from preliminary DC tests were recorded by the high speed camera images (at a rate of 1/1000 sec interval between successive images) and two images (before and after impact) by the digital still camera. Soil displacement was tracked by GeoPIV patches from the two cameras set of images.

For comparison, the GeoPIV displacement vectors from a single drop from images taken by a still camera (before and after an impact) and a high speed camera are shown in Figure 4.11. The picture from the high speed camera represents the cumulative displacement vectors from 50 successive pictures. The results indicate that high speed photography was able to reasonably capture the motion of the sand around the tamper whereas the still photographs before and after the drop were unable to provide reasonable estimates of such large soil displacements. It is clear that the displacement vectors generated from the series of continual digital images captured throughout the impact event, are more uniform and provide a

smoother displacement pattern with very few wild vectors compared to the displacement vectors produced from the before and after higher resolution images. This is because high speed photography (from a number of successive images) captures the continuous details of the soil spatial movement during the DC event. As a result, the displacement fields by high speed photography represent cumulative displacement vectors of better characterisation of the soil flow patterns.

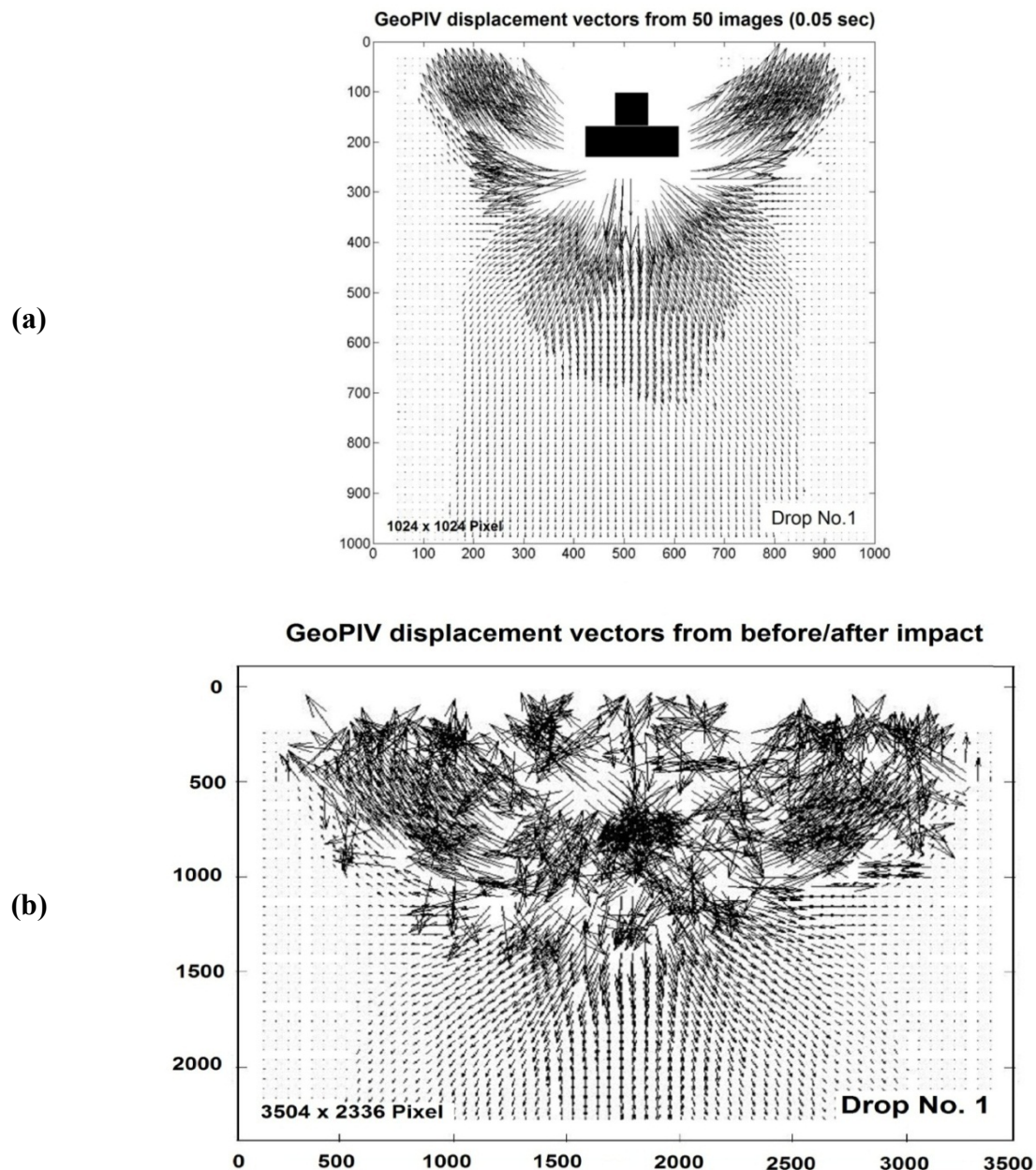


Figure 4.11. Cumulative displacement vectors at end of drop1 from high speed photographs (a) and displacement vectors at end of drop1 from still camera before and after impact (b).

Accordingly, the use of the digital still camera during the DC tests was limited to capturing the lower third of the high speed camera field of view (overlapped zone) where soil displacements were relatively small (around 4 mm) and wild vectors were minimal. The cameras set up was made so part of the model is overlapped in the field of views from both cameras. Figure 4.12 shows the set up that allowed an overlap between the high speed camera and still camera fields of views. This has also allowed using images from both cameras to cross check small magnitude displacements from the two different resolution images.

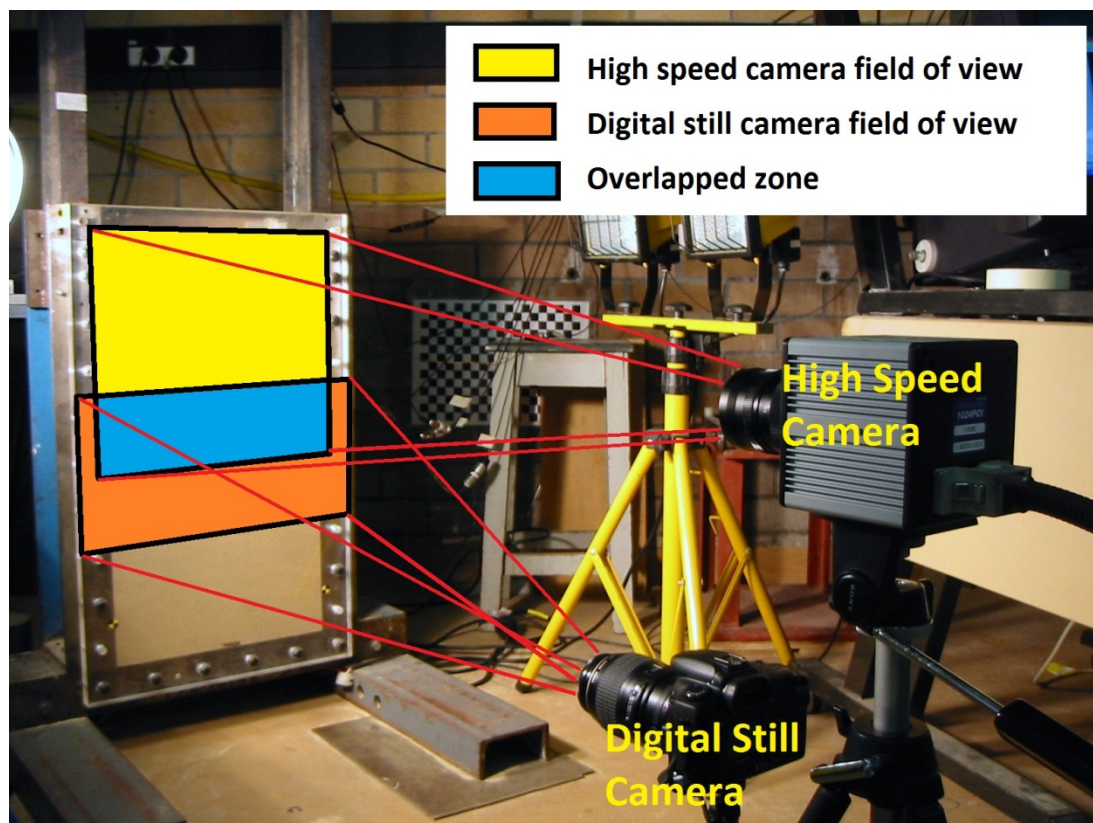


Figure 4.12. Illustration of the overlapped field of view merged by the high speed camera and digital still camera fields of view.

Figure 4.13 shows a comparison of the vertical displacements across the model container at a depth of 350 mm below the pre-impact surface. Both cameras indicated the same trends and similar magnitudes of displacement; however, the still camera suggested a smoother displacement gradient across the container, possibly due to its higher resolution images. By excluding the still images non-uniform displacements generated by wild vectors close to the model sidewalls, the difference between the two calculated displacements was around 12% (0.5mm).

For small spatial displacements, the higher the resolution of the digital images, the better displacement measurement the PIV can provide. However, for rapid loading events like the DC tests of this work where soil particles move quickly and randomly, it is a compromise between the image resolution and the amount of incremental details captured by the continuous high speed images.

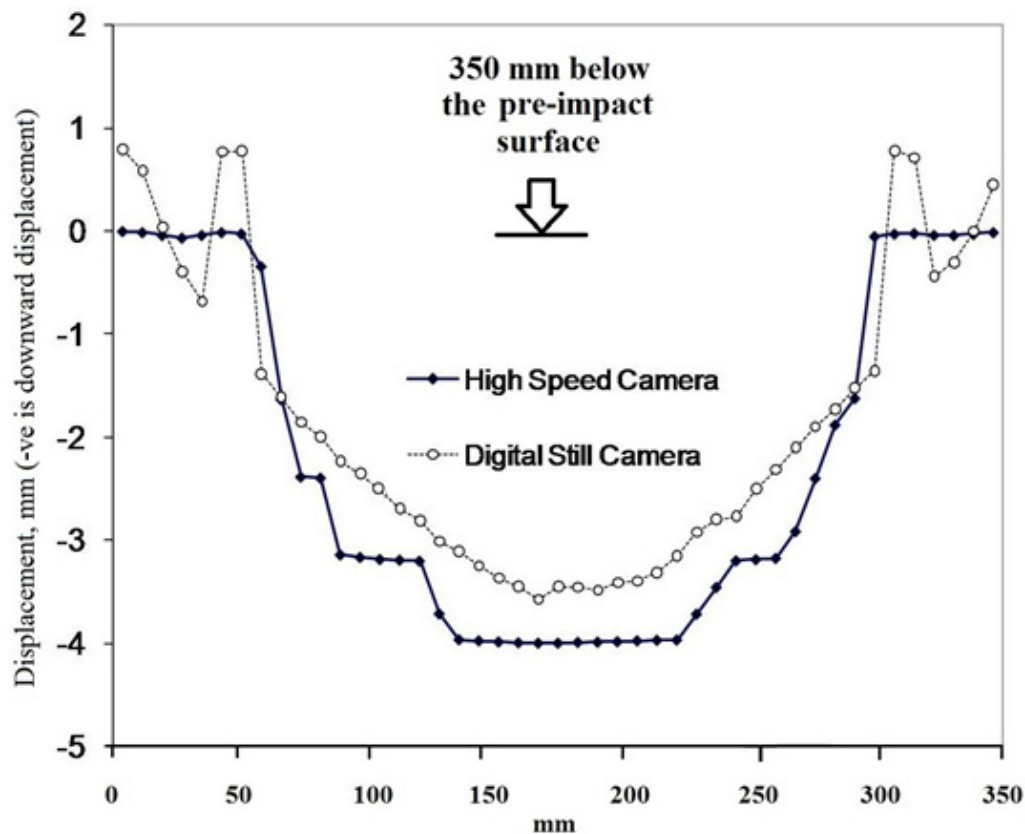


Figure 4.13. Comparison of displacement profiles from GeoPIV patches.

Analysing large numbers of images means longer computational times for the PIV algorithm to perform an analysis. To determine how many images from the high speed photography should be employed in the GeoPIV analyses that are sufficient to capture the mechanism of dynamic compaction, preliminary DC tests were carried out and the displacements at target locations were analysed. Figures 4.14 and 4.15 show selected measurements of vertical and lateral displacement, respectively, from preliminarily DC tests. Displacement histories suggested that no displacements at depth in the soil model could be detected after 0.05sec from the time of impact. This time corresponded to 50 high speed images at 1000fps. However, in some DC tests that involved large impacting energies, insignificant soil

movements at the surface continued beyond this time and up to 0.07sec. In this work, the majority of the GeoPIV analyses were conducted on sets of 50 and 75 images. The 50 and 75 image sets comprised a pre-impact reference image and series of 49 and 74 images that cover the impacting event. In very few cases 100 images that cover a time of 100milliseconds after impact were analysed.

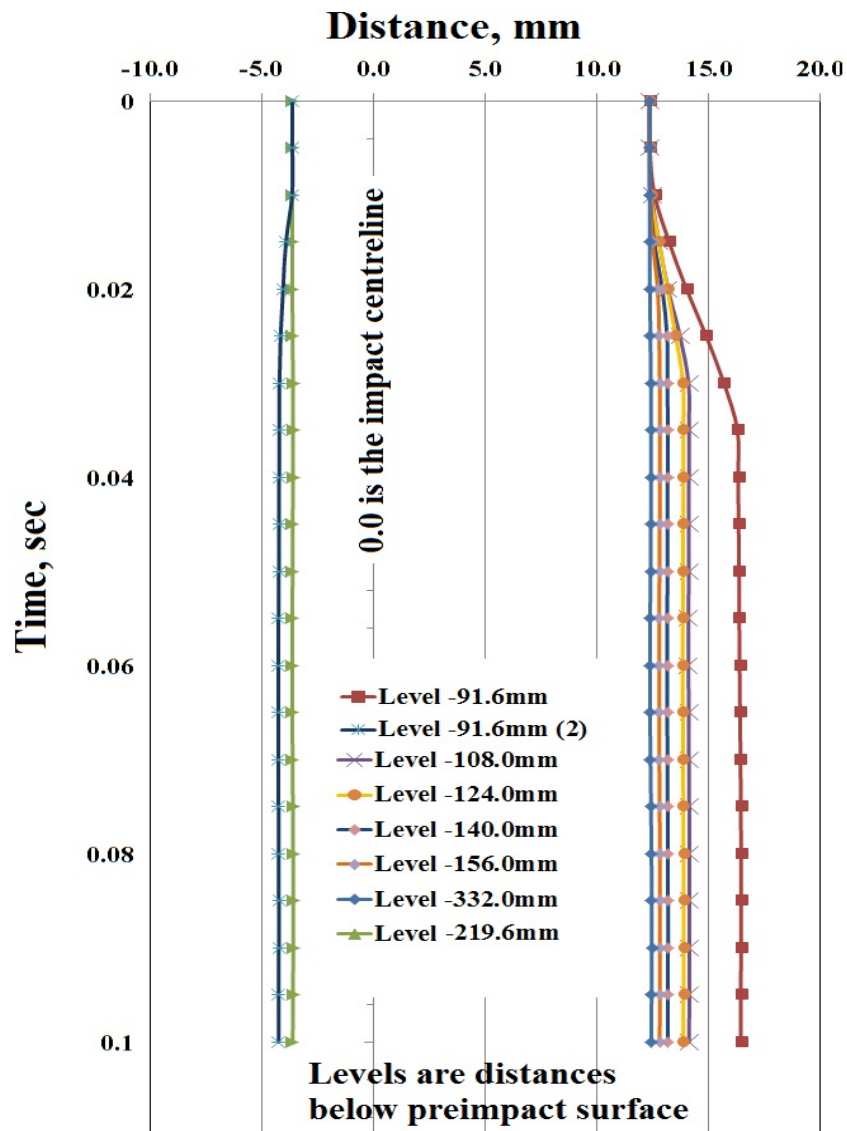


Figure 4.14. History of lateral displacements at 2 locations around the impact centreline from GeoPIV patches at different elevations.

GeoPIV allows users to set up a string (called Leapfrog) that specifies how often the reference image is updated during the analysis. Updating the reference image at each time step (Leapfrog =1) will lead to a low measurement precision over a long series of images but reduces the chance of wild vectors as patches are easily identifiable after each time step. To improve precision, higher leapfrog is preferable provided numbers of wild vectors remain reasonable. However, higher leapfrog requires more computational time. A leapfrog of 1 will suit the large displacements anticipated in the upper region of the models during the DC tests but it will lead to low precision in strain measurements within the lower region of the models where soil movements are less. Preliminary GeoPIV analyses were conducted to assess the sensitivity of this function on the amount of wild vectors and displacement measurements. It was found that a leapfrog between 10 to 25 provided the best balanced results from the DC tests.

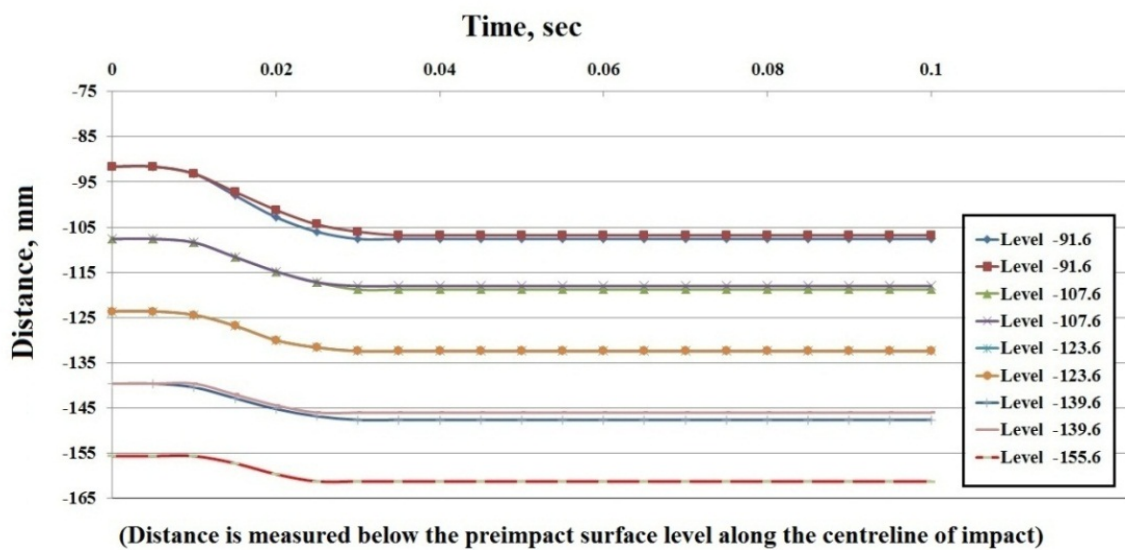


Figure 4.15. History of vertical displacements along the impact centreline from GeoPIV patches at different elevations.

4.6 SUMMARY

It has been shown that the GeoPIV algorithm has the capability for capturing large spatial deformation when the initial state of the model has sufficient texture, having good quality images and appropriate PIV analysis, using optimised sizes of the reference and target patches, are in use. Based on the above results, 30 x 30 pixels and 80 x 80 pixels were the patch sizes selected for majority of the GeoPIV analysis for 1024 x 1024 pixel and 3504 x 2336 pixel images respectively. Repeatable results were obtained using high speed photography during DC tests.

Chapter V: Experimental Results – Photography

Table of Contents

5	OVERVIEW	130
5.1	PHOTOGRAPHY RESULTS - ANALYSIS OF SOIL MOVEMENT	130
5.1.1	Soil Displacement During Static Load Tests	131
5.1.1.1	Steady Rate Static Load Tests	131
5.1.1.2	Pseudo-Static Load Tests.....	138
5.2	THE KINEMATICS OF DYNAMIC COMPACTION	144
5.2.1	Displacement Patterns & Soil Response to Impact Loading	144
5.2.2	Strain Uniformity and Micromechanics.....	158
5.3	QUANTIFYING THE DYNAMIC COMPACTION TESTING RESULTS.....	165
5.3.1	Cone Penetration Tests (CPT)	166
5.3.2	X-Ray Microtomography.....	168
5.3.3	Image analysis.....	174
5.3.3.1	Effect of Different Tamper Geometry on the Kinematics of Dynamic Compaction.....	177
5.3.3.2	Effect of Imparting Energy.....	190
5.3.3.2.1	Effect of Imparting Energy on Sand Models	190
5.3.3.2.2	Effect of Imparting Energy on Sand:Silt Models.....	194
5.4	SUMMARY	200

5 OVERVIEW

Results of the experimental works, based on photography, are presented in this chapter. These results reveal the mechanism of dynamic compaction as detected by the particle image velocimetry (PIV) technique outlined in *Chapter 4*. Selected GeoPIV displacement fields together with various types of strain plots are presented. The results disclose the observed densification mechanism and the kinematics and development of shear and volumetric strains during dynamic compaction tests. The chapter also provides results of the X-ray microtomography and cone penetrometer tests used as measures to quantify the photography results.

The aim of this chapter is to provide the factual outcomes of the photographic part of the experimental work and to draw general conclusions by quantitatively analysing the soil behaviour based on the results from the digital still images, high speed photography images and CT scan images. Further discussion, including attempts to explain the behaviour of soils during dynamic compaction linked to theoretical soil mechanics are intentionally left for further discussions in the following chapters. Results of the instrumentation output and the connection between the instrumentation physics and the photography results are presented in *Chapter 6*. Results of the numerical simulations and the supporting soil property experimental tests are presented in *Chapter 7*.

5.1 PHOTOGRAPHY RESULTS - ANALYSIS OF SOIL MOVEMENT

Quantitative analysis of the soil movements produced by dynamic compaction will be presented in this section by using the results obtained from image processing. The aim of exploring the soil movement during dynamic compaction is to understand the densification mechanism taking place below the surface and to investigate the extent of the improved zone by the dynamic compaction. The use of high speed photography for studying the real time soil behaviour during the rapid impact of dynamic compaction required the establishment of two key issues. First, the level of improvement high speed photography produces over conventional still images digital photography in the environment of rapid loading (discussed in *Section 4.5*). Second is the divergence in soil behaviour between static and rapid loading conditions.

5.1.1 Soil Displacement During Static Load Tests

As will be shown later the mechanism of soil deformation in the dynamic tests is dominated by a general bearing capacity mechanism similar to that widely reported in static tests. To enable the effects of the dynamic loading to be clearly appreciated, a series of static load tests have been conducted in which relatively large displacements have been applied. The results of these tests are reported in this section.

5.1.1.1 Steady Rate Static Load Tests

Stress-displacement responses during the steady state static load tests are shown in Figure 5.1. The differences between the loose and dense sand responses during the static load tests are similar to classical shear stress-shear strain results from a shear box test. For loose sand (Figure 5.1a), the stresses increase with displacements until an axial displacement of 10% of the footing width after which the mobilised stresses increase very slowly with increased displacements. In the case of tests on dense sand (Figure 5.1b), the stresses increase to higher peak values at relatively low displacements of about 5% of the footing width and thereafter stresses decrease with increasing displacements, and approach similar mobilised stress values to the loose sand. With further penetrations the stresses increase slowly with displacements, similarly to the loose sand, however the mobilised stresses are approximately double that of the loose sand at the same penetrations.

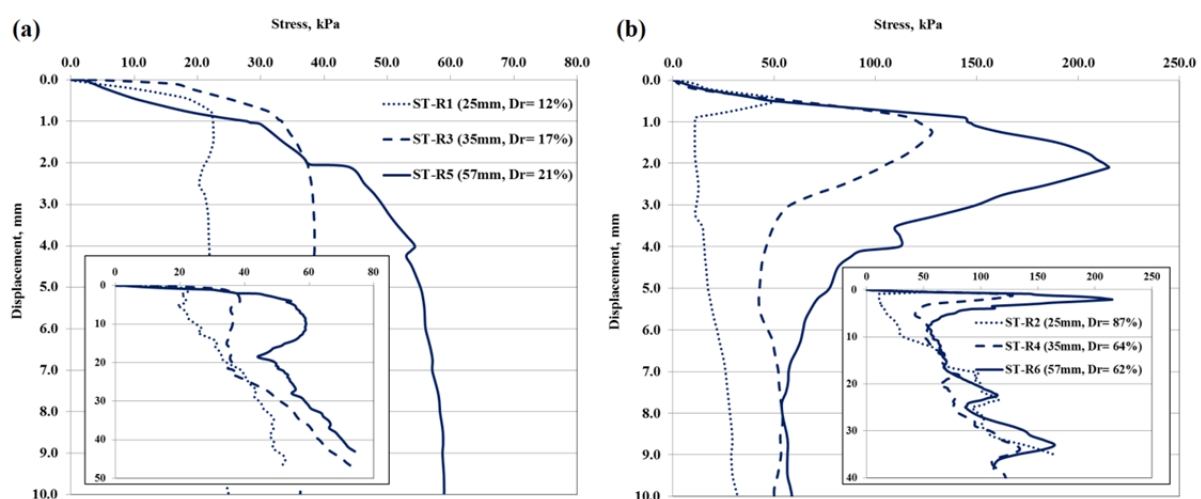


Figure 5.1. Stress-Displacement responses of steady rate static tests in loose (a) and dense (b) sands

In dense soil models, the 25mm footing showed a lower penetration resistance (beyond 1 mm penetration) than the corresponding loose case, which might be related to errors in the measured load.

Several researchers have reported similar loading settlement responses for surface foundations in their works examining the bearing capacity and failure mechanism of different types of foundations on sand using model scale footings (Shin *et al.*, 1999, White *et al.*, 2008 and Yamamoto *et al.*, 2009). The slightly irregular responses during these tests were due to the manual operation of the hydraulic ram used to push the pad footings into the sand. The effect of the size of the footing is clear with the wider footing having higher peak and residual stresses regardless of the sand initial relative density. For a surface strip foundation the ultimate bearing capacity q_u is defined as:

$$q_u = \frac{1}{2} \gamma B N_\gamma \quad (5.1)$$

where

γ = unit weight of soil

B = foundation width

N_γ = bearing capacity factor

For typical friction angles of 35° for loose sands and 45° for dense sands at low stress levels, the corresponding bearing capacity factors N_γ (Vesic, 1973) are 48.6 and 271.3, respectively. Soil unit weights were about 15 and 17kN/m³ for loose and dense sands during the tests. Thus, the theoretical ultimate bearing capacities for the 25, 35 and 57mm pad footings are 9, 13 and 21 kPa in loose sands and 58, 81 and 131 kPa in dense sand, respectively. The static test results showed a lack of agreement between the experimental findings and these estimated values. However, this discrepancy is expected due to the stress level-dependent nature of the soil shear strength parameters which are attributed to:

- The classic parametric studies by Ovesen (1975), Kimura *et al.*, (1985) and Cerato *et al.*, (2007) which have shown the decreasing of N_γ with footing width increases.

- Friction angles are generally found to be slightly higher for plane strain conditions, and a small variation of 2-3 degrees in the soil friction angle can result in a large variation in the value of $N\gamma$.
- Peak friction angle varies with footing size as a result of the different stress levels generated by the footing.
- The classical theories are conservative; they propose a conservative estimate for shape factor acceptable from a design point of view for low internal friction angles and small aspect ratios (Zhu and Michalowski, 2005).

Another important factor limiting the reliability of theoretical predictions is that the actual failure mechanism may differ from that which is assumed. Illustration of the typical mechanism of soil movement during static tests is provided by the velocity fields shown in Figure 5.2. These velocity fields consists of approximately 6200 individual vectors calculated from a series of 27 images through which the 35mm wide footing was displaced 51mm downwards. These displacement vectors represent the resultant trajectories of the GeoPIV patches (soil elements) from the preloading position to the target positions.

Figure 5.2 shows distinctive three zones of soil displacement. Directly below the pad footing is a zone of rigid soil that is translating with the footing movement. On either sides of this zone, and extending approximately 45° from the vertical is a zone of soil that is translating radially away from the centreline of symmetry before it changes direction and merges into a third zone of upwards translational displacement. The empty regions, on either sides of the footing had wild displacement vectors that have been removed for clarity. These occurred because sand particles flowed back into the void created by the footing.

Observation of the soil element trajectories during footing indentation provides further insight into the deformation mechanism and the degree of uniformity. Figure 5.3 shows the displacement trajectories of a selection of soil elements tracked through a steady rate static test. For clarity, only trajectories from 800 soil elements are shown, together with a magnified region under the footing showing the vectors and trajectories of three individual soil elements. This figure shows that GeoPIV software is providing reasonable estimates of the soil movement, and for example the displacements of the soil patches directly beneath the footing are identical to the footing displacement measured by the LVDT.

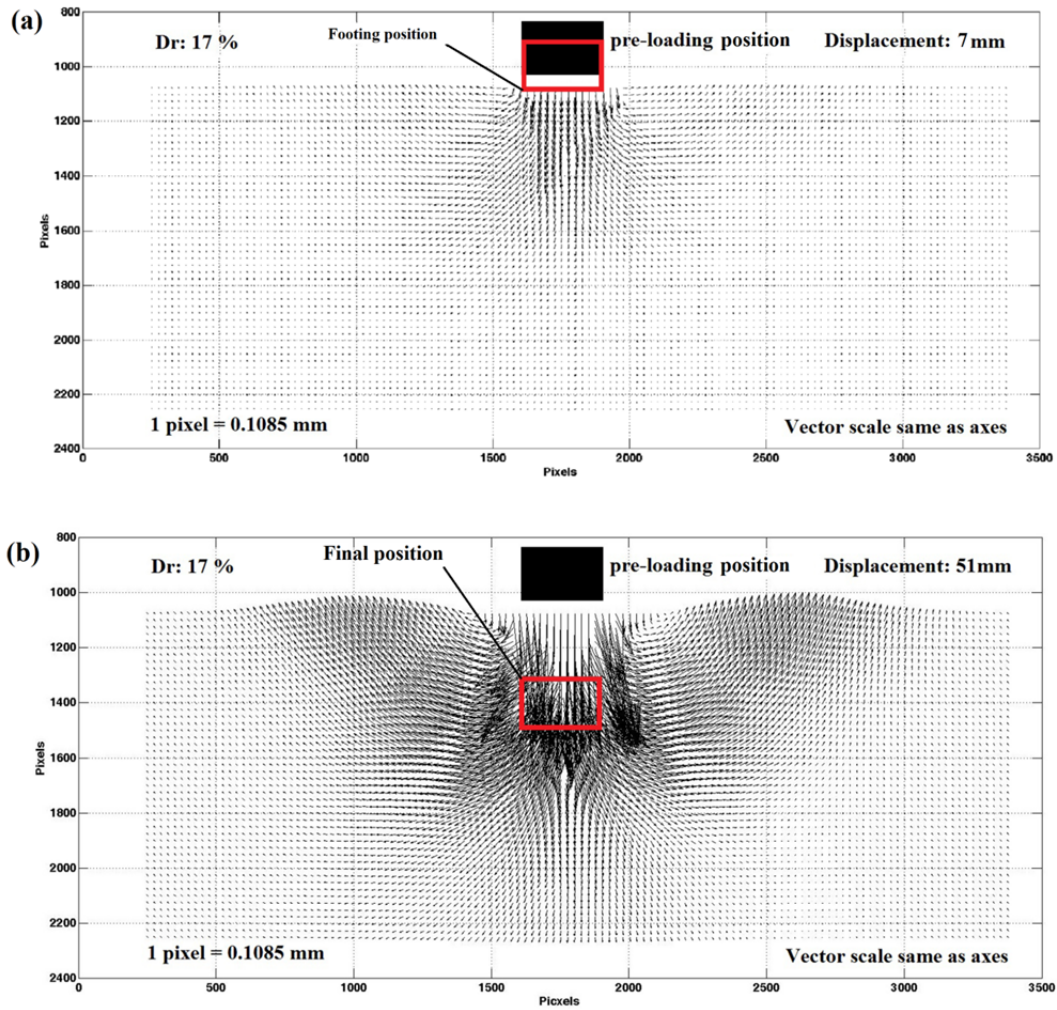


Figure 5.2. Cumulative displacement vectors at (a) 7mm and (b) 51mm displacements (end of static test ST-R3)

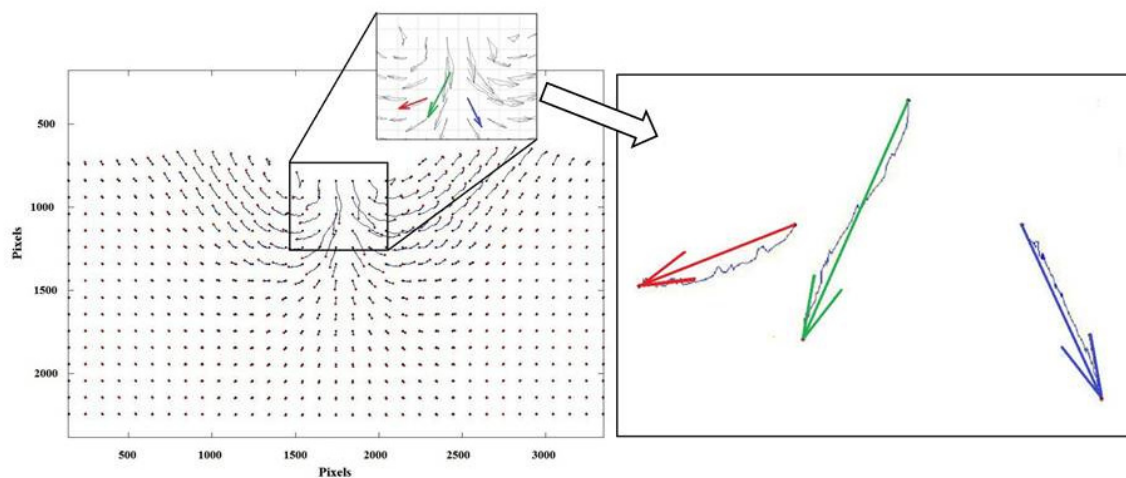


Figure 5.3. Displacement trajectories of soil elements tracked through a steady rate static test

More details of the deformation mechanism are visible in the strain fields determined by the image processing software, GeoPIV. Figure 5.4 shows the evolution of shear strain when the 35mm footing was pushed 13mm, 33mm and 51mm subsequent to loading during test ST-R3. Shear straining and intense localization of strains are visible within and inbetween the three zones of soil displacement. It is interesting to perceive similarities between the localised shear strain mechanism shown in Figure 5.4a and the observations made from plane strain bearing capacity experiments and numerical simulation work by Tatsuoka *et al.*, 1994 and 1997 (see Figure 2.25). Figure 5.5 shows total volumetric strains at the end of loading from tests ST-R3 (Dr:17%) and Figure 5.6 shows total shear and volumetric strains from test ST-R4 (Dr:64%).

Volumetric strains are generally concentrated along the same macrolines of shear strain localisation (Figures 5.4c and 5.5 and Figure 5.5a and 5.5b) and this is clearly evident for the initially denser sand. In addition, a “micro” mechanism of volumetric strains appears which is not evident in the pattern of shear strains. The characteristic feature of these microbands is that they show alternate behaviours of contraction (positive volume strain-red) and dilation (negative volume strain-blue). These alternate contraction/dilation microvolumetric lines are more evident in the case of dense sand and are associated with very highly sheared regions. This pattern of alternating dilation and contraction has been observed in the volumetric strains associated with shear bands in the static and dynamic tests presented below. It is believed that this pattern may be an artefact of the method of calculating volume strain, the relatively thin thickness of the shear band, and the size of the GeoPIV patches.

The overall mechanism defined by these shear bands is clearly a combination of two main internal deformation mechanisms, contraction and dilation. The mechanism has the features of a general bearing capacity mechanism, such as the inclined shear planes, radial shear zones, a zone of intense compaction directly beneath the footing, regions of intense shearing and dilation along the lower boundaries of the failed mechanism, and regions of dilated soil on either sides of the footing and close to the surface due to the low stress level. The details of the deformation mechanism that Figures 5.4 to 5.6 reveal, were consistent across all the steady rate static tests. In Figures 5.5 and 5.6b, the zones of intense compaction directly beneath the footing show contractile volume strains in excess of 10%, which theoretically brings the soil within these regions to the compaction limit of e_{\min} (0.58).

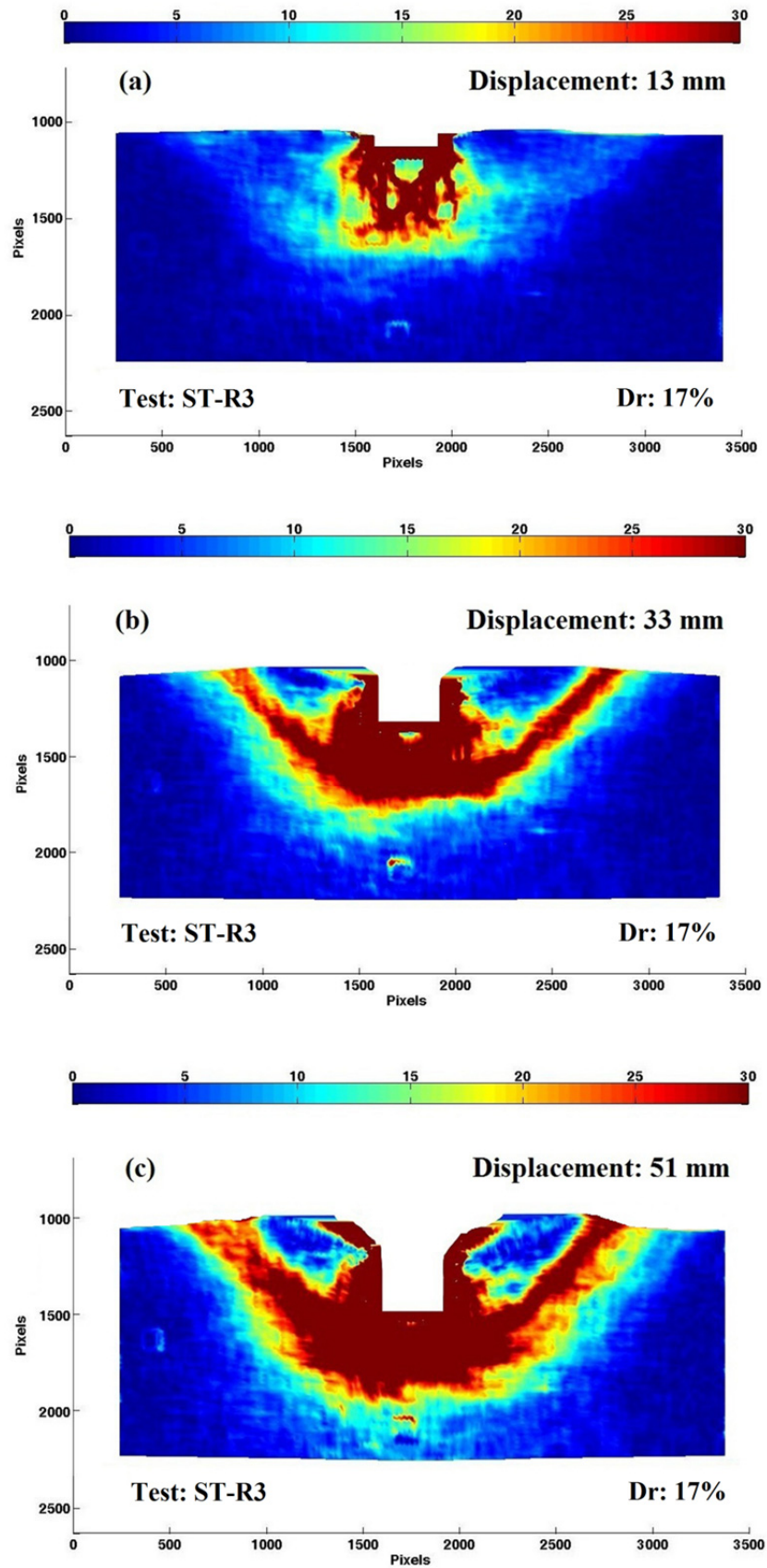


Figure 5.4. The evolution of total shear strain caused by (a) 13mm, (b) 33mm and (c) 51mm footing displacements during static test ST-R3

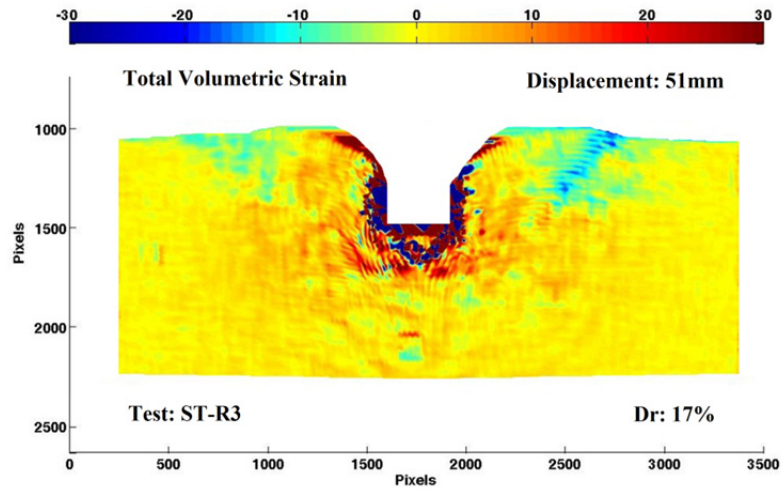


Figure 5.5. Total volumetric strain at the end of test ST-R3

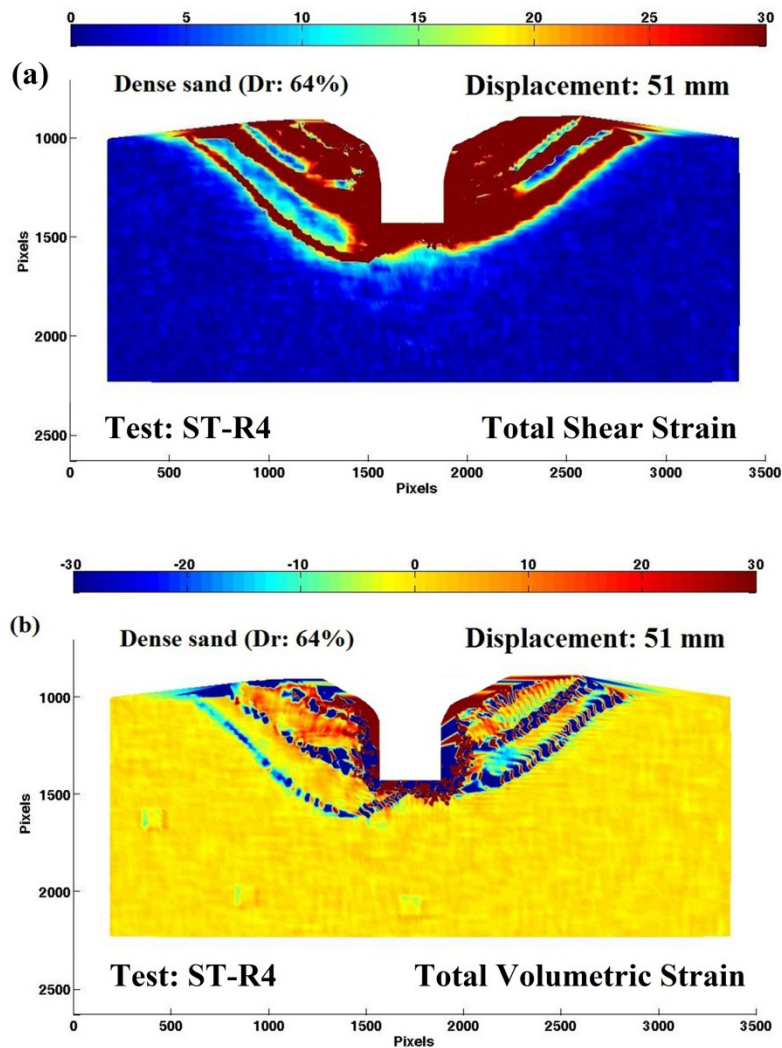


Figure 5.6. Total shear strain (a) and total volumetric strain (b) at the end of test ST-R4.

Because the vectors start from the centre of the soil patches there appears to be a gap between the plate and soil, however, the initial soil surface was horizontal and aligned with the base of the plate as demonstrated in Figure 5.7 which shows the trajectory of a single patch directly beneath the footing.

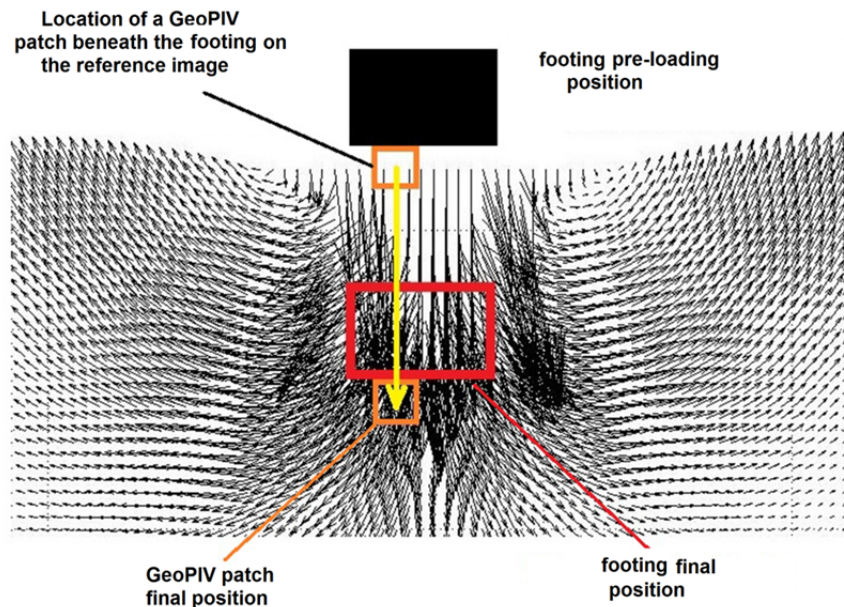


Figure 5.7. Illustration of soil displacement tracked by GeoPIV patch
(Extracted from Figure 5.2b)

Similar observations regarding the deformation patterns and failure mechanisms were made by Michalowski *et al.*, (2003) in their work investigating foundations on sand with reinforcing layers using an image correlation technique (Figure 2.26). They verified that the pattern of deformation under the footing from the image analysis was consistent with the classical bearing capacity mechanism of failure.

5.1.1.2 Pseudo-Static Load Tests

Stress-displacement responses during pseudo-static load tests on loose sands are shown in Figure 5.8, together with stress-displacement responses from relevant (footing size and nearest soil relative densities) steady-rate static load tests. The soil responses from the two

different techniques of load application (steady rate and pseudo-static) are similar within the stress levels the steady rate static tests reached. The lack of intermediate stress/displacement measurements before the first load increment (140N) during ST-P1 has resulted in poor representation of the pressure-displacement responses at small displacements (Figure 5.8a). However, at large displacements the incremental and steady rate tests track along the same response. Similarly comparable results were obtained between steady-rate and pseudo-static load tests from dense sand models.

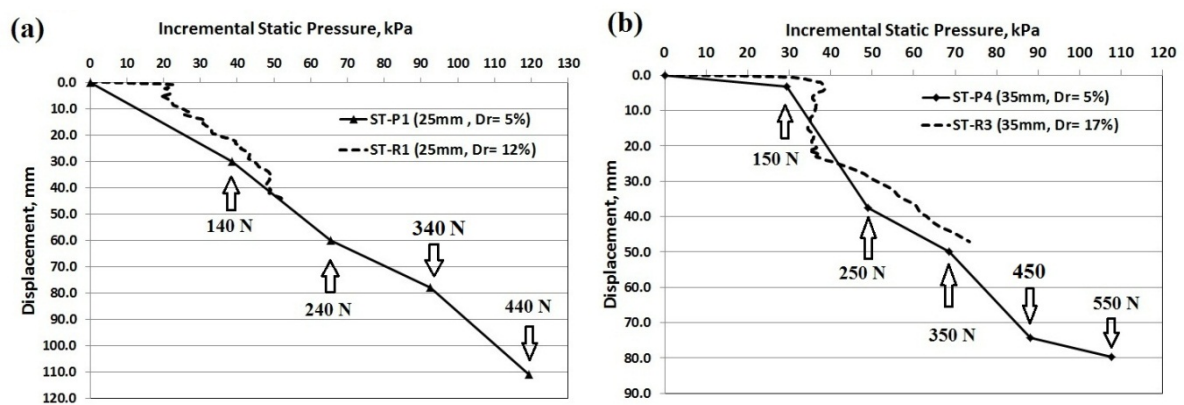


Fig. 5.8. Load-displacement curve for 25mm and 35mm pads during ST-P1 and ST-P4 tests.

To illustrate the evolution of the displacement field and strains during the pseudo-static tests high speed photography was used. This has enabled the mechanism of soil movement shown in Figure 5.9 to be produced. These velocity fields consist of approximately 4800 individual vectors calculated from a series of 75 images (0.075sec) following the application of each incremental loading.

Despite the rapid penetration of the footing that occurs after the application of each load increment, the distinctive three zones of soil displacement, similar to the steady rate static tests, are well-defined. Figure 5.9a shows the vectors just before the failure mechanism develops, and at this stage movements are predominantly downwards under the footing. At later stages of loading the soil moves predominantly to the side and upwards.

More details of the deformation mechanism are visible in the strain fields shown in Figure 5.10. This shows the evolution of total shear strain at the end of 150N, 350N, 450N and 550N

loading stages. Indeed, the mechanisms of soil deformation from steady rate static and pseudo-static tests demonstrate many characteristics of classical bearing capacity failures, even though penetrations of 5 times the footing width have been reached.

Results from both steady rate static and pseudo-static tests share a lot of similarities in the stress-displacement behaviour and the mechanisms of intense strain localisation at comparable stress levels. Nevertheless some differences in the strain patterns can be detected as shown in Figure 5.11, which shows the total shear strain at 70kPa stress level during ST-P4 and ST-R3 static tests. Both results indicate comparable footing displacements and depth of intense shearing (referenced to their pre-impact surface). But the pseudo-static test shows steeper upwards translational shearing (due to heaving around the footing). A unique feature from both types of static test was the occurrence of a localised deformation bulb that was formed beneath the zone of near rigid soil movement, and that moved deeper into the soil model with increased stress/penetration levels. This feature can be clearly detected in Figures 5.9(a) and 5.10(c-d). The shear strain localisations show that in this region the soil is moving down almost as a rigid block with shear strain concentrated around the perimeter of the region. Figures 5.10(c-d) suggest these bands develop towards the end of the penetration event, however, inspection of Figure 5.12 shows that these bands evolve even for penetrations of the order of the footing width.

The observation that this deformation bulb only develops during the pseudo-static tests indicates that the behaviour is associated with the relatively rapid rate of loading. It further suggests that the energy dissipation associated with the bearing capacity mechanism can not occur sufficiently rapid and it becomes possible for a block of soil to be pushed down into the underlying soil. As will be seen below in the dynamic tests, this effect becomes more dominant as the rate of load application increases.

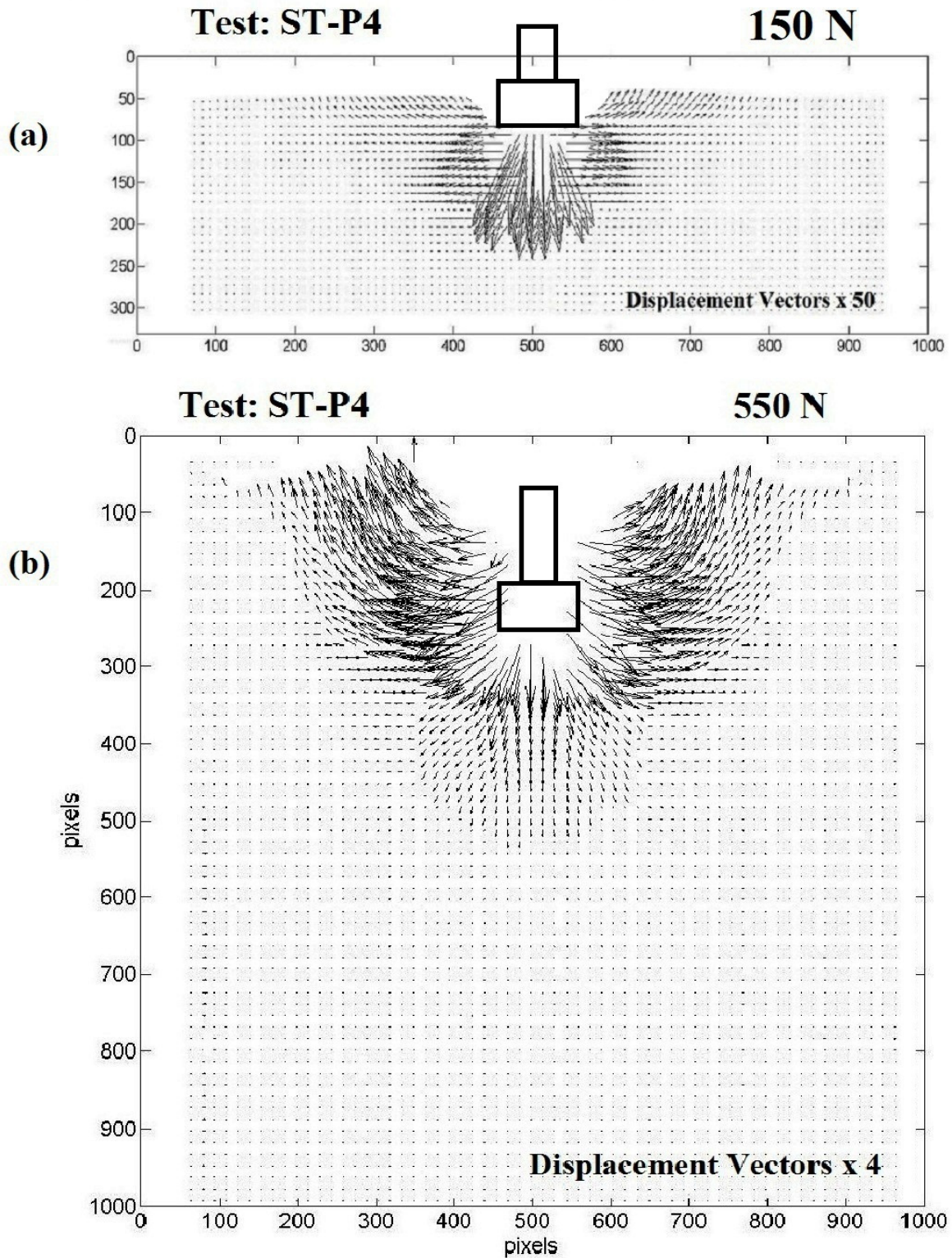


Figure 5.9. Cumulative displacement vectors (magnified 4 times) at the end of 150N (a) and 550N (b) static load applications (Test: ST-P4)

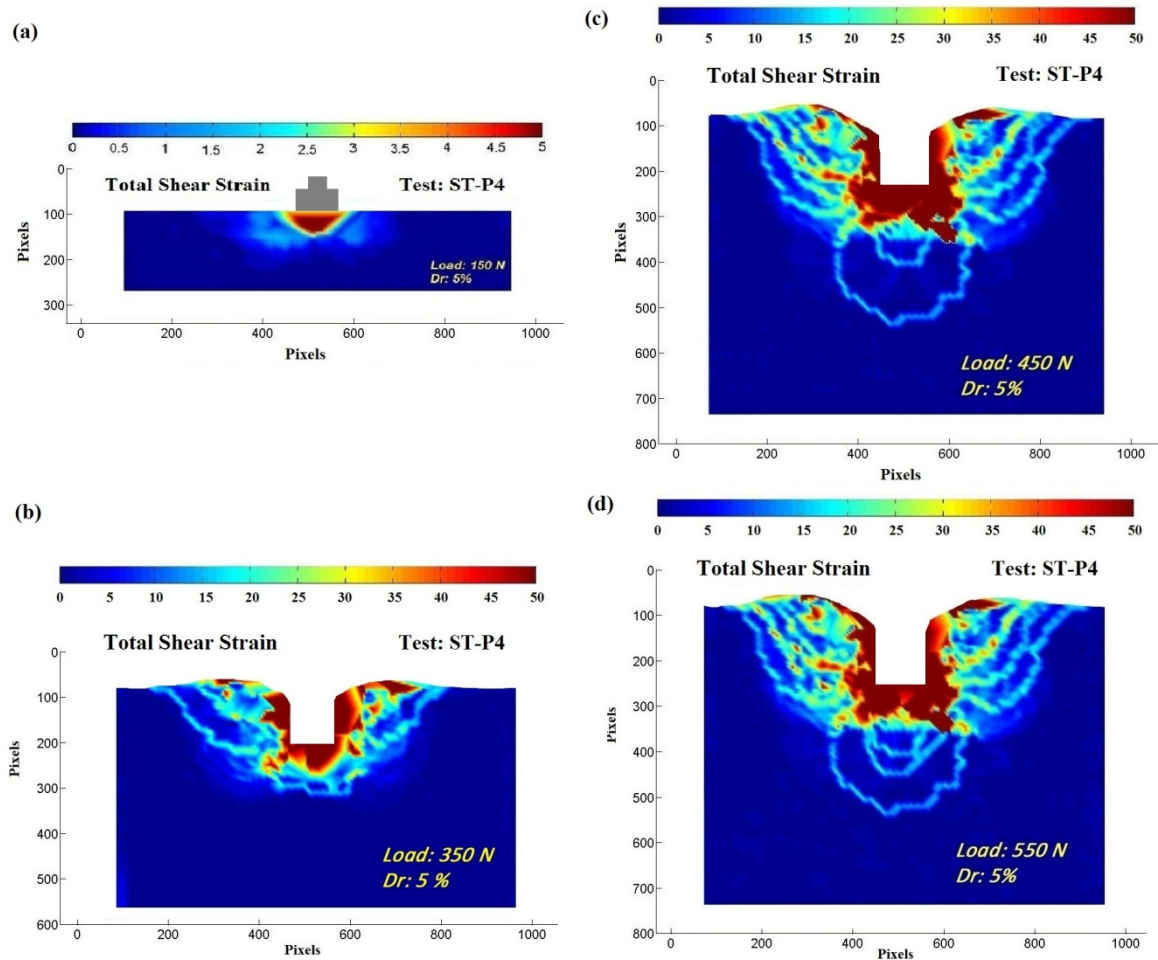


Figure 5.10. Evolution of total shear strain due to 150N, 350N, 450N and 550N during ST-P4

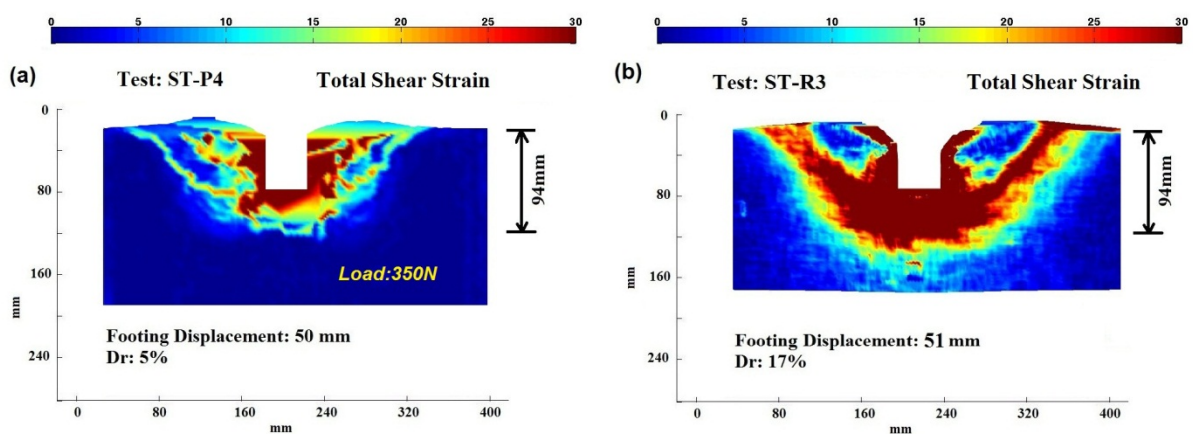


Figure 5.11. Comparison of total shear strain at 70kPa stress level during (a) ST-P4 and (b) ST-R3 static tests.

The evolution of incremental shear strains subsequent to a load increase from 150N to 250N are shown in Figure 5.12. Similar incremental shear strain patterns and evolution were observed in other load increments. The overall mechanism of strain localisation subsequent to a load increment has the same broad features (the general bearing failure mechanism) such as the inclined shear planes, radial shear zones, and intense strain directly beneath the footing, yet the evolution of this mechanism is different from the steady rate tests. Figure 5.13 shows schematic diagrams of the shear strain bands and the evolution of shear strain localisation observed during pseudo-static tests. Upon applying the load in the pseudo-static test, a localised deformation block develops immediately beneath the footing (Figure 5.12a) followed by the developing of localised strain along the outskirts of the passive triangles on either side (Figure 5.12b and c) and finally by localised strains arcs that originate at the opposite corners of the footing reaching the heads of the passive triangles (Figure 5.12d). A feature of the mechanism is that the shear strains are strongly localised and that the soil inbetween the shear bands experiences relatively little strain.

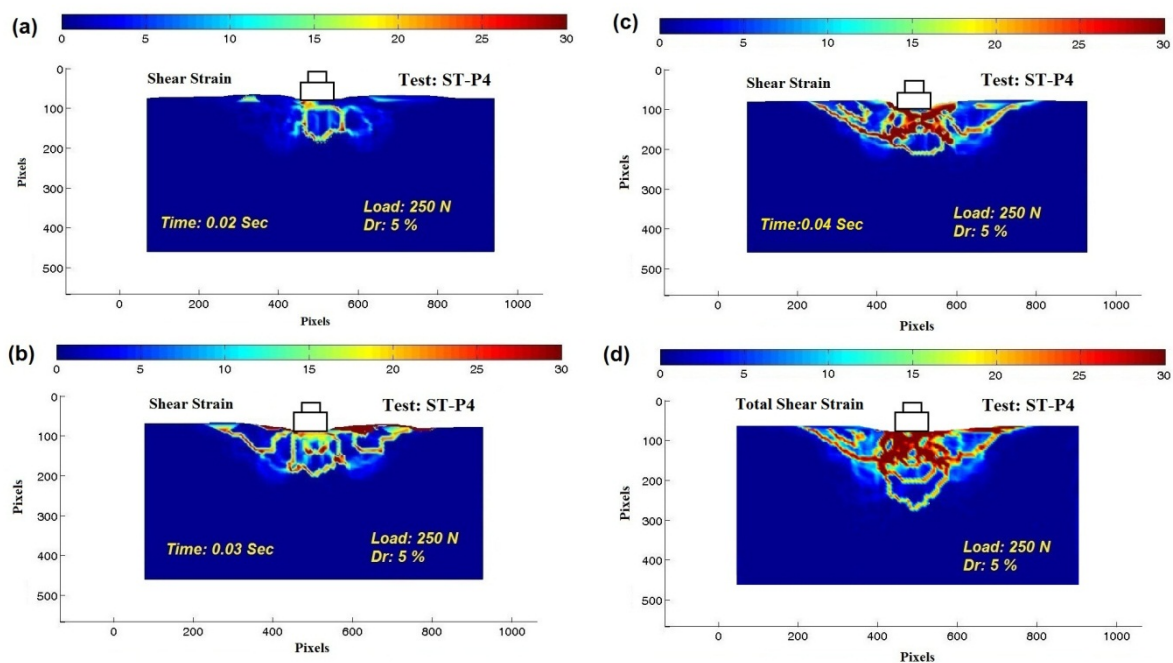


Figure 5.12. Evolution of shear strain subsequent to load increase from 150N to 250N during ST-P4.

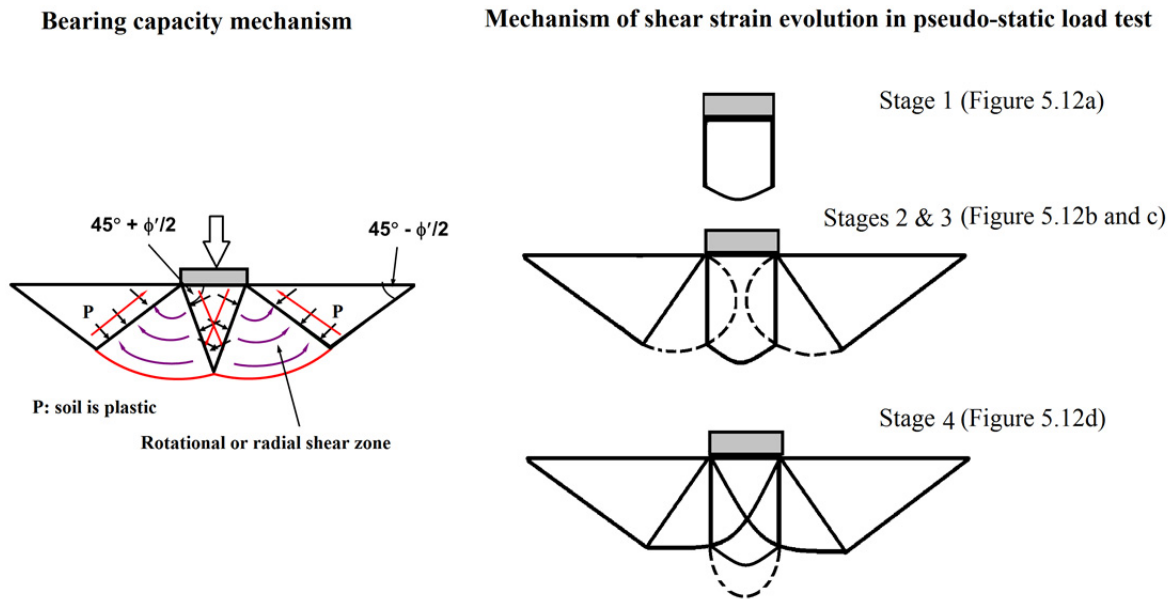


Figure 5.13 Schematic diagrams of general bearing capacity and shear strain localisation in pseudo-static mechanisms.

The static tests have involved penetrations of between 2 and 4 times the footing width. Despite these large penetrations the loose sand has developed a mechanism that involves the sand moving sideways and upwards. There has been only very slight deformation and strain in the soil below a depth of about one footing width below the penetrator.

5.2 THE KINEMATICS OF DYNAMIC COMPACTION

5.2.1 Displacement Patterns & Soil Response to Impact Loading

Studying geotechnical models using high speed photography and DIC enables continuous monitoring of displacement fields and internal strains at, and directly after, tamper impact. The photographic analysis provides continuous and smooth fields of motion of the soil particles and detailed information on the evolving patterns of strain localisation resulting from the rapid impact loading. The mechanism of soil movement during DC tests is provided

by the velocity fields and strain maps presented below. In general, the velocity fields and subsequent strain maps were made of 4000 to 4200 individual vectors calculated from series of 50 to 75 images for each single impact using patch sizes of 24 x 24 to 30 x 30 pixels.

Figure 5.14 shows the displacement vectors following the first impact by a 57mm wide poulder on initially loose sand in the small sized model container, DC11 (Dr: 25%), and large sized model container DC4L (Dr: 29%) delivering 48N.m and 56.6N.m per impact respectively. The displacement fields from DC, shown in Figure 5.14, are generally comprised of two significant regions. In the upper region the soil deformation pattern consists of a general bearing capacity failure mechanism where the soil is being pushed to the side and upwards, whereas in the lower region beneath the tamper the soil is pushed downwards and a confined soil compression takes place. The upper region affected by the bearing capacity mechanism experiences little if any compaction. The two tests retain the same features of having distinctive upper and lower displacement regions. However, the model container side boundaries are closer to the impact centreline in the case of the small sized model and thus appear to have affected the soil displacement by forcing the upper regions to heave further around the poulder and to have constrained the lateral spreading of soil movement within the lower region. On the other hand, there is less heaving around the poulder and lateral soil displacements extend further in the case of the large sized model where side boundaries are located further away. In the case of DC4L because the model container is double the depth of the small sized model, the poulder contact area is also double for the same poulder width, and thus the impact stress will have been smaller in this case, despite the comparable soil properties and imparting energies.

From Figure 5.14, it appears that there is a gradual reduction in displacement as one moves away from the tamper. This is consistent with standard interpretations of dynamic compaction which assume that a stress wave passes through the soil leading to soil densification. However, when the high speed photographs are analysed in more detail a different picture emerges, as shown below and in the following sections of this Chapter.

The effect of the imparting energy on poulder penetration and soil heaving around the poulder is shown in Figure 5.15. In this comparison, the two near identical soil beds of DC24 and DC30 were impacted by the same poulder (35mm wide) employing energy levels of

5.8N.m/drop and 17.4N.m/drop respectively, by increasing the drop height (see Table 3.2). After 6 drops, poulder penetration and soil heave were measured to be about 50% more in DC30. Records of poulder displacements over the course of 12 drops from 3 DC tests on loose sand are shown in Figure 5.16. For a particular energy level (N.m/drop), the results show the poulder penetrations are inversely proportional to the energy inputs, and that the deepest penetrations take place due to the first drops, and the penetration per blow declines and reaches a stabilised level after 9 to 10 drops where no further penetrations can be achieved.

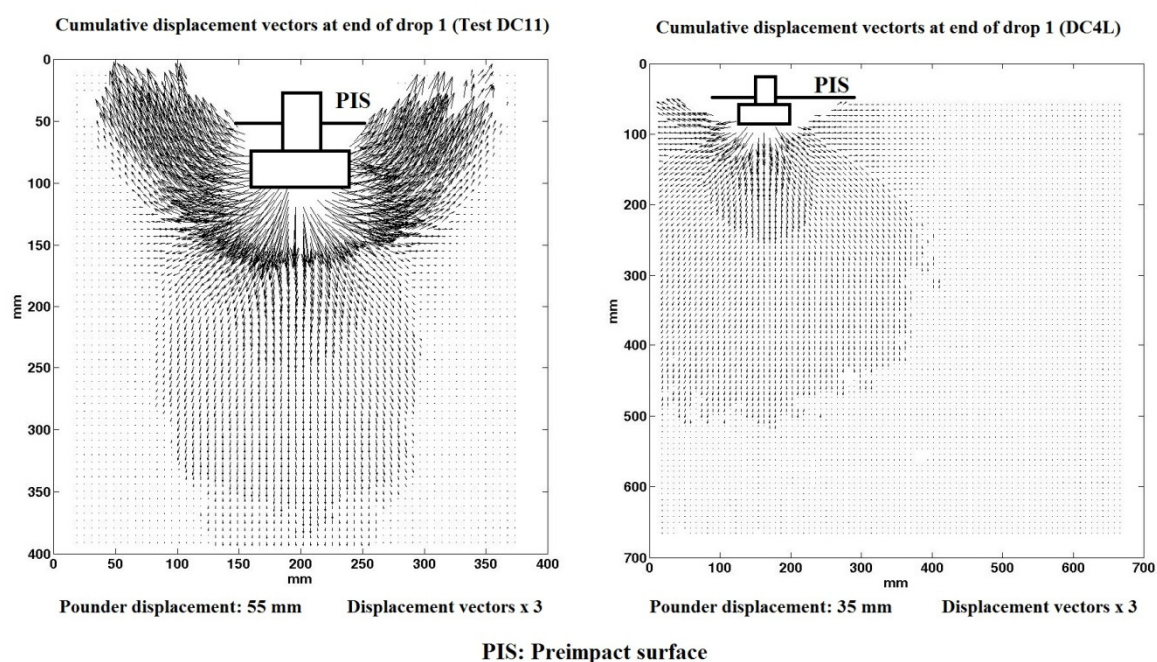


Figure 5.14. Cumulative displacement vectors at end of drop1 of tests DC11 (57mm poulder, Dr: 25%) and DC4L (57 mm poulder, Dr: 29%).

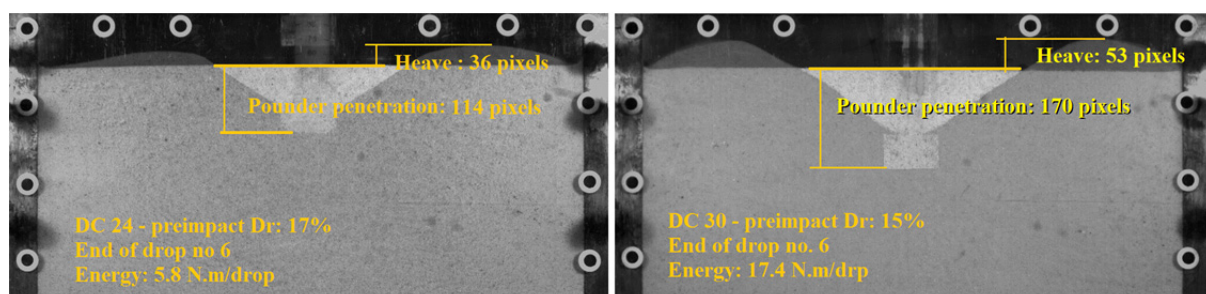


Figure 5.15. Effect of imparting energy level on poulder penetration and soil heave.

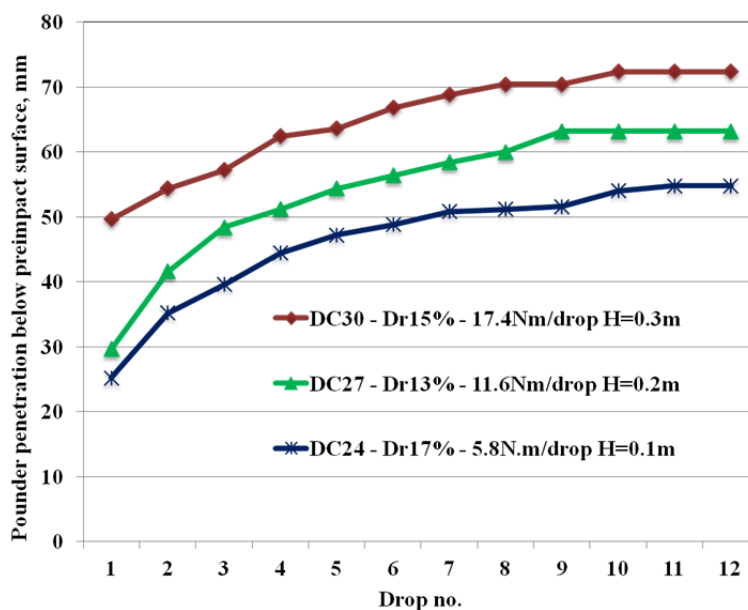


Figure 5.16. Effect of energy levels on pouncer penetrations

Figure 5.17 shows the incremental displacements in test DC11 that have taken place between successive photographs during the 0.001 sec duration following the times 0.007, 0.009, 0.014 and 0.024 seconds after the tamper has impacted the soil surface. At these times the pouncer had penetrated approximately 31 pixels (12.1mm), 41 pixels (16.0mm), 61 pixels (23.8mm) and 65 pixels (25.4mm) respectively. The displacement fields show that deformation beneath the tamper is concentrated in a series of bands or waves between which there is no significant displacement. This pattern shows that the soil particles do not deform uniformly starting with larger displacements directly beneath the point of impact that diminish with depth.

The photographs suggest an alternative interpretation with a series of compaction bands being generated as the tamper moves into the sand. These bands propagate downwards before stopping at some distance from the tamper, where they can still be detected in the cumulative displacement vectors from the jumps in the vectors (see Figure 5.14). Corresponding real time shear and volumetric strains during this impact are shown in Figures 5.18 to 5.20. The similarity between the cumulative shear strains at the times of 0.008 and 0.01 seconds after impact of the first drop (Figure 5.18a and b) and the incremental displacement at the same time in Figure 5.17 is clear, and is surprising given that one picture is incremental and the other cumulative from the time of impact.

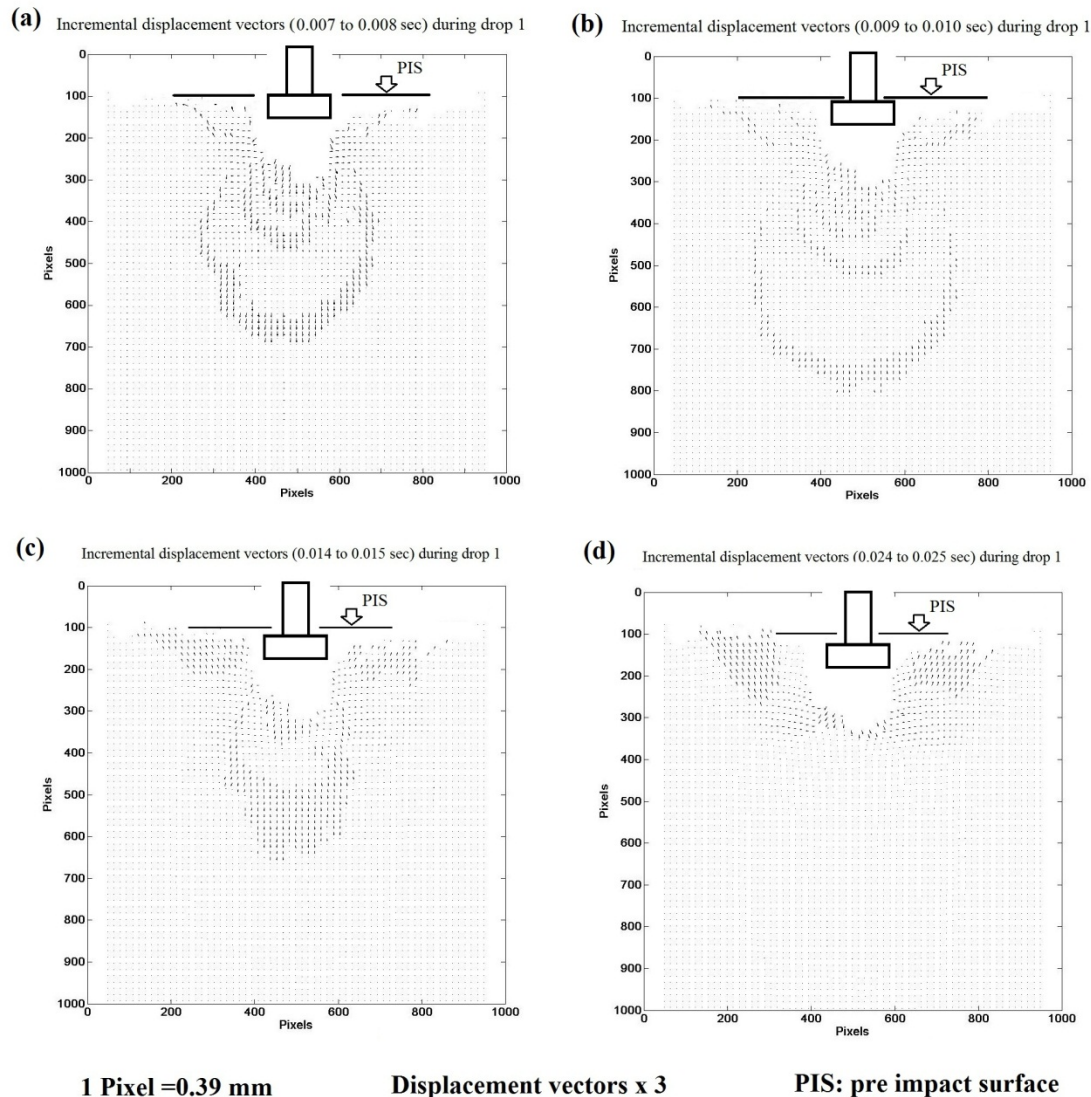


Figure 5.17. Incremental displacement vectors at four different times following the impact of drop no.1 (Test DC11)

No compaction bands were detected after a time of 0.025sec (Figure 5.17d), but the bearing capacity failure mechanism continued until 0.045sec, after which deformation ceased. The patterns of the incremental displacements of Figure 5.17 and the total shear strain of Figure 5.18 reveal the compaction mechanism. Velocities of the propagated compaction bands (identified by GeoPIV propagated incremental displacement fields) during DC tests ranged between 22 and 85 m/sec, depending on the soil bed relative density. Further discussion on the velocities of the propagated localisation and the relationship between these velocities and body wave (P-wave- and S-wave) velocities are provided in Section 6.4.1.1.

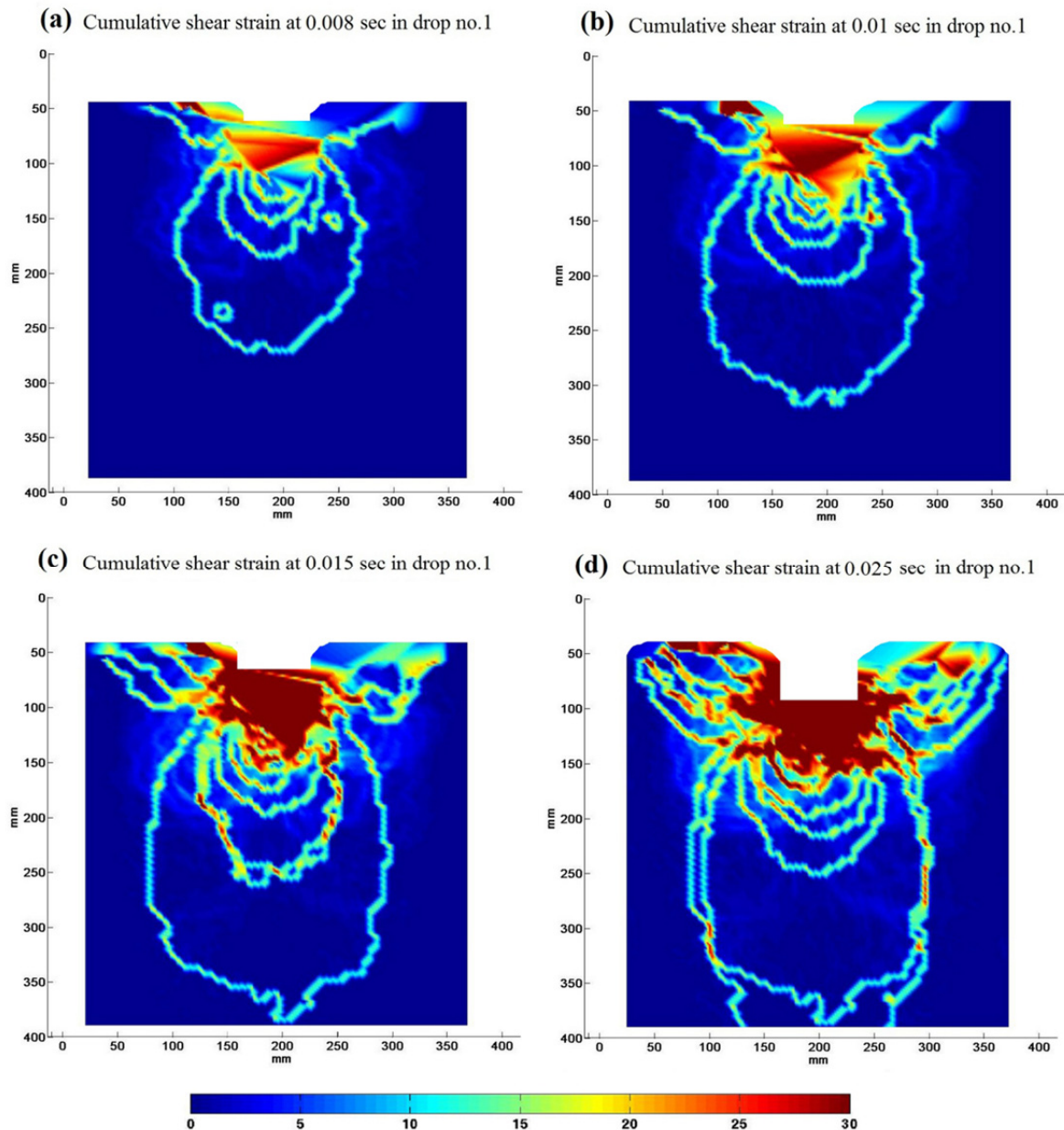


Figure 5.18. Cumulative shear strain at 0.008, 0.010, 0.015 and 0.025 sec during drop no.1 of Test DC11(compare with incremental displacement shown Figure 5.17)

These figures show that bands of high shear and volume strain (Figure 5.19) develop at the base of the intensely sheared zone and propagate downwards and outwards. However, the ends of these shear bands remain in the shear zone beneath the pounder. As the figures show several of these shear (or compaction) bands are produced as a result of each dynamic load application. The incremental displacement plot (Figure 5.17) shows the vectors moving down and outwards and diminishing as they move further from the pounder. However, the

cumulative plots show that the compaction bands are still visible even when all movement of the poulder has ceased. Close inspection of Figure 5.18 also reveals that it is not necessarily the first compaction band that travels furthest. Figure 5.18a shows the first band has moved down about 170mm at time 0.008sec, about 220mm at time 0.015sec and comes to a stop at about 300mm at time 0.025sec. In Figure 5.18c, it can be seen that there are two compaction bands overlapping at 250mm (150mm from the sheared zone) and that one of the bands continues down eventually finishing further from the poulder than the first compaction band.

Another feature of the shear strain plots is that they show significant strains at depth only occur in the compaction bands themselves. As the compaction bands pass through the soil there is little permanent strain despite the relatively large shear and volume strains within the compaction bands. Nevertheless at the conclusion of the dynamic event the compaction bands remain in the soil at the locations they reached furthest from the poulder. The absence of shear and volume strains after the compaction bands have passed is a result of positive strain in the front of the band being counteracted by the negative strains behind it. This result is surprising as large volume strains of 10% are indicated in the compaction bands.

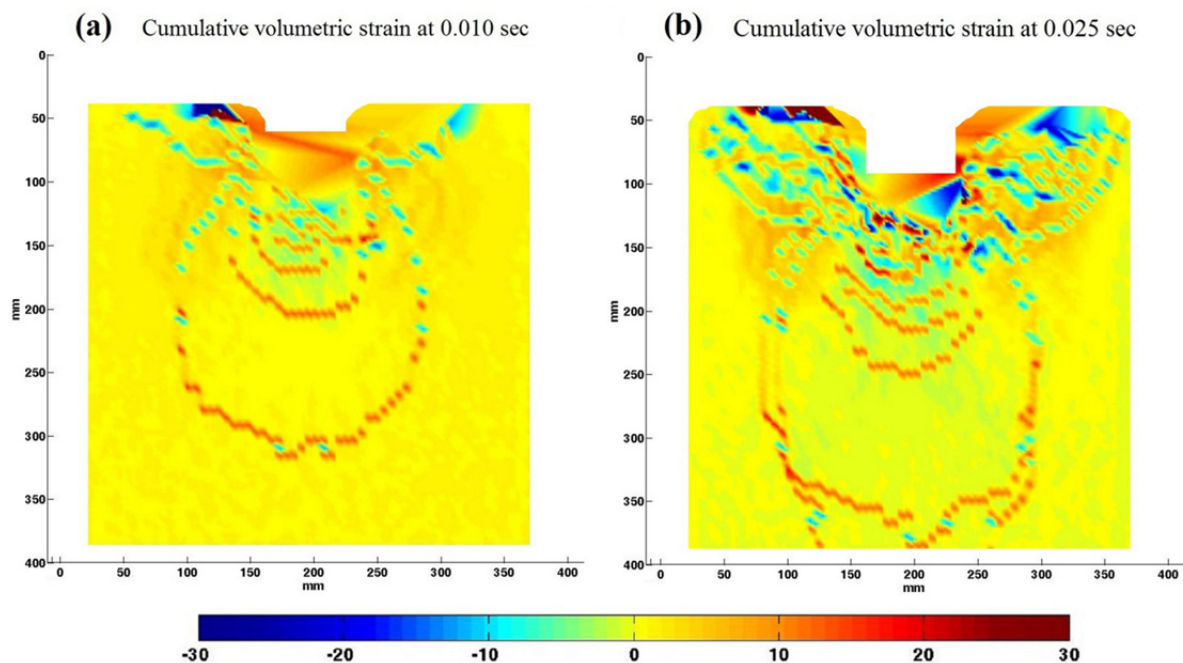


Figure 5.19. Cumulative volumetric strains at 0.01 and 0.025 sec during drop no.1
(Test DC11)

In 1-D compression (as assumed by many authors to represent conditions beneath the poulder) a volume strain of 10% would require a large normal stress and would result in significant residual compaction when the stress is removed.

As discussed above, after a certain level of poulder penetration, further penetration results in the bearing capacity mechanism with no compaction bands moving down into the soil. This is clearly seen by the concentrated incremental displacement (Figure 5.17d) and the intense shearing (Figure 5.18d) around the poulder at larger times. This can be seen even more clearly from the differences between the shear strain at 0.025sec (Figure 5.18d) and the total shear strain at the end of this drop (Figure 5.20a).

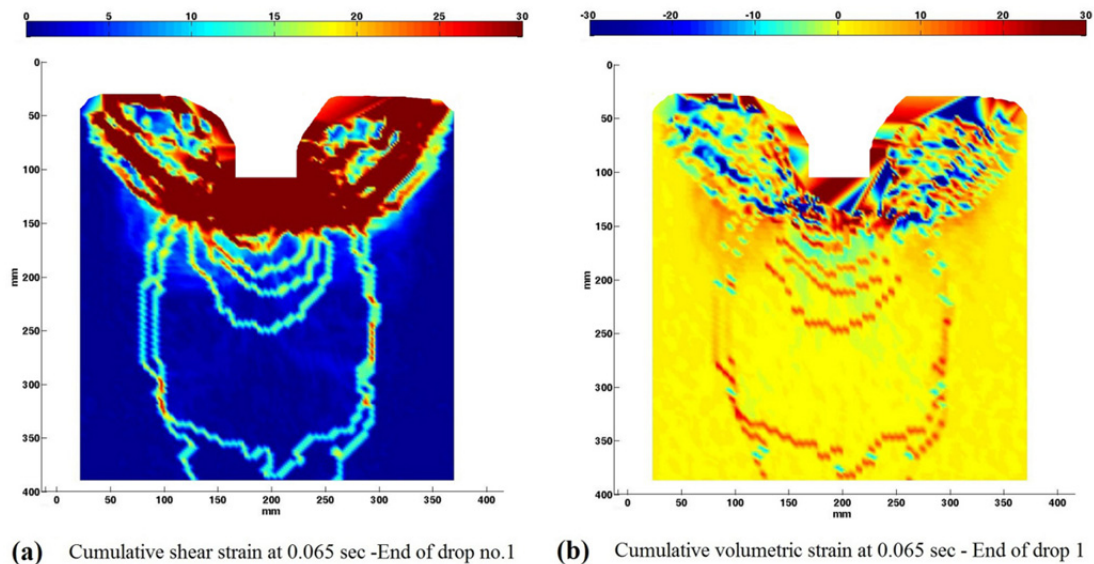


Figure 5.20 Cumulative shear (a) and volumetric strains (b) and end of drop 1 during DC11

After the tamper comes to rest the cumulative shear and volume strain plots looks similar to those at a time of 0.065 sec shown in Figures 5.20 and 5.21, and the effects of the first blow are effectively locked in the soil. With further impacts additional compaction/shear bands are formed which propagate down, through the existing bands, beneath the tamper, leading to the cumulative shear strains after two and four drops shown in Figure 5.21. A similar pattern is obtained for the volumetric strain. Figure 5.21 shows that continued blows have created additional shear (or compaction) bands which have filled in the region beneath the tamper, but there are still regions between these bands where no densification has occurred. In all

cases it has been observed that as the tamper moves into the soil new compaction bands develop until the tamper comes to rest. In a typical drop five or six of these bands are formed. It was difficult during the DC tests to maintain the shape of the deformed crater because of the collapsing nature of the dry sand tested. Subsequent to each drop, the sand falls into the deformed surface (crater that has been created by the drop) when the poulder is removed. Thus in subsequent drops, the poulder falls onto a zone of loosened sand. This limited the ability of the poulder to compact the soil at depth, and also explains why the poulder penetration reaches as shown in Figure 5.16.

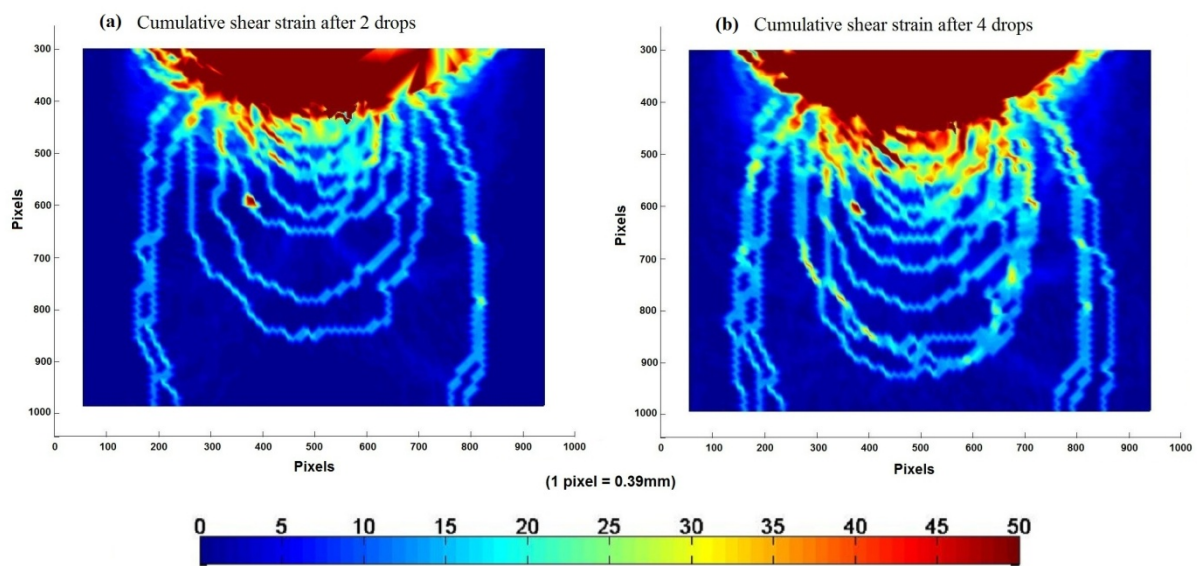


Figure 5.21. Cumulative shear strain after 2 (a) and 4 (b) drops (Test DC11-sand)

Remarkably the compaction bands following any single impact do not travel downward away from the impact point in sequential order, that is, the band travelling furthest from the tamper is generally the second or third band emanating from the tamper. The trend of the propagated strain bands shown in the previous strain plots have been observed in all compaction tests. Strain maps after 1, 6 and 12 drops on loose sand (large model) are shown in Figures 5.22, 5.23 and 5.24. The displacements and strain patterns from the large model DC tests are essentially similar to the displacements and strain patterns from the small model DC tests. However, the compaction bands are not as clearly defined, which is believed to be a result of the lesser image resolution in the case of the large sized model tests and additional reflections from the larger Perspex window which interfered with the image quality.

Although having similar energy inputs, a lesser number of strain bands of lesser strain intensity can be detected after the first drop from test DC1L (Figure 5.22a) comparing with the first drop from test DC11 (Figure 5.18d) due to the lesser impact stress as discussed previously. The effect of higher impacting energy can be detected by the more intense contractile volumetric strain shown in Figure 5.24 from the DC6L (82N.m/drop) than from Figure 5.23 from DC1L with an energy of 49.4N.m/drop.

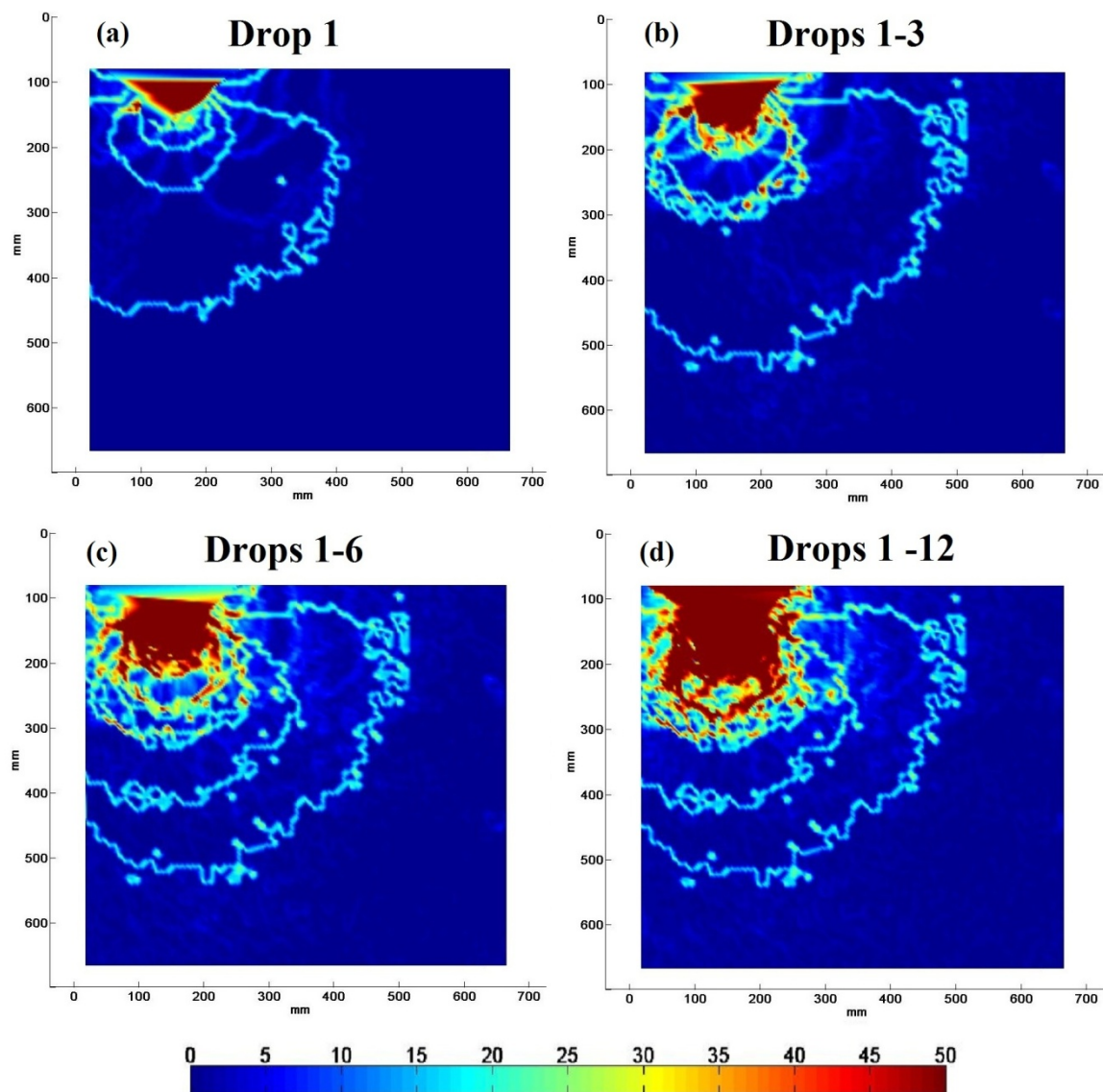


Figure 5.22 Cumulative shear strains after 1, 3, 6 and 12 drops (Test DC1L)

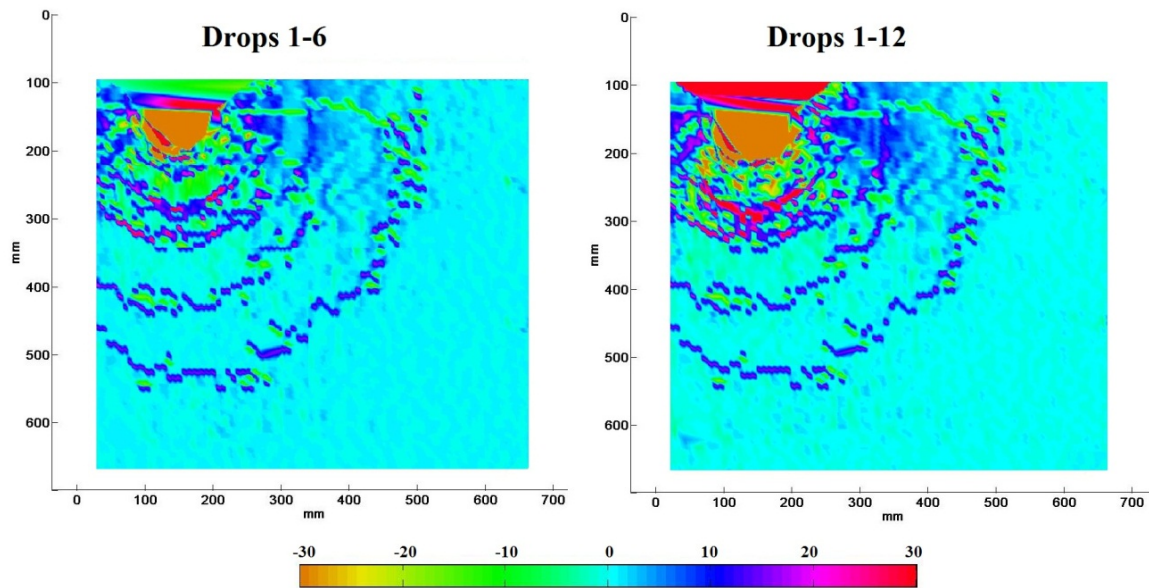


Figure 5.23. Cumulative volumetric strains after 6 and 12 drops during test DC1L
(DC1L: sand of Dr 8%, 35mm poulder and 49.4N.m/drop)

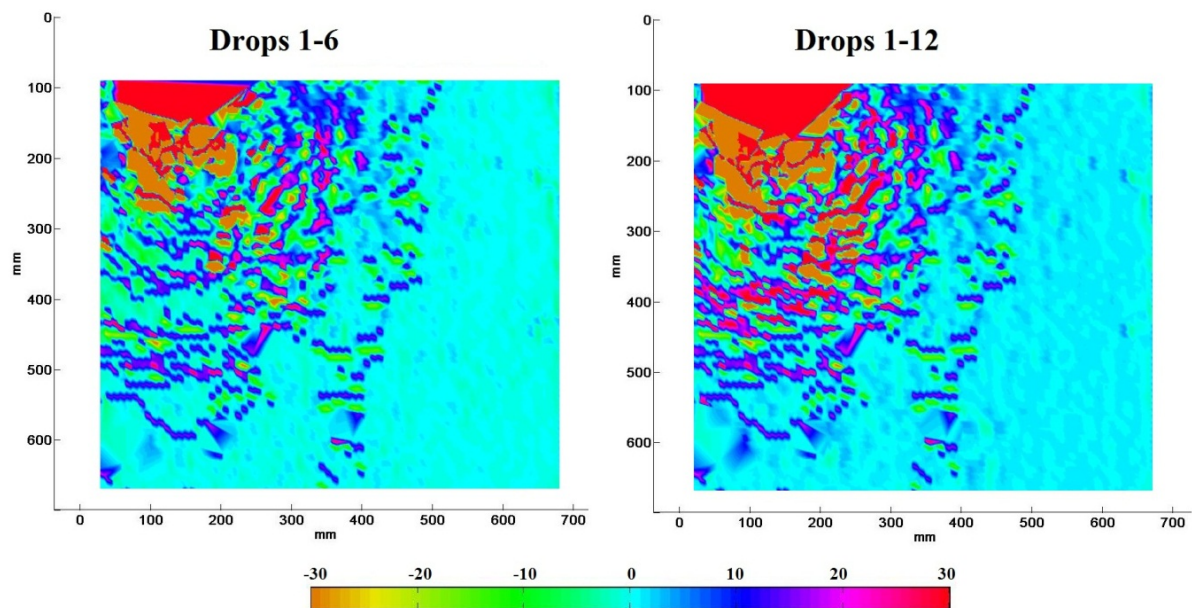


Figure 5.24. Cumulative volumetric strains after 6 and 12 drops during test DC6L
(DC6L: sand of Dr 30%, 105mm poulder and 82N.m/drop)

In dense sand, the impacting energies were unable to produce compaction (shear and volumetric strain) bands at depth, and the compaction energies were expanded by loosening the surface soil by the bearing capacity failure mechanism at the surface as shown in Figures 5.25 and 5.26. In these tests, there were only limited numbers of shallow compaction bands that emerged due to the first drop. Subsequent drops only caused more intense shearing and dilation in the upper region and around the poulder, but were unable to produce further compaction bands or to push the already formed ones deeper into the soil.

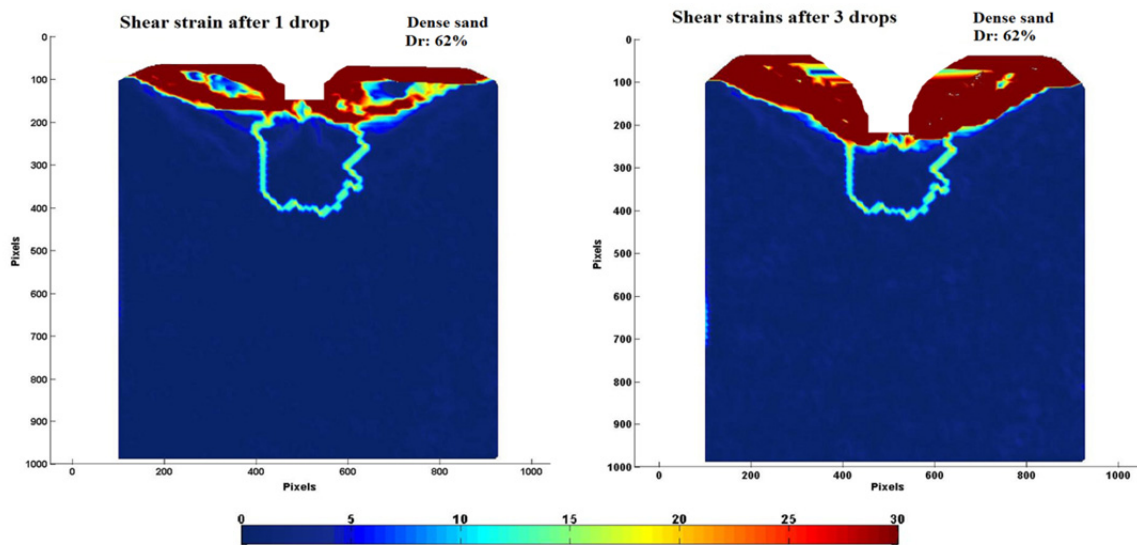


Figure 5.25. Cumulative shear strains after 1 and 3 drops (Test DC20)

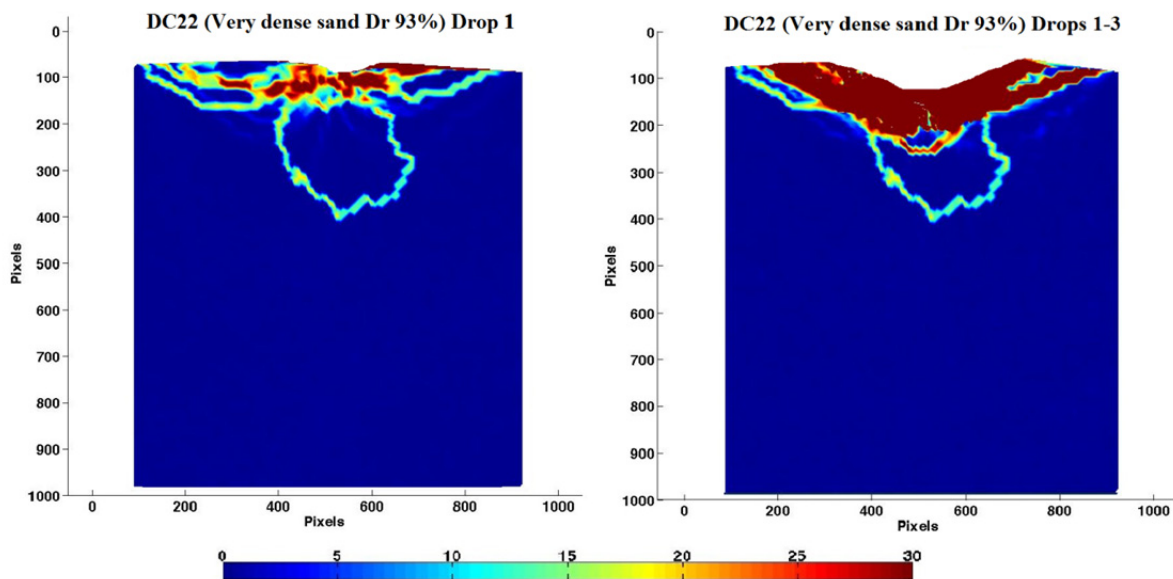


Figure 5.26. Cumulative shear strains after 1 and 3 drops (Test DC22)

Another feature observed from the GeoPIV strain plots was the occurrence of less intense shearing bands of the shape of half spirals that were generated at the poulder base and propagated laterally, and simultaneously with the downwards moving compaction bands. These shear bands could only be detected at the early stage of loading as shown in Figure 5.27, but they became masked by the intense shearing filling the upper bearing capacity region. Similar observations were made from plane strain bearing capacity experiments and numerical simulation work by Tatsuoka *et al.*, 1994 and 1997 (see Figure 2.25).

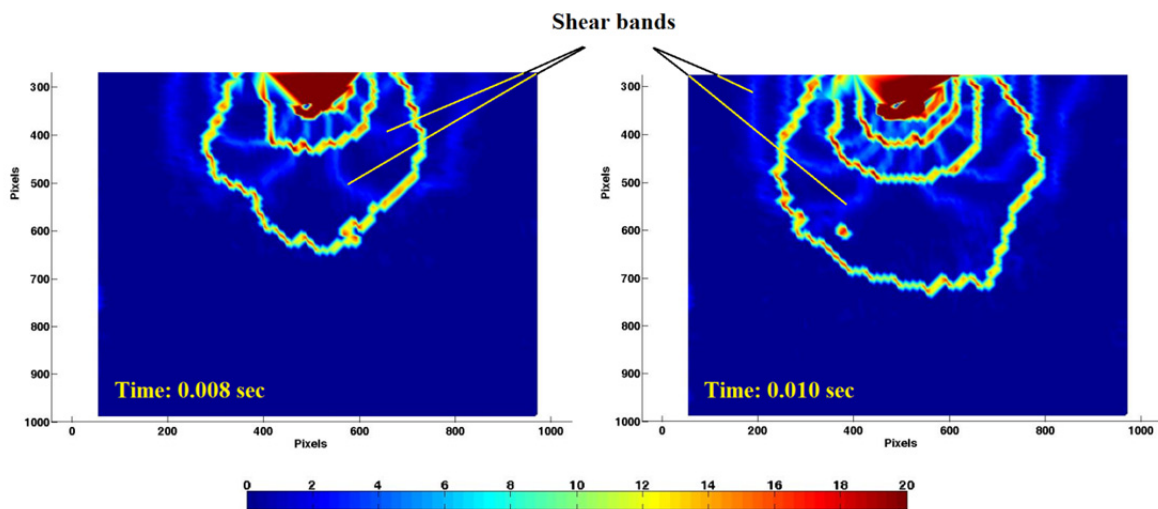


Figure 5.27. Cumulative shear strains after 0.008 and 0.01 seconds from drop 1 (Test DC12)

The behaviour and responses of sand and non-plastic feldspar silt mixtures (2sand:1silt) to DC have the same general features of the propagated compaction bands observed in the DC tests with sand only. Figure 5.28 shows examples of cumulative shear strain after 2 and 4 drops from test DC36. However, there were differences in the sand and the sand:silt mixture responses to DC which will be outlined in the following sections.

It has been widely believed that the densification of a soil following dynamic compaction occurs in a semi-prolate-spheroidal region with the largest density increase directly beneath the point of impact and the density change gradually decreasing with distance from the tamper. The reduction in cumulative displacement with distance from the tamper shown in Figures 5.14 (from both the small and the large sized model tests) supports this view, however, the results from the high speed photographs, shown by the strain profiles, are not

consistent with this simple interpretation. They show an alternative phenomenon of progressive but not homogeneous densification of the region beneath the tamper. Each tamper impact generates one or more shock bands, which are associated with high shear and volumetric strains, which pass down through the soil and eventually come to rest. The soil through which the shocks pass experiences a cycle of contraction and dilation, which produces little net change to the soil density. However, the soil in the shock band is significantly denser and this compacted band of soil is effectively locked in place when the shock band comes to a halt. With further impacts additional shock bands are generated and as these come to rest in different locations more of the soil is effectively compacted, particularly within a region of 4 to 5 times the poulder width beneath the poulder. However, even after six or up to twelve impacts much of the soil with the region bounded by the furthest travelled compaction band experiences little if any densification.

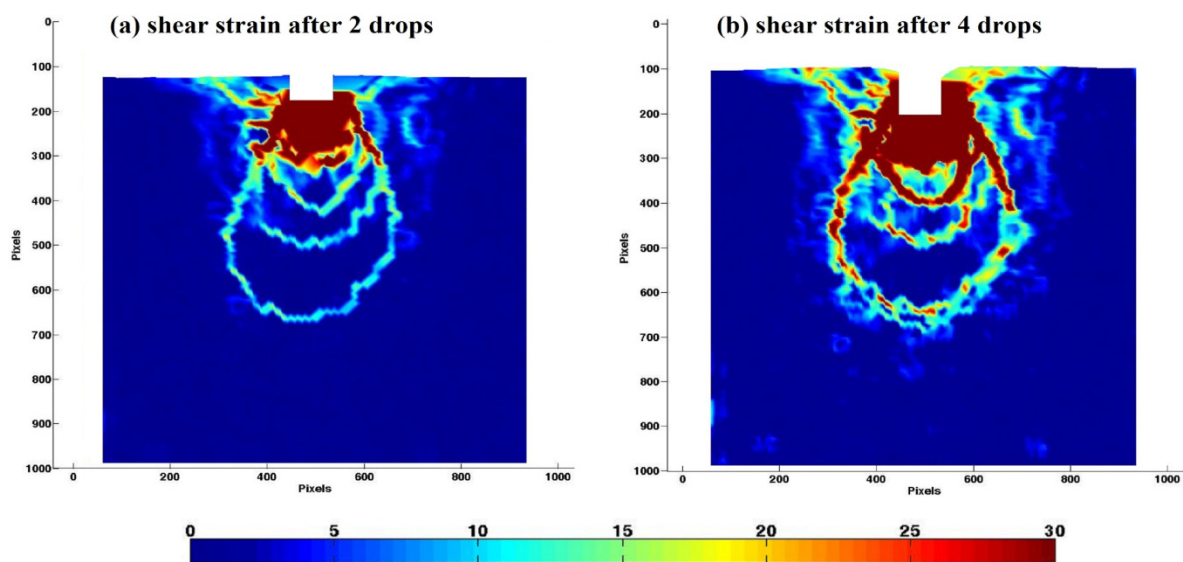


Figure 5.28. Cumulative shear strain after 2 (a) and 4 (b) drops (Test DC36-sand:silt)

It is inferred from the displacement and strain plots that strain localisation resulting from the dynamic impact leads to a phenomenon of progressive but not homogeneous strengthening of accumulated deformed and sheared zones. This pattern suggests that a cyclic mechanism of both incremental contractive and dilative behaviours is exhibited within the impacted soil mass, and that densification of the sand model will take place as a result of the accumulated strain localisations following a number of repeated impacts.

5.2.2 Strain Uniformity and Micromechanics

The results from DC tests show highly non-uniform strains. The detected strains had a very wide range with extreme shear strains greater than 50%, and extreme volumetric strains in excess of $\pm 30\%$. The parts of the model that experienced extreme high strains are in the upper region, immediately beneath the impact footprint, and on its sides due to the large displacement taking place within this region. To represent the gradient of strains within the upper region would result in a loss of definition in the rest of the model where strains are relatively small. As a compromise, the colour scaling of the shear strain and volumetric strain plots have been limited to up to 50% and $\pm 30\%$ for shear and volumetric strains respectively. The selected ranges for the strain values have allowed the monitoring of strain kinematics following the DC impact, but have resulted in loss of definition of the strains in the upper region of intense straining. Areas of very small strain magnitudes (less than 5% shear strain or $\pm 5\%$ volumetric strain) could only be examined by inspecting the GeoPIV data.

Figure 5.29 shows the variations in volumetric strain along the impact centreline at three different times from impact (including at the end), extracted from the GeoPIV strain matrices. For clarity, only the range of volumetric strain between -2% to +2% is shown between depths of 125mm and 400mm, the region below the highly sheared soil (the pre-impact surface is at 40mm), for times of 0.005sec, 0.02sec and at the end of the first impact. The volumetric strain plots shows a number of spikes, which correspond to the compaction bands, however for the majority of the soil the volumetric strain is zero. The compaction bands shown at about 200mm depth at time of 0.005sec have moved down at time of 0.025sec and have reached greater than 400mm at the end, except that three of the compacted bands at time of 0.02sec are retained at the end of the dynamic loading.

Figure 5.30 shows the accumulated volumetric strain at the end of one, six and twelve impacts during test DC24. The coordinates and magnitudes of the volumetric strain at five selected locations are presented in Table 5.1. After 12 impacts, only locations B and C exhibited significant contractive strains although they are deeper-seated and further away from the impact centreline than location A. Examining the volumetric strains at target locations at the end of the first drop indicates significant contractile volumetric strain in excess of +10% at the locations A, D and E and dilation (-ve volumetric strain) at locations B and C. Since volume strains change from positive strains in the front of the bands to negative

strains behind them after the compaction bands have passed as outlined in above, the net volumetric strain at any of the target locations continued changing with more compaction bands produced during the subsequent drops. This resulted in a non-uniform continuously changing volume strain profile.

Table 5.1 Coordinates and accumulated volumetric strain at locations shown in Figure 5.30

Location ID	Coordinates, mm			Volumetric Strain, %		
	X ¹	Y ²	Z ³	Drop 1	Drops 1 - 6	Drops 1 - 12
A	199.5	147.0	107.0	11.540	-2.314	1.243
B	230.0	175.5	135.5	-3.348	-2.604	34.900
C	299.0	185.0	145.0	-9.901	4.247	5.512
D	273.5	230.5	190.5	10.770	0.218	0.326
E	216.5	237.0	197.0	13.190	-0.040	-0.002

1. The centreline coordinate is 200mm
2. The pre-impact soil surface level Y coordinate is 40mm
3. Z= Depth below the pre-impact surface level

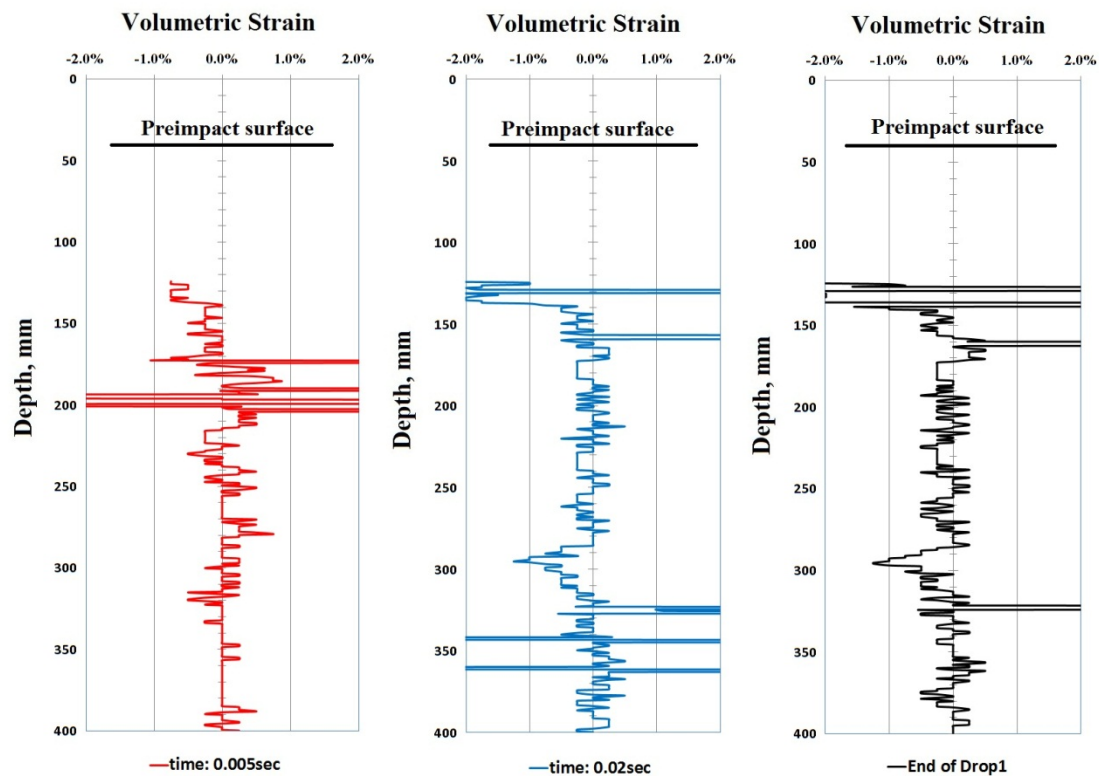


Figure 5.29. Fluctuation of volumetric strain along the centreline of impact at times 0.005sec, 0.020 sec and end of drop 1 (Test DC30)

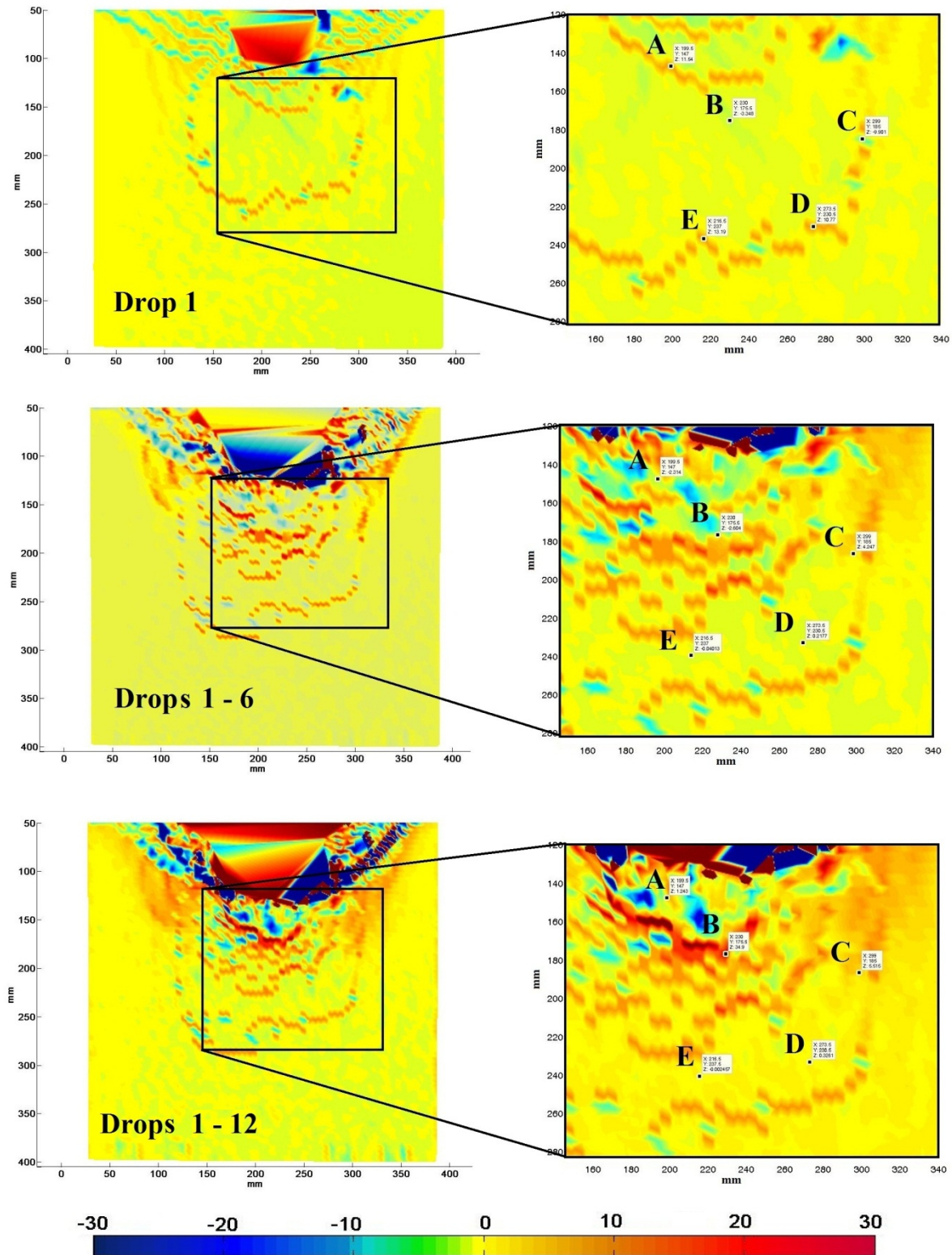


Figure 5.30. Cumulative volumetric strain after 1, 6 and 12 drops with zoomed in windows that illustrate the fluctuation of strain at 5 selected locations (Test DC24).

By examining all the test results, the primary zone of interest for DC was found to start at a depth equal to the tamper width (B) below the tamper base's final position. The selection of this zone, at a depth of B (tamper width) below the tamper's final position, was based on observations from the GeoPIV displacement fields and strain plots which showed regions above that level displayed a general bearing capacity failure type mechanism with very little net densification taking place. This is also consistent with observations from impact compaction (Berry, 2001) which showed highly variable densification directly beneath the tamper. At shallow depth, the tamping leads to monotonic strains in the form of a surface heaving bearing capacity mechanism type which drives the soil to a monotonic critical state, with no further densification. At depth, the tamping leads to cyclic (2-way) strains, which result in compaction, perhaps tending towards a denser form of critical state.

A volumetric strain analysis was carried out to establish the amount of dilation/contraction within this primary zone. For a particular DC test, the GeoPIV analysis started by placing a reference mesh of 900 patches of 30 x 30 pixels over the soil body within the reference image field of view as shown in Figure 5.31. The 900 patch mesh comprised 330 and 570 patches, overlaying the upper bearing capacity zone and the lower contraction zone, respectively. GeoPIV strain matrices provide the magnitude of strains at elements located in between the displaced patches. For this mesh, 1682, 1044 and 638 GeoPIV strain elements were generated for the 900, 570 and 330 patches, respectively.

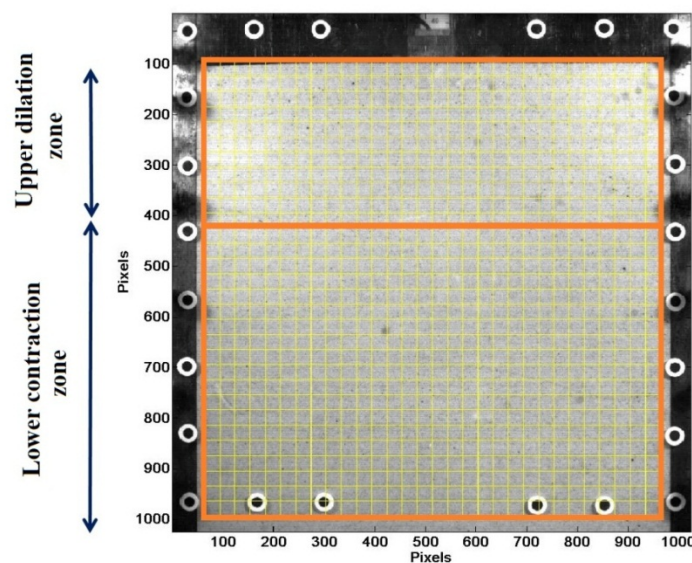


Figure 5.31. GeoPIV pre-impact patches for DC primary zone of influence calculations.

The example shown in Table 5.2 is to illustrate the volumetric strain calculation adopted in this work to distinguish the amounts of dilation/contraction resulting from the DC tests. Table 5.2 summarises the results from the first impact during test DC24 based on the GeoPIV patches and strain element configuration of Figure 5.31. The following explanations define the calculation:

V_m = volume of soil covered by GeoPIV mesh = mesh area x the depth of the model

V_e = volume of soil represented by a single strain element as $V_e = \frac{V_m}{N_e}$

VS_e = element's volumetric strain by GeoPIV

N_e = number of elements N_p = number of patches

The above conventions were selected to enable the conversion of strain values into a meaningful DC parameter called “net contracted volume”, abbreviated as NCV:

$$NCV = \Sigma (VS_e \cdot V_e) / V_m \quad (5.2)$$

In this example, the percentage of overall contraction by the full mesh is negative (-0.7653%) suggesting that no densification has taken place due to the studied impact. This global picture is controlled by the large amount of dilation occurring within the upper region, but analysing the upper and lower regions separately provides better understanding on the amount and location of primary compaction within the model. The results from Table 5.2 show that the upper soil region, represented by 330 patches, has experienced significant dilation having net contracted volume(s) (NCV) of -2.408% and -0.883% of the upper region and the full mesh volumes respectively. On the other hand, the lower soil region, represented by 570 patches, has experienced compaction having net contracted volume(s) (NCV) of 0.1862% and 0.1179% of the lower region and the full mesh volumes respectively. The small differences in the element volume (V_e) are due to slight differences between the N_e/N_p ratios among the three meshes.

Since the lower region of primary compaction is of the main concern from the DC point of view, the term “NCV” used in the remaining sections of this thesis presents the ratio of contracted volume to the volume of the lower region. Figure 5.32 shows the variation of the NCV parameter (lower region) over the 12 impacts of DC24.

Table 5.2. GeoPIV strain analysis of first impact during test DC24

Analysis	N_p	N_e	V_e, m^3	V_m, m^3	Sum($V_{S_e} \cdot V_e$)	NCV, % (by part)	NCV, % (Full mesh)
Full mesh	900	1682	1.10E-05	1.85E-02	-1.41E-04	-0.7653%	-0.7653%
Part1: Above 400	330	638	1.06E-05	6.78E-03	-1.63E-04	-2.4088%	-0.8832%
Part 2: Below 400	570	1044	1.12E-05	1.17E-02	2.18E-05	0.1862%	0.1179%
Sum of Part 1 & Part 2	900	1682		1.85E-02	-1.41E-04		-0.7653%

This approach may not be rigorous but the results provide a reasonable platform for an analytical methodology to be used for comparing the effect of different energy levels, initial relative density of soil and tamper geometry. The limitations of this approach can be considered as follows:

1. With the chosen camera setup, the field of view does not cover the entire soil body with the model. However, GeoPIV results showed very little displacement and strain taking place below the captured view and these might be reasonably considered as being insignificant.
2. The analysis might be sensitive to the GeoPIV setup such as the sizes of patches and search zone or number of images to be analysed. Sensitivity tests showed a variation of less than $\pm 10\%$ in NCV values with different GeoPIV setups, suggesting that this not a major concern.
3. Sensitivity of the results with respect to the nature of the DC tests generating highly non-uniform strains. Results from different tests showed acceptable statistical coefficients of correlation suggesting that the average strains are meaningful.

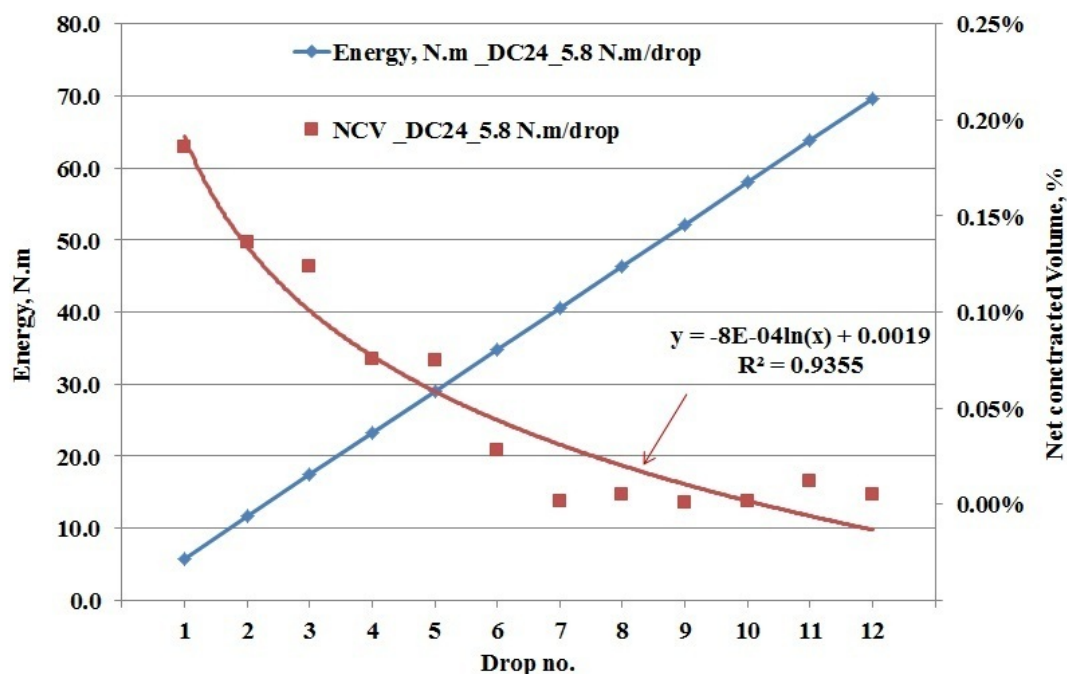


Figure 5.32. Variation of the net contracted volume parameter over the 12 impacts of DC24.

The relationship between the NCV parameter and the input energy shown by Figure 5.32 suggests a limiting level of energy (number of drops) after which the bulk of the energy is wasted through the upper region of the model with little incremental variation of the NCV parameter. Further discussion on the effect of energy input on the performance of DC tests and the separation of energy between the upper and the lower regions of the soil model is presented in Section 5.3.3.2.

5.3 QUANTIFYING THE DYNAMIC COMPACTION TESTING RESULTS

The high speed photography technique enabled measurements of the depth of influence, the lateral extent of the impacted zone at depth, and the magnitude of strains within the influence zone to be obtained. It also enabled quantified assessments of different aspects of dynamic compaction such as the level of energy, tamper geometries and soil types to be studied. However, the unique features of the propagated bands of high shear and volumetric strain observed in this work required independent verifying tests to support the photography results. For this purpose, the following testing and analytical approaches were used throughout the course of this work:

1. Before and after cone penetrometer tests were conducted at target locations in the soil models to detect changes in soil density.
2. X-ray Microtomography was used to investigate changes in soil density (void ratio) within the localised strain bands at a micro level.
3. Image analyses were carried out to quantify various aspects of the DC process including, imparting energy, tamper geometry, size of the model and type of soil treated by dynamic compaction.
4. Instrumentation (*see Chapter 6*) was used to provide additional measures of load and displacement.
5. Finite element simulation (*see Chapter 7*) was used to provide further insight into the deformation mechanism.

5.3.1 Cone Penetration Tests (CPT)

The CPT was introduced in the early stage of the testing programme to provide an indication of the change in soil density before and after the DC tests. Figures 5.33 and 5.34 show the change in soil resistance to the cone penetration from before and after 8 compaction drops of test DC3, performed at locations below the centreline of impact and 115mm to the side of the centreline respectively. The accumulated shear and volumetric strain from GeoPIV at the end of 8 drops are placed alongside the CPT results for better illustration. CPT tests were performed from the surface of soil and results were adjusted with reference to a datum depth (0.0mm) taken as the pre-impact surface level. The cone penetrometer resistance is usually normalized with the vertical stress (overburden) to the depth of the cone readings, as this allows a more meaningful relationship between density and normalized cone resistance. However, this was not possible in the case of the DC tests since after the impact vertical and lateral stresses at different levels were unknown because of the heterogenic change in soil density after the compaction drops. Consequently, there is no technique to give a precise analysis of the penetrometer measurements. Thus, the CPT results will be interpreted intuitively and in a qualitative way to correlate between the GeoPIV strains and CPT results.

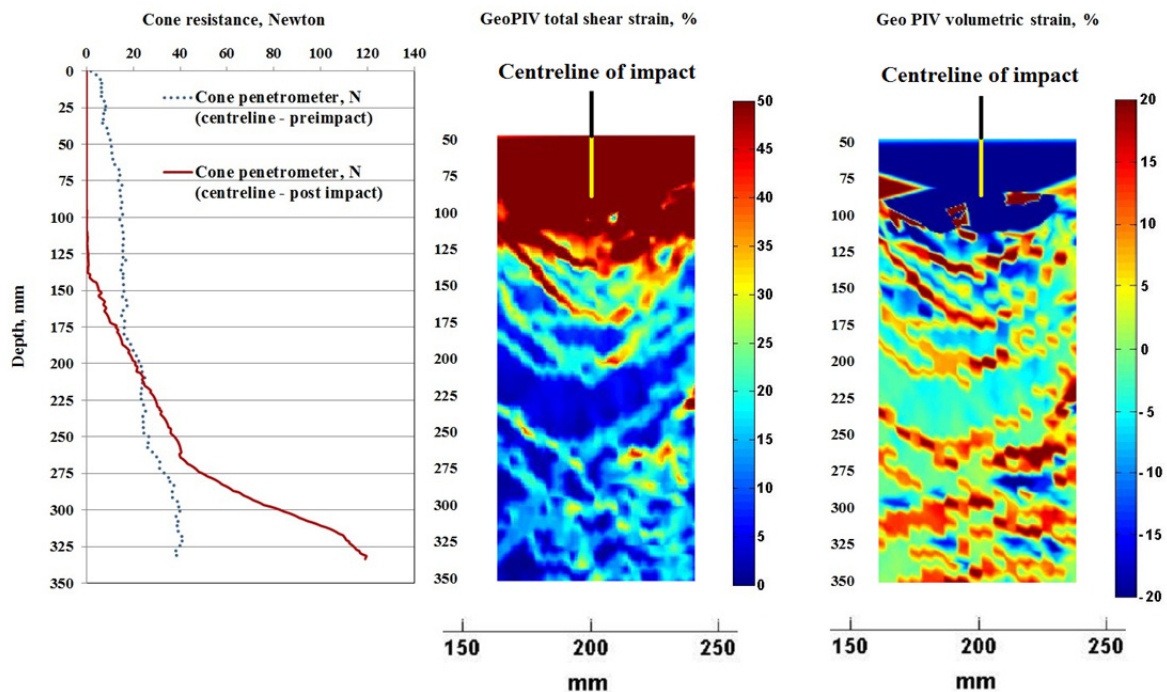


Figure 5.33. CPT soil resistance along the centreline of impact from before and after 8 drops of test DC3 with GeoPIV shear and volumetric strain.

The pre-impact cone resistances shown in Figures 5.33 and 5.34 indicate a pre-impact soil resistance of about 40N at depth of 325mm, which is consistent with a vertical stress at that depth for a uniformly placed sand of 14.52kN/m^3 unit weight. For the CPT tests that followed 8 DC drops, recorded cone results show increases in soil resistance with depth from the pre-impact status with soil resistance reached its peak at a depth of 325mm and 250mm from the pre-impact surface, beneath the centreline of impact and 115mm off centreline respectively. These peak resistances represent 300% and 170% increase of the pre-impact resistances beneath the centreline of impact and 115mm off centreline respectively.

The near zero cone resistance beneath the impact centreline down to about 130mm after 8 drops is consistent with the very small net volume change taking place along this profile. However, the after compaction CPT results show no evidence of the complexity of the diverse shearing and volume changes detected by the GeoPIV shown by the shear and volumetric strain profiles of Figures 5.33 and 5.34. This was reasoned to be due to limitations of the cone in detecting small volume changes at depth. The increase in the cone resistance is interpreted as reflecting the increase in the lateral stresses produced by the DC.

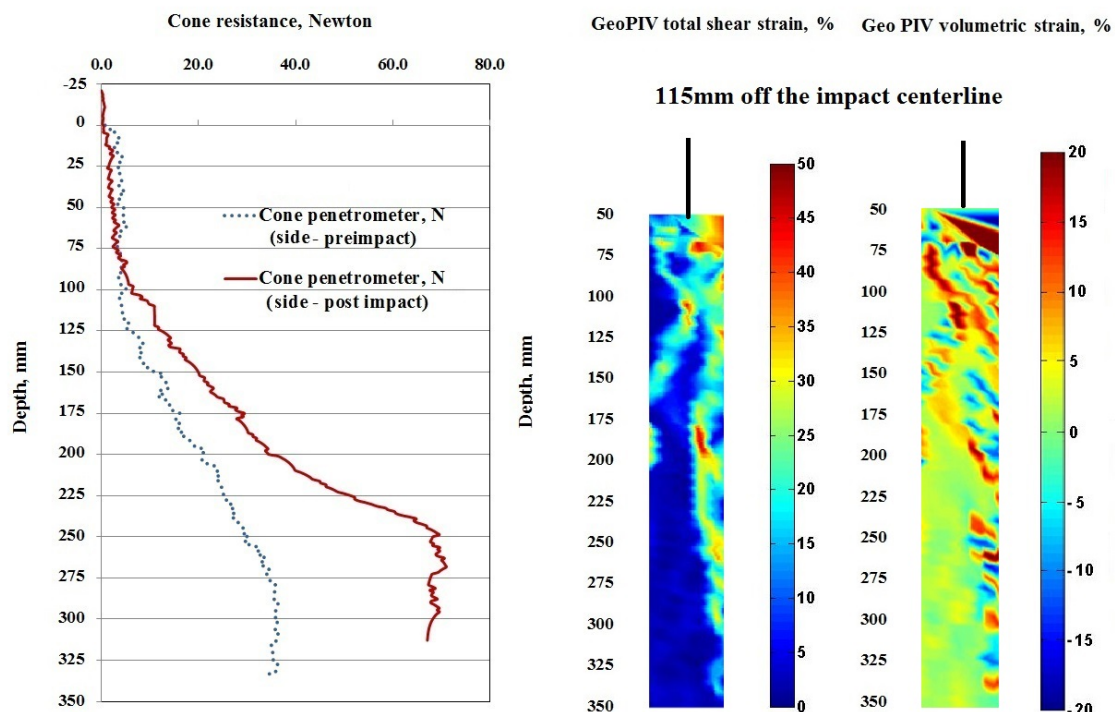


Figure 5.34. CPT soil resistance at 115mm off the impact centreline from before and after 8 drops of test DC3 with GeoPIV shear and volumetric strain.

5.3.2 X-Ray Microtomography

The CPT tests were not able to provide a method of verification to confirm and quantify the existence and the intensity of the compaction bands and the mechanism indicated by the high speed photography. Because the sand was loose and dry, and sensitive to any disturbance, there were limited options. While a number of studies of loose sands have used soil freezing techniques, these were not appropriate because the sand was dry. Attempts to X-ray the sample in a medical facility were unsuccessful due to collapse of the loose soil during transport, and the limited resolution of the medical X-ray equipment. The approach selected was to make use of a Micro-CT scan technique on collected undisturbed sand-resin specimens.

Typical thicknesses of shear bands for a variety of sands are in the order of $10\text{--}25d_{50}$ (Roscoe *et al.*, 1963, Mülhaus *et al.*, 1987). The observed strain localisations (bands) were generally of intense shearing of 5-7mm thickness with approximately 3mm of shear strain in excess of 10%. Figures 5.35 and 5.36 show typical shear and volumetric strain bands during a DC test. The 5-7mm thickness of the localised strain bands is about $20d_{50}$, as $d_{50} = 0.35\text{mm}$ for the Sydney sand.

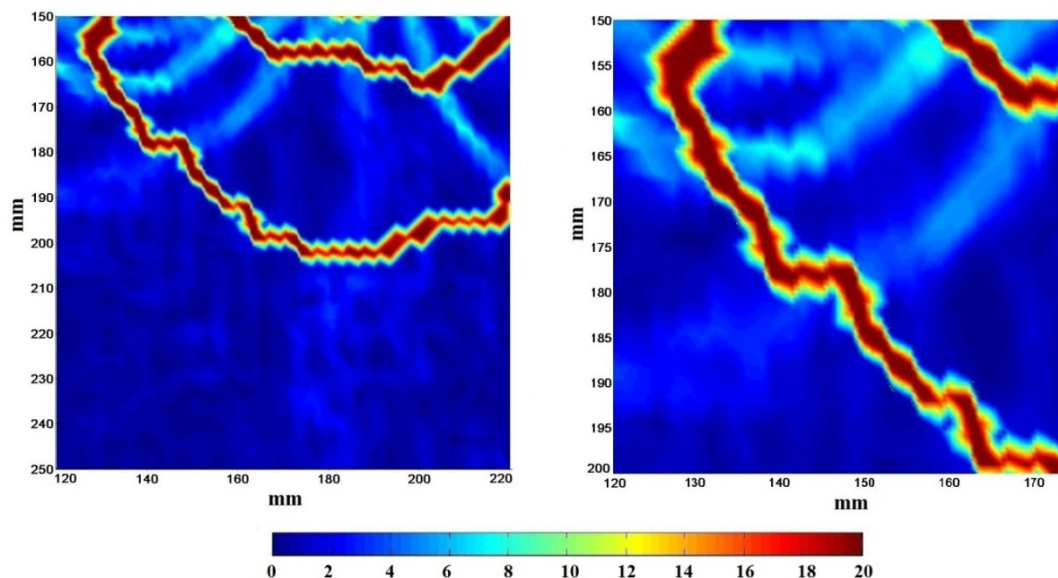


Figure 5.35. Bands of localised shear strain following the 1st drop during test DC2.

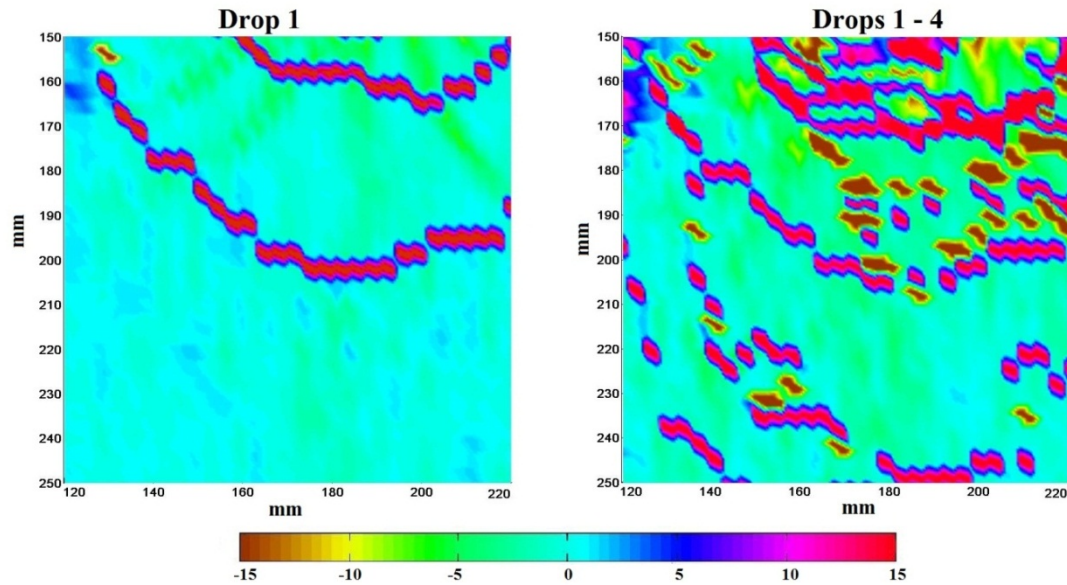


Figure 5.36. Bands of localised volumetric following 1st and 4th drops during test DC2.

To determine the local void ratio distribution along the scanned sand specimens, the created raw micro CT scan images (Section 3.4) were reconstructed using SkyScan NRecon software package to form a set of sliced images spaced at $95.5 \mu\text{m}$ (approximately 10 images per 1mm). Reconstructed images were then converted into 3D images using the CTAn software. The CTAn analysis provided quantitative parameters and constructed visual models from the scanned images. Figure 5.37 shows an illustration of the 3D CTAn software volumetric reconstruction from a scanned sand-resin sample. The determination of the porosity and void ratio from the reconstructed images requires the selection a greyscale threshold to determine which pixels are counted as particle and which as pore space. Possibly because of the resin filling the pore space a consistent threshold could not be determined, and calibration tests on specimens prepared with known porosities were conducted to assess the reliability of the inferred values.

Results from these calibration scans are shown in Figures 5.38 and 5.39 for the loose and dense reference samples respectively. The figures show an approximately linear relation between the inferred porosity and the greyscale threshold, and comparison between Figures 5.38 and 5.39 shows that the threshold can vary from scan to scan.

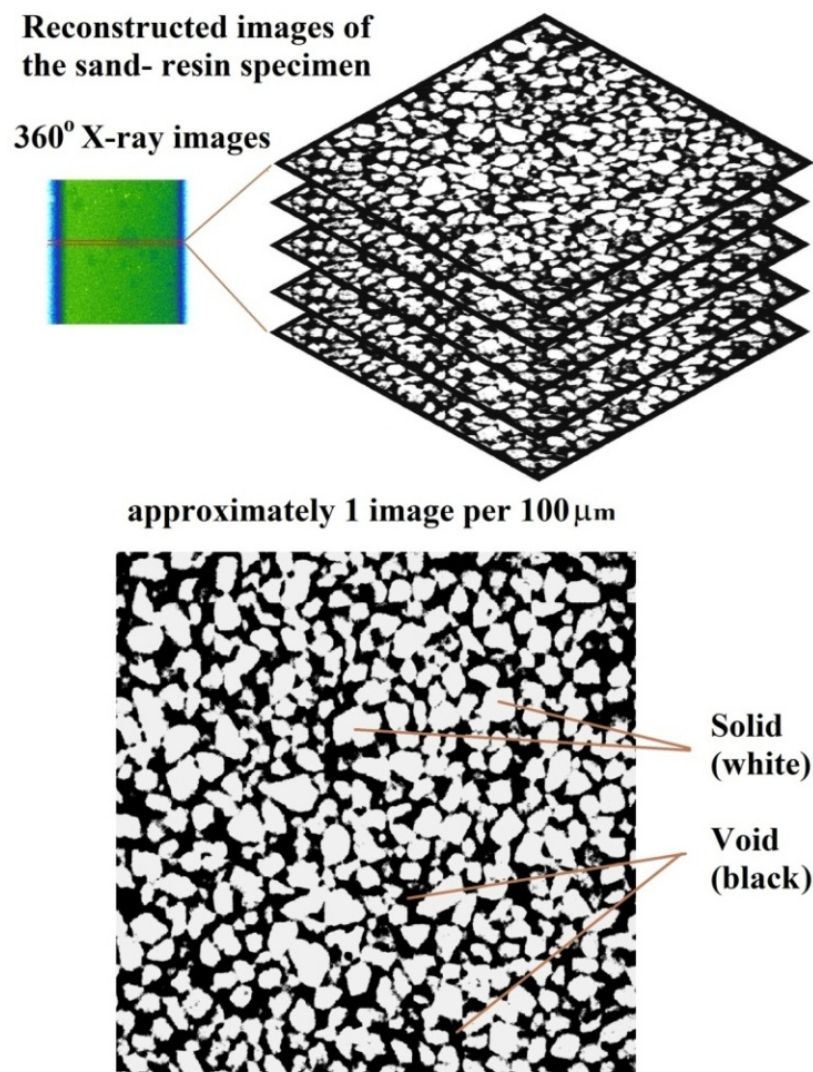


Figure 5.37. Schematic diagram demonstrates the sliced X-Ray images by NRecon software and the 3D volumetric reconstruction by CTAn software of a scanned sand-resin sample.

Results from different sections in the calibration tests suggest good correlation between the greyscale threshold from images of the same scan on the same sample but an inconsistent correlation between mean greyscale indices and sample porosities from images of different scans/samples. These results indicated that there was no single greyscale index that could be adopted in analysing samples of unknown porosities extracted following the dynamic compaction experiments, although differences in porosity would be detectable.

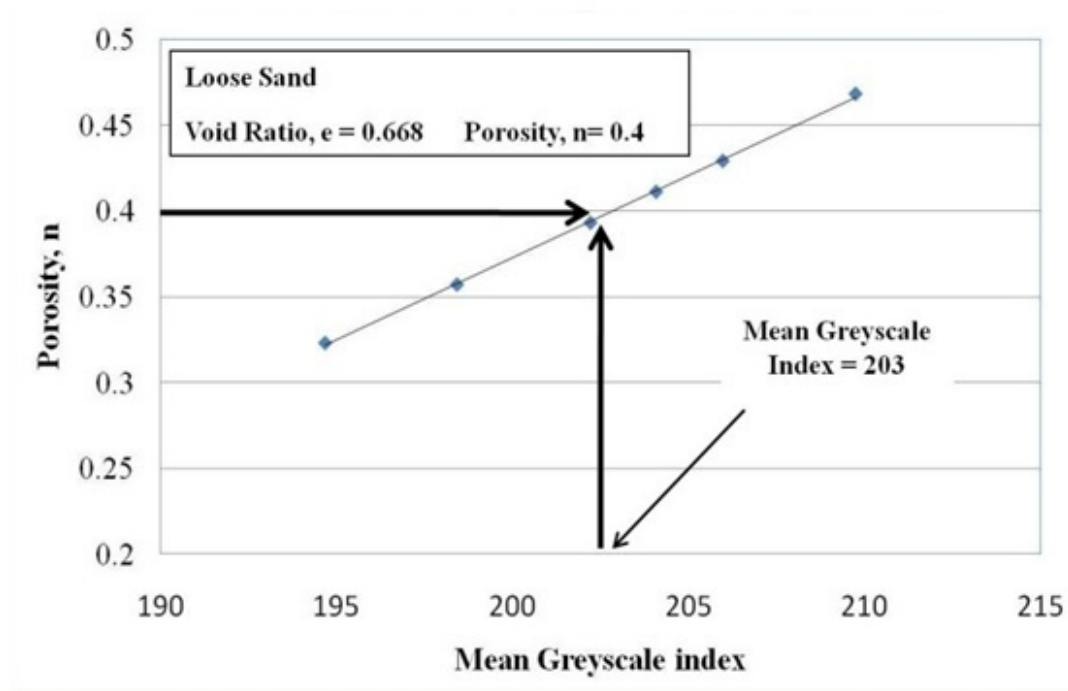


Figure 5.38. Correlation between sand porosity and CTScan mean greyscale index
(Loose sand)

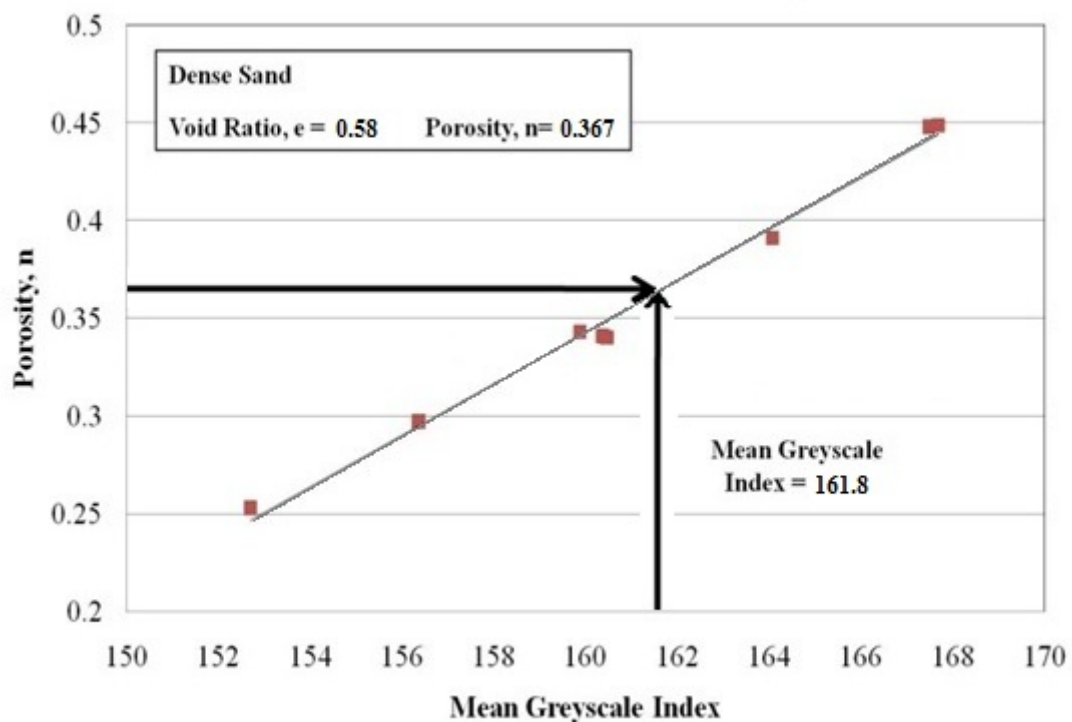


Figure 5.39. Correlation between sand porosity and CTScan mean greyscale index
(Dense sand).

To assist in the selection of an appropriate greyscale threshold, to achieve reasonable porosity measurements, the images were individually inspected to ensure that appropriate greyscale ranges were employed and a dependable contrast existed between the sand solid phase and the surrounding resin. Figures 5.40 and 5.41 demonstrate the sensitivity of the greyscale thresholds in determining the right contrast between solid particles of sand and the surrounding resin. Figure 5.41 most clearly shows the limitations of the porosity estimation as both images look reasonable, and the image on the right is similar to that of the loose specimen in Figure 5.40, but this is a dense specimen. A relatively small change in greyscale threshold would move this specimen from apparently loose to apparently dense. Without additional information on the porosity, it would have been impossible to reliably interpret the data from these pictures.

Despite the limitations of the micro-CT method to reliably interpret the porosity, the calibration tests have shown a consistent interpretation can be made for a given scan and specimen. Thus the method should be able to pick up porosity variations throughout a specimen, and limits on possible porosity values are available, as the sand density is expected to lie between its maximum and minimum values, to assist in selecting a grayscale threshold. Using this approach Figure 5.42 has been produced showing the estimated porosity distribution through a region of the model test across a predetermined compaction band. The variation of porosity from the 3D X-ray microtomography is generally in agreement with the strain localization pattern indicated by the high speed photography, and a region in the vicinity of the shear band has porosity close to the minimum value as might be expected.

The encountered non-uniform porosity gradient across the examined shear band suggests non-homogeneous deformation may be occurring within the model tests. The variation in porosity within and around the shear band zone is possibly attributed to the fact that the orientation of the shear bands is not perpendicular to the orientation of the extracted resin/sand samples.

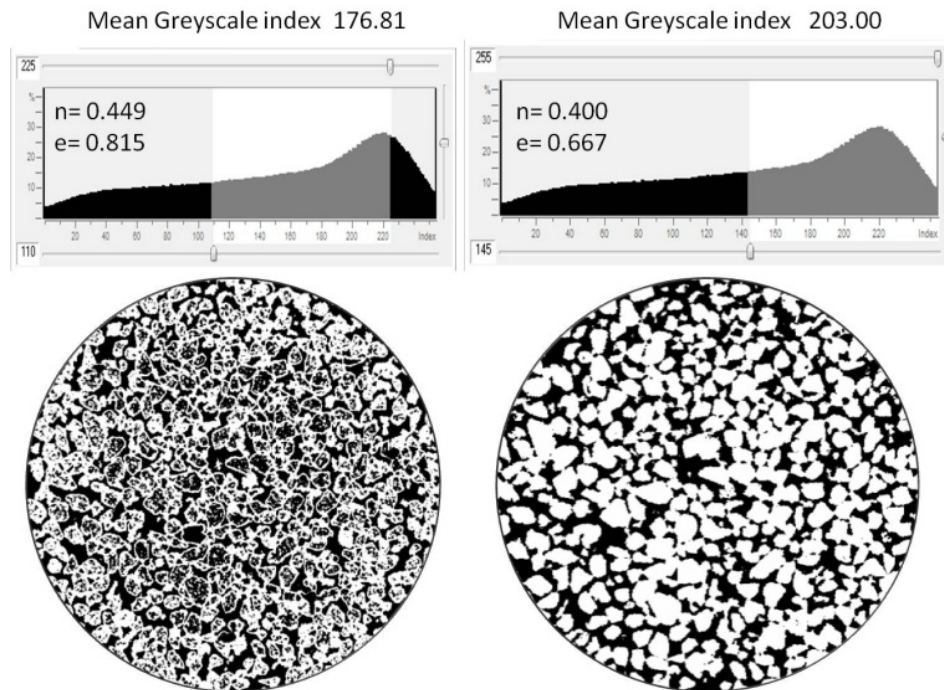


Figure 5.40. Sensitivity of greyscale thresholds and estimated sand porosity (Loose reference sample - void ratio, $e=0.668$ - porosity, $n= 0.40$)

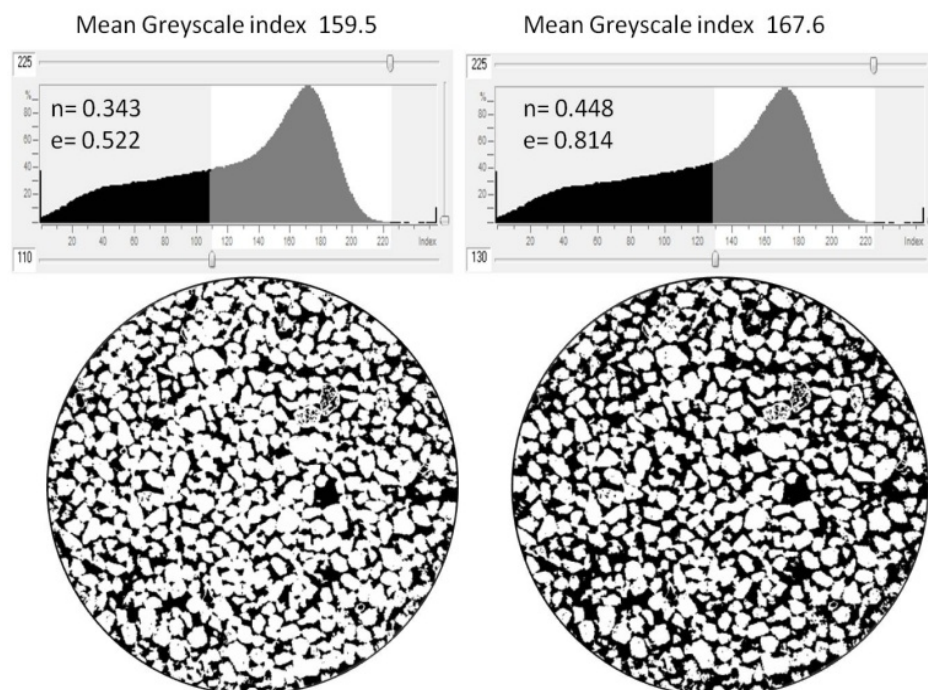


Figure 5.41. Sensitivity of greyscale thresholds and estimated sand porosity (Dense reference sample - void ratio, $e = 0.58$ - porosity, $n = 0.367$)

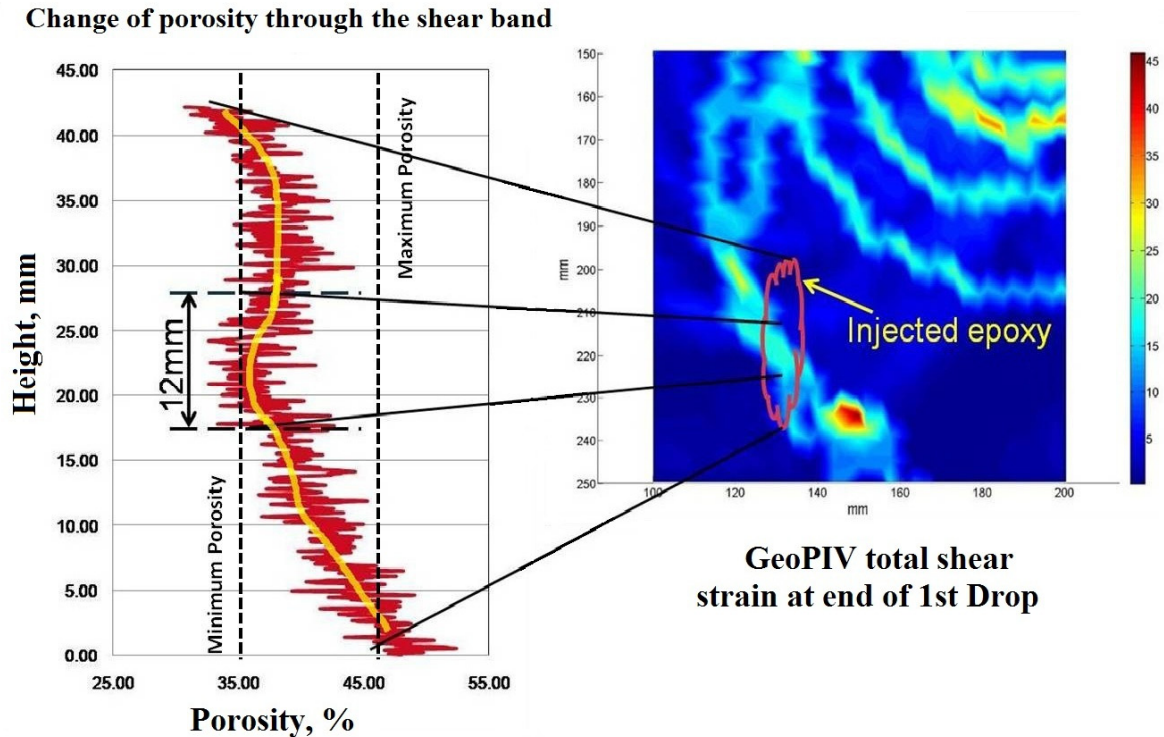


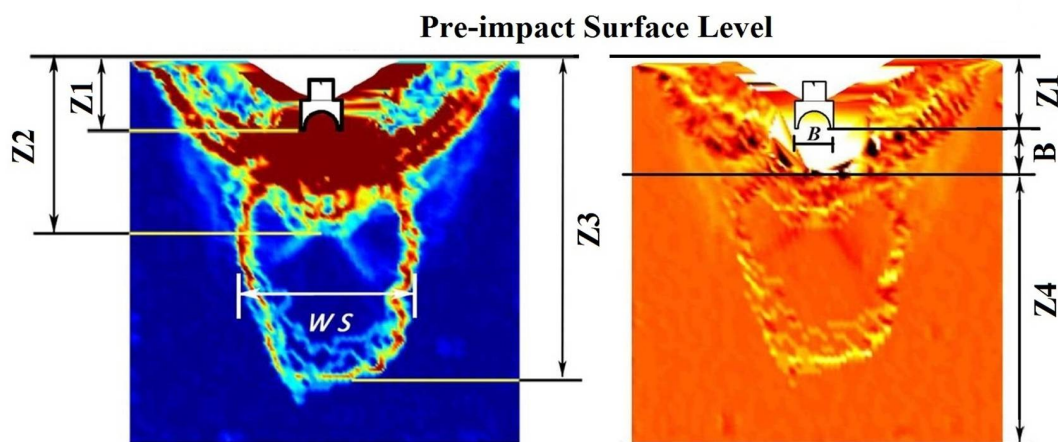
Figure 5.42. Change of sand porosity as estimated from the Micro-CTScan images at the location of a predetermined strain localisation at the end of Drop No. 1 during DC16

5.3.3 Image analysis

The high speed photography technique enables measurements of the depth of influence, the lateral extent of the impacted zone at depth, and the magnitude of the strains within the influence zone to be obtained and to enable a quantified assessment of the effect of different DC variables including different impact energies, tamper geometries and soil types on dynamic compaction. The following parameters have been chosen to assist in this process:

- I. Dimensions and characteristic features after number of impacts as illustrated in Figure 5.43 including:
 - i. Z1: Maximum depth of penetration (equivalent to tamper crater depth)
 - ii. Z2: Depth of highly sheared region below the tamper, measured from the original soil surface
 - iii. Z3: Maximum depth of localised strain bands (equivalent to DC influence depth, D_{\max})

- iv. Z4: Primary zone of interest for DC. Taken to start at a depth equal to the tamper width (B) below the tamper base's final position (approximately below the elevation of 400 pixels on the images).
 - v. WS: Maximum width of region within the outermost strain band
 - vi. Aspect ratio $Z3/Z1$ (influence depth/crater depth)
 - vii. Aspect ratio $Z3/Z2$
 - viii. Aspect ratio $Z3/WS$ (influence depth/influence lateral extent)
- II. Global volumetric strain (GVS, %) due to a number of impacts as defined in Figure 5.44.
 - III. The parameter “net contracted volume (NCV, %) as outlined in Section 5.2.2
 - IV. After a number of impacts, the difference between the percentages of the area experiencing contraction and dilation within the region of Z4 x the width of the model, referred to as the net contraction (NC, %) determined as shown in Figure 5.45.



B: Width of Tamper

Z1: Maximum Depth of Tamper Penetration

Z2: Depth of Major Shearing

Z3: Maximum Depth of Localised Strain Front

Z4 : Primary Zone of DC

WS: Maximum width of Strain Bulb

Figure 5.43. Characteristic features of DC selected measurements

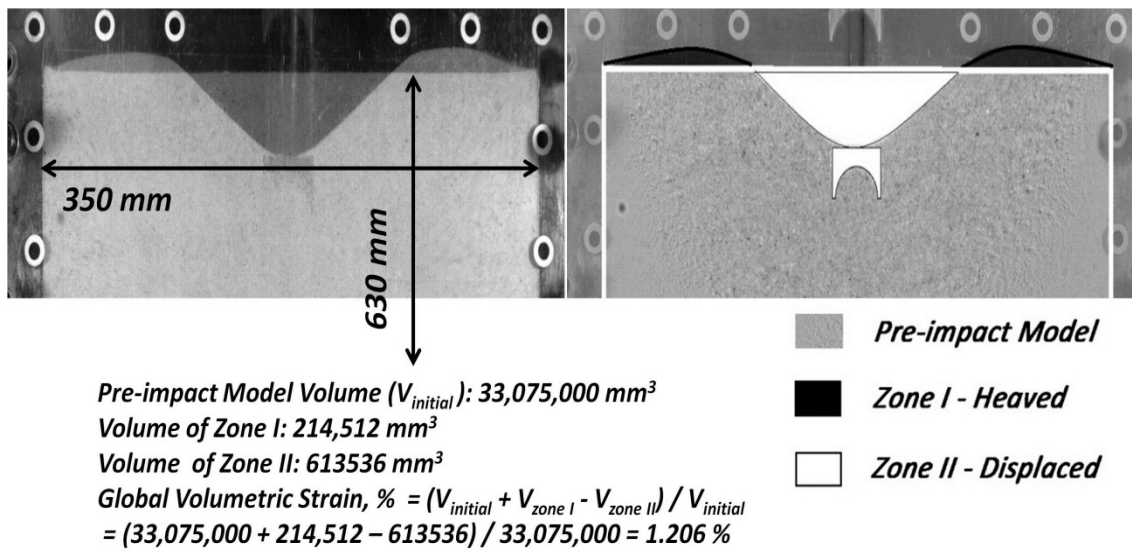


Figure 5.44. Calculation example of global volumetric strain

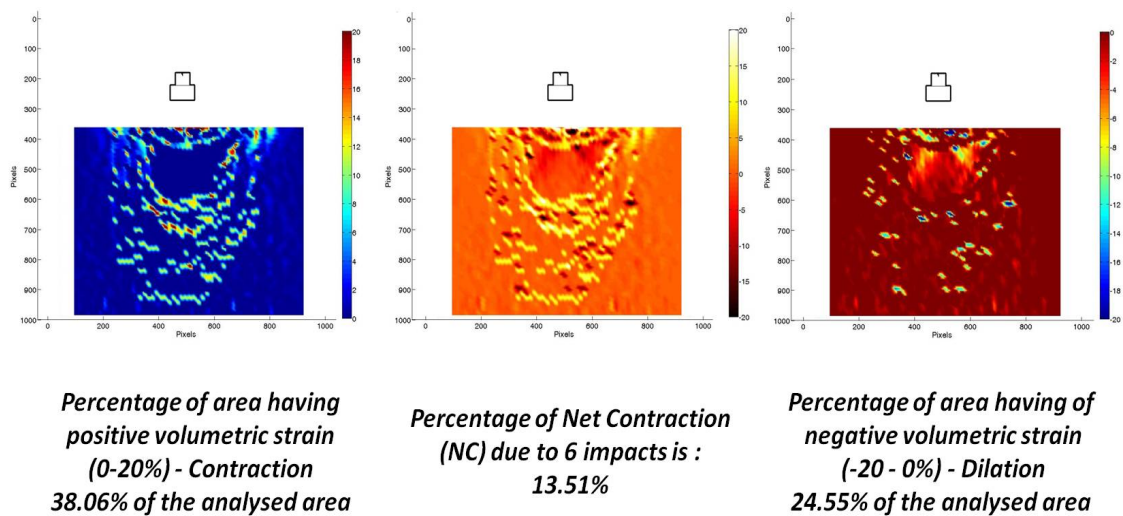


Figure 5.45. Calculation example of percentage of net contraction (NC) within the Z4 region.

5.3.3.1 Effect of Different Tamper Geometry on the Kinematics of Dynamic Compaction

Figures 5.46 and 5.47 show the cumulative displacements, captured by 1000 fps digital photographs, resulting from 6 impacts for each of the tamper shapes on sand and sand-silt mixture models, respectively. Figures 5.48 and 5.49 show the corresponding total shear strains and total volumetric strains for the sand and sand-silt mixtures, respectively. The results show distinct differences in the responses between the two different soils and between the different tamper shapes.

Irrespective of tamper geometry or type of soil, the features of the bearing capacity mechanism, such as the inclined shear planes and radial shear zones, are more evident in the case of sand models where the tampers generally penetrated less than for the sand-silt mixture models. For the sand-silt tests, the amount of soil heave around the tampers was significantly less and as the tampers penetrated deeper into the model this resulted in more of a local or punching shear failure mechanism. In these tests the inclined side shear planes only developed in later impacts with increasing impacting efforts. It is also evident from Figures 5.46 and 5.47 that the extent of the region beneath the tamper experiencing significant displacement varies with the tamper geometry.

Figure 5.46 shows that tamper shapes A and D affect the greatest amount of soil, and of these the curved tamper, which concentrates the deformation beneath the tamper, appears to be the most effective. For the sand-silt mixture Figure 5.47 shows that tamper shape B penetrates further, affects a much greater region and appears to be the most effective. The propagation of the compaction shock bands and the extent of the region affected by dynamic compaction differs between the two soil types and between the different tamper geometries. For the sand models the compaction bands reach their furthest extent in the first or second impact, and subsequent impacts create additional compaction bands that fill the region between the tamper and the outer band. This evolution of the compaction bands is shown in Figure 5.50 for the flat-bottomed tamper as it is dropped onto the sand.

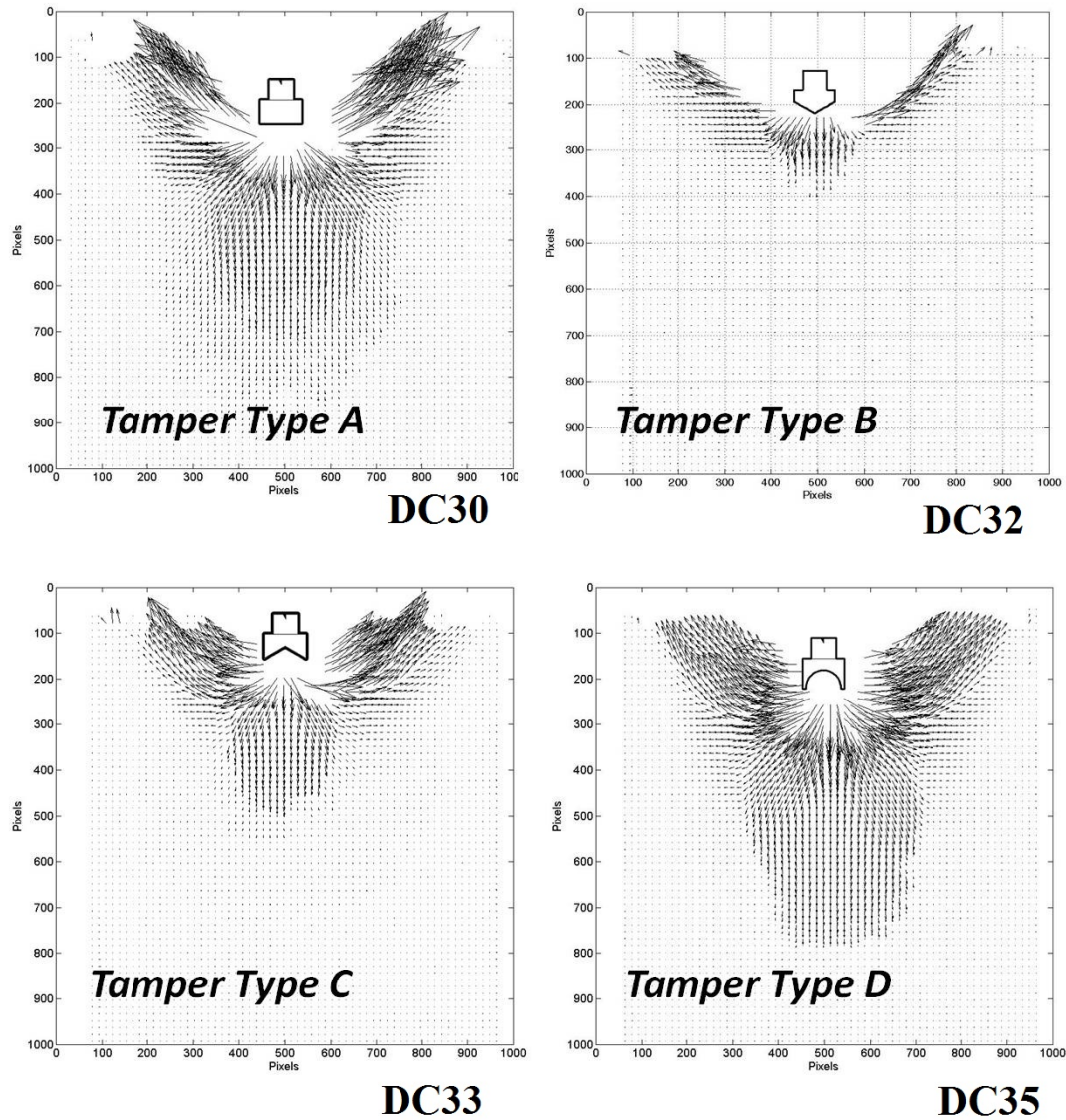


Figure 5.46. Cumulative displacement vectors (magnified x 2 for clarity) after 6 impacts – sand models (1000 pixels = 400mm).

Although only shear strains are shown in Figure 5.50, the areas of high shear strain are also areas of high volume strain. It may also be noted from Figure 5.50 that the small region of very high strains directly beneath the tamper also grows with successive impacts.

The compaction bands developed similarly in the other tests on sand using the different shaped tampers. In contrast, the evolution of the compaction bands for the sand-silt models occurs differently, with the distance travelled by the compaction bands increasing with number of blows as shown in Figure 5.51, at least for the six blows used here. The evolution of the compaction band patterns was similar in all the sand-silt mixture models for all four tamber shapes.

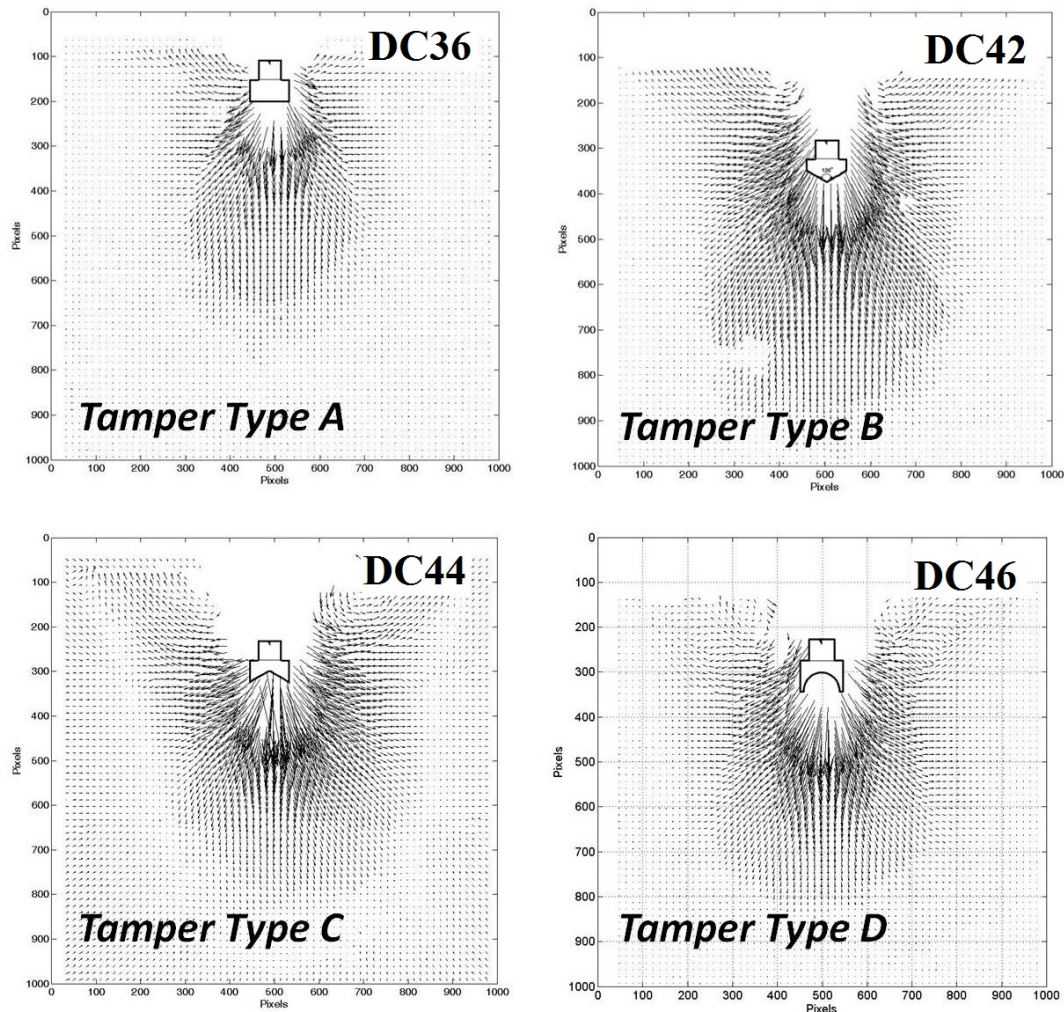


Figure 5.47. Cumulative displacement vectors (magnified $\times 2$ for clarity) after 6 impacts – Sand- Silt mixture models (1000 pixels = 400mm).

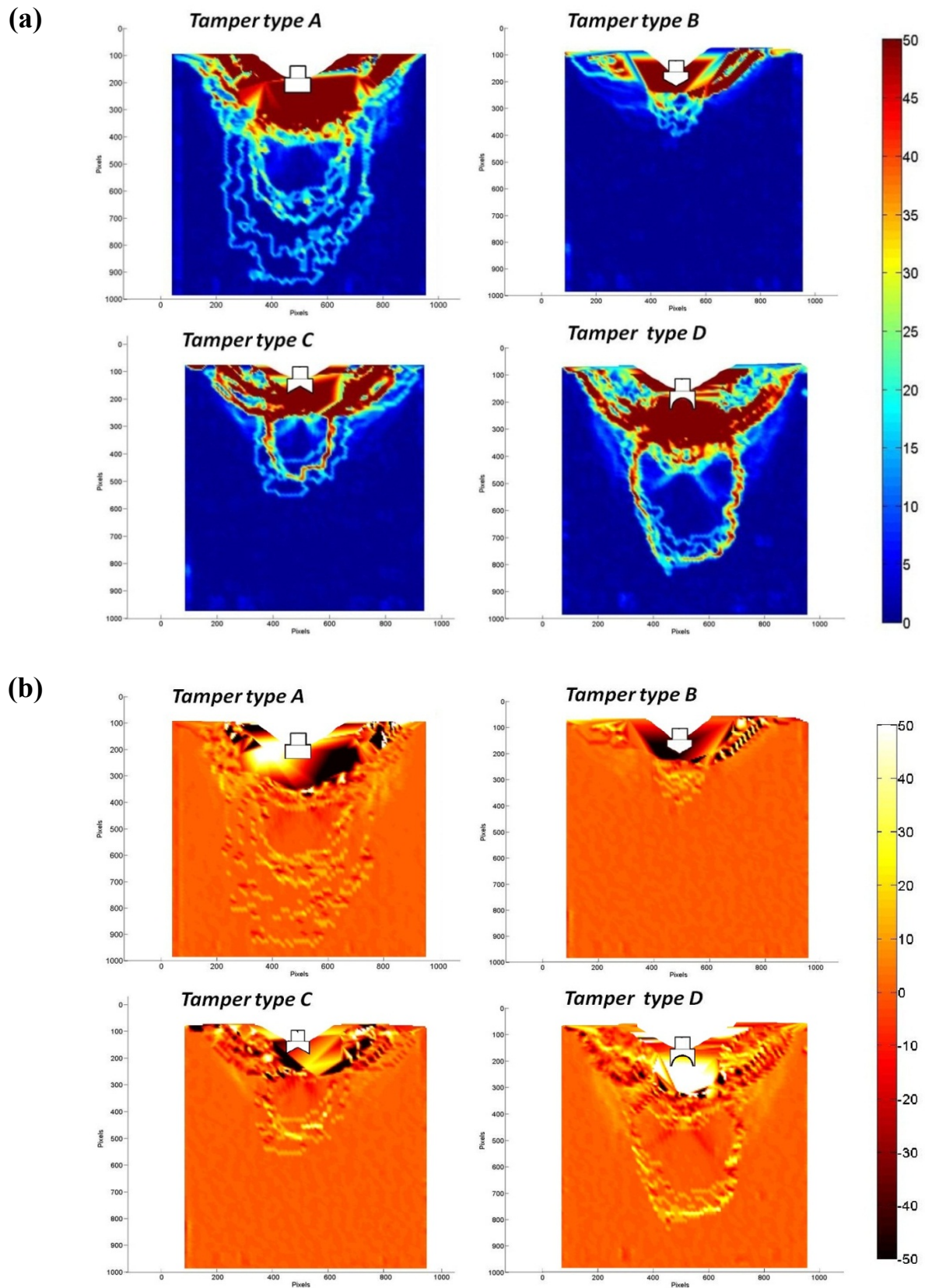
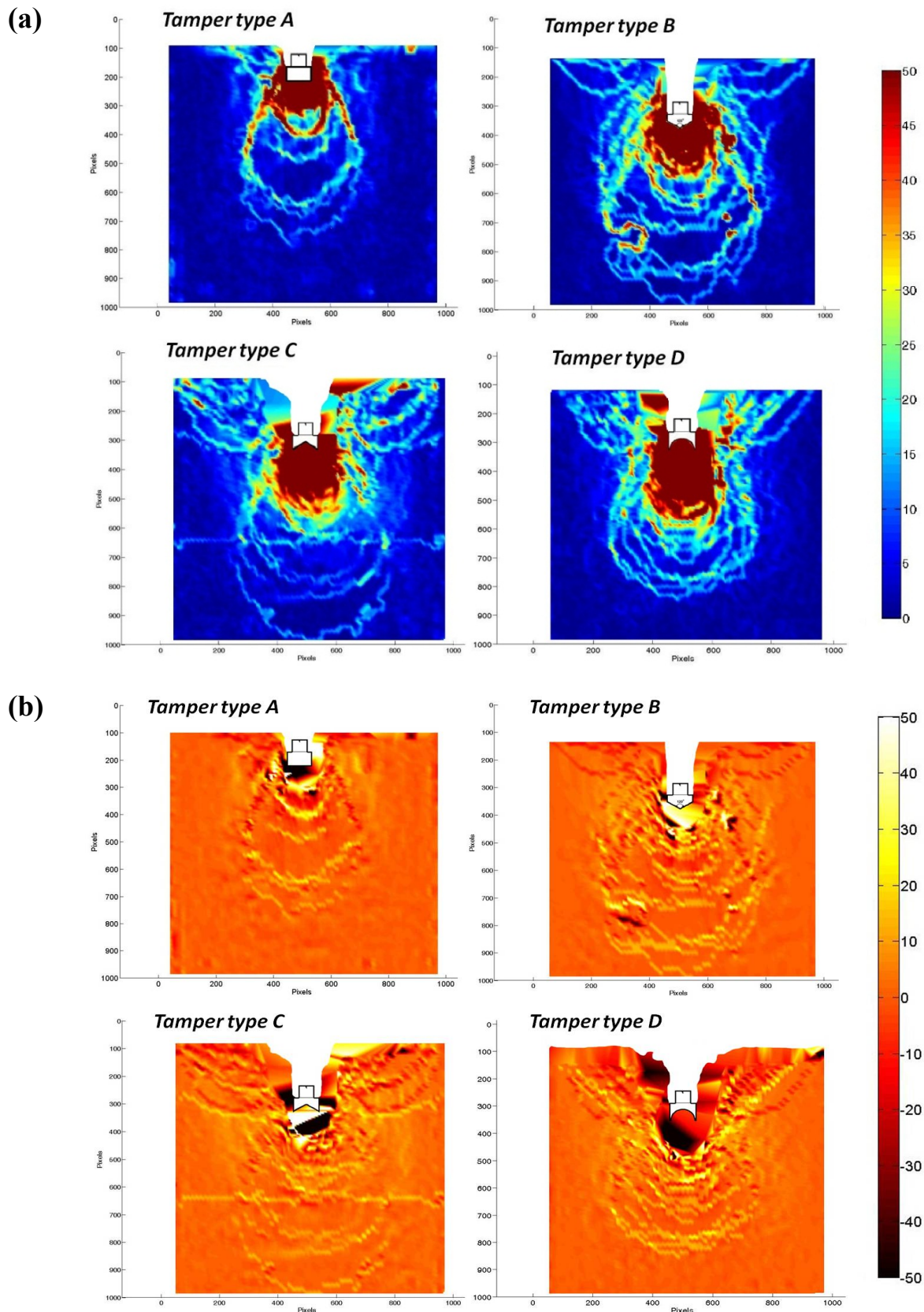


Figure 5.48. Total Shear Strain (a), and total volumetric strain (b) at end of 6 impacts on dry sand models using four types of tampers



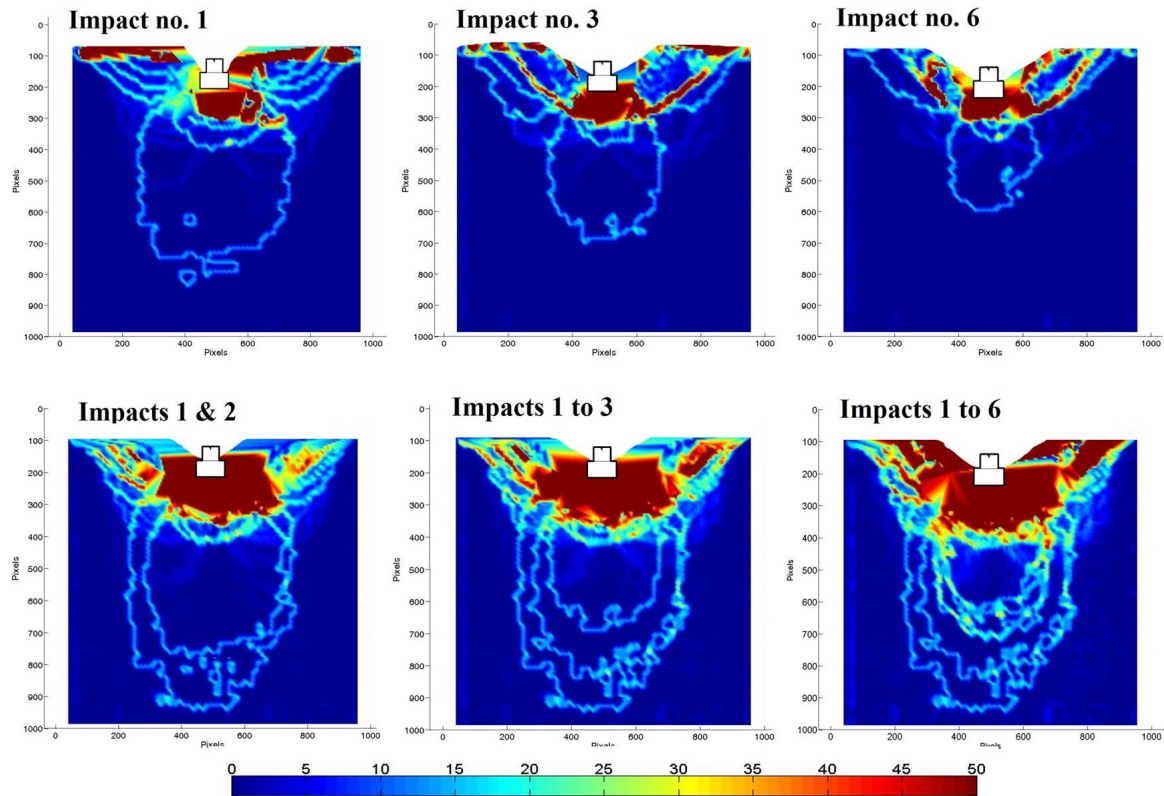


Figure 5.50. Incremental shear strains and history of total shear strain over the course of 6 impacts on a sand model using tamper type A (test DC30).

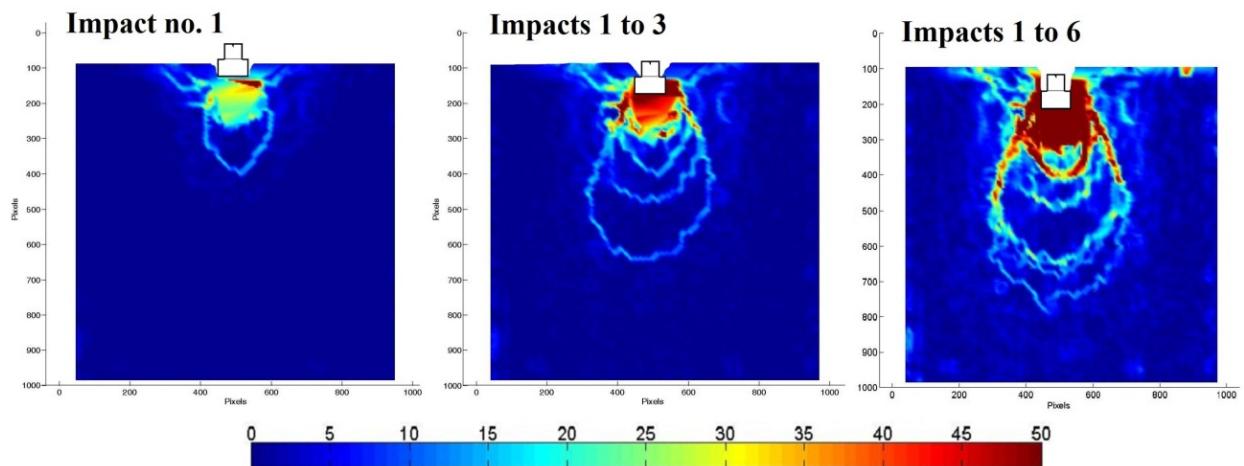


Figure 5.51. History of total shear strain over the course of six impacts on a sand-silt model using tamper type A (test DC36).

The detailed NCV analyses examining the effect of tamper geometry on the sand models are shown in Figures 5.52 and 5.53 respectively. In Figure 5.52, the magnitudes and variation of the NCV parameters confirm the visual reading from the fields of displacement (Figure 5.46) and strain plots (Figure 5.48). The declining trends and magnitudes of densification over the course of 6 impacts are similar among tampers types A and D. However, the variations of the NCV parameter over the course of the 6 impacts is more scattered in the case of the tamper type D.

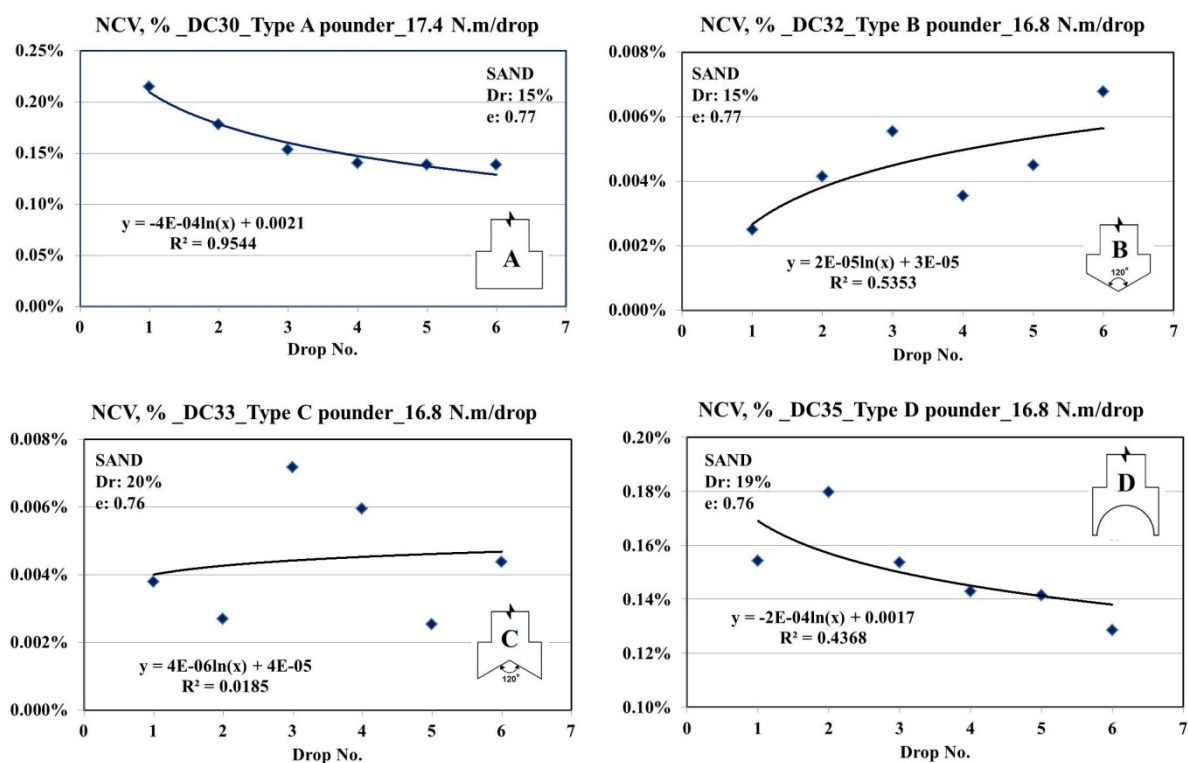


Figure 5.52. Variation of the NCV parameter over the course of 6 impacts on sand models using four types of tampers

On the other hand, the magnitudes of densification are very small in the case of tamper types B and C. However, the variation of the NCV parameter is of an improving trend with subsequent drops in the case of tamper type B but very scattered for tamper type C. The above relationships can be better illustrated by the normalised NCV ratios from different drops/tamper types in reference to the NCV value of the corresponding drops by tamper type A as shown in Figure 5.53. It is obvious from Figure 5.53 that the effectiveness of tamper types B or C is less than 10% of tamper type A in sand models. Tamper type D can be

considered of equivalent effectiveness to that of tamper type A in sand models. Despite the nearly equal NCV by pounders A and D, Figure 5.48b provides better understanding regarding the locations of volumetric strain bands buildup and depths the strain fronts have reached.

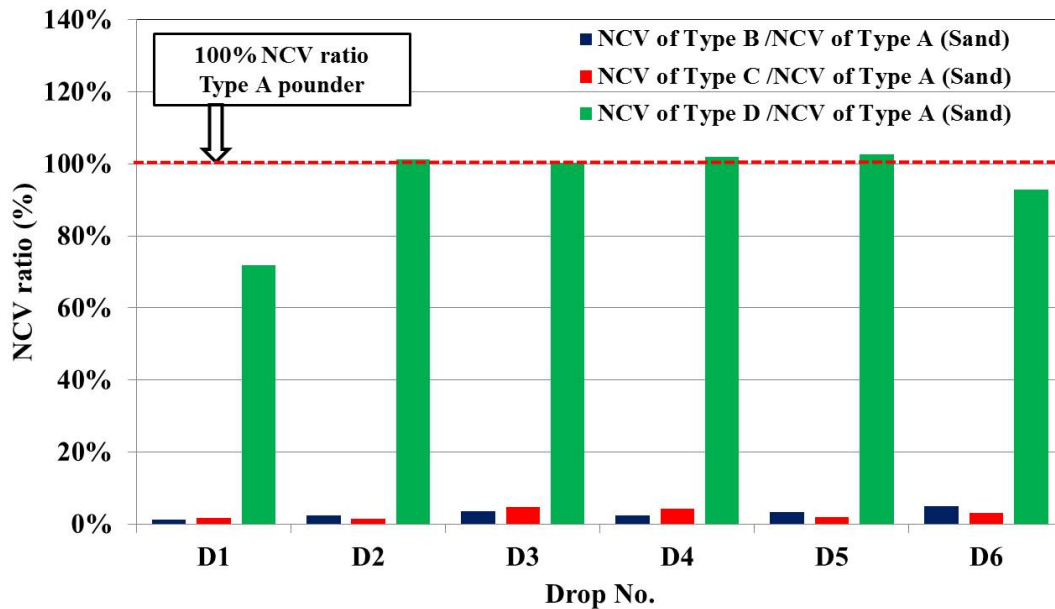


Figure 5.53. NCV ratios (NCV of drop “n” / NCV of drop “n” by tamper type A) from DC tests on sand models.

Similarly, the detailed NCV analyses examining the effect of tamper geometry on sand-silt models are shown in Figures 5.54 and 5.55 respectively. In the sand-silt models, all the non-flat based tampers showed declining trends of the amount of densification over the course of 6 impacts the opposite trend to that shown by the flat base tamper type A. However, the magnitudes of densification (NCVs) from the first impact by any of the non-flat based tampers were much higher than the corresponding densification (NCVs) by the first impact of tamper type A. The above relationships are illustrated by the normalised NCV ratios from different drops/tamper types in reference to the NCV value of the corresponding drops by tamper type A as shown in Figure 5.55. The first impacts by tamper types B, C and D have caused NCV ratios of 357%, 261% and 413% taking tamper type A as of 100% NCV ratio. Despite the declining trends of the NCV parameters for tamper types B, C and D, their better performance over tamper type A continued over the course of the first 5 impacts and even continued to the sixth impact for tamper type B.

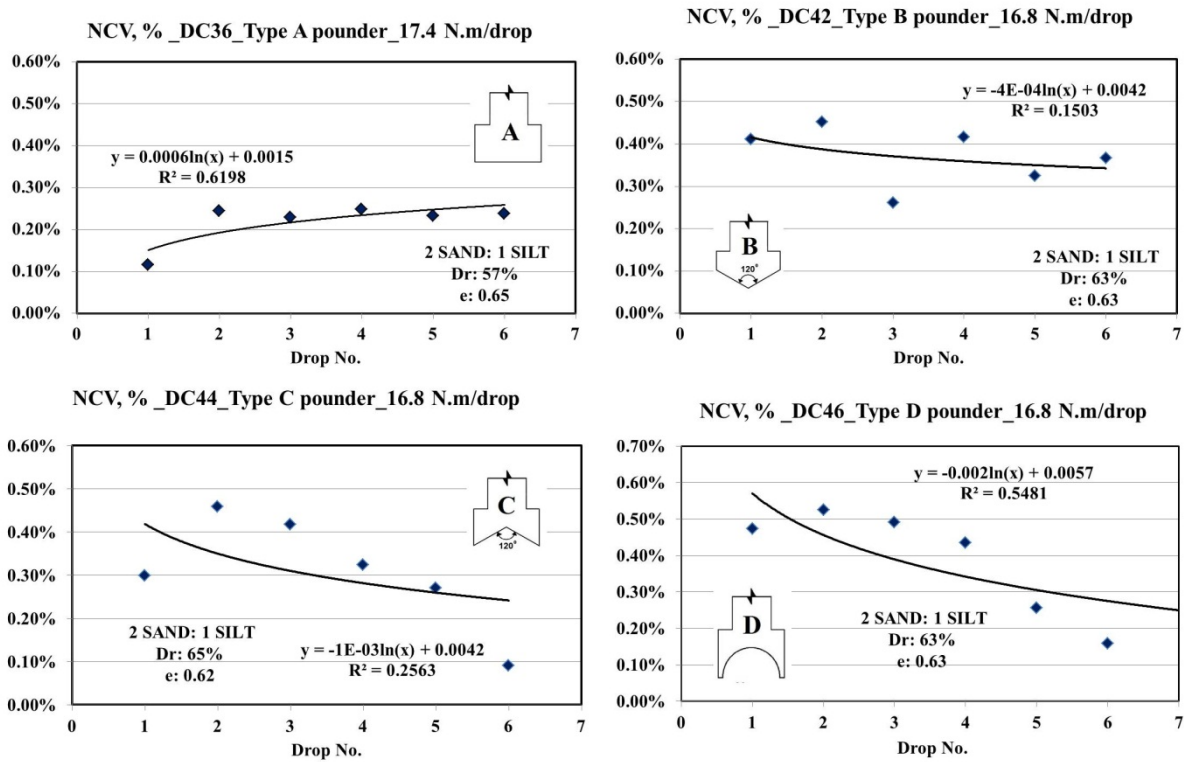


Figure 5.54. Variation of the NCV parameter over the course of 6 impacts on sand-silt models using four types of tampers

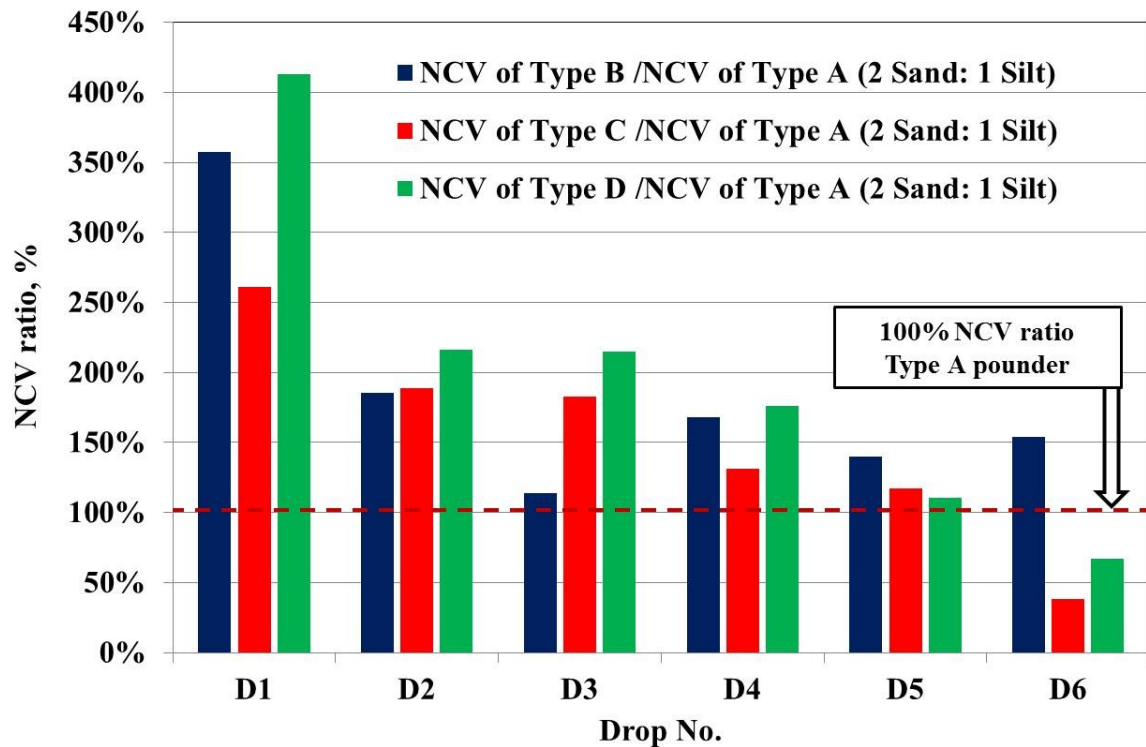


Figure 5.55. NCV ratios (NCV of drop “n” / NCV of drop “n” by tamper type A) from DC tests on sand-silt models.

As discussed previously there are significant differences in the amount and extent of densification produced by the different tamper geometries and between the responses of the two investigated target materials. Despite the essentially identical pre-impact relative densities of the models of either material, there were noticeable differences in all characteristic feature measurements as well as the estimated global volume strain (GVS), percentage of net contraction (NC) and (NCV) parameters. In the sand models, there was 26% difference between the smallest and largest depths of penetration (Z1) and these were associated with variations of 150% in Z3 and 180% WS. The greatest and smallest Z3 were produced by tamper types A and B, while the widest WS was achieved by tamper type A. For the sand-silt mixtures there was a greater difference of 54% difference between smallest and largest depths of penetration (Z1) but these were associated with smaller variations in Z3, 26% and WS, 24% . In the sand-silt mixtures the greatest and smallest (Z3) were produced by tamper types C and A, and the widest (WS) was achieved by tamper type B. The effects of different tamper base profiles on the studied characteristic features as well as on the GVS, NC and NCV adjudicator parameters are summarised in Figures 5.56 and 5.57.

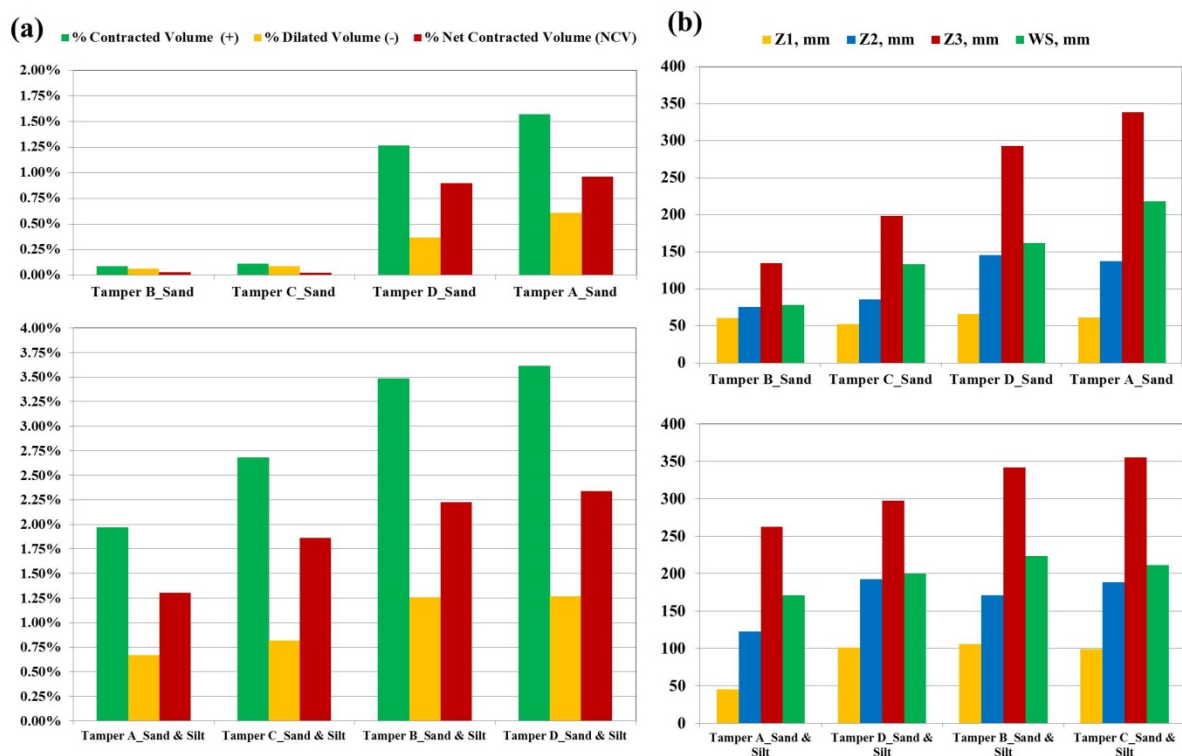


Figure 5.56. Variation in volumetric strain intensities - arranged from smallest to largest NCV (a) and DC measured characteristic features - arranged from smallest to largest Z3 (b).

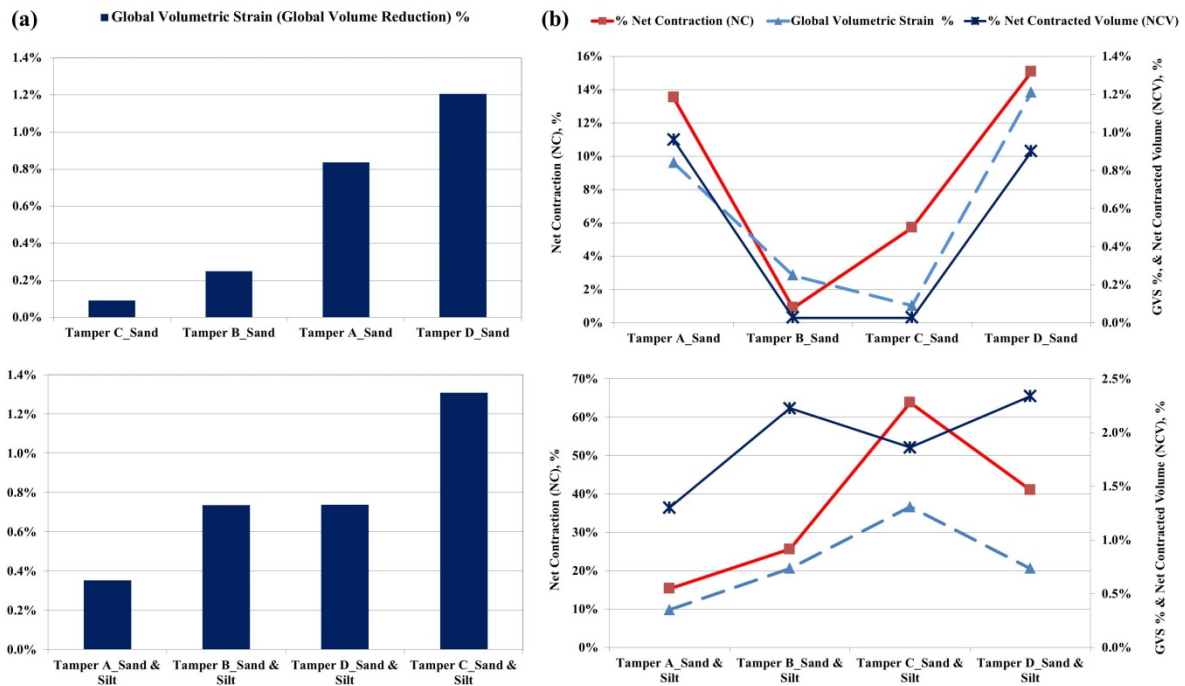


Figure 5.57. Variation in global volumetric strain with respect to tamper geometries (a) and correlation between the global volumetric strains (GVS) and adjudicator net contraction (NC) and (NCV) parameters within the region of Z4 (b.)

These figures show that all the selected quantities vary significantly with tamper geometry and soil type, despite the similar impact energies and similar relative densities of tests for each soil type. The results show that the use of crater dimension measures such as the displaced volume and crater depth (expressed here by the global volumetric strain GVS, and tamper penetration depth, Z1) to estimate the tamper efficiency and DC degree of improvement may provide misleading results particularly in the case of loose sand. For example, the results show a difference of less than 1% in the penetrations (crater depths) of tamper types A and B in near identical sand models, however the GVS from tamper type A is 3.4 times greater than the GVS of tamper type B. On the other hand, the GVS due to tamper type B is about three times the GVS of tamper type C while the difference between their depths of penetration (Z1) is around 15%. The precise values are not important as there are important differences between these small scale laboratory tests and field tests, but they indicate the limitations of surface measurements for predicting compaction at depth. Apart from the different scales between the laboratory and the field, the use of loose, dry materials has affected the estimates of the depth of penetration (Z1), the shape of the deformed surface

and the subsequent calculation of GVS. This is because the dry sand is able to flow freely into the crater, and to partially fill in the crater between impacts, in contrast to typical field behaviour where suctions in moist natural soil often prevent collapse of the soil into the formed crater.

The percentage of area experiencing compression (NC) and the magnitude of densification (NCV) in the primary zone of interest, over depth Z4, provide a more meaningful and accurate measure for quantifying soil mass displacement and densification in the studied models. The magnitude of the NCV parameter is preferred to a sum of the volume strains at each point from pixel-by-pixel data. In all the tests significant areas in the zone of interest are indicated to experience both compression and dilation, and there is generally more compression than dilation as would be expected. It is interesting to observe from Figure 5.61a that a much greater area experiences compression with the silty sand mixture when compared to the loose sand, and tampers B and C in the loose sand produce almost no net compaction at depth. Although this trend is reflected in the global volume strains, GVS, measured from the surface measurements shown in Figure 5.57, the GVS provides a poor indication of the response at depth. Figure 5.57b shows a reasonable correlation between GVS and the values of NC and NCV parameters for tamper types A, B and D with the sand-silt models and tamper types A and D with the sand, which suggests that the surface heave in sand is an important factor limiting the usefulness of the surface measures in estimating DC effectiveness.

For tampers B and C in the loose sand, the poor densification at depth was reflected in all the measured parameters like Z3, WS, NC and NCV, and the majority of the GVS was a result of the larger sideways and upward (heaving) displacements of its dart front rather than any significant compaction at depth as also illustrated by the GeoPIV displacement vectors and strain map shown in Figures 5.46 and 5.48 respectively.

Figure 5.56 shows the penetration depths, Z1, in the sand-silt models were almost double the corresponding depths in the sand models for all tampers except the flat base tamper type A, and from Figure 5.57 it is clear that there is no correlation between Z1 and GVS. Relationships between various aspect ratios and NCV are presented in Figure 5.58. These relationships address the diverse responses of the two target materials to the different tamper

geometries during DC model tests. The aspect ratio $Z3/Z1$, the ratio of depth of soil improvement to penetration depth was found to be more affected by the type of the target material in the cases of tamper types B and D while it was less affected in the cases of tamper types A and C. Nevertheless, the higher $Z3/Z1$ ratio did not necessarily imply that greater densification has taken place as can be seen from the trend relationships between $Z3/Z1$ and NCV in the cases of tamper types C and D. The aspect ratios $Z3/Z2$ and $Z3/WS$ were found to be less sensitive to the soil type or the tampers geometry.

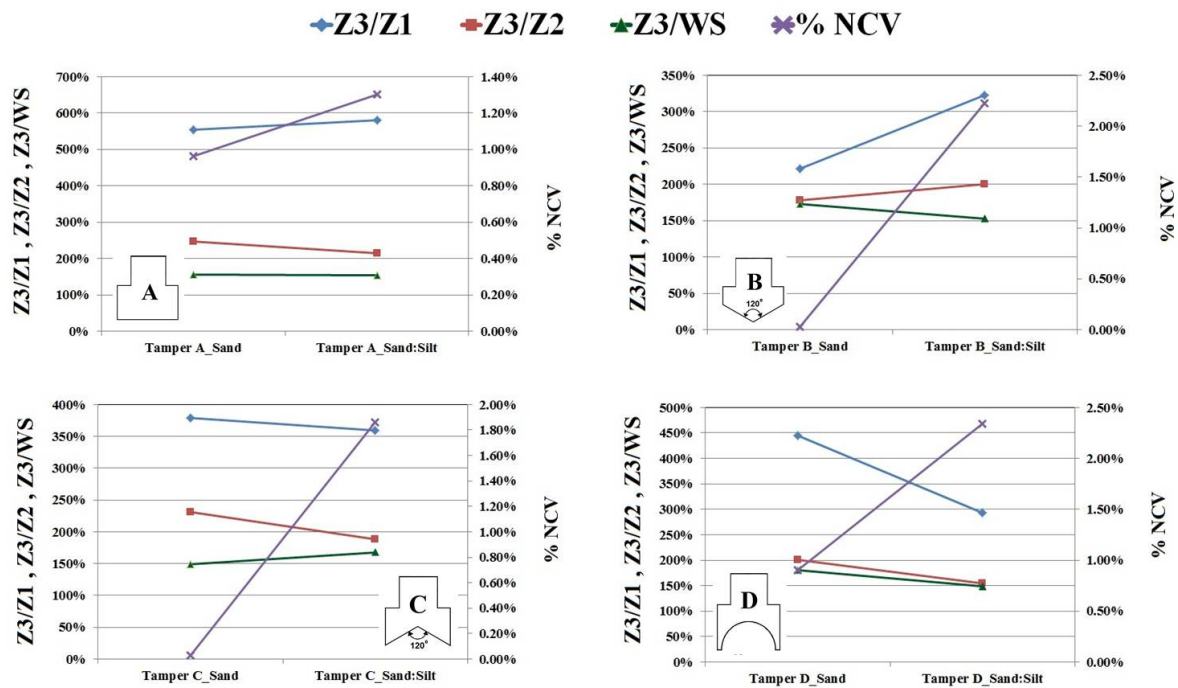


Figure 5.58. Correlations between tamper geometries, key DC aspect ratios and intensities of net contracted volume (NCV) in sand and sand-silt models.

5.3.3.2 Effect of Imparting Energy

The experimental results indicate that soil response to imparting energy can be characterised based on three distinctive features: first is the amount of soil disturbance directly beneath and around the impact footprint, second is the depth for which significant shearing/compaction is taking place and third is the magnitude of densification within the zone identified by the two previous features.

5.3.3.2.1 Effect of Imparting Energy on Sand Models

The strain distribution and variation of strain levels with depth in the sand models due to different imparting energies have been captured by the GeoPIV strain plots. Figure 5.59 shows the total shear strains after 12 drops from tests DC24, DC27 and DC30 which were performed using sand having essentially the same pre-impact void ratio, but different energies of 5.8, 11.6 and 17.4N.m/drop respectively. The accumulated total shear strains after 1, 6 and 12 impacts, shown in Figure 5.59 provide a visual assessment of the effect of impact energy on the dynamic compaction of these three sand models.

The detailed NCV analyses of these tests are shown in Figures 5.60 and 5.61. The analyses show strong regression coefficient (R^2) for both linear and logarithmic trend correlations between the accumulated energy input and the NCV parameters. This suggests the presence of a threshold energy after which the bulk of the input energy is wasted (dissipated) within the upper region of the models, causing further soil heaving at the surface, but with less densification at depth. NCV results from tests DC11 and D12, which employed an elevated energy level of 48N.m/drop over the course of 5 impacts, show the same trend of threshold energy shown by tests DC24, DC27 and DC30. Figure 5.62 shows NCV parameters from tests DC11 and DC12 together with the NCV parameters from the first 5 impacts of test DC30 which used 17.4N.m/drop. The results indicates insignificant difference in the magnitude of soil densification at depth after 5 drops even with the nearly 3 fold difference of energy input being used in tests DC11 and DC12.

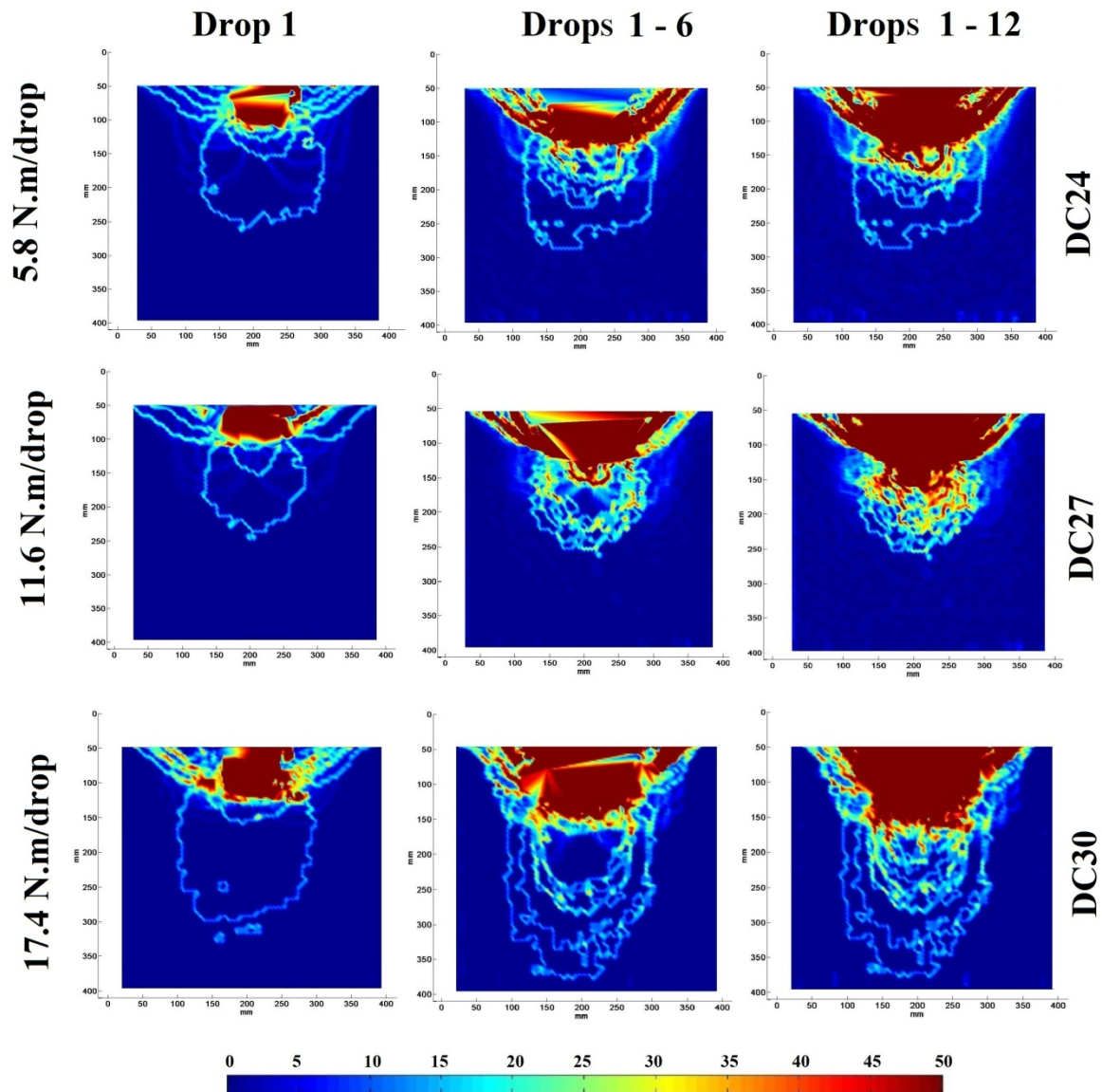


Figure 5.59. History of accumulated total shear strain over the course of 12 drops due to three levels of imparting energy on three loose sand models (Dr: 13-17%)

Combining the propagation patterns of strain and compaction bands with the magnitudes of the net contracted volume parameter (NCV) provides an explanation for the observation of a threshold energy. In DC tests on sand, the first drop causes compaction bands that reach deeper into the soil body causing some compaction at depth, which is registered in the initially higher magnitudes of the NCV parameters. Compaction bands from subsequent impacts do not penetrate as far, and this leads to lower NCV values.

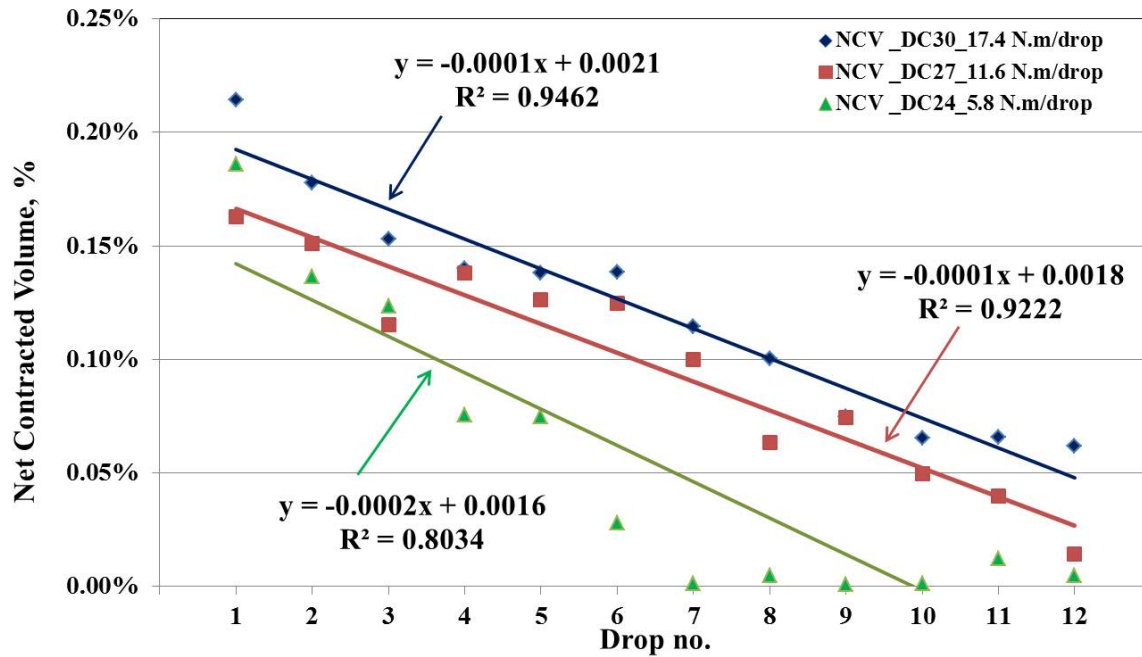


Figure 5.60. Variation in the NCV parameter by three energy levels over the course of 12 drops (sand models of void ratio 0.76-0.77) with their linear correlations.

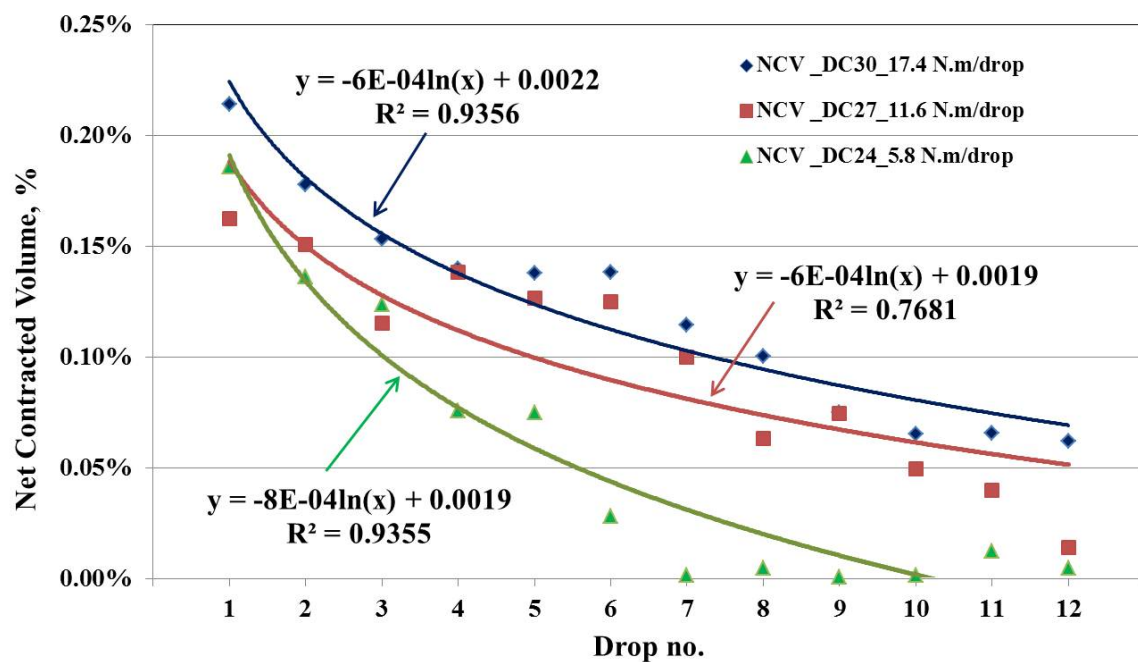


Figure 5.61. Variation in the NCV parameter by three energy levels over the course of 12 drops (sand models of void ratio 0.76-0.77) with their logarithmic correlations.

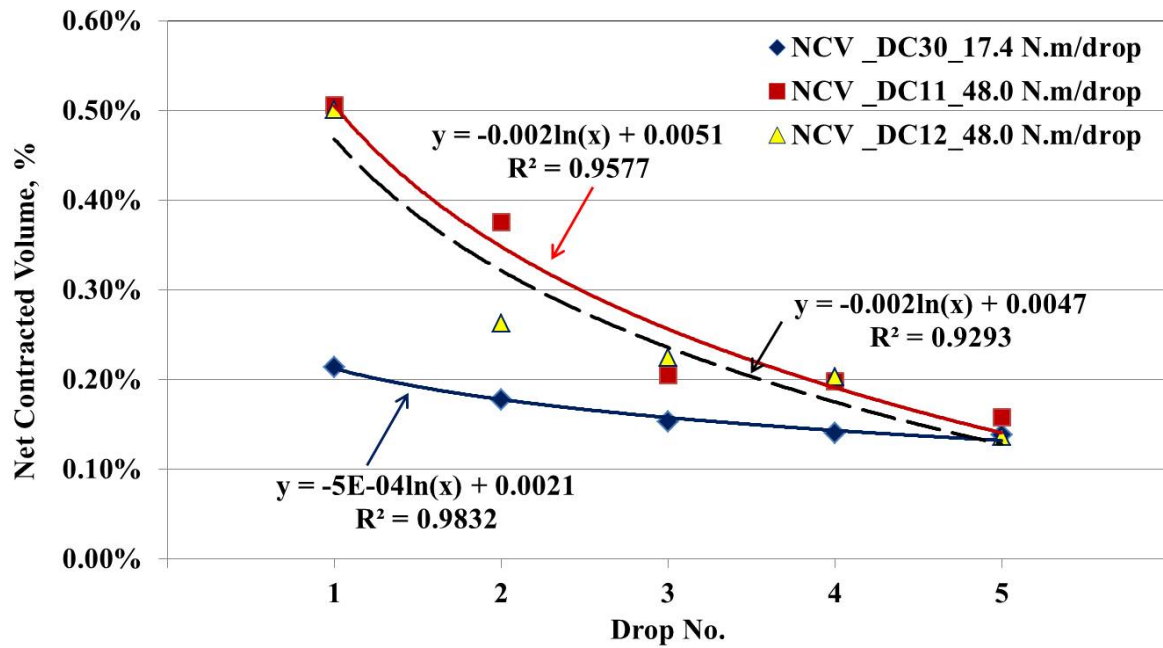


Figure 5.62. Effect of the imparting energy on the NCV parameter over the course of 5 drops (sand models of void ratio 0.71-0.77) with their logarithmic correlations.

This can be seen from the shear strain plots shown in Figure 5.59. This figure shows that the compaction band that moves furthest in the first drop is close to the limit of the compacted zone even after 12 drops. In between drops 1 and 6 some compaction bands can travel slightly further than the first blow, but the majority fill in the region defined by the furthest compaction band from the first blow. Beyond 7 drops no further expansion of the compacted zone occurs.

The result of the above behaviour is why the amount of densification (NCV) caused by the first impact was the highest in all sand models tests despite the accumulated energy from subsequent drops. This trend can be perceived from Figures 5.60 to 5.62 and better illustrated by the normalised NCV percentage ratios (NCV of any drop as a percentage of the NCV of drop 1) shown in Figure 5.63.

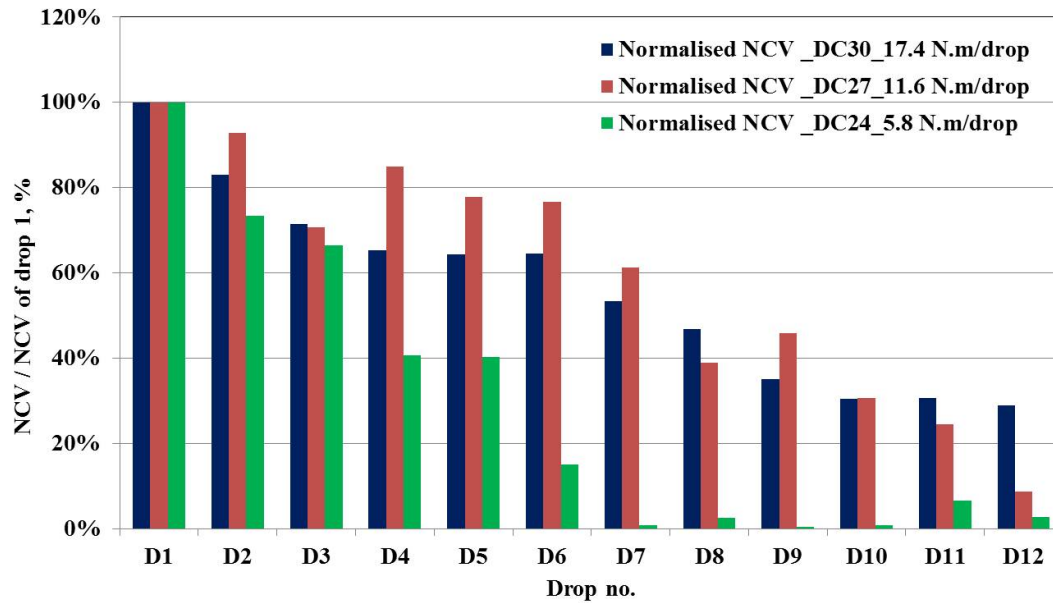


Figure 5.63. Normalised NCV (NCV of drop “n” / NCV of drop 1) from three DC tests in sand models employing three energy levels.

5.3.3.2.2 Effect of Imparting Energy on Sand:Silt Models

For the sand-silt mixture a bigger portion of the imparted energy is utilised by the compaction mechanism beneath the tamper rather than being wasted in pushing the soil aside and upwards, suggesting that DC will be more effective in compressible soils. Strain distribution and variation of strain levels with depth in sand-silt models due to different imparting energies are illustrated by the volumetric strain plots, shown in Figure 5.64, from tests DC36 and DC37 which were made of sand-silt mixtures that had essentially the same pre-impact void ratio. The tests were performed by imparting the sand-silt soils 6 times with energy levels of 17.4N.m/drop and 5.8N.m/drop respectively. The accumulated volumetric strains after 1, 3 and 6 impacts shown in Figure 5.64 provide visual assessment of the energy effect on the dynamic compaction of the two sand-silt models.

Unlike the sand response, the correlations between accumulated energy inputs and NCV parameters from the sand-silt models are less well correlated. However, the trends show greater densifications at depth than the first impact have occurred in the second and subsequent tamper drops. This trend can be perceived from Figures 5.65 and better illustrated by the normalised NCV percentage ratios shown in Figure 5.66. Despite the limited numbers

of data available for this analysis, the presence of a threshold energy level can still be detected from the plateau NCV correlation with number of drops after the third drop.

The better response from the sand-silt models which has resulted in increased compaction efficiency is due to two reasons: (1) the better packing achieved when the smaller particles of the silt lodge themselves in the voids between the larger particles of the sand; and (2) the presence of fines which makes it easier for rearrangement of the soil particles. This response from the sand-silt soil was prevailed even when the sand-silt mixture was overlaid by different thicknesses of sand above it. In model tests DC38 and DC39, the surface of the sand silt mixture was placed 180mm and 85mm from the impact surface elevation respectively and the models were topped up by sand to the target level as shown in Figure 5.67.

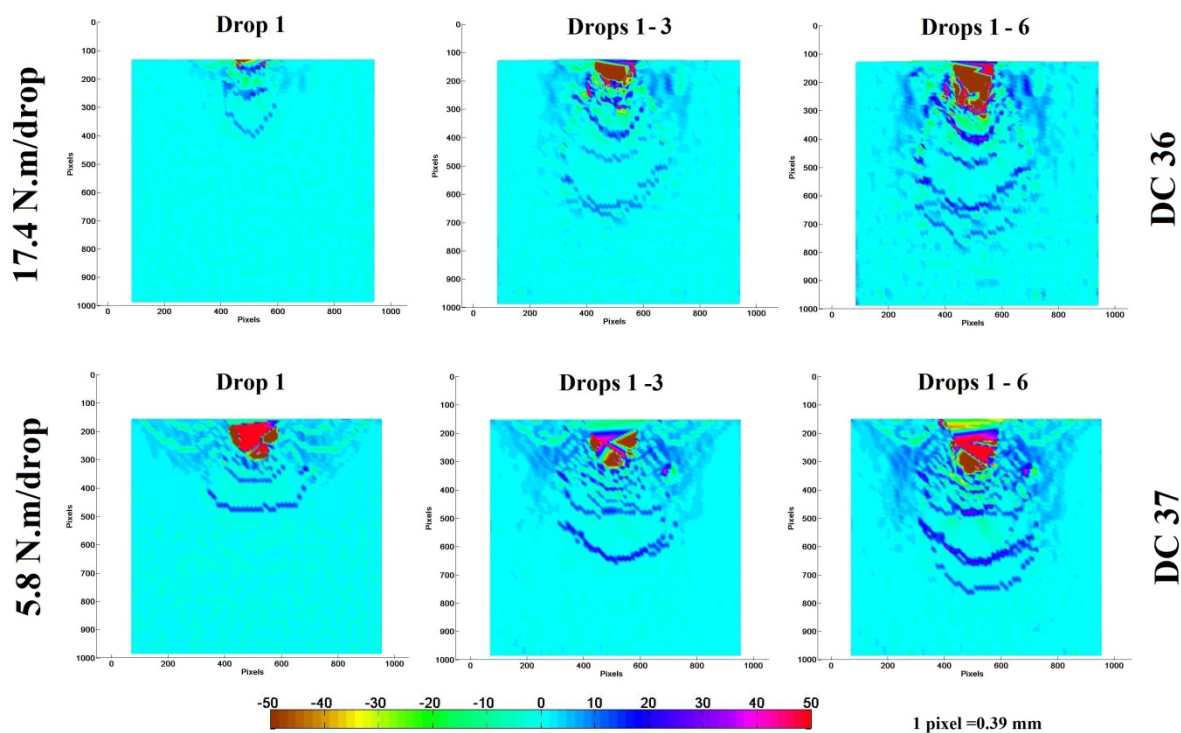


Figure 5.64. History of accumulated volumetric strain over the course of 6 drops due to two levels of imparting energy on sand-silt models (Dr: 55-57%)

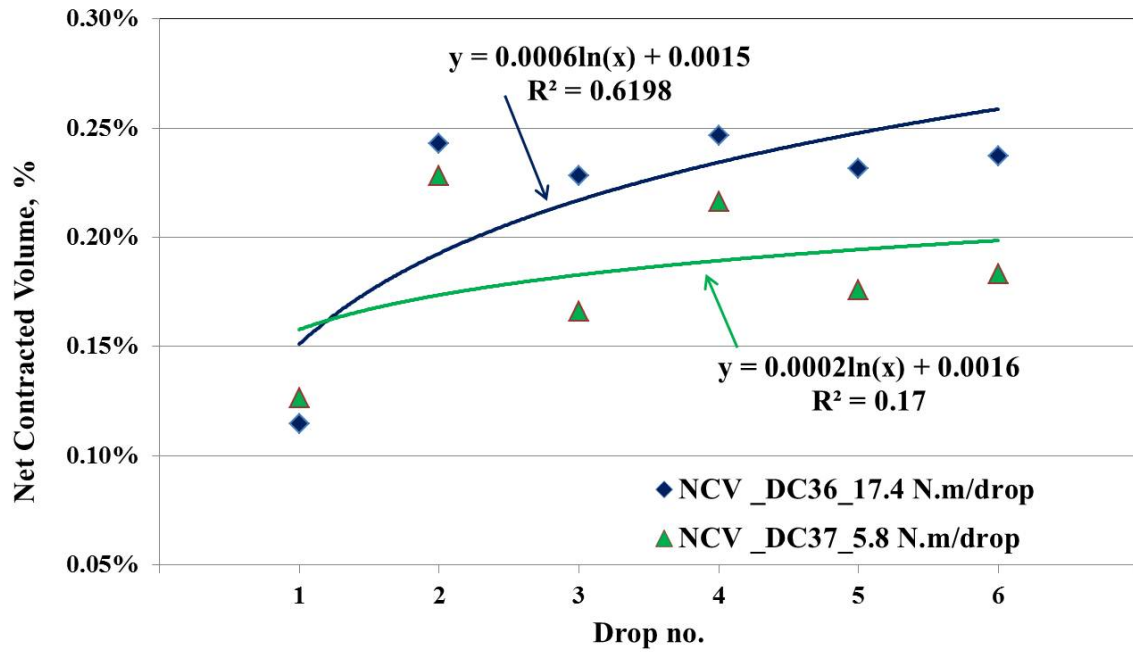


Figure 5.65. Variation in the NCV parameter by two energy levels over the course of 6 drops (sand-silt models of void ratio 0.65-0.66) with their logarithmic correlations.

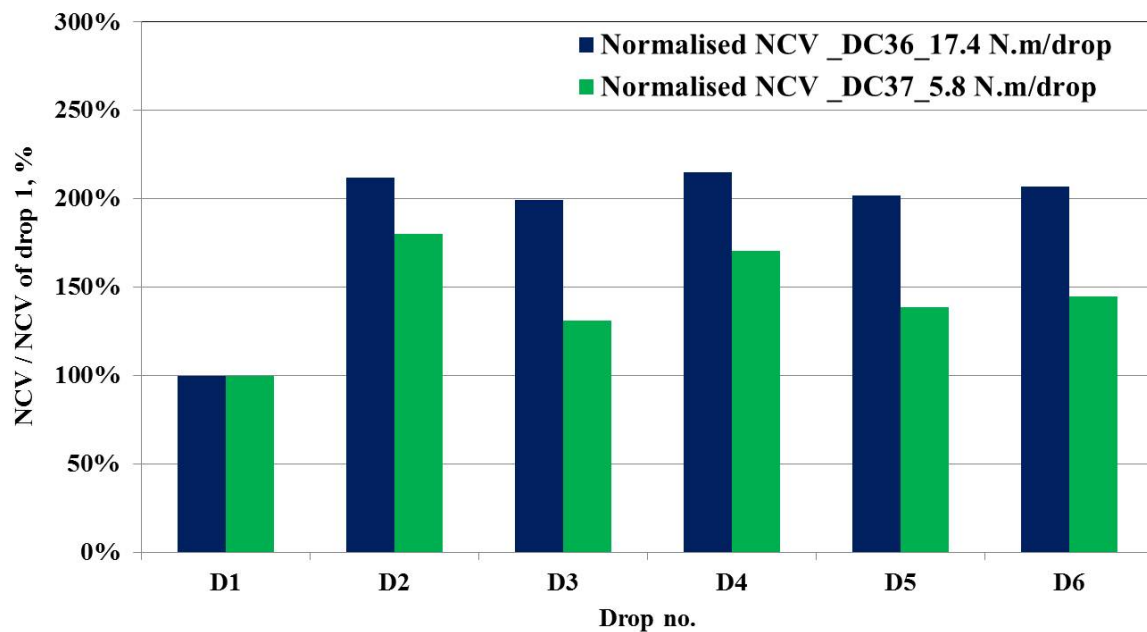


Figure 5.66. Normalised NCV (NCV of drop “n” / NCV of drop 1) from two DC tests in sand-silt models employing two energy levels

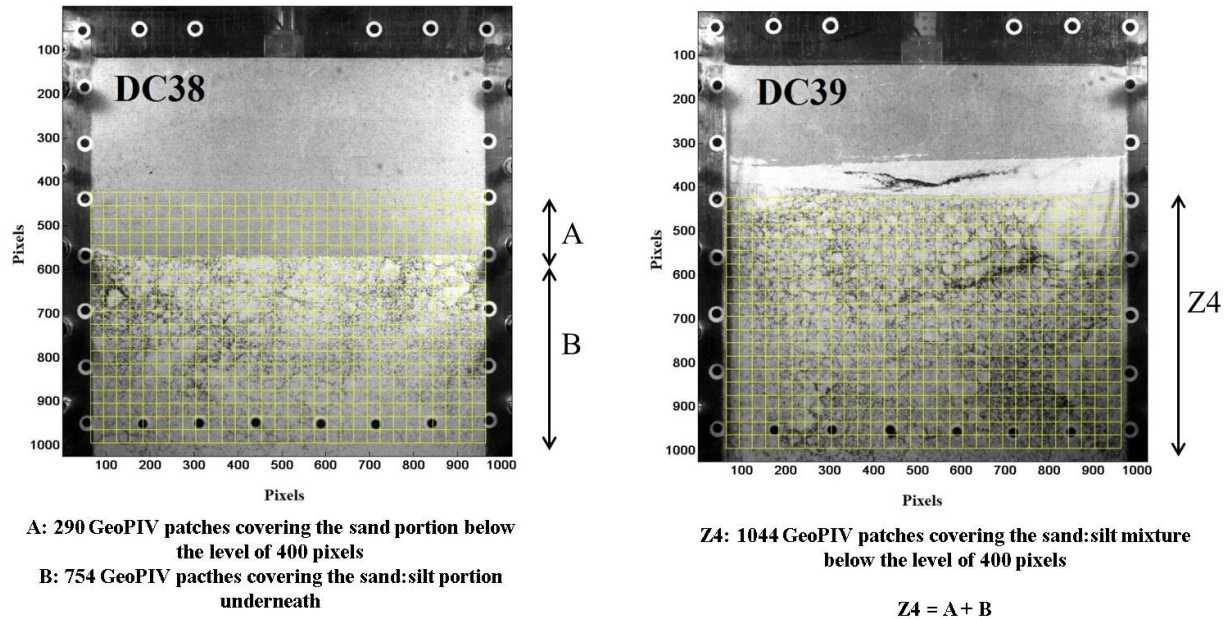


Figure 5.67. DC tests with 180mm (DC38) and 85mm (DC39) of sand overlaid sand-silt soil.

These heights were chosen so the sand layer extended into the region below the elevation 400 pixels ($Z4$) in test DC 38, and ended just above the 400 pixels elevation in tests DC39. Results from these special tests confirmed the better response of the sand-silt soils to dynamic compaction over the sand. Correlations between accumulated energy inputs and NCV parameters from these special tests are shown in Figure 5.68. Both tests showed similar correlation trends between accumulated energy and NCV parameters. The amount of net volume contraction (NCV parameter) in test DC39, where the sand-silt extends over the entire $Z4$ region, was higher than DC38. Separation of the NCV values between the sand and the sand-silt portions extending over the $Z4$ region in test DC38 is shown in Figures 5.69 and 5.70.

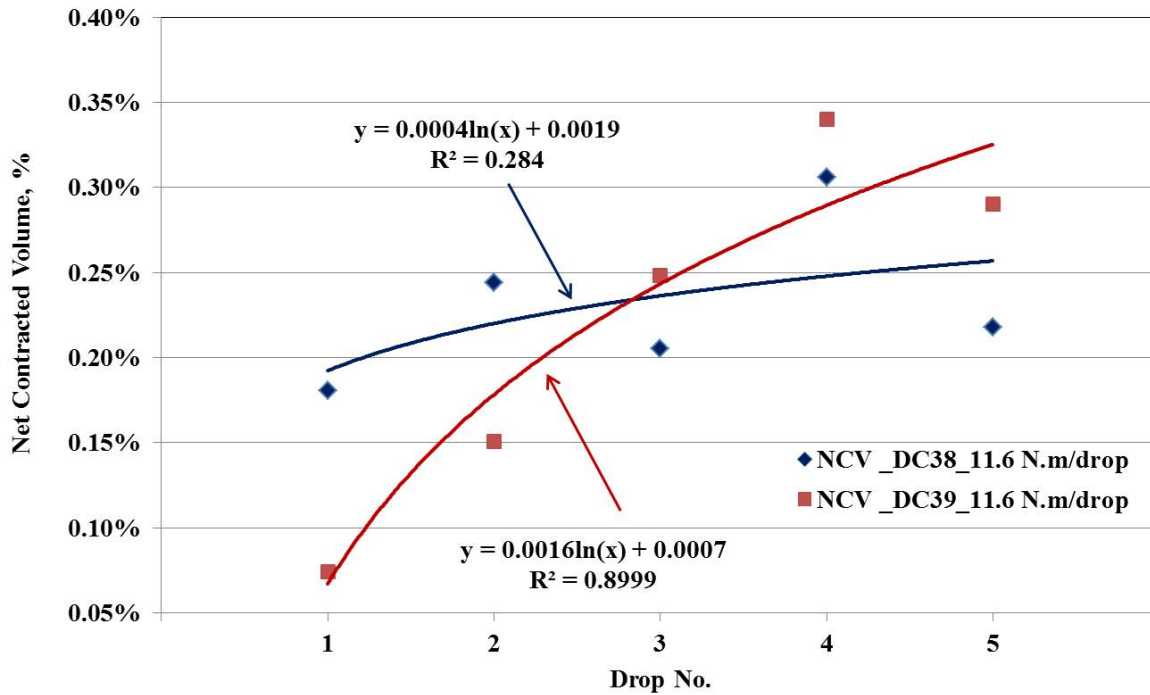


Figure 5.68. Variation in the NCV parameter by same energy input over the course of 5 drops (sand-silt models overlaid by sand) with their logarithmic correlations

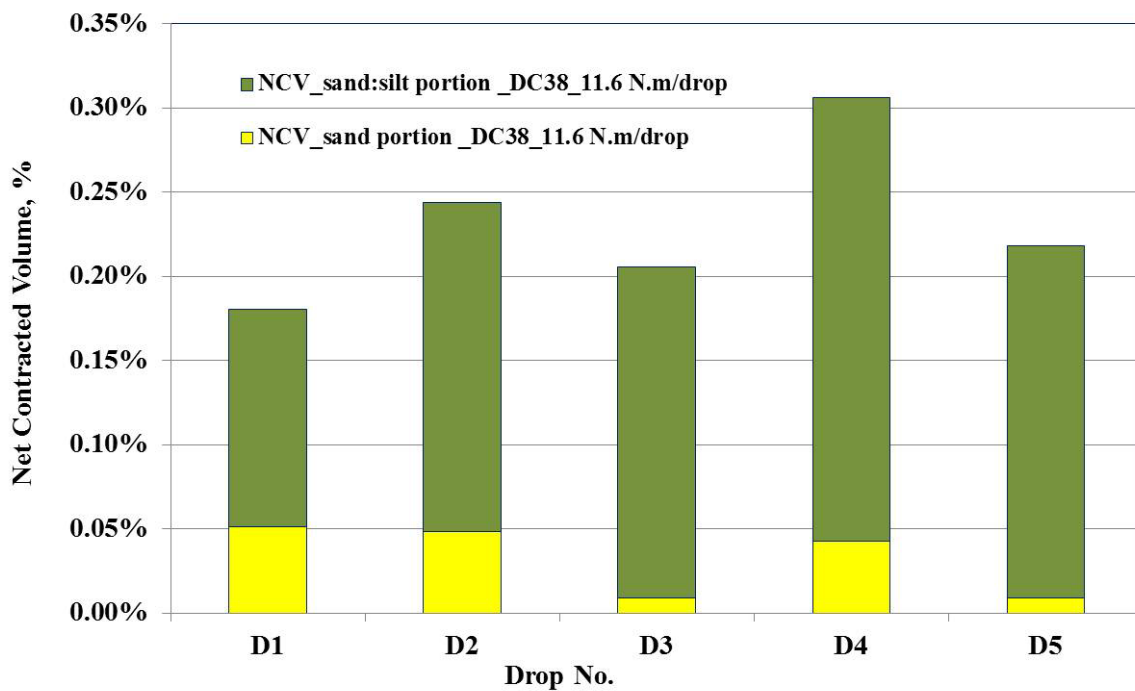


Figure 5.69. Separation of NCV values among the sand (A) and sand-silt (B) portions along the Z4 regain shown by Figure 5.67.

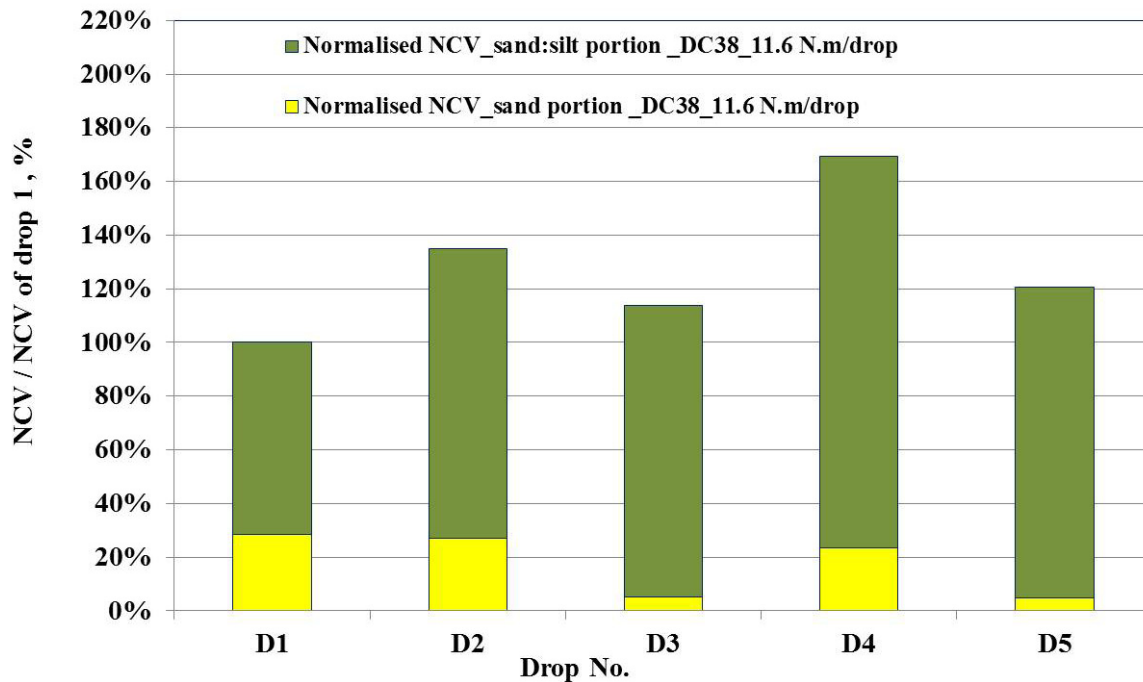


Figure 5.70. Separation of normalised NCV ratios among the sand (A) and sand-silt (B) portions along the Z4 regain shown by Figure 5.67.

The results of the NCV magnitudes and normalised NCV ratios for test DC38 are interpreted as showing that the impact shock has transmitted through the overlaid sand and down into the sand-silt causing greater displacement and net contracted volume strain (densification) in the sand-silt portion. The better response, in terms of higher NCV values and the better correlation, of the results from DC39 (85mm of sand at top) over the ones from DC38 (180mm of sand at top) signifies that a larger portion of the imparted energy is utilised by the compaction mechanism at depth rather than being wasted in pushing the soil aside and upwards, suggesting that DC will be more effective in compressible soils.

5.4 SUMMARY

The use of high speed photogrammetry as a quantitative tool has allowed the evolution of localised deformation and strain fields in dynamic tests to be revealed, and has suggested that compaction shock bands are an important mechanism in dynamic compaction. Digital high speed photography has allowed the propagation of localised deformation and strain fields to be identified and has suggested that compaction shock bands control the kinematics of dynamic compaction. The results have revealed distinctive internal densification mechanisms that depend on the tamper geometry and the type of target soil.

Micro-CT scans were performed on a small specimen from the model tests to provide volumetric parameters describing the particles, pores and porosity across the scanned field. It was found to be very difficult to reliably interpret the porosity, in the absence of other data, because the estimated value was very sensitive to the grayscale threshold selected in the analysis. Results from the X-ray microtomography revealed variations in porosity across a specimen that were broadly consistent with the data from photogrammetry, however, because of the small specimen size, the difficulty of knowing its precise location relative to the photographs, possible disturbance during sample extraction, and the cost of the procedure it is considered that this technique is currently of limited value.

The after impact non-uniform volume change concentrated in localised strain bands limits the value of before/after compaction CPT tests as quantitative tool for assessing the effectiveness of DC in increasing soil density.

The direct applicability of the results may be limited by the small scale and low stress levels in the model tests, however, they indicate that the response of soil to dynamic compaction is likely to be strongly influenced by the soil type and tamper geometry. The results show that there are significant differences in the extent and magnitude of the compacted zone at depth, and suggest that there may be significant benefits from considering different tamper shapes in future field studies. It was found that no single tamper shape performed well across both soil types investigated. The tests suggest potential to improve dynamic compaction practice by using combinations of different tamper geometries on alternate grids to achieve the most effective densification.

Chapter VI: Experimental Results – Physics of Dynamic Compaction

Table of Contents

6	OVERVIEW	202
6.1	THE ROLE OF INSTRUMENTATION IN DC TESTS	202
6.2	MEASUREMENT VALIDITY	203
6.2.1	Soil-instrumentation interaction.....	203
6.2.2	Effect of Reflected Signals	204
6.2.3	Signal noise.....	204
6.3	VALIDATION OF PHOTOGRAPHY RESULTS.....	206
6.4	INSTRUMENTATION RESULTS	208
6.4.1	Accelerometers	208
6.4.1.1	Soil Accelerations.....	208
6.4.1.2	Pounder Accelerations.....	216
6.4.2	Stress Cell (EPC) Data.....	223
6.4.2.1	Impact Stresses by Pounder EPC.....	223
6.4.2.2	Dynamic Soil Stresses	226
6.5	TYPICAL RESULTS DURING DC TESTS.....	228
6.6	SUMMARY	236

6 OVERVIEW

The aim of this chapter is to analyse the soil dynamic response during DC tests from the instrumentation (accelerometers and stress cells) attached to the falling poulder and embedded in the soil beds. The measurements included poulder acceleration and impact stress as well as measurements of stress and acceleration at target locations within the soil models.

The load cell and embedded accelerometer data are presented to demonstrate the effect of DC impact on the performance of the soil beds with increasing number of drops, tamper energy and momentum. Instrumentation output was used to validate the results from the high speed photography. The reliability and consistency of the instrumentation measurements as indicators of the soil mechanical behaviour during dynamic loading is discussed.

6.1 THE ROLE OF INSTRUMENTATION IN DC TESTS

The role of the instrumentation was to obtain the amplitude and characteristics of signals in the time domain, such as peak accelerations, peak pressures and the arrival times of the signals, upon, during, and after DC impacts. During DC, dynamic pressure should increase and arrival times measured from the time of impact, should diminish as the soil becomes stiffer with increasing number of drops (Wetzel and Vey, 1970, Mayne and Jones, 1983, and Thilakasiri *et al.*, 1996). The measurements from the embedded stress cells were also used to infer changes in the soil properties at depth due to repeated surface impacts. The measurements in each drop can be summarised as follows:

1. The acceleration history of the tamper was measured from the time of release until it stopped penetrating the soil.
2. An indication of the impacting stress was provided by a load cell mounted at the base of the poulder.
3. The soil response to the compaction shock wave was recorded by embedded stress cells and accelerometers.

Integration of the accelerometer data was used to provide velocity of pounder and soil, and double integration used to provide displacements. Hence, both the magnitude and the arrival time from these signals can be derived.

6.2 MEASUREMENT VALIDITY

Considering the relatively small size of the physical models employed in this work and the dynamic environment of the compaction tests, there were three main issues associated with the instrumentation measurements that had to be addressed:

1. Interaction between the gauges (stress cell or accelerometer) and the soil
2. Wave reflections from the model container
3. Signal noise

6.2.1 Soil-instrumentation interaction

It is generally acknowledged that the measurement of stresses and strains in granular materials is a difficult task since any embedded instrumentation will have physical properties different from the surrounding soil, affecting the stress and strain fields in the vicinity of the introduced gauges. The use of miniature stress cells and small uniaxial accelerometers was intended to reduce such unavoidable interaction, and, more importantly, to ensure an uninterrupted flow of soil particles around these inclusions so as not to influence the photography results. Despite the adopted calibration scheme, stresses from the embedded cell were found to be inconsistent relative to the cell position within the model, and inconsistent between repeat tests.

Unlike the stress cells, soil accelerometers are not sensitive to the soil-cell interactions. However, they were observed to move, tilt and rotate with the surrounding soil during the course of DC experiments, making velocity measurements based on differences between the acceleration-time responses and the pre-impact positions of the accelerometers unreliable. Triaxial accelerometers would have enabled the position of the accelerometers to be tracked but they were not considered for this work because of concerns that the accelerometer size would interfere with the photography results.

6.2.2 Effect of Reflected Signals

Spatial attenuation and soil damping will result in the impact wave attenuating rapidly with distance from the wave source (point of impact) and therefore reflected waves from the model container base and sidewalls should be much smaller than the incident wave at the locations of the embedded instrumentation. Nevertheless, it was important to substantiate that the measured signals captured by the embedded instrumentation were unaffected by base or sidewall reflections. To investigate this, a few preliminary DC tests were conducted with a bender element placed at the model container base and the travelling times of the impact wave from the point of impact to the bender element (container base) and back to the target locations of instrumentation were measured. Signal arrival times were measured to be between 30 to 55 milliseconds which were 20-35 times greater than the signal arrival times to the stress cells and accelerometers embedded close to the surface of the soil models. Signals from embedded instrumentation were found to be free from apparent secondary peak arrivals that could have been caused by boundary interference.

6.2.3 Signal noise

The size of the model container and the close proximity of the gauges to the impact surface required accurate timing to reliably differentiate the arrival times at different target gauges. This was made more difficult by inevitable signal noise generated by the electrical components of the accelerometers, cables and data logger and noise due to vibration of the falling assembly.

Raw accelerometer signals were found to be relatively noisy and this made it difficult to determine an accurate evaluation of the time shift between arrival responses. Thus, it was more appropriate to analyse their response in frequency domain rather than in time domain. This change from time domain to frequency domain was accomplished by means of an inverse discrete Fourier transform (IFFT) algorithm readily available in several numerical modules. The frequency domain analyses by the IFFT algorithm provided rather more reasonable estimations of the time shifts between sets of accelerometer signals. Figure 6.1 shows an example of typical acceleration time histories and the signals cross-correlation by the IFFT algorithm. Although time shifts can be determined from differences of the arrivals

and peaks from the acceleration time domain responses in Figure 6.1a, this procedure often did not provide reasonable results.

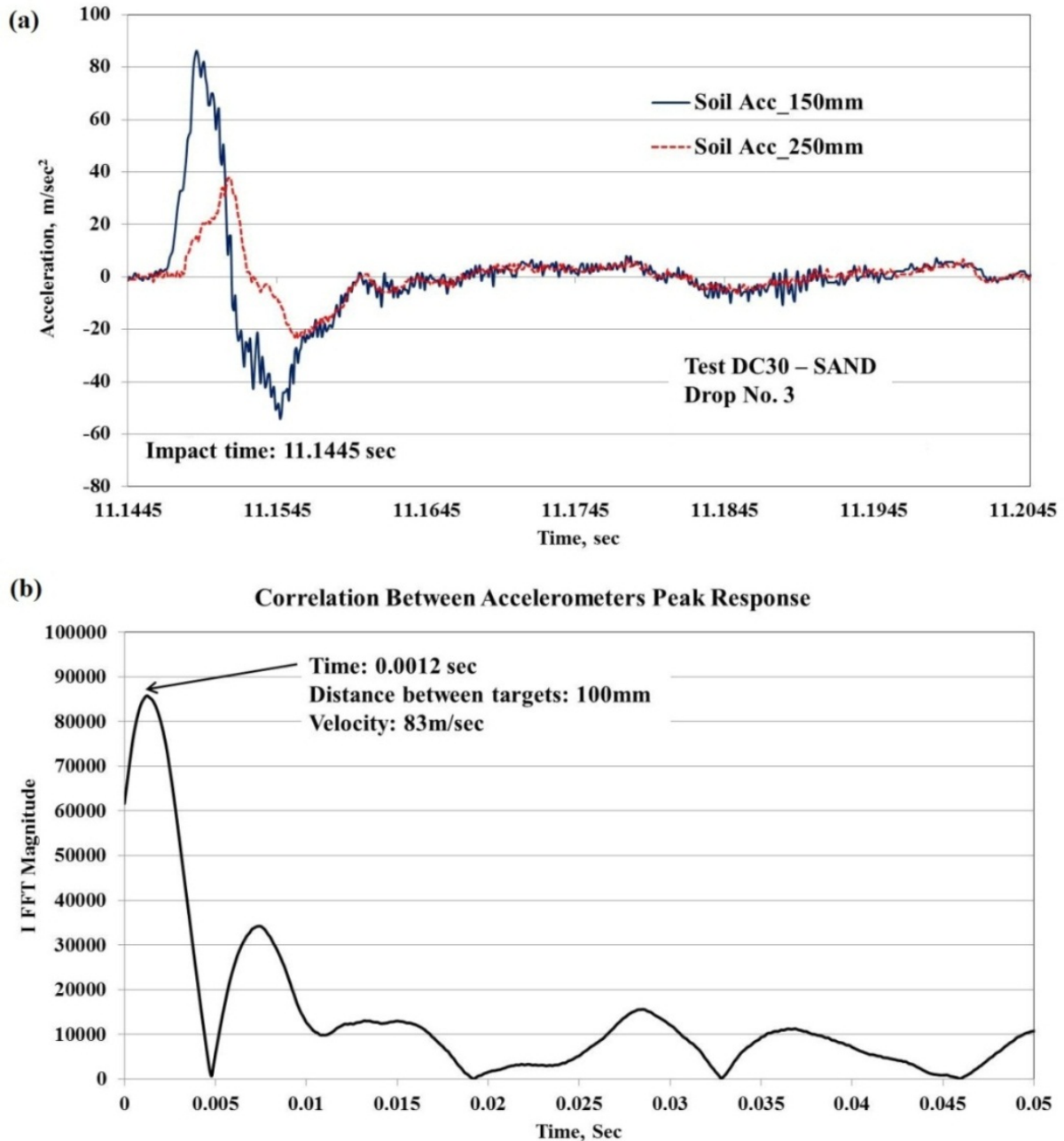


Figure 6.1. Time history of two embedded accelerometers signals (a) and time shift by IFFT cross-correlation (b).

6.3 VALIDATION OF PHOTOGRAPHY RESULTS

Instrumentation results were used to assess the precision of GeoPIV measurements. This process comprised the comparison of two main events:

1. Comparison of poulder penetration by integrated poulder acceleration verses poulder penetration tracked by GeoPIV.
2. Comparison of soil displacement by integrated soil accelerations verses soil displacement at target locations tracked by GeoPIV.

In some DC tests, physical measurement of poulder penetration was not possible because of the collapsing nature of the dry sand and sand:silt mixtures used. Also, tracking the position of the poulder by GeoPIV was difficult because soil particles entered the narrow gap that separated the poulder from the Perspex face, which prevented the GeoPIV algorithm from accurately tracking patches positioned on the poulder.

The results from 23 random impacts have been used to compare the poulder penetrations from the accelerations and photography as shown in Figure 6.2. The figure shows there is a reasonable correlation between the displacements estimated by the poulder acceleration and tracked by GeoPIV with a variance of 12.85%. The slightly greater displacements from the acceleration records are believed to be a consequence of the slightly uneven surface of the sand. The agreement between the two measurements appears to be better for deeper penetrations.

GeoPIV patches were also used to track soil displacements at the locations of the embedded accelerometers to establish the agreement between the GeoPIV displacement vectors and the double integrated accelerometer signals (displacement). This validation exercise was valid only for the first drop of any DC test since the exact locations of the embedded accelerometers subsequent to the first impact were not known accurately. The correlation between the soil displacements estimated from integrated accelerations and from tracked GeoPIV patches is shown in Figure 6.3.

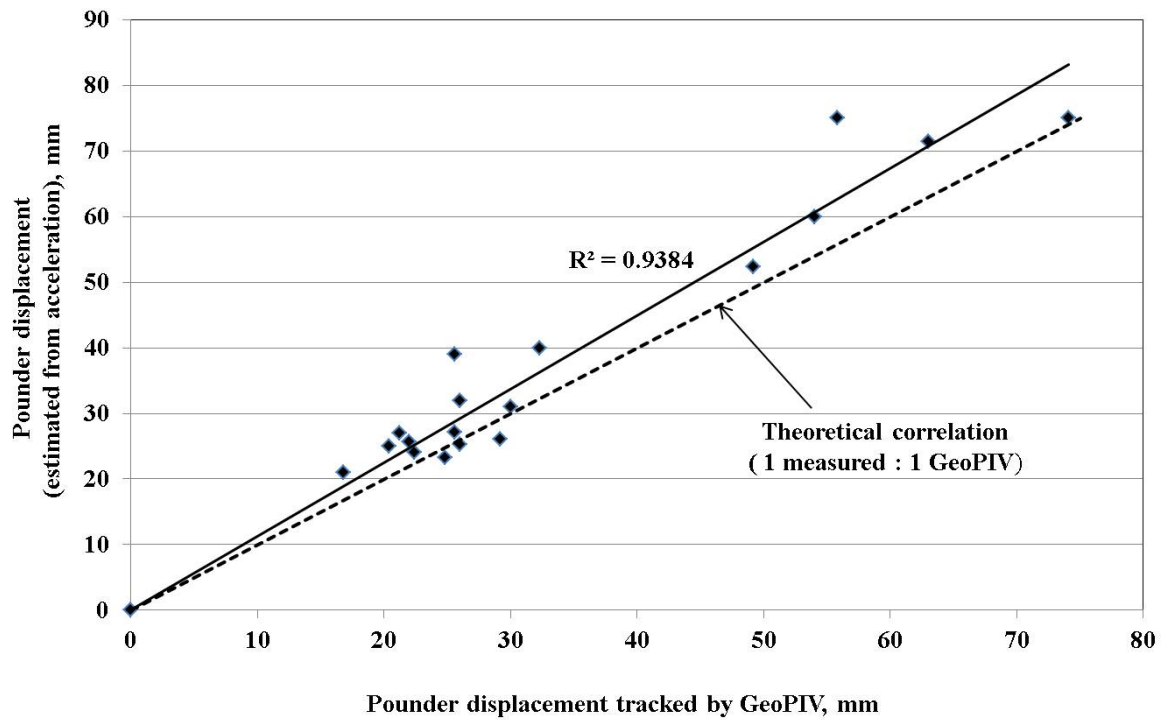


Figure 6.2. Correlation between measured poulder penetration by poulder acceleration, and poulder penetration tracked by GeoPIV.

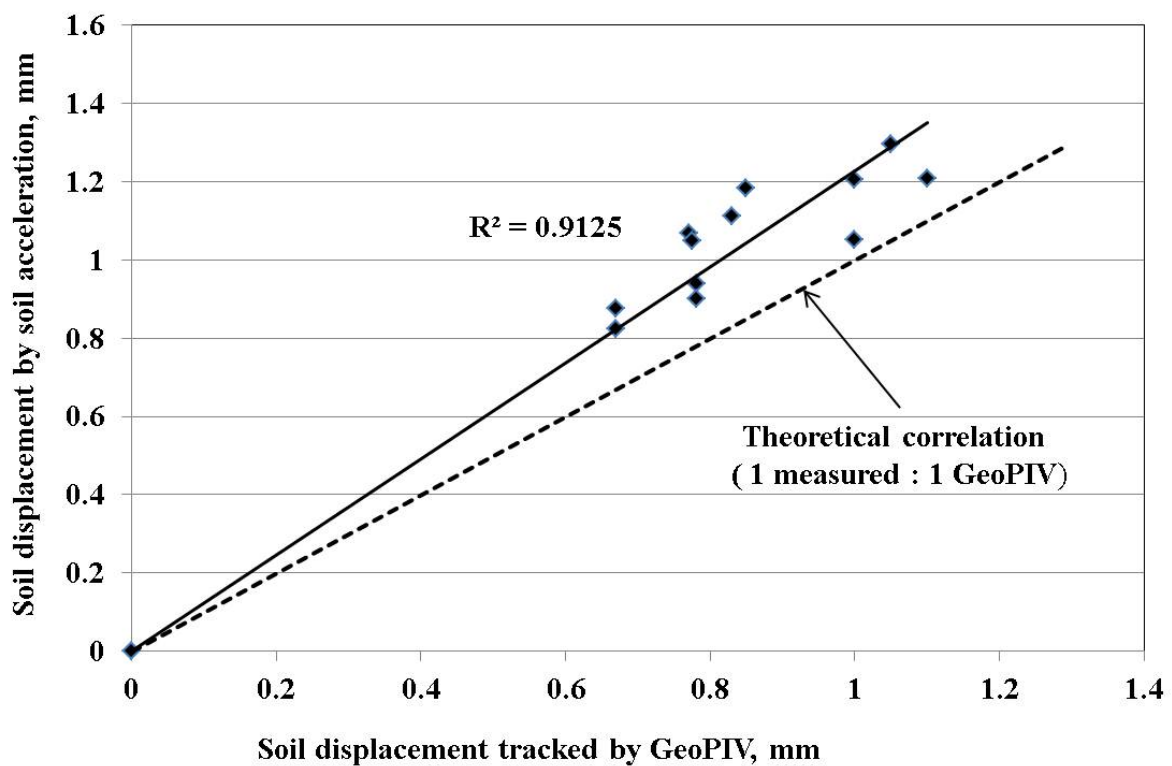


Figure 6.3. Correlation between measured soil displacements from integrated accelerations and tracked GeoPIV patches.

This figure shows that the displacements estimated from the accelerometer slightly overestimate the values from GeoPIV. This could be a result of friction between the Perspex face and the sand which restricts motion at the face and hence reduces the PIV estimated values, but it was also observed that the accelerometers had moved out of their measurement plane. When these factors are considered, the agreement shown in Figure 6.3 looks reasonable.

The GeoPIV measurements were not expected to be in full agreement with the instrumentation due to the limited accuracy and precision of both results. The limited range of the camera focus, the accuracy of the conversion from image-space to object-space, and the limited resolution of the accelerometers were all possibly contributing to the minor discrepancies between the two different measurements. Nevertheless, agreement between the instrumentation based displacements and corresponding GeoPIV displacement fields was generally satisfactory and has provided further confidence in the photographic results.

6.4 INSTRUMENTATION RESULTS

6.4.1 Accelerometers

6.4.1.1 Soil Accelerations

Peak soil accelerations plotted against drop numbers provide an indication of the response of different soil densities to different imparting energies at target depths below the point of impact. Typical variations in the peak soil accelerations at depths of 150 and 250mm below the initial surface level from DC tests on loose sand are shown in Figure 6.4. In these results, soil accelerations appear to be proportional to the magnitude of the imparting energy, and due to energy dissipation decay with depth. In loose sand, the first impacts cause the soil to accelerate rapidly but in subsequent drops the accelerations were essentially constant and only 50% of the accelerations caused by the first impact. The soil accelerations at 250mm were about 60% less than their corresponding values from 150mm throughout all the drops. The response of the dense sand bed was different. Variations in the peak soil accelerations at 150 and 250mm depths from DC tests on dense sand are shown in Figure 6.5. Here, the peak soil accelerations from the second impact were the highest before soil accelerations declined sharply and stabilised for the remaining drops.

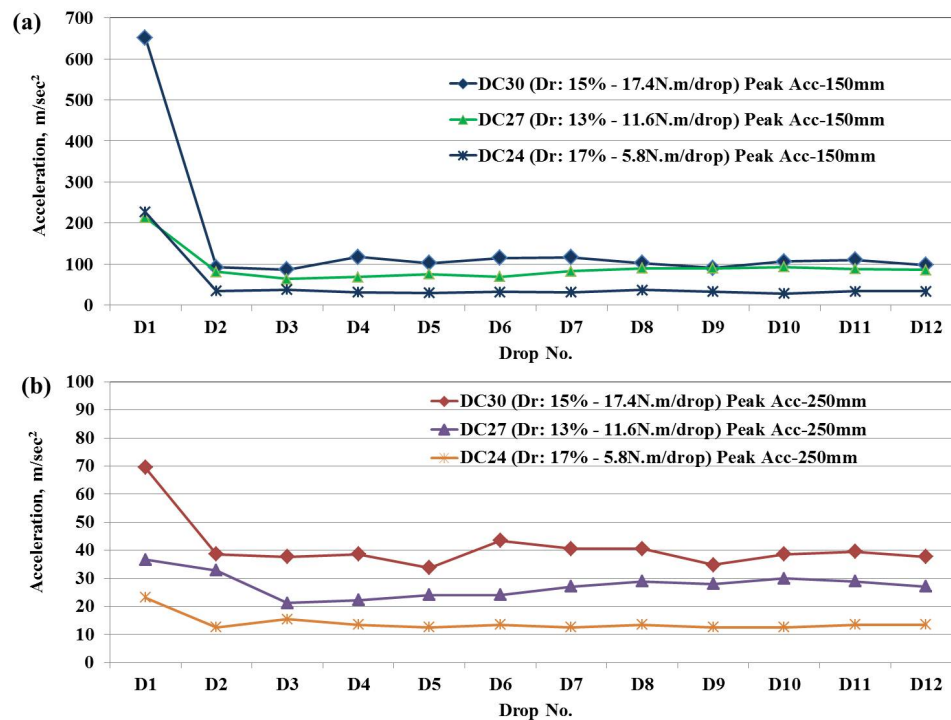


Figure 6.4. Peak soil accelerations at 150mm (a) and 250mm (b) below point of impact over 12 drops on loose sand models.

Soil accelerations in the dense sand beds were generally higher than their corresponding accelerations in the loose sand beds. In dense sand, irrespective of the response in the first couple of impacts, subsequent soil accelerations appear to be also proportional to the magnitude of the imparting energy, and due to energy dissipation decay with depth. For drops 3-12, the accelerations were varied between 8% and 35% of the highest accelerations at depths of 150 and between 8% and 17% of the highest accelerations from depths 250mm, respectively. Similar to the response from loose sand, ratios of soil accelerations at 250mm were about 45-60% less than their corresponding values from 150mm. In dense sand, impacting the surface of the soil bed disturbs (loosening) the surface without causing any significant densification in the soil resulting in higher soil acceleration at depth. The sudden drop in soil accelerations subsequent to the first impacts in loose sand models or the second impacts in dense sand models could be a result of tilted accelerometers or of them being moved aside off the impact centreline. As noted above, the accelerometers were found to have moved during the tests, but when and by how much are unknown, and thus interpretation of the accelerations after the first drop involves some uncertainty.

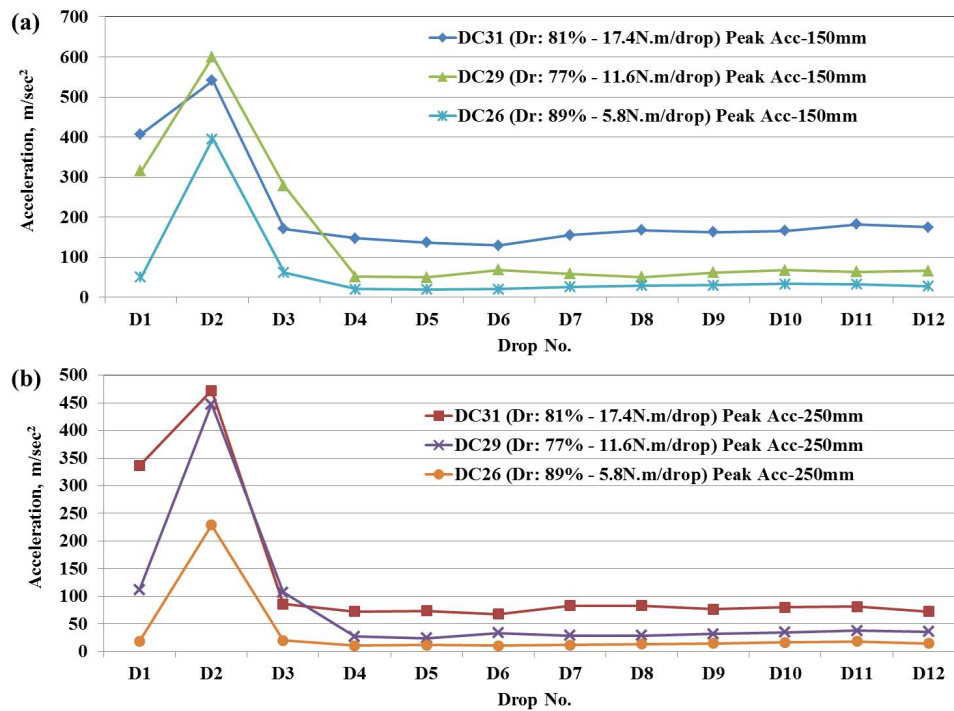


Figure 6.5. Peak soil accelerations at 150mm (a) and 250mm (b) below point of impact over 12 drops on dense sand models.

Velocities of the impact front shock waves (from the arrival of the first and largest acceleration pulse) were calculated from the differences between the arrival responses using signal cross-correlations by the IFFT algorithm among accelerometers embedded at two or three different levels. Variations in the shock passing velocities from dense sand models impacted by two energy levels and from tests with two different sand densities are shown in Figures 6.6 and 6.7 respectively.

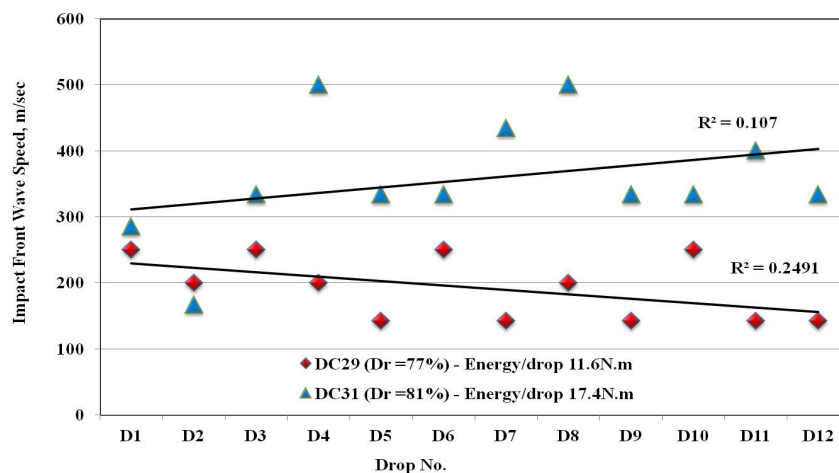


Figure 6.6. Variation in shock passing velocities in dense sand models.

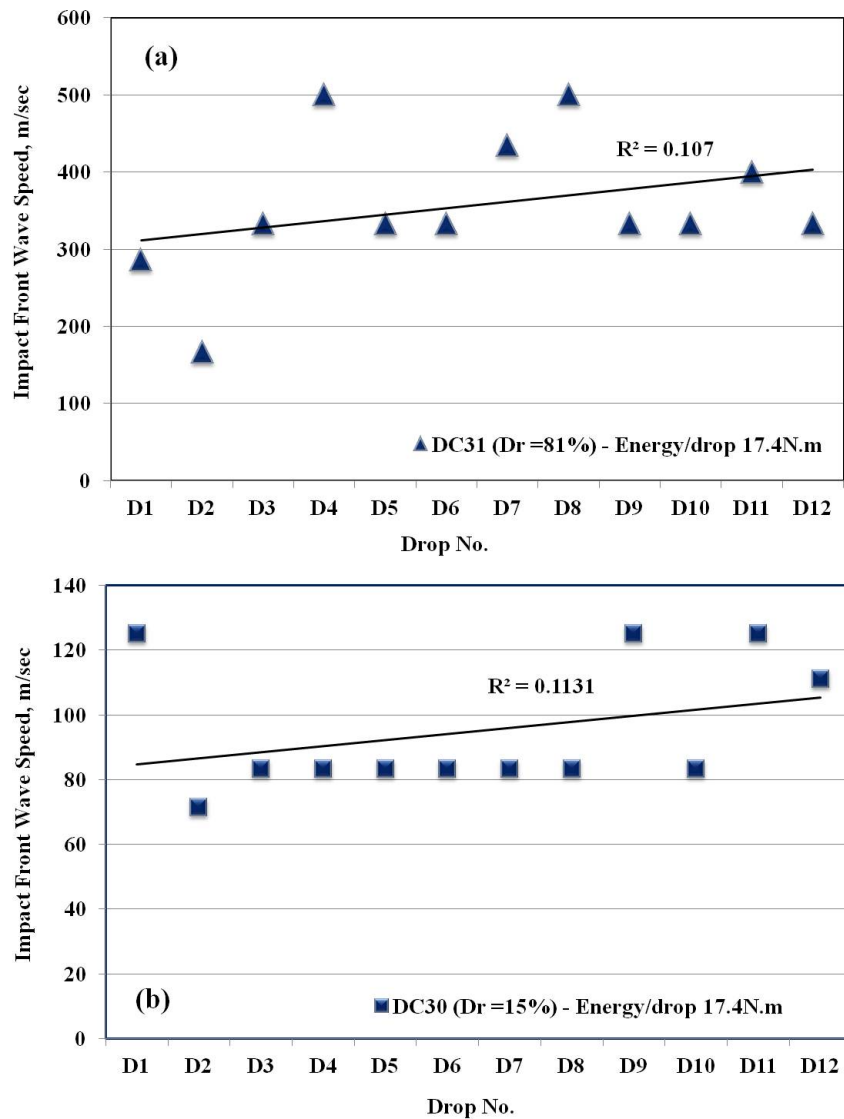


Figure 6.7. Variation in shock passing velocities in dense (a) and loose (b) sand models

The results from the accelerometers arrival responses are scattered as they reflect the fact that distances between the embedded accelerometers were reducing with successive impacts, and after the first impact the distances were not accurately known. Nevertheless, a reasonably consistent pattern is indicated suggesting that the wave speed does not change significantly despite the changes in density and stress state occurring beneath the poulder. Figures 6.8 and 6.9 show that the peak soil accelerations during DC tests on dense sand are of significantly greater amplitudes, higher frequencies and shorter wave lengths than from tests on loose sand. Since amplitude is an indication of the power of the acceleration signal, this implies that denser sand carries greater energy per unit volume than loose sand.

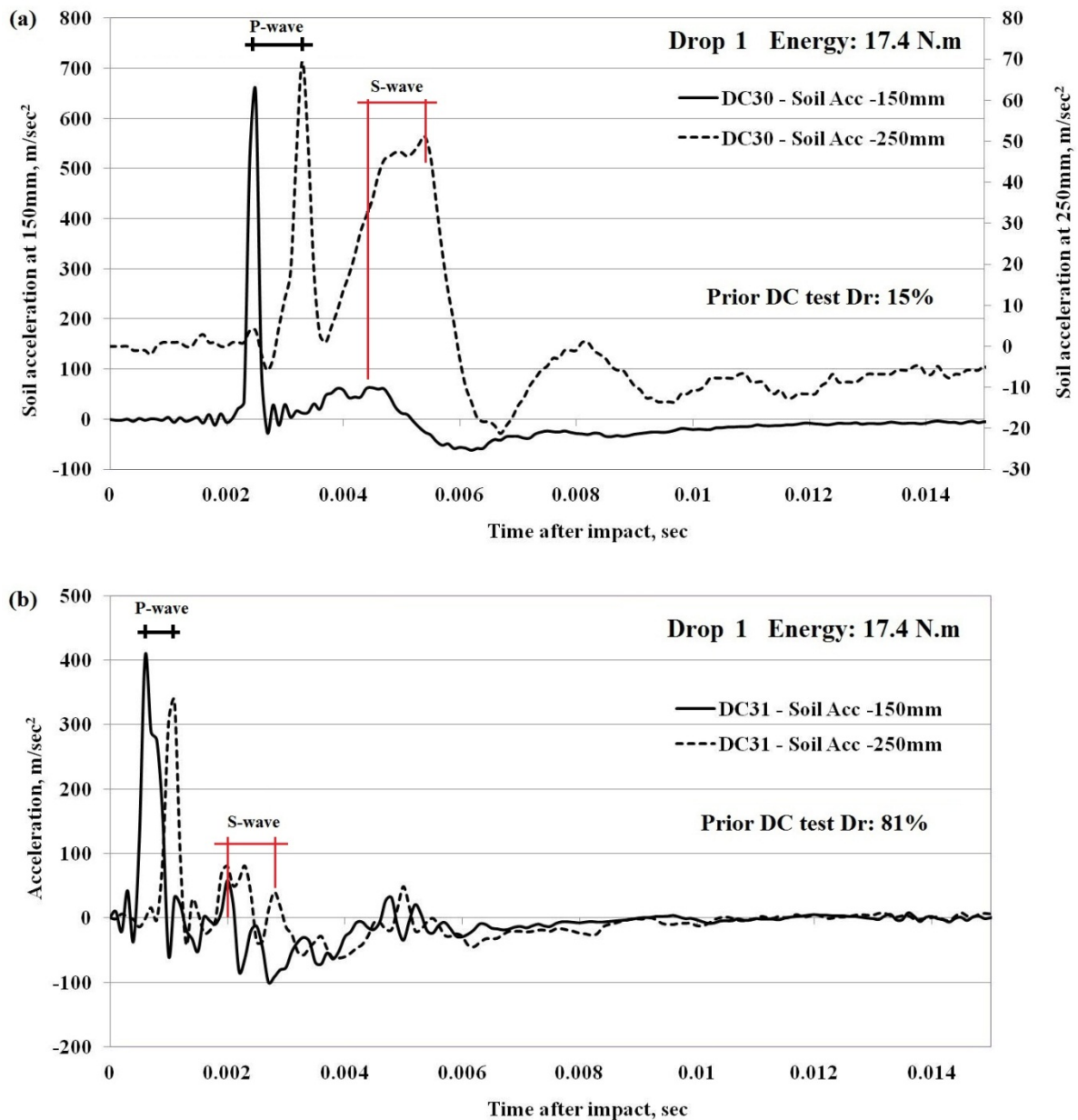


Figure 6.8. Soil accelerations at 150 and 250mm depths during drop no. 1 on loose sand model (a) and dense sand model (b) employing the same energy level.

For waves travelling through an elastic material, the relations between the Rayleigh wave velocity V_R , shear wave velocity V_s and compression wave velocity V_p as functions of Poisson's ratio are known (see Figure 6.10). For a point located beneath a concentrated load applied instantaneously at the surface of a semi-infinite elastic half-space two body wave front arrivals are experienced, corresponding to the compression (P-wave) and shear (S-wave) waves. The wave velocities between each pair of either source (impact) and receiver (buried accelerometer) or between different receivers were measured.

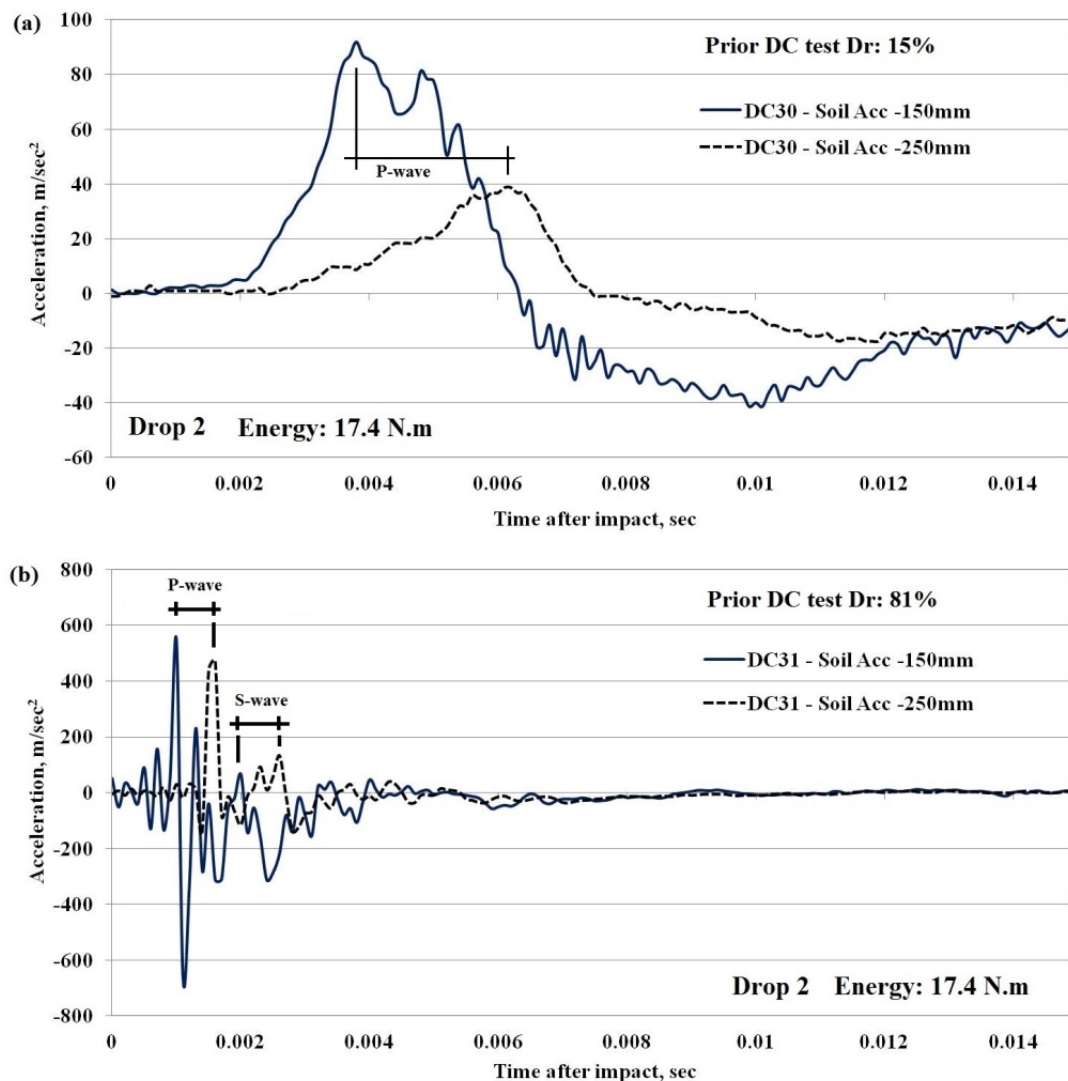


Figure 6.9. Soil accelerations at 150 and 250mm depths during drop no. 2 on loose sand model (a) and dense sand model (b) employing the same energy level.

Time differences between acceleration peaks were obtained by IFFT analysis and were used to determine the wave velocities from DC tests. These time differences could also be estimated visually from acceleration-time records as shown in Figures 6.8 and 6.9. These figures show that the P-wave could generally be determined without too much difficulty, however estimation of the S-wave velocity required some judgement and in some cases (e.g. Figure 6.9a) it was not possible to detect. Table 6.1 summarises the range of P-wave and S-wave velocities obtained during the DC tests on loose and dense sand.

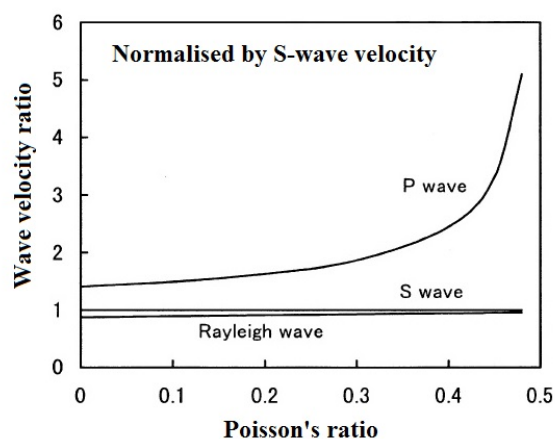


Figure 6.10 Variation of Rayleigh wave, P-wave, and S-wave velocities with Poisson's ratio
(after Richart *et al.*, 1970)

Table 6.1. Ranges of P-wave and S-wave velocities measured during DC tests

Preimpact sand density	P-wave Velocity (V_p) m/sec		S-wave Velocity (V_s) m/sec		V_p/V_s	V_p/V_s	Velocities of propagated localised strain during drop 1 by GeoPIV, m/sec
	Drop 1	Drop 2-12	Drop 1	Drop 2-12	Drop 1	Drop 2-12	
Loose sand (Dr: 3-35%) 1480 – 1540 kg/m ³	67 – 135 (101)*	35 - 68	50 – 115 (82.5)*	38 - 58	1.2 – 1.3	0.9 – 1.2	56 - 85
Dense sand (Dr: 77-93%) 1625 – 1660 kg/m ³	255 – 375 (315)*	156 - 288	214 – 275 (244.5)*	163 - 232	1.2 - 1.4	0.9 – 1.2	22 - 35

* average values

The measured P and S-wave velocities during the first impacts are consistent with typical wave velocities in granular soils. Back calculated shear moduli of 10.3 MPa and 98 MPa for loose and dense sand, respectively, are derived from the average S-wave velocity measurements of first drops. As shown in Appendix V, these shear moduli are within the range of the values measured in the triaxial tests, but the moduli vary significantly with stress level and void ratio. The G_{\max} values of 10MPa and 98MPa imply mean stresses of less than

50 and about 100kPa for the loose and dense sands, respectively. These values are within the stress level experienced during the DC tests. Most importantly, it should be emphasised that V_p/V_s ratio was found to be less than 1.5 for loose and dense models as well as subsequent to 12 drops in both. Since there is correlation between the ratio E/G (i.e. elasticity/rigidity ratio) and the velocity ratio V_p/V_s (Uyanik, 2010), this implies that compressional and shear-wave velocity measurements in porous and air-filled environment provide unreliable indicators of increased density/stiffness within the models. On the contrary, the velocities of propagated localised strain by GeoPIV provide more meaningful indications regarding the density of the soil bed they travel through with the velocities of propagated localised strain in loose model being twice that in the corresponding dense model.

It may be noted that neither the P nor the S-wave velocities were in agreement with the speed of propagation of the localised strain bands into the model soils. Figure 6.11 shows the compaction band velocities estimated from the GeoPIV strain and displacement plots. They typically started at around 80m/sec and decreased in speed as they moved away from the impact until the speed reached 10m/sec, after which the speed decreased rapidly to zero. The P and S-wave velocities estimated from subsequent impacts are not very reliable because as outlined earlier, the sensors moved and tilted as a result of the impact loading.

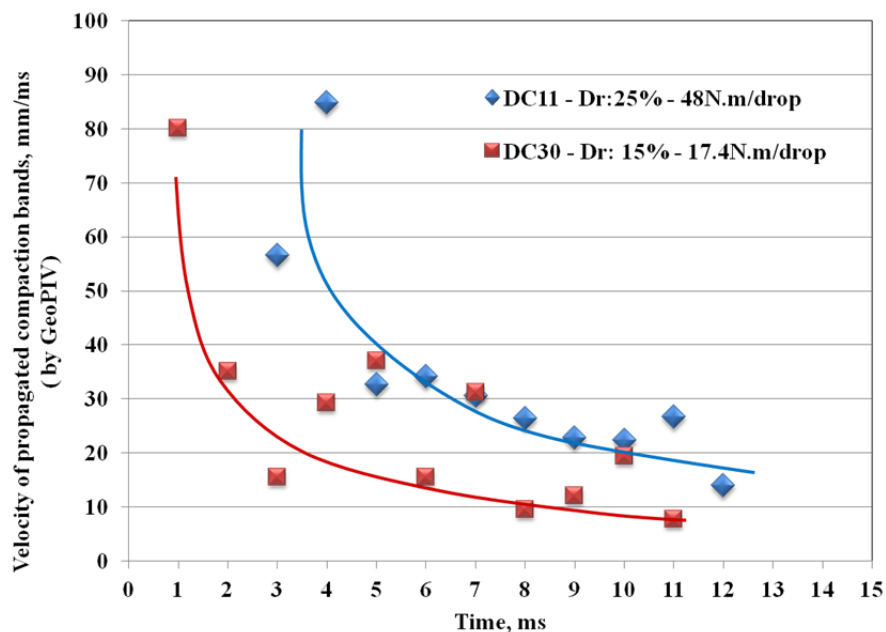


Figure 6.11 Trends of compaction band velocities by GeoPIV

6.4.1.2 Pounder Accelerations

Pounder acceleration signals were unaffected by interaction with the soil and were considered to be the most trustworthy of the instrumentation data. Typical acceleration results are provided in provided in *Section 6.5*. Data analysis from pounder decelerations is based on simple mechanics (Newton's laws). These have been used to estimate the velocities, displacements, dynamic settlement moduli (DSMs), work and peak dynamic stiffness from the pounder accelerations and are presented below. For each acceleration record, a , the first processing step was to integrate once with respect to impact time, t , to obtain the tamper velocity, V as:

$$V = \int a . dt + c \quad 6.1$$

Where c was a constant determined at the end of the acceleration record when the velocity approaches zero. The next step was to obtain tamper displacement history after impact, Z , by integrating the digitized velocity, V over the impact duration, as:

$$Z = \int V dt \quad 6.2$$

The net impact force and stress applied by the pounder over the impact durations were then determined from the digitized acceleration signals as:

$$\text{Net Impact Force } (F) = m (g - a) \quad 6.3$$

$$\text{Impact Stress } (\sigma) = F/A \quad 6.4$$

Where " m " and " A " are the pounder mass and contact area respectively, " a " is the post impact deceleration of the pounder and " g " is the gravitational acceleration. By identifying the pounder penetration (*Eq 6.2*) and the net impact force (*Eq 6.3*), the external work done on the soil surface by the pounder can then be calculated as:

$$\text{Work} = F.Z \quad 6.5$$

The tangent of the loading portion from the poulder stress-strain curve represents the dynamic settlement modulus (DSM) of a particular impact as:

$$\text{Dynamic Settlement Modulus (DSM)} = \frac{\text{Impact stress}(\sigma)}{\text{Relative displacement}(\epsilon)} \quad 6.6$$

where the relative displacement " ϵ " is the poulder penetration/poulder width

During dynamic loading, both impact force and displacement are functions of time. However, the time-based spectra of these quantities are not usually coincident. Therefore, it is considered more meaningful to estimate the peak dynamic stiffness (k_{dy}) of an impact from the peak values of the impact force (F) and displacement (Z) time histories as:

$$\text{Peak dynamic stiffness} (k_{dy}) = \frac{F_{peak}}{Z_{peak}} \quad 6.7$$

Correlations between peak impact dynamic stiffness (k_{dy}), dynamic settlement modulus (DSM) and other characteristics of the DC tests are presented in the following sections. Typical results of impact force, dynamic settlement modulus (DSM) and work by DC tests are provided in *Section 6.5 (Figures 6.28 and 6.29)*.

Figure 6.12 shows the variation in measured DSM values during impacts onto loose sand (Dr:13-17%) using the same poulder dropped from 100, 200 and 300mm in tests DC24, DC27 and DC30 respectively. The general trend of the DSM results for any particular test shows that the soil global stiffness increases with subsequent impacts. However, interpreting the results just based on the magnitude of the DSM values can be misleading since higher DSM values can be obtained from impacts of lesser energy levels and lower impact stresses. Figure 6.13 shows the variation of the maximum impact stress (MIS) for the higher (DC30-17.4N.m/drop) and lower (DC24-5.8N.m) energy levels for the DSM values presented in Figure 6.12.

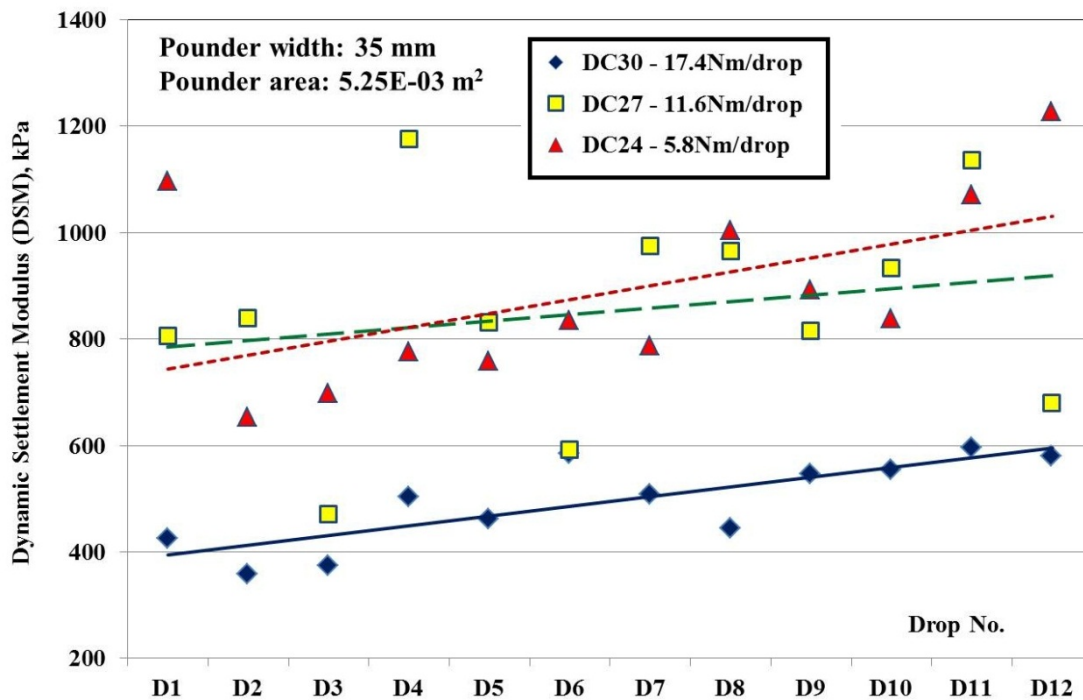


Figure 6.12. Variation in DSM values for three DC tests employing three energy levels on loose sand models (Dr: 13-17%).

From Figure 6.13, it is evident that the MIS values have more significant correlation with energy level (number of repeating impacts) than their corresponding DSM measurements. Correlations between DSM, MIS and peak dynamic stiffness (k_{dy}) with the degree of densification indicated by the accumulated NCV values are shown in Figure 6.14. Unlike DSM and peak dynamic stiffness (k_{dy}) measurements, for a certain poulder size, measurements of maximum impact stress are independent of poulder displacement (equivalent to crater depth). Among these relationships, MIS measurements provided the most significant correlation with accumulated NCV parameters. Although there are limitations of the tests from the small size and scale effects, the presented results indicate the inappropriateness of using surface measurements (depth of crater, which is equivalent to poulder displacement during DC tests) as a tool to gauge the global effectiveness of dynamic compaction.

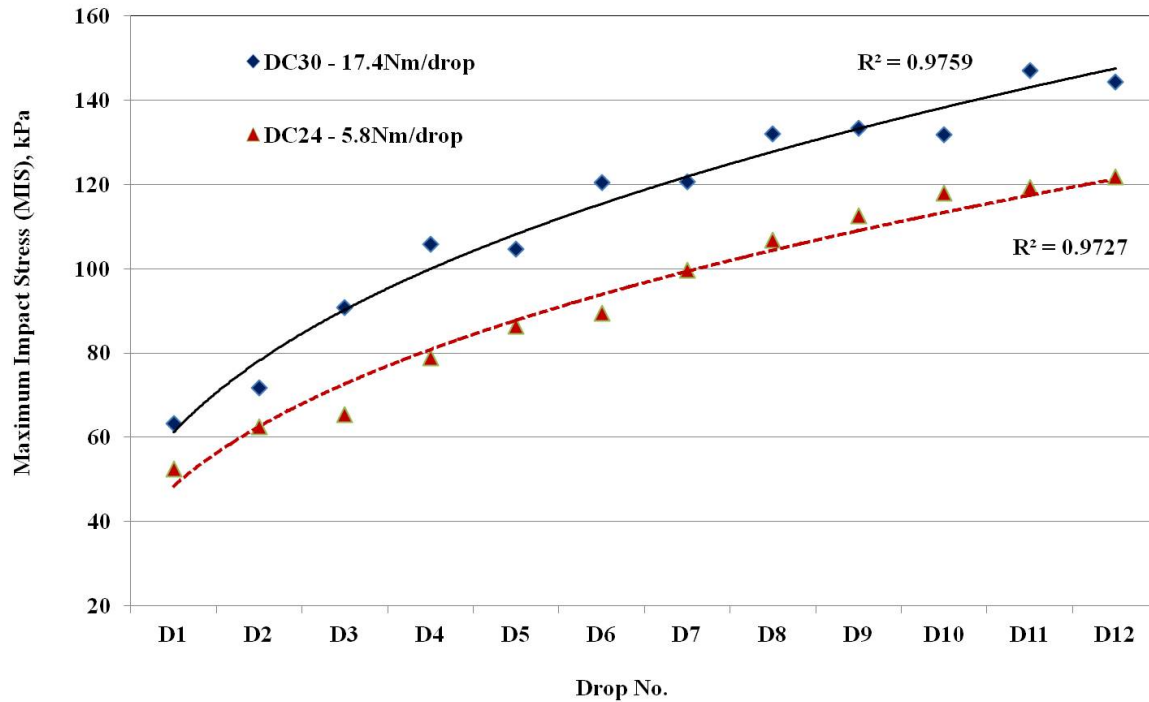


Figure 6.13. Variation in maximum impact stress for tests on loose sand models using 35mm pounder falling from 100 and 200mm heights.

DSM values appear to vary greatly based on the pounder size, the initial relative density and the type of soil. However, this measurement depends only on the initial slope of the dynamic load-settlement response and thus it represents an incomplete picture of the response. In particular it does not capture the large displacement “plastic” soil response. This might be the reason of the less significant correlation between DSM and the degree of densification measured by the accumulated NCV values. On the other hand, taking the effect of the irregular variable impacting force over the entire pounder displacement history, expressed by the pounder work, provides better interpretation of the relationship between the compaction effort, expressed by the external work, and the degree of densification (NCV). This significant correlation is illustrated by the good correlation between accumulated work and accumulated NCV shown in Figure 6.15.

It is important to differentiate between the input energy (pounder weight x drop height) and the pounder work created by displacing the soil after impact. The accumulated pounder work from both model sizes have a similar tendency with increased number of impacts as shown in Figure 6.16. It may also be noted from Figure 6.16 that the pounder work is about 50% of the input for all of the tests. The reduced resolution of the high speed photography images from the large model DC tests has limited the reliability of NCV calculations from these experiments and it has not been possible to confirm whether the accumulated work/accumulated NCV trends shown by Figure 6.15 are equally applicable for the large model experiments.

In dynamic compaction practice, researchers have interpreted the response of soil strata to an impact of a large pounder as being influenced by the global properties of the soil mass under the impact point. This global dynamic response is usually expressed by correlating the dynamic settlement modulus (DSM) with a soil elastic modulus estimated by plate bearing tests to extrapolate increases in soil density. DSM measurements from the better controlled physical models of this study indicate that DSM values are sensitive to soil properties, pounder size and impacting energies, and variations in DSM values do not correlate directly with changes in subsurface densities.

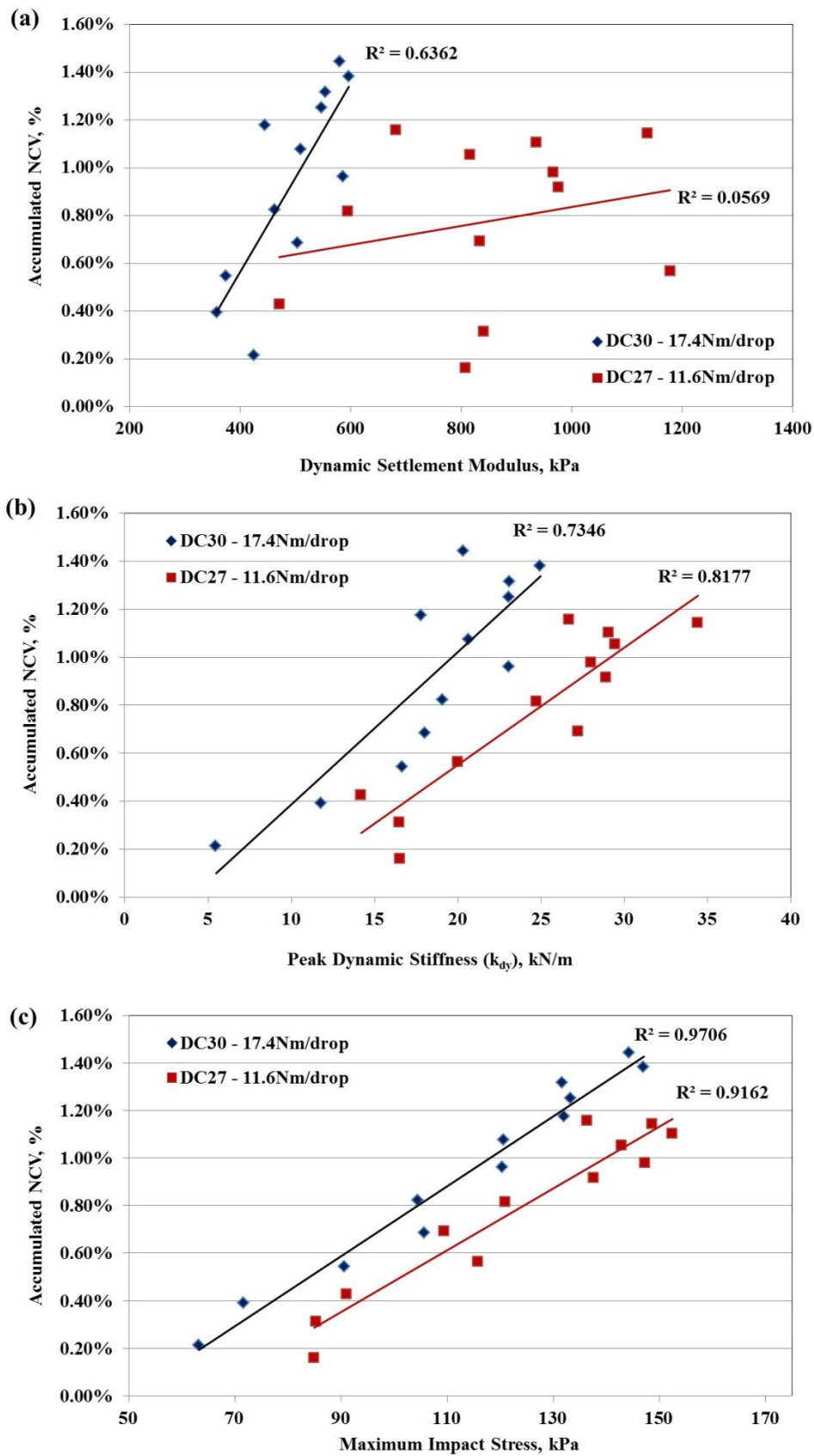


Figure 6.14. Correlation of accumulated NCV with DSM (a), peak dynamic stiffness (b) and MIS (c) from DC tests on loose sand models using 35mm pounder.

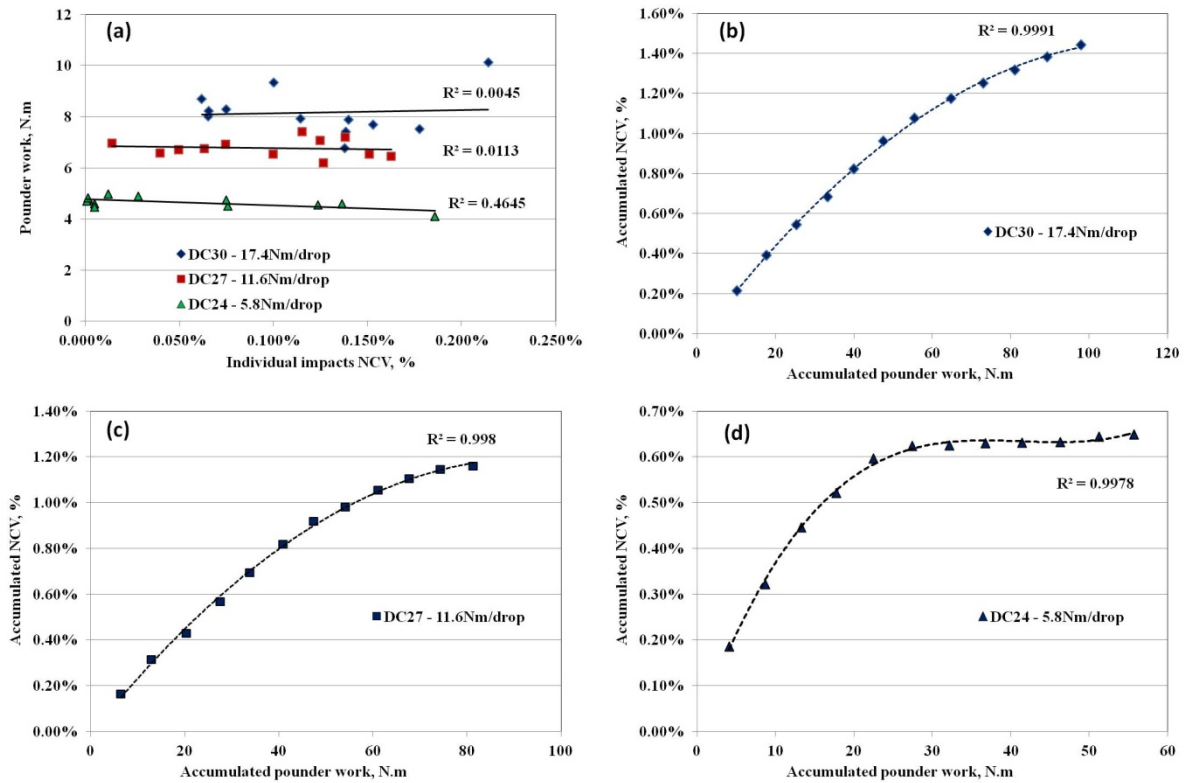


Figure 6.15. Poulder work verses NCV values of individual impacts (a) and correlation between accumulated NCV and accumulated poulder work from DC tests on loose sand models using 35mm poulder with 17.4N.m/drop (b), 11.6N.m/drop (c) and 5.8N.m (d) over the course of 12 impacts.

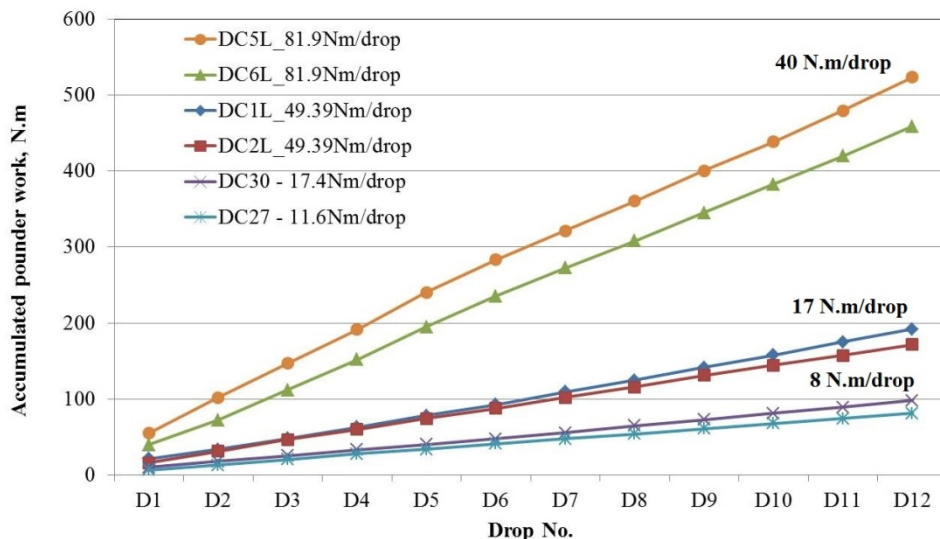


Figure 6.16. Accumulated poulder work over the course of 12 drops from both small size models (DC27 and DC30) and large size models (DC1L, DC2L, DC5L and DC6L).

6.4.2 Stress Cell (EPC) Data

6.4.2.1 Impact Stresses by Pounder EPC

Figure 6.17 shows a comparison between the maximum impact stresses for two different impacting energies on near identical sand models registered by the pounder stress cell and established from the pounder acceleration signals, over a series of 12 impacts. The results show poor agreement between stresses registered by the pounder EPC and stresses derived from the pounder decelerations. The stresses measured by the EPC were scattered and generally significantly higher than the estimated impact stresses. These discrepancies between the two measured stresses are shown by the relationships between MIS and EPC stresses presented in Figure 6.18.

Impact stresses from the stress cell (EPC) attached to the pounder base and stress levels derived from pounder accelerations were not expected to be identical since the impact stress may not necessarily be uniform across the pounder base. The pressure measured by the EPC can not be assumed to approximate the average normal stress on the face of the pounder. This assumption would be correct if the pounder behaves as a flexible member, but it is a rigid pounder of high stiffness, and thus non-uniform contact stresses should be expected. Unlike the average contact pressure derived from the pounder accelerations, the true contact pressure distribution is unknown. A range of pressure distributions have been proposed in the literature (Holtz, 1991) and the two extreme situations are shown in Figure 6.19. Because of the small contact area and the uncertainty in the distribution, differences between the EPC and MIS are not surprising.

On the other hand, it was only during the first drop that the pounder came into full contact with the soil surface instantaneously while the pre-impact surface was level. During subsequent impacts, the pounder penetrated a deformed surface of the shape of the letter "V" as shown in Figure 6.20. The V-shaped trench around the pounder may have also changed the rate of the pounder penetration and potentially also the resulting acceleration of the soil contributing in the rapid fall in the internal soil acceleration after the first and second drops shown in Figures 6.4 and 6.5.

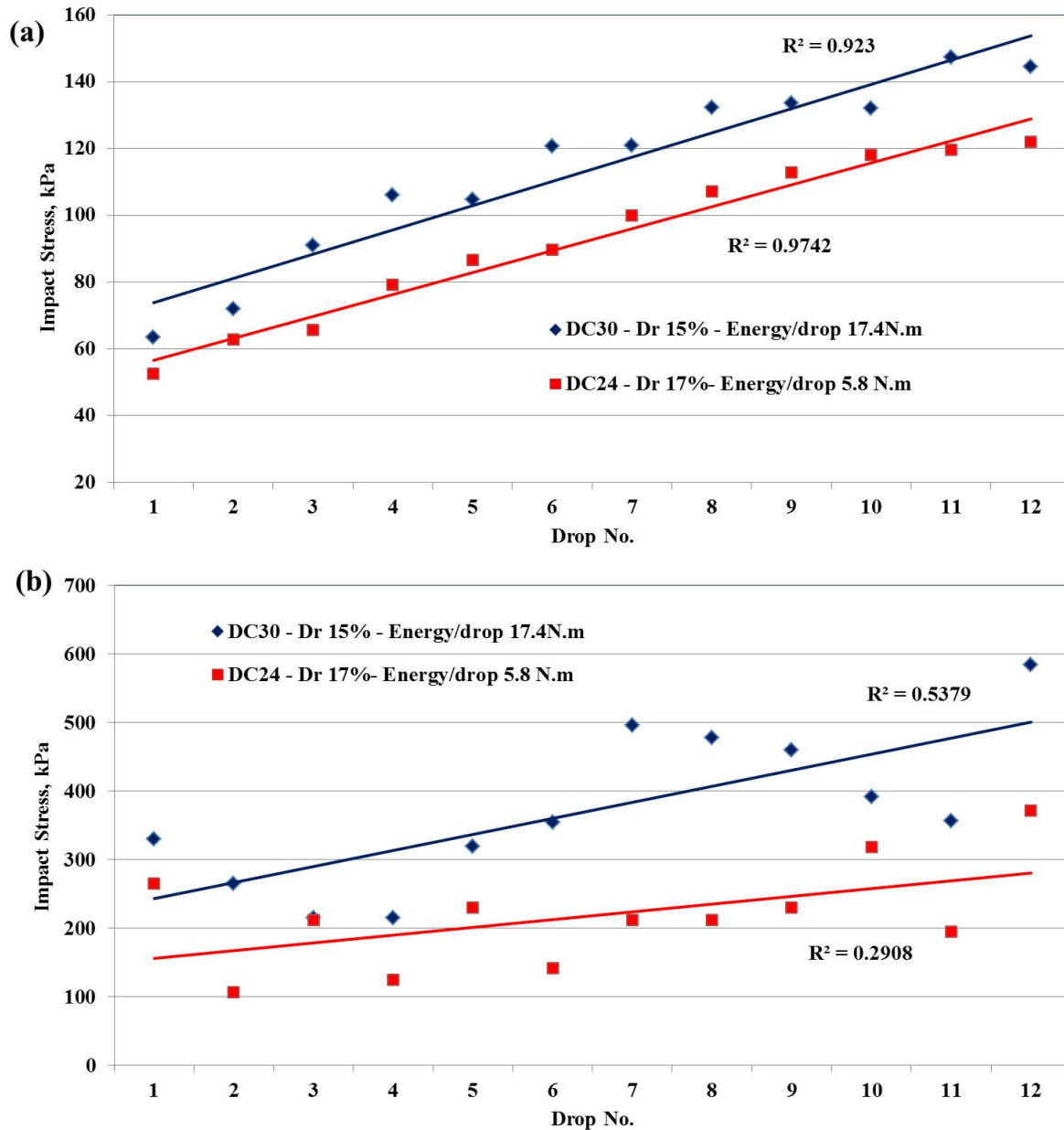


Figure 6.17. Variation in impact stresses with number of drops for two energy levels calculated from poulder post impact decelerations (a) and measured by poulder EPC (b).

Therefore, the poulder EPC did not come in contact with the soil until it had travelled some distance into the deformed soil, during which the momentum of the poulder was dampened by resistance from the soil on either sides of the poulder resulting in relatively lower stresses being registered by the centrally located EPC. This could be contributing to the stresses during the second and subsequent drops being less than the recorded stress from the first drop as shown in Figure 6.17b.

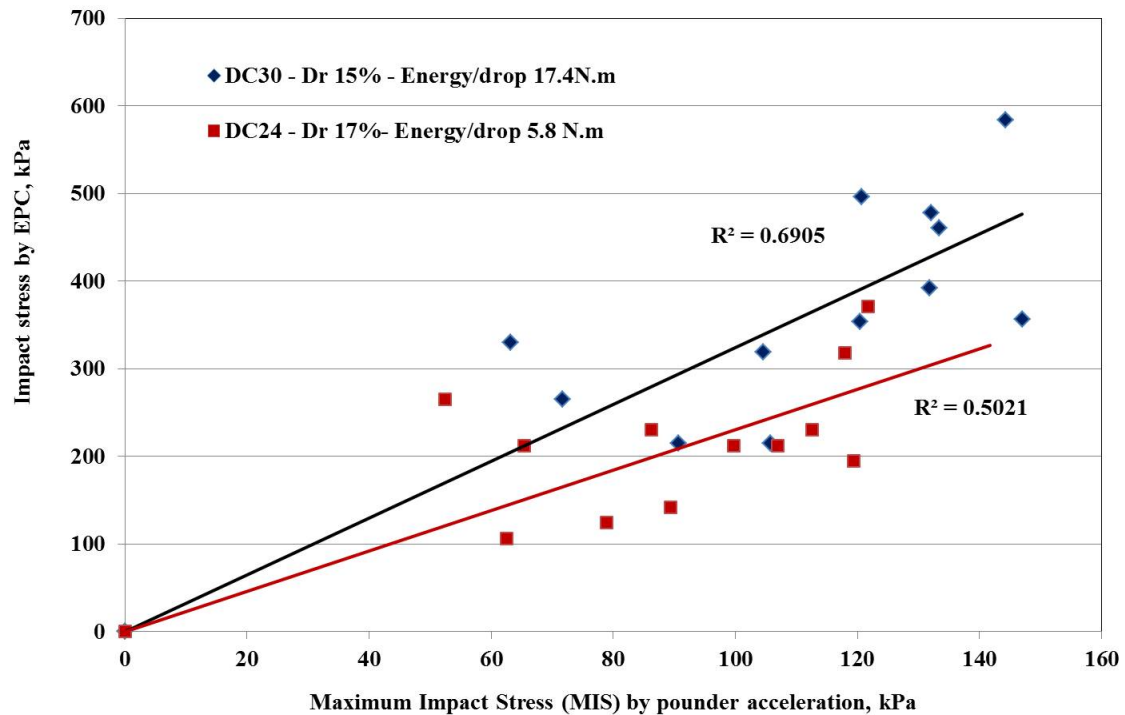


Figure 6.18. Correlations between maximum impact stresses (MIS) calculated from poulder post impact decelerations and impact stresses measured by poulder EPC form DC tests by two energy levels.

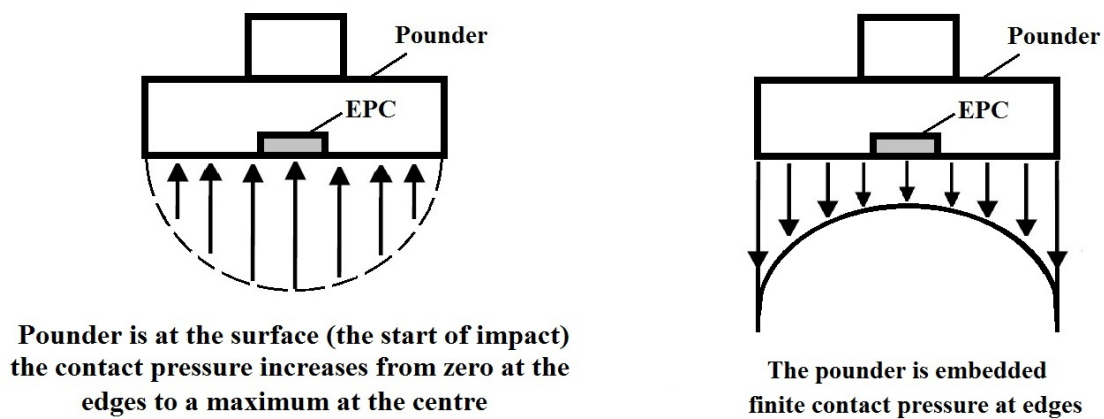


Figure 6.19. Contact stress against rigid poulder penetrating sand.

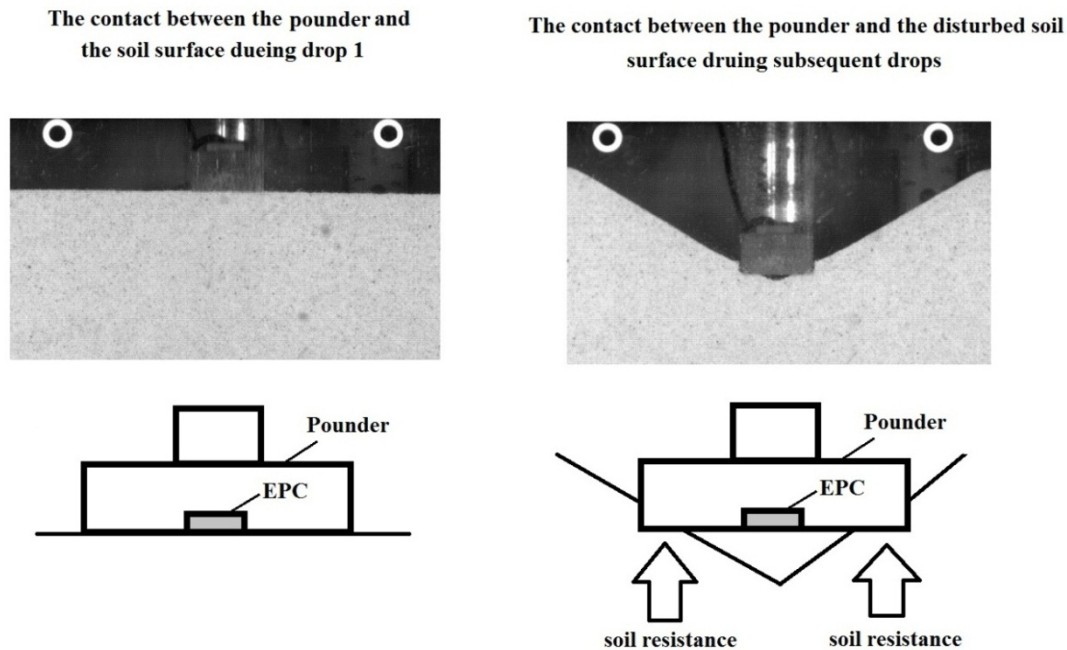


Figure 6.20. Effect of the non-flat disturbed soil surface on the contact stress against rigid pounder penetrating sand.

6.4.2.2 Dynamic Soil Stresses

Examples of maximum soil stresses (from buried soil stress cells) during dynamic compaction are shown in Figure 6.21. It is expected that soil dynamic stresses resulting from a DC impact should decrease with depth for any particular drop and that the stress level at any depth should increase with an increasing number of drops. Although, these trends are shown in Figure 6.21, there are very large differences between the stresses at 150mm despite the consistent imparting energies and the near identical sand beds of tests DC11 and DC12. In DC11, the distribution of soil stresses with respect to their depths/locations and the average impact stresses (derived from pounder accelerations) appeared to be reasonable. On the contrary, stress measurements during DC12 were doubtful with stresses at 150mm depth reaching values 5 -10 times of their corresponding values during DC11 and up to three times higher than the impact stress at the soil surface. As the EPC subsequently ceased to function, it is suspected that the high results from DC12 were a function of damage to the EPC. Measurements from the EPC mounted on the model container wall appeared to be the least erratic with consistent stress values that corresponded to 4 - 7% of the impact stress in both tests. Similarly, inconsistent soil stresses were obtained from other DC tests with embedded

instrumentation and all the buried EPCs ceased to function after a few tests. As a result, it has been difficult to develop any confidence in the values obtained, even though they look reasonable in some tests.

The responses of the soil EPCs during the DC tests are believed to have been influenced by their small size as well as the non-uniform distribution of stresses in the soil. Also as discussed in Chapter 3, the calibration of the EPCs was difficult and they did not provide a linear repeatable and reversible response. All these factors may have contributed to the poor performance of the buried EPCs.

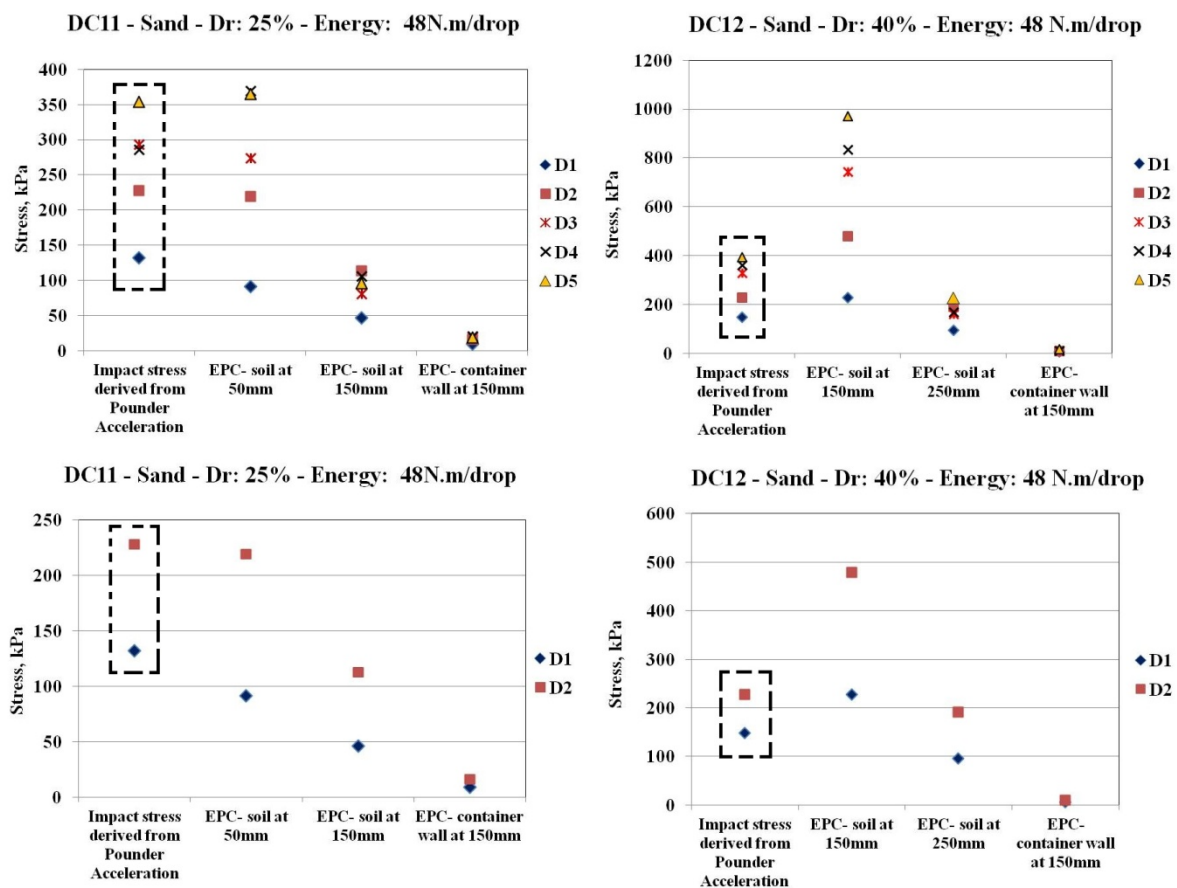


Figure 6.21. EPC soil stresses from dynamic compaction during DC11 and DC12 tests – (for clarity, results from the first and second drops are shown separately). The range of impact stresses from the pounder accelerations are enclosed by dashed lines.

6.5 TYPICAL RESULTS DURING DC TESTS

Accelerometers and earth pressure cells (EPC), both mounted on the pounder and embedded in the soil, recorded the signals generated by each impact during the DC tests. Figure 6.22 shows typical time domain signals of pounder acceleration and its integrated velocity and displacement. The figure shows the increase of pounder acceleration from rest, reaching an acceleration of about 7.5m/sec^2 during free fall before impacting the soil after 0.307sec from the start. Upon impact, the pounder started to decelerate rapidly before it stopped after 0.435sec from the start (0.128sec after impact). During the free fall, pounder velocity and displacement increased to reach their highest magnitude just after impact then rapid deceleration occurred as the pounder come to rest. Impact time was determined by inspecting the pounder acceleration signal and determining the time at which the acceleration started to change from its steady free fall acceleration. This visual inspection to determine the impact time was considered satisfactory because of the high frequency (1/10000sec) of the data acquisition which enabled the change in the acceleration signal to be picked with an accuracy of $\pm 0.0005\text{sec}$. The after impact pounder deceleration and displacement verses the penetration velocity for test DC1 (shown in Figure 6.22) are shown in Figure 6.23.

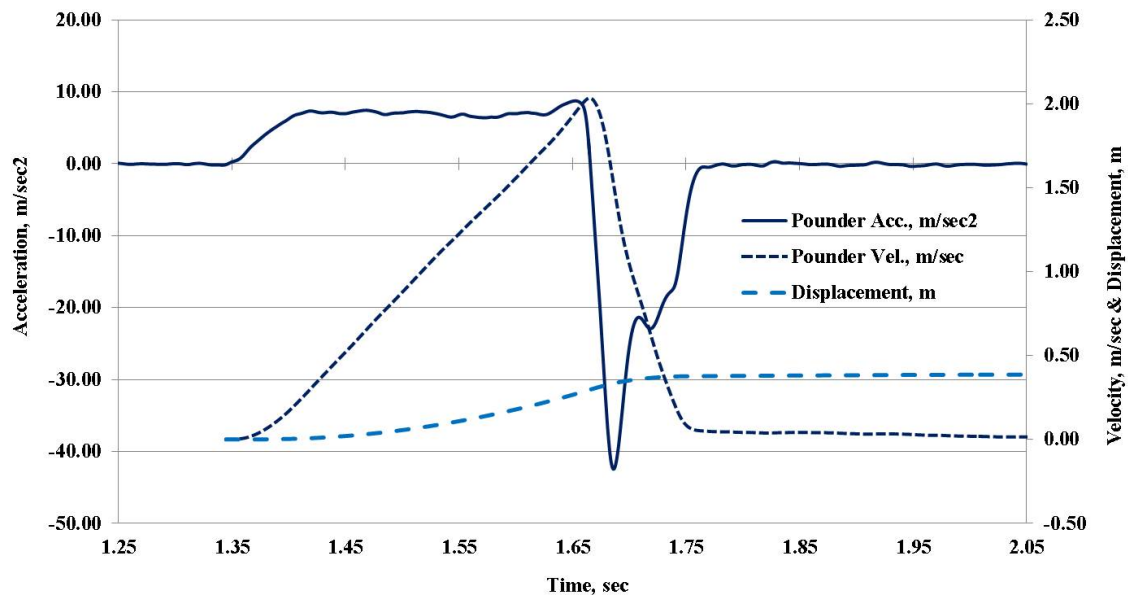


Figure 6.22. Typical time domain of pounder acceleration and its integrated velocity and displacement – drop 1 test DC1.

It is worth mentioning that due to the relatively short fall heights during the DC experiments and the presence of friction between the falling assembly and the steel frame of the Type 1 configuration, or between the falling assembly and the release mechanism of the Type 2 configuration gearbox, the free falling acceleration of the pounder was generally less than the typical free-fall gravitational acceleration of 9.8 m/sec^2 .

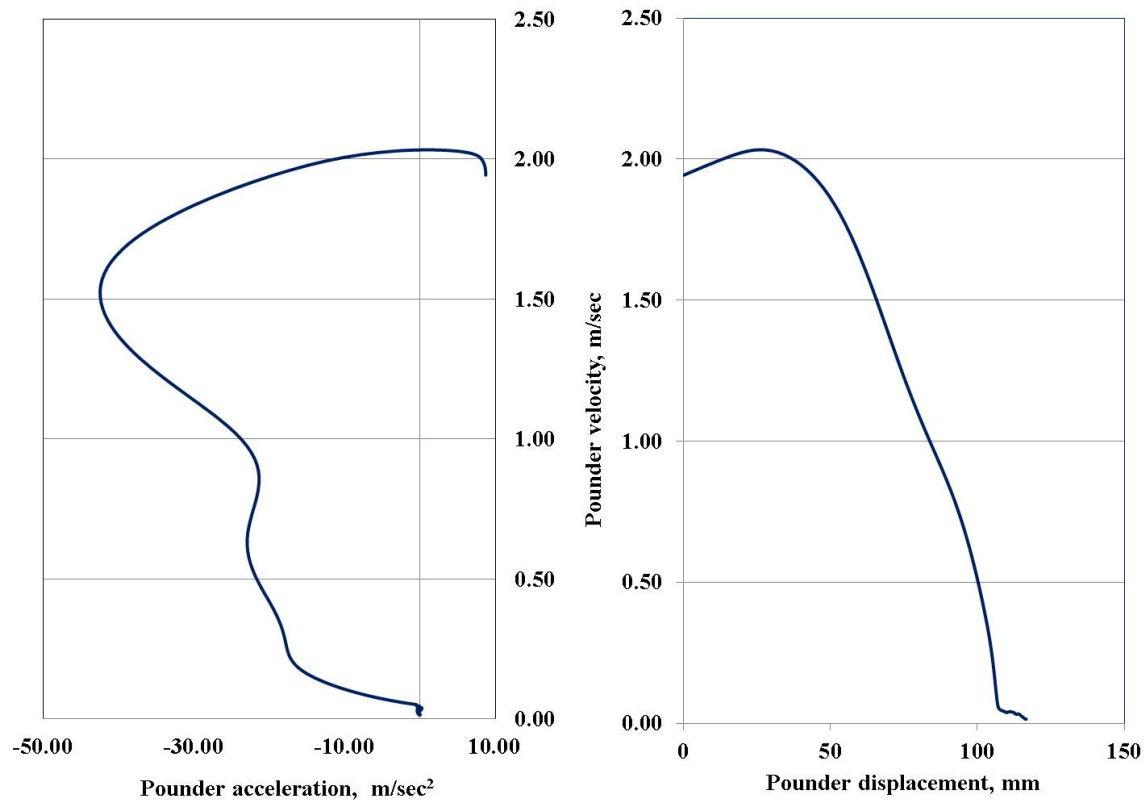


Figure 6.23. Typical after impact pounder deceleration and displacement versus pounder penetration velocity (drop 1 test DC1).

Typical time histories of soil accelerations measured by accelerometers embedded in the soil body at depths of 100, 200 and 300mm are shown in Figure 6.24. The figure shows the attenuation of the soil acceleration amplitude due to the passing compressive stress wave as it travels from the point of impact at the soil surface through the soil.

However, the magnitudes of the signals' peaks are more distinct than the signals' arrival times. According to the time shift between impact time (determined by inspecting the pounder acceleration signal) and acceleration peaks during drop 1 of DC2, the impact wave has travelled at a speed of 77m/sec between point of impact and the first target at 100mm before reducing to about 50m/sec travelling between the three accelerometers. The peak soil acceleration declines significantly with depth as the energy transmitted is decreasing due to radiation damping and energy dissipation mechanisms.

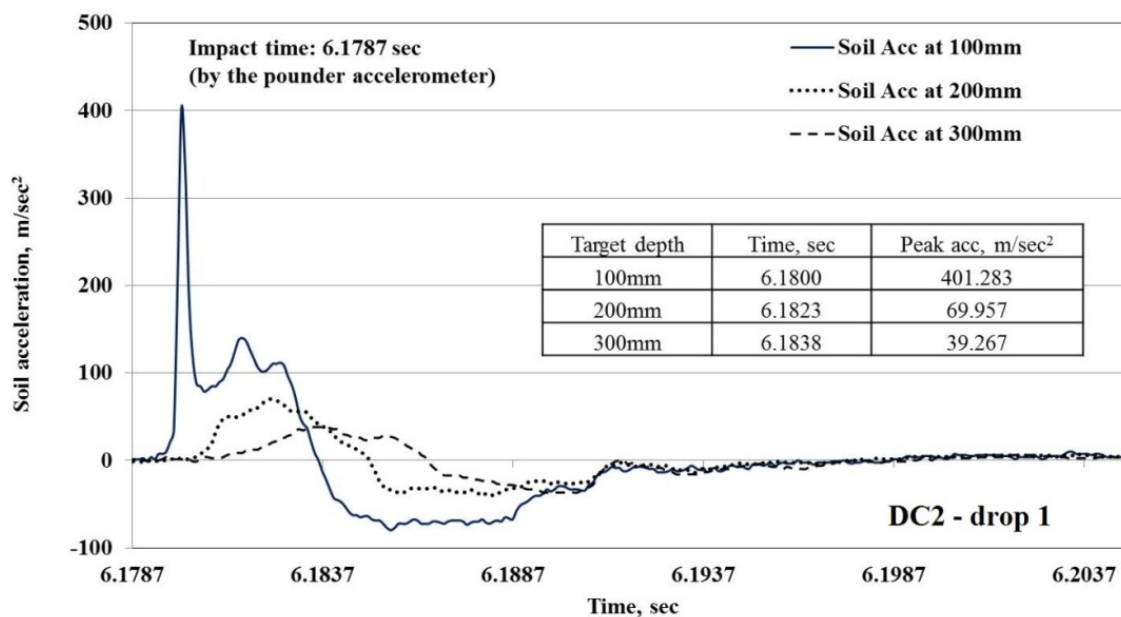


Figure 6.24. Typical time domain signals of the dynamic soil acceleration (drop 1 of DC2 - Dr: 95%).

Typical time domain responses of the dynamic pressures measured by the earth pressure cells embedded in the soil at depths of 50 and 150mm, measuring the vertical stresses along the impact centreline, and at a depth of 150mm attached to the model container sidewall, measuring the lateral stress, are shown in Figure 6.25. The figure also shows time domain responses of the impact stresses from the EPC mounted flush with the pounder base and the pounder acceleration signals. The unloading responses of the EPC signals were adjusted to account for the non-linear unloading responses of the EPC calibrations (*Section 3.2.7.1*).

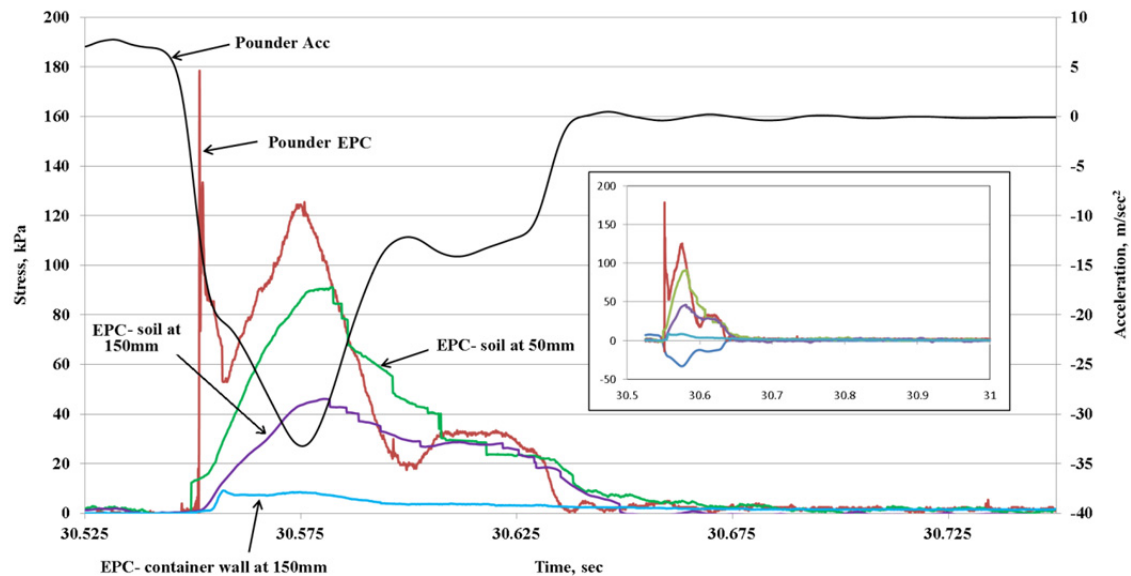


Figure 6.25. Typical time domain signals of soil dynamic pressure measured by earth pressure cells during drop 1 of DC11.

The attenuation of the amplitude of the pressure signals due to the compressive stress wave as it travels from the point of impact at the soil surface through the soil bed is clear. Similarly to the soil accelerometer signals, the magnitudes of signals from the stress cells are more distinct than the signals arrival times. The sudden after impact decrease, followed by the less rapid increase in impact stress recorded by the pounder EPC shown in Figure 6.25 could be a result of a slightly uneven sand surface. From Figure 6.25, soil stresses by EPCs are consistent with the target depths. These typical instrumentation results confirm the relatively low stress levels in the soil away from the centreline of the impact (less than 10 kPa by the EPC attached to the model container sidewall at 150mm depth). The residual low stress by the EPC at the container wall implies a coefficient of lateral earth pressure of 2 which is consistent with the at rest coefficient of lateral earth pressure " k_0 " of 0.435 measured from the 1-D compression tests (*Section 3.6*) and the limiting coefficient of passive earth pressure " k_p " of 3.

Typical after impact pounder deceleration records are shown in Figure 6.26. The increase in pounder acceleration maximum amplitude and the shortening of time to the arrival peak with increased number of drops indicates an increase in the soil stiffness beneath the impact footprint. This increase in soil stiffness is the reason for the increased impact stress (Figures 6.13 and 6.17a) and dynamic settlement modulus (Figure 6.12) with subsequent drops. Time

domain responses of poulder displacements have then been obtained by double integration of poulder acceleration signals.

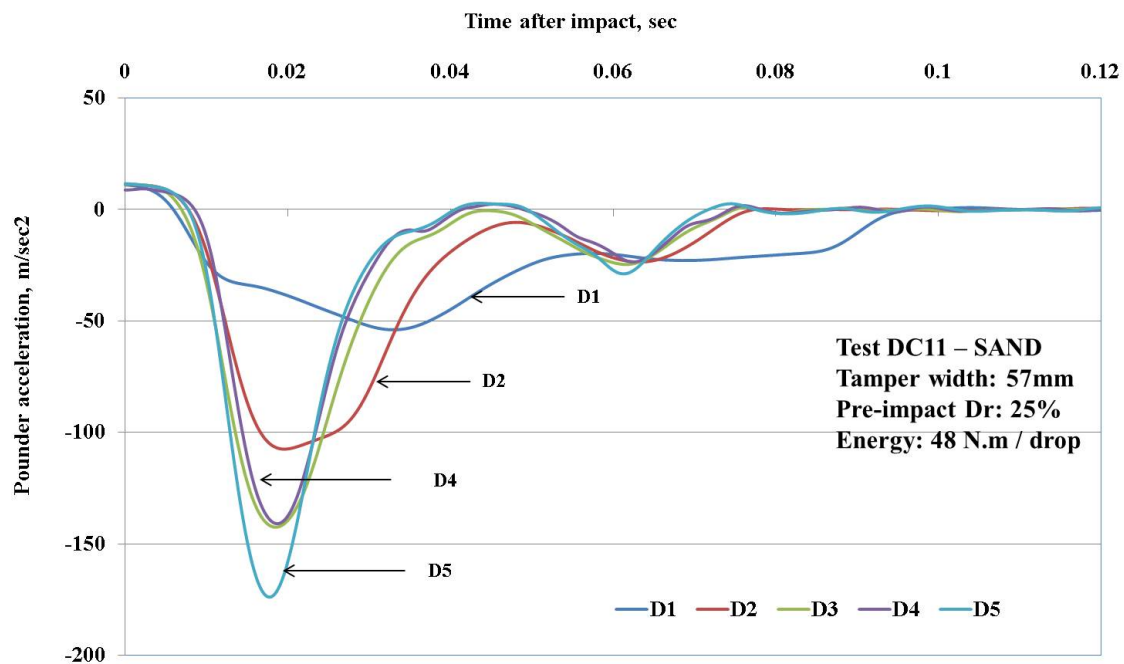


Figure 6.26. Records of after impacts poulder accelerations (decelerations).

Figure 6.27 shows records of poulder displacements (by double integration of poulder accelerations) from selected impacts due to two different imparting energies on near identical sand models. Poulder penetration is clearly a function of the impacting energy as can be seen from the nearly double the penetration in drop 1 of DC27 compared to drop 1 of DC24 as a result of doubling the drop height. The dynamic settlement modulus, which is a function of the impact stress and poulder displacement (*Eq.6.6*), increases by the increased impact stresses and decreased poulder displacement with subsequent drops as shown in Figure 6.12. On the other hand, the work done by the poulder remains relatively steady since it is the product of an increasing impact forces and reducing poulder displacements. This relatively uniform work provides the linear relationships between accumulated works and number of drops shown in Figure 6.16.

Figure 6.28 shows examples of computed net impact force and poulder work. The history of the dynamic stress after impact was also determined by plotting the impact stress versus the poulder strain (poulder relative displacement with respect to poulder width) as shown in Figure 6.29.

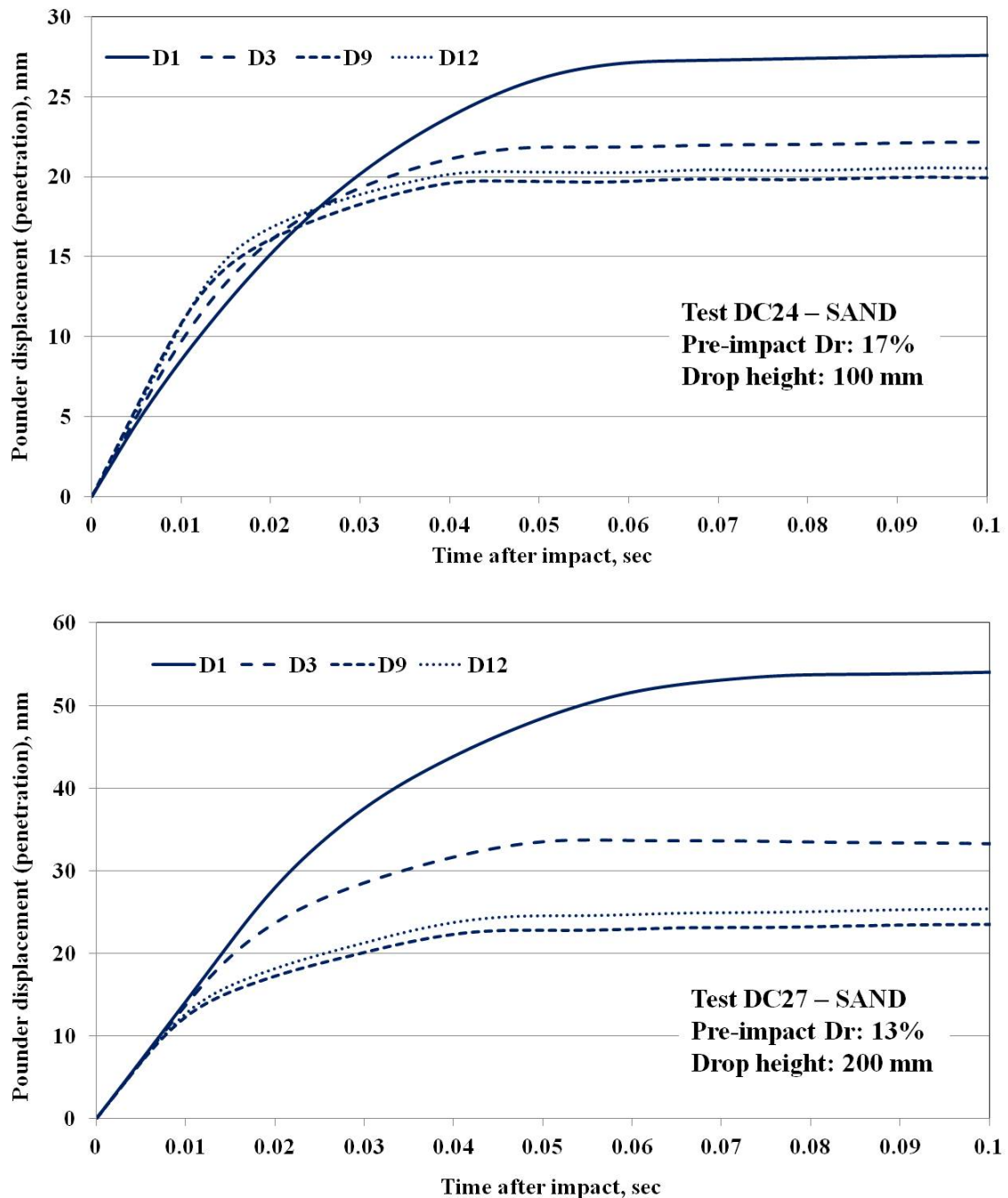


Figure 6.27. Poulder displacements (by double integration of poulder accelerations).

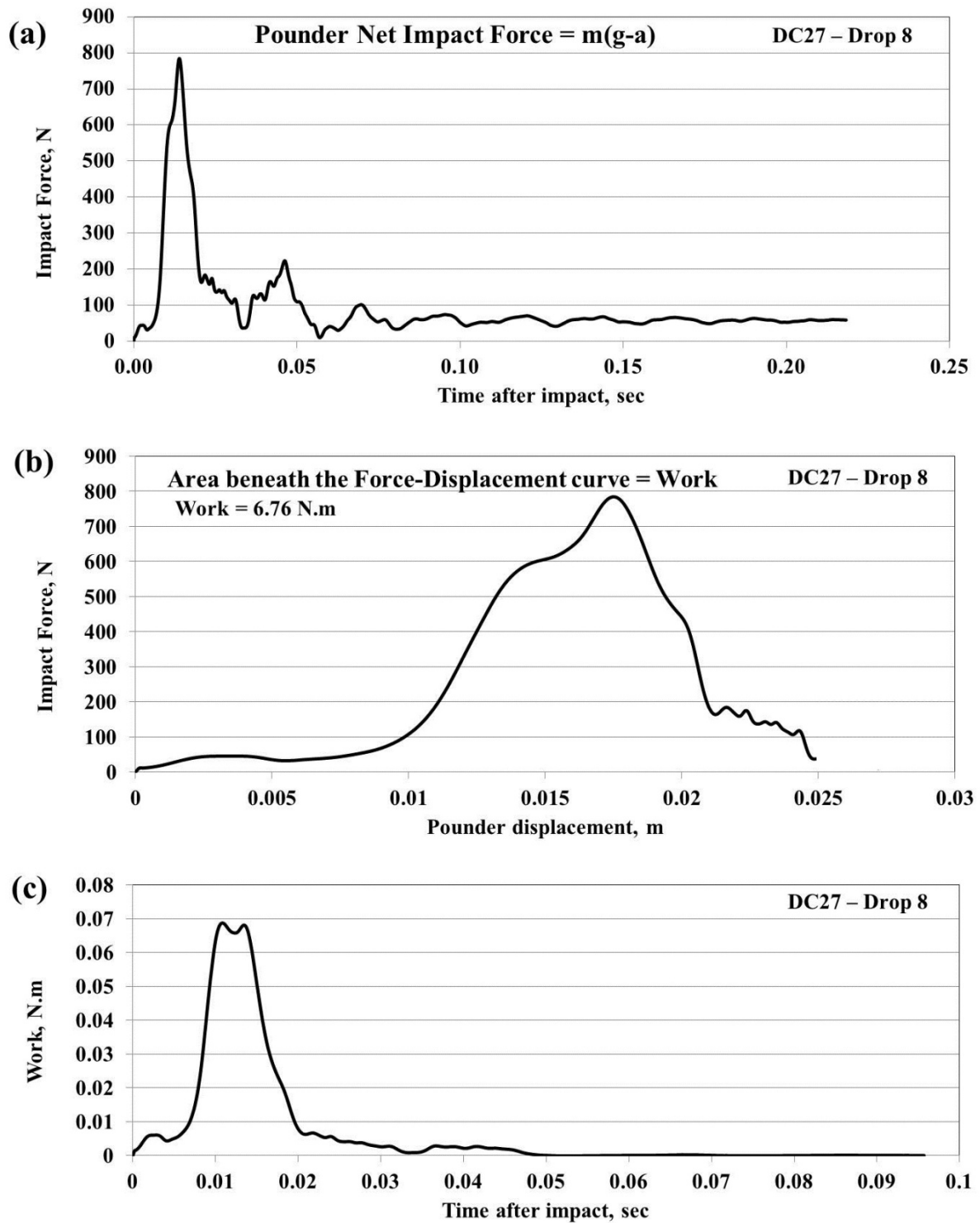


Figure 6.28. Examples of pounder net impact force history (a), pounder net impact force vs. displacement (b) and history of work done by the pounder (c).

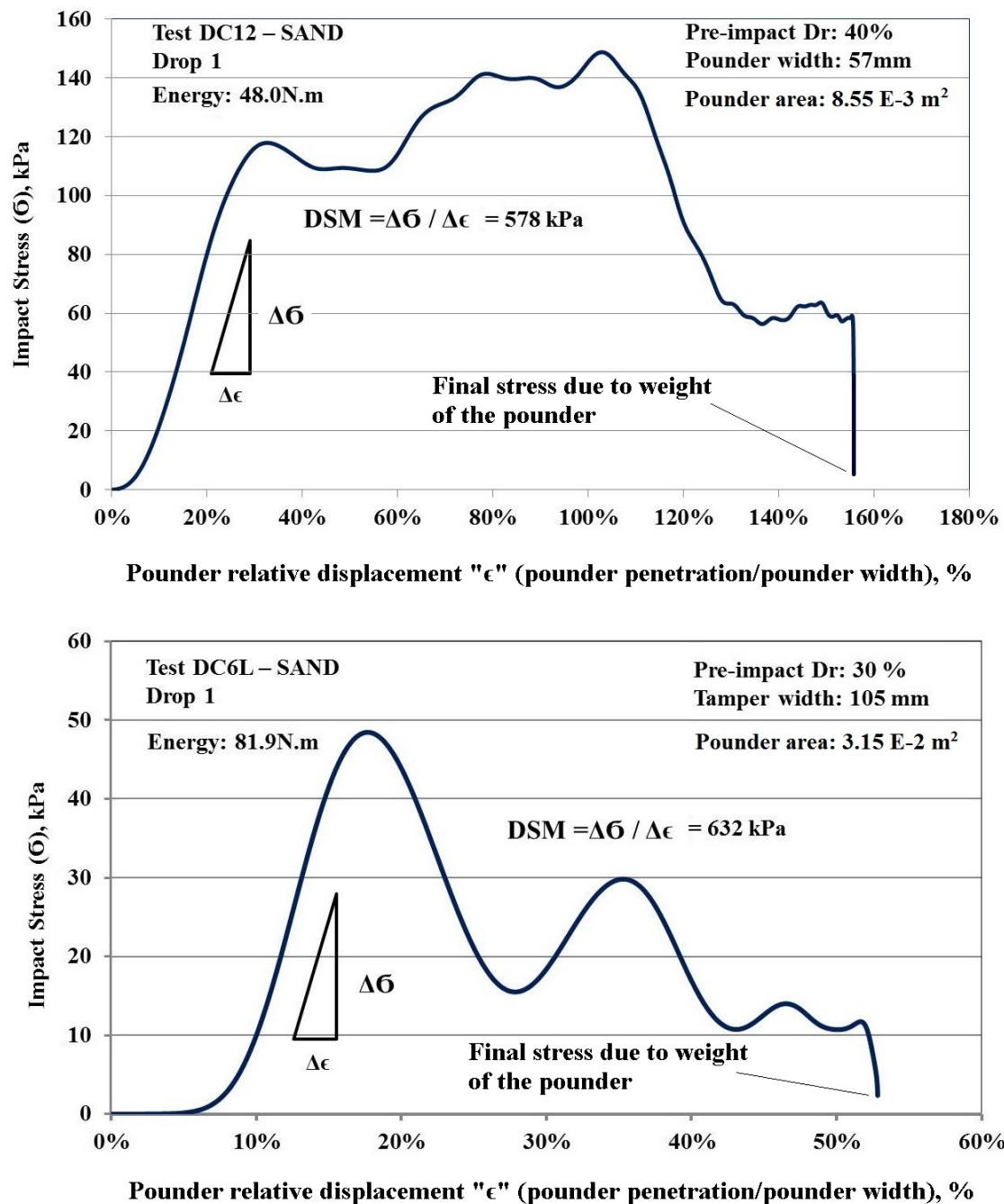


Figure 6.29. Poulder impact stresses verses poulder relative displacements (strain) from two different setups (poulder widths, energy levels and model sizes).

6.6 SUMMARY

Results from the poulder acceleration signals have been used to estimate the poulder velocities, displacements and impact forces and have proved to be very useful in establishing the simple physics of the DC impacts and have allowed the amount of external work delivered to be estimated. Soil accelerations have provided valid indications of the changes in soil response with respect to repeated impacts. Velocities of shock wave fronts were calculated from differences between the arrival times among accelerometers embedded at different levels within the models. Since wave speed in the soil is proportional to soil density, information of wave speed should be very helpful in assessing the degree of achieved densification during DC tests. However, the results were scattered and not very conclusive.

Consistency between the displacements estimated from the instrumentation signals and from GeoPIV have provided confidence in the precision of the photography technique in tracking the soil behaviour during dynamic loading. The least valuable instrumentation results were obtained from the soil stress sensors (EPC). These sensors provided a qualitative picture of the stress changes occurring in the soil and at the tank boundary. However, the results were not repeatable and thus there are concerns about the value of these data.

Chapter VII: Simulation of Dynamic Compaction by Finite Element LS-DYNA Code

Table of Contents

7	OVERVIEW	238
7.1	THE LS-DYNA CODE.....	238
7.2	LS-DYNA SYSTEM OF UNITS.....	239
7.3	SELECTION OF SOIL MODELS.....	240
7.4	LABORATORY TESTS TO CHARACTERISE THE GEOMATERIALS	240
7.4.1	Derivation of Soil Parameters for LS-DYNA Material Model.....	243
7.5	MODEL DEVELOPMENT	245
7.6	SENSITIVITY STUDY	248
7.6.1	Sensitivity of the results to the FE mesh size	248
7.6.2	Sensitivity of the Soil Model Material Parameters	251
7.6.3	Model Stability.....	255
7.6.4	Lagrangian verses ALE models	256
7.6.5	Summary of preliminary sensitivity analysis.....	258
7.7	SIMULATION RESULTS.....	258
7.8	SUMMARY OF THE LS-DYNA MODELLING RESULTS.....	274

7 OVERVIEW

The objective of this chapter is to investigate the suitability of the LS-DYNA finite element code and selected LS-DYNA material models to simulate soil response under dynamic loading conditions. Simulations were intended to reproduce the physical models of the DC experimental work presented in Chapters 5 and 6. The chapter presents the material models used in the simulations and describes the process used to select the soil model parameters.

Comparisons between the numerical simulations and physical DC model tests are discussed along with any areas of agreement and discrepancies between the two sets of results.

7.1 THE LS-DYNA CODE

LS-DYNA is a nonlinear explicit computer code with a movable mesh solution. It currently contains around two-hundred material models (including 11 possible soil models) of different capabilities. The LS-DYNA soil models possess the ability to handle post-failure responses and strain rate effects to simulate various strain dependent and dynamic applications of geomaterials. The LS-DYNA material models that are intended to simulate geomaterials are listed in Table 7.1.

The LS-DYNA solution methodology is based on explicit integration by contact-impact algorithms that permit difficult contact problems to be simulated. Spatial discretisation is achieved by the use of shell or rigid bodies with a large variety of element types and formulations.

The pre and post modelling for this work was developed on a personal computer while the code execution was performed by the National Computational Infrastructure (NCI) supercomputers. Outputs and results were then downloaded to a personal computer for analysis.

Table 7.1. LS-DYNA possible Geomaterial models

Model no.	Model Name	Material properties	Post Failure Modelling	Strain rate
MAT_005	Soil & Foam	Foam/Soil	N	N
MAT_025	Inviscid Geologic cap	Soil	N	N
MAT_192	Soil Brick	General	N	N
MAT_193	Drucker-Prager	General	N	N
MAT_014	Soil & Foam with Failure	Foam/Soil	Y	N
MAT_078	Soil Concrete	Soil	Y	N
MAT_079	Elasto-Perfectly Plastic Soil	Soil	Y	N
MAT_016	Pseudo Geological Model	Soil/Concrete	Y	Y
MAT_026	Honeycomb	Foam/Soil	Y	Y
MAT_072	Concrete Damage	Soil/Concrete	Y	Y
MAT_096	Brittle damage	concrete	Y	Y

7.2 LS-DYNA SYSTEM OF UNITS

The LS-DYNA software has no default unit system but users need to provide all the values in a consistent system of units according to which the results are provided. There are 15 systems of units the users can select from. Table 7.2 provides the system of units chosen for this work. As points of reference, density and Young's modulus of steel, gravitational acceleration and an arbitrary velocity are provided in this system of units.

Table 7.2. Selected consistent system of units for LS-DYNA inputs and results

Mass	Length	Time	Force	Stress	Energy	Density	Young's Modulus	velocity 10m/sec	Gravitational Acceleration
kg	mm	ms [*]	kN	GPa	kN.mm	7.83E-06 kg/mm ³	2.07E+02 GPa	10 mm/ms	9.81E-03 mm/ms ²

* ms: millisecond = 1/1000 second

7.3 SELECTION OF SOIL MODELS

The soil and foam models (MAT_005 and MAT_014) are among the basic geomaterial models available in LS-DYNA. However, they are quite robust and have long well documented usage in modelling geotechnical problems (Fasanella *et al.*, 2008, Qin *et al.*, 2008 and Bojanowski *et al.*, 2010) that involve large soil deformations. The two models are essentially the same except that material model type 14 does not allow the soil elements to carry tension when the pressure reaches the failure pressure. Both material models are simple and work in some ways like a fluid and can only be used to simulate situations when soils are confined within a structure or when geometric boundaries are present. The Material model MAT_014, essentially an extended version of MAT_005, was chosen to perform the finite element simulation of the DC tests of this work. The theoretical backgrounds of these two soil models (extracted from the LS-DYNA theory manual) are listed in Appendix IV.

7.4 LABORATORY TESTS TO CHARACTERISE THE GEOMATERIALS

Soil laboratory testing such as uniaxial compression tests and triaxial tests are needed so the material model parameters in appropriate constitutive models can be derived. The MAT_014 model requires a minimum amount of input data, and hence material characterization. The soil characteristic parameters required for the LS-DYNA material input card are listed in Table 7.3.

Table 7.3. List of soil parameters required for LS-DYNA material 014 input card

Characteristic input	Description	
RO	Mass density	
G	Shear modulus	
BULK	Bulk modulus (unloading)	
PC	Pressure cutoff for tensile fracture	
A0, A1 and A2	Yield function coefficients for plastic yield function.	
VCR	Volumetric crushing option (default VCR= 0)	
REF	Use reference geometry to initialize the pressure (default REF= 0)	
EPS1-EPS10	Logarithmic volume strains	Stress-volume strain relationship
P1-P10	Corresponding pressures for EPS1-EPS10	

The pressure-volume strain relationship can be determined from uniaxial compression or triaxial tests. The relationship that describes the compaction behaviour of soil materials is shown schematically in Figure 7.1, where four typical phases of geomaterial compaction response can be recognised. These phases are:

1. $P_0 < P < P_1$ is the initial elastic response. The slope of this segment is the elastic bulk modulus, K ,
2. $P_1 < P < P_2$ is when the voids are compressed (non-reversible).
3. $P > P_2$ fully compacted material (removal of voids).
4. The slope of the unloading segment (IV) represents the unloading bulk modulus, K_{un} , which is a user input for the soil material model.

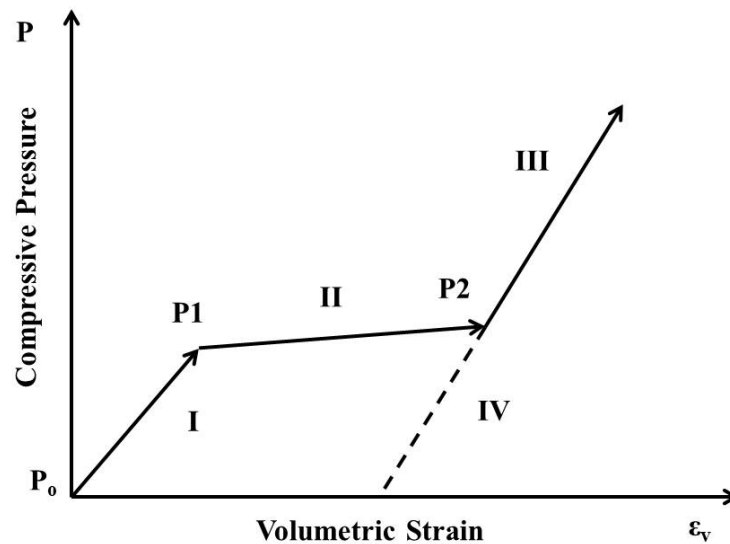


Figure 7.1 Schematic of geomaterial general compression response

It is important to note that LS-DYNA expects strain to be input as true strain (natural logarithmic strains). Volumetric strains “ ε_v ” can be converted to logarithmic volumetric strain using the following relation:

$$\ln \frac{V}{V_0} = \ln(1 + \varepsilon_v) \quad (7.1)$$

Where V_0 and V are the initial and current volumes at any loading stage. The conversion becomes more significant for volumetric strains greater than 10%. According to LS-DYNA

theoretical manual, the shear failure envelope for MAT_005 and MAT_014 has the following form written in terms of a quadratic pressure as (Fasanella *et al.*, 2009):

$$\text{Shear failure envelope, } \sigma_s = \frac{1}{2} S_{ij} S_{ij} = (A_0 + A_1 p' + A_2 p'^2) \quad (7.2)$$

where, p' , is the mean effective pressure, S_{ij} is the deviatoric stress tensor, and the “A” coefficients are determined from triaxial compression tests. In a compression test, stress difference, q , is the difference between the axial stress, σ_a , and the confining stress, σ_c , and the maximum stress difference, q , is determined when shear failure takes place. Test data is normally plotted with the mean effective stress, p' , on the X-axis and the stress difference, q , on the Y-axis. This plot provides the shear strength envelope or the yield surface of the soil from which the values of the “A” coefficients can be determined.

The left hand side of Eq 7.1 is the stress invariant J'_2 associated with soil shearing. By expanding the stress tensor, it can be shown that:

$$J'_2 = \frac{1}{3} (\sigma_c - \sigma_a)^2 = \frac{1}{3} (q)^2 \quad (7.3)$$

Therefore, a linear fit of the mean effective stress, p' , versus the stress difference, q , gives a form

$$q = mp' + C \quad (7.4)$$

where m is the slope of the yield line and C is the Y-intercept (apparent cohesion of the soil). Since the cohesion is very small or non-existent in the case of sandy soil, then $C=0$. By squaring Eq 7.3:

$$\frac{1}{3} (q)^2 = \left(\frac{1}{3} m^2\right) p'^2 + \left(\frac{2}{3} mC\right) p' + \frac{1}{3} C^2 = A_0 + A_1 p' + A_2 p'^2 \quad (7.5)$$

The coefficients A_0 , A_1 , and A_2 are found by equating the coefficients in Eq 7.4. For the case where C equals zero or is very small, then A_0 and A_1 will approach zero and A_2 will be the only remaining term and is equal to $1/3$ the square of the slope of the yield curve. The governing relationship between yield surface coefficients and the soil friction angle is

considered as a special kind of cap model, but the cap is a plane cap in principal stress space similar to Druker and Prager yield criterion (Krieg, 1972).

7.4.1 Derivation of Soil Parameters for LS-DYNA Material Model

A series of uniaxial (oedometric) strain compression tests and triaxial tests were performed to determine the shear strength parameters and the compression response of the modelled sandy soils. Loose densities and low stress levels were deployed in the uniaxial compression tests to depict the pre-impact soil densities and stress levels exhibited in the soil from the DC tests. In the uniaxial compression tests, soil specimens were placed in an oedometer ring, which prevents lateral displacement, and axial compressive loads were applied (outlined in *Section 3.6*).

The stress-strain responses from uniaxial compression and triaxial tests performed on dry sand and sand:silt mixture are shown in Figures 7.2 and 7.3 (note that axial and volumetric strains are equal in uniaxial compression). These responses are referred to as “SA” and “SSL” for sand and sand:silt mixture respectively. The compression response could not be accurately determined from triaxial tests on dry specimens. The response from a triaxial test of a saturated specimen is shown in Figure 7.2. The results from this test are broadly consistent with uniaxial test results and support the use of the uniaxial responses in the numerical analysis.

Triaxial tests were performed on specimens made of Sydney sand and sand:silt mixtures to measure the dynamic properties (small-strain shear modulus (G_{\max}) and unloading bulk modulus) of the soils. Parameters used to define the soil materials in accordance with MAT_014 formulation are listed in Table 7.4. Typical shear failure envelopes from compression triaxial tests on sand and sand:silt specimens indicated failure envelopes with ϕ' of about 35° and $q=1.4p'$ (triaxial testing results are provided in Appendix V). The adopted shear and bulk moduli values are also consistent with typical values for the sandy soils (Salgado *et al.*, 2000). It is important to note that soil moduli may vary significantly with the stress level in the soil. Therefore, and for validation purposes, the range of soil densities and moduli were set to the conditions of the DC experimental work.

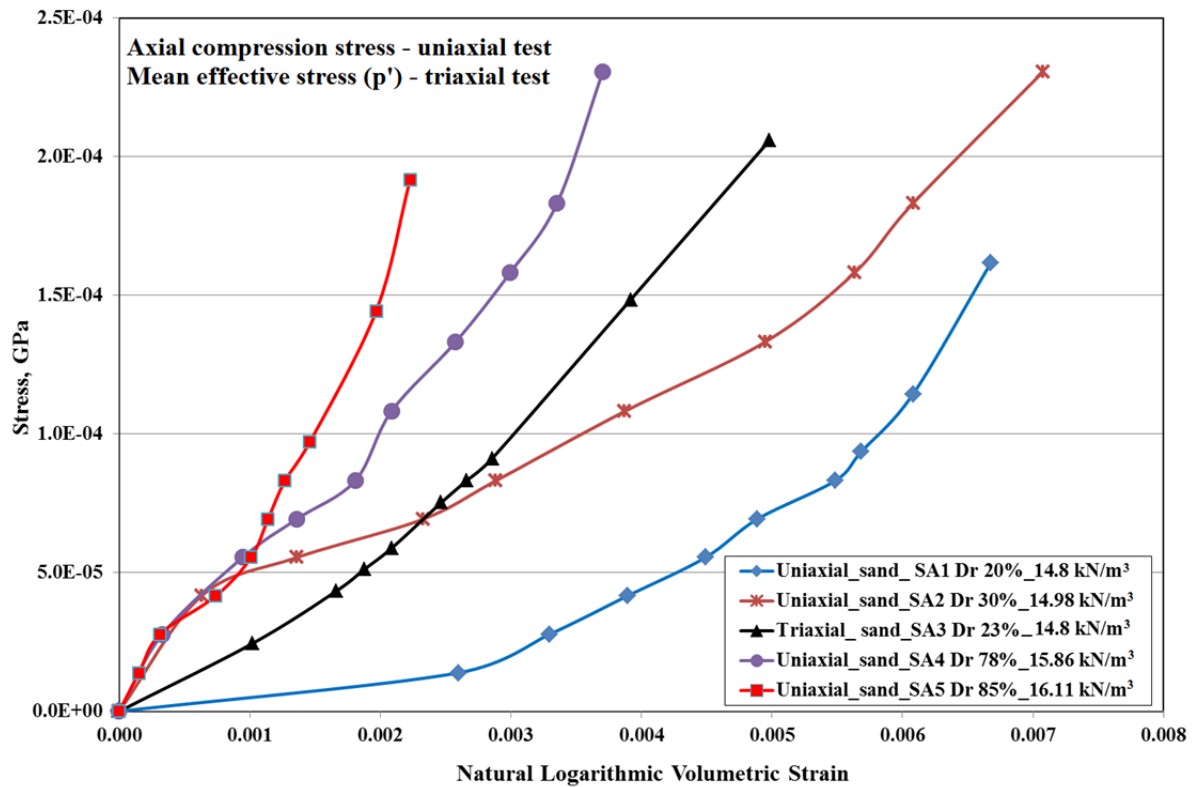


Figure 7.2. Triaxial and uniaxial compression response (strain dependency) of sand

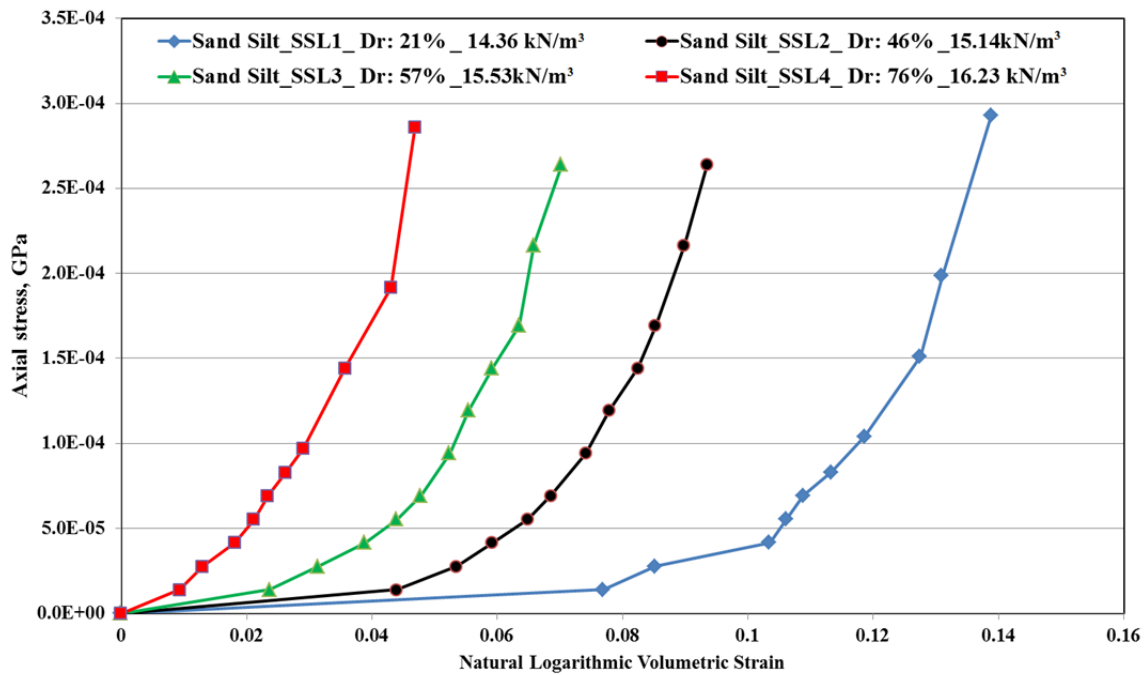


Figure 7.3. Uniaxial compression response (strain dependency) of sand:silt mixture

Table 7.4. Parameters used to define the soil materials using MAT_014 formulation

Soil Parameters, (units)	Sand	Sand	Sand	2 Sand: 1Silt	2 Sand: 1Silt	2 Sand: 1Silt
	SA1	SA3	SA5	SSL1	SSL2	SSL4
RO, (kg/mm ³)	1.51E-06	1.51E-06	1.65E-06	1.46E-06	1.580E-06	1.650E-06
Shear Modulus, G (GPa)	0.03	0.04	0.06	0.02	0.03	0.04
Unloading Bulk Modulus, K _{un} (GPa)	0.065	0.085	0.13	0.043	0.065	0.087
PC (GPa)	0	0	0	0	0	0
A0	0	0	0	0	0	0
A1	0	0	0		0	0
A2	0.65	0.65	0.65	0.65	0.65	0.65
VCR	0 (on)	0 (on)	0 (on)	0 (on)	0 (on)	0 (on)
REF	0 (off)	0 (off)	0 (off)	0 (off)	0 (off)	0 (off)
EPS1-EPS10	Figure 7.2-SA1	Figure 7.2-SA3	Figure 7.2-SA5	Figure 7.3-SSL1	Figure 7.3-SSL2	Figure 7.3-SSL4
P1-P10, (GPa)	Figure 7.2-SA1	Figure 7.2-SA3	Figure 7.2-SA5	Figure 7.3-SSL1	Figure 7.3-SSL2	Figure 7.3-SSL4

7.5 MODEL DEVELOPMENT

The LS-DYNA models are made up of two body parts, two sections and two materials simulating the soil body and the falling assembly in the physical models as shown in Figure 7.6. The soil body was modelled as a box having the dimensions of either the small or the large containers. The steel pounder was modelled as a rigid body using the material type MAT_020_RIGID from the directory of LS-DYNA material models.

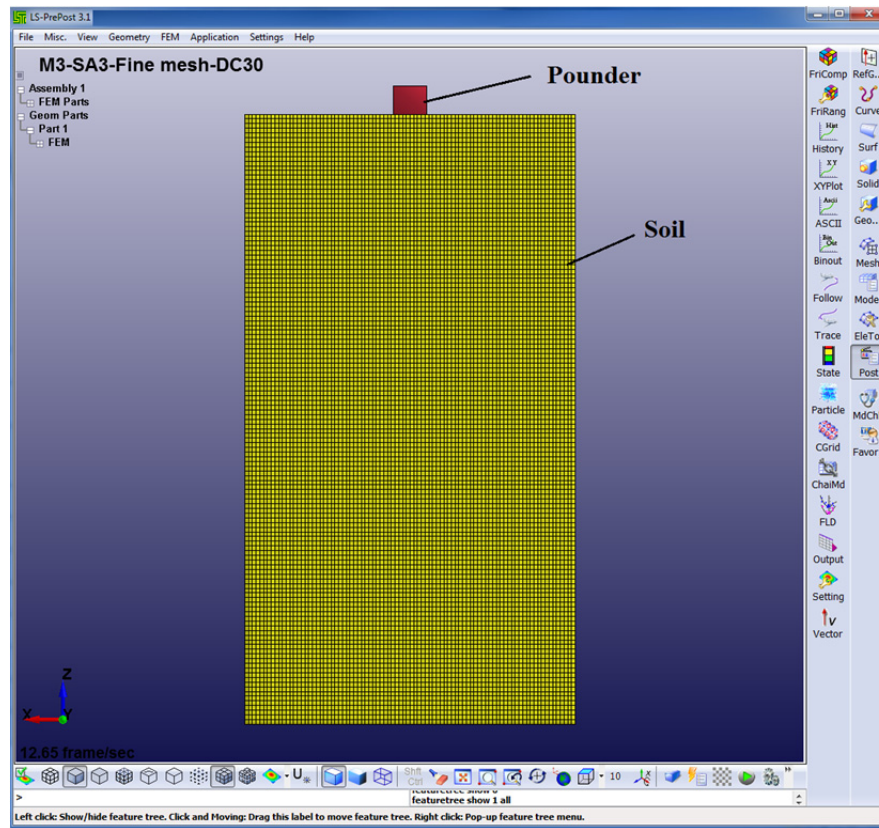


Figure 7.4. LS-DYNA two parts, two sections and two materials model

The poulder was modelled to have the same contact area as the simulated DC tests but was made to be 30mm high for all the simulations rather than modelling the whole falling assembly. Therefore modified steel densities were introduced in the simulations to achieve the actual mass of the falling assemblies during the DC tests being modelled. Impact velocities from the DC tests were applied in the model simulations. Except for the freely moving top surface of the soil body, the bottom and side faces of the soil body were constrained to simulate the confinement and rigidity of the steel and Perspex faces of the physical model container. Translational degrees of freedom (fixities) that correspond to boundary conditions of the 2-D plane-strain DC tests were applied.

The soil and poulder were modelled as two solid elements. Contact between the soil and the poulder was modelled using the LS-DYNA automatic type of contact. Since the orientation of parts relative to each other cannot always be anticipated as the model undergoes large deformations during DC simulation, the automatic contact is considered suitable for this application because this type of contact is non-oriented, meaning it can detect penetration coming from either side of an element.

Since the strength of the soil is pressure dependent in the MAT_014 soil model, gravitational load was introduced in the simulations to produce a pressure gradient with soil depth. Based on the displacement and strain field results from the high speed photography and the monitored timing of the poulder penetrations, a termination time of 100millisecond was used in the majority of the LS-DYNA models. This time is equal or greater than the time windows of up to 100 milliseconds (50, 75 and 100 images at the rate of 1/1000 fps) considered in the PIV analysis.

Traditionally, researchers and engineers have used three different types of finite element (FE) approaches to simulate large deformation problems in soils. These approaches are:

- 1 Lagrangian (LAG)
- 2 Arbitrary Lagrangian - Eulerian (ALE)
- 3 Smoothed Particle Hydrodynamic (SPH)

The Lagrangian approach represents the main finite element approach of the LS-DYNA software. Traditionally, it has been believed that the ALE approach can better deal with the mesh distortion problems normally confronted in high deformation simulations. However, it requires more time to adjust the contact parameters and requires more processing (CPU) time for the simulation. The SPH approach requires more CPU time unless a hybrid model is created with the SPH formulation in the region with expected high soil deformation and a Lagrangian or ALE formulation being used in regions of less distorted soil. This hybrid approach would have its own issues of dealing with interfaces along the contacts between the different elements of the soil material. The hybrid SPH approach would be more attractive in simulating further complicated soil structure interaction problems than the DC experiments of this work. A comparison study of the three FE approaches for modelling large soil deformation problems by Bojanowski *et al.*, (2010) showed marginal advantages of using the hybrid SPH approach over the Lagrangian or ALE approaches. The FE simulations conducted for this work were limited to the Lagrangian approach. However, preliminarily simulations were reproduced using the ALE approach for comparison and sensitivity analysis. A summary of the LS-DYNA models and the physical models they simulated are listed in Table 7.5. An example of LS-DYNA model is provided in Appendix IV.

Table 7.5. List of LS-DYNA models

LS-DYNA model ID- Soil response	DC test to simulate	Pounder width, mm	Mass of falling assembly kg	Volume of modelled pounder, mm ³	Equivalent density used in DYNA model, kg/mm ³	Impact speed, mm/ms
M1-SA3	DC11	57	16.34	256500	6.37E-05	2
M1-SA5	DC4	57	16.34	256500	6.37E-05	2
M2-SA3	DC24	35	5.91	157500	3.75E-05	1
M2-SA5	DC26	35	5.91	157500	3.75E-05	1
M3-SA3	DC30	35	5.91	157500	3.75E-05	1.5
M4-SSL1*	DC36	35	5.91	157500	3.75E-05	1.5
M4-SSL2	DC36	35	5.91	157500	3.75E-05	1.5
M4-SSL4*	DC36	35	5.91	157500	3.75E-05	1.5
M5-SA3 *	DC6L	105	11.13	945000	1.18E-05	2.5
M5-SA5 *	DC5L	105	11.13	945000	1.18E-05	2.5

Notes:

1. All models are based on Lagrangian approach.
2. "*" denotes coarse mesh configuration (see Section 7.6.1)

The DC simulations were limited to the first impact of the corresponding DC test as modelling repeated impacts requires an interactive contact approach that is not available in LS-DYNA. Attempts were made to simulate the static load tests presented in Section 5.1.1, but the results were irrelevant due to the limited capabilities of LS-DYNA implicit solver in solving slow statically loaded problems.

7.6 SENSITIVITY STUDY

7.6.1 Sensitivity of the results to the FE mesh size

Preliminary analyses using LS-DYNA showed the DC simulation results changed when employing coarse and fine uniform meshes. Slight variations in estimated penetrations, energies and stresses were observed as expected when using finer meshes in the FE models. Model M3-SA3 was selected as an example to demonstrate these effects. The soil body in model M3-SA3 was first generated with 42,900 elements as the basic "coarse" model and

then regenerated by adopting a fine mesh of 57,200 and then a very fine mesh of 236,250 soil elements. The effects of mesh size on poulder penetration, soil body internal energy and maximum shear stress (along the soil elements immediately beneath the poulder) are shown in Figures 7.5 to 7.7 to illustrate the influence of the mesh sensitivity on the LS-DYNA simulation results.

The FE results were found to be sensitive to the FE element size, yet all the compared models had the same material properties. Thus, these variations are the result of numerical issues. Soil elements of the smaller size meshes presented a softer medium for the solid poulder resulting in more penetration than the coarser mesh model as shown in Figure 7.5. This softer response from the fine meshes resulted in less of the poulder kinetic energy being transferred to the modelled soil bodies, resulting in less stored internal energy as shown in Figure 7.6. Results from poulder penetrations and soil internal energies suggest that no further improvement can be gained by refining the mesh of the soil body beyond the fine mesh.

On the other hand, the maximum shear stress in the soil elements located along the top surface of the soil body, directly beneath the poulder, straight after impact continued to increase with the number of elements. The maximum shear stress increased by about 26% and 9% as the mesh was refined from coarse to fine and from fine to very fine meshes respectively, as shown in Figure 7.7. It is known that oscillations can occur in the numerical solutions at locations of high-speed flow and in compressible elements around a shock, and this may be responsible for the different responses presented by the different size meshes.

Simulations adopting the very fine mesh configuration required large memory and long computation times and therefore were considered undesirable. The fine mesh model configuration made of 57,200 soil elements was considered robust enough to perform the simulations without compromising the results or requiring unnecessary computation. However, the preliminary sensitivity analysis investigating the performance of the simulations with respect to different soil models, the models stability and the FE approach were performed adopting the coarse mesh model. The coarse models are considered to be adequate to perform the remaining sensitivity analysis presented in the following sections and some of the final simulation results. Simulations performed adopting the coarse mesh configuration are listed in Table 7.5 with (*) next to the model name.

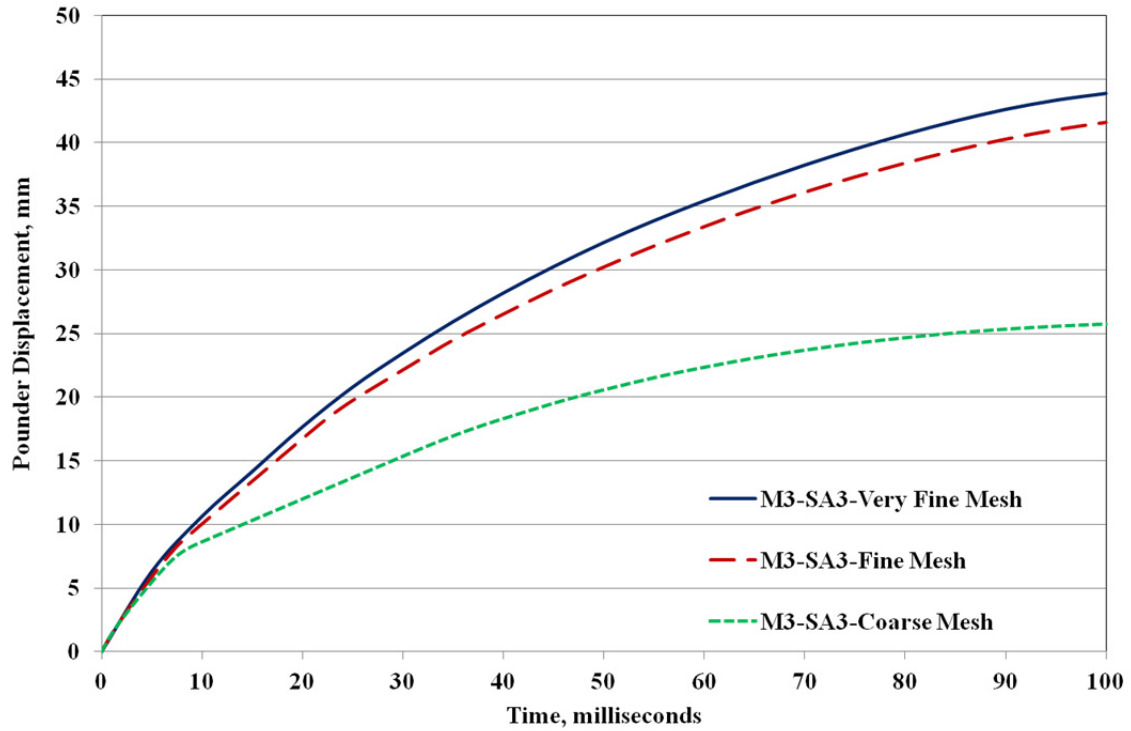


Figure 7.5. History of poulder displacements from the model M3 generated by three different mesh sizes.

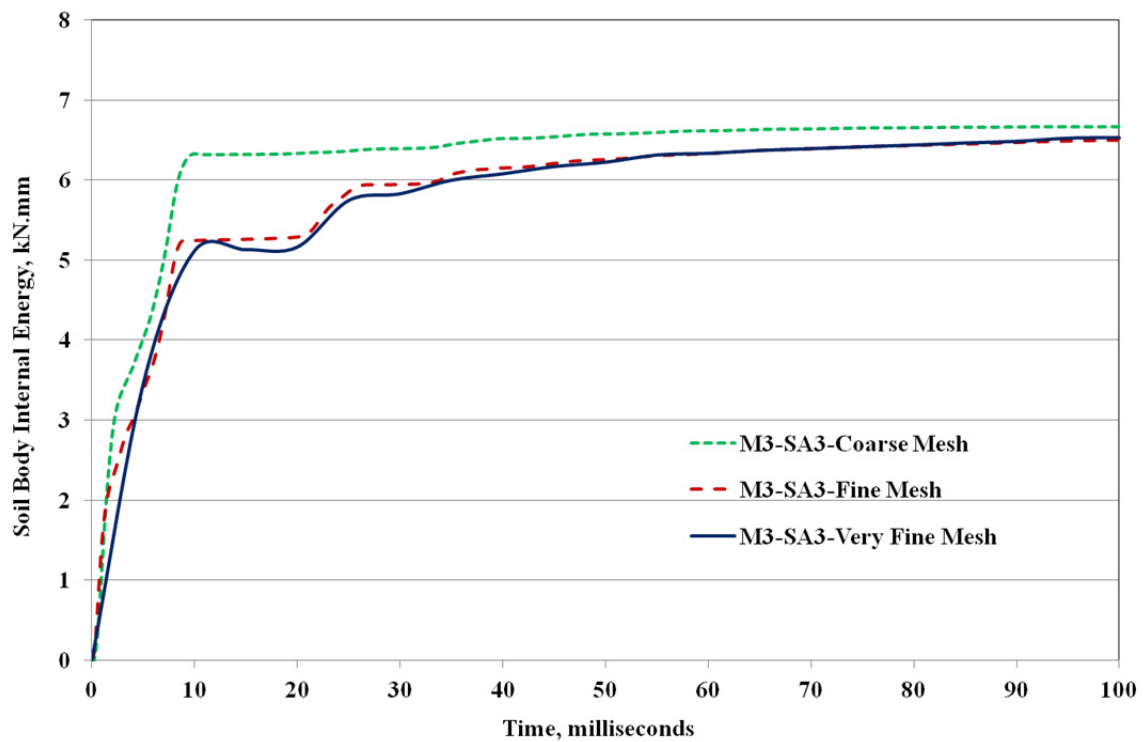


Figure 7.6. History of soil body internal energies from the model M3 generated by three different mesh sizes.

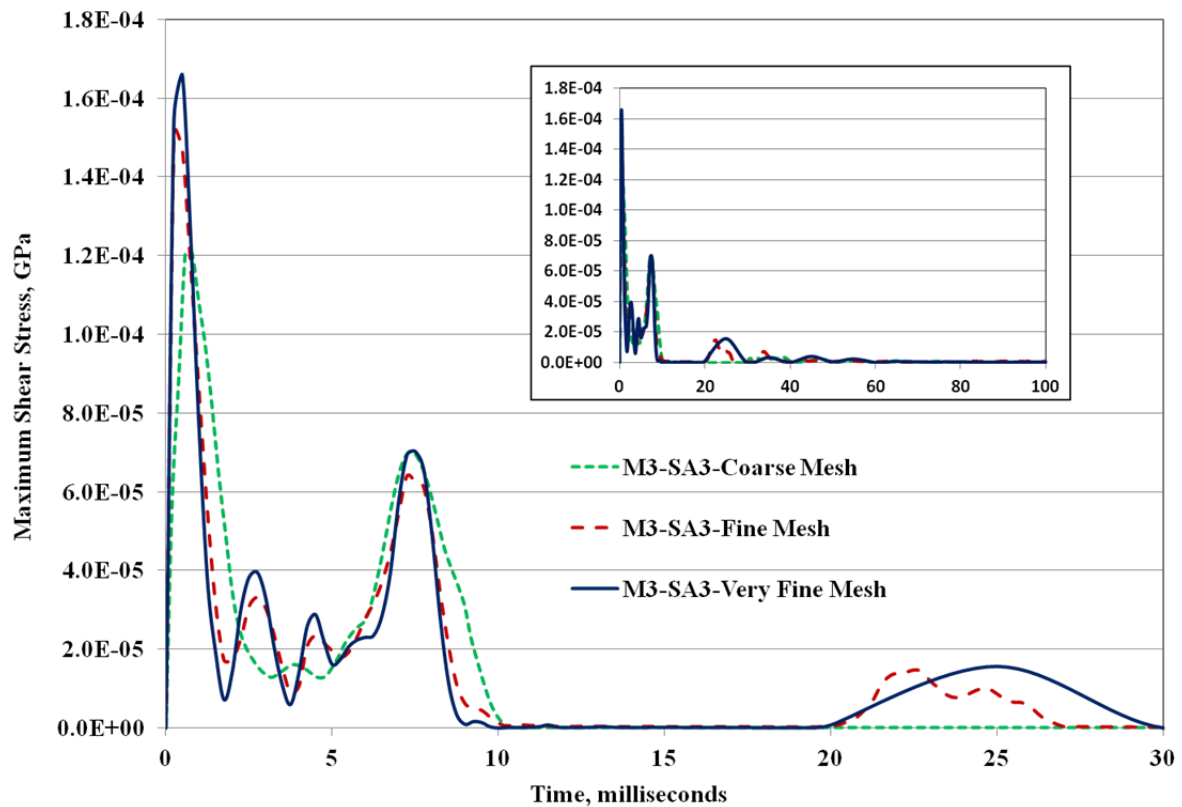


Figure 7.7. History of maximum shear stress in soil elements immediately beneath the impacting contact from the model M3 generated by three different mesh sizes.

7.6.2 Sensitivity of the Soil Model Material Parameters

To investigate the effect of the soil parameters on the modelling results, a sensitivity analysis was carried out by studying the effect of different soil densities, shear moduli, soil stiffnesses, the soil shear strength expressed by different values of the “A2” yield function coefficient and the stress-strain dependency of models M1-SA1, M1-SA5 and modified versions of model M1. The LS-DYNA sensitivity analysis models together with investigated variables are listed Table 7.6.

The poulder penetration is the most apparent LS-DYNA output and it can be used to scale the effect of varying soil parameters on the modelling output. Despite their inconsistency with the physically measured poulder penetrations during the DC tests (to be discussed later), resultant poulder penetrations decreased significantly with increased soil strength and were not significantly affected by changes of the other parameters.

Table 7.6. List of LS-DYNA sensitivity analysis models

LS-DYNA model ID	RO, (kg/mm ³)	Shear Modulus, G (GPa)	Unloading Bulk Modulus, K _{un} (GPa)	Yield function coefficient "A2"	Stress-strain dependency
M1-SA1	1.51E-06	0.03	0.065	0.65	SA1
M1A	1.51E-06	0.03	0.065	0.5	SA1
M1B	1.51E-06	0.03	0.065	0.4	SA1
M1C	1.51E-06	0.05	0.11	0.65	SA1
M1D	1.65E-06	0.03	0.065	0.65	SA1
M1-SA5	1.65E-06	0.06	0.13	0.65	SA5

The effect of soil properties on the penetration results are shown in Figures 7.8 and 7.9. The sensitivity analysis shows that the yield surface (A2 coefficient) has the most significant effect on the penetration results. A near 50% increase in predicted poulder penetration has occurred between M1-SA1 and M1B models by reducing the A2 coefficient from 0.65 (friction angle of 35°) to 0.45 (friction angle of 29°) as shown in Figure 7.9a.

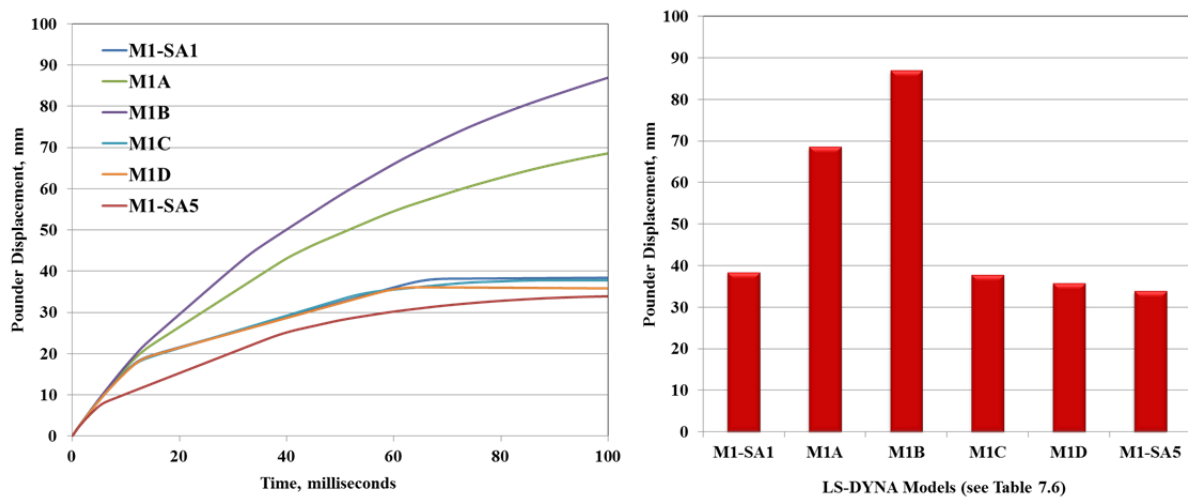


Figure 7.8. Effect of the soil model parameters on predicted poulder penetration

Increasing the soil stiffness (shear and bulk moduli) or soil density were found to have less effect on the poulder penetration as shown by Figures 7.9b and 7.9c, respectively. Variations in the predicted poulder penetrations of the two sand models SA1 and SA5 are shown in Figure 7.9d. The lesser penetration in the case of sand SA5 is due to combined effects of higher soil density, higher shear and bulk moduli (Table 7.6), and the strain-stress responses (Figure 7.2) of the SA5 soil model. However, the majority of the lesser penetration in the case of the SA5 sand must be related to the stress-strain response considering the minor effects of soil stiffness and soil density on the predicted penetration (Figures 7.9b and 7.9c).

Since internal energy includes elastic strain energy and work done in permanent deformation, the internal energies should be consistent with the displacement results among the investigated models listed in Table 7.6. Comparison of soil body energies was used to further compare the sensitivity of the soil material models on the FE analysis results and to have more confidence in the studied soil models. Figure 7.10 shows the time histories of the soil internal energies from five soil models, which indicates that the internal energies decrease as the poulder displacement increases.

The greater poulder penetration due to the softer soil of model M1B over the stiffer soils of models M1-SA1, M1C, M1D and M1-SA5 (Figure 7.9) is consistent with the higher internal energies stored in the soil bodies of these soils. Although the LS-DYNA models simulated the same impact, the models with stiffer soil bodies possessed more resistance to penetration and a greater portion of the poulder kinetic energy has transferred to the soil bodies as stored internal energy.

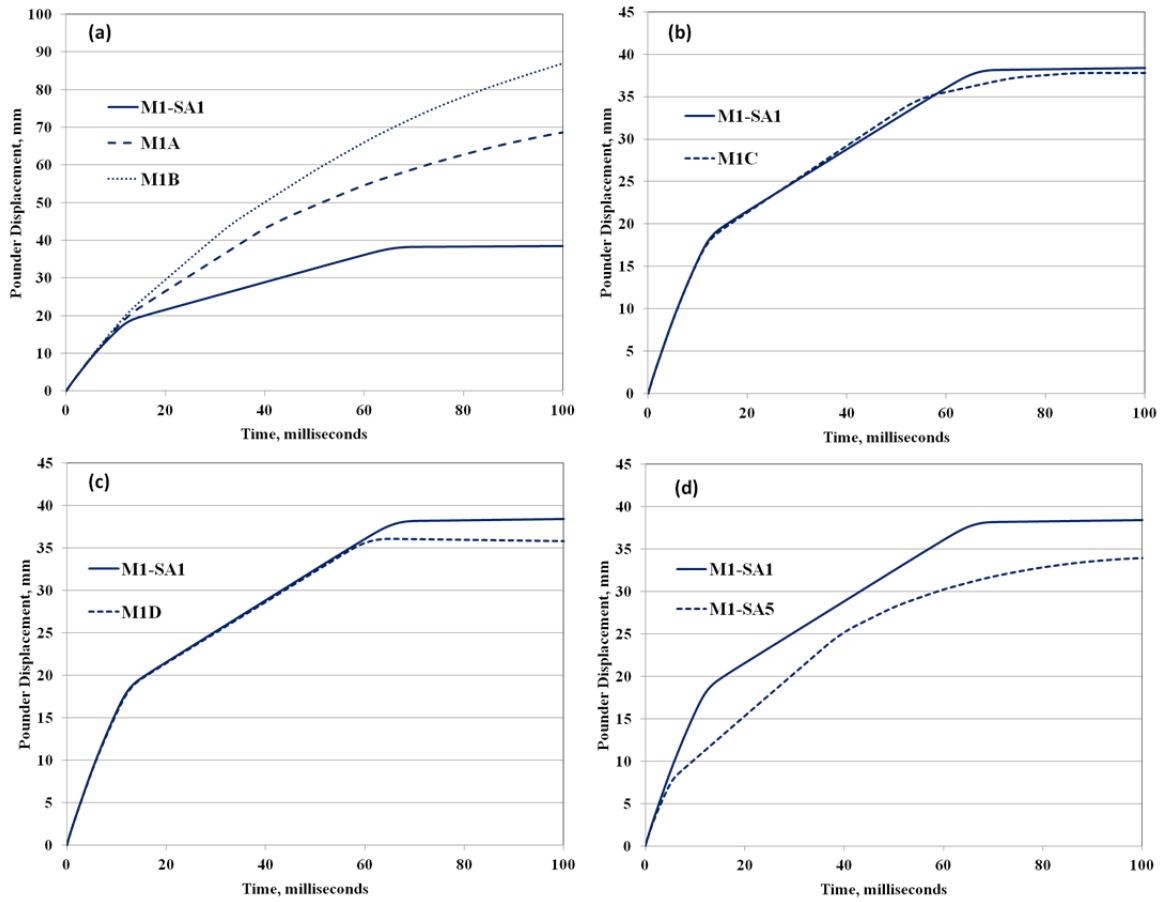


Figure 7.9. Effect of soil strength (a), stiffness (b), density (c) and stress-strain responses on predicted pounder penetration.

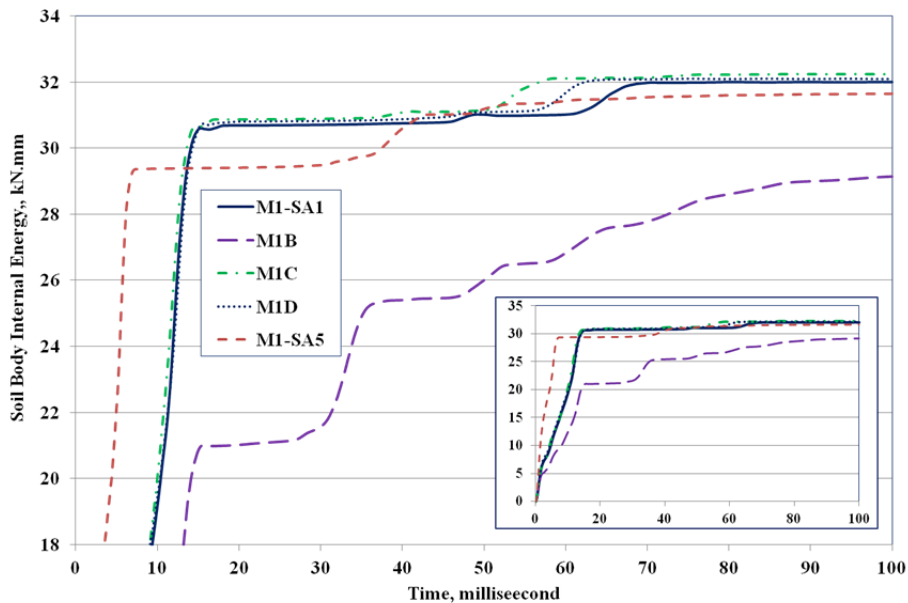


Figure 7.10 History of Soil body internal energies from four different soil model parameters.

7.6.3 Model Stability

Examining the balance of system energy components during a dynamic FE simulation can be useful in identifying the factors affecting the model response. Monitoring energy components is a key step in identifying the presence and causes of numerical instabilities that may arise in dynamic finite element impact simulations. In these simulation problems, a perfect energy balance is when the energy ratio is equal or close to 1.0 (Consolazio *et al.*, 2003). By considering the principle of the conservation of energy for a physical system, the energy ratio can be defined as:

$$\frac{T+W_{internal}-W_{external}+U_{dissipation}}{E} = 1 \quad (7.6)$$

where:

T: kinetic energy

W: work

$W_{internal} - W_{external}$ = potential energy

U_{dissipation}: energy dissipated by frictional forces, plastic deformation, and system damping

E: total energy

The energy ratios from the LS-DYNA simulations of this work were found to be between 1.035 and 1.065 in simulations modelling DC tests of sand and between 1.2 and 1.4 in the simulations modelling DC tests of sand:silt mixture. Thus, results from simulating the DC tests of sand are acceptable and the simulated DC models were considered stable. The unbalanced energies in the simulations of the sand:silt mixtures will be discussed in the following sections.

Another important requirement for stability in dynamic FE modelling is to minimise and prevent hourglassing. Hourglassing is a zero-energy mode of deformation in which oscillations occur at a frequency much higher than the body's global response. This zero-energy mode is mathematically stable, but is physically impossible, and it can result in an erratic deformed mesh. It is considered good modelling practice to keep the hourglass energy to less than 10% of the internal energy of the model. At the end of the analysis the internal soil body and hourglass energies from models M1-SA1, M1-SA3 M3-SA3, M4-SSL1 and M4-SSL2 (models with large deformed soil bodies and anticipated higher hourglassing) are shown in Figure 7.11. It can be seen that hourglass energy is much less than the internal

energy and the hourglass energy / internal energy ratios were 5% in the M3-SA3, 4% in M1-SA3 and 3% in the M1-SA1 and M4-SSL1 simulations respectively. The hourglass energy to internal energy ratio varied between 3.0 – 7% in the simulations reported in this chapter, which is considered to be acceptable.

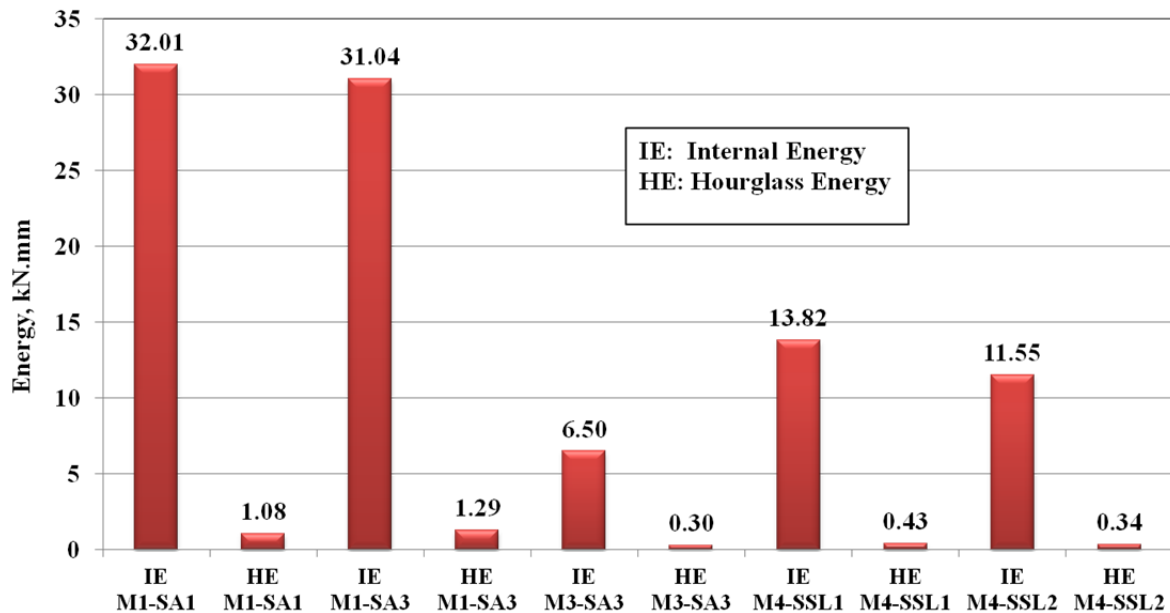


Figure 7.11. Total internal and hourglassing energies from M1 models.

7.6.4 Lagrangian versus ALE models

The sensitivity of the modelling results to the two FE approaches (Lagrangian and ALE) was also evaluated and the results from two preliminary simulations were found to be nearly identical. For example, poulder penetrations at the end of the analysis from the LAG models were found to be within $\pm 6.0\%$ of the corresponding penetrations from the ALE models. Figure 7.12 shows an example of the slight variation in the poulder penetrations by Lagrangian (M1A-LAG) and ALE (M1A-ALE) methods of analysis. Similarly, the maximum shear stress in the soil elements located at the impact frontline directly beneath the poulder reached similar peak values with slightly different attenuation as shown in Figure 7.13. The similar results from the two solution methods have been reported by others, as discussed above, and thus the more computationally efficient Lagrangian approach has been used in subsequent analyses.

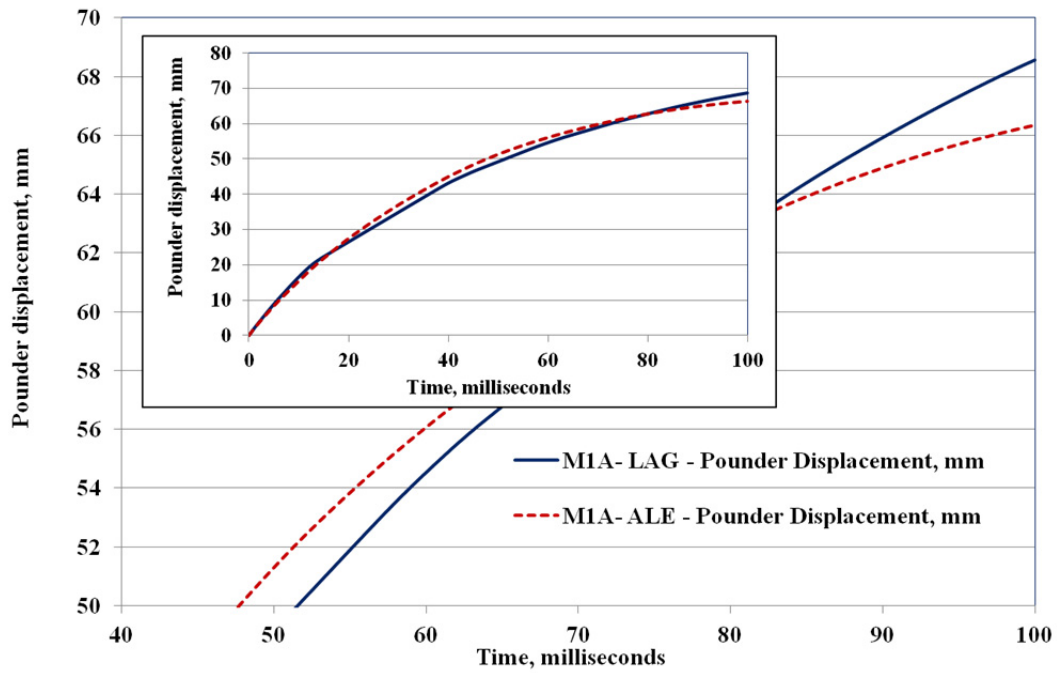


Figure 7.12. Ponder displacements from M1A-LAG (Lagrangian) and M1A-ALE models.

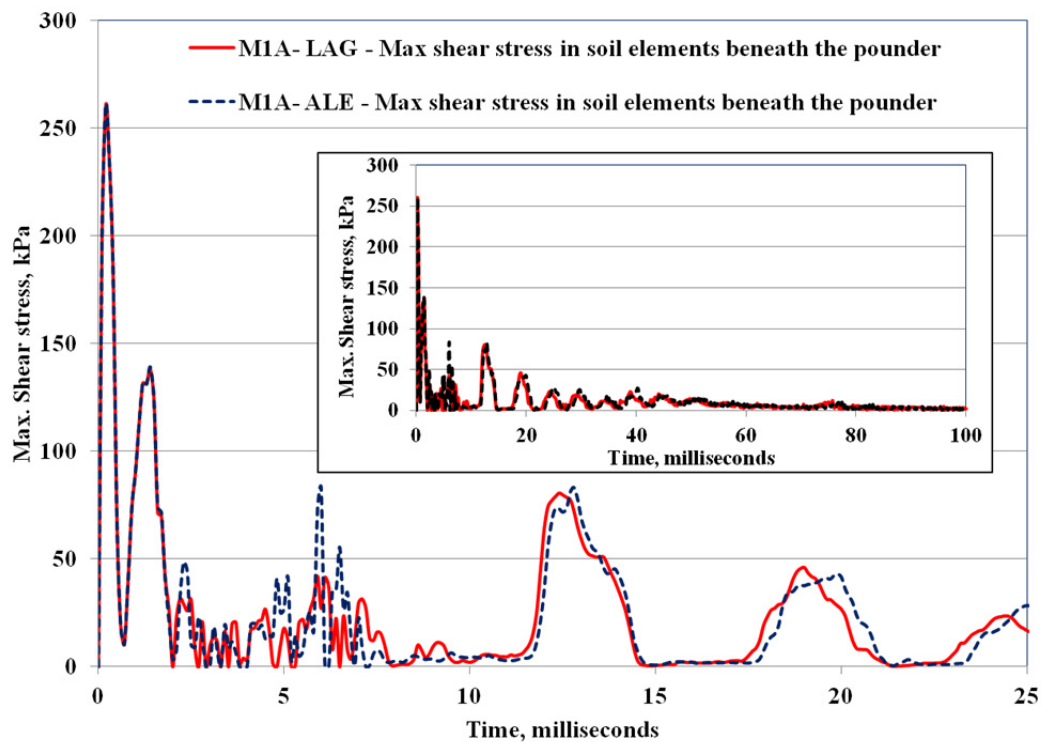


Figure 7.13. Maximum shear stress in soil elements immediately beneath the impacting contact from M1A-LAG (Lagrangian) and M1A-ALE models.

7.6.5 Summary of preliminary sensitivity analysis

The objective of the preliminary sensitivity work was to develop a reliable FE model that can simulate the DC tests. The performance of the FE simulations was checked for stability and hourglassing and was found to be satisfactory. The results indicate that the simulation results are sensitive to the mesh size and some of the soil material properties. To compare simulation results with the findings from the DC tests, the majority of the results presented in the following section were obtained from simulations performed using the fine mesh configuration of 57200 soil elements. Considering the nearly identical outcomes from simulations performed using Lagrangian and ALE approaches and the significantly lesser computation time needed for the Lagrangian simulations, the simulations have adopted the Lagrangian approach only.

7.7 SIMULATION RESULTS

The soil body deformations and final resultant displacement vectors (after 100 milliseconds) for models M1-SA3, M3-SA3, M4-SSL2 and M5-SA3 during the course of simulations are shown in Figures 7.14 to 7.17. It is important to note that the range of any output's fringe levels extends from the minimum to the maximum of that particular result. The resultant displacements represent the absolute values and therefore the provided fringe scales all are positive. The time dependent poulder displacement and the maximum soil surface soil heave from model M1-SA3 are shown in Figure 7.18. In this case, the downward poulder displacements are negative in accordance with LS-DYNA default outputs.

Figure 7.14 shows the results of a high impact energy by a 57mm poulder of 160N (16.4kg) with an impact velocity of 2.0m/sec on loose sand simulating test DC11. This is shown to cause large heave around the poulder as elements of the soil body continued to move laterally towards the sides, reached the side boundaries of the model, and then moved upward as shown by the displacement vectors of Figure 7.14d. Displacement vectors 50 milliseconds after the impact in test DC11 estimated by GeoPIV and from the LS-DYNA simulation for DC11 are shown in Figure 7.19. Both GeoPIV and the simulation show similar patterns of soil displacement around the poulder, but unlike the experimental pattern from GeoPIV, the simulation results show very little measurable displacement at depth. Although poulder

penetrations at the end of the simulation time (100 milliseconds from impact) are in reasonable agreement with the results from the physical model, the real time photography and subsequent GeoPIV analysis showed that no further penetration or soil displacement occurred after 65 milliseconds, whereas the poulder continued penetrating the soil body in the simulation up to the termination time and beyond (will be discussed later). Figure 7.15 shows the effect of a lower energy impact by a 35mm of 58N (5.9kg) weight with an impact velocity of 1.5m/sec. Comparison with Figure 7.14 shows that this causes less poulder penetration and produces less soil heaving around the poulder, and has many of the characteristics of the DC30 test results (see Figure 5.50). Nevertheless, the simulation was also unable to show any noticeable soil displacements/strains at depth. Both DC11 (M1-SA3) and DC30 (M3-SA3) were carried out on near identical loose sand by different energy inputs (mass of the falling assembly, poulder size and impact speed), and in each case the simulation outputs were not entirely consistent with the results from the physical models, captured by high speed photography. In both cases the simulation results show a strong “bearing capacity” mechanism, similar to that observed in the model tests, but there is no evidence of significant shear or volume strain beneath the poulder.

Figure 7.16 shows the simulated displacements for DC36 (sand:silt mixture). Here, the predicted displacement at the termination time of 100 milliseconds is nearly twice the predicted displacement from the simulation for the sand shown in Figure 7.15d even though they had the same impact energy. Thus, the difference is a result of the different stress-strain dependency and greater compressibility of the sand:silt mixture. The predicted poulder displacements for the sand:silt mixture were found to be many times higher than measured displacements during the DC tests. More importantly the simulations were unable to reproduce the physical model response with any of the three different sand:silt soil models (SSL1, SSL2 and SSL3). The simulation results (Figure 7.16c and d) also show that some displacements took place at depth and extended laterally to reach the model side boundaries towards the simulation termination time. This behaviour was not detected by the photographic results during the DC tests. This might be a result of numerical instability which resulted in slightly unbalanced energies being encountered during the sand:silt simulations, but is more likely to be a result of the more rapid damping of the wave propagation that was observed in all the physical model tests.

Figure 7.20 shows the responses of sand:silt mixture at the end of drop 1 during DC36 as well as the predicted soil displacement by three simulations using the three sand:silt soil models (stress-strain responses). The stress-strain response of model SSL1 indicates a collapse like behaviour which is responsible for the significantly greater predicted displacement. The stiffer response of soil model SSL4 provides a better prediction of displacement, however, the predicted poulder penetration was still more than twice the measured penetration. Simulation M4-SSL4 (DC36) provided reasonable prediction of the physical model surface heave but shows the soil moving laterally as the poulder penetrates, whereas in this and several tests on loose sands this was not observed. The results from the simulation using soil model SSL2 were intermediate between the two others.

By extending the termination time to 300 milliseconds in simulation M3-SA3, the poulder was found to continue to penetrate the soil body till 125 milliseconds after the impact, after which the soil mesh started falling back into the cavity around the poulder as shown in Figure 7.21a. At that stage, the poulder penetration was 43.6mm (only 2mm deeper than the predicted displacement at 100milliseconds). In simulation M4-SSL2, poulder penetration ceased at 76.74 milliseconds however when the termination time was extended to 300 milliseconds, the heaved soil was observed to flow around the poulder as shown in Figure 7.21b. The different responses by the sand and sand:silt mixture were very clear in the photographic results (Chapter 5) and laboratory testing (Figure 7.2 verses Figure 7.3). In the FE simulations, the difference in the displacements and/or deformation patterns can also be recognized from the simulation results.

The effect of the model width on the behaviour of the soil body can be perceived from the lateral extent of the displacement contours. In the small size models (Figures 7.14 to 7.16), displaced soil elements have reached the model side boundaries while the boundary soil element remained virtually stationary in the large size model (Figure 7.17). The effect of the model width can be detected also by the larger energy dissipation (including the Rayleigh damping) shown in Figure 7.22. The results show an increase of 5 times in the Rayleigh damping dissipated energy for only an 18% increase in the internal body energy moving from simulations M1-SA3 (DC11 of the small tank) to M5-SA3 (DC6L of the large tank) as the wider model provides more room for the Rayleigh wave to dissipate. Energy dissipation including the Rayleigh damping energy dissipation was found to be very small compared to

the total soil body internal energy. This is expected given the relatively small size of the DC models. The effect of the model width on internal strains will be discussed below.

Results from M5-SA3 show very little detectable displacement from the end of simulation (100 milliseconds) at depth as shown in Figure 7.17b. However, considering the less maximum displacement (pounder penetration) and different fringe levels, the magnitudes of detectable displacement at depth are very minute perceiving the 14.33 mm range of the simulation's fringe levels.

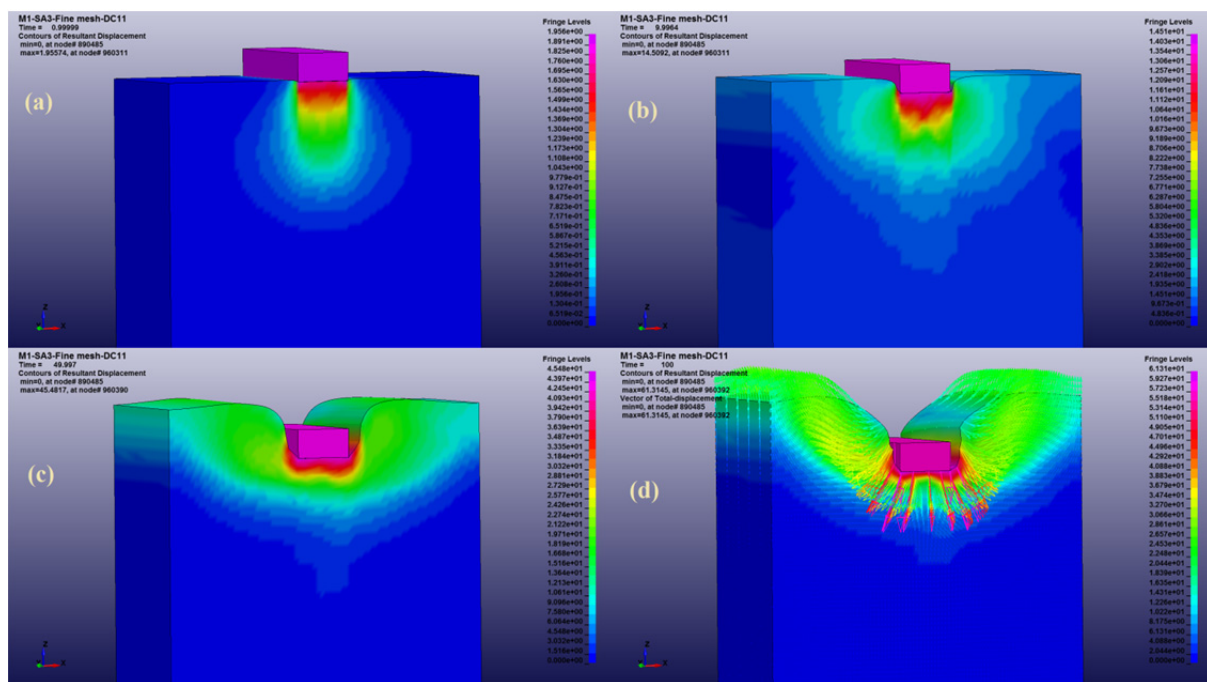


Figure 7.14. Progressing displacements (a, b and c) and end displacement vectors at 100 milliseconds (d) for model M1-SA3 (DC11).

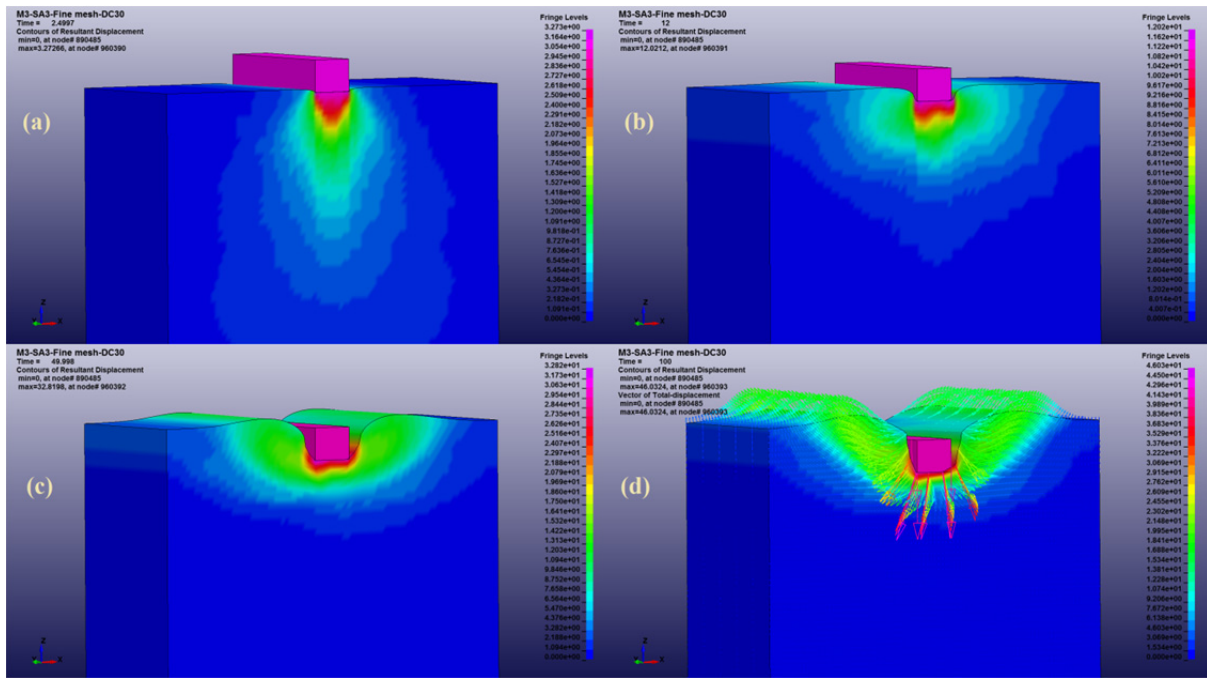


Figure 7.15. Progressing displacements (a, b and c) and end displacement vectors at 100 milliseconds (d) for model M3-SA3 (DC30).

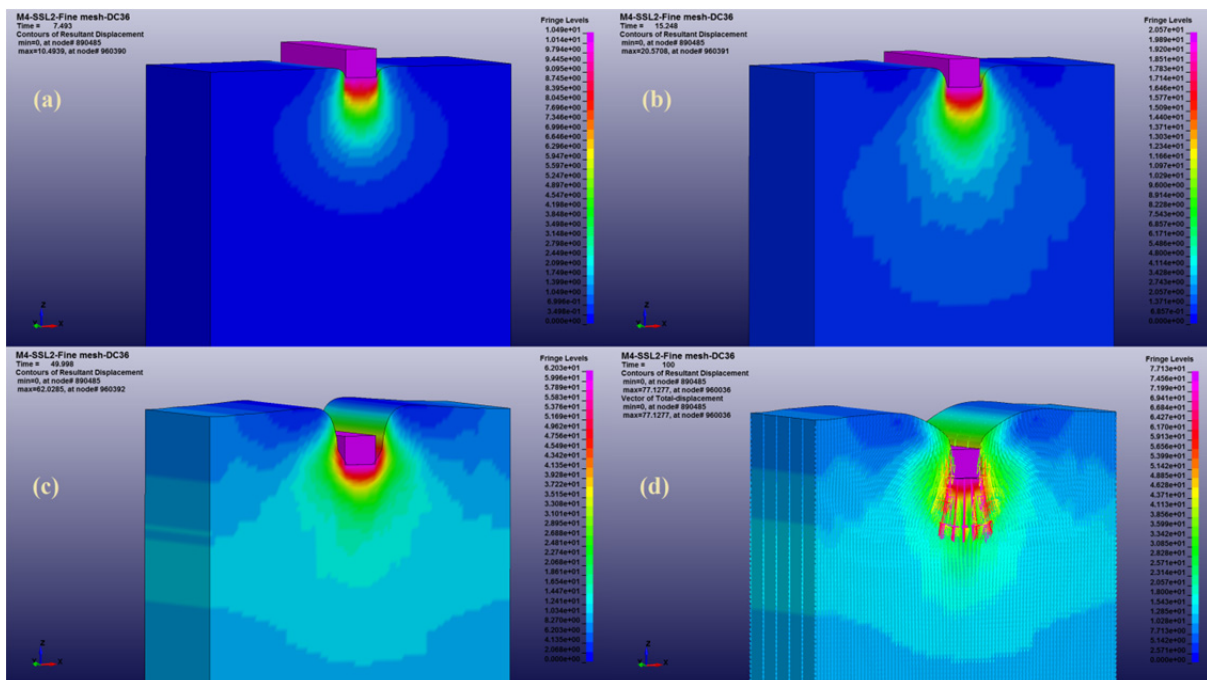


Figure 7.16. Progressing displacements (a, b and c) and end displacement vectors at 100 milliseconds (d) for model M4-SSL2 (DC36).

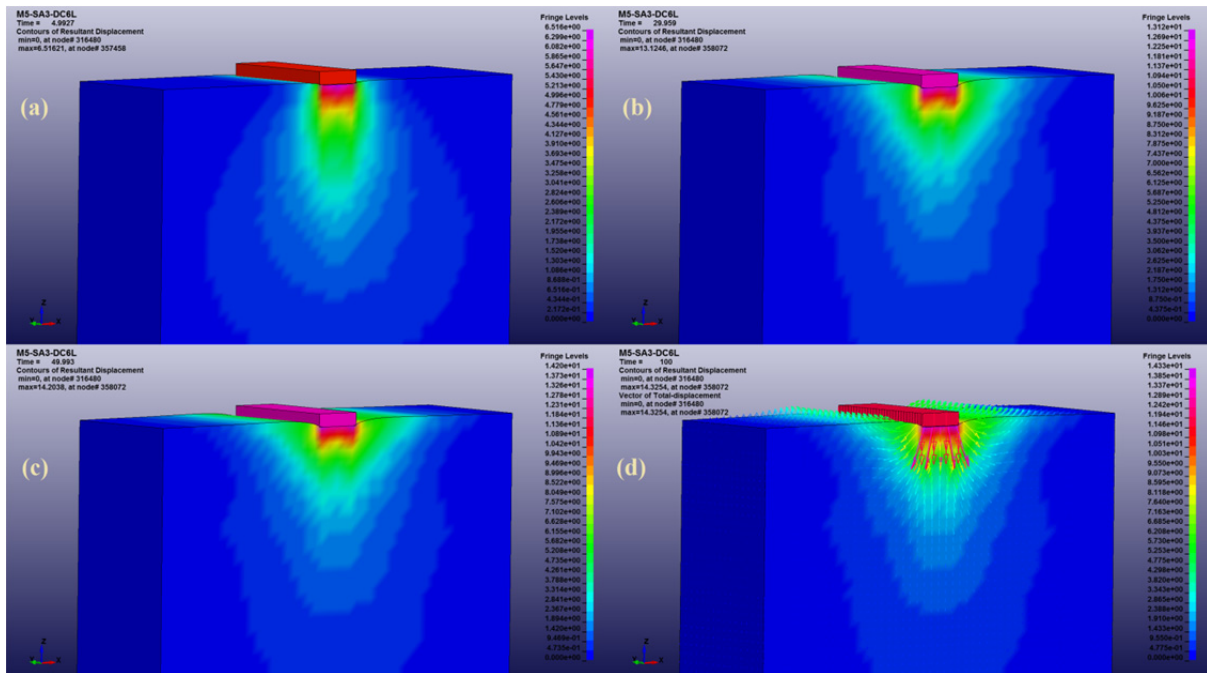


Figure 7.17. Progressing displacements (a, b and c) and end displacement vectors at 100 milliseconds (d) for model M5-SA3 (DC6L).

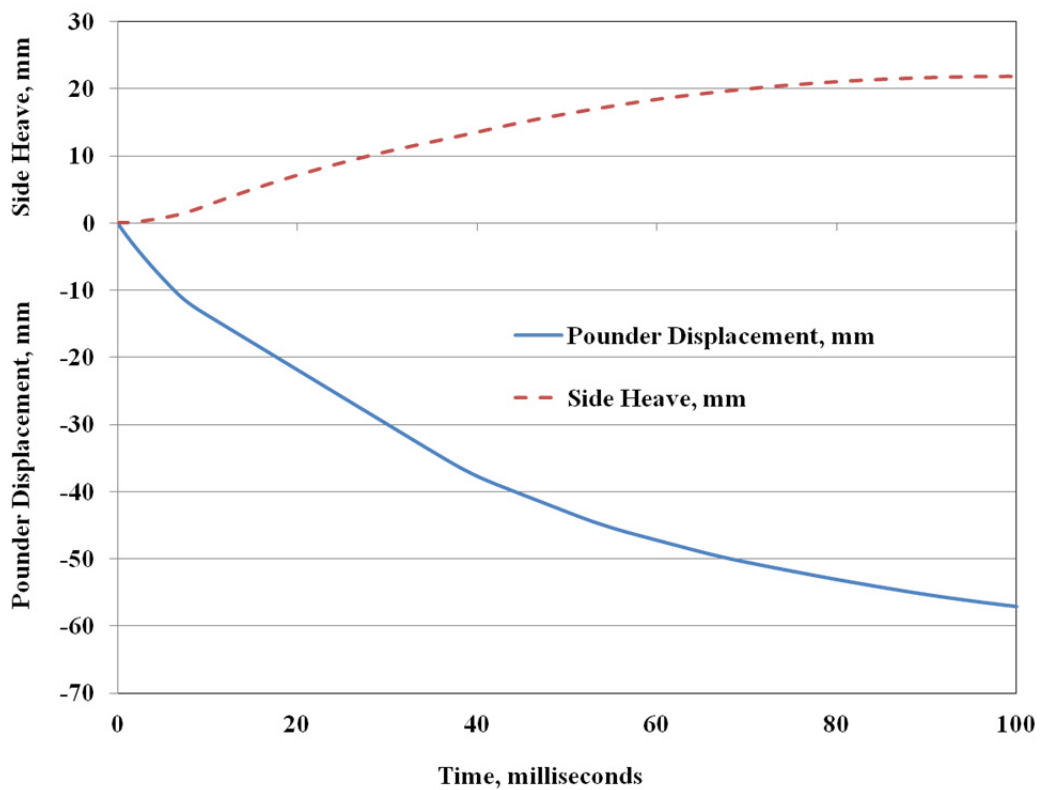


Figure 7.18. History of poulder displacement and surface soil heave from model M1-SA3.

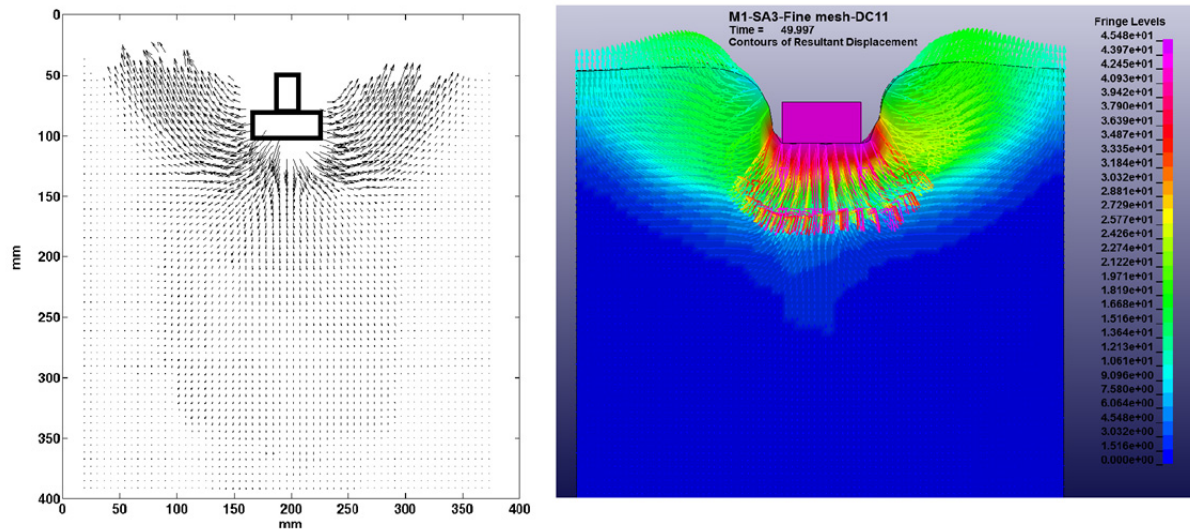


Figure 7.19. Displacement vectors by GeoPIV and LS-DYNA simulation (at 50 milliseconds) for model M1-SA3 (DC-11) - displacement vector scale x 1.0.

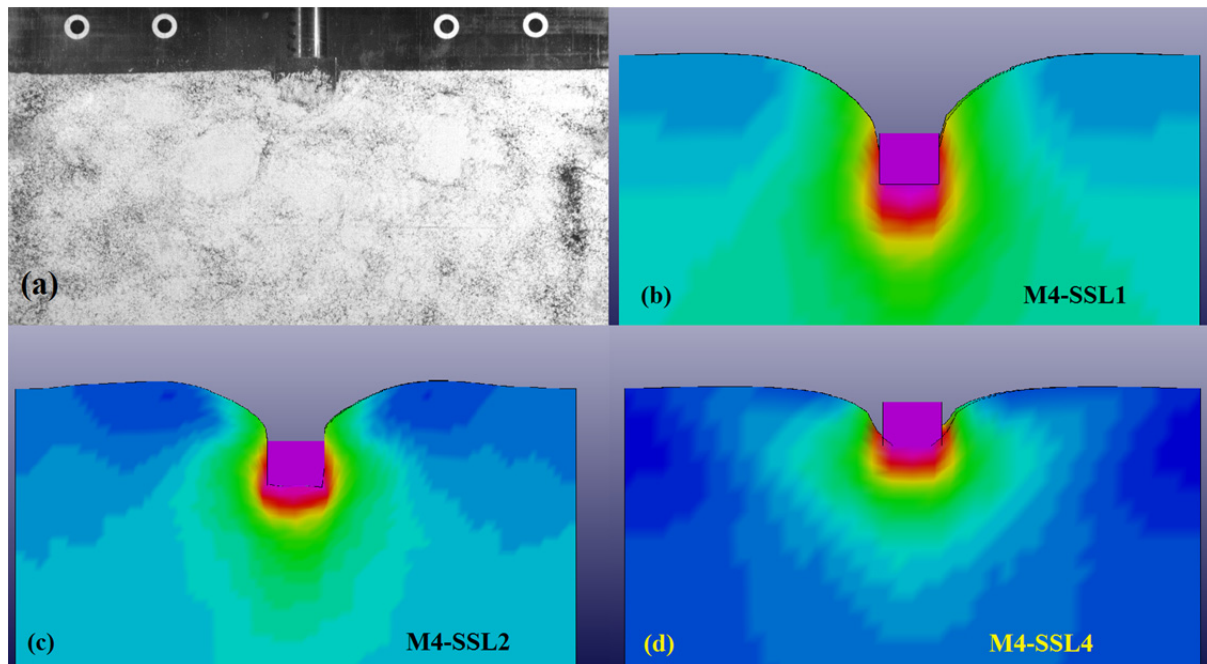


Figure 7.20. Response of sand:silt mixture during drop 1 captured by the high speed photography (a) and by LS-DYNA simulations (b, c and d) for DC36.

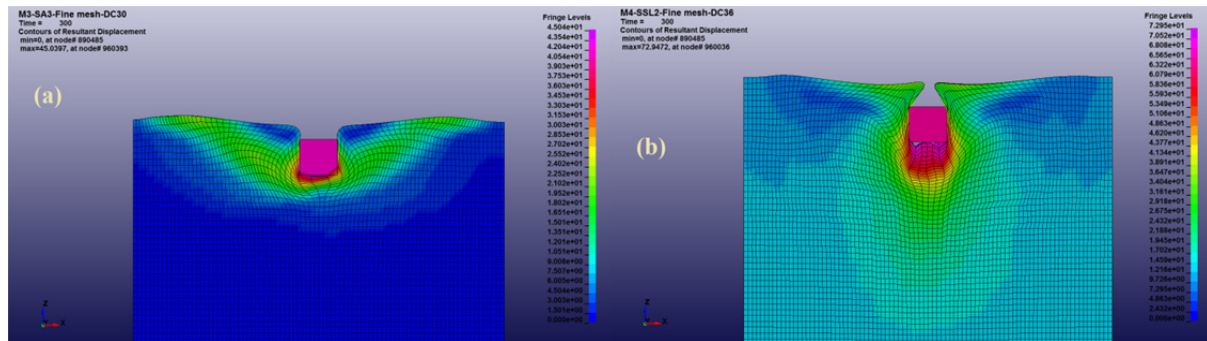


Figure 7.21. Displacement at time 300 milliseconds from simulations M3-SA3 (a) and M4-SSL2 (b).

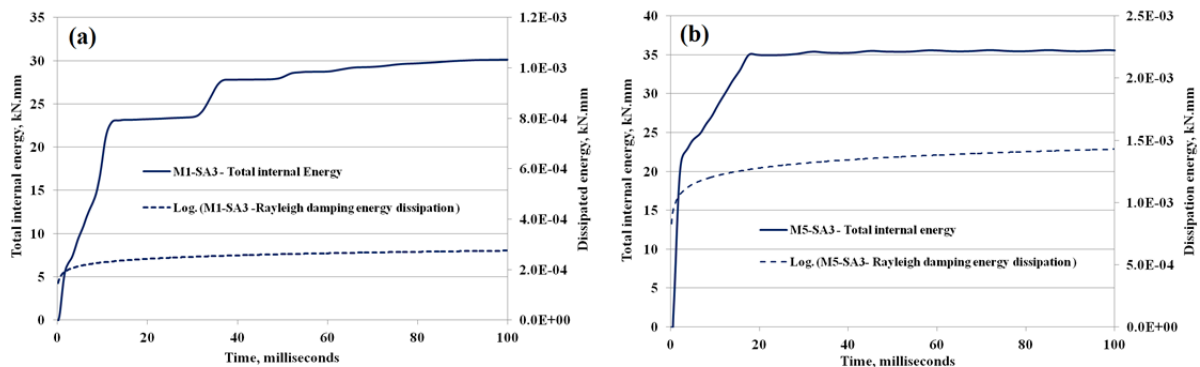


Figure 7.22. Total soil body internal energy and Rayleigh damping dissipated energy during simulations M1-SA3 (a) and M5-SA3 (b).

Table 7.7 presents the differences between the poulder penetrations predicted by the LS-DYNA models and their corresponding values physically measured during the DC tests. The correlation between measured and simulated results from simulations of the small size DC tests on sand is shown in Figure 7.23. There is reasonable agreement between the measured and the simulated poulder penetrations. Modifying some of the soil model parameters (such as reducing the soil density and/or the yield function parameters) can force the models to produce comparable penetration results, but the FE models would not then be replicating the intended physical models. However, the simulations of the sand:silt DC tests significantly overestimated the poulder displacements and unreasonable adjustments to the input parameters would be required to force agreement with the measured penetrations.

Table 7.7. Pounder penetrations by LS-DYNA simulations and physical models.

LS-DYNA Model ID	Physical Model ID	Predicted pounder penetration by LS-DYNA, mm		Pounder penetration from physical models, mm
		Time: 50 ms after impact	Time: 100 ms after impact (simulation terminated)	
M1-SA3	DC11	43.07	57.15	67
M1-SA5	DC4	38.93	53.40	54
M2-SA3	DC24	23.16	33.53	28
M2-SA5	DC24	15.97	21.12	28
M3-SA3	DC30	30.21	41.58	52
M4-SSL1*	DC36	61.06	88.96	14
M4-SSL2	DC36	61.59	74.82	14
M4-SSL4*	DC36	33.32	37.65	14
M5-SA3*	DC6L	13.07	11.98	55
M5-SA1*	DC6L	18.46	18.30	55

* simulation result by coarse mesh configuration

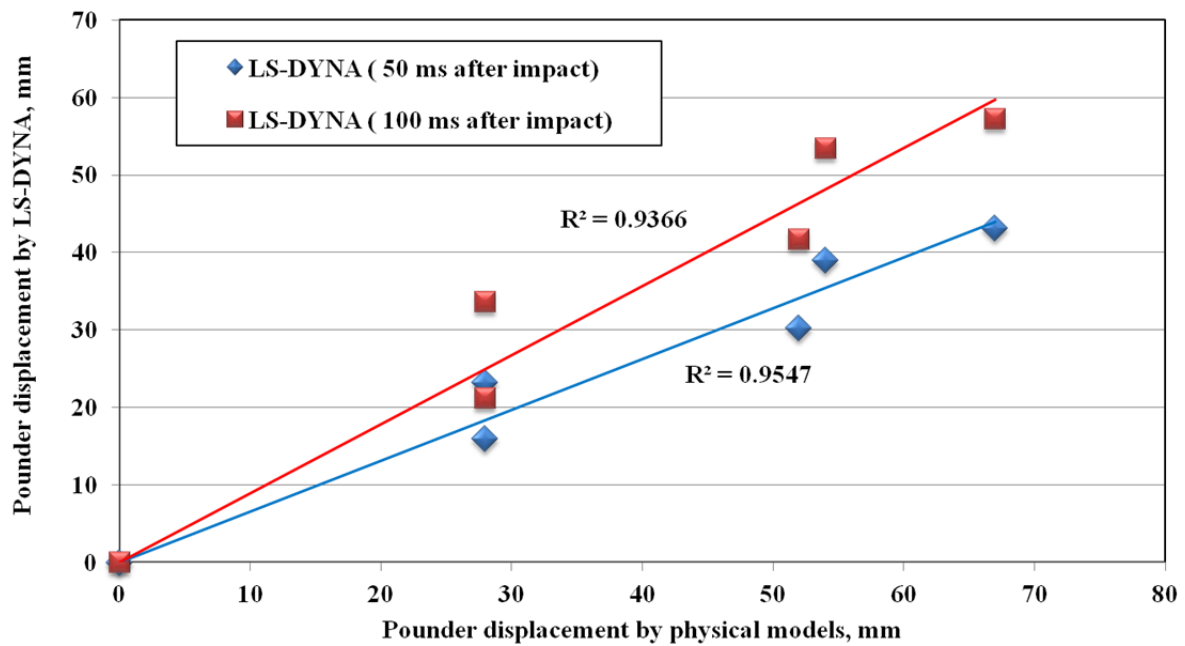


Figure 7.23. Measured (GeoPIV) and predicted (LS-DYNA) pounder penetrations (results are only for simulations of the small size DC models using sand).

Another important difference between FE models and reality was in the variation of the timing at which the pounder ceases penetration. Soil materials (particularly the sand:silt, SSL, models) in the FE simulations continued deforming beyond the times that all movement in corresponding physical models had ceased, typically between 35 to 50 ms after impact. As seen from Table 7.7, soil bodies made of MAT_014 continued deforming beyond 50ms with displacement trends suggesting they would continue deforming beyond 100ms.

These results suggests that the elasto-viscoplastic fitness of the material MAT_014 constitutive model which is sensitive to strain rate (controlled by the initial impact velocities of the models) is unable to accurately adjust the increased stiffness in the soil elements located close to the impact. Other measurements such as accelerations and element internal stresses were found to be much higher, or highly divergent from, the acceleration and stress measurements recorded by soil accelerometers and stress cells during the DC tests. Figure 7.24 shows soil accelerations at 150mm below the pre-impact surface measured during DC11 and simulated by model M1-SA3.

The peak soil acceleration predicted by the simulation is about 20 times the measured soil acceleration during DC11. During DC11, peak soil acceleration occurred 11.9 milliseconds after impact, while the peak soil acceleration from the same level took place only 1.25 milliseconds after impact in the simulation. Figure 7.25 shows the simulation prediction of the lateral stress at 150mm depth at the wall of the DC container. The high stresses predicted within the first 10ms after the impact are a result of the elastic shock wave passing through the model immediately after the impact. Beyond 60ms after the impact, the LS-DYNA simulation prediction of about 3kPa lateral stress is comparable with the 5.0kPa measured by EPC stress sensor during test DC11.

Another objective of the LS-DYNA simulations was to investigate if the densification mechanism with localised strain bands, revealed by the high speed photography could be reproduced by the FE codes. Contours of maximum shear strain at different times from impact for M3-SA3 (DC30-small physical model) and M5-SA3 (DC6L-large physical model) are shown in Figures 7.26 to 7.28. There are evident similarities between the FE shear strain contours and the strain maps from GeoPIV analyses. Evidence of strain bands starting beneath the pounder and propagating downward into the soil body can be seen. However in

the FE analysis these are associated with elastic wave travel and produce little resultant change in density or soil stresses.

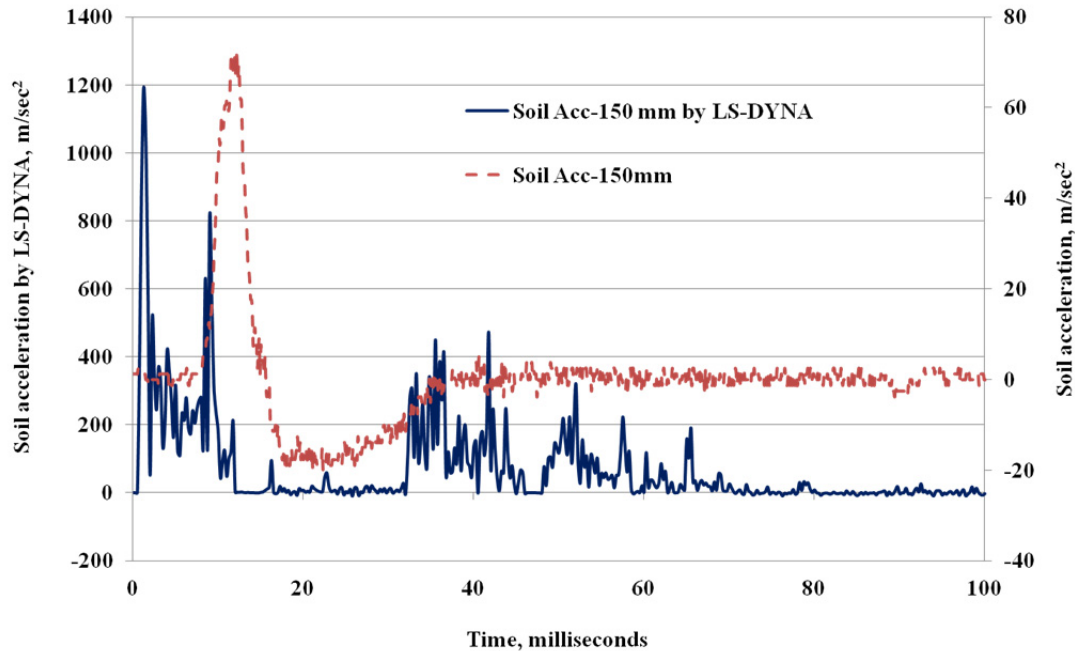


Figure 7.24. Soil accelerations measured during DC11 and simulated by model M1-SA3.

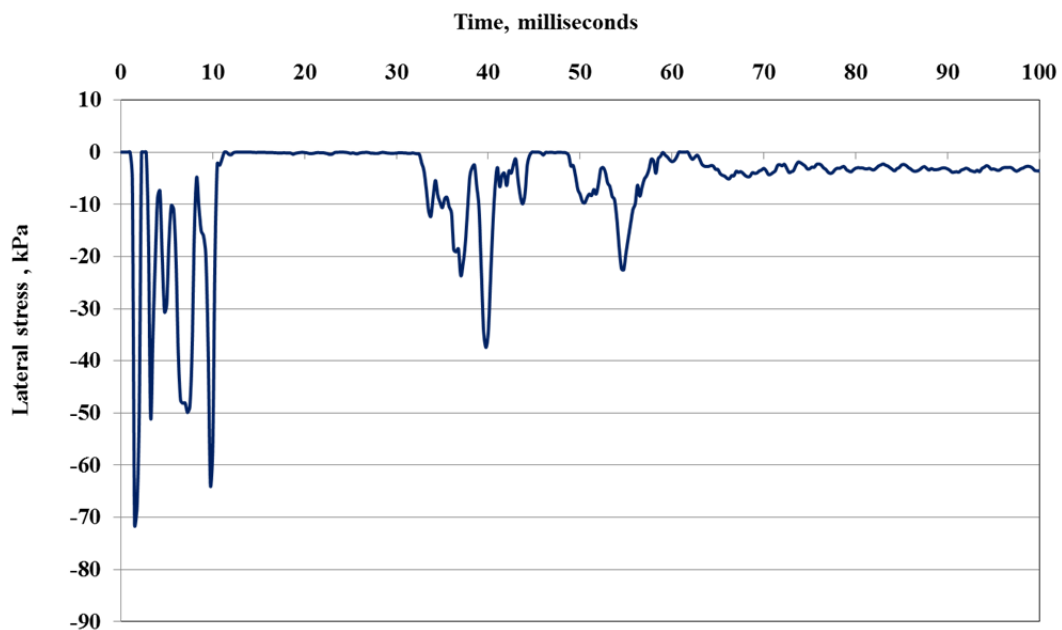


Figure 7.25. Lateral stress at 150mm depth at the wall of the DC container simulated by model M1-SA3 (DC11), (-ve is for stress in compression).

Features of a general bearing capacity mechanism such as the inclined shear planes and radial shear zones are also evident towards the end of penetration as shown by the shear strain contours at the times of 10.747ms (Figures 7.26d) and 49.998ms (Figure 7.27) of M3-SA3 model and at the time of 38.598ms of M5-SA3 model (Figure 7.28). The same features are also evident in all the displacement contours previously shown in Figures 7.14-7.17.

The most important similarity between the LS-DYNA and GeoPIV strain contours is the capturing of the parabolic shaped shear bands that move down into the soil body without significant compaction occurring in the region through which they have propagated as shown by the shear strains from Figure 7.26 (0.48908, 0.7421, 0.99352, 1.244 and 1.7435ms) and Figure 7.27 (2.3545, 3.1667 and 3.5464ms). However, there are significant differences in the rates at which the localised strain bands travel between the real soil and in the simulations. In theory, a point located beneath a concentrated load that is applied instantaneously at the surface of an elastic half-space experiences two body wave front arrivals, corresponding to the compression (P-wave) and shear (S-wave) waves. Velocities at which the observed shear strain bands travel within the soil body are important measurements as the mechanism of propagated waves represents the earliest response, i.e. the arrival of the P- wave (compression wave) of the material model to impact. There is also a possibility of boundary effects due to the relatively small sizes of the models, so that distorted elastic waves of different frequencies travel at different speeds.

From the simulation results, it was possible to estimate these velocities by tracking the timing and elevations of the shear band fronts from the LS-DYNA maximum shear strain contours or by detecting the difference in timing between peak accelerations of target soil elements as shown in Figures 7.29 and 7.30. The trend of shear strain velocities that occurred in the selected simulations is shown in Figure 7.31. The average wave velocities from these simulations were 203m/sec and 190m/sec for the simulated small model DC tests on sand and sand:silt respectively. Wave velocities from the simulated large model DC tests were about 17% less than velocities measured from the simulated small model DC tests. These velocities are 1.5 -3 times higher than the velocities calculated from GeoPIV strain maps or velocities derived from differences between soil accelerometers arrival times.

Table 7.8 presents velocities measured during two DC tests and their simulations which were identical except for the impacting energy as 100mm and 300mm drop heights were employed during DC24 and DC30 respectively. Both approaches show the impact velocities are higher with the higher impact energy and this produces higher wave velocities as well. However, the P-wave velocities measured by the instrumentation signal arrivals are only 35-62% of the velocities predicted from the simulations. However, the predicted wave velocities from the simulations are consistent with the input stiffness parameters (shear and bulk moduli).

Table 7.8. Impact velocities from two types of measurements

Physical Model ID	by time shift (IFFT cross-correlation) of embedded soil accelerometers, mm/ms		Velocity by LS-DYNA, (Model) mm/ms	
	P-wave velocity	S-wave velocity	P-wave velocity	S-wave velocity
DC24	67	50	200	N/A**
DC30	135	115	205	N/A**
DC6L	N/A*	N/A*	166	143

“*” Instrumentation was not employed in the physical model

“**” Unnoticeable difference between second peak acceleration arrivals

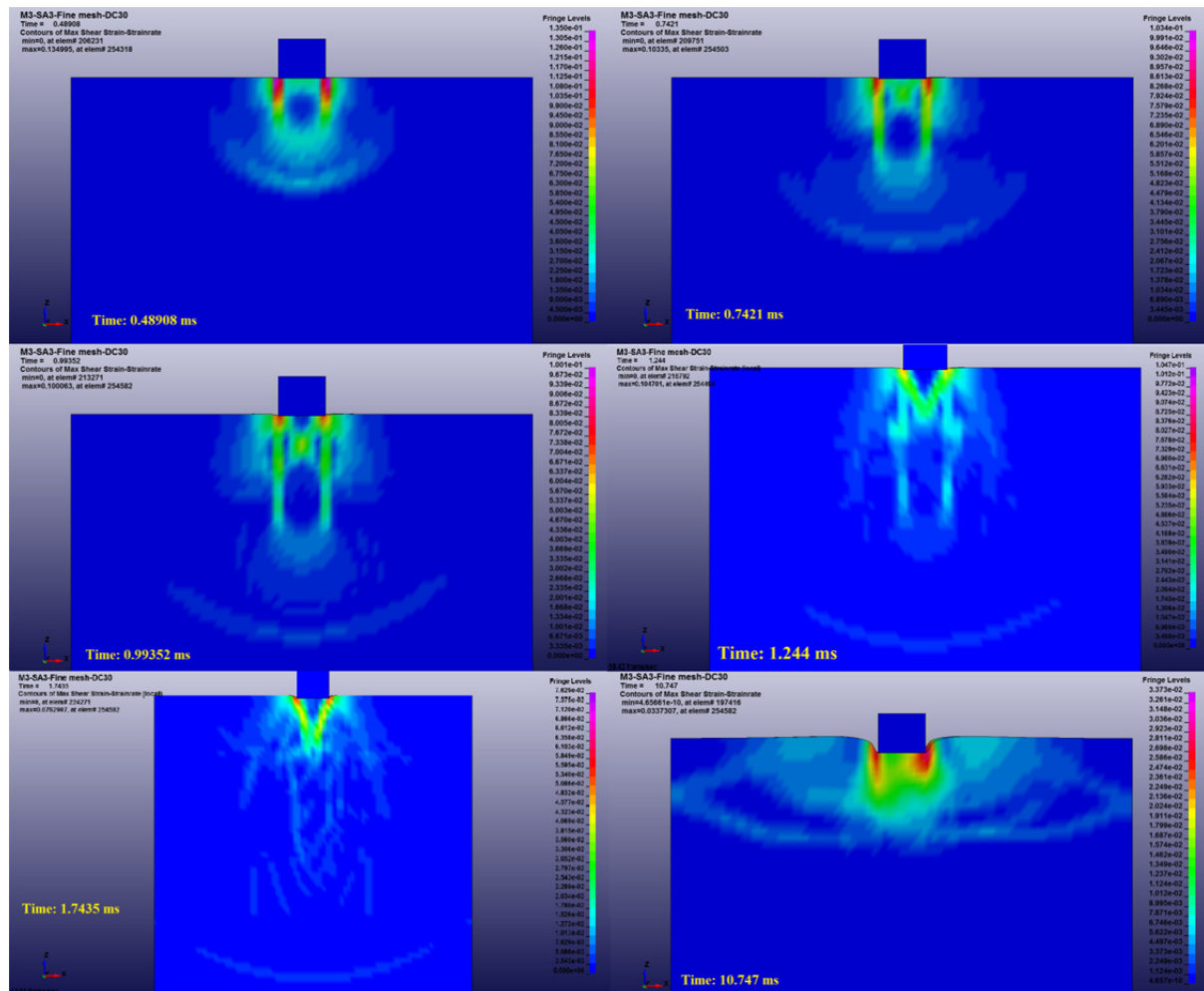


Figure 7.26. Contours of maximum shear strain during M3-SA3 simulation (DC30).

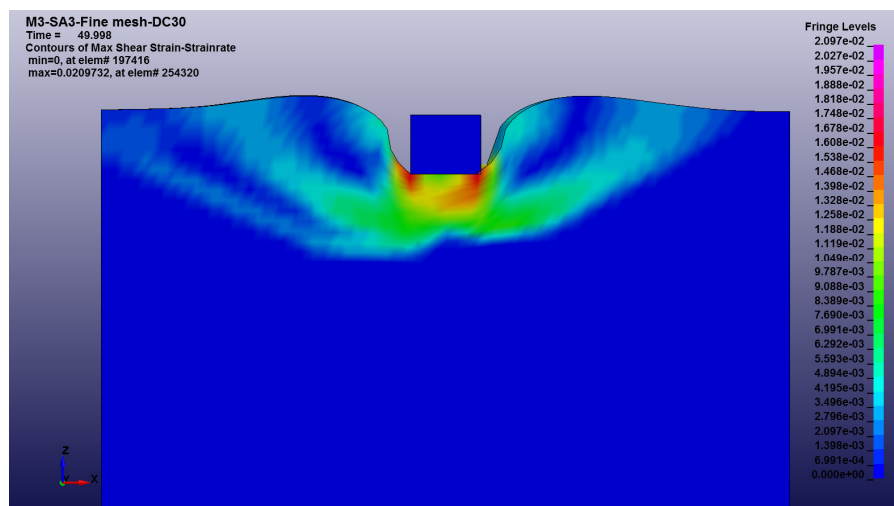


Figure 7.27. Contours of maximum shear strain after 49.998 milliseconds from impact during M3-SA3 simulation (DC30).

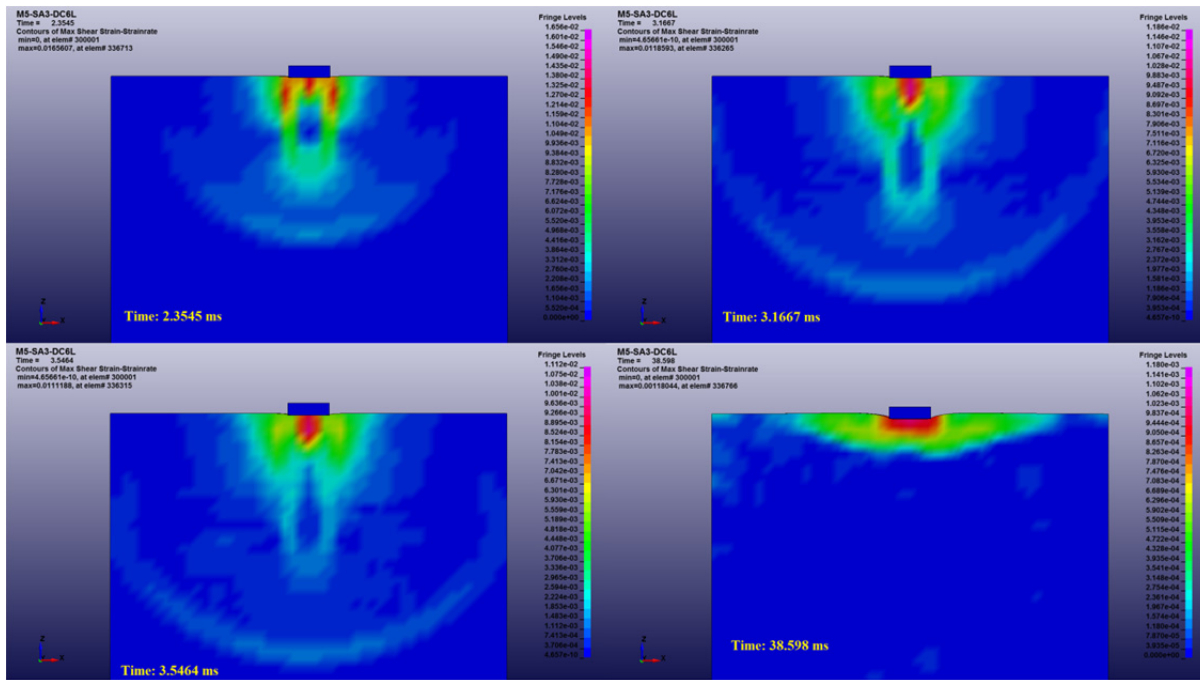


Figure 7.28. Contours of maximum shear strain during M5-SA3 simulation (DC6L).

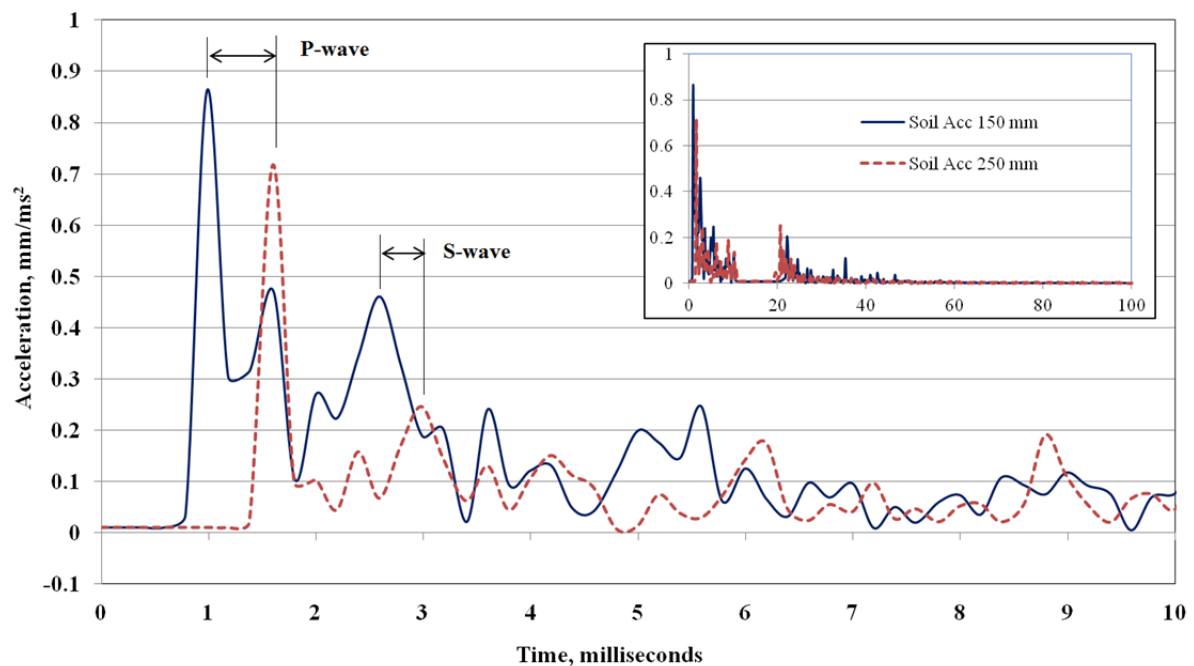


Figure 7.29. Soil accelerations at 150 and 250 mm depths by M3-SA3 -DC30.

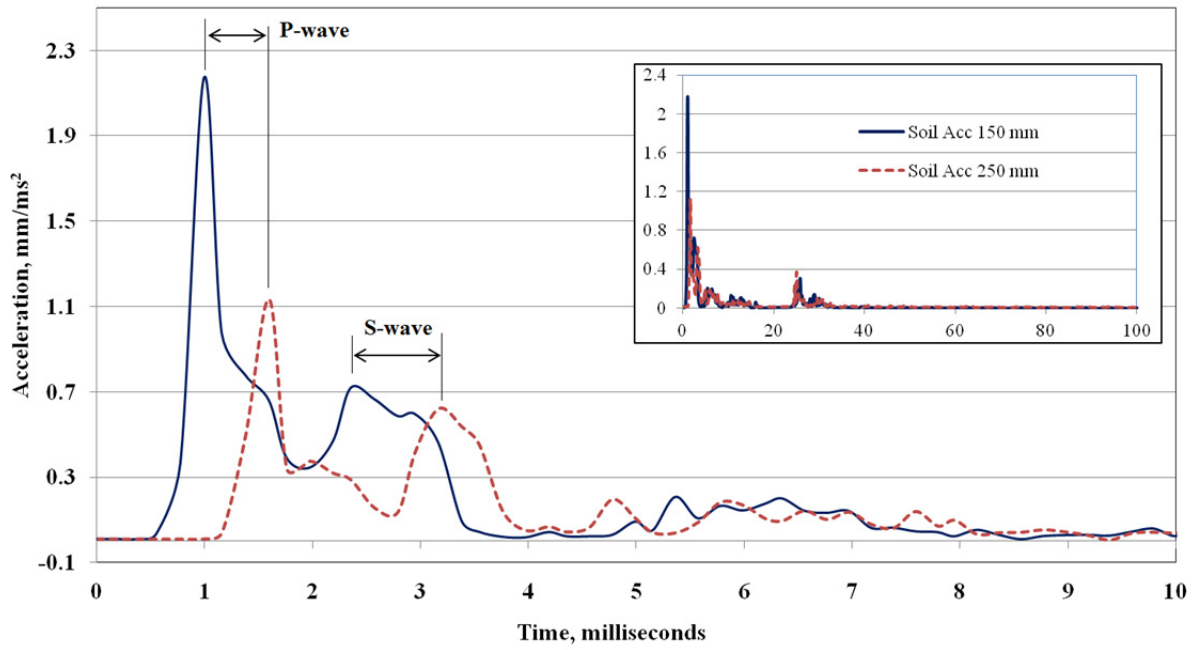


Figure 7.30. Soil accelerations at 150 and 250 mm depths by M5-SA3-DC6L.

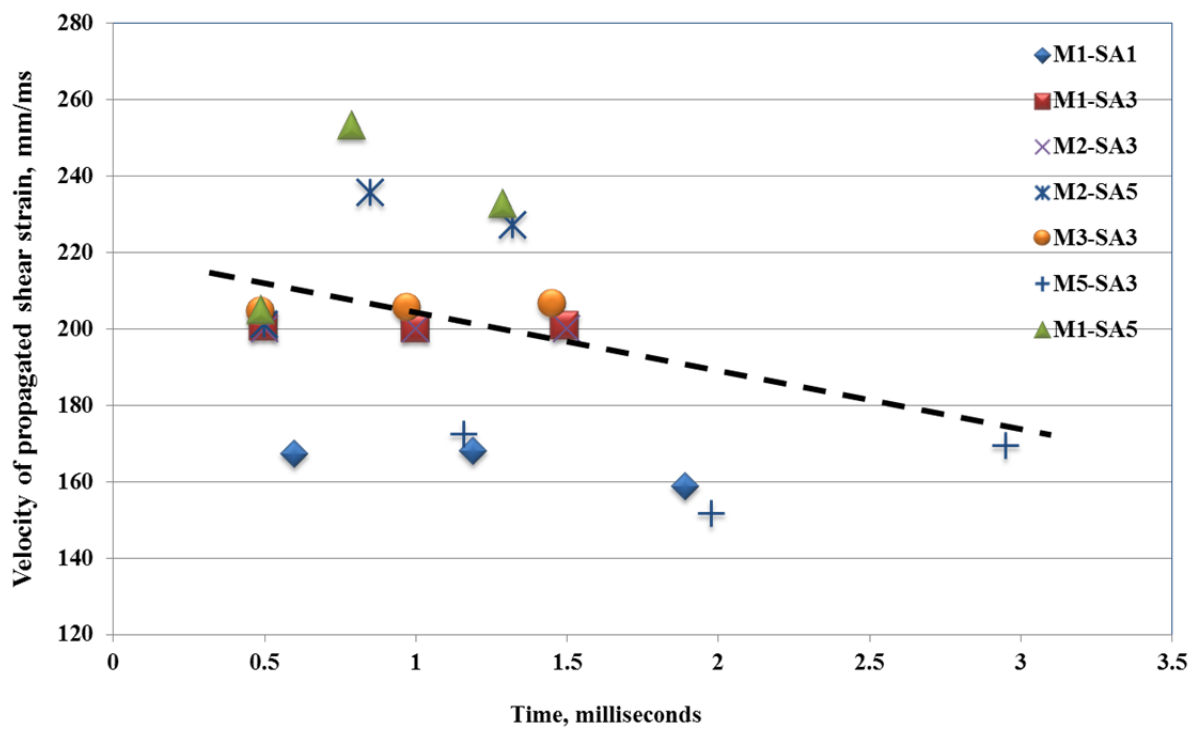


Figure 7.31. Velocities of propagated shear strain bands tracked from LS-DYNA simulations (note: mm/ms = m/sec).

7.8 SUMMARY OF THE LS-DYNA MODELLING RESULTS

The results from the sensitivity analyses (soil material parameters and size of FE mesh) have demonstrated the effect of those variables on the modelling output. Results were found to be more sensitive to small changes of the plastic yield function coefficient "A2" of the soil material model than other material parameters. The LS-DYNA simulations predicted the general behaviour of the soil response to dynamic impact loading, but showed typical limitations of a continuum type model in capturing the free surface behaviour of sandy soils.

The simulations were able to predict some of the DC test features and provided reasonable prediction of poulder penetration in the case of sand. However, the FE models were unable to reproduce the exact way granular soils responded to impact loading. In the case of simulating the sand:silt mixture, we see the soil moving around the penetrating poulder and falling back into the cavity that formed around the poulder sides only when the simulations surface displacement is two times or beyond the measured displacement during actual DC tests.

This is the effect of combined limitations of the material model and the way the soil body was constructed in the FE code as a continuum section that is made of numbers of attached elements that can not move freely to simulate the behaviour of something that is made of discrete particles like sand. This could be the reason behind the variation between measurements from actual physical models and simulations. With the right soil parameters derived from thorough soil laboratory testing, the LS-DYNA material model MAT_014 may better suit modelling clayey soils rather than loose sand.

Chapter VIII: Summary, Conclusions, and Recommendations for Further Studies

Table of Contents

8.1	SUMMARY	276
8.2	CONCLUSIONS	277
8.3	RECOMMENDATIONS FOR FURTHER STUDIES	279

8.1 SUMMARY

It has been shown by large numbers of previous researchers and case studies that dynamic compaction, a method that involves repeated application of high-energy impacts on the soil surface, can increase the density and bearing capacity of treated granular soil deposits and improve their resistance to liquefaction. Despite the wide use of dynamic compaction as a ground improvement technique in granular soil sites, there are no well established design procedures. It has been suggested that this is because there is no clear understanding of the unseen kinematic processes taking place beneath the ground surface.

This research work has investigated the kinematics occurring during lab-based dynamic compaction tests using high speed photography and image correlation techniques. This has enabled the displacement and strain fields to be determined from the digital images. The aim has been to establish a methodology for studying the densification of sandy soils during 2D dynamic compaction model tests. The main outcomes from this study are briefly presented below.

The literature related to the dynamic loading of sandy soil especially during ground improvement by dynamic compaction has been reviewed in *Chapter 2*. The nature of dynamic loading and its effects on the densification mechanism and degree of improvement have been reported. A chronological review of the development of physical and numerical techniques used in the prediction of dynamic compaction depth of improvement has been presented. In *Chapters 5* and *6*, results from combining the high speed photography and from physical measurements have been presented. Micro-CT scans were performed on a small specimen from the model tests to provide volumetric parameters describing the particles, pores and porosity across the scanned field, and these have also been presented in *chapter 5*.

Comparisons of the experimental results with finite element simulations has been presented in *Chapter 7* together with a sensitivity study of the effect of the soil material model input on the simulation results. Overall, the simulations were able to predict the general characteristics of to the experimental results. However, the simulations were unable to reproduce details of the response to compaction at depth.

8.2 CONCLUSIONS

The material presented in this thesis and the main output of this research calls into question what has been long believed about ground improvement by dynamic compaction. It has been thought that DC increases relative densities in a bulb of soil the shape of a semi prolate-spherical with the effect of DC reducing as one moves away from the impact footprint. The results also suggest that the degree of densification due to dynamic compaction can not be simply quantified by the common practises of before and after subsurface field testing and surface measurements.

The results have shown that GeoPIV suits the analysis of rapid loading geotechnical model tests. The use of high speed photogrammetry as a quantitative tool has allowed the evolution of localised deformation and strain fields in dynamic tests to be revealed, and has suggested that compaction shock bands are an important mechanism in dynamic compaction. The results have revealed a distinctive mechanism that should affect how we understand the kinematics of soil rapid loading process, towards better design of ground improvement by dynamic compaction.

The displacement and strain results from high speed photography showed that soil deformation in the dynamic tests was dominated by a general bearing capacity mechanism similar to that widely stated in classic soil mechanics texts. This close to the surface mechanism plays significant role in the process of energy dissipation around the impact location depending on the soil type and density. The tendency for the soil to heave and be loosened near the surface has been reported in many field studies, however, this mechanism has not been widely reported from laboratory scale experiments. This could possibly because the focus is on the densification at depth.

Results from the X-ray microtomography revealed variations in porosity across tested specimens that were broadly consistent with the data from photogrammetry. However, micro CT scans were found to be difficult to reliably interpret since the estimated porosity values were very sensitive to the grayscale threshold selected in the analysis. It is considered that this technique is currently of limited value due to the high cost of the procedure.

Results from using different tamper geometries have revealed the internal densification mechanisms depend on the tamper geometry and the type of target soil. The results of the DC model tests using different tamper geometries may benefit the ground improvement industry, as they suggest there is significant potential to improve dynamic compaction practice by using combinations of different tamper geometries on alternate grids to achieve the most effective densification.

The LS-DYNA simulations were able to predict some of the DC test features and provided reasonable prediction of poulder penetration in the case of sand. The simulations predicted the general behaviour of the soil response to dynamic impact loading, but showed typical limitations of a continuum type model in simulating the exact way granular soils responded to impact loading such as capturing the free surface behaviour of sandy soils. The FE simulations were found to predict the strain localisation in the granular material models with low dependency on the finite element mesh size, but underestimated the timing response of the soil model.

8.3 RECOMMENDATIONS FOR FURTHER STUDIES

Further study to explore the response of sandy soils under dynamic loading and the propagation of compaction bands is required. Research works are needed to build on the findings of this work to advance the understanding of the kinematic of the rapid loading of sandy soils, and to improve the analysing and simulation procedures. Some areas in which this effort can be continued are:

- Verification of image analysis results is not possible for dynamically loaded tests as the granular material samples experience large and non-uniform displacements. This makes it difficult, if not impossible, to physically track individual particles for the purpose of verifying the image-based deformations without the aid of other techniques like X-ray scanning. However, transporting bulk samples from physical models to a high resolution CT scanner without causing disturbance is not possible. Further research may consider a specially designed model made entirely of non-metal materials tested in an X-ray protected chamber where x-ray scanning can be performed during and after dynamic loading without disturbing the test models.
- The direct applicability of the results from this research may be limited by the small scale and low stress levels in the model tests, however, they indicate that the response of soil to dynamic compaction is likely to be strongly influenced by the soil type and tamper geometry. The results show that there are significant differences in the extent and magnitude of the compacted zone at depth, and suggest that there may be significant benefits from considering different tamper shapes in future field studies. It was found that no single tamper shape performed well across both soil types investigated. The effect of tamper geometry on the dynamic compaction process should be further investigated, both experimentally by employing larger physical modelling and field trials.
- Development of a soil material model that can be employed by LS-DYNA or other similar FE codes that can simulate the discrete nature of granular soils. The key goal of the proposed material model is to have the ability of simulating the permanent increase of soil stiffness due to DC blows based on increases in the relative density of compacted soil.

- Conducting field tests and/or large scale physical model tests to explore the importance of compaction bands in DC practice and establishing correlations between compaction levels and dynamic settlement modulus (DSM) and impact stress measurements which both were found to be sensitive to soil properties, poulder size and impacting energies.

REFERENCES

- Abbiss, C P 1981, 'Shear wave measurements of the elasticity of the ground', *Géotechnique*, vol. 31, no. 1, pp. 91-104.
- Abdel-Aziz, YI & Karara HM 1971, 'Direct linear transformation into object space coordinates in close-range photogrammetry' *Proc Symposium on Close-Range Photogrammetry*, Urbana, Illinois, pp. 1-18.
- Adam, D, Brandl H, Kopf, F & Paulmichl I 2007, 'Heavy tamping integrated dynamic compaction control' *Ground Improvement*, vol. 11, no. 4, pp. 237–243.
- Adrian R 1991, 'Particle-imaging techniques for experimental fluid mechanics' *Annual Review Fluid Mechanics*, vol. 23, pp. 261-304.
- Alshibli, K & Sture, S 1999, 'Sand shear band thickness measurement by digital imaging techniques' *Journal of Computing in Civil Engineering*, ASCE, vol. 13, no. 2, pp. 103-109
- Alshibli, KA., & Sture, S 2000, 'Shear Band formation in plane strain experiments of sand', *Journal of Geotechnical & Geoenvironmental Engineering*, ASCE, vol. 126, no. 6, pp. 495-503.
- Allersma, HGB 1982, 'Photo-elastic stress analysis and strains in simple shear', *Proc, IUTAM Symposium on Deformation and Failure of Granular Materials*, P A Vermeer and H J Luger, eds, IUTAM, Delft, The Netherlands, pp. 345–353.
- Altaee, A & Fellenius, BH 1994, 'Physical modeling in sand', *Canadian Geotechnical Journal*, vol.31, no.3, pp 420-431.
- Arduino P & Macari EJ 2001, 'Numerical analysis of geomaterials within theory of porous media', *Journal of Engineering Mechanics*, vol. 127, no. 2, pp. 167–175.
- Arslan, H, Baykal, G & Ertas, O 2007 'Influence of tamper weight shape on dynamic compaction', *Proceedings of the ICE- Ground Improvement*, vol. 11, no. 2, pp. 61–66.
- Arulnathan, R, Boulanger, RW & Riemer, MF 1998, 'Analysis of bender element tests', *Geotechnical Testing Journal*, vol. 21, no. 2, pp. 120–131.
- Atkinson, JH & Sallfors, G 1991, 'Experimental determination of stress-strain-time characteristics in laboratory and in situ tests', *Proceedings of the International Conference on Soil Mechanics and Foundation Engineering*, vol.3, pp. 915-956.
- Beckett, TS Augarde, CE 2011, 'A novel image-capturing technique for the experimental study of soil deformations during compaction', *Geotechnical Testing Journal*, vol. 34, no. 6, pp. 571- 578.
- Berril, JB & Davis RO 1985, 'Energy dissipation and seismic liquefaction of sands: revised model', *Soils and Foundations*, vol. 25, no. 2, pp. 106 - 118.

- Berry, A, Visser, AT & Rust, E 2000, 'State of the art review of the prediction of ground improvement using impact compaction equipment', *South African Transport Conference 'Action in Transport for the New Millennium'* South Africa.
- Berry, AD 2001, 'Development of a Volumetric Strain Influence Ground Improvement Prediction Model with Special Reference to Impact Compaction', Mater Thesis, University of Pretoria.
- Bo, MW, Na, YM, Arulrajah, A & Chang, MF 2009, 'Densification of granular soil by dynamic compaction', *Proceedings of the ICE - Ground Improvement*, vol. 162, no. GI3, pp. 121–132.
- Bolton, MD, Gui, MW, Garnier, J, Corte, JF, Bagge, G, Laue, J & Renzi, R 1999, 'Centrifuge cone penetration tests in sand', *Geotechnique*, vol. 49, no. 4, pp. 543 – 552.
- Bojanowski, C & Kulak, RF 2010, Comparison of Lagrangian, SPH and MM-ALE approaches for modeling large deformations in soil, *11th International LS-DYNA Users Conference*, Dearborn, MI, USA, no. 11, pp. 45-56.
- Bourdeau, P 1993, 'Radiographic visualization in experimental soil mechanics', *Proc, Conf on Digital Image Processing: Techniques and Applications in Civil Engineering*, ASCE, New York, pp. 125–134.
- Brandl, H & Sadgorski, W 1977, 'Dynamic stresses in soils caused by falling weights', *Proceedings of the 8th International Conference on Soil Mechanics and Foundation Engineering*, Moscow, pp. 187–194.
- Bransby, PL & Milligan, GWE 1975, 'Soil deformation near cantilever sheet pile', *Geotechnique*, vol. 25, no. 2, pp. 175–195.
- Butterfield, R & Andrawes, K 1971, 'The visualization of planer displacement field', *Proc, Roscoe Memorial Symposium: Stress Strain Behavior of Soils*, R Perry, ed, Cambridge University, Cambridge, UK, pp. 467–475.
- Cerato, AB & Lutenege AJ 2007, 'Scale effects of shallow foundation bearing capacity on granular material', *Journal of Geotechnical and Geoenvironmental Engineering*, ASCE vol. 133, no. 10, pp.1192-1202.
- Chan, D & Morgenstern, NR 1988, 'Program User Manual for SAGE', A Finite Element Program for Stress Analysis in Geotechnical Engineering Geotechnical Group, University of Alberta,
- Chandrasekaran, VS 2001, 'Numerical and centrifuge modeling in soil-structure interaction', *Indian Geotechnical Journal*, vol. 31, no. 1, pp. 30–59.
- Chen, Z, Steeb, H & Diebels, S 2006, 'A time-discontinuous Galerkin method for the dynamic analysis of porous media', *International Journal for Numerical and Analytical Methods in Geomechanics*, vol. 30, pp. 1113–1134.

Choa, V, Karunaratne, GP, Ramaswamy, SD, Vijiaratnam, A & Lee, SL 1979, 'Compaction of sand fill at Changi airport', *Proc, 6th Asian Regional Conf on Soil Mechanics and Found Engineering*, Southeast Asian Society of Soil Engineering, pp.137-140.

Chow, SH, Nazhat, Y & Airey, DW 2010, 'Applications of high speed photography in dynamic tests', *Proceeding of 7th International Conference on Physical Modelling in Geotechnics*, ICPMG, Zurich, pp. 313-318.

Chow, YK, Yong, DM, Yong, KY & Lee, SL 1992a, 'Dynamic compaction analysis', *Journal of Geotechnical Engineering*, ASCE, vol. 118, no. 8, pp. 1141-1157.

Chow, YK, Yong, DM, Yong, KY & Lee, SL 1992b, 'Dynamic compaction of loose sand deposits' *Soils and Foundation*, vol. 32, no. 4, pp. 93-106.

Chow, YK, Yong, DM, Yong, KY & Lee, SL 1994, 'Dynamic compaction of loose granular soils: effect of print spacing' *Journal of Geotechnical Engineering*, ASCE, vol. 120, no. 7, pp. 1115-1133.

Chow, YK, Yong DM, Yong, KY & Lee, SL 2000, 'Improvement of granular soils by high-energy impact', *Proceedings of the ICE - Ground Improvement*, vol. 4, no. 1, pp. 31 –35.

Consolazio, GR, Chung, JH and Gurley, KR 2003, 'Impact simulation and full scale crash testing of a low profile concrete work zone barrier', *Computers and Structures* no. 81, pp. 1359–1374.

De Jong, JT, Randolph, ME & White, DJ 2003, 'Interface load transfer degradation during cyclic loading: a microscale investigation', *Soils and Foundations*, vol. 43, no. 4, pp. 81–93.

Diebels, S & Ehlers W 1996, 'Dynamic analysis of fully saturated porous medium accounting for geometrical and material non-linearities', *International Journal for Numerical Methods in Engineering*, vol. 39, no. 1, pp. 81–97.

Drescher, A & De Josselin de Jong, G 1972, 'Photoelastic verification of a mechanical model for the flow of a granular material', *Journal of the Mechanics and Physics of Solids*, vol. 20, no. 5, pp. 337–351.

Drescher, A 1976, 'An experimental investigation of flow rules for granular materials using optically sensitive glass particles', *Géotechnique* 26, no. 4, pp. 591–601.

Duncan JM, & Seed RB 1986, 'Compaction induced earth pressures under k_0 conditions', *Journal of Geotechnical Engineering*, ASCE, vol. 112, no 1, pp 1-43.

Dumas, J. & Beaton, N 1988, 'Discussion of "Practical Problems from Surprising Soil Behavior" by James K. Mitchell (March, 1986, vol. 112, no. 3). *Journal of Geotechnical Engineerin.*, ASCE, vol. 114, no. 3, pp 367–368.

Dyvik, R & Madshus, C 1985, 'Lab measurements of G_{max} using bender elements', *Proceedings, Advances in the Art of Testing Soils under Cyclic Conditions*, ASCE, New York, pp. 186–196.

Elias, V, Welsh, J, Warren, J & Lukas, R 1999, 'Ground improvement technical summaries demonstration project 116, Publication No FHWA-SA-98-086, Federal Highway Administration, Washington DC.

Faisal, A, Kenny Yee & Varaksin, S 1997, 'Treatment of highly compressible soils' *Proceedings, Conference on Recent Advances in Soft Soil Engineering*, vol. 1, Kuching.

Fasanella, EL, Jackson, KE & Kellas, S 2008, 'Soft soil impact testing and simulation of aerospace structures', *10th International LS-DYNA Users Conference*, Dearborn, Michigan USA, pp. 18-29.

Fasanella, EL, Lyle KH, Jackson, KE 2009, 'Developing soil models for dynamic impact simulations', *American Helicopter Society (AHS) International Forum 65*, Texas, USA

Feng TW, Chen KH, Su YT & Shi YC 2000, 'Laboratory investigation of efficiency of conical based pounders for dynamic compaction', *Géotechnique*, vol. 50, no. 6, pp. 667-674.

Feng, TW and Chih-Chung, K 2005, 'A study on using conical bottom tamper for dynamic compaction in platy sand', *Proceedings of the Fifteenth International Offshore and Polar Engineering Conference*, Seoul, Korea, pp. 674-678.

Ferriera, NH 1983, 'The earth pressure of compacted soils', *Proceedings 8th European Regional Conference on Soil Mechanics and Foundation Engineering*, Helsinki, pp. 279-282.

Figuroa JL, Saada, AS, Liang L & Dahisaria MN 1994, 'Evaluation of soil liquefaction by energy principles', *Journal of Geotechnical Engineering*, ASCE, vol. 120, no. 9, pp. 1554-1569.

Fröhlich, OK 1934, '*Druckverteilung im Baugrunde*', Springer Verlag, Wien, pp. 178.

Gambin, MP 1985, 'Dix ans de consolidation dynamique', *Annales de L'Institute technique du bâtiment st des travaux publics*, Series SF/193, no. 433, pp. 11-30.

Gerber E 1929, *Untersuchungen uber die Druckverteilung im Oertlick Belasteten Sand*, Dissertation, Technische Hochschule, Zurich.

Ghassemi, A, Pak, A & Shahir, H 2009, 'Validity of Menard relation in dynamic compaction operations', *Proceedings of the ICE, Ground Improvement*, vol. 162, no. 1, pp. 37-45.

Ghassemi, A, Pak, A & Shahir, H 2010, 'Numerical study of the coupled hydro-mechanical effects in dynamic compaction of saturated soil layers', *Computers and Geotechnics*, vol. 37, pp. 10-24.

Ghazavi, M & Niazipour, M 2010, 'An experimental setup for the investigation of tamper geometry effects', *Proceedings of the 7th International Conference on Physical Modelling in Geotechnics*, Zurich, pp. 235-238.

Goh, SH 1995, *Propagation and attenuation of ground shock in dry soils*, MEng thesis, National University of Singapore.

Goh, SH, Lee, FH, & Tan, TS 1998, 'Effects of lateral constraints and inertia on stress wave propagation in dry soil columns', *Géotechnique*, vol. 48, no. 4, pp. 449–463.

Gonzalez, RC, Woods, RE & Eddins, SL 2004, *Digital image processing using MATLAB*, Pearson Prentice Hall, New Jersey, USA.

Graff K F 1975, *Wave Motion in Elastic Solids*. Clarendon Press, Oxford

Green R & Mitchell JK 2004, 'Energy-based evaluation and remediation of liquefiable soils', *Geotrans 2004*, ASCE, *Proceedings Geotechnical Engineering for transportation projects*, 1961-1970.

Gu, Q & Lee, FH 2002, 'Ground response to dynamic compaction of dry sand', *Géotechnique*, vol. 52, no. 7, pp. 481–493.

Guler M, Edil TB & Bosscher, PJ 1999, 'Measurement of particle movement in granular soils using image analysis', *Journal of Computing in Civil Engineering*, ASCE, vol. 13, no. 2, pp. 116–122.

Gustafsson, L & Gustafsson, P 1996, 'Studying mixed granular flows by image analysis', *Proceedings of 11th Conference of the ASCE Engineering Mechanics Division*, ASCE, Reston, Virginia, pp. 100–103.

Hainsworth, JM & Aylmore, LAG 1983, 'The use of computer-assisted tomography to determine spatial distribution of soil water content', *Australian Journal of Soil Research*, vol. 21, pp. 435-443.

Hajjalilue-Bonab, M & Rezaei, AH 2009, 'Physical modelling of low-energy dynamic compaction', *International Journal of Physical Modelling in Geotechnics*, vol. 9, no. 3, pp. 21–32.

Hall, SA, Wood, DM, Ibraim, E & Viggiani, G 2010, 'Localised deformation patterning in 2D granular materials revealed by digital image correlation', *Granular Matter*, vol. 12, no. 1, pp. 1–14.

Handy, R L, 2011, 'Lateral in-situ stress measurements to diagnose liquefaction', *Advances in Geotechnical Earthquake Engineering – Soil Liquefaction and Seismic Safety of Dams and Monuments*, Abbas Moustafa (Ed.), ISBN: 978-953-51-0025-6, <http://www.intechopen.com/>

Hallquist, JO 2006, *LS-DYNA theory manual*, Livermore software technology corporation, Livermore, California, USA. ISBN 0-97785-40-0-0.

Heikkila, J, & Silven, O 1997, 'A four-step camera calibration procedure with implicit image correction', *IEEE Computer Society Conference on Computer Vision and Pattern Recognition (CVPR '97)*, San Juan, Puerto Rico, pp. 1106–1112.

Heukolom, W & Foster, CR 1962, 'Dynamic testing of pavements', *Transactions of the American Society of Civil Engineers*, vol. 127, no. 1, pp. 425-456.

- Heyns, S 1998, 'Response analysis of an impact compactor', Report LGI98/013, Project No 020-DP, Laboratory for Advanced Engineering (Pty) Ltd, University of Pretoria.
- Holtz, R 1991, Stress Distribution and Settlement of Shallow Foundations. In: H. Fang, ed. *Foundation Engineering Handbook*. 2nd ed. New York: Chapman and Hall Inc., pp. 167-222.
- Hounsfield, GN 1972, 'A method of and apparatus for examination of a body by radiation such as X- or gamma-radiation, British Patent No 1283915, London.
- Hounsfield, GN 1973, 'Computerized transverse axial scanning tomography Part 1: Description of system', *British Journal of Radiology*, vol. 46, no. 552, pp. 1016-22.
- Hwang, JH & Tu, TU 2006, 'Ground vibration due to dynamic compaction', *Soil Dynamics and Earthquake Engineering*, vol. 26, pp 337–346.
- Jafarzadeh, F 2006, 'Dynamic compaction method in physical model tests' *Scientia Iranica*; vol. 13, no. 2: pp.187-192.
- James, RG 1965, 'Stress and strain fields in sand', Cambridge University PhD thesis.
- James, RG 1971, 'Some aspects of soil mechanics model testing', SOILS/TR No.6, University of Cambridge.
- Jessberger, HL & Beine RA 1981, 'Heavy tamping: theoretical and practical aspects', *Proceedings: 10th ICSMFE, AA Balkema, ISSMFE*, Stockholm, vol. 3, session 12: Soil Improvement, pp. 695-699.
- Jones, RB 1958, 'In-situ measurement of the dynamic properties of soil by vibration methods', *Géotechnique*, vol. 8, no. 1, pp. 1-21.
- Krieg, RD 1972, 'A simple constitutive description for cellular concrete, Report SCDR-72-0883, Livermore Software Technology Corporation, Livermore, CA.
- Kimura, T, Kusakabe, O & Saitoh, K 1985, 'Geotechnical model test of bearing capacity problems in a centrifuge', *Geotechnique*, vol. 35, no. 1, pp. 33–45.
- Kirpatrick, WM & Belshaw, DJ 1968, 'On interpretation of triaxial test', *Géotechnique*, vol. 18, no. 3, pp. 336–350.
- Konagai, K, Tamura, C, Rangelow, P & Matsushima, T 1992, 'Laser-aided tomography: A tool for visualization of changes in the fabric of granular assemblage', *Proceedings JSCE Number 455 I-21, Structural Engineering/Earthquake Engineering, Japan Society of Civil Engineers*, Tokyo, vol. 9, no. 3, pp. 193s–201s.
- Konagi, K, Rangelow, P & Sato, T 1994, 'Real-time observation of dynamic changes in the fabric of granular material structures through laser-aided tomography', *Proceedings, Tenth European Conference on Earthquake Engineering*, pp. 459-466.

- Kopf, F, Paulmichl, I &, Adam D 2010, 'Modelling and simulation of heavy tamping dynamic response of the ground', *14th Danube-European Conference on Geotechnical Engineering 'From Research to Design in European Practice'* Bratislava, Slovakia. ISBN: 978-80-227-3279-6, S. 107.
- Kerisel, J 1985, "The history of geotechnical engineering up until 1700." in Golden Jubilee Volume. Proceedings of the Eleventh International Conference on Soil Mechanics and Foundation Engineering, San Francisco, 12-16 August pp. 3–93.
- Lade, PW 2003, 'Analysis and prediction of shear banding under 3D conditions in granular materials', *Soils and Foundations*, vol. 43, no. 4, pp. 161–172.
- Lai, CG & Rix, GJ 2002, 'Solution of the rayleigh eigen problem in viscoelastic materials', *Bulletin of the Seismological Society of America*, vol. 92, no. 6, pp. 2297- 2309.
- Lee, C, Take, WA & Hoult, NA 2011, 'Optimum accuracy of two dimensional strain measurements using digital image correlation', *Journal of Computing in Civil Engineering*, Submitted July 28, 2011; accepted November 30, 2011; posted ahead of print December 3, 2011 doi:10.1061/ASCECP1943-54870000182.
- Lee, FH & Gu, Q 2004, 'Method for estimating dynamic compaction effect on sand' *Journal of Geotechnical and Geoenvironmental Engineering*, ASCE, vol. 130, no. 2, pp. 139-152.
- Lee, SL, Yong, KY, Tham, SW, Singh, J & Chen, WP, 1989, 'Treatment of examining land by fibredrains, surcharge and high energy impact', *Symposium on the Application of Geosynthetic and Geofibre in South Asia*, Selangor, Sect 5, pp. 18–22.
- Leong, EC, Yeo, SH & Rahardjo, H 2005, 'Measuring shear wave velocity using bender elements', *Geotechnical Testing Journal*, vol. 28, no.5, pp. 488–498.
- Leonards, GA, Cutter, WA & Holtz, RD 1980, 'Dynamic compaction of granular soils' *Journal of Geotechnical Engineering Division*, ASCE, vol. 106, no. GT1, Proc. Paper 15144, pp. 35-44.
- Lewis, WA 1975, 'A study of some of the factors likely to affect the performance of impact compactors on soil', *Proceedings of the 4th International Conference on Soil Mechanics and Foundations*, London.
- Li, C, Borja, RI & Regueiro, RA 2004, 'Dynamics of porous media at finite strain', *Computer Methods in Applied Mechanics and Engineering*, vol. 193, pp. 3837–3870.
- Liu, J and Iskander, M 2004, 'Adaptive Cross Correlation for Imaging Displacements in Soils', *Journal of Computing in Civil Engineering*, vol. 18, no. 1, pp. 46 – 57.
- Lo, KW, Ooi, PL, & Lee, SL 1990, 'Unified approach to ground improvement by heavy tamping', *Journal of Geotechnical Engineering*, ASCE, vol. 116, no. 3, pp. 514-527.

Lohani, TN, Imai, G & Shibuya, S 1999, 'Determination of shear wave velocity in bender element test', *Proceedings of 2nd International Conference on Earthquake Geotechnical Engineering*, Lisbon, Portugal, pp. 101–106.

L'opez-Querol, S, Fern'andez-Merodo, JA, Mira P & Pastor, M 2008, 'Numerical modelling of dynamic consolidation on granular soils', *International Journal for Numerical and Analytical Methods in Geomechanics*, vol. 32, pp. 1431–1457.

Lueptow, RM, Akonur, A & Shinbrot, T 2000, 'PIV for granular flows', *Experiments in Fluids*, vol 28, no. 2, pp. 183-186.

Lukas, RG 1980 'Densification of loose deposits by pounding', *Journal of Geotechnical Engineering*, ASCE, vol. 106, no. GT4, pp. 435-446.

Lukas RG, 1986, '*Dynamic compaction for highway construction vol.1 1: Design and construction guidelines*', FHWA report No RD-86/133, Washington DC.

Lukas RG, 1995, '*Geotechnical Engineering Circular No. 1 – Dynamic Compaction*' FHWA Publication no: FHWA-SA-95-037, NTIS no: PB96-146105, Washington DC.

Matthews, MC, Hope, VS & Clayton, CRI, Rayleigh 1996, 'The use of surface waves in the determination of ground stiffness profiles', *Proceedings of ICE - Geotechnical Engineering*, vol. 119, no. 2, pp. 84 – 95.

Mayne, PW & Jones JS 1983, 'Impact stresses during dynamic compaction', *Journal of Geotechnical Engineering*, ASCE, vol. 109, no. 10, pp. 1342-1346.

Mayne, P W, Jones, J S & Dumas, J C 1984, 'Ground response to dynamic compaction', *ASCE, Journal of Geotechnical Engineering*, vol. 110, no. 6, pp. 757-774.

Mayne, PW 1985, 'Ground vibrations during dynamic compaction', *Vibration Problems in Geotechnical Engineering Proceedings of Symposium, Geotechnical Engineering Division*. ASCE, New York, pp. 247-265.

Mayne, PW 1988, *Ground Improvement by Dynamic Compaction, Civil Engineering Practice: Geotechnical and Ocean Engineering, Chapter 32*, Technomic Publishing, N.J.

Mees, F, Swennen, R, Geet MV & Jacobs, P 2003, 'Applications of X-ray computed tomography in the geosciences', *Geological Society*, London, Special Publications, vol. 215, pp. 1-6.

Melen, T 1994, '*Geometrical Modelling and Calibration of Video Cameras for under Water Navigation*' Dr ing Thesis, Norges Tekniske Hogskole, Institutt for Teknisk Kybernetikk (Norwegian Institute of Technology).

Menard, L & Broise, Y 1975, 'Theoretical and practical aspects of dynamic consolidation', *Géotechnique*, vol. 25, no. 1, pp. 3-18.

- Michalowski, RL and Shi, L 2003, 'Deformation patterns of reinforced foundation sand at failure' *Journal of Geotechnical and Geoenvironmental Engineering*, ASCE, vol. 129, no. 6, pp. 439-449.
- Michalowski, RL and Nadukuru, SS 2012, 'Static fatigue, time effects, and delayed increase in penetration resistance after dynamic compaction of sands' *Journal of Geotechnical and Geoenvironmental Engineering*, ASCE, vol. 138, no. 5, pp. 564-574.
- Mitchell, JK & Keaveny, JM 1986, 'Determining sand strength by cone penetrometer', *Proceedings of In Situ 86, ASCE Specialty Conference, Use of In Situ Tests in Geotechnical Engineering*, Blacksburg, Virginia, pp. 823-839.
- Mitchell, JK, Cooke, HG & Schaeffer, JA 1998, 'Design considerations in ground improvement for seismic risk mitigation', *Proceedings of Geotechnical Earthquake Engineering and Soil Dynamics III*, ASCE Geotechnical Special Publication, no. 75, vol. 1, pp. 580– 613.
- Mohsin, AKM and Airey, DW 2003, 'Automating Gmax measurement in triaxial tests', *3rd International Symposium on the Deformation Characteristics of Geomaterials*, Lyon, France, pp. 73–80.
- Mülhaus, HB & Vardoulakis, I 1987, 'The thickness of shear bands in granular materials', *Géotechnique*, vol. 37, no. 3, pp. 271–283.
- Mullins, G, Gunaratne, M, Stinnette, P & Thilakasiri, S 2000, 'Prediction of dynamic compaction tamper penetration', *Soils and Foundations*, vol. 40, no. 5, pp. 91-97.
- Nashed, R 2005, '*Liquefaction mitigation of silty soils using dynamic compaction*' PhD thesis The State University of New York at Buffalo.
- Nashed, R, Thevanayagam, S & Martin, GR 2009a, 'Dynamic compaction of saturated sands and silty sands: results', *Proceedings of the ICE - Ground Improvement*, vol. 162, no. 2, pp. 69 –79.
- Nashed, R, Thevanayagam, S & Martin, GR 2009b, 'Dynamic compaction of saturated sands and silty sands: design', *Proceedings of the ICE - Ground Improvement*, vol. 162, no. 2, pp. 81 –92.
- Ng, T-T, Kelley, M & Sampson, J 1996, 'MRI studies of direct shear tests on round particles', *Proceedings of 11th Conference of ASCE, Engineering Mechanics Division*, ASCE, Reston, Virginia, pp. 572–575.
- Niedostatkiewicz, M, Lesniewska, D & Tejchman, J 2011, 'Experimental analysis of shear zone patterns in cohesionless for earth pressure problems using particle image velocimetry', *Strain*, vol. 47, no. S2, pp. 218-231.

- Nouri, HR, Elahi, HA, Jalili, M & Hosseininia, E 2008, 'Evaluation of empirical relationships for dynamic compaction in liquefiable reclaimed silty sand layers using pre/post cone penetration tests', *The Sixth International Conference on Case Histories in Geotechnical Engineering*, Arlington, Virginia, paper no. 7.32a, pp. 1-8.
- O'Reilly, MP & Brown, SF 1991, *Cyclic loading of soils*, Blackie and Son, Inc, New York, NY.
- O'Rourke, TD and Druschel SJ 1990, 'Shear Strength Characteristics of Sand-Polymer Interfaces'. *Journal of Geotechnical Engineering* vol. 116, no. 5, pp. 451-469.
- Oshima, A & Takada, N 1994, 'Effect of ram momentum on compaction by heavy tamping', *International Conference on Soil Mechanics & Foundation Engineering*, vol. 13, no. 3, pp. 1141-1144.
- Oshima, A & Takada, N 1997, 'Relation between compacted area and ram momentum by heavy tamping', *Proceedings of the 14th International Conference on Soil Mechanics and Foundation Engineering*, vol. 3, 1641-1644.
- Oshima, A & Takada, N 1998, 'Evaluation of compacted area of heavy tamping by cone point resistance', *Proceedings of International Conference of Centrifuge*, Tokyo, vol. 1, pp. 813-818.
- Ovesen, NK 1975, 'Centrifugal testing applied to bearing capacity problems of footings on sand', *Geotechnique*, vol. 25, no. 2, pp. 394-401.
- Paige-Green P 1998, *The use of impact compaction in ground improvement*, Report CR-97/098 (prepared for Landpac), CSIR, Pretoria.
- Pan, B, Xie, H, Wang, Z, Qian, K and Wang, Z 2008 'Study on subset size selection in digital image correlation for speckle patterns', *Optics Express*, vol. 16, no. 10, pp. 7037-7048.
- Pan, B, Qian, K, Xie, H & Asundi, A 2009, 'Two-dimensional digital image correlation for in-plane displacement and strain measurement: a review', *Measurement Science and Technology*, vol. 20, no. 6, pp. 1-17.
- Pan, JL & Selby, AR 2001, 'Analysis of dynamic compaction of loose soils under impact loads', *Proceedings of 4th International Conference on recent advances in Geotechnical Earthquake Engineering and Soil Dynamics*, San Diego, California.
- Pan JL & Selby AR 2002, 'Simulation of dynamic compaction of loose granular soils', *Advances in Engineering Software*, vol. 33, pp. 631-640.
- Parvizi, M & Merrifield, CM 2004, 'Centrifuge validation of soil improvement prediction using the WAK test analysis', *Proceedings of the ICE- Ground Improvement*, vol. 8, no. 1, pp. 33-37.
- Parvizi, M 2009, 'Soil response to surface impact loads during low energy dynamic compaction', *Journal of Applied Sciences*, vol. 9, no. 11, pp. 2088 - 2096.

- Parvizi, M & Sharif, H 2011, 'Obtaining soil stiffness using WAK test and numerical methods', *Scientific Research and Essays*, vol. 6, no. 29, pp. 6082-6094.
- Perret, J, Prasher, SO, Kantzas, A & Langford, C 1999, 'Three-dimensional quantification of macropore networks in undisturbed soil cores', *Soil Science Society of America Journal*, vol. 63, pp. 1530- 1543.
- Petrovic, AM, Siebert, JE & Rieke, PE 1982, 'Soil bulk density analysis in three dimensions by computed tomographic scanning', *Soil Science Society of America Journal*, vol. 46, pp. 445-450.
- Pierret, A, Capowiez, Y, Belzunces, L & Moran, CJ 2002, '3D reconstruction and quantification of macropores using X-ray computed tomography and image analysis', *Geoderma*, vol. 106, no. 3-4, pp. 247-271.
- Poran, CJ & Rodriguez, JA 1992a, 'Design of dynamic compaction', *Canadian Geotechnical Journal*, vol. 2, no. 5, pp. 796-802.
- Poran, CJ & Rodriguez, JA 1992b, 'Finite element analysis of impact behavior of sand', *Soil and Foundation*, vol. 32, no. 4, pp. 68-80.
- Poran, CJ, Heh, KS & Rodriguez, JA 1992, 'Impact behavior of sand', *Soils and Foundations*, vol. 32, no. 44, pp. 81- 92.
- Qian, JH 1987, 'Dynamic consolidation: from practice to theory' proceedings, 8th Asian Regional Conference on Soil Mechanics and Foundation Engineering, Kyoto, Vol 1, pp. 213-217.
- Qin, X, Luan, M, Yang, Q, Li, X & Zhao, Z 2008, 'Numerical simulation of dynamic compaction using LS-DYNA', *Geotechnical Engineering for Disaster Mitigation and Rehabilitation, Proceedings of the 2nd International Conference GEDMAR08*, Nanjing, China, part 4, pp. 412-420.
- Raschke, S, Hryciw, R & Donohoe, G 1996, 'Microdeformations in sands by digital image processing and analysis', *Transportation Research Record 1548, Transportation Research Board*, Washington, DC, pp. 31–37.
- Rechenmacher, AL & Finno, RJ 2004, 'Digital image correlation to evaluate shear banding in dilative sands' *ASTM Geotechnical Testing Journal*, vol. 27, no.1, pp. 13-22.
- Richart, F E, Hall, JR, and Woods, RD 1970, *Vibrations of soils and foundations*, Prentice-Hall, Englewood Cliffs, NJ.
- Ringrose-Voase, AJ 1993, 'Some principles to be observed in the quantitative analysis of sections of soil, In: A.J. Ringrose-Voase and G.S. Humphreys, Editor(s), *Developments in Soil Science*, Elsevier, vol. 22, pp. 483-493.
- Robinsky, E & Morrison, C 1964, 'Sand displacement and compaction around model friction piles', *Canadian Geotechnical Journal*, vol. 1, no. 2, pp. 81–91.

- Rocha, M 1957, 'The possibility of solving soil mechanics problems by the use of models', *Proceeding of the 4th International Conference on Soil Mechanics*, London, no.1, pp 183.
- Rollins, KM, Jorgensen, SJ & Ross, TE 1998, 'Optimum moisture content for dynamic compaction of collapsible soils', *Journal of Geotechnical and Geoenvironmental Engineering*, ASCE, vol. 124, no. 8, pp. 699 -708.
- Roscoe KH, Arthur JRF & James RG 1963, 'The determination of strains in soils by an X-ray method', *Civil Engineering & Public Works Review*, 58:873- 876, 1009-12.
- Saada, A, Liang, L, Figueroa, J & Cope, T 1999, 'Bifurcation shear band propagation in sands', *Géotechnique*, vol. 49, no. 3, pp. 367–385.
- Sadek, S, Iskander, MG & Liu, J 2003, 'Accuracy of digital image correlation for measuring deformations in transparent media', *Journal of Computing in Civil Engineering*, ASCE, vol. 17, no. 2, pp. 88-96.
- Salgado, R, Bandini, P & Karim, A 2000, 'Shear strength and stiffness of silty sand', *Journal of Geotechnical and Geoenvironmental Engineering*, ASCE, vol. 126, no. 5, pp. 451-462.
- Santamarina, JC and Goodings, DJ 1989, 'Centrifuge Modeling: A Study of Similarity', *Geotechnical Testing Journal*, vol. 12, no. 2, pp. 163-166.
- Santamarina, JC, Klein, KA & Fam, MA 2001, *Soils and waves*, Wiley, New York.
- Schaefer, VR, 1997, 'Ground improvement, ground reinforcement, ground treatment', ASCE, *Geotechnical special publication No 69*.
- Schmertmann, JH, Baker, W, Gupta, R & Kessler, K 1986, 'CPT/DMT Quality control of ground modification at a power plant', *Proceedings In situ '86 ASCE Special Conference on 'Use of In Situ Tests in Geotechnical Engineering'* Virginia Tech, Blacksburg, VA, ASCE Geotechnical Special Publication no 6, pp. 985-1001.
- Scott, RA & Pearce, RW 1975, 'Soil compaction by impact', *Géotechnique*, vol. 25, no. 1, pp. 19-30.
- Serridge, CJ & Synac, O 2006, 'Application of the rapid impact compaction (RIC) technique for risk mitigation in problematic soils', *The 10th IAEG International Congress*, Nottingham, United Kingdom, IAEG2006, Paper number 294, pp. 1-8.
- Shenthan, T, Nashed, R, Thevanayagam, S & Martin GR 2004, 'Liquefaction mitigation in silty soils using composite stone columns and dynamic compaction', *Journal of Earthquake Engineering and Engineering Vibration*, vol. 3, no. 1, pp. 39–50.
- Shi, B, Murakami, Y, Wu, Z, Chen, J & Inyang, H 1999, 'Monitoring of internal failure evolution in soils using computerization X-ray tomography', *Engineering Geology*, vol. 54, no. 3-4, pp. 321–328.

- Shin, EC, Lee, JB, and Das, BM 1999, 'Bearing capacity of a model scale footing on crude oil-contaminated sand', *Geotechnical and Geological Engineering*, vol. 17, no. 2, pp. 123-132.
- Shirley, DJ & Hampton, LD 1978, 'Shear-wave measurements in laboratory sediments', *Journal of the Acoustical Society of America*, vol. 63, no. 2, pp. 607-613.
- Siskind, DE, Stachura, VJ, Stagg, MS & Kopp, JW 1980, *Structure response and damage produced by ground vibrations from surface mine blasting*, U.S. Department of Interior, Bureau of Mines, RI 8507.
- Slocombe, BC 1993, *Dynamic Compaction Chapter 2 of Ground Improvement*, CRC Press Inc, Boca Raton, Florida, pp. 21-39.
- Slominski, C, Niedostatkiewicz, M & Tejchman, J 2007, 'Application of particle image velocimetry PIV for deformation measurement during granular silo flow', *Powder Technology*, vol. 173, no. 1, pp. 1-18.
- Smits, M, Th, JH & De Quelerij, L 1989, 'The effect of dynamic compaction on dry granular soils', *Proceedings of the Twelfth International Conference on Soil Mechanics and Foundation Engineering*, Rio de Janeiro, vol. 2. pp. 1419-1422.
- Smoltczyk, U 1983, 'Deep compaction- General report', *Proceedings, 8th European Regional Conference on Soil Mechanics and Foundation Engineering*, Helsinki vol. 1.
- Sousa, J 2002, 'Turbulent flow around a surface mounted obstacle using 2D-3C DPIV' *Experiments in Fluids*, vol. 33, no. 6, pp. 854-862.
- Tagliaferri, F, Waller, J, Andò, E, Hall, SA, Viggiani, G, Bésuelle, P & DeJong, JT 2011, 'Observing strain localisation processes in bio-cemented sand using x-ray imaging', *Granular Matter*, vol. 13, no. 3, pp. 247-250.
- Take, WA 2002, 'The influence of seasonal moisture cycles on clay slopes' PhD dissertation University of Cambridge.
- Tatsuoka, F, Okahara, M, Tanaka, T, Tani, K, Moritomo, T and Siddiquee, MSA 1991, "Progressive failure and particle size effects in bearing capacity of footing on sand", *Geotechnical Engineering Congress*, ASCE, vol. 27, pp. 788-802.
- Tatsuoka, F, Siddiquee, MSA and Tanaka, T 1994, "Link among design, model tests, theories and sand properties in bearing capacity of footing on sand", *Proceedings of 13th ICSMFF*, vol. 5, pp. 87-88.
- Tatsuoka, F, Goto, S, Tanaka, T, Tani, K and Kimura, Y 1997, "Particle size effects on bearing capacity of footings on granular material", *Asaoka, Adachi, Oka (Eds.), Deformation and Progressive Failure in Geomechanics*, Pergamon, Nagoya (Japan), pp. 133-138.
- Taylor, RN 1995, 'Centrifuges in modelling: principles and scale effects', *Geotechnical Centrifuge Technology*, Chapter 1, edited by Taylor RN, Blackie Academic and Professional, London, pp. 19-33.

The MathWorks, Inc 2010, 'Image Processing Toolbox 7; MATLAB User Guide', The MathWorks, Inc, Massachusetts, USA.

Thevanayagam, S, Liang, J, Shenthan, T 2000, 'A contact index for liquefaction potential analysis of silty/gravelly soils', *ASCE, EM2000, Proceedings 14th EMD Special Conference*, Tassoulas, Ed, Austin, Texas.

Thevanayagam, S, Shenthan, T, Kanagalingam, T 2003, 'Role of intergranular contacts on mechanisms causing liquefaction and slope failures in silty sands', *USGS Award no. 01HQGR0032 and 99HQGR0021*, US Geological Survey.

Thevanayagam, S, Nashed, R & Martin, GR 2009, 'Dynamic compaction of saturated sands and silty sands: theory', *Proceedings of the ICE - Ground Improvement*, vol. 162, no. 2, pp. 57–68.

Thilakasiri, HS, Gunaratne, M, Mullins, G, Stinneite, P & Jory, B 1996, 'Investigation of impact stresses induced in laboratory dynamic compaction of soft soils', *International Journal for Numerical and Analytical Methods in Geomechanics*. vol. 20, pp. 753-767.

Tovey, NK, Smart, P, and Hounslow, MW 1994, 'Quantitative methods to determine microporosity in soils and sediments', *Development in soil science 22, Soil micromorphology: Studies in management and genesis*, Elsevier, Amsterdam, The Netherlands, pp. 531–539.

Tsai, RY 1987, 'A versatile camera calibration technique for high-accuracy 3d machine vision metrology using off-the-shelf TV cameras and lenses' *IEEE Journal of Robotics and Automation*. RA-3, no. 4, pp. 323-344.

Uyanik, O 2010, 'Compressional and shear-wave velocity measurements in unconsolidated top-soil and comparison of the results', *International Journal of the Physical Sciences*, vol. 5, no.7, pp. 1034-1039.

Valliappan S, Yazdi JT & Zhao, C 1995, 'Analytical solution for two-dimensional dynamic consolidation in frequency domain', *International Journal for Numerical and Analytical Methods in Geomechanics*, vol. 19, no. 10, pp. 663–682.

Van Impe, WF 1994, *Soil Improvement Techniques and Their Evolution*, A.A.Balkema, Rotterdam, Netherlands, 125 pp.

Varaskin S, 1981, 'Recent development in soil improvement techniques and their practical applications', *Solcompact Sols/Soils*, 38/39-1981, Techniques Louis Menard, 15, rue des Sablons, Paris.

Vesic AS, 1973, 'Analysis of ultimate loads on shallow foundations', *Journal of Soil Mechanics and Foundation Engineering Division*, ASCE, vol. 99, no.1, pp :45–73.

Viggiani, G & Atkinson, JH 1995, 'Interpretation of Bender element tests', *Géotechnique*, vol. 45, no. 1, pp. 149–154.

- Viggiani, G, Lenoir, N, Bésuelle, P, Di Michiel, M, Marelo, S, Desrues, J & Kretschmer, M 2004, 'X-ray microtomography for studying localized deformation in fine-grained geomaterials under triaxial compression', *Comptes Rendus Mécanique*, vol. 332, no. 10, pp. 819–826.
- Wallays M, 1983, 'Speciality session 3: Deep compaction', *Proceedings, 8th European Regional Conference on Soil Mechanics and Foundation Engineering*, A.A. Balkema, Helsinki, p1126-1128.
- Welsh, J P 1986, 'In situ testing for ground modification techniques', Use of in situ tests in geotechnical engineering, *ASCE, Geotechnical special publication No 6*, pp. 322-335.
- Weiler, WA, Jr and Kulhawy, FH 1982, 'Factors affecting stress cell measurements in soil', *Journal of the Geotechnical Engineering Division*, ASCE, vol. 108, no. 12, pp. 1529-1548.
- Weng, J, Cohen, P & Herniou, M 1992, 'Camera calibration with distortion models and accuracy evaluation', *IEEE Transactions on Pattern Analysis and Machine Intelligence*, PAMI-14, no. 10, pp. 965-980.
- Wetzel, RA & Vey, E 1970, 'Axisymmetric stress wave propagation in sand', *Journal of Soil Mechanics & Foundation Engineering Division*, ASCE, vol. 96, no. SM5, pp. 1763-1786.
- White, DJ, Take, WA and Bolton MD 2001a, 'Measuring soil deformation in geotechnical models using digital images and PIV analysis', *10th International Conference on Computer Methods and Advances in Geomechanics*, Tucson, Arizona, Balkema, Rotterdam, pp. 997-1002.
- White, DJ, Take, WA, Bolton, MD and Munachen, SE 2001b, 'A deformation measuring system for geotechnical testing based on digital imaging, close-range photogrammetry, and PIV image analysis', *Proceedings of the 15th International Conference on Soil Mechanics and Geotechnical Engineering*. Istanbul, Turkey. Balkema, Rotterdam, pp 539-542.
- White, DJ and Take, WA 2002, '*Particle Image Velocimetry (PIV); software for use in geotechnical testing*', Cambridge University, Engineering Department, Technical Report CUED/D-SOILS/TR322.
- White D J 2002, '*An investigation into the behaviour of pressed-in piles*', University of Cambridge, PhD Dissertation.
- White, DJ, Take, WA & Bolton MD 2003, 'Soil deformation measurement using particle image velocimetry PIV and photogrammetry', *Géotechnique*, vol. 53, no. 7, pp. 619–631.
- White, D, Randolph, M & Thompson, B 2005, 'An image-based deformation measurement system for the geotechnical centrifuge', *International Journal of Physical Modelling in Geotechnics*, vol. 3, pp. 01-12.
- White, DJ, Teh, KL, Leung, CF & Chow, YK 2008, 'A comparison of the bearing capacity of flat and conical circular foundations on sand', *Géotechnique*, vol. 58, no. 10, pp. 781–792.

- Wiss, JF, 1981, 'Construction vibrations: state of the art', *Journal of the Geotechnical Engineering Division*, ASCE, vol. 107, no. GT2, pp. 167-181.
- Wolinsky, ED & Take, WA 2010, 'Application of digital signal processing to the measurement of landslide acceleration using PIV image analysis', *7th International Conference in Physical Modelling and Geotechnics*, Zurich, Switzerland, pp. 405-410.
- Wong, R 1999, 'Mobilized strength components of Athabasca oil sand in triaxial compression', *Canadian Geotechnical Journal*, vol. 36, no. 4, pp. 718-735.
- Woods, R, Barnett, N & Sagesser, R 1974, 'Holography - a new tool for soil dynamics', *Journal of Geotechnical Engineering Division*, ASCE, vol. 100, no. 11, pp. 1231-1247.
- Yamamoto, K, Lyamin, AV, Abbo, AJ, Sloan, SW and Hira, M 2009, 'Bearing capacity and failure mechanism of different types of foundations on sand', *Soils and Foundations*, vol. 49, no. 2, 305-314.
- Yaofeng, S & Pang, JHL 2007, 'Study of optimal subset size in digital image correlation of speckle pattern images', *Optics and Lasers in Engineering*, vol. 45, no. 9, pp. 967-974.
- Yee, IK 1999, Upgrading of existing landfills by dynamic compaction – A geotechnical aspect, *Master Builders Journal*, Malaysia, pp. 21-29 & 210-215.
- Yue, ZQ, Bekking, W & Morin, I 1995, 'Application of digital image processing to quantitative study of asphalt concrete microstructure', *Transportation Research Record, 1492*, Transportation Research Board, Washington, DC, pp. 53-60.
- Yue, ZQ & Morin, I 1996, 'Digital image processing for aggregate orientation in asphalt concrete mixtures', *Canadian Journal of Civil Engineering*, vol. 23, no. 2, pp. 480-489.
- Zhao, H & Ge, L 2007, 'camera calibration using neural network for image-based soil deformation measurement system', *Geotechnical Testing Journal*, vol. 31, no. 2, *Technical Note*, pp. 6.
- Zhu, M & Michalowski, RL 2005, 'Shape Factors for Limit Loads on Square and Rectangular Footings', *Journal of Geotechnical and Geoenvironmental Engineering*, ASCE, vol. 131, no. 2, pp. 223-231.

Appendix I

Table of contents

A1.1	Data sheets of the data Acquisition System – StrainSmart 6000	A-2
A1.2	Accelerometers Data Sheets	A-5
A1.3	Stress cell data sheet	A-9
A1.4	Megapoxy data sheet	A-10

A1.1 Data sheets of the data Acquisition System – StrainSmart 6000

System 6000

MEME Micro-Measurements



StrainSmart® Data Acquisition System



FEATURES

- From 1 to 1200 input channels
- Individual input cards for strain gage and strain-gage-based transducers (Model 6010A), thermocouples (Model 6020), sensors with high-level voltage outputs (Model 6030A), LVDT's (Model 6040A), piezoelectric sensors (Model 6050), and digital tachometer (Model 6095)
- Built-in bridge completion for 120-, 350-, and 1000-ohm strain gages
- Maximum scan rate of 10 000 samples per second per channel; maximum throughput of 200 000 samples per second
- Simultaneous sampling with anti-aliasing filter and analog-to-digital conversion for each channel
- Stable, accurate, low-noise signal conditioning
- Selectable digital filtering of measurement signals
- High-speed PCI hardware interface (Model 6100) and Ethernet network interface (Model 6200A)
- Digital I/O for triggering external events

DESCRIPTION

System 6000 features data acquisition rates of up to 10,000 samples per second per channel. The hardware is designed to incorporate all the features required for precision strain measurement under a variety of loading conditions, while maintaining flexibility and ease of use. A system can be configured with 1 to 1200 sensors. Strain gages, strain-gage-based transducers, thermocouples, LVDT's, potentiometers, accelerometers, piezoelectric sensors and other transducers can be intermixed by choosing the appropriate sensor card. All System 6000 components can be easily configured for each test requirement. Both the Model 6100 Scanner (holding up to 20 input cards) and the Model 6200A Scanner (holding up to 16 input cards) function independently. Additionally, the smaller, lighter, portable Model 6200A can operate from a variety of dc power sources, and can be configured to remotely perform data acquisition and storage.

Utilizing the benefits of individual analog-to-digital conversion on each channel and simultaneous sampling data acquisition for all channels, System 6000's Model 6100 Scanners record test data at rates of up to 10,000 samples per second per channel of instrumentation hardware. The PCI hardware interface between the scanners and a PC running Strain-Smart software in the Windows NT/2000/XP environment enables a combined throughput of up to 200 000 samples per second for all channels (for example, 20 channels at 10 000 samples per second per channel or 40 channels at 5000 samples per second per channel).

Selectable, digital FIR low-pass filtering is incorporated into each instrumentation channel to meet a variety of testing requirements. Custom filters are also available.



System 6000

Micro-Measurements

StrainSmart® Data Acquisition System

MODEL 6100 SCANNER SPECIFICATIONS



- AC powered
- 19-in rack-mountable, 3.5-in high package
- Accepts up to 20 plug-in input cards
- Support high-speed data transfer and setup of the plug-in cards
- Supports local diagnostics
- Supports software identification and setup of each type of plug-in card

OPERATION:

Direct software control.

INPUTS:

Accepts up to 20 cards (one channel per card and up to 20 channels per unit).

SYNC: Automatic**DATA STORAGE:** None.**INTERFACE:** Proprietary PCI.**SIZE:**

3.5 H x 19 W x 16 D in (89 x 483 x 381mm)

WEIGHT:

17lb (7.7kg) empty

19.5lb (8.8kg) loaded with 20 plug-in cards

POWER:115 or 230Vac user-selectable; $\pm 10\%$ of setting; 50/60Hz; 200W max.

MODEL 6200A SCANNER SPECIFICATIONS



- DC powered (AC optional)
- Compact package
- Accepts up to 16 plug-in input cards
- Supports network communication via a 100BASE-T Ethernet connection
- Multiple units can be linked together to provide common control and synchronous sampling
- Offers user-selectable decimal-based (radix 10) and binary-based (radix 2) scanning rates
- On-board program and data storage
- Supports local diagnostics
- Supports software identification and setup of each type of plug-in card

OPERATION:

Stand-alone or direct software control.

INPUTS:

Accepts up to 16 cards (one channel per card and up to 16 channels per unit).

SYNC: Multiple scanners synchronized with synchronization cable links.**DATA STORAGE:**

Can be configured:

Internal: 2GB solid state.

Removable: ATA form factor removable storage devices, solid state.

INTERFACE: Type : Ethernet

Topology : 100Base-T

Protocol : TCP/IP (HTTP)

OPERATING VIBRATION:

6G peak in all three axes. Sweep to 10Hz (solid state media).

OPERATING SHOCK:

20G peak in all three axes, 5 shocks in each axis (solid state media).

SIZE:

4 H x 10 W x 12.3 D in (102 x 254 x 312mm)

WEIGHT:

9.1lb (4.1kg) empty, 11.1lb (5.0kg) loaded with 16 plug-in cards.

POWER:

Designed for use with dc power; 9-32Vdc, 100W max. Optional power adapter (Model 6207); 120/240Vac.

Document Number: 11270
Revision: 22-Jan-10For technical questions, contact: micro-measurements@vishaypg.comwww.micro-measurements.com

41

System 6000

MEME Micro-Measurements

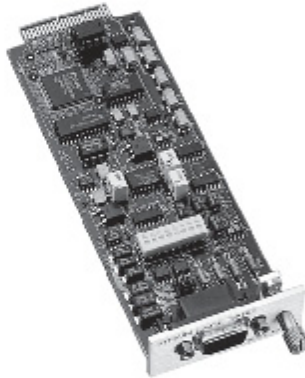


StrainSmart® Data Acquisition System

SENSOR CARD SPECIFICATIONS



MODEL 6010A STRAIN GAGE CARD



- Supports software identification and setup of each type of plug-in card
- Complete strain gage signal conditioner with 16-bit analog-to-digital converter
- Programmable digital filter
- Programmable excitation supply per channel. The supply is settable to 0, 0.5, 1, 2, 5, and 10V. Up to 50mA of excitation current is available on each channel. Remote sense is provided for full-bridge transducers.
- Programmable gain to complement the excitation steps of 1, 2, 5, and 10V. Full-scale input range will be $\pm 16\ 383\ \mu\text{V}$. An excitation setting of 0.5V will use the 1V gain range, but with one-half the resolution. Gain settings are independent per channel.
- Internal bridge completion resistors: 120 Ω , 350 Ω , and 1000 Ω dummy resistors (jumper selectable); 1000 internal half bridge
- Programmable coarse balance range of $\pm 16\ 300\ \mu\text{V}$ (4096 μV steps)

- Fixed low-pass anti-aliasing filter (six-pole)
- Two programmable shunt calibration circuits
- Input connections to user's strain gage via nine-pin D-sub connector

CHANNELS: One per card.

INPUTS:

Strain Gages:

120 Ω , 350 Ω , 1000 Ω quarter bridges; 60 Ω to 5000 Ω half and full bridges.Jumper-selectable completion resistors (0.01% \pm 2.5ppm/ $^{\circ}\text{C}$ typical).

Measurement Range:

Normal range mode: $\pm 16\ 380\ \mu\text{V}$
High range mode: $\pm 163\ 800\ \mu\text{V}$
Low range mode: $\pm 1638\ \mu\text{V}$

Resolution:

Normal range mode: 0.5 μV
High range mode: 5 μV
Low range mode: 0.05 μV Strain Gage Based Transducers:
60 Ω to 5000 Ω impedance

Measurement Range:

Normal range mode: $\pm 8\text{mV/V}$
High range mode: $\pm 80\text{mV/V}$
Low range mode: $\pm 0.8\text{mV/V}$

Resolution:

Normal range mode: 0.25 $\mu\text{V/V}$
High range mode: 2.5 $\mu\text{V/V}$
Low range mode: 0.025 $\mu\text{V/V}$

Input Impedance:

220M Ω each input.Source Current: $\pm 25\text{nA}$ max.

Input Connector: Nine-pin D-sub style.



A1.2 Accelerometers Data Sheets

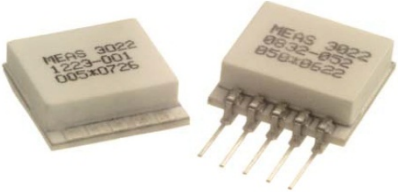
Model 3022 Accelerometer

Piezoresistive MEMS
DC Response
Circuit Board Mountable
Low Cost

The Model 3022 is a silicon MEMS accelerometer in a Wheatstone bridge configuration. The accelerometer is packaged on a ceramic substrate with an epoxy sealed ceramic cover and is designed for adhesive mounting. The accelerometer is offered in ranges from $\pm 2g$ to $\pm 200g$ range and provides a flat frequency response to minimum 2000Hz. The silicon MEMS sensor is gas damped and incorporates over-range stops for high-g shock protection.

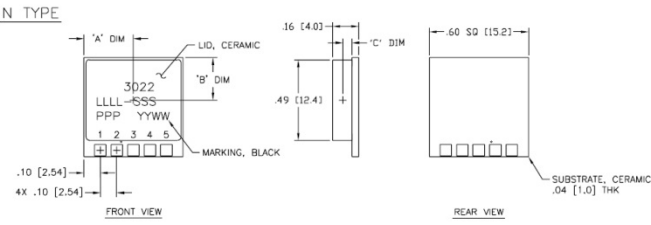
For a similar accelerometer designed for bolt mounting, see the model 3028.



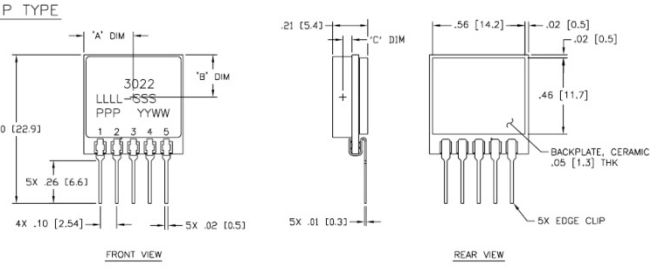
dimensions

N TYPE



FRONT VIEW REAR VIEW

P TYPE



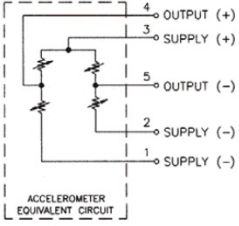
FRONT VIEW REAR VIEW

FEATURES

- Adhesive Mounted
- $\pm 0.5\%$ Non-linearity
- Open Wheatstone Bridge
- DC Response
- Gas Damping
- Built-in Overrange Stops
- Low Power Consumption

APPLICATIONS

- Vibration & Shock Monitoring
- Motion Control
- Impact & Shock Testing
- Modal Analysis
- Embedded Applications
- Machinery



ACCELEROMETER EQUIVALENT CIRCUIT

Model 3022 Rev 2

32 Journey Ste. 150 Aliso Viejo, CA 92656

www.meas-spec.com

949-716-5377

10/14/2009

t&m@meas-spec.com

Model 3022 Accelerometer



performance specifications

All values are typical at +24°C, 100Hz and 5Vdc excitation unless otherwise stated. Measurement Specialties reserves the right to update and change these specifications without notice. Standard product parameters are described in PSC-1002 for Embedded DC Accelerometers.

Parameters

DYNAMIC

Parameters	±2	±5	±10	±20	±50	±100	±200	Notes
Range (g)	±2	±5	±10	±20	±50	±100	±200	
Sensitivity (mV/g) ¹	8.0-20.0	6.0-15.0	3.0-6.0	1.5-3.0	0.6-1.5	0.3-0.6	0.15-0.3	@5Vdc Excitation
Frequency Response (Hz)	0-150	0-250	0-400	0-600	0-1000	0-1500	0-2000	±5%
Natural Frequency (Hz)	700	800	1000	1500	4000	6000	8000	
Non-Linearity (%FSO)	±0.5	±0.5	±0.5	±0.5	±0.5	±0.5	±0.5	
Transverse Sensitivity (%)	<3	<3	<3	<3	<3	<3	<3	<1 Typical
Damping Ratio	0.7	0.7	0.7	0.7	0.7	0.7	0.6	
Shock Limit (g)	5000	5000	5000	5000	10000	10000	10000	

ELECTRICAL

Zero Acceleration Output (mV)	±25	±25	±25	±25	±25	±25	±25	Differential
Excitation Voltage (Vdc)	2 to 10	2 to 10	2 to 10	2 to 10	2 to 10	2 to 10	2 to 10	
Input Resistance (Ω)	2500-6500	2500-6500	2500-6500	2500-6500	2500-6500	2500-6500	2500-6500	
Output Resistance (Ω)	2500-6500	2500-6500	2500-6500	2500-6500	2500-6500	2500-6500	2500-6500	
Insulation Resistance (MΩ)	>100	>100	>100	>100	>100	>100	>100	@50Vdc
Residual Noise (μV RMS)	10	10	10	10	10	10	10	Maximum
Ground Isolation	Isolated from Mounting Surface							

ENVIRONMENTAL

Thermal Zero Shift (%FSO/°C)	-0.09	-0.09	-0.09	-0.09	-0.09	-0.09	-0.09	Typical
Thermal Sensitivity Shift (%/°C)	-0.15	-0.15	-0.15	-0.15	-0.15	-0.15	-0.15	Typical
Operating Temperature (°C)	-40 to +125							
Compensated Temperature (°C)	Uncompensated							
Storage Temperature (°C)	-40 to +125							

PHYSICAL

Case Material	Ceramic
Cable	Not applicable
Weight (grams)	3.1
Mounting	Adhesive or solder
Mounting Torque	Not applicable
AWG	Not applicable

¹ Output is ratiometric to excitation voltage

Wiring color code: See schematic

The information in this sheet has been carefully reviewed and is believed to be accurate; however, no responsibility is assumed for inaccuracies. Furthermore, this information does not convey to the purchaser of such devices any license under the patent rights to the manufacturer. Measurement Specialties, Inc. reserves the right to make changes without further notice to any product herein. Measurement Specialties, Inc. makes no warranty, representation or guarantee regarding the suitability of its product for any particular purpose, nor does Measurement Specialties, Inc. assume any liability arising out of the application or use of any product or circuit and specifically disclaims any and all liability, including without limitation consequential or incidental damages. Typical parameters can and do vary in different applications. All operating parameters must be validated for each customer application by customer's technical experts. Measurement Specialties, Inc. does not convey any license under its patent rights nor the rights of others.

ordering info

PART NUMBERING Model Number+Range+Electrical Connection

3022-GGG-P

Example: 3022-010-P
Model 3022, 10g, Pins

Model 3022 Rev 2

www.meas-spec.com

10/14/2009

32 Journey Ste. 150 Aliso Viejo, CA 92656

949-716-5377

t&m@meas-spec.com

Model 3038 Accelerometer

measurement
SPECIALTIES™



Miniature Piezoresistive MEMS
SMD Accelerometer
Hermetically Sealed
10,000g Shock Protection



The **Model 3038** is a hermetically sealed SMD accelerometer designed for high performance applications. The accelerometer incorporates a gas-damped piezoresistive MEMS sensing element providing outstanding long-term stability. The model 3038 provides a millivolt output signal and features mechanical overload stops that provide shock protection to loads greater than 10,000g.

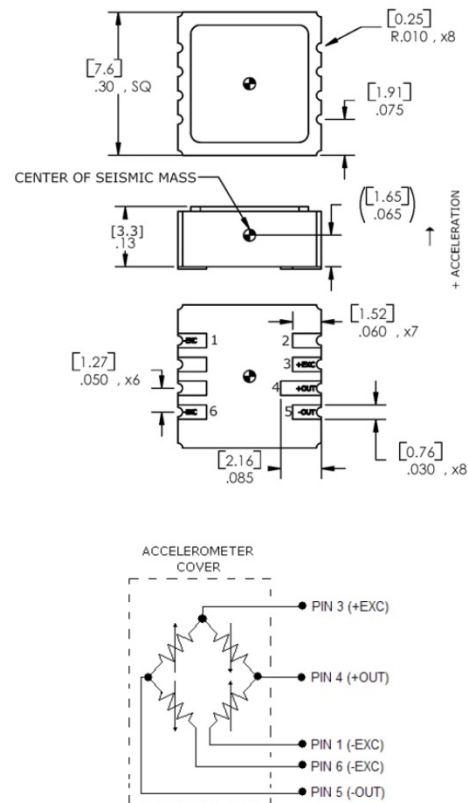
FEATURES

- $\pm 50g$ to $\pm 6000g$ Dynamic Ranges
- Board Mountable Accelerometer
- Low Power Consumption
- Hermetic LCC Package
- DC Response, Gas Damping
- 5000Hz Bandwidth

APPLICATIONS

- Harsh Environments
- Vibration & Shock Monitoring
- Impact Testing
- Embedded Applications
- Instrumentation
- Machinery

dimensions



US Patents 5,103,667; 5,253,510; 5,445,006 apply

Model 3038 Rev D

www.meas-spec.com

03/26/2012

32 Journey Ste. 150 Aliso Viejo, CA 92656

949-716-5377

t&m@meas-spec.com

Model 3038 Accelerometer



performance specifications

All values are typical at +24°C, 100Hz and 5Vdc excitation unless otherwise stated. Measurement Specialties reserves the right to update and change these specifications without notice. Standard product parameters are described in PSC-1002 for Embedded DC Accelerometers.

Parameters

DYNAMIC

	±50	±100	±200	±500	±2000	±6000	Notes
Range (g)							
Sensitivity (mV/g) ¹	1.0	0.50	0.40	0.20	0.08	0.05	@5Vdc Excitation
Frequency Response (Hz)	0-1000	0-1200	0-1400	0-2000	0-4500	0-5000	±5%
Natural Frequency (Hz)	4000	6000	8000	15000	24000	26000	
Non-Linearity (%FSO)	±1	±1	±1	±1	±1	±2	
Transverse Sensitivity (%)	<3	<3	<3	<3	<3	<3	<1 Typical
Damping Ratio	0.4-0.9	0.4-0.9	0.2-0.6	0.2-0.6	0.05-0.30	0.05-0.30	
Shock Limit (g) ³	10000	10000	10000	10000	10000	10000	

ELECTRICAL

Zero Acceleration Output (mV)	±25						Differential
Excitation Voltage (Vdc)	2 to 10						
Input Resistance (Ω)	2400-6500						
Output Resistance (Ω)	2400-6500						
Insulation Resistance (MΩ)	>100						@50Vdc
Residual Noise (μV RMS)	10						Maximum
Ground Isolation	Isolated from Mounting Surface						

ENVIRONMENTAL

Thermal Zero Shift (%FSO/°C)	-0.09						Typical
Thermal Sensitivity Shift (%/°C)	-0.15						Typical
Operating Temperature (°C)	-55 to 125						
Compensated Temperature (°C)	Uncompensated						
Storage Temperature (°C)	-55 to 125						
Humidity	Hermetically Sealed						

PHYSICAL

Case Material	Ceramic
Weight (grams)	0.6
Mounting	Solder

¹ Output is ratiometric to excitation voltage. 10Vdc excitation will increase output by a factor of 2x.

² The maximum recommended soldering temperature is +260°C

³ 10,000g shock limit in normal axis; 5,000g in transverse axes

Calibration supplied: CS-SENS-0100 NIST Traceable Amplitude Calibration at 100Hz and 5Vdc Excitation

The information in this sheet has been carefully reviewed and is believed to be accurate; however, no responsibility is assumed for inaccuracies. Furthermore, this information does not convey to the purchaser of such devices any license under the patent rights to the manufacturer. Measurement Specialties, Inc. reserves the right to make changes without further notice to any product herein. Measurement Specialties, Inc. makes no warranty, representation or guarantee regarding the suitability of its product for any particular purpose, nor does Measurement Specialties, Inc. assume any liability arising out of the application or use of any product or circuit and specifically disclaims any and all liability, including without limitation consequential or incidental damages. Typical parameters can and do vary in different applications. All operating parameters must be validated for each customer application by customer's technical experts. Measurement Specialties, Inc. does not convey any license under its patent rights nor the rights of others.

ordering info

PART NUMBERING Model Number+Range

3038-GGGG

| _____ Range (0100 is 100 g)

Example: 3038-0100

Model 3038, 100g

Model 3038 Rev D

www.meas-spec.com

03/26/2012

32 Journey Ste. 150 Aliso Viejo, CA 92656

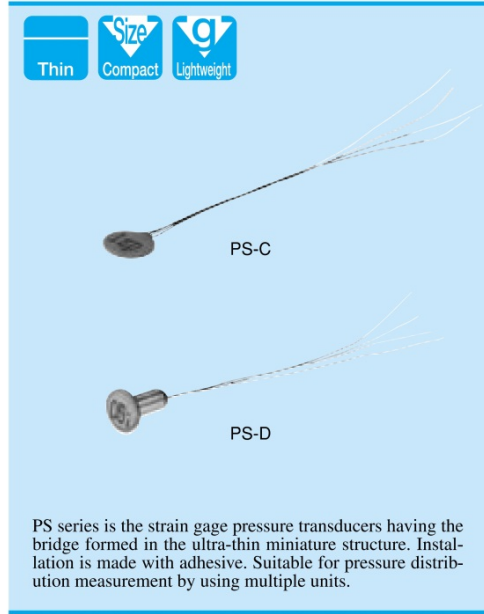
949-716-5377

t&m@meas-spec.com

A1.3 Stress cells data sheet

PS Miniature Pressure Sensors

● For Pressure Distribution Measurement ● 50 kPa to 7 MPa



Thin Compact Lightweight

PS series is the strain gage pressure transducers having the bridge formed in the ultra-thin miniature structure. Installation is made with adhesive. Suitable for pressure distribution measurement by using multiple units.

Features

- Ultra-thin design
- Compact
- Wide range of rated capacities

Specifications

Performance

Rated Capacity:

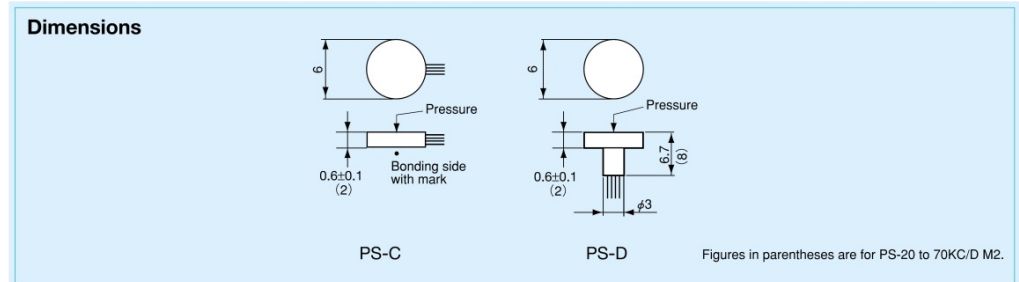
Model		Rated Capacity	Natural Frequency (Approx.)
Cable Direction to Sensing Surface			
Horizontal	Vertical		
PS-05KC	PS-05KD	50 kPa	10 kHz
PS-1KC	PS-1KD	100 kPa	10 kHz
PS-2KC	PS-2KD	200 kPa	14 kHz
PS-5KC	PS-5KD	500 kPa	20 kHz
PS-10KC	PS-10KD	1 MPa	37 kHz
PS-20KC M2	PS-20KD M2	2 MPa	46 kHz
PS-30KC M2	PS-30KD M2	3 MPa	58 kHz
PS-50KC M2	PS-50KD M2	5 MPa	71 kHz
PS-70KC M2	PS-70KD M2	7 MPa	86 kHz

Measuring liquids of PS-20 to 70KC/D M2 are limited to oils.
Nonlinearity: Within ±1% RO
Hysteresis: Within ±1% RO
Rated Output:
 0.25 mV/V (500 μm/m) or more (PS-05KC/D)
 0.5 mV/V (1000 μm/m) or more (PS-1KC/D)
 0.85 mV/V (1700 μm/m) ±30% (PS-2KC/D)
 1 mV/V (2000 μm/m) ±20% (PS-5 to 70KC/D)
 Note: Rated output is sorted to one of the classes divided by every 2% difference in output value. Since the rated output stated in the Test Data Sheet is the center value of the class, it may have a maximum error of ±1%.

Environmental Characteristics
Safe Temperature Range: -20 to 70°C
Compensated Temperature Range: 0 to 50°C
Temperature Effect on Zero Balance:
 Within ±0.8% RO/°C (PS-05KC/D)
 Within ±0.4% RO/°C (PS-1KC/D)
 Within ±0.3% RO/°C (PS-2KC/D)
 Within ±0.2% RO/°C (PS-5 to 70KC/D)
Temperature Effect on Output:
 Within ±0.3%/°C (PS-05 to 2KC/D)
 Within ±0.2%/°C (PS-5 to 70KC/D)

Electrical Characteristics
Safe Excitation Voltage: 3 VAC or DC
Recommended Excitation Voltage: 1 to 2 VAC or DC
Input Resistance: 350 Ω ±10%
Output Resistance: 350 Ω ±10%
Cable: Polyurethane coated copper wires, 0.1 mm diameter (0.08 mm diameter with PS-05KD & 1KD) by 5 cm long, soldering finish at each tip (Shield wire is not connected to mainframe.)

Mechanical Properties
Safe Overload Rating: 150% (100% with PS-70KC/D M2)
Materials: Metallic finish
Weight: Approx. 0.5 g ±20% (including cable)
Dedicated Adhesive: RC-19 (Request when ordering, charge-free)



2 TRANSDUCERS

A1.4 Megapoxy HX data sheet

Technical Bulletin

Megapoxy

317A1

MEGAPOXY HX

SOLVENT FREE HYDROPHILIC EPOXY EXTRA LOW VISCOSITY

Recent advances in epoxy resin technology enabled the development of very low viscosity 100% reactive epoxy resin system for repair of cracked concrete by gravity penetration or low pressure injection. Megapoxy HX is also suitable for impregnation of porous substrates such as masonry and timber. Megapoxy HX has also been used successfully as a low viscosity laminating resin for fibreglass work.

PROPERTIES CURED

Ultimate compressive strength	: 95 MPa
Ultimate flexural strength	: 35 MPa

INSTRUCTIONS FOR USE

Mixing Ratio by Volume	: Part A - 3 parts : Part B - 1 part
Pot Life (1 litre mix)	: 30 minutes at 25°C
Initial mixed viscosity	: 60 cps at 25°C
Working time	: 30 minutes at 25°C
Full cure	: 48 hours at 25°C

Megapoxy HX should be used in manner similar to Megapoxy H Multi Purpose Hydrophilic Resin where extra low viscosity is required. The cured properties of Megapoxy HX are very similar to those of Megapoxy H and mixing and working recommendations for Megapoxy H apply to Megapoxy HX.

PACKAGING

Megapoxy HX is available in 4 litre and 20 litre kit. Each kit contains the resin and hardener pre-metered in correct mixing ratio for immediate use.



VIVACITY ENGINEERING PTY. LTD.
 3 Sefton Road, Thornleigh, NSW 2120 • P.O. Box 71, Hornsby, NSW Australia, 1630
 Telephone +61-2-9875 3044 Fax +61-2-9875 3865 email:info@megapoxy.com
 www.megapoxy.com A.B.N. 78 305 545 664

Appendix II

Table of Contents

A2.1	Calibrations of earth pressure sensors	A-12
A2.2	Calibration of load cell- Steady rate static test	A-15
A2.3	Calibrations of oedometer ring strain gauges	A-16

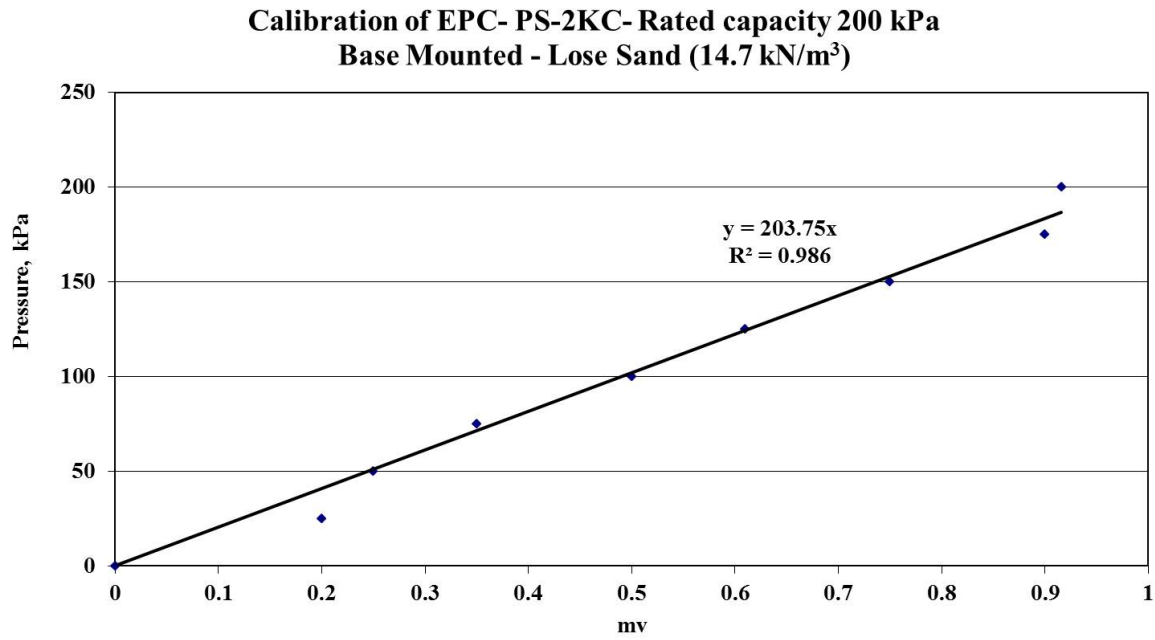


Figure A2.1. Calibration of EPC- PS-2KC- Rated capacity 200 kPa – Loose Sand

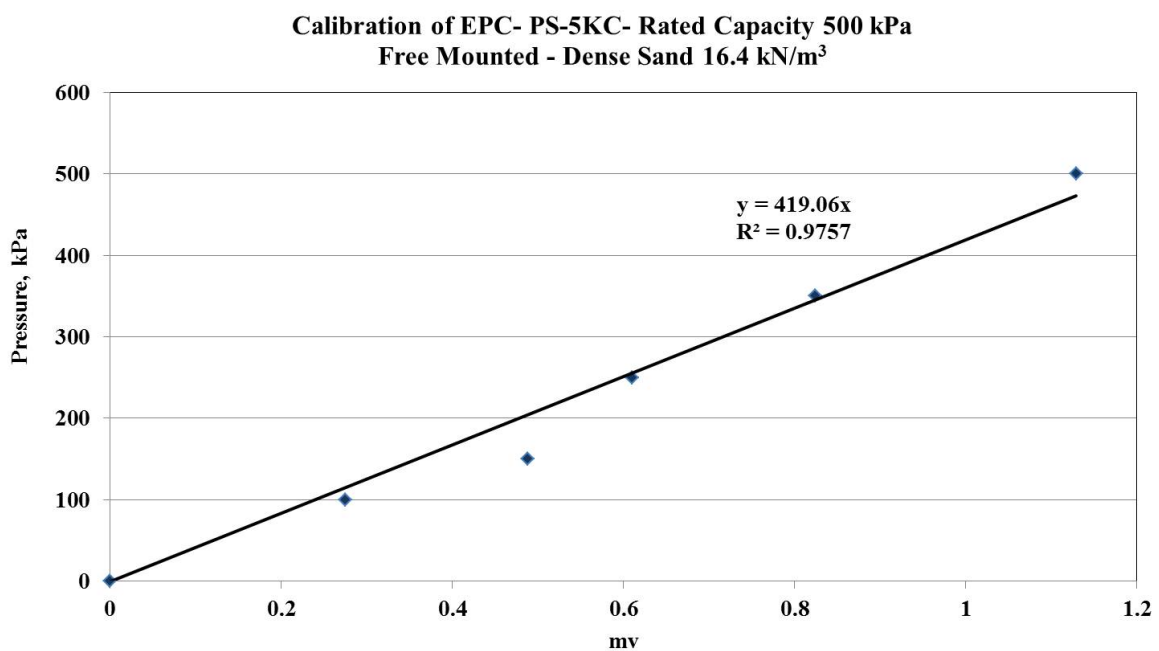


Figure A2.2. Calibration of EPC- PS-5KC- Rated capacity 500 kPa – Dense Sand

Note:

Free mounted: the EPC sensor is placed at the middle of the calibration chamber

Base mounted: the EPC sensors is placed on the calibration chamber's base

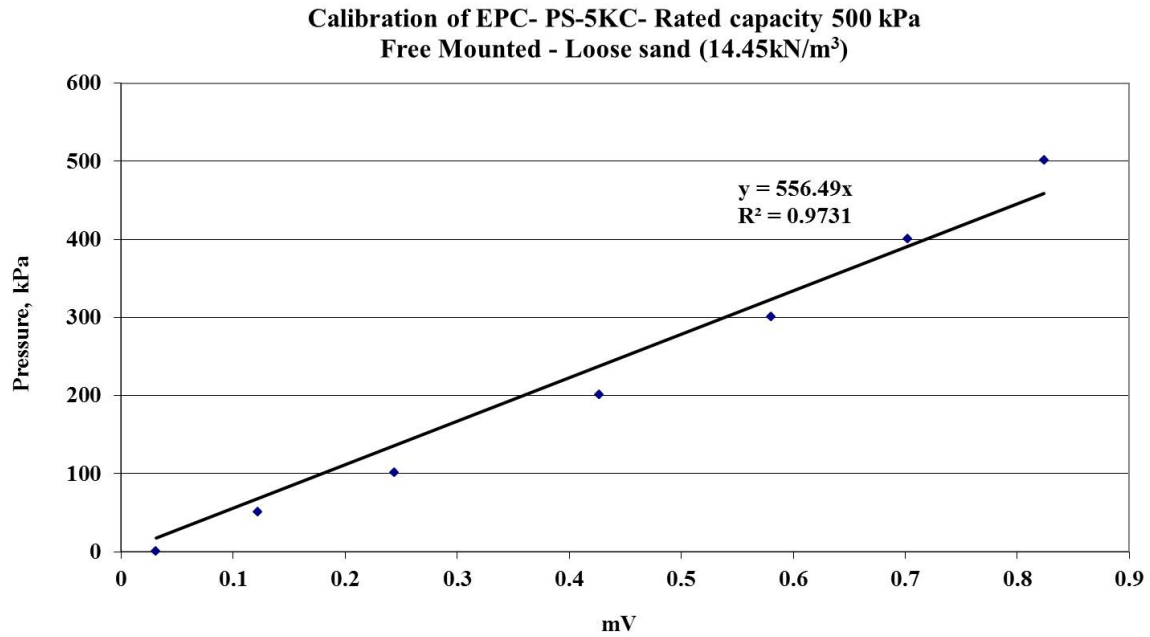


Figure A2.3. Calibration of EPC- PS-5KC- Rated capacity 500 kPa – Loose Sand

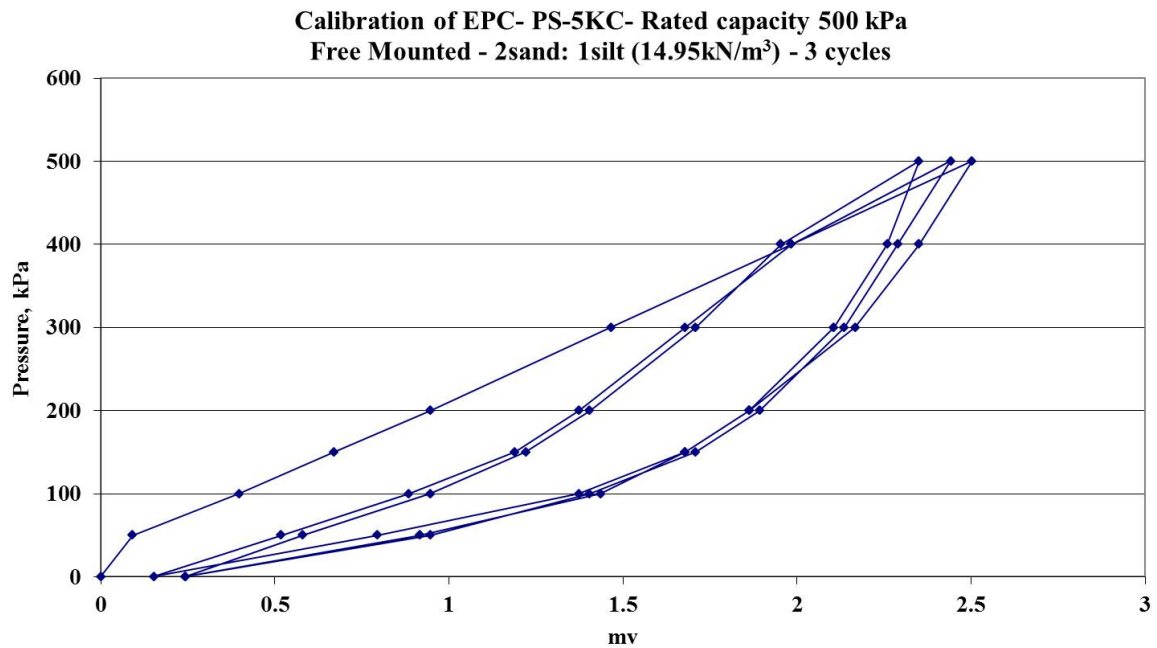


Figure A2.4. Calibration of EPC- PS-5KC- Rated capacity 500 kPa – 2Sand:1Silt

Note:

Free mounted: the EPC sensor is placed at the middle of the chamber

Base mounted: the EPC sensors is placed on the calibration chamber's base

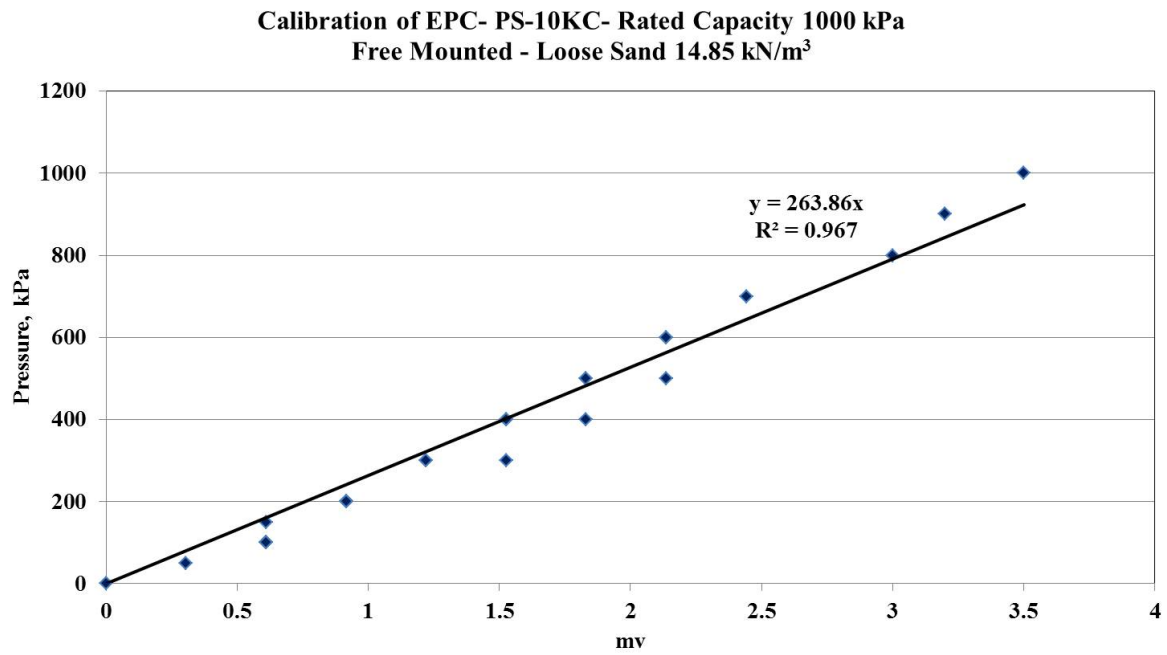


Figure A2.5. Calibration of EPC- PS-10KC- Rated capacity 1000 kPa – Loose Sand

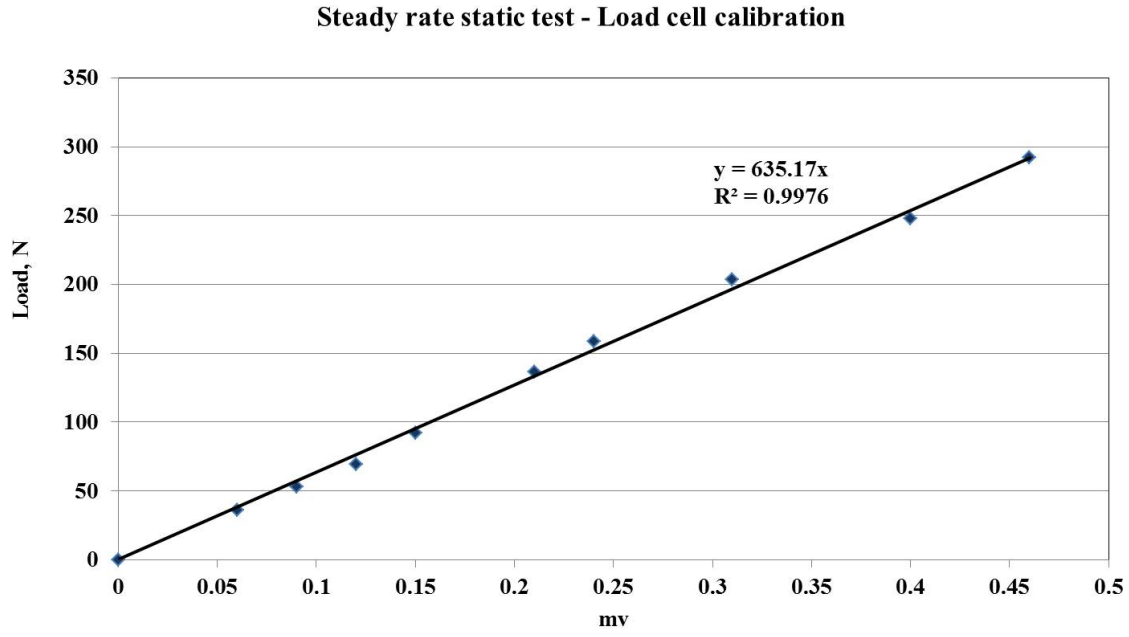


Figure A2.6. Calibration of load cell – Steady rate static test

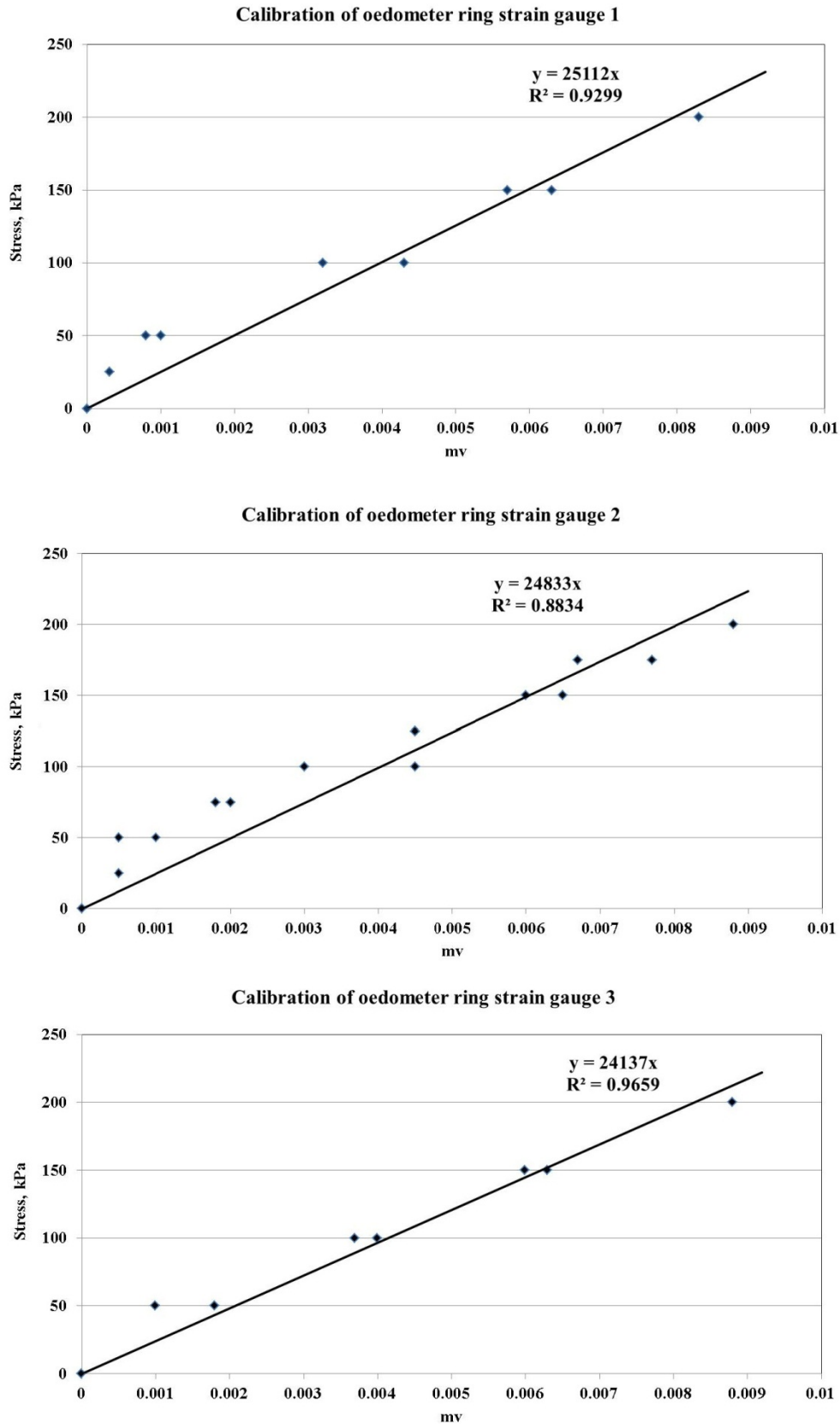


Figure A2.7. Calibration of oedometer ring strain gauges

Appendix III

Table of Contents

A3.1	Syntaxes and algorithms of the Matlab routine "histeq"	A-18
A3.2	Syntaxes and algorithms of the Matlab routine "wiener2"	A-20
A3.3	Calibration of control markers object-space coordinates	A-21

A3.1 Syntaxes and algorithms of the Matlab routine "histeq"

histeq - Enhance contrast using histogram equalization

Syntax

```
J = histeq(I, hgram)
J = histeq(I, n)
[J, T] = histeq(I,...)
newmap = histeq(X, map, hgram)
newmap = histeq(X, map)
[newmap, T] = histeq(X,...)
```

Description

`histeq` enhances the contrast of images by transforming the values in an intensity image, or the values in the colormap of an indexed image, so that the histogram of the output image approximately matches a specified histogram.

`J = histeq(I, hgram)` transforms the intensity image `I` so that the histogram of the output intensity image `J` with `length(hgram)` bins approximately matches `hgram`. The vector `hgram` should contain integer counts for equally spaced bins with intensity values in the appropriate range: `[0, 1]` for images of class `double`, `[0, 255]` for images of class `uint8`, and `[0, 65535]` for images of class `uint16`. `histeq` automatically scales `hgram` so that `sum(hgram) = prod(size(I))`. The histogram of `J` will better match `hgram` when `length(hgram)` is much smaller than the number of discrete levels in `I`.

`J = histeq(I, n)` transforms the intensity image `I`, returning in `J` an intensity image with `n` discrete gray levels. A roughly equal number of pixels is mapped to each of the `n` levels in `J`, so that the histogram of `J` is approximately flat. (The histogram of `J` is flatter when `n` is much smaller than the number of discrete levels in `I`.) The default value for `n` is 64.

`[J, T] = histeq(I,...)` returns the grayscale transformation that maps gray levels in the image `I` to gray levels in `J`.

`newmap = histeq(X, map, hgram)` transforms the colormap associated with the indexed image `X` so that the histogram of the gray component of the indexed image (`X, newmap`) approximately matches `hgram`. The `histeq` function returns the transformed colormap in `newmap`. `length(hgram)` must be the same as `size(map,1)`.

`newmap = histeq(X, map)` transforms the values in the colormap so that the histogram of the gray component of the indexed image `X` is approximately flat. It returns the transformed colormap in `newmap`.

`[newmap, T] = histeq(X,...)` returns the grayscale transformation `T` that maps the gray component of `map` to the gray component of `newmap`.

Class Support

For syntax that include an intensity image `I` as input, `I` can be of class `uint8`, `uint16`, `int16`, `single`, or `double`. The output image `J` has the same class as `I`.

For syntax that include an indexed image `X` as input, `X` can be of class `uint8`, `single`, or `double`; the output colormap is always of class `double`. The optional output `T` (the gray-level transform) is always of class `double`.

Examples

Enhance the contrast of an intensity image using histogram equalization.

```
I = imread('tire.tif');
J = histeq(I);
imshow(I)
figure, imshow(J)
```

Algorithms

When you supply a desired histogram `hgram`, `histeq` chooses the grayscale transformation T to minimize

$$|c_1(T(k)) - c_0(k)|,$$

where c_0 is the cumulative histogram of A , c_1 is the cumulative sum of `hgram` for all intensities k . This minimization is subject to the constraints that T must be monotonic and $c_1(T(a))$ cannot overshoot $c_0(a)$ by more than half the distance between the histogram counts at a . `histeq` uses the transformation $b = T(a)$ to map the gray levels in x (or the colormap) to their new values.

If you do not specify `hgram`, `histeq` creates a flat `hgram`,

```
hgram = ones(1,n)*prod(size(A))/n;
```

and then applies the previous algorithm.

See Also

`brighten` | `imadjust` | `imhist`

A3.2 Syntaxes and algorithms of the Matlab routine "wiener2"

wiener2 - 2-D adaptive noise-removal filtering

Note The syntax `wiener2(I, [m n], [mblock nblock], noise)` has been removed. Use the `wiener2(I, [m n], noise)` syntax instead.

Syntax

```
J = wiener2(I, [m n], noise)
[J, noise] = wiener2(I, [m n])
```

Description

`wiener2` lowpass-filters a grayscale image that has been degraded by constant power additive noise. `wiener2` uses a pixelwise adaptive Wiener method based on statistics estimated from a local neighborhood of each pixel.

`J = wiener2(I, [m n], noise)` filters the image `I` using pixelwise adaptive Wiener filtering, using neighborhoods of size `m`-by-`n` to estimate the local image mean and standard deviation. If you omit the `[m n]` argument, `m` and `n` default to 3. The additive noise (Gaussian white noise) power is assumed to be `noise`.

`[J, noise] = wiener2(I, [m n])` also estimates the additive noise power before doing the filtering. `wiener2` returns this estimate in `noise`.

Class Support

The input image `I` is a two-dimensional image of class `uint8`, `uint16`, `int16`, `single`, or `double`. The output image `J` is of the same size and class as `I`.

Examples

For an example, see [Removing Noise By Adaptive Filtering](#).

Algorithms

`wiener2` estimates the local mean and variance around each pixel.

$$\mu = \frac{1}{NM} \sum_{n_1, n_2 \in \eta} a(n_1, n_2)$$

and

$$\sigma^2 = \frac{1}{NM} \sum_{n_1, n_2 \in \eta} a^2(n_1, n_2) - \mu^2,$$

where η is the N -by- M local neighborhood of each pixel in the image `A`. `wiener2` then creates a pixelwise Wiener filter using these estimates,

$$b(n_1, n_2) = \mu + \frac{\sigma^2 - v^2}{\sigma^2} (a(n_1, n_2) - \mu),$$

where v^2 is the noise variance. If the noise variance is not given, `wiener2` uses the average of all the local estimated variances.

References

Lim, Jae S., *Two-Dimensional Signal and Image Processing*, Englewood Cliffs, NJ, Prentice Hall, 1990, p. 548, equations 9.44 -- 9.46.

A3.3 Calibration of control markers object-space coordinates

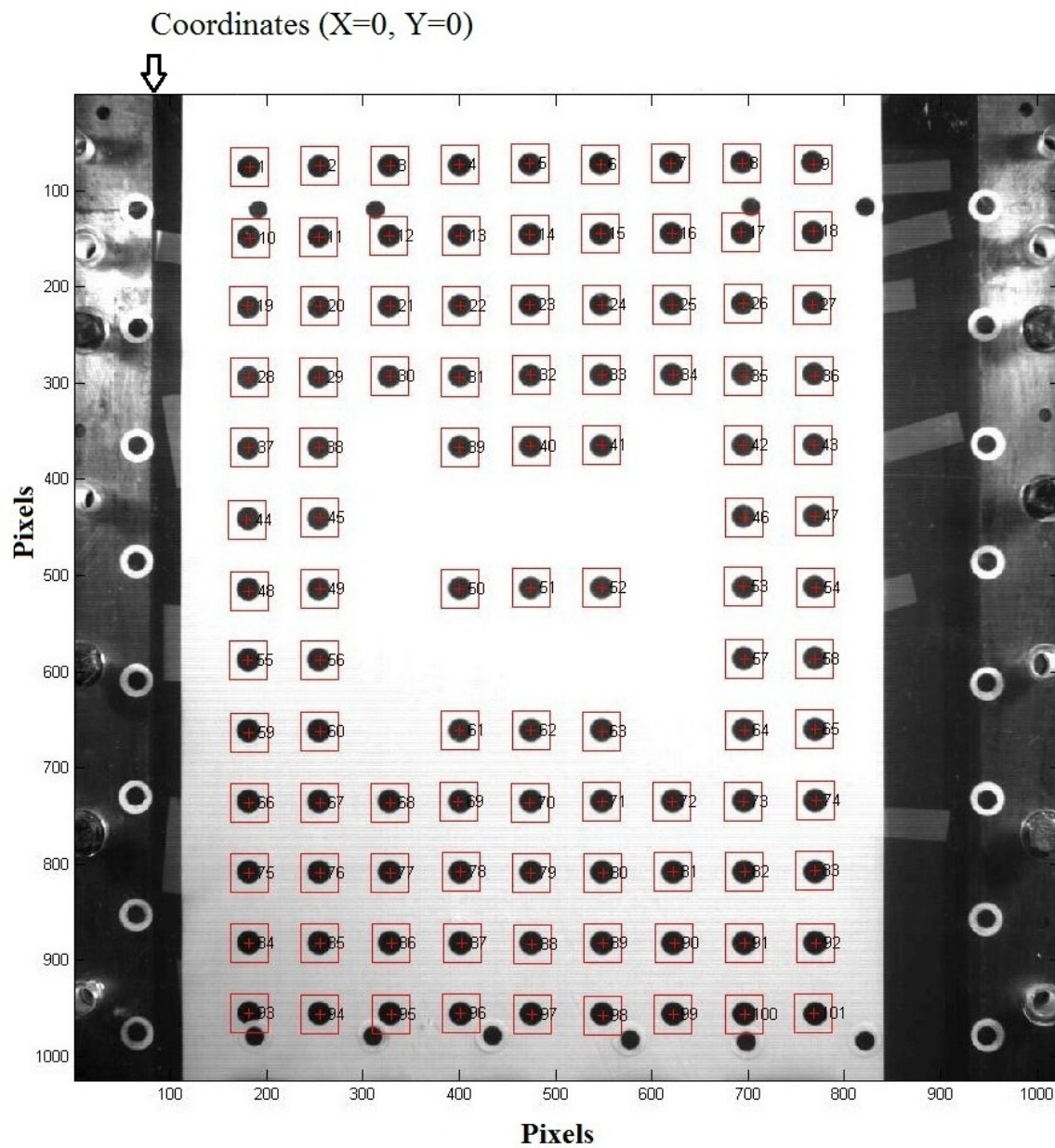


Figure A3.1. Calibration of control markers by 101 stationary dots

Table A3.1. Object-space coordinates of 101 stationary calibration dots

Dot No.	X, mm	Y, mm	Dot No.	X, mm	Y, mm	Dot No.	X, mm	Y, mm	Dot No.	X, mm	Y, mm	Dot No.	X, mm	Y, mm
1	30	30	21	90	90	41	180	150	61	120	270	81	210	330
2	60	30	22	120	90	42	240	150	62	150	270	82	240	330
3	90	30	23	150	90	43	270	150	63	180	270	83	270	330
4	120	30	24	180	90	44	30	180	64	240	270	84	30	360
5	150	30	25	210	90	45	60	180	65	270	270	85	60	360
6	180	30	26	240	90	46	240	180	66	30	300	86	90	360
7	210	30	27	270	90	47	270	180	67	60	300	87	120	360
8	240	30	28	30	120	48	30	210	68	90	300	88	150	360
9	270	30	29	60	120	49	60	210	69	120	300	89	180	360
10	30	60	30	90	120	50	120	210	70	150	300	90	210	360
11	60	60	31	120	120	51	150	210	71	180	300	91	240	360
12	90	60	32	150	120	52	180	210	72	210	300	92	270	360
13	120	60	33	180	120	53	240	210	73	240	300	93	30	390
14	150	60	34	210	120	54	270	210	74	270	300	94	60	390
15	180	60	35	240	120	55	30	240	75	30	330	95	90	390
16	210	60	36	270	120	56	60	240	76	60	330	96	120	390
17	240	60	37	30	150	57	240	240	77	90	330	97	150	390
18	270	60	38	60	150	58	270	240	78	120	330	98	180	390
19	30	90	39	120	150	59	30	270	79	150	330	99	210	390
20	60	90	40	150	150	60	60	270	80	180	330	100	240	390
												101	270	390

Note: coordinates (X=0, Y=0) are shown in Figure A3.1.

Table A3.2. Control markers object space coordinates with reference to the 101 calibration dots (Figure A3.1. & Table A3.1)

Control Marker	X, mm	Y, mm
1	-18.18	46.54
2	33.50	47.92
3	82.90	48.41
4	243.44	49.76
5	291.65	48.42
6	343.17	48.67
7	-18.01	97.31
8	342.33	99.00
9	-17.90	147.90
10	342.42	149.10
11	-17.82	197.50
12	341.77	199.10
13	-17.78	247.50
14	342.00	249.38
15	-17.83	296.60
16	341.90	299.20
17	-17.92	347.42
18	341.40	348.70
19	-18.02	397.90
20	32.20	399.30
21	82.65	398.70
22	132.93	398.90
23	191.70	400.10
24	240.90	401.30
25	291.00	401.00
26	341.50	399.20

Table A3.3. Control markers object space coordinates with reference to the coordinates of the top let corner control marker

Control Marker	X, mm	Y, mm
1	0.00	0.00
2	51.67	1.37
3	101.08	1.87
4	261.61	3.21
5	309.83	1.88
6	361.35	2.12
7	0.16	50.76
8	360.51	52.46
9	0.28	101.36
10	360.59	102.56
11	0.36	150.96
12	359.94	152.56
13	0.39	200.96
14	360.18	202.84
15	0.34	250.06
16	360.08	252.66
17	0.26	300.87
18	359.58	302.16
19	0.16	351.36
20	50.38	352.76
21	100.83	352.16
22	151.11	352.36
23	209.88	353.56
24	259.08	354.76
25	309.18	354.46
26	359.68	352.66

Appendix IV

Table of Contents

A4.1	Theoretical backgrounds of LS-DYNA soil models (extracted from LS-DYNA theory manual)	A-26
A4.2	Examples of LS-DYNA model	A-28

A4.1 Theoretical backgrounds of LS-DYNA soil models (extracted from LS-DYNA theory manual)

Material Model 5: Soil and Crushable Foam

This model, due to Krieg [1972], provides a simple model for foam and soils whose material properties are not well characterized. We believe the other foam models in LS-DYNA are superior in their performance and are recommended over this model which simulates the crushing through the volumetric deformations. If the yield stress is too low, this foam model gives nearly fluid like behavior.

A pressure-dependent flow rule governs the deviatoric behavior:

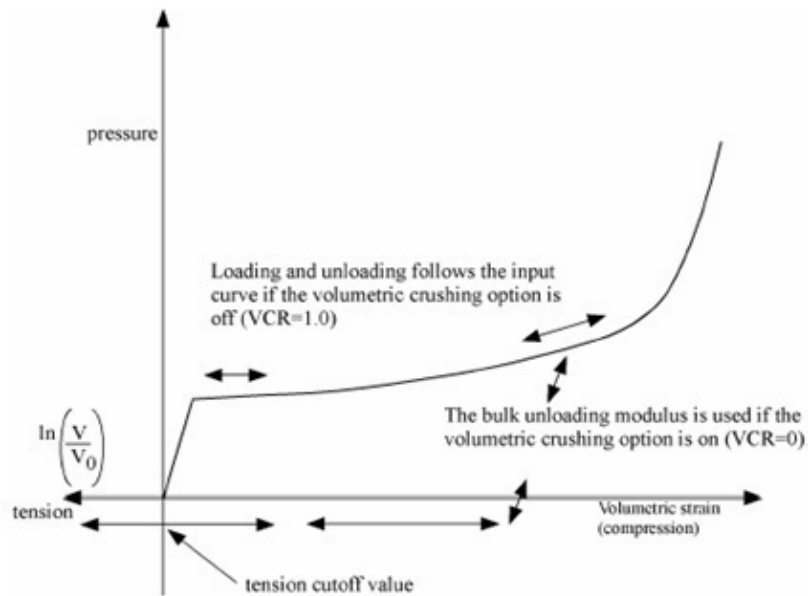
$$\phi_s = \frac{1}{2} s_{ij} s_{ij} - (a_0 + a_1 p + a_2 p^2)$$

where a_0 , a_1 , and a_2 are user-defined constants. Volumetric yielding is determined by a tabulated curve of pressure versus volumetric strain. Elastic unloading from this curve is assumed to a tensile cutoff as illustrated in Figure 19.5.1.

Implementation of this model is straightforward. One history variable, the maximum volumetric strain in compression, is stored. If the new compressive volumetric strain exceeds the stored value, loading is indicated. When the yield condition is violated, the updated trial stresses, s_{ij}^* , are scaled back using a simple radial return algorithm:

$$s_{ij}^{n+1} = \left(\frac{a_0 + a_1 p + a_2 p^2}{\frac{1}{2} s_{ij}^* s_{ij}^*} \right)^{1/2} s_{ij}^*$$

If the hydrostatic tension exceeds the cutoff value, the pressure is set to the cutoff value and the deviatoric stress tensor is zeroed.



Volumetric strain versus pressure curve for soil and crushable foam model.

Material Model 14: Soil and Crushable Foam With Failure

This material model provides the same stress update as model 5. However, if pressure ever reaches its cutoff value, failure occurs and pressure can never again go negative. In material model 5, the pressure is limited to its cutoff value in tension.

A4.2 Example of LS-DYNA model

```

$# LS-DYNA Keyword file created by LS-PrePost 3.1 - 09Apr2011(10:30)
$# Created on Apr-27-2013 (15:49:30)
*KEYWORD
*TITLE
$# title
M3-SA3-Coarse mesh
*CONTROL_CONTACT
$# slsfac      rwpnal      islchk      shlthk      penopt      thkchg      orien      enmass
   0.100000    0.000          1          0          0          0          1          0
$# usrstr      usrfrc      nsbcs      interm      xpene      ssthk      ecdt      tiedprj
   0          0          0          0      4.000000    0          0          0
$# sfric      dfrcic      edc      vfc      th      th_sf      pen_sf
   0.000      0.000      0.000      0.000      0.000      0.000      0.000
$# ignore      frceng      skiprwg      outseg      spotstp      spotdel      spothin
   0          0          0          0          0          0          0.000
$# isym      nserod      rwgaps      rwgdt      rwksf      icov      swradf      ithoff
   0          0          0          0.000      1.000000    0          0.000      0
$# shldg
   0
*CONTROL_DAMPING
$# nrcyck      drtol      drfctr      drterm      tssfdr      irelal      edttl      idrflg
   250 0.001000 0.995000 35.000000 0.000          1 2.000000 -1
*CONTROL_DYNAMIC_RELAXATION
$# nrcyck      drtol      drfctr      drterm      tssfdr      irelal      edttl      idrflg
   250 0.001000 0.995000 0.000      0.000          0 0.040000 0
*CONTROL_ENERGY
$# hgen      rwen      slnten      rylen
   2          2          2          2
*CONTROL_HOURLASS
$# ihq      qh
   1 0.100000
*CONTROL_OUTPUT
$# npopt      neecho      nrefup      iaccop      opifs      ipnint      ikedit      iflush
   0          0          0          0          0.000          0          100          5000
$# iprtf      ierode      tet1      msgmax      ipcurv
   0          0          2          50          0
*CONTROL_RIGID
$# lmf      jntf      orthmd      partm      sparse      metalf
   0          1          0          0          0          0
*CONTROL_SOLID
$# esort      fmatrix      niptets      swloc1      psfail
   1          1          4          2          0
$# pm1      pm2      pm3      pm4      pm5      pm6      pm7      pm8      pm9      pm10
   0          0          0          0          0          0          0          0          0          0
*CONTROL_TERMINATION
$# endtim      endcyc      dtmin      endeng      endmas
 100.000000 0          0.000      0.000      0.000
*DATABASE_GLSTAT
$# dt      binary      lcur      ioopt
 0.200000 0          0          1
*DATABASE_MATSUM
$# dt      binary      lcur      ioopt
 0.200000 0          0          1
*DATABASE_RCFORC
$# dt      binary      lcur      ioopt
 0.200000 1          0          1
*DATABASE_SLEOUT
$# dt      binary      lcur      ioopt
 0.200000 0          0          1
*DATABASE_BINARY_D3PLOT
$# dt      lcdt      beam      npltc      psetid
 0.200000 0          0          0          0
$# ioopt

```

```

0
*DATABASE_BINARY_D3THDT
$#   dt      lcdt      beam      npltc      psetid
0.200000      0      0      0      1
*BOUNDARY_SPC_SET
$#   nsid      cid      dofx      dofy      dofz      dofrx      dofry      dofrz
48      0      1      1      1      1      1      1
*SET_NODE_LIST_TITLE
NODESET(SPC) 48
$#   sid      da1      da2      da3      da4      solver
48      0.000      0.000      0.000      0.000MECH
$#   nid1      nid2      nid3      nid4      nid5      nid6      nid7      nid8
807657      807658      807659      807660      807661      807662      807663      807664
807665      807666      807667      807668      807669      807670      807671      807672
807673      807674      807675      807676      807677      807678      807679      807680
807681      807682      807683      807684      807685      807686      807687      807688
807689      807690      807691      807692      807693      807694      807695      807696
807697      807698      807699      807700      807701      807702      807703      807704
807705      807706      807707      807708      807709      807710      807711      807712
807713      807714      807715      807716      807717      807718      807719      807720
808241      808242      808243      808244      808245      808246      808247      808248
808249      808250      808251      808252      808253      808254      808255      808256

808257      808258      808259      808260      808261      808262      808263      808264
808265      808266      808267      808268      808269      808270      808271      808272
808273      808274      808275      808276      808277      808278      808279      808280
808281      808282      808283      808284      808285      808286      808287      808288
808289      808290      808291      808292      808293      808294      808295      808296
808297      808298      808299      808300      808301      808302      808303      808304
808305      808306      808307      808308      808309      808310      808311      808312
808313      808314      808315      808316      808317      808318      808319      808320
808321      808322      808323      808324      808325      808326      808327      808328
808329      808330      808331      808332      808333      808334      808335      808336
808337      808338      808339      808340      808341      808342      808343      808344
808345      808346      808347      808348      808349      808350      808351      808352
808353      808354      808355      808356      808357      808358      808359      808360
808361      808362      808363      808364      808365      808366      808367      808368
808369      808370      808371      808372      808373      808374      808375      808376
*BOUNDARY_SPC_SET
$#   nsid      cid      dofx      dofy      dofz      dofrx      dofry      dofrz
49      0      0      1      0      0      0      0
*SET_NODE_LIST
$#   sid      da1      da2      da3      da4      solver
49      0.000      0.000      0.000      0.000MECH
$#   nid1      nid2      nid3      nid4      nid5      nid6      nid7      nid8
807657      807658      807659      807660      807661      807662      807663      807664
807665      807666      807667      807668      807669      807670      807671      807672
807673      807674      807675      807676      807677      807678      807679      807680
807681      807682      807683      807684      807685      807686      807687      807688
807689      807690      807691      807692      807693      807694      807695      807696
807697      807698      807699      807700      807701      808377      808378      808379
808380      808381      808382      808383      808384      808385      808386      808387
808388      808389      808390      808391      808392      808393      808394      808395
808396      808397      808398      808399      808400      808401      808402      808403
808404      808405      808406      808407      808408      808409      808410      808411
808412      808413      808414      808415      808416      808417      808418      808419
808420      808421      809097      809098      809099      809100      809101      809102
809103      809104      809105      809106      809107      809108      809109      809110
809111      809112      809113      809114      809115      809116      809117      809118
809119      809120      809121      809122      809123      809124      809125      809126
809127      809128      809129      809130      809131      809132      809133      809134
809135      809136      809137      809138      809139      809140      809141      809142
853022      853023      853024      853025      853026      853027      853028      853029
853030      853031      853032      853033      853034      853035      853036      853037
853038      853039      853040      853041      853042      853043      853044      853045
853046      853047      853048      853049      853050      853051      853052      853053

```

```

853054      853055      853056      853057      853058      853059      853060      853061
853737      853738      853739      853740      853741      853742      853743      853744
853745      853746      853747      853748      853749      853750      853751      853752
853753      853754      853755      853756      853757      853758      853759      853760
853761      853762      853763      853764      853765      853766      853767      853768
853769      853770      853771      853772      853773      853774      853775      853776
853777      853778      853779      853780      853781      854457      854458      854459
854460      854461      854462      854463      854464      854465      854466      854467
854468      854469      854470      854471      854472      854473      854474      854475
854476      854477      854478      854479      854480      854481      854482      854483
854484      854485      854486      854487      854488      854489      854490      854491
854492      854493      854494      854495      854496      854497      854498      854499
854500      854501      0          0          0          0          0          0
*BOUNDARY_SPC_SET
$#      nsid      cid      dofx      dofy      dofz      dofrx      dofry      dofrz
      50          0          0          1          0          0          0          0
*SET_NODE_LIST
$#      sid      da1      da2      da3      da4      solver
      50      0.000      0.000      0.000      0.000MECH
$#      nid1      nid2      nid3      nid4      nid5      nid6      nid7      nid8
808332      808333      808334      808335      808336      808337      808338      808339
808340      808341      808342      808343      808344      808345      808346      808347
808348      808349      808350      808351      808352      808353      808354      808355
808356      808357      808358      808359      808360      808361      808362      808363
808364      808365      808366      808367      808368      808369      808370      808371
808372      808373      808374      808375      808376      809052      809053      809054
809055      809056      809057      809058      809059      809060      809061      809062
809063      809064      809065      809066      809067      809068      809069      809070
809071      809072      809073      809074      809075      809076      809077      809078
809079      809080      809081      809082      809083      809084      809085      809086
809087      809088      809089      809090      809091      809092      809093      809094
809095      809096      809772      809773      809774      809775      809776      809777
809778      809779      809780      809781      809782      809783      809784      809785
809786      809787      809788      809789      809790      809791      809792      809793
809794      809795      809796      809797      809798      809799      809800      809801
809802      809803      809804      809805      809806      809807      809808      809809
809810      809811      809812      809813      809814      809815      809816      810492

854428      854429      854430      854431      854432      854433      854434      854435
854436      854437      854438      854439      854440      854441      854442      854443
854444      854445      854446      854447      854448      854449      854450      854451
854452      854453      854454      854455      854456      855132      855133      855134
855135      855136      855137      855138      855139      855140      855141      855142
855143      855144      855145      855146      855147      855148      855149      855150
855151      855152      855153      855154      855155      855156      855157      855158
855159      855160      855161      855162      855163      855164      855165      855166
855167      855168      855169      855170      855171      855172      855173      855174
855175      855176      0          0          0          0          0          0
*BOUNDARY_SPC_SET
$#      nsid      cid      dofx      dofy      dofz      dofrx      dofry      dofrz
      51          0          1          1          0          0          0          0
*SET_NODE_LIST_TITLE
NODESET(SPC) 51
$#      sid      da1      da2      da3      da4      solver
      51      0.000      0.000      0.000      0.000MECH
$#      nid1      nid2      nid3      nid4      nid5      nid6      nid7      nid8
807657      807702      807747      807792      807837      807882      807927      807972
808017      808062      808107      808152      808197      808242      808287      808332

853737      853782      853827      853872      853917      853962      854007      854052
854097      854142      854187      854232      854277      854322      854367      854412
854457      854502      854547      854592      854637      854682      854727      854772
854817      854862      854907      854952      854997      855042      855087      855132
*BOUNDARY_SPC_SET
$#      nsid      cid      dofx      dofy      dofz      dofrx      dofry      dofrz
      52          0          1          1          0          0          0          0

```

```

*SET_NODE_LIST_TITLE
NODESET(SPC) 52
$#      sid      da1      da2      da3      da4      solver
      52      0.000      0.000      0.000      0.000MECH
$#      nid1      nid2      nid3      nid4      nid5      nid6      nid7      nid8
      807701      807746      807791      807836      807881      807926      807971      808016
      808061      808106      808151      808196      808241      808286      808331      808376
      808421      808466      808511      808556      808601      808646      808691      808736
      808781      808826      808871      808916      808961      809006      809051      809096
      809141      809186      809231      809276      809321      809366      809411      809456
      809501      809546      809591      809636      809681      809726      809771      809816
      809861      809906      809951      809996      810041      810086      810131      810176
      810221      810266      810311      810356      810401      810446      810491      810536
      810581      810626      810671      810716      810761      810806      810851      810896
      810941      810986      811031      811076      811121      811166      811211      811256
      811301      811346      811391      811436      811481      811526      811571      811616
      811661      811706      811751      811796      811841      811886      811931      811976
      812021      812066      812111      812156      812201      812246      812291      812336

      848381      848426      848471      848516      848561      848606      848651      848696
      848741      848786      848831      848876      848921      848966      849011      849056
      849101      849146      849191      849236      849281      849326      849371      849416
      849461      849506      849551      849596      849641      849686      849731      849776
      849821      849866      849911      849956      850001      850046      850091      850136
      850181      850226      850271      850316      850361      850406      850451      850496
      850541      850586      850631      850676      850721      850766      850811      850856
      850901      850946      850991      851036      851081      851126      851171      851216
      851261      851306      851351      851396      851441      851486      851531      851576
      851621      851666      851711      851756      851801      851846      851891      851936
      851981      852026      852071      852116      852161      852206      852251      852296
      852341      852386      852431      852476      852521      852566      852611      852656
      852701      852746      852791      852836      852881      852926      852971      853016
      853061      853106      853151      853196      853241      853286      853331      853376
      853421      853466      853511      853556      853601      853646      853691      853736
      853781      853826      853871      853916      853961      854006      854051      854096
      854141      854186      854231      854276      854321      854366      854411      854456
      854501      854546      854591      854636      854681      854726      854771      854816
      854861      854906      854951      854996      855041      855086      855131      855176

*BOUNDARY_SPC_SET
$#      nsid      cid      dofz      dofry      dofz      dofry      dofz      dofry
      53      0      1      1      0      1      1      1
*SET_NODE_LIST_TITLE
NODESET(SPC) 53
$#      sid      da1      da2      da3      da4      solver
      53      0.000      0.000      0.000      0.000MECH
$#      nid1      nid2      nid3      nid4      nid5      nid6      nid7      nid8
      855177      855178      855179      855180      855181      855182      855183      855184
      855185      855186      855187      855188      855189      855190      855191      855192
      855193      855194      855195      855196      855197      855198      855199      855200
      855201      855202      855203      855204      855205      855206      855207      855208
      855209      855210      855211      855212      855213      855214      855215      855216
      855217      855218      855219      855220      855221      855222      855223      855224
      855225      855226      855227      855228      855229      855230      855231      855232
      855233      855234      855235      855236      855237      855238      855239      855240

*LOAD_GRAVITY_PART
$#      pid      dof      lc      accel      lcdr      stga      stgr
      7      3      0      0.009810      0      0      0

*CONTACT_AUTOMATIC_SINGLE_SURFACE_ID
$#      cid      title
      1CONTACT DEFINITION
$#      ssid      msid      sstyp      mstyp      sboxid      mboxid      spr      mpr
      1      0      2      0      0      0      0      0
$#      fs      fd      dc      vc      vdc      penchk      bt      dt
      0.000      0.000      0.000      0.000      0.000      0      0.0001.0000E+20
$#      sfs      sfm      sst      mst      sfst      sfmt      fsf      vsf
      1.000000      1.000000      0.000      0.000      1.000000      1.000000      1.000000      1.000000
*SET_PART_LIST_TITLE

```

```

SET CONTACT
$#   sid      da1      da2      da3      da4      solver
    1      0.000    0.000    0.000    0.000MECH
$#   pid1     pid2     pid3     pid4     pid5     pid6     pid7     pid8
    7       8       0       0       0       0       0       0
*PART
$# title
SAND
$#   pid      secid     mid      eosid     hgid      grav      adpopt     tmid
    7       7       4       0       1       1       0       0
*SECTION_SOLID_TITLE
SOIL_SAND
$#   secid     elform      aet
    7       1       0
*MAT_SOIL_AND_FOAM_FAILURE_TITLE
SOIL_FOAM_FAILURE_SA3
$#   mid      ro      g      bulk      a0      a1      a2      pc
    4 1.5100E-6 0.040000 0.085000 0.000 0.000 0.650000 0.000
$#   vcr      ref
    0.000    0.000
$#   eps1     eps2     eps3     eps4     eps5     eps6     eps7     eps8
    0.000 0.001023 0.001665 0.001876 0.002088 0.002466 0.002661 0.002856
$#   eps9     eps10
    0.003918 0.004979
$#   p1      p2      p3      p4      p5      p6      p7      p8
    0.000 2.4500E-5 4.3400E-5 5.1100E-5 5.8900E-5 7.5200E-5 8.3200E-5 9.1200E-5
$#   p9      p10
    1.4800E-4 2.0600E-4
*HOURLASS_TITLE
HRGLASS
$#   hgid      ihq      qm      ibq      q1      q2      qb/vdc      qw
    1       1 0.100000 0 1.500000 0.060000 0.100000 0.100000
*PART
$# title
Tamper
$#   pid      secid     mid      eosid     hgid      grav      adpopt     tmid
    8       6       3       0       1       0       0       0
*SECTION_SOLID_TITLE
TAMPER
$#   secid     elform      aet
    6       1       0
*MAT_RIGID_TITLE
STEEL_RIGID
$#   mid      ro      e      pr      n      couple      m      alias
    3 3.7500E-5 207.00000 0.300000 0.000 0.000 0.000
$#   cmo      con1      con2
    0.000    0       0
$#   lco or a1  a2      a3      v1      v2      v3
    0.000 0.000 0.000 0.000 0.000 0.000
*INITIAL_VELOCITY_NODE
$#   nid      vx      vy      vz      vxr      vyr      vzr      icid
    855177 0.000 0.000 -1.500000 0.000 0.000 0.000 0
    855178 0.000 0.000 -1.500000 0.000 0.000 0.000 0
    855179 0.000 0.000 -1.500000 0.000 0.000 0.000 0
    855180 0.000 0.000 -1.500000 0.000 0.000 0.000 0
    855181 0.000 0.000 -1.500000 0.000 0.000 0.000 0
    855182 0.000 0.000 -1.500000 0.000 0.000 0.000 0
    855183 0.000 0.000 -1.500000 0.000 0.000 0.000 0
    855184 0.000 0.000 -1.500000 0.000 0.000 0.000 0
    855185 0.000 0.000 -1.500000 0.000 0.000 0.000 0
    855186 0.000 0.000 -1.500000 0.000 0.000 0.000 0
    855187 0.000 0.000 -1.500000 0.000 0.000 0.000 0
    855188 0.000 0.000 -1.500000 0.000 0.000 0.000 0
    855189 0.000 0.000 -1.500000 0.000 0.000 0.000 0
    855190 0.000 0.000 -1.500000 0.000 0.000 0.000 0
    855191 0.000 0.000 -1.500000 0.000 0.000 0.000 0
    855192 0.000 0.000 -1.500000 0.000 0.000 0.000 0

```

855193	0.000	0.000	-1.500000	0.000	0.000	0.000	0.000	0		
855194	0.000	0.000	-1.500000	0.000	0.000	0.000	0.000	0		
855195	0.000	0.000	-1.500000	0.000	0.000	0.000	0.000	0		
855196	0.000	0.000	-1.500000	0.000	0.000	0.000	0.000	0		
855197	0.000	0.000	-1.500000	0.000	0.000	0.000	0.000	0		
855198	0.000	0.000	-1.500000	0.000	0.000	0.000	0.000	0		
855199	0.000	0.000	-1.500000	0.000	0.000	0.000	0.000	0		
855200	0.000	0.000	-1.500000	0.000	0.000	0.000	0.000	0		
855201	0.000	0.000	-1.500000	0.000	0.000	0.000	0.000	0		
855202	0.000	0.000	-1.500000	0.000	0.000	0.000	0.000	0		
855235	0.000	0.000	-1.500000	0.000	0.000	0.000	0.000	0		
855236	0.000	0.000	-1.500000	0.000	0.000	0.000	0.000	0		
855237	0.000	0.000	-1.500000	0.000	0.000	0.000	0.000	0		
855238	0.000	0.000	-1.500000	0.000	0.000	0.000	0.000	0		
855239	0.000	0.000	-1.500000	0.000	0.000	0.000	0.000	0		
855240	0.000	0.000	-1.500000	0.000	0.000	0.000	0.000	0		
*DAMPING_PART_MASS										
\$#	pid	lcid	sf	flag						
	7	0	0.100000	0						
*DAMPING_PART_MASS										
\$#	pid	lcid	sf	flag						
	8	0	0.100000	0						
*DAMPING_PART_STIFFNESS										
\$#	pid	coef								
	7	0.010000								
*DAMPING_PART_STIFFNESS										
\$#	pid	coef								
	8	0.010000								
*ELEMENT_SOLID										
\$#	eid	pid	n1	n2	n3	n4	n5	n6	n7	n8
	154516	7	807657	807658	807703	807702	808377	808378	808423	808422
	154517	7	807658	807659	807704	807703	808378	808379	808424	808423
	154518	7	807659	807660	807705	807704	808379	808380	808425	808424
	154519	7	807660	807661	807706	807705	808380	808381	808426	808425
	154520	7	807661	807662	807707	807706	808381	808382	808427	808426
	154521	7	807662	807663	807708	807707	808382	808383	808428	808427
	154522	7	807663	807664	807709	807708	808383	808384	808429	808428
	154523	7	807664	807665	807710	807709	808384	808385	808430	808429
	154524	7	807665	807666	807711	807710	808385	808386	808431	808430
	154525	7	807666	807667	807712	807711	808386	808387	808432	808431
	154526	7	807667	807668	807713	807712	808387	808388	808433	808432
	185043	7	840947	840948	840993	840992	841667	841668	841713	841712
	185044	7	840948	840949	840994	840993	841668	841669	841714	841713
	185045	7	840949	840950	840995	840994	841669	841670	841715	841714
	185046	7	840950	840951	840996	840995	841670	841671	841716	841715
	185047	7	840951	840952	840997	840996	841671	841672	841717	841716
	185048	7	840952	840953	840998	840997	841672	841673	841718	841717
	185049	7	840953	840954	840999	840998	841673	841674	841719	841718
	185050	7	840954	840955	841000	840999	841674	841675	841720	841719
	185051	7	840955	840956	841001	841000	841675	841676	841721	841720
	185052	7	840957	840958	841003	841002	841677	841678	841723	841722
	185053	7	840958	840959	841004	841003	841678	841679	841724	841723
	185054	7	840959	840960	841005	841004	841679	841680	841725	841724
	185055	7	840960	840961	841006	841005	841680	841681	841726	841725
	185056	7	840961	840962	841007	841006	841681	841682	841727	841726
	185057	7	840962	840963	841008	841007	841682	841683	841728	841727
	185058	7	840963	840964	841009	841008	841683	841684	841729	841728
197420	8	855185	855186	855188	855187	855217	855218	855220	855219	
197421	8	855187	855188	855190	855189	855219	855220	855222	855221	
197422	8	855189	855190	855192	855191	855221	855222	855224	855223	
197423	8	855191	855192	855194	855193	855223	855224	855226	855225	
197424	8	855193	855194	855196	855195	855225	855226	855228	855227	
197425	8	855195	855196	855198	855197	855227	855228	855230	855229	
197426	8	855197	855198	855200	855199	855229	855230	855232	855231	
197427	8	855199	855200	855202	855201	855231	855232	855234	855233	

197428	8	855201	855202	855204	855203	855233	855234	855236	855235
197429	8	855203	855204	855206	855205	855235	855236	855238	855237
197430	8	855205	855206	855208	855207	855237	855238	855240	855239
*NODE									
\$#	nid	x	y	z	tc	rc			
807657	-9.7747119e-037	-9.7747119e-037	-9.7747119e-037	-9.7747119e-037	0	0			
807658	8.0000000	-9.7747119e-037	-9.7747119e-037	-9.7747119e-037	0	0			
807659	16.0000000	-9.7747119e-037	-9.7747119e-037	-9.7747119e-037	0	0			
807660	24.0000000	-9.7747119e-037	-9.7747119e-037	-9.7747119e-037	0	0			
807661	32.0000000	-9.7747119e-037	-9.7747119e-037	-9.7747119e-037	0	0			
807662	40.0000000	-9.7747119e-037	-9.7747119e-037	-9.7747119e-037	0	0			
807663	48.0000000	-9.7747119e-037	-9.7747119e-037	-9.7747119e-037	0	0			
807664	56.0000000	-9.7747119e-037	-9.7747119e-037	-9.7747119e-037	0	0			
807665	64.0000000	-9.7747119e-037	-9.7747119e-037	-9.7747119e-037	0	0			
807666	72.0000000	-9.7747119e-037	-9.7747119e-037	-9.7747119e-037	0	0			
807667	80.0000000	-9.7747119e-037	-9.7747119e-037	-9.7747119e-037	0	0			
807668	88.0000000	-9.7747119e-037	-9.7747119e-037	-9.7747119e-037	0	0			
807682	200.0000000	-9.7747119e-037	-9.7747119e-037	-9.7747119e-037	0	0			
807683	208.0000000	-9.7747119e-037	-9.7747119e-037	-9.7747119e-037	0	0			
807685	224.0000000	-9.7747119e-037	-9.7747119e-037	-9.7747119e-037	0	0			
807686	232.0000000	-9.7747119e-037	-9.7747119e-037	-9.7747119e-037	0	0			
807687	240.0000000	-9.7747119e-037	-9.7747119e-037	-9.7747119e-037	0	0			
807688	248.0000000	-9.7747119e-037	-9.7747119e-037	-9.7747119e-037	0	0			
807689	256.0000000	-9.7747119e-037	-9.7747119e-037	-9.7747119e-037	0	0			
855198	194.0000000	100.0000000	650.0000000	650.0000000	0	0			
855199	158.0000000	110.0000000	650.0000000	650.0000000	0	0			
855200	194.0000000	110.0000000	650.0000000	650.0000000	0	0			
855201	158.0000000	120.0000000	650.0000000	650.0000000	0	0			
855202	194.0000000	120.0000000	650.0000000	650.0000000	0	0			
855203	158.0000000	130.0000000	650.0000000	650.0000000	0	0			
855204	194.0000000	130.0000000	650.0000000	650.0000000	0	0			
855205	158.0000000	140.0000000	650.0000000	650.0000000	0	0			
855206	194.0000000	140.0000000	650.0000000	650.0000000	0	0			
855207	158.0000000	150.0000000	650.0000000	650.0000000	0	0			
855208	194.0000000	150.0000000	650.0000000	650.0000000	0	0			
855209	158.0000000	-9.7747119e-037	680.0000000	680.0000000	0	0			
855210	194.0000000	-9.7747119e-037	680.0000000	680.0000000	0	0			
855211	158.0000000	10.0000000	680.0000000	680.0000000	0	0			
855212	194.0000000	10.0000000	680.0000000	680.0000000	0	0			
855213	158.0000000	20.0000000	680.0000000	680.0000000	0	0			
855214	194.0000000	20.0000000	680.0000000	680.0000000	0	0			
855215	158.0000000	30.0000000	680.0000000	680.0000000	0	0			
855216	194.0000000	30.0000000	680.0000000	680.0000000	0	0			
855217	158.0000000	40.0000000	680.0000000	680.0000000	0	0			
855222	194.0000000	60.0000000	680.0000000	680.0000000	0	0			
855223	158.0000000	70.0000000	680.0000000	680.0000000	0	0			
855224	194.0000000	70.0000000	680.0000000	680.0000000	0	0			
855225	158.0000000	80.0000000	680.0000000	680.0000000	0	0			
855226	194.0000000	80.0000000	680.0000000	680.0000000	0	0			
855227	158.0000000	90.0000000	680.0000000	680.0000000	0	0			
855228	194.0000000	90.0000000	680.0000000	680.0000000	0	0			
855229	158.0000000	100.0000000	680.0000000	680.0000000	0	0			
855230	194.0000000	100.0000000	680.0000000	680.0000000	0	0			
855231	158.0000000	110.0000000	680.0000000	680.0000000	0	0			
855232	194.0000000	110.0000000	680.0000000	680.0000000	0	0			
855233	158.0000000	120.0000000	680.0000000	680.0000000	0	0			
855234	194.0000000	120.0000000	680.0000000	680.0000000	0	0			
855235	158.0000000	130.0000000	680.0000000	680.0000000	0	0			
855236	194.0000000	130.0000000	680.0000000	680.0000000	0	0			
855237	158.0000000	140.0000000	680.0000000	680.0000000	0	0			
855238	194.0000000	140.0000000	680.0000000	680.0000000	0	0			
855239	158.0000000	150.0000000	680.0000000	680.0000000	0	0			
855240	194.0000000	150.0000000	680.0000000	680.0000000	0	0			
*END									

Appendix V

Table of Contents

A5.1	Triaxial testing results	A-36
------	--------------------------	------

A5.1 Triaxial Testing Results

A series of cyclic CID triaxial and bender element tests on specimens made of dry sand and sand:silt mixtures having different dry densities were used to determine the shear strength parameters of the soils and the shear modulus under different soil densities and loading conditions. Table A5.1 presents the details of triaxial tests adopted in this work.

Table A5.1. Details of triaxial tests.

Test ID	Soil Type	Specimen density, kN/m^3	Specimen initial void ratio "e"	Cycles of Confining stress " σ_c " during consolidation, kPa	Maximum mean effective stress, p' , kPa	Maximum deviator Stress, q , kPa
TX-S1	Sand	15.95	0.62	0-100 100-10 10-1000 1000-100	266	494
TX-S2	Sand	16.01	0.62	0-1000	2119	3358
TX-S3	Sand	16.28	0.59	0-500 500-800	210	301
TX-SS1	Sand:silt mixture	14.85	0.74	0-200	377	517
TX-SS2	Sand:silt mixture	15.17	0.70	0-100 100-10 10-100 100-1000 1000-100	264	490
TX-SS3	Sand:silt mixture	16.80	0.52	0-100 100-10 10-1000 1000-100	277	531

The relationships between G_{max} values and effective mean stresses are shown in Figures A5.1 and A5.2 for sands and sand:silt mixtures, respectively. Stress ratio (q/p') versus axial strain from selected tests on sand and sand:silt specimens are shown in Figures A5.3 and A5.4 respectively. Stress paths during triaxial tests on sand and sand:silt specimens are shown in Figures A5.5 and A5.6, respectively.

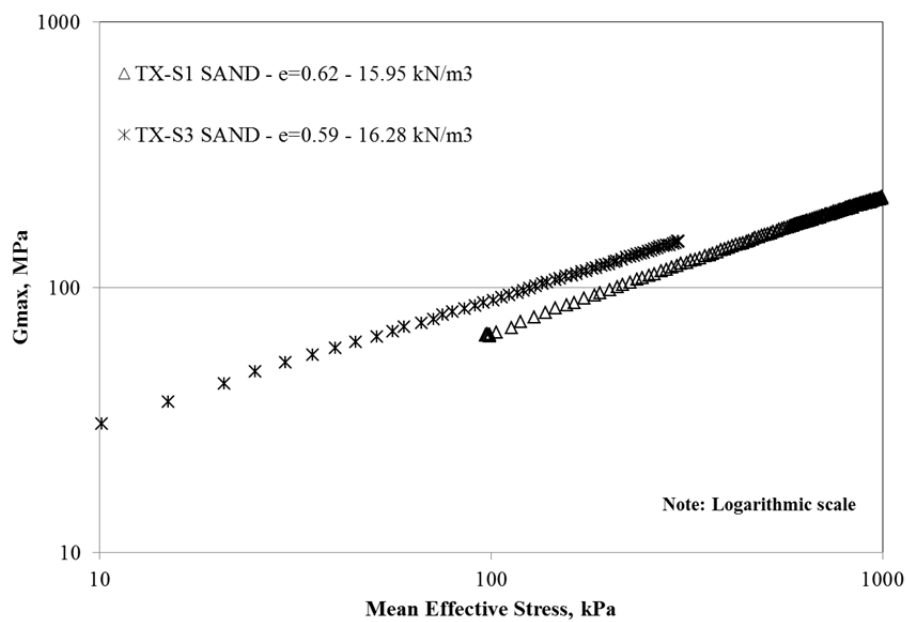


Figure A5.1. Correlation between G_{max} and mean effective stress (p') in sand

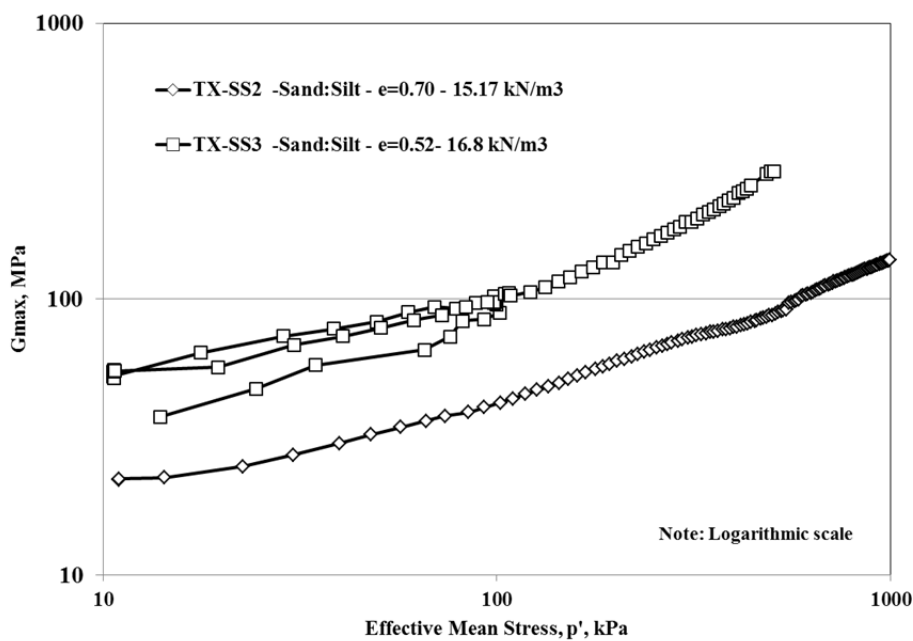


Figure A5.2. Correlation between G_{max} and mean effective stress (p') in sand:silt mixture

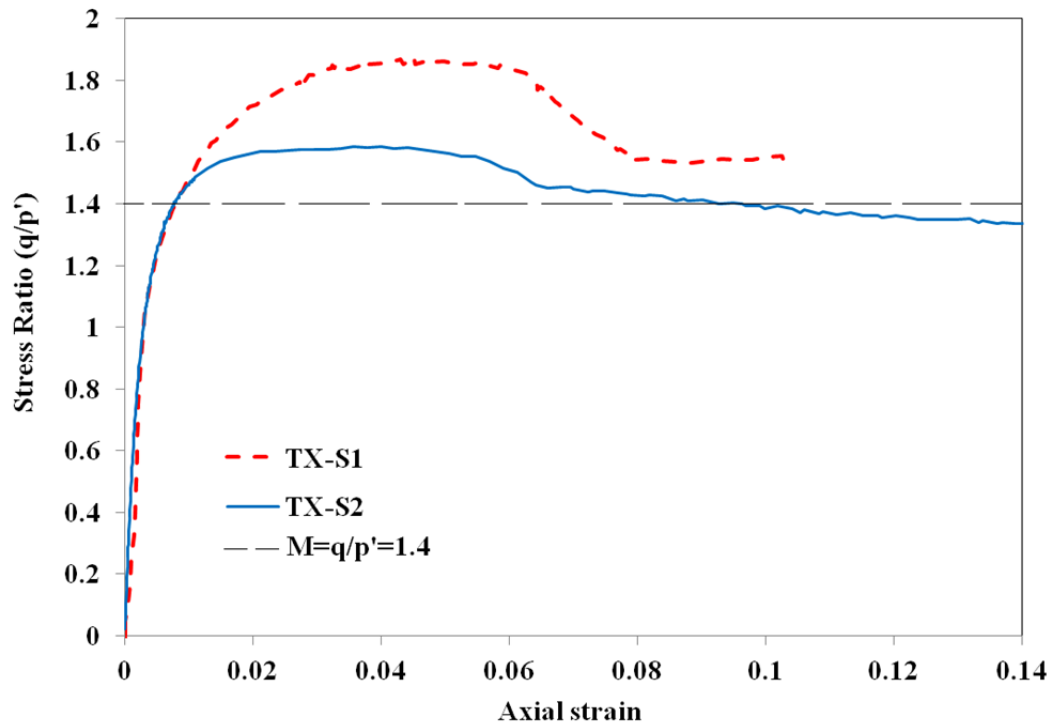


Figure A5.3. Stress ratio vs. axial strain from triaxial tests (sand).

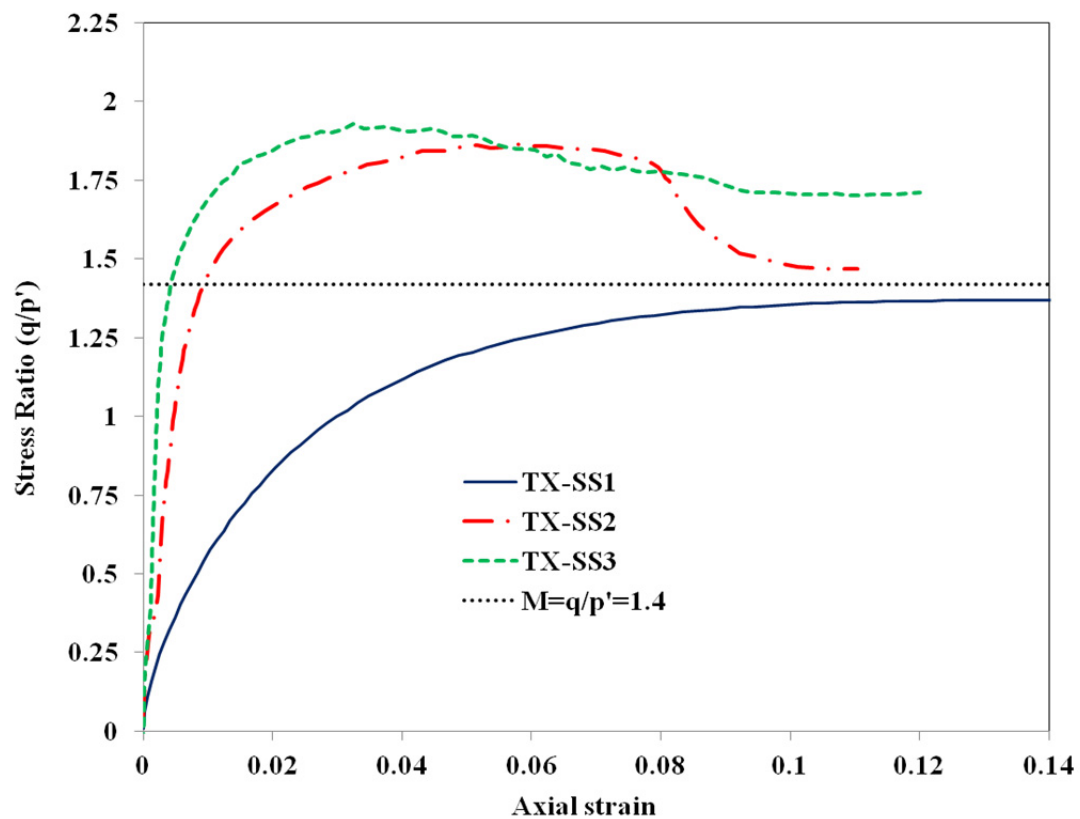


Figure A5.4. Stress ratio vs. axial strain from triaxial test (sand:silt).

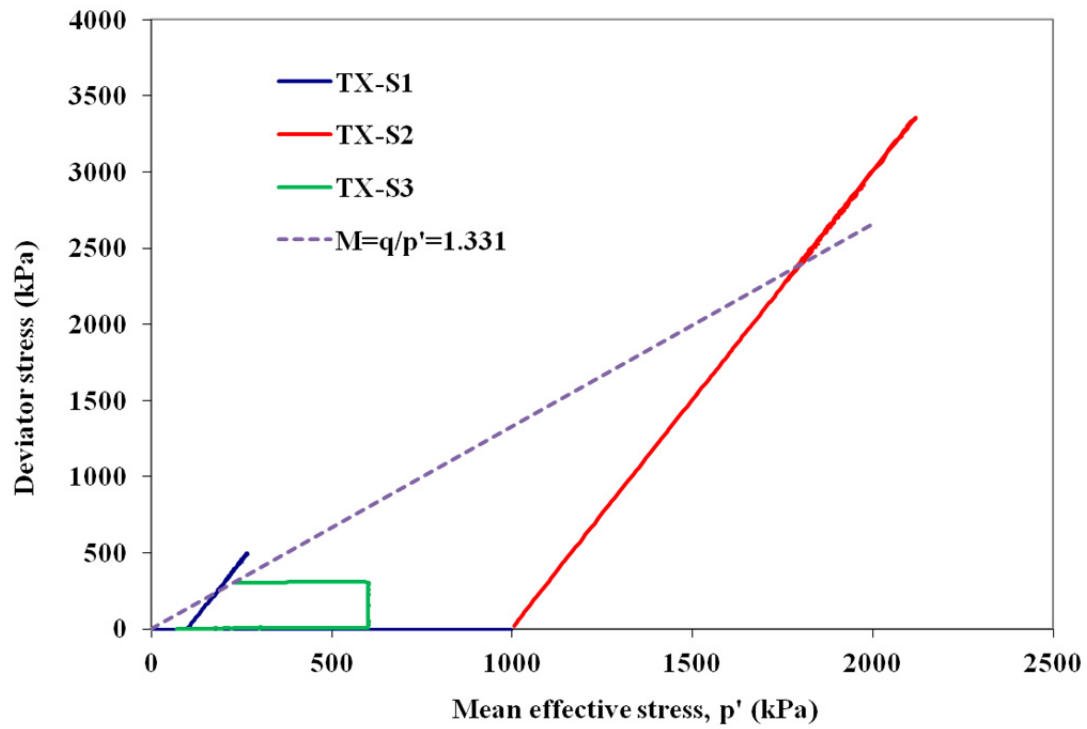


Figure A5.5. Stress paths of triaxial tests (sand).

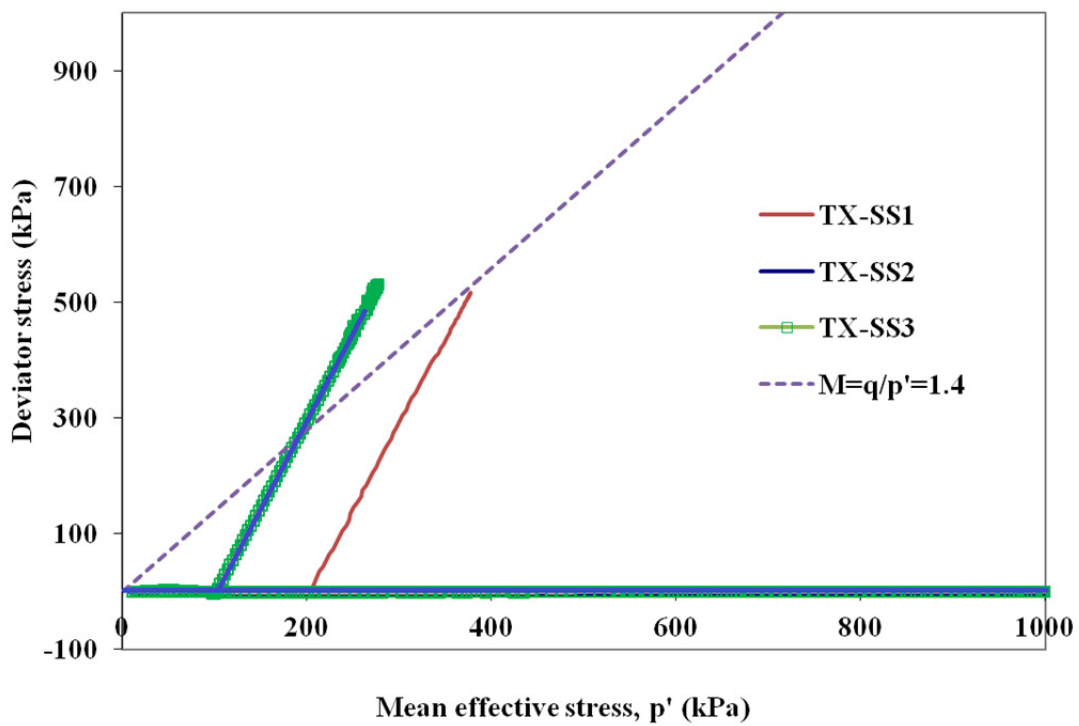


Figure A5.6. Stress paths of triaxial tests (sand:silt).